ANL/ET/PROC-112803

Metal Dusting

Proceedings of the International Workshop
September 26-28, 2001

Edited by
K. Natesan
Argonne National Laboratory

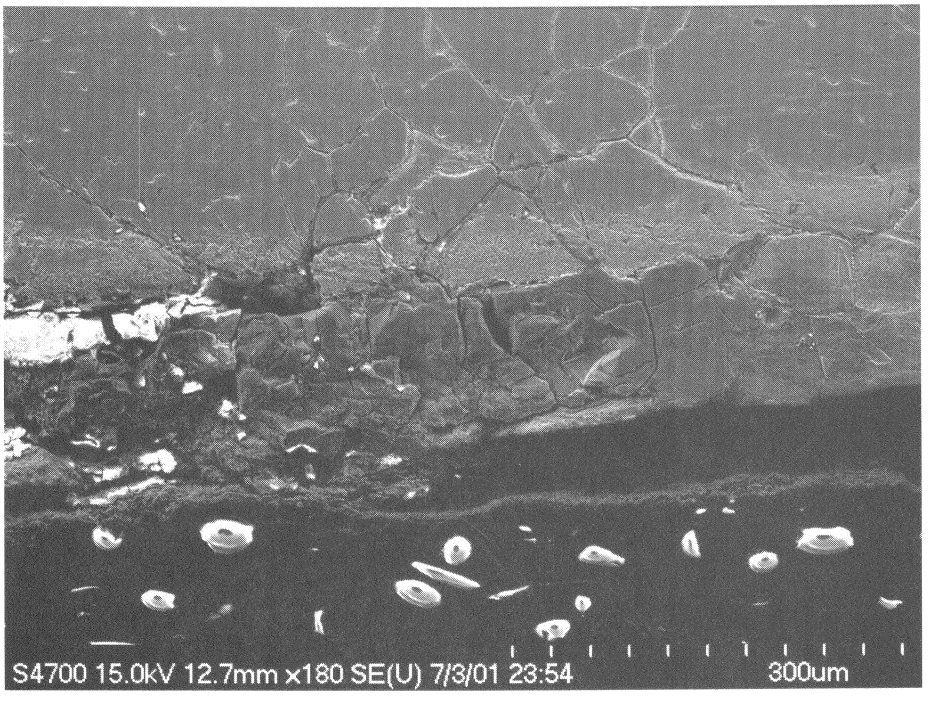

Published by
Argonne National Laboratory
Argonne, IL 60439

Argonne National Laboratory, a U.S. Department of Energy Office of Science laboratory, is operated by The University of Chicago under contract W-31-109-Eng-38.

DISCLAIMER

This report was prepared as an account of work sponsored by an agency of the United States Government. Neither the United States Government nor any agency thereof, nor The University of Chicago, nor any of their employees or officers, makes any warranty, express or implied, or assumes any legal liability or responsibility for the accuracy, completeness, or usefulness of any information, apparatus, product, or process disclosed, or represents that its use would not infringe privately owned rights. Reference herein to any specific commercial product, process, or service by trade name, trademark, manufacturer, or otherwise, does not necessarily constitute or imply its endorsement, recommendation, or favoring by the United States Government or any agency thereof. The views and opinions of document authors expressed herein do not necessarily state or reflect those of the United States Government or any agency thereof.

Available electronically at http://www.osti.gov/bridge/

Available for a processing fee to U.S. Department of Energy and its contractors, in paper, from:

U.S. Department of Energy
Office of Scientific and Technical Information
P.O. Box 62
Oak Ridge, TN 37831-0062
phone: (865) 576-8401
fax: (865) 576-5728
email: reports@adonis.osti.gov

Metal Dusting

Proceedings of the International Workshop
September 26-28, 2001
Sponsored by
ANL, DOE-OIT, and MTI

Edited by

K. Natesan
Argonne National Laboratory

Published by
Argonne National Laboratory
Argonne, IL 60439

This proceedings is dedicated to the brave men and women who lost their lives in the fatal disasters at New York, Washington DC, and Pennsylvania On September 11, 2001

Forward

This Workshop was held soon after the September 11 incident under a climate of sorrow and uncertainty among the people of the world, in particular the Workshop participants and their host organizations. With considerable help from the participants, the Workshop was conducted as planned and we had excellent participation (more than anticipated) in spite of the circumstances. A good fraction of the attendees in the Workshop were from abroad and from several industries, indicating the importance and relevance of the subject for the chemical process industry. Degradation of structural metallic alloys by metal dusting has been an issue for over 40 years in the chemical, petrochemical, syngas, and iron ore reduction plants. However, the fundamental scientific reasons for the degradation of complex alloys in high carbon activity environments are not clear. One of the major parameter of importance is the variation in gas chemistry in both the laboratory experiments and in the plant-service environments. The industry has questioned the applicability of the laboratory test data, obtained in low steam environments, in assessment and life prediction for the materials in plant service where the environments contain 25-35% steam. Several other variables such as system pressure, gas flow velocity, incubation time, alloy chemistry, surface finish, and weldments, were also identified in the literature as to having an effect on the initiation and propagation of metal dusting attack. It is the purpose of this Workshop to establish a forum in which the researchers from scientific and industrial laboratories, alloy manufacturers, end users, and research and development sponsors can exchange information, discuss different points of view, prioritize the issues, and to elaborate on the trends in industry for the future. I believe that we have accomplished these goals successfully and sincerely thank the participants for their contributions.

K. Natesan
Workshop Chairman
Argonne National Laboratory

List of Participants

Dinesh C. Agarwal, Krupp VDM Technologies, Houston, TX, USA

David W. Alley, UOP, Des Plaines, IL, USA

Brian A. Baker, Special Metals Corporation, Huntington, WV, USA

Kenneth L. Baumert, Air Products and Chemicals, Allentown, PA, USA

Steven A. Bradley, UOP, Des Plaines, IL, USA

Annette M. Brenner, General Motors, Honeoye Falls, NY, USA,

Timothy J. Carney, Rolled Alloys, Inc. Temperance, MI, USA

Nitin P. Chitgopekar, UOP, Des Plaines, IL, USA

Peter S. Christensen, Haldor Tops□e A/S, Lyngby, Denmark

Charlie Chun, ExxonMobil Research & Engg., Annandale, NJ, USA

LeRoy R. Clavenna, ExxonMobil Research & Engg, Baton Rouge, LA, USA

Gary E. Coates, Nickel Development Institute, Toronto, Canada

Howard L. Craig, Jr., Materials Technology Institute, Richmond, VA, USA

Hendrik J. de Bruyn, Statoil ASA, Trondheim, Norway

Malcolm Dixon, Kvaerner Process, Houston, TX, USA

Harvey Drucker, Argonne National Laboratory, Argonne, IL, USA

Peter W. Farnell, Synetix, Billingham, England

Emory A. Ford, Materials Technology Institute, Florence, MA, USA

Gerald E. Gapinski, MetalTek International, Waukesha, WI, USA

Hans J. Grabke, Max-Planck Institut für Eisenforschung GmbH, Düsseldorf, Germany

Richard T. Jones, Materials Technology Institute, Murrysville, PA, USA

Shoji Kinomura, Sumitomo Metal USA Corporation, Chicago, IL, USA

Tomoaki Kiso, JGC Corporation, Ibaraki Prefecture, Japan

Dwaine L. Klarstrom, Haynes International, Inc., Kokomo, IN, USA

Allen K. Lee, University of Illinois at Chicago, Chicago, IL, USA

Jan Links, Dow Benelux n.v.. Terneuzen, The Netherlands

Victor A. Maroni, Argonne National Laboratory, Argonne, IL, USA

Michael J. McNallan, University of Illinois at Chicago, Chicago, IL, USA

Ramkumar Natarajan, University of Illinois at Chicago, Chicago, IL, USA

Ken Natesan, Argonne National Laboratory, Argonne, IL, USA

Maria Jose L. Oestergaard, Haldor Tops□e A/S, Lyngby, Denmark

YoungSoo Park, Haynes International, Inc., Kokomo, IN, USA

Karen A. Payne, Diffusion Alloys, Ltd., Hatfield, Hertfordshire, England

Roger B. Poeppel, Argonne National Laboratory, Argonne, IL, USA

Ankur Purohit, Argonne National Laboratory, Argonne, IL, USA

Covadonga Rosado, DECHEMA e.V., Frankfurt am Main, Germany

Jenny E. Rosendahl, AvestaPolarit, Inc., Schaumburg, IL, USA

Michael Schütze, DECHEMA e.V., Frankfurt am Main, Germany

Charles A. Sorrell, Office of Industrial Technologies, U.S. DOE, Washington, DC, USA

Peter K. M. Szakalos, Swedish Institute for Metals Research, Stockholm, Sweden

Charles Thomas, Industrial Research Ltd., Lower Hutt, New Zealand

Peter F. Tortorelli, Oak Ridge National Laboratory, Oak Ridge, TN, USA

J. C. van Wortel, TNO Institute of Industrial Technology, Apeldoorn, The Netherlands

Randall E. Winans, Argonne National Laboratory, Argonne, IL, USA

Zuotao Zeng, Argonne National Laboratory, Argonne, IL, USA

Ranyi Zhu, University of Illinois at Chicago, Chicago, IL, USA

Table of Contents

Office of Industrial Technologies and Chemical Vision 1
C. Sorrell and D. M. Soboroff, Office of Industrial Technologies,
U. S. Department of Energy, Washington, D. C.

Thermodynamics, Mechanisms, and Kinetics of Metal Dusting 5
H. J. Grabke, Max-Planck-Institut für Eisenforschung GmbH, Düsseldorf, Germany

Theoretical Studies on Metal Dusting: Boudourd and Steam-Carbon Reactions and Iron Carbonyl Formation 15
K. L. Baumert and H. Cheng, Air Products and Chemicals, Allentown, PA

Metal Dusting Research at Argonne National Laboratory 19
K. Natesan, Z. Zeng, V. A. Maroni, W. K. Soppet, and D. L. Rink,
Argonne National Laboratory, Argonne, IL

Applications of Molecular Spectroscopy Methods to the Study of Metal Dusting Corrosion 41
V. A. Maroni, Argonne National Laboratory, Argonne, IL 60439

Metal Dusting of Steel Alloys: Raman, FT-IR, and XPS Results 55
G. L. Johnson, K. L. Baumert, T. Mebrahtu, and G. Xiaoping,
Air Products and Chemicals, Allentown, PA

Mechanisms of Metal Dusting Corrosion of Pure Metals 77
C. M. Chun, T. A. Ramanarayanan, ExxonMobil Res. & Engg. Annandale, NJ
L. Clavenna, ExxonMobil Process Research, Baton Rouge, LA

Study of Metal Dusting Mechanism in Iron Using Raman Spectroscopy and X-ray Diffraction 93
Z. Zeng, K. Natesan, and V. A. Maroni,
Argonne National Laboratory, Argonne, IL

A New Corrosion Mechanism for Metal Dusting on 304L Stainless Steel 109
P. Szakalos, R. Pettersson, and S. Hertzman,
Swedish Institute for Metals Research, Stockholm, Sweden

Application of ESEM for In-Situ Study of High Temperature Corrosion Processes 123
H. J. de Bruyn, N. Aas, Statoil ASA, Trondheim, Norway and
B. Schmid, Hydro Aluminium, Holmestrand, Norway

Metal Dusting and Pressure - Is There a Relationship? 139
T. P. Levi, C. W. Thomas, N. Briggs, and I. E. Minchington,
Industrial Research Ltd., Lower Hutt, New Zealand

Role of Alloying Elements in Fe-base and in Ni-base Alloys on Metal Dusting 147
H. J. Grabke, E. M. Müller-Lorenz, S. Strauss,
Max-Planck-Institut für Eisenforschung GmbH, Düsseldorf, Germany

Metal Dusting Failures on Fe-Cr-Ni Alloys in Petrochemical Plants 155
T. Kiso, H. Mochizuki, and K. Hosoya,
JGC Corporation, Ibaraki, Japan

Metal Dusting in a Laboratory Environment - Alloying Addition Effects 163
B. A. Baker and G. D. Smith,
Special Metals Corporation, Huntington, WV

The Metal Dusting Behavior of Several High Temperature Alloys 177
D. L. Klarstrom, Haynes International, Inc., Kokomo, IN and
H. J. Grabke, Max-Planck-Institut für Eisenforschung GmbH, Düsseldorf, Germany

Effects of Chlorine Contamination on the Kinetics of Oxidation/Carburization of
Chromium Containing Austenitic Alloys 183
M. McNallan, S. Thongtem, Y. S. Park and J. Tomei
University of Illinois at Chicago, Chicago, IL

Analysis of Metal Dusting in a Waste Heat Boiler 191
K. Natesan, A. Purohit, and D. L. Rink, Argonne National Laboratory,
Argonne, IL, USA and W. J. Salot, Honeywell International, Hopewell, VA

Development of Coating Systems Against Metal Dusting Attack 213
C. Rosado, F. Dettenwanger, and M. Schütze,
Karl-Winnacker-Institut der DECHEMA e.v.,
Frankfurt am Main, Germany

Metal Dusting and Coking – Ways and Means of Protection 225
H. J. Grabke, E. M. Müller-Lorenz, A. Schneider,
Max-Planck-Institut für Eisenforschung GmbH, Düsseldorf, Germany

Metal Dusting Behavior of Coatings 233
K. Natesan, Z. Zeng, W. K. Soppet, and D. L. Rink,
Argonne National Laboratory, Argonne, IL, USA

Controlling/Mitigating Metal Dusting Problems with a New Nickel Base
Ni-Cr-Al-Y High Carbon Alloy 602CA 245
D. C. Agarwal, Krupp VDM Technologies, Houston, TX and
U. Brill, Krupp VDM GmbH, Altena, Germany

Development of Metal Dusting Resistant Materials for Use in GTL Production 257
B. J. Crewdson and P. W. Farnell,
Synetix, Cleveland, United Kingdom

Panel Discussion 265

Panelists: K.Baumert, Air Products and Chemicals, Allentown, PA, USA
H. J. de Bruyn, Statoil ASA, Trondheim, Norway
P. W. Farnell, Synetix, Billingham, United Kingdom
H. J. Grabke, Max-Planck-Institut, Düsseldorf, Germany
C. W. Thomas, Industrial Research Ltd., New Zealand
H. Van Wortel, TNO Inst. of Ind. Tech., The Netherlands

Moderator: K. Natesan, Argonne National Laboratory, Argonne, IL

Workshop Summary
K. Natesan, Argonne National Laboratory, Argonne, IL

THE OFFICE OF INDUSTRIAL TECHNOLOGIES AND THE CHEMICAL INDUSTRY VISION

C. A. SORRELL* AND D. M. SOBOROFF
Office of Industrial Technologies, U. S. Department of Energy, Washington, DC

ABSTRACT

The Office of Industrial Technologies, Energy Efficiency and Renewable Energy, embarked on a new strategy in 1994, called the Industries of the Future (IOF). The major energy consuming industries are encouraged to, and assisted with, completion of Vision documents that outline the major technology developments foreseen as essential to the future health of the industry and then to prepare Technology Roadmaps to identify short, intermediate, and long term needs to achieve the goals of the Visions. The Chemical Industry has completed nine Technology Roadmaps, one of which identifies the need for materials of construction for chemical processing. The metal dusting project at Argonne National Laboratory is a direct result of that Roadmap and a solicitation for projects that will improve energy efficiency and productivity in the chemical industry. The IOF strategy and some of the projects for materials of construction in the industry are described.

INTRODUCTION

The Industries of the Future

The Office of Industrial Technologies (OIT) is one of four offices in Energy Efficiency and Renewable Energy, the others being Automotive, Building, and Power Technologies. The mission of OIT is to identify and fund research and development in the industrial sector of the U.S. economy. In order to accomplish the mission of improving energy efficiency and reducing waste in industry, OIT embarked on a new strategy in 1994. Rather than leaving it to program managers in OIT to select R&D projects based on their expertise and knowledge, the major processing industries were encouraged, through industry organizations, to do an in-depth analysis of the current status of each industry; identifying technical, economic, environmental, and policy drivers for changes; and major technology areas needing attention to ensure future health and competitiveness. This analysis was undertaken in order to prepare industry Visions of the Future. Following the Visions of the Future exercise, each industry was encouraged to look in more detail at technology needs in order to prioritize and plan R&D. Each of the industries has prepared one or more Technology Roadmaps that provide the basis for issuance of competitive solicitations for proposals to address those needs. It is important to note that the Visions and Roadmaps were prepared by industry, with OIT providing funds for facilitated workshops and publication. The major process industries in the IOF strategy are:

- Agriculture
- Aluminum
- Chemicals
- Forest Products
- Glass
- Metalcasting
- Mining
- Petroleum
- Steel

* C.A. Sorrell, Office of Industrial Technologies, U.S. Department of Energy, Washington, D.C.

Each of these industries has a budget line and an active portfolio of R&D projects being funded by OIT, with 50% cost share by industry. After the IOF process was well underway, the forging, heat treating, and welding industries asked for OIT's assistance with formulation of Vision documents and Technology Roadmaps. These requests were honored and, following completion of the documents, a budget line for "supporting industries" was established and several projects are underway. The Carbon Products industry has also formulated a Vision and is working on a Technology Roadmap.

VISION 2020: CHEMICAL INDUSTRY VISION AND TECHNOLOGY ROADMAPS

In 1996, under the auspices of the American Chemical Society, the American Institute of Chemical Engineers, the Council for Chemical Research, the Synthetic Organic Chemicals Manufacturing Association, and the Chemical Manufacturers Association, the industry produced a document, "Technology Vision 2020 – the U.S. Chemical Industry. Subsequently, the Materials Technology Institute of the Chemical Process Industry produced, with OIT assistance became involved, with a primary concern for materials of construction. To date, the following Technology Roadmaps have been completed:

- Biocatalysis (2000)
- Combinatorial Chemistry (2001)
- Computational Chemistry (1999)
- Computational Fluid Dynamics (1998)
- Materials of Construction (1998)
- Materials Technology (2000)
- New Process Chemistry (2001)
- Reaction Engineering (2001)
- Separations (2000)

The Chemical Industry portfolio of OIT includes projects in all these areas.

MATERIALS OF CONSTRUCTION FOR THE CHEMICAL INDUSTRY

"Technology Roadmap for Materials of Construction, Operation, and Maintenance in the Chemical Process Industries," prepared by the Materials Technology Institute (MTI), lists the following high priority opportunities:

- Metals with high temperature/corrosion capabilities (strong, ductile, corrosion and wear resistant)
- Materials for halogen-based processes (fluorine, chlorine)
- High temperature refractory coatings/materials
- Better corrosion-resistant thermal spray coatings
- Prediction of materials performance without empirical tests
- Materials that resist metal dusting
- Materials for high pressure environments – 10,000 bars
- Self-sensing systems for fitness of service

Based on these recognized priority needs and those from other Technology Roadmaps, the Chemical Industry Team in OIT, issued a competitive solicitation for cost-shared R&D in 1999. The corporate members of MTI submitted five proposals in response. All the proposals involved multiple chemical process and supplier companies, in cooperation with the National Laboratories; all received very favorable merit reviews by chemical industry experts and were

funded by OIT through the Chemical Industry Team. The projects currently underway with the corporate leads and Laboratory partners are:

- Metal Dusting Phenomenon – Air Products and Chemicals and Argonne National Laboratory
- Intermetallics and Alloys for Ethylene Production – Exxon Mobil Chemicals and Oak Ridge National Laboratory
- Corrosion Monitoring System – Honeywell and Oak Ridge
- Corrosion in Mixed Solvents – OLI Systems and Oak Ridge
- Alloy Selection System for Elevated Temperatures (ASSET) – Shell Chemicals and Oak Ridge

All projects are progressing satisfactorily. The materials program managers are monitoring the progress of the projects for the Chemical Industry Team.

THE INDUSTRIAL MATERIALS FOR THE FUTURE PROGRAM

In addition to the Industries of the Future budgets, OIT also supports technology development in three cross-cutting areas – materials, combustion, and sensors and controls. The missions of these programs are to support technology of benefit to multiple industries and to maintain a technology base by supporting longer range research aimed at ensuring continuing materials and processing. The Industrial Materials for the Future Program, newly formed from the Advanced Industrial Materials and the Continuous Fiber Ceramic Composites Programs, supports a wide variety of projects in the following areas:

- Alloy Development
- Infrared and Plasma Processing
- Refractories and Insulation
- Hard Materials and Coatings
- Combinatorial Methods, Thermochemical Data Acquisition, and Modeling
- Novel Processing Materials, Processing and Welding
- Membrane Materials and Reactive Systems for Separations

CONCLUSIONS

The Industries of the Future strategy provides Technology Roadmaps for intelligent selection of research and development activities for the benefit of U.S. industry. The Roadmaps also are invaluable for prioritization in the cross-cut areas to benefit multiple industries. The metal dusting effort is a direct outcome of the IOF process and, like other projects proposed by the Materials Technology Institute, has resulted in assembly of very strong teams – industry, universities, and National Laboratories to ensure successful development and applications to benefit entire industries.

THERMODYNAMICS, MECHANISMS AND KINETICS OF METAL DUSTING

H.J. GRABKE*
Max-Planck-Institut für Eisenforschung GmbH, Düsseldorf, Germany

Metal dusting of Fe, Ni, steels and Ni-base alloys occurs in carburizing atmospheres, $CO-H_2$, $CO-CO_2$, CH_4-H_2 and hydrocarbons, at carbon activities $a_C > 1$ ($a_C = 1$, in equilibrium with graphite). Carbon dissolution into the metal phase, oversaturation and growth of graphitic carbon destroys the materials. Ni and Ni-based alloys disintegrate by direct inward or internal graphite growth

C (dissolved) $\rightarrow$ C (graphitic).

At the surface of iron and steels, cementite is formed as an intermediate, after graphite nucleation it decomposes according to $Fe_3C \rightarrow 3\ Fe + C$ (graphitic). At temperatures <600 °C the decomposition is by growth of graphite into the cementite, outward migration of Fe through the graphite and its agglomeration to fine metal particles, which catalyze carbon deposition from the atmosphere (coking). This mechanism leads to a well-understood kinetics of metal wastage and coking, which is summarized here.

At higher temperatures >700°C the iron from cementite decomposition forms a dense layer, through which the carbon must diffuse to form graphitic carbon. This mechanism leads to an outer layer of coke, an inner layer of ferrite and cementite beneath, and its kinetics is retarded compared to the mechanism at lower temperatures. At even higher temperatures >900 °C, no cementite is formed, but the decay of iron is by direct inward growth of graphite, as in the case of nickel. So, metal dusting is a most interesting corrosion phenomenon, with different mechanisms and kinetics depending on material, temperature and gas compositions.

INTRODUCTION : DEFINITION OF METAL DUSTING

Metal dusting is a disintegration of metallic materials into a dust of fine metal particles and graphitic carbon, containing sometimes also carbides and oxides. This corrosion phenomenon occurs in carburizing atmospheres, containing CO and/or hydrocarbons, at carbon acitivities
$a_C > 1$ which means that a tendency for graphite formation prevails (in equilibrium with graphite $a_C = 1$). Susceptible are metals and alloys which dissolve carbon, i.e. Fe, Ni and Co and their alloys. The carbon is transferred from the atmosphere and dissolved into the metal phase, at $a_C > 1$ to oversaturation, leading to growth of graphite which destroys the materials. In the case of iron and steels cementite is formed as an intermediate into which the graphite grows (Grabke et al. 1993; Grabke 1997; Grabke 1998; Pippel et al. 1995; Schneider et al. 1997)

Fe and Ni and low alloyed materials are attacked uniformly. In the most critical temperature range 400–800°C mostly chromia forming steels and Ni-based alloys are used, on

*Corresponding author address: Prof Dr. H.J. Grabke, Max-Planck-Institut für Eisenforschung GmbH, Max-Planck-Str. 1, 40237 Düsseldorf; e-mail: grabke@mpie.de

these materials metal dusting starts locally, where the oxide scale fails, and leads to pitting and hole formation.

THERMODYNAMICS AND KINETICS OF GAS-METAL REACTIONS

Metal dusting is caused by the tendency to graphite formation, the Gibbs free energy for the process is

$$\Delta G = -RT \ln a_C$$

which is zero in equilibrium with graphite ($a_C = 1$). The main reactions for carbon transfer from the atmosphere are CO-reduction:

$$CO + H_2 = H_2O + C \qquad (1)$$

$$(a_C)_1 = K_1 \frac{pCO \cdot pH_2}{pH_2O} \qquad \log K_1 = \frac{7100}{T} - 7.496$$

Boudouard-reaction:

$$2CO = CO_2 + C \qquad (2)$$

and dissociation of hydrocarbons (Grabke 2000)which is not discussed here in detail.

Metal dusting is mainly a problem in gas for synthesis of ammonia, methanol etc. or gas for reduction of iron ores, produced by either conversion or oxidation of natural gas (CH_4). Such process gas or reduction gas is obtained at high temperatures and not in equilibrium in the critical temperature range for metal dusting. For a nonequilibrium atmosphere generally the values $(a_C)_1$ and $(a_C)_2$ are different and may be very high, both values are rising with decreasing temperature. On a catalytically active surface, i.e. free metal surface, a steady-state a_C is established which is nearer to the value $(a_C)_1$ because of the faster kinetics of reaction (1) (Turkdogan and Vinters 1974; Grabke and Tauber 1975; Shatynski and Grabke 1978). The reaction (1) transfers carbon into solid solution in Fe according to the rate equation (Grabke and Tauber 1975).

$$v_1 = \frac{dn_C}{A\,dt} = k_1 \cdot pCO \cdot \frac{1}{1 + K_O \cdot pH_2O / pH_2} \left(1 - a_C/(a_C)_1\right) \qquad (3)$$

where v is the rate (mol carbon per area A and time), k_1 a rate constant and K_O an adsorption constant. The rate equation indicates that the CO-dissociation on iron is rate determining:

$$CO(gas) = O(adsorbed) + C(dissolved) \qquad (1a)$$

and that the adsorbed oxygen is rapidly removed by reaction with hydrogen:

$$H_2(gas) + O(adsorbed) = H_2O(gas) \qquad (1b)$$

so that the equilibrium for the second reaction step is virtually established. The first step (1a) is proportional to pCO and the part of surface free of oxygen which is given by a Langmuir term:

$$1 - \theta_{O_o} = 1 / (1 + K_O \cdot pH_2O / pH_2)$$

The Boudouard-reaction is composed of the steps

$$CO(gas) = O(adsorbed) + C(dissolved) \quad (2a)$$

and $$CO(gas) + O(adsorbed) = CO_2(gas) \quad (2b)$$

so the first step is the same as in reaction (1), but the second step (2b) is much slower than (1b) and becomes rate determining. Therefore the Boudouard-reaction plays a minor role in kinetics and thermodynamics of nonequilibrium gas mixtures, compared to the CO-reduction (1) and the latter reaction is decisive for the steady state a_C.

Another thermodynamic value is the oxygen pressure which is important for the formation of oxides. Again two reactions deliver oxygen, the H_2O-dissociation

$$2\,H_2O = 2\,H_2 + O_2 \quad (4)$$

and the CO_2-dissociation

$$2\,CO_2 = 2\,CO + O_2 \quad (5)$$

In nonequilibrium atmospheres generally reaction (3) is decisive for the pO_2, again according to its more rapid kinetics. In fact, these reactions take place on catalytically active surfaces at the temperatures of interest 400–800°C and a steady state activity of atomic oxygen is established, by the reaction steps of the watergas-shift reaction (Meschter and Grabke 1979; Münster and Grabke 1980)

$$H_2O = H_2 + O(adsorbed) \quad (1b)\ backward$$

$$O(ad) + CO = CO_2 \quad (2b)$$

$$H_2O + CO = CO_2 + H_2 \quad (6)$$

which is generally not in equilibrium in process and reduction gases.

Another reaction to be considered is the oxidation of methane (Münster and Grabke 1980)

$$CH_4 + H_2O = CO + 3H_2 \quad (7)$$

by which the synthesis and reduction gas is produced. This reaction needs catalytic acceleration and is performed generally on Ni-catalysts at temperatures >700°C. Its back reaction, the methanation of CO may occur when metal dusting has produced fine metal particles, catalyzing the methanation already at rather low temperatures. The methane formation can indicate the occurrence of metal dusting.

So, the elementary reactions in a CO-H_2-H_2O-CO_2-CH_4 gas mixture, i.e. synthesis or reduction gas on a metal surface can be illustrated by the schematics Fig. 1, where the thicker arrows designate fast reaction steps – leading to the predominance of reactions (1) and (3).

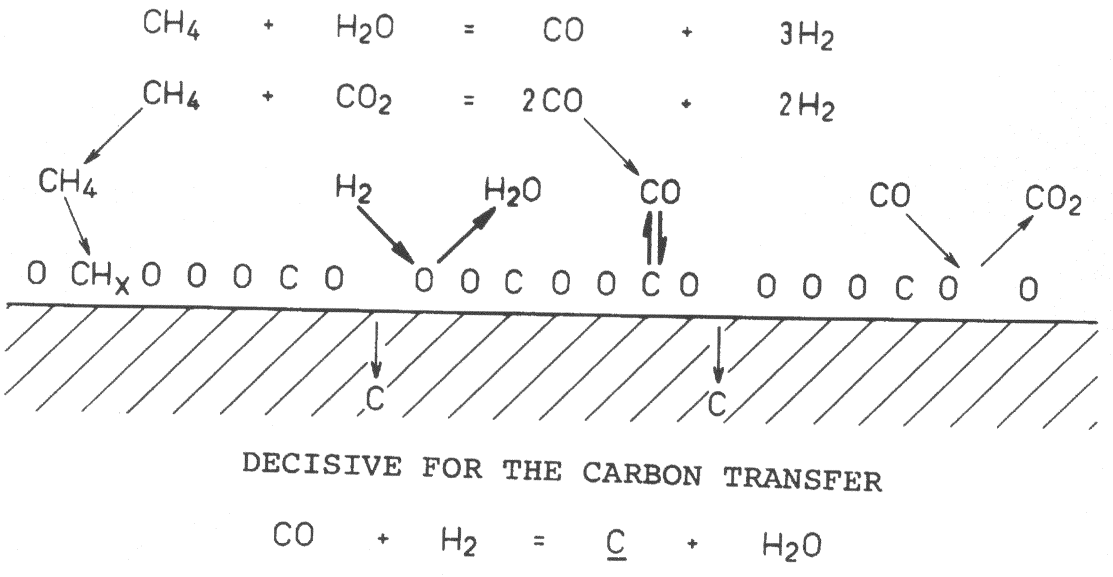

FIGURE 1 Schematic representation of the partial reactions in carburization in a CO-CO_2-H_2-H_2O-CH_4 atmosphere (the thickness of the arrows characterizes the rates).

MECHANISMS OF METAL DUSTING

Metal Dusting on Iron and Low Alloy Steels

The following mechanism was proven by thermogravimetric studies, optical and electron microscopy on metallographic cross sections and high resolution transmission electron microscopy (Grabke et al. 1993; Grabke 1995,1998; Pippel et al. 1995; Schneider, R. et al. 1997; Chun et al. 1999). In the temperature range 400–650°C in a H_2-CO-H_2O mixture the reaction sequence occurs on iron and low alloy steels:

- transfer of carbon by reaction (1) into solid solution, up to oversaturation, concerning equilibrium with graphite (a_C=1) and cementite $(a_C)_{Fe\text{-}Fe3C}$, i.e. somewhat higher than one, relatively high oversaturations have been observed by electron microprobe.

- growth of cementite, mainly at the surface but also at grain boundaries. A rather irregular layer of cementite crystals grows with characteristic protrusions into the bulk metal phase. Due to the low carbon diffusivity in cementite (Ozturk et al. 1984, Schneider et. al. 2000; Schneider et al. 2000), it is a barrier against further carbon ingress, the carbon activity at the surface rises and locally.

- graphite nucleates. This means a decrease of carbon activity to $a_C = 1$ and thus cementite becomes instable.

- cementite decomposes to graphite and iron, according to $Fe_3C = 3\ Fe + C$, in fact by growth of graphite into the cementite. Carbon atoms from Fe_3C attach to graphite planes, growing more or less vertically into the cementite (Pippel et al. 1995). HRTEM shows graphite tongues or roots invading the cementite. The iron diffuses outward through the graphite, concentrations of 3-4% Fe have been detected in the graphite. The iron atoms agglomerate

under formation of fine particles, of about 20 nm average diameter. Into these particles carbon is transferred, again by reaction (1) from the atmosphere with $a_C>1$.

The carbon diffuses through the particle to some site where graphite nucleation is easy. Here graphite growth starts, often growth of graphitic carbon filaments is observed. The rate of carbon transfer into the particles filaments therefore should be governed by the rate law (3) for carbon transfer given above (Grabke and Tauber 1975).

This mechanism can be retarded and altered by the presence of sulfur (Grabke and Müller-Lorenz 1995; Grabke et al. 2001). Adsorption of sulfur on the metal surface hinders the transfer of carbon into solid solution, i.e. step (i), and also the carbon deposition is retarded. But, more important, the nucleation of graphite is impeded and reaction step (iii) may not take place at all or is delayed for a long time. In this way, cementite is stabilized and its properties concerning thermodynamics, diffusion and stoichiometry could be studied (Schneider et al. 2000; Schneider et al. 2000). Suppression of metal dusting depends on carbon and sulfur activity in the atmosphere, carburizing gas CO or CH_4, temperature and time (Grabke et al. 2001).

At higher temperatures >700°C the morphology of the reaction products changes. The iron from the Fe_3C decomposition does not form fine particles but agglomerates to an iron layer through which the carbon must diffuse, to attach to the outer graphite layer. Thereby the processes are slowed down and metal dusting becomes controlled by carbon diffusion in ferrite, or at higher temperature in austenite. In the system: outer graphite layer, metal layer, cementite layer, metal phase, the phase boundary graphite/metal is instable, since the diffusion control causes that graphite intrusions into the metal layer grow faster, until that layer is disrupted and perturbed (Schneider et al. 2002).

At even higher temperatures, 900 and 1000°C, in CH_4-H_2-mixtures at $a_C>1$ no cementite formed (Forseth and Grabke, unpublished), but from the oversaturated metal phase, carbon diffuses through an austenite layer to the graphite growing on the surface. Again the strong growth of graphite protrusions indicates carbon diffusion control and unstable phase boundaries. After longer duration also metal disintegration is to be expected which means that metal dusting occurs also at 1000°C, but not via cementite formation.

Metal Dusting of Nickel and Ni-Based Alloys

The latter mechanism, just described for iron at high temperatures >900°C is valid also for Ni and Ni-based alloys. Such materials are destroyed by direct inward growth of graphite into the oversaturated solid solution, as shown by high-resolution transmission-electron microscopy (Schneider, R. et al. 1997; Chun et al. 2000). The roots and filaments of graphite growing into the metal phase, separate particles from the material which are considerably bigger than in the mechanism via cementite. Therefore, the catalytic surface area generated is less and coke formation is minor compared to iron and steels (Müller-Lorenz and Grabke 1999; Strauß et al. 1999).

The attack on nickel and its alloys is dependent on the crystal orientation on the surface, due to orientation dependent graphite nucleation and growth. On (111) and some other planes of nickel graphite grows epitaxially, its layers parallel to the metal surface (Blakely 1978), and on these planes no direct metal dusting attack occurs. On other planes such as Ni(100), graphite nucleates more or less vertical and here its layers grow into the metal phase, which leads to materials destruction.

KINETICS OF METAL WASTAGE AND COKING ON IRON AND LOW ALLOY STEELS

The rate of metal wastage was determined on iron and low alloy steels in discontinuous exposures at 400–600°C. After exposures for 1-2 days the coke was removed and its metal content was determined by chemical analysis. The rates of metal wastage (in mg/cm^{2}h) were constant and independent of time from the beginning. At 475°C experiments in various gas mixtures were conducted and the rate of metal wastage was shown to be independent of carbon and oxygen activity (Grabke et al. 1994). Thus the rate law results:

$$r_M = \frac{d m_M}{A\,dt} = k_M \tag{8}$$

for metal wastage per unit area A and time.

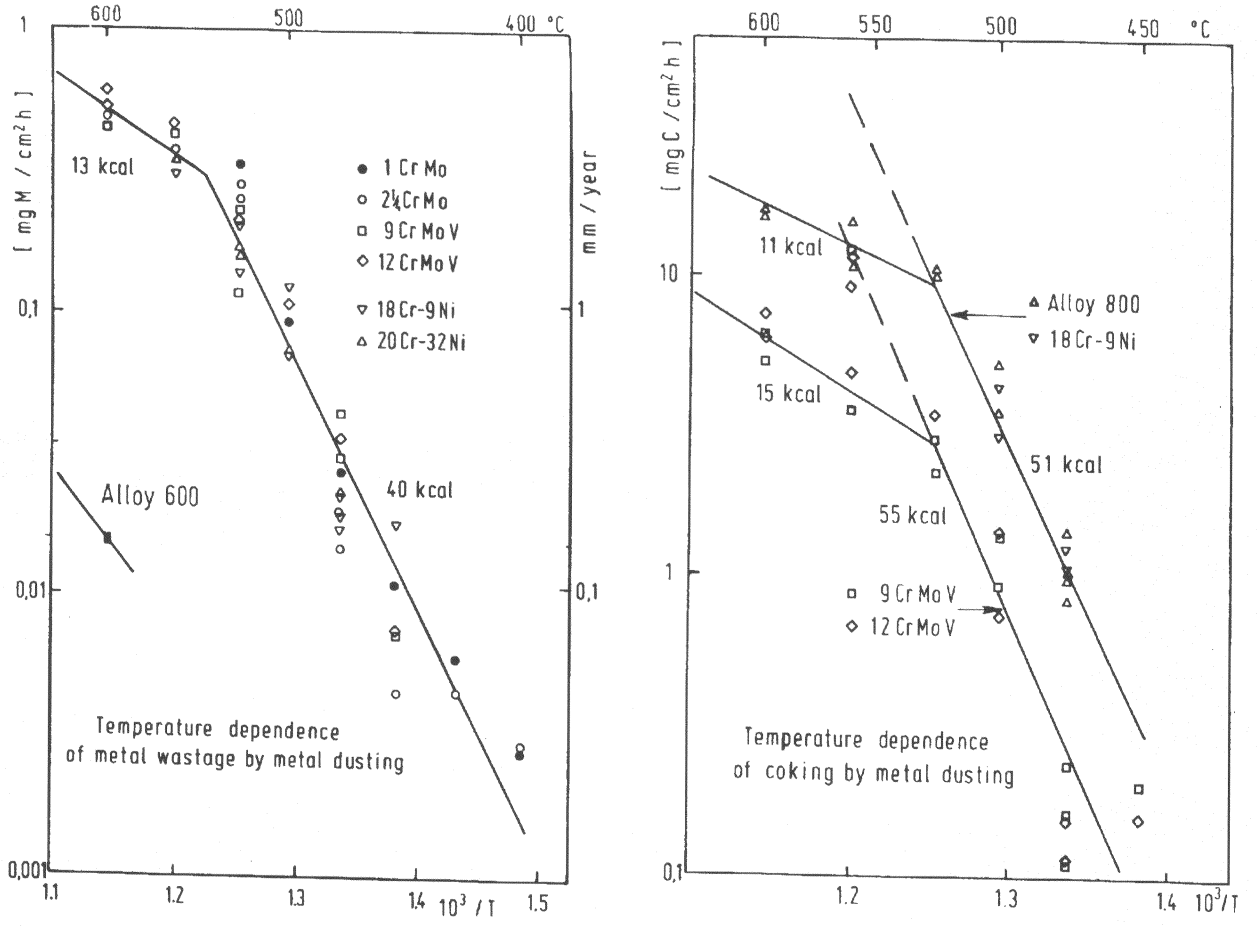

FIGURE 2 Arrhenius-diagrams, from exposures of various steel samples, attacked on their whole surface a) metal wastage rates, determined by coke analysis for its metal content, b) coking rates, determined by weighing the removable coke after repeated exposures

This rate law most probably describes the solid state reaction:

$$Fe_3C = 3\,Fe + C \tag{9}$$

i.e. the cementite decomposition. Studies on various steels yield one line in the Arrhenius-plot log r_M vs. 1/T (Fig. 2), up to about 540°C, which indicates that for these ferritic and austenitic 1-20% Cr steels the cementite decomposition is the rate determining step in metal dusting, with an activation energy of about 40 kcal/mol (Protection by oxide scales is not considered here, the data in Fig. 2 a and b are for samples, attacked on their whole surface).

The cementite decomposition leads to a great number of fine metal particles of about the same size, their mass increases with time according to the expression, obtained by integration of the rate law (8)

$$\Delta m_M / A = k_M \cdot t \tag{10}$$

Carbon deposition is catalyzed by those fine metal particles and one may assume that the rate of carbon deposition is proportional to their mass:

$$\begin{aligned} r_C = \frac{dm_C}{Adt} &= k_C \cdot (\Delta m_M / A) \cdot f(p_i) \\ &= k_C \cdot k_M \cdot f(p_i) \cdot t \end{aligned} \tag{11}$$

where k_C and k_M are the rate constants of carbon deposition and metal wastage and $f(p_i)$ a function of the partial pressures. Integration yields the result

$$2(\Delta m_C/A) = k_C \cdot k_M \cdot f(p_i) \cdot t^2 \tag{12}$$

i.e. the rate of carbon deposition should increase with t^2 which in fact was proven for coking on steels in experiments upto 10-15 hours (Grabke et al. 1994).

The Arrhenius-plot for coking rates shows differences for ferrites and austenites, on the austenitic steels coking is more severe. The activation energy of coking contains two values, since a product of rate constants $k_C \cdot k_M$ is contained in equation (11). Therefore it is the sum of the value for metal wastage, 40 kcal/mol, plus the value for carbon transfer and results to be 55 kcal/mol for the ferritic steels and 51 kcal/mol for the austenitic steels. The dependence on partial pressures $f(p_i)$ was investigated at 475°C (Grabke et al. 1994) and it was shown that the coking rate is proportional to pCO, it increases with pH_2 and decreases with pH_2O. These dependencies are in agreement with the kinetic equation (3) for carbon transfer.

The above statements are true for the temperature range below about 550°C, at higher temperatures the kinetics change. The activation energies for metal wastage and coking are lower and the metal wastage rate becomes dependent on the product $pCO \cdot pH_2$ (Müller-Lorenz et al. 1999) which indicates that carbon transfer is rate determining. More detailed studies of the dependencies of metal wastage and coking on temperature, time and partial pressures are needed for a full description of the very complex mechanisms and kinetics of metal dusting on iron and steels in the temperature range 550–750°C (Schneider et al. 2002). At even higher temperatures >750°C, the kinetics change again and carbon diffusion in austenite appears to be rate determining for the coke growth.

References

Blakely, J.M., 1978, "Segregation to Surfaces: Dilute Alloys of the Transition Metals", CRC Critical Reviews in Solid State and Materials Science", Nov. 1978:333-355.

Chun, C.M., J.D. Mumford and T.A. Ramanarayanan, 1999, "Relationship between Coking and Metal Dusting", *Materials and Corrosion* 50:634-639.

Chun, C.M., J.D. Mumford and T.A. Ramanarayanan, 2000, "Carbon-Induced Corrosion of Nickel Anode", *Journal Electrochem. Soc.* 147:3680-3686.

Grabke H.J. and G. Tauber, 1974, "Kinetics of the Decarburization of α and γ-iron in H_2-H_2O mixtures and of the Carburization in CO-H_2-Mixtures", *Archiv Eisenhüttenwes.* 45:215-222.

Grabke, H.J., R. Krajak, and J.C. Nava Paz, 1993, "On the Mechanism of Catastrophic Carburization," *Corrosion Sci.* 35:1141-1150.

Grabke, H.J., C.B. Bracho-Troconis, E.M. Müller-Lorenz, 1994, "Metal Dusting of Low Alloy Steels," *Werkst. und Korr.* 45:215-221.

Grabke, H.J., 1995, "Metal Dusting of Low and High Alloy Steels," *Corrosion NACE* 51:711-720.

Grabke, H.J. and E.M. Müller-Lorenz, 1995, "Effect of Sulfur on the Stability of Cementite," *Steel Research* 66:252-258.

Grabke, H.J., 1998, "Thermodynamics, Mechanisms and Kinetics of Metal Dusting," *Mat. Corr.* 49:303-308.

Grabke, H.J., 2000, "Carburization and Metal Dusting by Hydrocarbons," *Proceed. International Conference Corrosion in Refinery Petrochemical and Power Generation Plants,* Venice 18-19 May 2000, Ass. Italiana di Metallurgia, Milano, ISBN 88-85298-36-2, 1-11.

Grabke, H.J., E.M Müller-Lorenz, A. Schneider, 2001, "Carburization and Metal Dusting of Iron," *ISIJ International* 41, Supplement S1-S8.

Meschter, P. and H.J. Grabke, 1979 "Kinetics of the Water-Gas Shift Reaction on an FeO Surface," *Metallurg. Trans.* 10B:323-329.

Müller-Lorenz, E.M. and H.J. Grabke, 1999, "Coking by Metal Dusting of Steels," Mat. Corr. 50:614-621.

Münster, P. and H.J. Grabke, 1980, "Kinetics of the Water-Gas Shift Reaction on Iron", *Archiv Eisenhüttenwes.* 51:319-324.

Münster, P. and H.J. Grabke, 1980, "Kinetics of the Steam-Reforming of Methane on Iron as a Catalyst", *Berichte Bunsenges. Phys. Chem.* 84:1068-1071.

Ozturk, B., V.L. Fearing, J. A. Ruth and G. Simkovich, 1984, "The Diffusion Coefficient of Carbon in Cementite, Fe_3C at 450 °C", *Solid State Ionics* 12:145-151.

Pippel, E., J. Woltersdorf, H.J. Grabke, and S. Strauss, 1995, "Microprocesses of Metal Dusting and Their Investigation by Transmission Electron Microscopy," *Steel Research* 66:217-221.

Schneider, A., G. Inden, H.J. Grabke, Q. Wei, E. Pippel, J. Woltersdorf, 2000, "Effect of H_2S on Formation and Decomposition of Fe_3C and Fe_5C_2 Under Metal Dusting Conditions," *Steel Research* 71:179-184, No. 5.

Schneider, A., G. Inden, H.J. Grabke, 2000, "Growth kinetics of Iron Carbide Layers During Gas Carburization", EUROMAT 99, *Interface Controlled Materials*, Vol. 9, M. Rühle, H. Gleiter (EDS), Wiley-VCH 30-37.

Schneider, A., J. Zhang and G. Inden, 2002, "Cementite Decomposition and Coke Formation During Carburization of Iron, I. Iron Layer Formation, II. Effect of Gas Composition," *Corrosion Sci. in press.*

Schneider, R., E. Pippel, J. Woltersdorf, S. Strauss, and H.J. Grabke, 1997, "Microprocesses of Metal Dusting on Nickel and Ni-Base Alloys," *Steel Research* 68: 326-332.

Shatynski, S.R. and H.J. Grabke, 1978, "The Kinetics of Carburization of γ-Iron in $CO-H_2$ and $CO-H_2$ Atmosphere at 920 °C", *Archiv Eisenhüttenwes.* 49:129-133.

Strauss, S., R. Krajak and H.J. Grabke, 1999, "Coking by Metal dusting of Nickel-Base Alloys", Mat. Corr. 50:622-627.

Turkdogan, E.T. and J.V. Vinters, 1974, "Catalytic Effect of Iron on Decomposition of Carbon Monoxide: I. Carbon Depostion in $CO-H_2$-Mixtures", *Metallurg. Trans.* 5:11-19.

THEORETICAL STUDIES ON METAL DUSTING: BOUDOUARD AND STEAM-CARBON REACTIONS AND IRON CARBONYL FORMATION

K.L. BAUMERT* and H. CHENG,
Air Products and Chemicals, Inc.
Allentown, PA

ABSTRACT

Quantum-mechanical calculations based on density functional theory were performed to study surface reactions resulting in metal depletion. The mechanisms and energetics of two major metal dusting processes represented by Boudouard and steam-carbon reactions on the FeO(100) surface were investigated. The reaction process involving direct abstraction of O from the surface by CO was excluded from consideration of the overall dusting processes due to unfavorable energetics. The present study suggests a "digging" mechanism of surface carbonyl formation that the strong adsorption of CO at the hollow sites pushes the metal atom out of surface, leading to the depletion of metal atom to form iron pentacarbonyl.

INTRODUCTION

The technique used for this study is the ab initio density functional theory. The method is entirely based on quantum-mechanical first principles without any empirical and experimental input. It has been widely benchmarked against numerous experimental results and has been shown to be highly accurate in providing realistic molecular/crystal structures (within 0.1 Å of experimental values) and energetics (within 5 kcal/mol of experimental values). Both cluster and slab models were used to describe the surface structures. Normally, the top three to five surface layers were included in the calculations.

This effort has been mainly focused on the mechanistic aspects of metal dusting. Specifically, Boudouard reaction and steam carbon reaction at transition metal and metal oxide surfaces and carbonyl formation on Fe and Ni surfaces were examined. All these processes lead to metal depletion from the materials.

On the Boudouard and Steam Carbon Reactions

The Boudouard and steam carbon reactions at transition metal oxide surfaces are given below:

$$CO + CO \rightarrow C + CO_2,$$
$$CO + H_2 \rightarrow C + H_2O.$$

Using the FeO (100) surface as an example, the possible reaction mechanisms were explored by considering the most plausible reaction pathways as illustrated in Fig. 1.

*Corresponding author address: Kenneth L. Baumert, Air Products and Chemicals, Inc., 7201 Hamilton Boulevard, Allentown, PA 18195-1501; e-mail: baumerkl@apci.com.

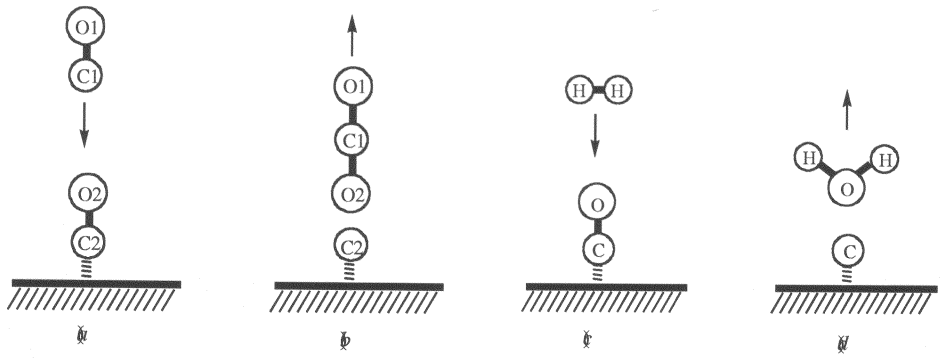

FIGURE 1 Reaction Paths for Boudouard Reaction, Shown in (a) and (b), and Steam Carbon Reaction, Shown in (c) and (d)

The calculated adsorption energy for CO (-7.9 kcal/mol) suggested that CO binds weakly at the atop site of FeO(100) on the metal atom and thus the molecule is not activated for further reactions. Indeed, the subsequent reaction path calculations suggested that the activation barrier for these two reactions is extremely high. For the Boudouard reaction, the activation energy is 128.5 kcal/mol and for the steam carbon reaction, it is 99.3 kcal/mol. Therefore, it is kinetically very difficult. Even thermodynamically these reactions are very endothermic on FeO(100) surface. The calculated heats of reaction for Boudouard and steam carbon reactions are 45.8 kcal/mol and 59.2 kcal/mol, respectively. The reason for lack of reactivity can be readily understood based on the charge transfer analysis. Briefly, the oxygen atoms surround the adsorption site on the FeO surfaces prevent electrons of the metal atom from being transferred to CO, which is necessary in order to activate CO for metal dusting reactions. Therefore, we conclude that in order to sustain the dusting attack it is essential to make the electrons on the metal unavailable to CO and the metal oxides did just that. This conclusion is in excellent agreement with the observations by corrosion engineers for many years. Nevertheless, the theoretical studies provide fundamental insight into the underlying mechanism.

The adsorption energy was calculated for CO at various sites of metal surfaces. Here, the Fe(100) surface as an example. This is far less reactive surface than other high index surfaces. However, we still found that CO can be readily activated. The molecule prefers adsorption at the hollow site with a much larger adsorption energy, -40.1 kcal/mol. The C-O bond distance is also significantly elongated from 1.10 to 1.31 Å. The bond is much weaker and thus the oxygen atom can be easily picked up by the gas-phase CO or H_2, which results in the formation of CO_2 and H_2O, respectively, in addition to surface carbides.

The calculation on Fe and FeO surfaces have important implications. First, the results can be used to explain why metal dusting often results in pitts. In most cases the normal oxides present on stainless steels should prevent Boudouard carbon deposition. However, the presence of defects in these oxides will yield sites for local carbon deposition to occur. As a result, the attack should take the form of pits occurring at these local sites as carbon diffuses into the metal at these sites, ultimately causing the loss of metal from these sites. The observation of pitting attack as a result of metal dusting has not been adequately explained in the prior literature, but based on this work it is clear that pitting should be the preferred mode of attack. Second, the calculation suggests that CO chemisorption at surfaces is the most important step in the metal dusting process. A strong adsorption usually leads to large activation of the C-O bond, making it easier for dusting attack. The adsorption can be readily detected with the surface Fourier transform infrared spectroscopic (known as FTIR in literature) technique. Based on the calculation, we proposed to initiate the spectroscopic experiments

On the Metal Carbonyl Formation

In this project, we examined the possibility of depleting metal atoms from metal surfaces by CO molecules to form carbonyl species. Use the iron pentacarbonyl formation at Fe(100) surface as an example by considering the following reaction processes:

1. CO adsorption on Fe surface to form surface iron pentacarbonyl species:

$$Fe(s) + 5CO(g) \rightarrow Fe\text{-}5CO(s);$$

The abstraction of surface $Fe(CO)_5$ into the gas phase to form a meta-stable structure of ironpentacarbonyl with a C_{4v} symmetry, creating a vacancy per unit cell on the surface:

$$Fe\text{-}5CO(s) \rightarrow Fe(s, \text{vacancy}) + Fe(CO)_5\ (g, C_{4v});$$

2. The evolution of the gas phase $Fe(CO)_5$ from the meta-stable structure to the final product:

$$Fe(CO)_5(C_{4v}) \rightarrow Fe(CO)_5(D_{3h}).$$

To effectively model these reaction processes, we selected a surface slab model with a large unit cell as shown in Fig. 2. The calculated reaction energies are shown in Table 1. The optimized adsorption structure and the calculated thermochemical energies seem to suggest a "digging" mechanism for the $Fe(CO)_5$ formation: the CO molecules are initially adsorbed at the hollow site, push the surrounded metal atom out of the surface, and then deepen their roots by forming strong bonding with the surface atoms. The structural optimization shows this is an energetically downhill process.

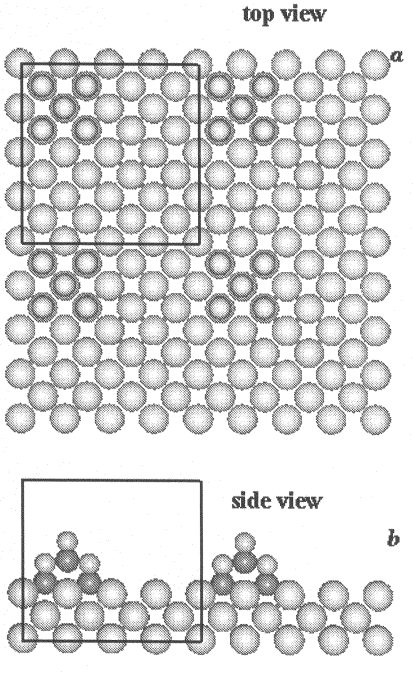

FIGURE 2 Slab Model Used to Model CO Adsorption and Carbonyl Formation on Fe(100) Surface.

TABLE 1 The Calculated Reaction Energies

Reaction Process	ΔE (kcal/mol)
$Fe(s) + 5CO(g) \rightarrow Fe\text{-}5CO(s)$	-187.6
$Fe\text{-}5CO(s) \rightarrow Fe(s, \text{vacancy}) + Fe(CO)_5\ (g, C_{4v})$	88.9
$Fe(CO)_5(C_{4v})? \rightarrow Fe(CO)_5(D_{3h})$	-0.9

The calculated reaction energy for step 2 indicates that the desorption of the surface $Fe(CO)_5$ species is very endothermic, as expected. The carbonyl species must overcome a stiff activation barrier before evolving into a stable trigonal bipyramid structure. However, the energy required is easily off set by the extremely exothermic adsorption energy. The activation barrier likely represents the upper bound of the energy required to form iron pentacarbonyl for the following reasons. First, the present study deals with a perfectly aligned and close-packed Fe surface, which is much less reactive than the surfaces with terraces, defects or sharp edges. Second, the calculation yields an activation energy to form a gas-phase carbonyl species. In practice, however, the carbonyl complexes remain on surfaces as a liquid. The overall energy required to form these complexes is therefore expected to be much smaller. Nevertheless, the information about the upper bound activation energy is still useful for us to understand the corrosion process.

CONCLUSIONS

Using the ab initio density functional theory we calculated the likely mechanisms of metal removal from a surface exposed to carbon monoxide. We find that the overall processes of iron pentacarbonyl formation are energetically favorable even at the least reactive surface of iron. The theory also predicts that an oxide on the surface inhibits the metal dusting reaction.

METAL DUSTING RESEARCH AT ARGONNE NATIONAL LABORATORY

K. Natesan*, Z. Zeng, V. A. Maroni, W. K. Soppet, and D. L. Rink
Argonne National Laboratory
Argonne, IL 60439

ABSTRACT

The deposition of carbon from cabonaceous gaseous environments is prevalent in many chemical and petrochemical processes such as reforming systems, syngas production systems, and iron reduction plants. One of the major consequences of carbon deposition is the degradation of structural materials by a phenomenon known as "metal dusting." There are two major issues of importance in metal dusting. First is formation of carbon and subsequent deposition of carbon on metallic materials. Second is the initiation of metal dusting degradation of the alloy. Details are presented on a research program that is underway at Argonne National Laboratory to study the metal dusting phenomenon from a fundamental scientific base involving laboratory research in simulated process conditions and field testing of materials in actual process environments. The project has participation from the U.S. chemical industry, alloy manufacturers, and the Materials Technology Institute, which serves the chemical process industry.

INTRODUCTION

Production of synthesis gas (mixtures of carbon monoxide and hydrogen) is an important first step in the manufacture of numerous chemicals. The most common process for production of synthesis gas production is steam reforming, where hydrocarbons are converted by reaction with steam over a nickel catalyst at high temperatures. The synthesis gas from the reformer is purified in order to meet the requirements of the downstream process. It can be separated into pure H_2, pure CO, H_2/CO mixtures, etc. Pure CO is required for the production of isocyanates, polycarbonates, and acetic acid, while for example, synthesis of oxo-alcohols requires an H_2/CO mixture with a molar ratio close to 1. By decreasing the steam/carbon ratio and by increasing the outlet temperature of the reformer furnace, great savings in feedstock consumption and in investment can be realized. However, the carbonaceous gases catalyzed by metallic components in these processes result in carbon deposition. Consequences of deposited carbon are the deleterious effect on heat transfer and degradation of structural materials by a phenomenon known as "metal dusting."

Metal dusting is a catastrophic corrosion phenomenon that leads to the disintegration of structural metals and alloys into dust composed of fine particles of the metal/alloy, carbides, and carbon. Metal dusting occurs at intermediate temperatures of 400-800°C, but this type of corrosion is possible at any temperature at which the carbon activity (a_C) in the gas phase is >>1. Such high carbon activities are prevalent in certain locations in chemical processes such as methanol production, hydrocarbon and ammonia synthesis, hydrogen production, and syngas generation. Even though dusting-related failures have occurred most often in the petroleum and petrochemical industries, and this deterioration has been studied for more than 50 years (Camp et

*Corresponding author address: Ken Natesan, Argonne National Laboratory, 9700 South Cass Avenue, Argonne, IL 60439; e-mail: ntesan@anl.gov

al. 1945; Hoyt and Caughey 1959), its mechanism and driving force are not evident in all cases, and no approach is currently available to mitigate this problem.

A research program is being conducted at Argonne National Laboratory (ANL) to study the metal dusting phenomenon from a fundamental scientific base involving laboratory research in simulated process conditions and field testing of materials in actual process environments with participation from the U.S. chemical industry, alloy manufacturers, and the Materials Technology Institute, which serves the chemical process industry.

Our approach involves characterization, using thermodynamic modeling, of environments prevalent in several process streams in terms of their chemical activities for carbon, oxygen, and other elements. The results are used to assess their chemical potential and temperature windows for metal dusting to initiate and propagate in metallic materials. The thermodynamic assessment would also establish the consequences of equilibrium and nonequilibrium gas chemistries on the metal dusting process.

Bench-scale laboratory experiments are being conducted at ANL with candidate commercial alloys, developmental alloys, and surface-engineered materials, including coatings. Experiments are conducted over a wide range of gas chemistries and temperatures that encompass the environments prevalent in various process systems such as reformers for the production of hydrogen, ammonia, and methanol. Results are used to establish the conditions for onset of metal dusting and to evaluate the influence of alloy chemistry on the occurrence of metal dusting. It is planned to expose candidate commercial, developmental, and surface-engineered alloys in process streams of production plants for hydrogen, methanol, ammonia, and other hydrogen-bearing compounds. The field-exposure results and the laboratory test data will be used to develop performance envelopes for alloys in service with minimum risk of metal dusting.

PRELIMINARY CALCULATIONS

Gas Phase Reactions

Chemical process environments were characterized by computer modeling of gas-phase reactions under both equilibrium and nonequilibrium conditions. Calculations were made to evaluate carbon activities (a_C) for different gas mixtures as a function of temperature at atmospheric pressure (14.7 psia) and at plant system pressures. Chemical compositions are listed in Table 1 for seven gas mixtures, which include the reformer streams and laboratory simulation environments. The carbon deposition process can be influenced by two possible reactions, as follows:

$$CO(g) + H_2(g) = C + H_2O(g) \quad (1)$$

$$2CO(g) = C + CO_2(g) \quad (2)$$

Since the gas composition is maintained fairly constant during the passage through the waste-heat boiler for the reformer streams, either Reaction 1 or Reaction 2 may dictate the a_C at different temperatures. If it is dictated by Reaction 1, a_C will be directly proportional to the H_2 and CO partial pressures and inversely proportional to the H_2O partial pressure. On the other hand, if a_C is dictated by Reaction 2, then it will be directly proportional to square of the CO partial pressure and inversely proportional to the CO_2 partial pressure. In addition, if gas-phase equilibrium does prevail, albeit at high temperatures and/or for long residence times, then the

calculated a_C value will be the same (i.e., irrespective of Reaction 1 or 2) since thermodynamically the gas composition will adjust to give the most stable (lowest free energy) composition. Therefore, a_C was calculated as a function of temperature (496°C or 925°F to the maximum test temperatures and 1 atm to the maximum test pressures) for the seven gas mixtures assuming Reaction 1 or 2 is dominant and the gas phase is in assumption of thermodynamic equilibrium.

Carbon Activity Calculations

Table 2 lists a_C values calculated for the seven gas mixtures (Table 1) at 593°C (1100°F) and 704°C (1300°F), based on whether Reaction 1 or 2 was dominant or equilibrium among different gas species prevailed. Figures 1-3 show plots of a_C as a function of temperature for the three reformer outlet-gas mixtures listed in Table 1. Figure 1 shows six curves for Gas Mixture 1, as follows:

Case 1:	Reaction 1 dominant, P = 1 atm (14.7 psia)
Case 2:	Reaction 1 dominant, P = 37 atm (543, psia)
Case 3:	Reaction 2 dominant, P = 1 atm (14.7 psia)
Case 4:	Reaction 2 dominant, P = 37 atm (543 psia)
Case 5:	Equilibrium condition, 1 atm (14.7 psia)
Case 6:	Equilibrium condition, P = 1 atm (543 psia)

Similar curves are shown in Fig. 2 for Gas Mixture 2, and in Fig. 3 for Gas Mixture 3. The maximum pressures for Gas Mixtures 2 and 3 are 15 atm (215 psia) and 32 atm (470 psia), respectively.

TABLE 1 Chemical compositions of gas mixtures relevant for metal dusting study.

	Composition in mole %						
Gas species	**Gas 1**	**Gas 2**	**Gas 3**	**Gas 4**	**Gas 5**	**Gas 6**	**Gas 7**
CH_4	4.1	1.1	0.2	-	-	-	-
CO	7.2	18	8.4	17.5	17.6	12.7	70.0
CO_2	5.7	5.6	5	8.3	8.3	10.1	4.0
H_2	43.8	52	36.3	74.2	72.2	77.2	25.25
H_2O	39.2	23	35	0	1.96	0	0.007
N_2	-	-	15	-	-	-	-
Ar	-	-	0.1	-	-	-	-

Gases 1, 2,and 3: Reformer outlet gases. Gases 4, 5, and 6: Used in ANL experiments. Gas 7: Used in Special Metals Program.

TABLE 2 Carbon activity values at 593°C (1100°F) and 704°C (1300°F) based on reactions 1, 2, and equilibrium, calculated for gas mixtures listed in Table 1.

	593°C (1100°F)			704°C (1300°F)		
Gas #	**Rxn 1**	Rxn 2	**Eqm**	**Rxn 1**	**Rxn 2**	**Eqm**
1	0.4	1.2	0.3	0.05	0.08	0.09
2	2.0	7.9	0.7	0.24	0.53	0.25
3	0.4	1.9	0.2	0.05	0.13	0.04
4	∞	5.0	1.3	∞	0.34	0.8
5	32.3	5.0	1.2	3.8	0.34	0.7
6	∞	2.2	0.01	∞	0.15	0.02
7	117.4	165.4	32.6	13.8	11.1	6.2

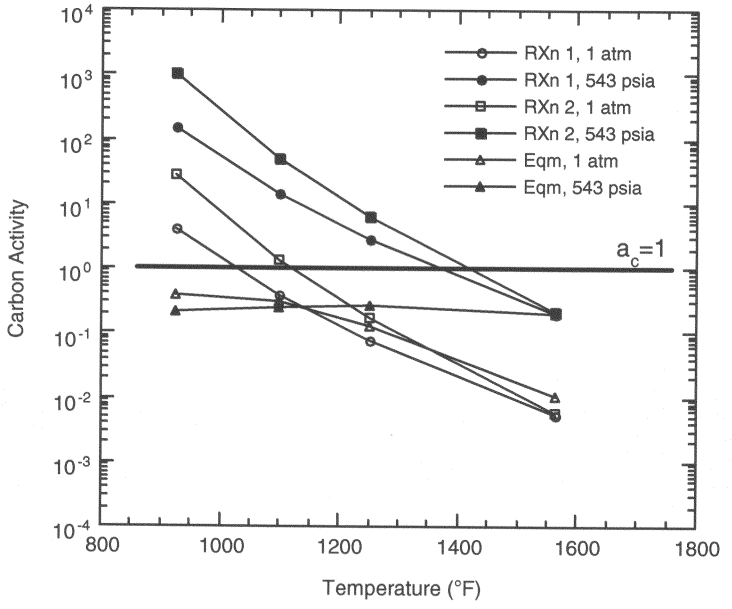

FIGURE 1 Carbon activity curves calculated as a function of temperature for Gas Mixture 1.

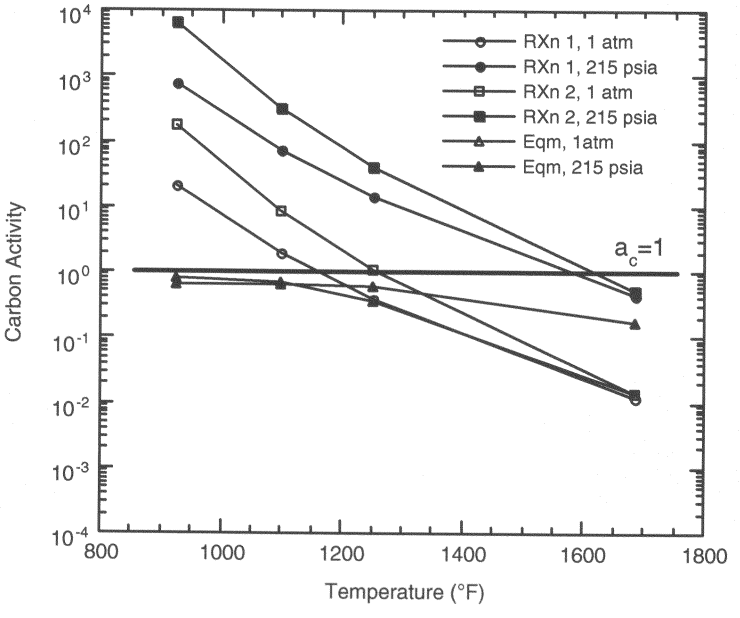

FIGURE 2 Carbon activity curves calculated as a function of temperature for Gas Mixture 2.

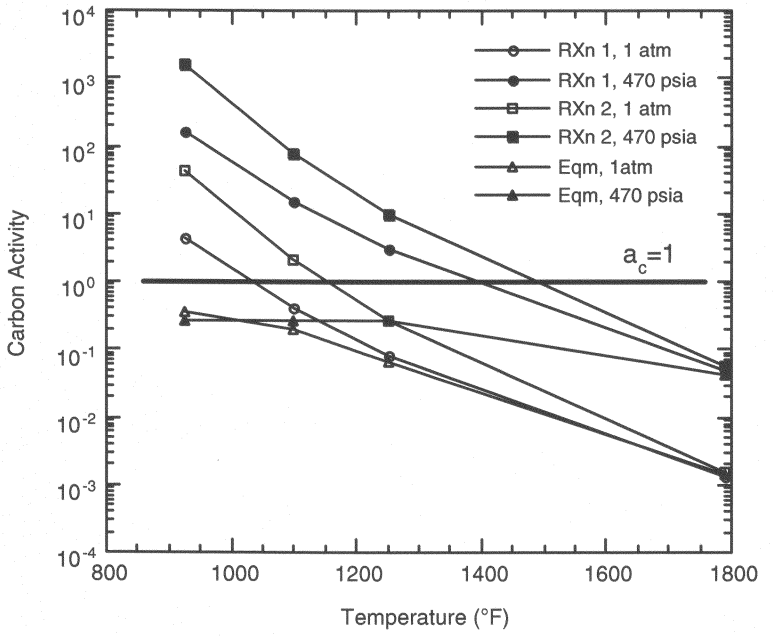

FIGURE 3 Carbon activity curves calculated as a function of temperature for Gas Mixture 3.

The implications of the carbon activity calculations are as follows:

1 Under nonequilibrium conditions, Reaction 1 control at 1 atm pressure results in the lowest a_C for all reformer gas mixtures (Gases 1-3). Even under these conditions, a_C is 1 or higher at temperatures below ≈565°C (≈1050°F) for Gas Mixtures 1 and 3 and below ≈621°C (≈1150°F) for Gas Mixture 2. At 496°C (925°F), a_C is ≈4 for Gas Mixtures 1 and 3 and ≈20 for Gas Mixture 2. These a_C values can result in carbon deposition at 496°C (925°F) and may lead to metal dusting of several alloys, depending on the incubation time and alloy composition.

2 Reaction 2 control always results in higher a_C. This trend is evident at all temperatures and pressures for the present calculations. Furthermore, this trend is independent of the gas mixture used in the calculation. The differences in the absolute value of a_C established under Reaction 1 versus Reaction 2 control can be used to assess the role of these reactions in carbon deposition and associated metal dusting. For example, if an experiment is run in Gas Mixture 1 at 579°C (1075°F) and 1 atm pressure, Reaction 1 control (with a_C of ≈0.6) would result in no carbon deposition whereas Reaction 2 control (with a_C of ≈3) would result in carbon deposition.

3 Increased system pressure increases the a_C calculated for both reactions, irrespective of the gas composition. The carbon activity increases in direct proportion to the total pressure, and the value could be extremely large at lower temperatures. Furthermore, the effect of increased pressure is to widen the temperature window in which $a_C >> 1$. For example, in Gas Mixture 1 with Reaction 1 control, an increase in pressure from 1 atm (14.7 psia) to 37 atm (543 psia) increases the temperature window with $a_C > 1$ from 427-565°C (800-1050°F) to 427-732°C (800-1350°F). This assumes that temperatures <427°C (<800°F) is too low to initiate metal dusting degradation, even though a_C is high.

4 Calculations also indicate that under equilibrium conditions, all reformer gas mixtures exhibit a_C <1 (even at high pressures); therefore, no deposit of carbon and associated metal dusting should occur. Since carbon deposition and metal dusting of structural alloys are widely observed in reformer systems, the gas mixtures in these systems are not really in equilibrium, and a_C is established by individual reactions and is dictated by the reformer effluent gas composition.

5 Calculations further show that experiments need to be conducted under nonequilibrium gas chemistry to deposit carbon (coke) and also allow sufficient incubation time for metal dusting to initiate.

6 For gas mixtures 4 and 5, a_C will be >1 if Reaction 1 is dominant. If Reaction 2 is dominant, a_C will be >1 at 593°C (1100°F) and <1 at 704°C (1300°F).

Results from these analyses were used to select gas compositions and temperatures for the experimental effort on metal dusting of structural alloys.

EXPERIMENTAL PROGRAM

Equipment Description

In all, five experimental systems were used in the metal dusting experiments. Two existing systems at ANL were modified to accommodate the requirements of the program. Each of the modified systems consisted of a horizontal, tubular, high-temperature furnace capable of operation up to 900°C. The reaction chamber, with gas inlet/outlet fittings, fabricated from quartz was positioned within the furnace chamber. A chromel-alumel thermocouple, inserted from one end of the reaction chamber, was used to monitor the specimen temperature. Specimens were suspended from quartz rods held on the top of a high-purity alumina boat. The specimens and the boat were positioned in the constant-temperature section of the reaction chamber. High-purity gases such as CO, CO_2, CH_4, and H_2 were procured and piped into the reaction chamber through flow meters to obtain the desired composition. In some experiments, H_2 gas was bubbled through a water bath to saturate the H_2 with water prior to entering the reaction chamber.

While the two systems described above enabled study of the key variables in metal dusting research, additional facilities were needed for long-term testing of metallic alloys, surface-engineered materials, and coatings, especially in environments that contained a large H_2O content. For this purpose, three new systems were designed and assembled in a metal dusting research laboratory. Figure 4 shows a schematic diagram for the three test facilities. The three test fixtures were positioned horizontally on a laboratory bench top in a staggered linear arrangement with a common gas supply. Each test fixture consists of a quartz retort chamber (74-cm length, 5-cm OD, 0.32-cm thick), which was centered in a 30-cm diameter resistive heating furnace. A Barber-Coleman Model 560 three-mode controller was used to control the furnace temperature. Type 316 stainless steel (SS) flange caps with an O-ring seal closed the ends of the quartz retort tube. The flange caps provided port fittings for the gas flow, steam/vapor preheater, and ceramic thermowells used for specimen temperature measurements.

The gas that flowed through the retort chamber had various ratios of H_2, CH_4, CO, CO_2, and steam/water vapor. Gases from the low-pressure manifold lines were supplied to respective individual Brooks model 5850S computer-controlled digital mass flow controller (DMFC) valves.

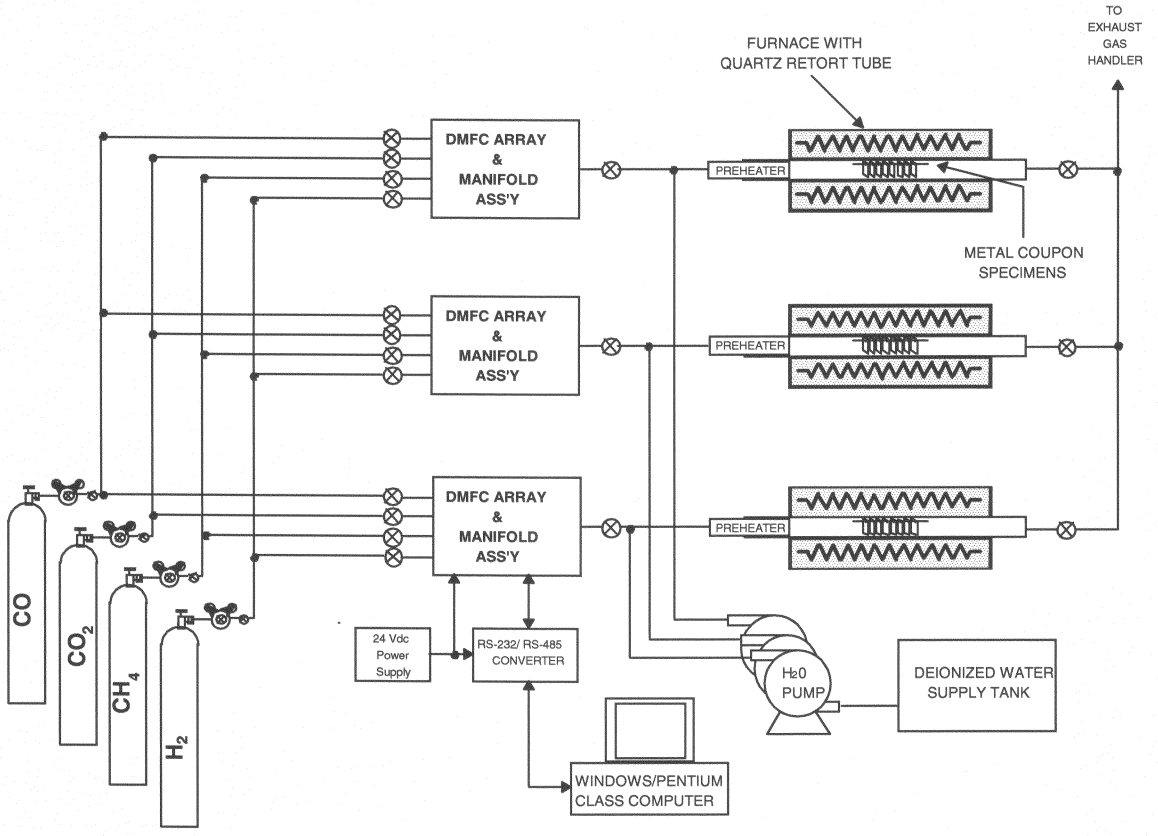

FIGURE 4 Schematic diagram for three test facilities set up for metal dusting experiments.

The output from each DMFC combined into a central manifold tube that connected to the steam/vapor preheater assembly at the input cover flange for the retort tube. The steam/ vapor preheater had a coaxial-design mixing chamber, enabling the water vapor to be entrained by the flowing gas mixture prior to passing the preheat element. The gas mixture flow rate was typically 200-400 cc/min, and the water flow rate was 1-5 cc/h. Distilled water was supplied to the preheat mixing chamber by a Watson-Marlow Model MPL micro-metering pump that was fed from a 20 L polycarbonate carboy. The micro-metering pump is based on peristaltic action, and the flow rate was adjusted by varying the rotational speed of the roller cam and/or the diameter of the flexible tubing. The gas-steam mixture flowed past the alloy test specimens to the exit port at the rear flange cap. After the gas-steam mixture exited the retort, it was passed through a chilled-water pyrex condenser to collect water vapor while the remaining gas mixture was vented to a room exhaust vent handler. Gas analysis during the exposure tests was provided by a Stanford Research Systems Model QMS100 gas analyzer. Each test system had sampling ports at the inlet of the preheat mixing chamber and at the outlet of the chilled water condenser.

Alloy test specimens were mounted on a quartz specimen tree (see Fig. 5) that was centered in the heat zone of the retort chamber. Metal-dusting experiments were conducted under isothermal conditions at temperatures between 427°C (800°F) and 704°C (1300°F). A chromel-alumel thermocouple controlled the furnace temperature. Specimen temperature was monitored with a second, sheathed chromel-alumel thermocouple inserted into the reaction chamber in the vicinity of the specimens. The actual composition of the gas mixture had a wide

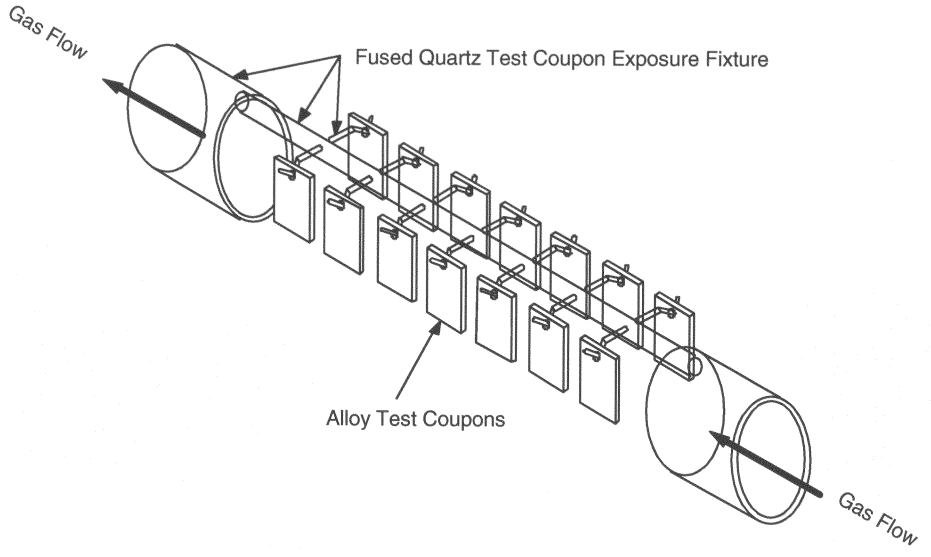

FIGURE 5 Schematic diagram of quartz specimen holder and test coupon arrangement used for metal dusting experiments.

enough range to establish a_C of ≈0.5 to ≈100 at the temperatures and pressures of interest. The exposure time periods in different experiments ranged between 5 and 1000 h, depending on the objective of the test.

Materials

The test material include a number of Fe- and Ni-base alloys, predominantly those commercially available, selected on the basis of Steering Committee discussions. Table 3 lists the nominal compositions of various alloys selected for evaluation in the program.

The Fe-base alloys included a low-Cr ferritic steel (T22), an intermediate-Cr ferritic steel (T91), and several high-Cr ferritic and austenitic steels and other alloys. The chromium and nickel contents of the high-Cr alloys were in the range of 17.3-26.7 wt.% and 9.3-36.6 wt.%, respectively, except for alloys MA 956 and APMT, which contained no nickel. Several of the Fe-base alloys contained a third element,such as Al or Si, which has a high affinity for O. For example, MA956 and APMT contained 4.5 and 4.9 wt.% Al, respectively. Alloys 153MA, 253MA, and 353MA contained Si in a range of 1.3-1.6 wt.%, whereas Alloy 38815 contained 5.8 wt.% Si.

Generally, the Ni-base alloys had a much more complex chemical composition since they contained Cr (in a range of 15.4-28 wt.%) and several other elements, such as Mo (alloys 617 and 625), Al (601, 617, 602CA, and 214), and Si (45TM and HR 160). Further, several alloys contained Nb, W, and Co, which can also influence their oxidation behavior and their resistance to metal dusting attack.

Surface engineering of select alloys is planned to examine the influence of such treatment on their resistance to metal dusting. The pretreatment involves oxidation of the alloys in an air or a low-pO_2 environment at elevated temperatures. In addition, metallic coatings (primarily

TABLE 3 Nominal chemical compositions of alloys selected for the experimental program (wt.%).

Material	C	Cr	Ni	Mn	Si	Mo	Al	Fe	Other
T22	0.20	2.3	–	0.6	0.5	1.0	-	Bal	–
T91	0.08	8.6	0.1	0.5	0.4	1.0	-	Bal	N 0.05, Nb 0.07, V 0.2
153MA	0.05	18.4	9.5	0.6	1.4	0.2	-	Bal	N 0.15, Ce 0.04
253MA	0.09	20.9	10.9	0.6	1.6	0.3	-	Bal	N 0.19, Ce 0.04
353MA	0.05	24.4	34.7	1.4	1.3	0.1	-	Bal	N 0.18, V 0.06
321L	0.02	17.4	9.3	1.8	0.5	-	-	Bal	N 0.02, Ti 0.3
310	0.03	25.5	19.5	1.7	0.7	-	-	Bal	-
800	0.08	20.1	31.7	1.0	0.2	0.3	0.4	Bal	Ti 0.31
803	0.08	25.6	36.6	0.9	0.7	0.2	0.5	34.6	Ti 0.6
38815	0.01	13.9	15.3	0.6	5.8	1.0	0.13	Bal	-
MA956	-	20.0	-	-	-	-	4.5	Bal	Ti 0.5, Y_2O_3 0.6
321	0.04	17.3	10.3	1.2	0.4	-	-	Bal	Ti 0.4, N 0.01
APMT	0.04	21.7	-	0.1	0.6	2.8	4.9	Bal	-
4C54	0.17	26.7	0.3	0.7	0.5	-	-	Bal	N 0.19
									-
600	0.04	15.4	Bal	0.2	0.1	-	-	9.7	-
601	0.03	21.9	61.8	0.2	0.2	0.1	1.4	14.5	Ti 0.3, Nb 0.1
690	0.01	27.2	61.4	0.2	0.1	0.1	0.2	10.2	Ti 0.3
617	0.08	21.6	53.6	0.1	0.1	9.5	1.2	0.9	Co 12.5, Ti 0.3
625	0.05	21.5	Bal	0.3	0.3	9.0	0.2	2.5	Nb 3.7, Ti 0.2
602CA	0.19	25.1	62.6	0.1	0.1	-	2.3	9.3	Ti 0.13, Zr 0.19, Y 0.09
214	0.04	15.9	Bal	0.2	0.1	0.5	3.7	2.5	Zr 0.01, Y 0.006
230	0.11	21.7	60.4	0.5	0.4	1.4	0.3	1.2	W 14, La 0.015
45TM	0.08	27.4	46.4	0.4	2.7	-	-	26.7	RE 0.07
HR 160	0.05	28.0	Bal	0.5	2.8	0.1	0.2	4.0	Co 30.0

RE = rare earth.

enrichment of Al or Cr in the surface regions of the alloys) will be applied by a pack diffusion process on several Fe- and Ni-base alloys. Prior to evaluation under metal dusting conditions, the coatings will be oxidized in air at elevated temperatures to develop adherent chromia or alumina scales.

TEST RESULTS AND DISCUSSION

Key Variables for Carbon Deposition and Metal Dusting

Ten short-term runs were conducted to evaluate the role of several variables in the carbon deposition process and in the initiation of metal dusting reactions. The key variables included exposure time, temperature, water content in the exposure gas, and presence/absence of catatytic material during exposure. The range of parameters in the scoping tests included exposure times of 5-100 h, temperatures of 593°C (1100°F) and 704°C (1300°F), gas mixtures with and without H_2O, and presence and absence of catalyzing agent. The specimens included pure Fe, pure Ni, Type 304 stainless steel, Alloys 800 and 601, and Fe aluminide intermetallic.

Runs 2 and 3 were conducted for 100 h at 593°C (1100°F) in Gases 4 and 5, respectively. Gases 4 and 5 had similar composition (see Table 1), except that Gas 5 had 2 vol % H_2O in addition to other gases. The carbon activity values established by the two gases are listed in Table 2. Since Gas 4 contained no H_2O, the a_C values at at 593°C (1100°F), are infinity and 4.98, based on Reactions 1 and 2, respectively. The a_C values for Gas 5 at 593°C (1100°F) are 32.3 and 5.04, based on Reactions 1 and 2, respectively.

In runs 4 and 5, the specimens were exposed to the same two gases at the higher temperature of 704°C (1300°F). The carbon activities established by Gases 4 and 5 at 704°C (1300°F) are infinity and 3.80, based on Reaction 1, whereas the values for both gases would be 0.34, based on Reaction 2. The calculations indicate that, if Reaction 1 determined carbon deposition, a carbon deposit is expected because $a_C > 1$; on the other hand, if Reaction 2 determined the deposition, no deposit of carbon is anticipated because a_C is <1. The observation of significant deposit of carbon in the runs at 704°C (1300°F) indicates that Reaction 1 determines a_C in the exposure environment.

Additional experiments showed that the gas phase reactions, accentuated by the catalytic effect of the metallic specimens consisting of Fe- and Ni-base alloys, lead to $a_C >> 1$, causing a copious amount of carbon deposit even within a short time period of 5 h.

Characteristics of Deposits

Scanning electron microscopy (SEM), Raman spectroscopy, energy dispersive X-ray spectroscopy (EDX), and X-ray diffraction (XRD) have been used to study the microstructure, electron binding, and phase chemistry of the metal dusting products. Graphite has a layered structure with the space group $P6_3/mmc$. Carbon atoms within the layers bond strongly through sp^2 hybridization and arrange in a two-dimensional honeycomb network. The layers are stacked in a hexagonal crystal structure and are bound together by van der Waals force. Because this force is weak, the C-C distance of 335.4 pm between layers is large (Franklin 1951). For this reason, graphite crystals readily disorder along the c-axis (Krebs 1968). The Raman scattering from various forms of carbon is sensitive to the structural disorder of the material (Tuinstra and Koenig 1970; Nakamizo et al. 1977; Nakamizo et al. 1978; Dillon and Woollam 1984). As a result, Raman spectroscopy, a useful nondestructive technique for structural characterization of carbon materials, was used to analyze the characteristics of the carbon that was generated in the metal dusting experiments. Details on the results and analysis are discussed in a companion paper, presented in this workshop (Zeng et al. 2002).

Behavior of Fe- and Ni-base Alloys

Several of the screening tests were used to establish the testing conditions for long-term experiments with Fe- and Ni-base alloys. One of the important results was that the Fe- and Ni-base alloys should not be exposed simultaneously in the same run, since the Fe-base alloys exhibited a carbon deposit much earlier than the Ni-base alloys, and significant cross contamination occurred between these classes of alloys. Even among the Fe-base alloys, the ones with lower Cr contents (e.g., T22) were much more susceptible to carbon deposition and metal dusting attack when exposed under the same conditions of temperature, time, and gas composition.

Several 1000-h experiments were conducted at 482°C (900°F) and 593°C (1100°F) with Fe- and Ni-base alloys in Gas 2 environment, which simulated the chemistry of the reformer effluent. This gas contained 23 vol.% H_2O, which was achieved by pumping water into the reaction chamber through a specially designed heater.

Detailed analysis of the specimens after exposure at 593°C (1100°F) showed little, if any, deposit of carbon on the specimen surfaces. Carbon was noted primarily on the T22 specimen, and virtually no carbon was detected on Ni-base alloys. The major difference between these runs and the scoping tests was the amount of H_2O in the exposure environment. Note that a_C

established by Gas 2 at 593°C (1100°F) is ≥2 (see Table 2), yet no deposit of carbon was noted, even after 1000 h of exposure.

Another experiment was conducted to examine the competing effects of oxidation and carbon deposition/metal dusting on alloy behavior. In this experiment, Fe-base alloys were exposed in Gas 2, but with only 2 vol.% H_2O, instead of the 23 vol.% tested earlier. The calculated values for a_C in experiments at 593°C (1100°F) with 23 and 2 vol.% H_2O were 2 and 30, respectively. In the experiment with low H_2O, a copious amount of carbon was observed on specimen surfaces. Figure 6 shows a macroscopic photograph of the specimens exposed in the two experiments.

Detailed analysis of the surfaces of specimens exposed in the gas environment containing 23 vol.% H_2O indicated development of oxide layers on most of the specimens. Figures 7-9 show SEM photomicrographs of surfaces of several Fe-base alloys after 1000-h exposure at 593°C (1100°F). In general, most of the alloys exhibited oxide scales on the surface; however, at isolated locations some carbon deposit adhered to the surface. No significant pitting-type attack was noted in any of the high-Cr specimens. The only alloy that exhibited a copious amount of carbon deposit and metal dusting was T22 steel, which contained 2.25 wt.% Cr.

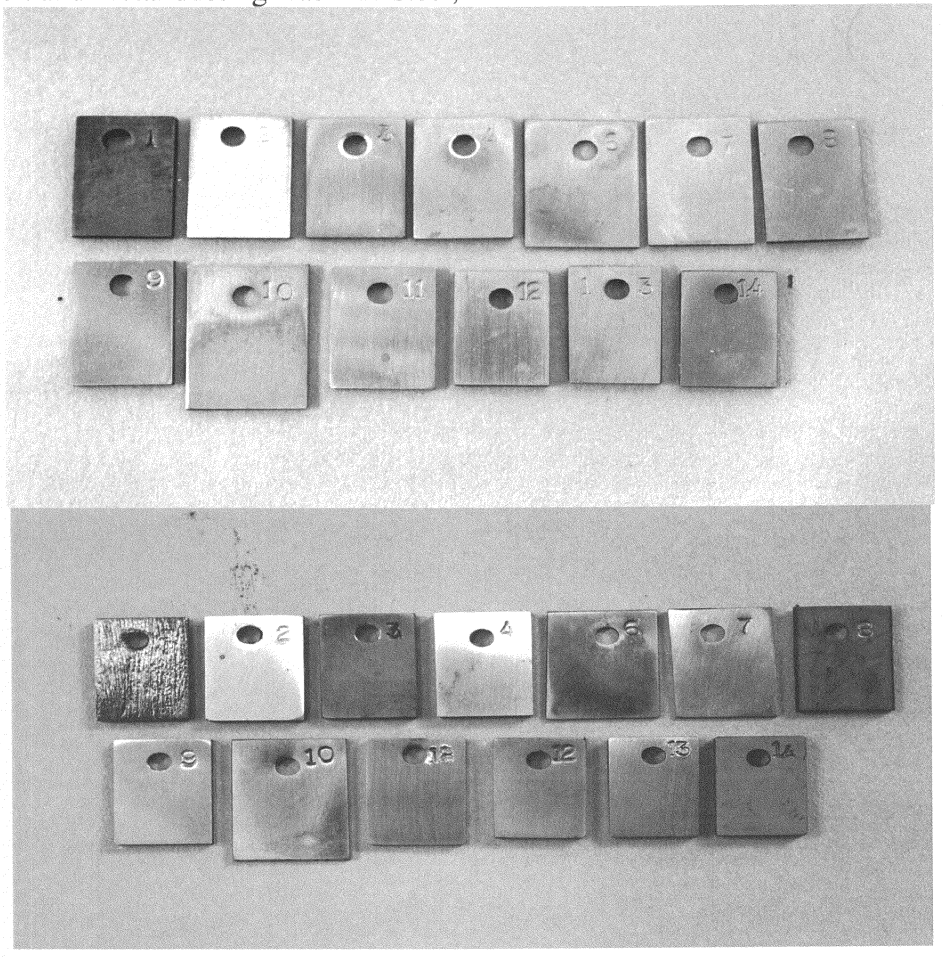

FIGURE 6 Macrophotographs of Fe-base alloy specimens after 1000-h exposure at 593°C (1100°F) in (top) Gas 2 with 23.1 vol.% H_2O and (bottom) Gas 2 with 2 vol.% H_2O.

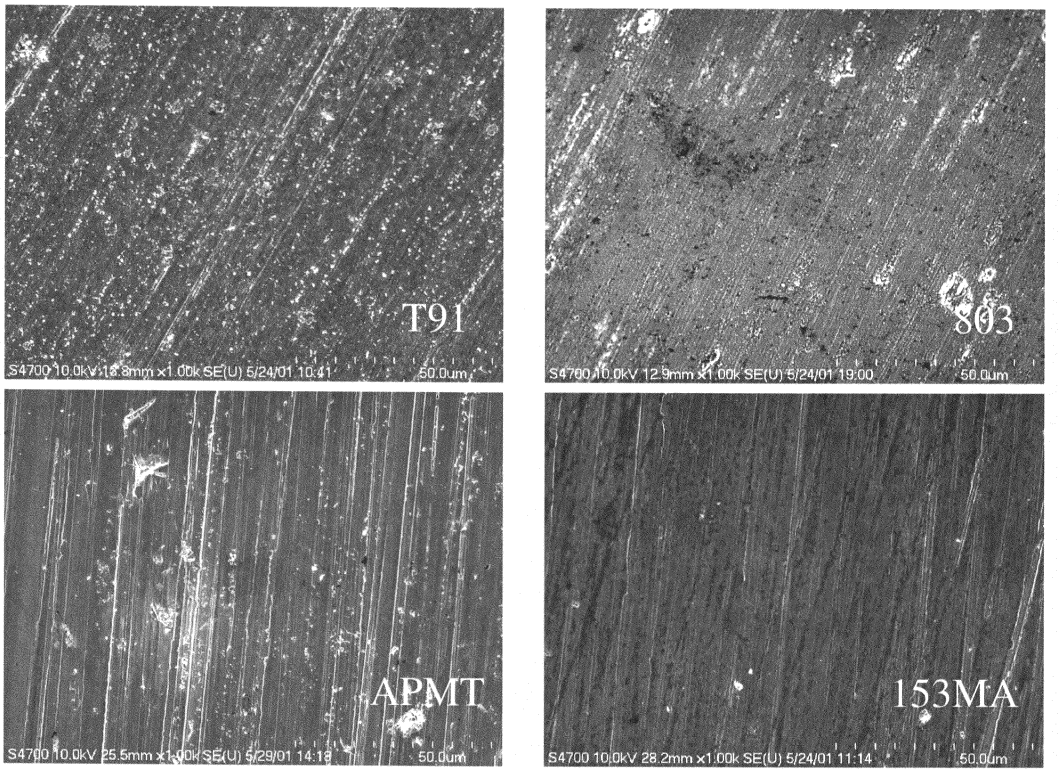

FIGURE 7 SEM photomicrographs of surfaces of (top left) T91, (top right) 803, (bottom left) APMT, and (bottom right) 153MA after 1000 h exposure in Gas 2 environment.

EDX analysis showed that MA956 and APMT (which contained 4.5 and 4.9 wt.% Al, respectively) developed thin alumina scales, whereas 253MA and 38815 (even though they contained 1.6 and 5.8 wt.% Si, respectively) only developed chromia or (Fe,Cr) oxide scales.

Figures 10 and 11 show SEM photomicrographs of surfaces of several Ni-base alloys after 1000-h exposure in Gas 2 environment at 593°C (1100°F). In general, Ni-base alloys develop much thinner oxide scales than the Fe-base alloys. However, carbon adherence onto the surface of Ni-base alloy is much stronger, as evidenced by the presence of it even after prolonged ultrasonic cleaning. Furthermore, the carbon deposit can be seen as striations, forming preferentially along the polishing lines on the surface and in a nonuniform distribution.

To examine carbon penetration, if any, into the alloys, several of the exposed specimens were cut, mounted, polished, and cross sectioned for SEM and EDX. Figures 12 and 13 show the SEM photomicrographs of cross sections of several Fe- and Ni-base alloys, respectively, after 1000-h exposure in the metal dusting environment. T91 alloy developed a thin oxide scale and virtually no carbon penetration, even after 1000-h exposure. The oxide scale developed on Alloy 800 was porous and discontinuous, and several pits initiated from the surface (see Fig. 12). Alloy 321 developed a thin oxide scale with almost no carbon penetration into the alloy, indicating that the spots of carbon observed on the surface (see Fig. 8) are primarily adherent to the thin oxide layer.

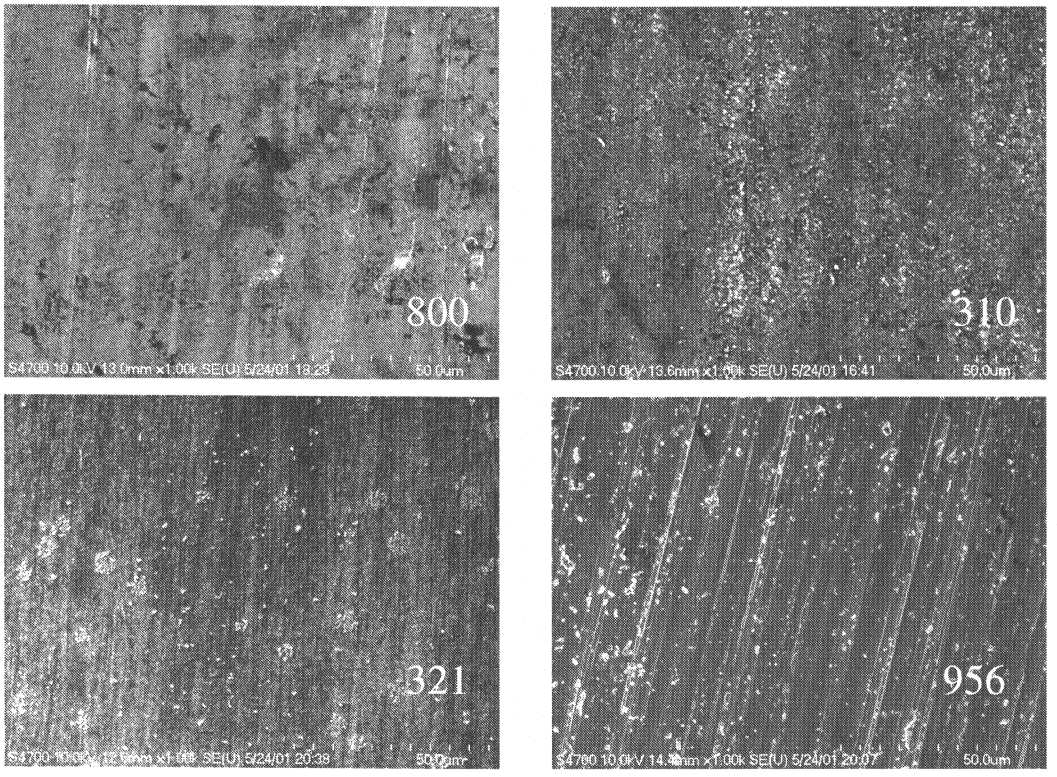

FIGURE 8 SEM photomicrographs of surfaces of (top left) Alloy 800, (top right) 310 SS, (bottom left) 321 SS, and (bottom right) MA956 after 1000-h exposure in Gas 2 environment.

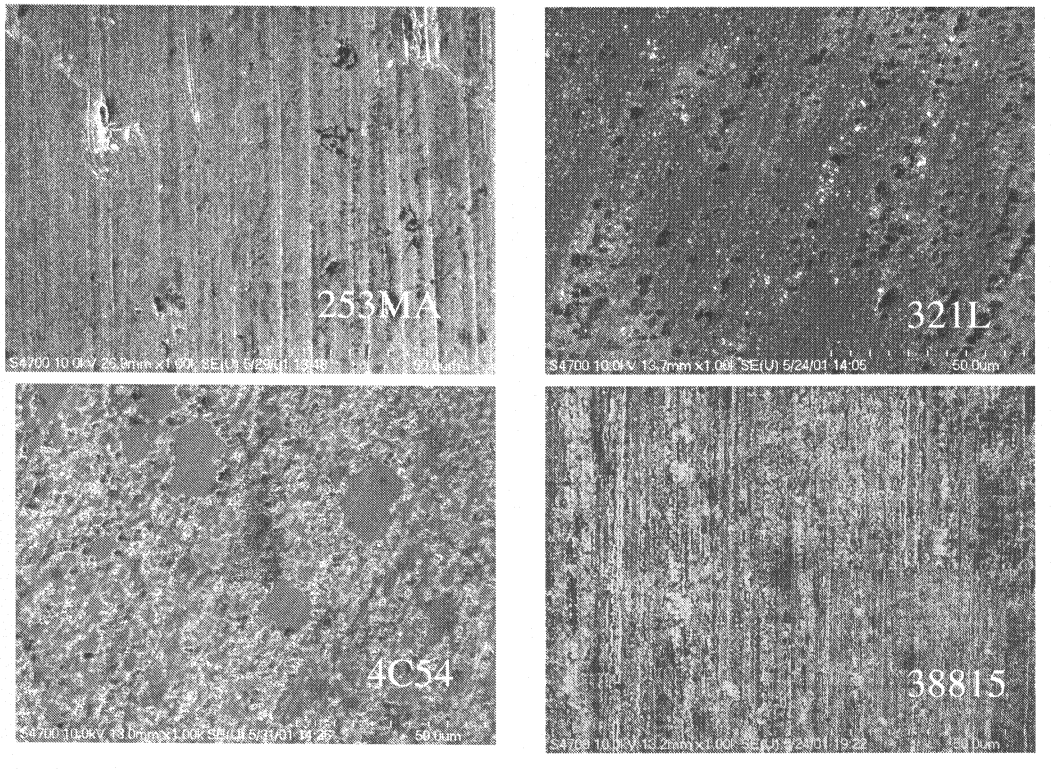

FIGURE 9 SEM photomicrographs of surfaces of (top left) 253MA, (top right) 321L, (bottom left) 4C54, and (bottom right) 38815 after 1000-h exposure in Gas 2 environment.

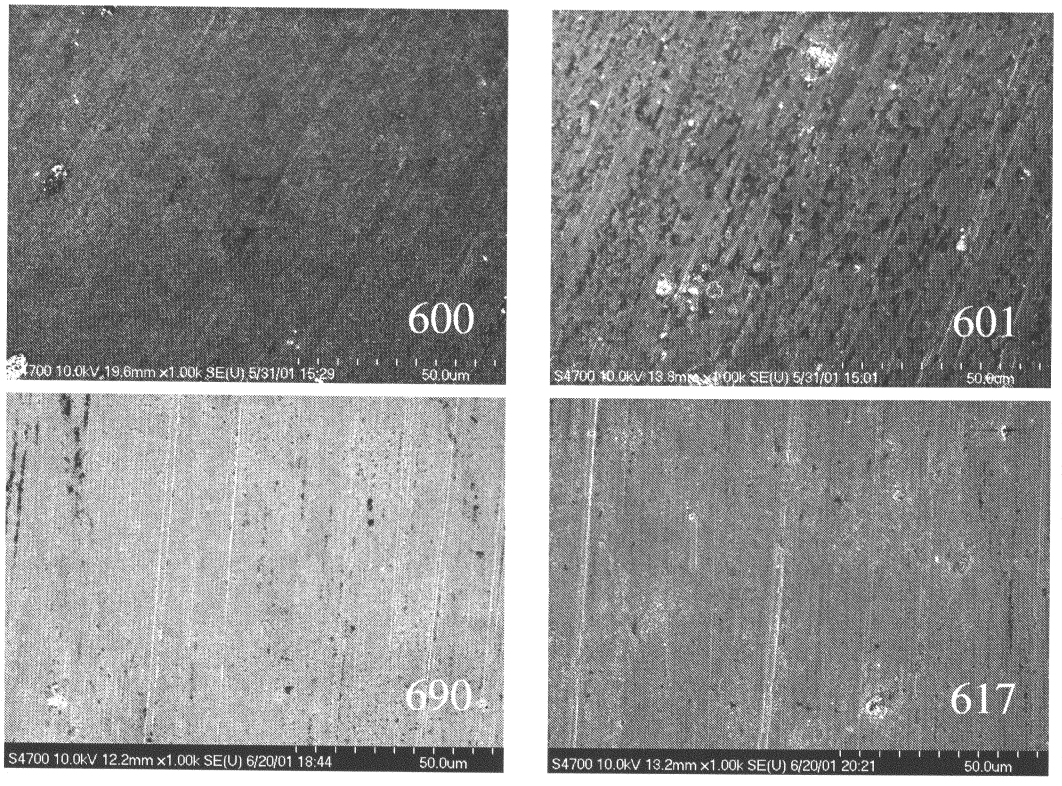

FIGURE 10 SEM photomicrographs of surfaces of (top left) 600, (top right) 601, (bottom left) 690, and (bottom right) 617 after 1000-h exposure in Gas 2 environment.

Among the Ni-base alloys, 600, 690, 602CA, and 45TM were examined in cross section. Figure 13 shows the SEM photomicrographs of these specimens. The scales were continuous and adherent to the substrate, and the thickness was 0.1-0.2 μm after 1000-h exposure in Gas 2 at 593°C (1100°F). None of the alloys exhibited internal penetration of carbon or pitting attack.

Raman spectroscopy was used to analyze the carbon that adhered to the surface on Fe- and Ni-base alloys exposed in Gas 2 environment at 593°C (1100°F). Figure 14 shows Raman spectra (frequency range 1200-1700 cm^{-1}) for carbon that adhered to the surface of alloys T22, T91, 153MA, and 253MA (which had Cr contents of 2.25, 8.6, 18.4, and 20.9, respectively). The alloy T22, which exhibited severe metal dusting attack, had much sharper peaks for carbon when compared with those for the other alloys. Figure 15 shows the Raman spectra (frequency range 200-800 cm^{-1}) obtained on the surfaces of several Fe-base alloys with different Cr contents, after 1000-h exposure. The Raman spectra in the frequency range 200-800 cm^{-1} clearly show that alloys with Cr >8.6 wt.% develop oxide scales, as evidenced by the SEM photomicrographs presented earlier. The peaks at ≈550 and ≈680 cm^{-1} correspond to Cr_2O_3 and (Fe,Cr) oxide spinel, respectively. Lack of oxide scale on alloy T22 (which contained 2.3 wt.% Cr) led to metal dusting attack during the 1000-h exposure.

Figure 16 shows the Raman spectra (frequency range 200-800 cm^{-1}) for three Ni-base alloys with different Cr contents after 1000-h exposure in the metal dusting environment at 593°C (1100°F). The alloys predominantly developed Cr_2O_3, as indicated by the peak at ≈550 cm^{-1}. The peak height seems to be strongly dependent on the Cr content of the alloy; for example, among the three alloys, the peak height is smallest for Alloy 600 (15.4 wt.% Cr)

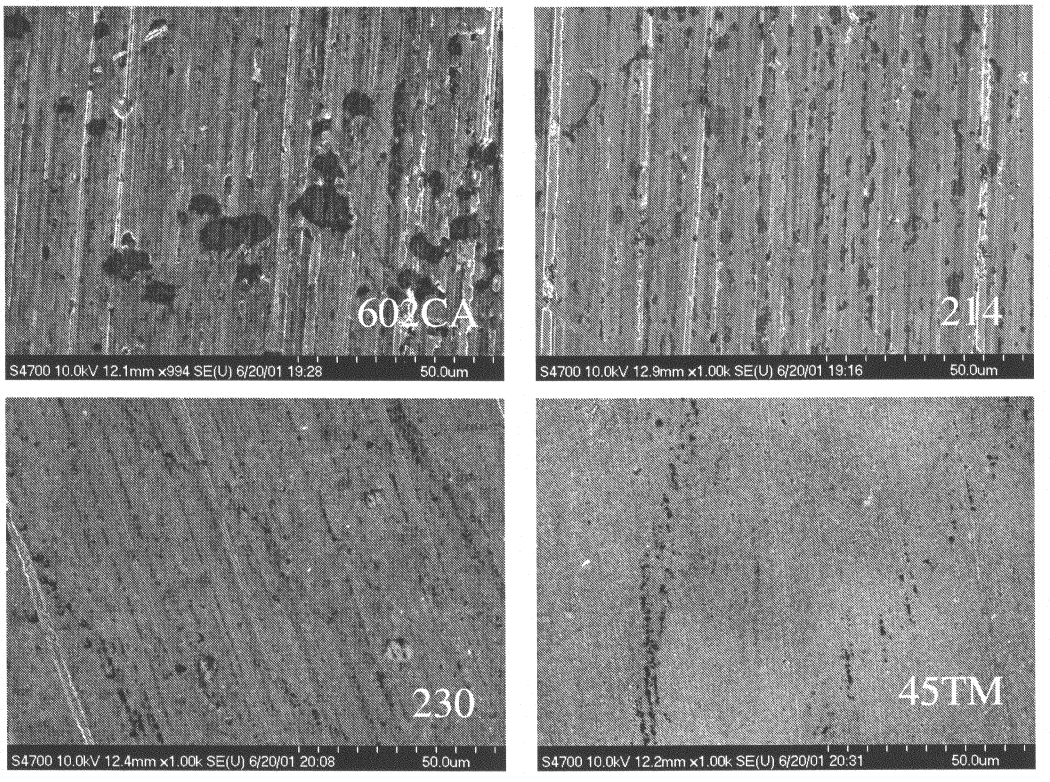

FIGURE 11 SEM photomicrographs of surfaces of (top left) 602CA, (top right) 214, (bottom left) 230, and (bottom right) 45TM after 1000-h exposure in Gas 2 environment.

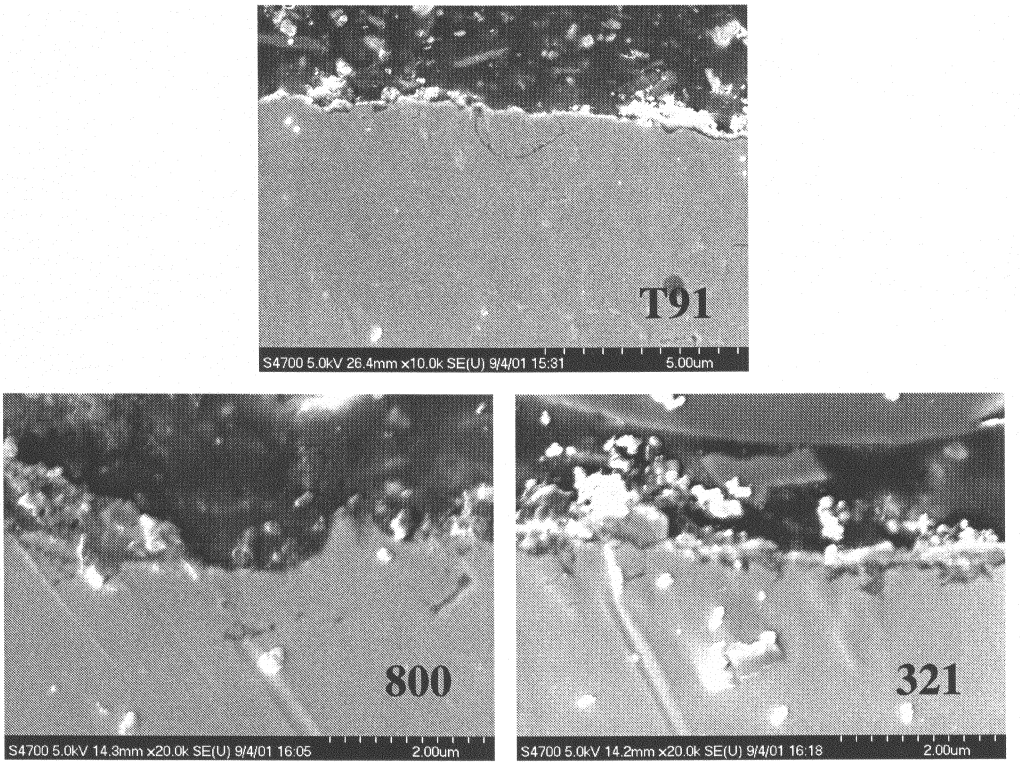

FIGURE 12 SEM photomicrographs of cross sections of (top) T91, (bottom left) 800, and (bottom right) 321 after 1000-h exposure in Gas 2 environment.

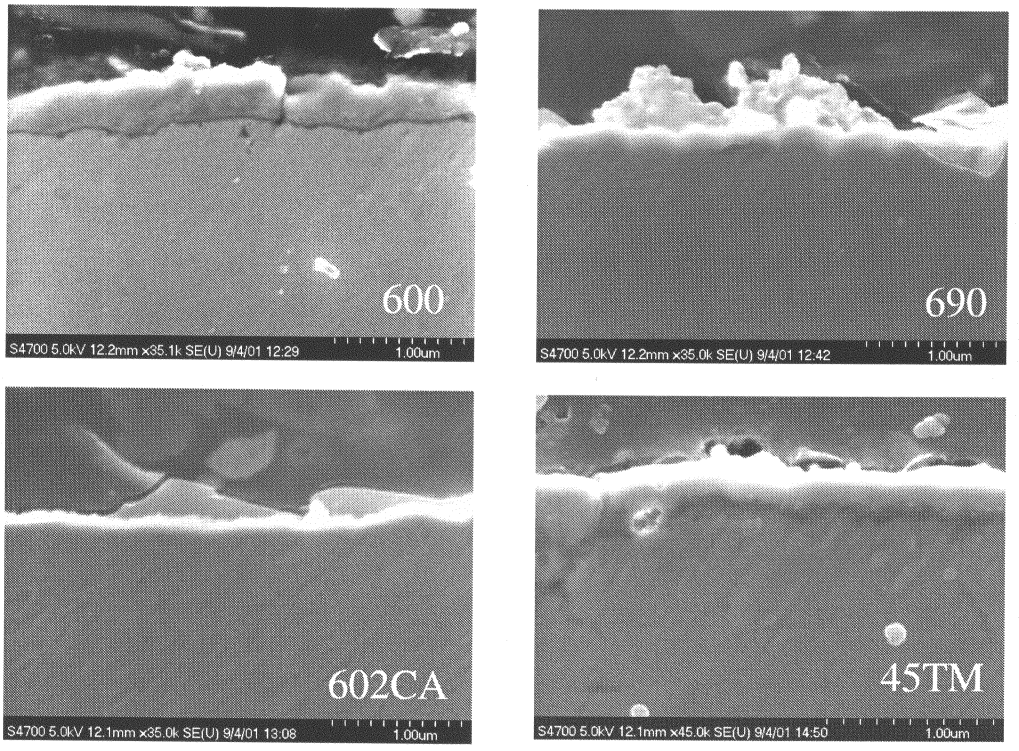

FIGURE 13 SEM photomicrographs of cross sections of (top left) 600, (top right) 690, (bottom left) 602CA, and (bottom right) 45TM after 1000-h exposure in Gas 2 environment.

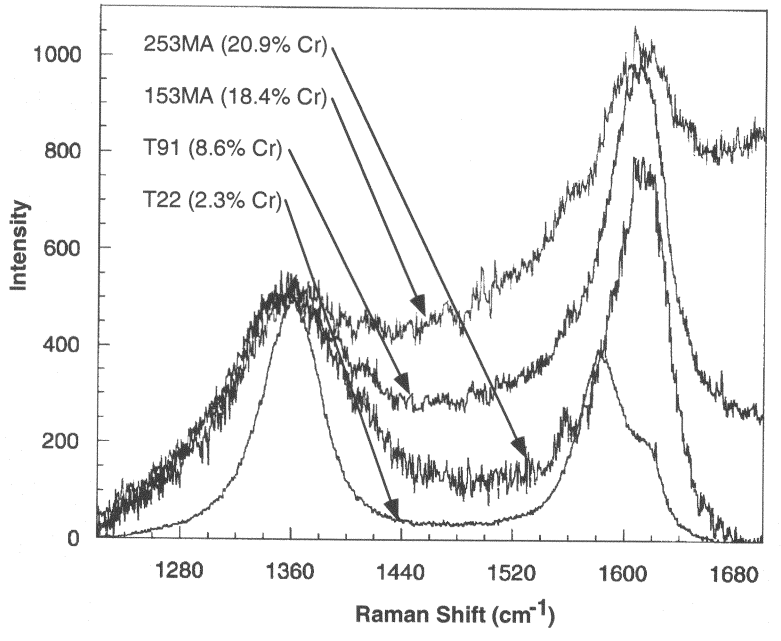

FIGURE 14 Raman spectra for carbon adhered to several alloys with different Cr contents after 1000-h exposure in Gas 2 environment at 593°C (1100°F).

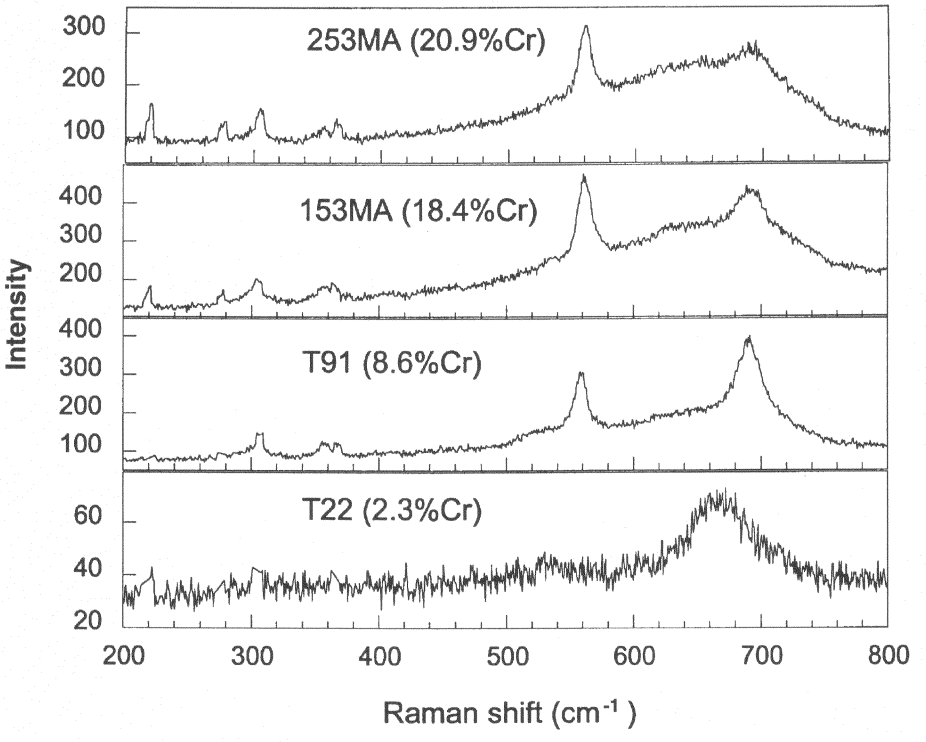

FIGURE 15 Raman spectra for surfaces of several Fe-base alloys with different Cr contents after 1000-h exposure in Gas 2 environment at 593°C (1100°F).

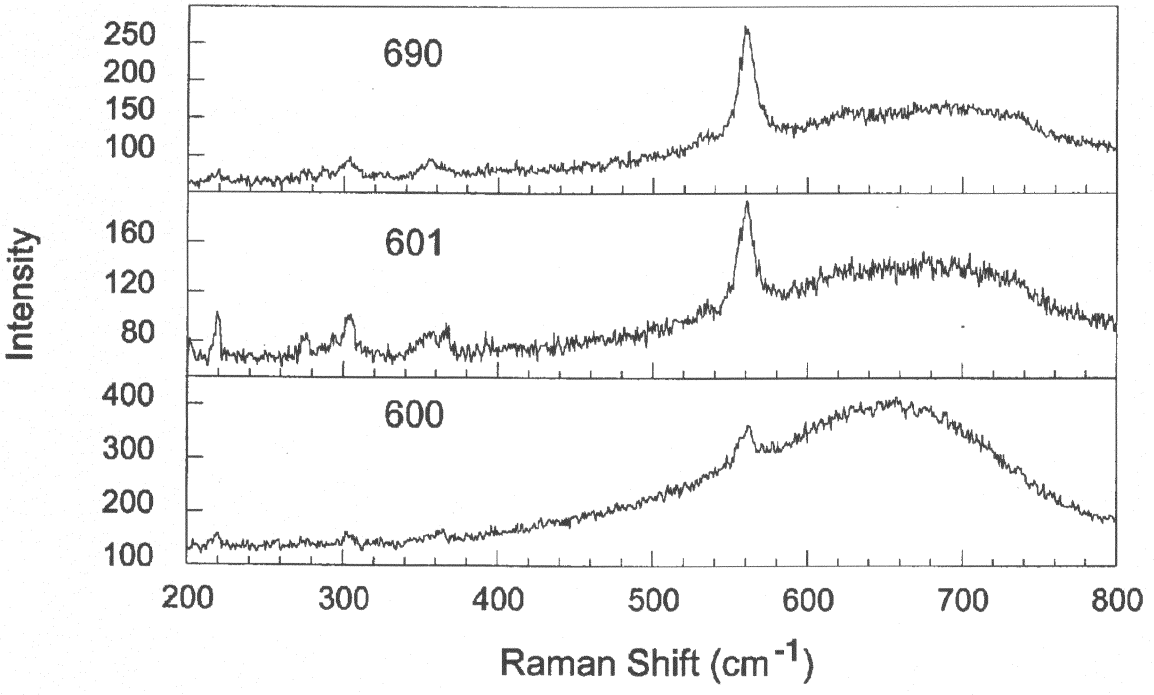

FIGURE 16 Raman spectra for surfaces of several Ni-base alloys with different Cr content after 1000-h exposure in Gas 2 environment at 593°C (1100°F).

and largest for Alloy 690 (27.2 wt.% Cr). The broad feature in these spectra at ≈660 cm^{-1} is not currently identified but seems to disappear as the Cr level in the alloy increases.

Raman analysis was also performed on several alloys that had deliberate additions of Al (Zeng et al 2001). Even though the Al content of alloys MA956 and APMT is similar, their scaling behavior is somewhat different. Alloy APMT predominantly developed Cr_2O_3 scale, as evidenced by a sharp peak at ≈550 cm^{-1}, whereas the alloy MA956 (which exhibited a much thinner scale) showed a less developed peak at a frequency >550 cm^{-1}. A peak at ≈700 cm^{-1} was observed in the APMT alloy; this peak is not presently identified, but it does not correspond to any of the Al_2O_3 phases. Even in the higher frequency range (corresponding to carbon), the relative intensities for the D-to-G band for the two alloys are different, but the cause is not known. The Raman spectra for the alloys 602CA and 214 (with a lower Al content) were similar in the entire frequency range.

Raman analysis was also performed on several alloys that had deliberate additions of Si (Zeng et al 2001). The alloys selected for comparison included 253MA, 38815, 45TM, and HR160, which contain 13.9-28.0 wt.% Cr and 1.6-5.8 wt.% Si, respectively. The results showed that all four alloys developed predominantly Cr_2O_3 scale, which is expected based on oxidation studies of Si-containing alloys. In general, Si can form a silica scale at the Cr_2O_3/alloy interface since the diffusion coefficient for Si is much smaller than that for either Cr or Fe, and these alloys can rarely form an external scale of silica at the concentration levels present. The Raman spectra in the frequency range of 1200-1800 cm^{-1} showed similar peaks on all four alloys, indicating that the variation in Si content had virtually no effect on the carbon deposition.

Initiation of Metal Dusting

The results presented thus far clearly indicate that the gas chemistry used (simulating reformer effluent) in our study can deposit carbon by the two reactions discussed earlier. Furthermore, decreasing the H_2O content (e.g., from 23 to 2.0 vol.%) in the gas can increase a_C, thereby accelerating carbon deposition. However, whether the deposited carbon can initiate metal dusting in Fe- and Ni-base alloys is strongly influenced by the oxidation characteristics of the alloys. The competition between the oxidation process to form a continuous oxide scale on a given alloy surface and deposition and penetration of carbon will determine the incubation time for metal dusting attack to occur. If an alloy can develop a protective oxide scale fast enough and early during exposure, then subsequent deposition of carbon on top of the oxide layer can delay initiation of metal dusting.

In most earlier studies on metal dusting, the researchers selected gas compositions that yielded carbon activities >>1, which led to deposition of carbon on the specimens from the beginning of the exposure (Grabke 1998; Maier et al. 1998; Baker and Smith 2001; Levi et al. 2001). Besides exposure to high carbon activity, the alloys did not have much time (before carbon deposition) to develop a protective oxide scale. Therefore, the earlier studies emphasized interaction of the deposited carbon with the constituents of the structural alloys and examined the role of alloy-related variables (such as alloy composition; Fe, Cr, and Ni contents; surface preparation; and surface roughness) on alloy degradation. A comparative analysis was conducted on the carbon activities and oxygen partial pressures established in several studies to better understand the role of gas chemistry in the metal dusting behavior of structural alloys.

Table 4 lists the chemical compositions of gases used in several of the studies. The H_2O content in the past studies was in the range of 0-2.4 vol.%, whereas in the present studies, we used H_2O contents of 0, 2, and 23 vol.% (the last one is typical of the effluent from a H_2 reformer). Similar to results presented in an earlier section, we calculated a_C for the gas mixtures (used in earlier studies) at several temperatures in the range of 425-760°C (800-1400°F).

Table 5 lists the carbon activity values at 593°C (1100°F) calculated for gas mixtures used in past studies and the current program. The calculations are based on whether Reaction 1 or 2 was dominant or equilibrium between different gas species prevailed at the elevated temperature. The carbon activities in past studies have been >>1, irrespective of whether Reaction 1 or 2 dominated the process. If the gases were in thermodynamic equilibrium, the carbon activity in most cases is around 1. A carbon activity value of infinity under the Reaction 1 column (in Table 5) arises because the inlet gas mixture in the study did not contain H_2O, whereas infinity under Reaction 2 arises because the mixture did not contain CO_2. The calculated carbon activity values are based on initial gas compositions. Once Reaction 1 starts, H_2O will be generated, and the local carbon activity will be less than the calculated values in Table 5. However, carbon deposition would have occurred, and it would be almost impossible to develop a protective oxide scale on the alloy surface.

Table 4 Gas chemistries used in metal dusting research.

	Composition in vol.%				
Researcher	**CO**	**CO_2**	**CH_4**	**H_2**	**H_2O**
Grabke	24.7	-	-	73.4	1.9
Maier et al.	24.4	-	-	73.2	2.4
Baker/Smith	70.0	4.0	-	25.3	0.75
Levi et al.	25.0	-	-	75.0	-
Natesan et al. (gas 4)	17.5	8.3	-	74.2	-
Natesan et al. (gas 5)	17.6	8.3	-	72.2	2.0
Natesan et al. (gas 2)	18.0	5.6	1.1	52.0	23.0

Table 5 Carbon activity and oxygen partial pressure values at 593°C (1100°F), calculated for gas mixtures used by various researchers.

	Carbon activity			Oxygen pressure (in atm), based on		
Researcher	**Rxn 1**	**Rxn 2**	**Eqm**	**CO/CO_2**	**H_2/H_2O**	**Eqm**
Grabke	47.5	∞	1.2	-	6.7×10^{-28}	7.6×10^{-26}
Maier et al.	37.1	∞	1.2	-	1.1×10^{-27}	7.7×10^{-26}
Baker/Smith	118.0	165.0	0.8	3.1×10^{-28}	1.0×10^{-28}	3.9×10^{-25}
Levi et al.	∞	∞	1.2	-	-	6.9×10^{-26}
Natesan et al. (gas 4)	∞	5.0	1.3	2.2×10^{-26}	-	1.1×10^{-25}
Natesan et al. (gas 5)	32.5	5.0	1.2	2.2×10^{-26}	7.6×10^{-28}	1.2×10^{-25}
Natesan et al. (gas 2)	2.0	7.9	0.7	9.5×10^{-27}	1.2×10^{-25}	2.4×10^{-25}

Table 5 also lists the pO_2 values at 593°C (1100°F), calculated for three possible assumptions: (1 and 2) CO/CO_2 or H_2/H_2O ratio determines the pO_2, or (3) thermodynamic equilibrium exists among all the gaseous species at the elevated temperature. The calculations indicate that for a given gas composition, the equilibrium pO_2 values are always higher than those established by either CO/CO_2 or H_2/H_2O ratios. If one assumes that the gas composition does not change significantly during flow from the exit of the reformer to low-temperature sections of the waste-heat boiler (i.e., the carbon deposition reactions are slow enough that the generation of carbon by catalysis of gas-phase constituents causes little change in bulk gas chemistry), then the pO_2 in the environment will be dictated by the higher of the two values calculated from the CO/CO_2 and H_2/H_2O ratios.

From the materials standpoint, one can analyze the type of interactions between the constituents of the alloy and the environment by means of thermochemical diagrams. Since carbon deposition and formation of the oxide layer on the metal surface are of interest for materials exposed to metal dusting environments, oxygen/carbon diagrams were generated for several temperatures in the range of 400-700°C. Figure 17 shows the oxygen/carbon thermochemical diagrams for Fe, Cr, and Ni calculated for 593°C (1100°F). The diagrams depict the stability fields for the metals, oxides, and carbides of Fe, Cr, and Ni in terms of carbon and oxygen partial pressures. Superimposed on these diagrams (indicated by boxes) are the oxygen and carbon partial pressure ranges for gas mixtures used by various researchers in metal dusting studies. The calculations show that Fe_3C, Cr_2O_3, Ni, and Ni_3C are the phases that will be stable in the environments used in the laboratory research and in gas mixtures corresponding to the effluent of the H_2 reformer (Gas 2).

For pure Fe and for Fe-base alloys containing low concentrations of Cr (e.g., T22), the calculations indicate that Fe_3C would be the primary phase that forms upon exposure to the metal dusting environment. In the case of Fe- and Ni-base alloys containing high Cr concentration, pure Cr oxide or Cr-rich oxide will be the stable phase that forms upon exposure of the alloy to metal dusting environments, unless precipitous deposition of carbon occurs from the beginning of exposure such that the alloy surface is completely covered with carbon and no time is available to develop an oxide scale. We believe such was the case in most of the earlier studies, which had $a_C >> 1$ and extremely low H_2O content. In the study conducted at ANL, the H_2O content of Gas Mixture 2 was 23 vol.%, and a_C was somewhat greater than 1. For this condition, the alloys exhibited oxide scales with subsequent deposition of carbon on top of the oxide.

In reformers, the metal dusting attack generally occurs over a period of years of service, while in laboratory studies the attack occurs over a period of a few hours to few days. Thus, in the reformer, the degradation process is dictated by the breakdown of the oxide scale, while in the laboratory studies, attack begins right from the start. The ongoing program at ANL will examine the competition between the oxide scale development and its breakdown leading to metal dusting attack. Therefore, an understanding of the incubation period and initiation time for development of metal dusting morphology (such as surface pits) will be emphasized, in addition to evaluation of the role(s) of alloy chemistry and surface modification in mitigating metal dusting degradation.

SUMMARY

The deposition of carbon from cabonaceous gaseous environments is prevalent in many chemical and petrochemical processes such as reforming systems, syngas production systems, iron reduction plants, and others. One of the major consequences of carbon deposition is the

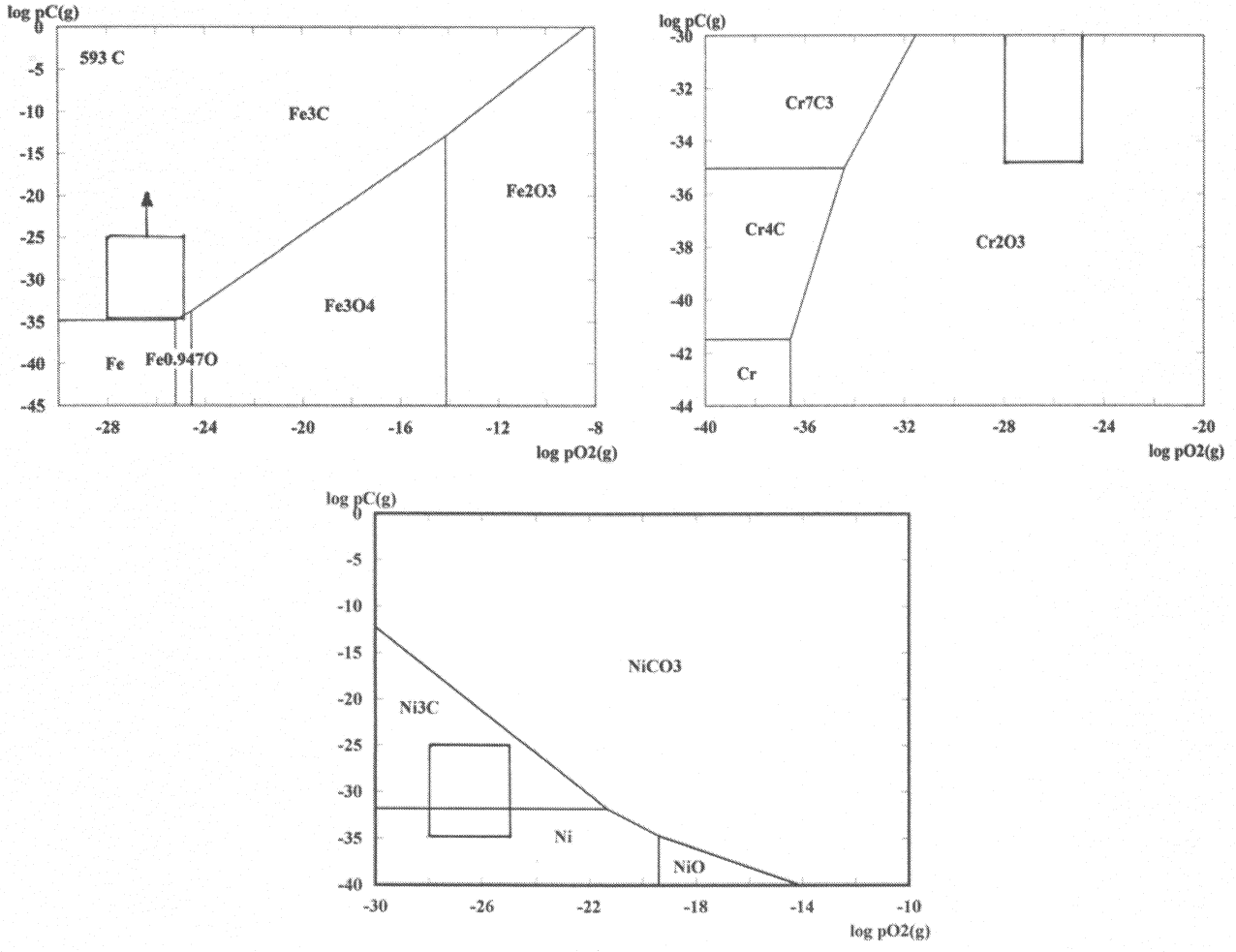

FIGURE 17 Oxygen/carbon thermochemical diagrams for Fe, Cr, and Ni calculated for 593°C (1100°F).

degradation of structural materials by a phenomenon known as "metal dusting." There are two major issues of importance in metal dusting. First is formation of carbon and subsequent deposition of carbon on metallic materials. Second is the initiation of metal dusting degradation of the alloy. The first is influenced by a_C in the gas mixture and availability of the catalytic surface for carbon-producing reactions to proceed. There may be a threshold in a_C (>>1) for carbon deposition. Metal dusting of the alloy in the reformer environments is determined by a competition between the oxide scale development and access of the virgin metal surface to the carbon deposit. The presence of an oxide scale may not prevent metal dusting but can delay its initiation, thereby slowing the overall attack.

The local nature of dusting (initiated by pits on the alloy surface) on both Fe- and Ni-base alloys shows that defects in the oxide scales play a large role in initiation. Oxide scaling may not occur if a_C is >>1 and/or if the H_2O content in the environment is very low. Laboratory experiments have clearly indicated the effect of gas chemistry (in particular H_2O content) in the scaling, carbon deposition, and dusting initiation. It is evident that the environment in reformers is high enough in pO_2 that a Cr-rich alloy will develop a chromia scale (given enough exposure time) before carbon deposition.

ACKNOWLEDGMENTS

This work was sponsored by the U.S. Department of Energy, Office of Industrial Technologies, and Dr. Charles Sorrell was the Program Manager for the project. Specimens of various alloys were supplied by Haynes International, AvestaPolarit, Sandvik Steel, Special Metals, Allegheny Ludlum, and Krupp VDM.

REFERENCES

Baker, B. and G. D. Smith, 2001, NACE Corrosion 2001, Paper # 01375.

Camp, E. Q., C. Phillips, and L. Gross, 1945, Corrosion, 1, 149.

Dillon, R. O. and J. A. Woollam, 1984, Physical Review B, 29, 3482.

Franklin, R. E., 1951, Acta Cryst., 4, 253.

Grabke, H. J., Materials and Corrosion, 1998, 49, 303.

Hoyt, W. B., R. H. Caughey, 1959, Corrosion, 15, 627.

Krebs, H., 1968, Fundamentals of Inorganic Crystal Chemistry, McGraw-Hill, p. 150.

Levi, T. P., N. Briggs, I. Minchington, and C. W. Thomas, 2001, NACE Corrosion 2001, Paper # 01375.

Maier, M., J. F. Norton, and P. D. Frampton, 1998, Materials and Corrosion, 49, 330-335.

Nakamizo, M., H. Honda, M. Inagaki, and Y. Hishiyama, 1977, Carbon, 15, 295.

Nakamizo, M., H. Honda, and M. Inagaki, 1978, Carbon, 16, 281.

Tuinstra, F. and J. L. Koenig, J. Chem. Phy. 1970, 53, 1126.

Zeng, Z., K. Natesan, and V. Maroni, 2001, this workshop proceedings.

APPLICATIONS OF MOLECULAR SPECTROSCOPY METHODS TO THE STUDY OF METAL DUSTING CORROSION

V. A. MARONI
Argonne National Laboratory, Argonne, Illinois*

ABSTRACT

The interrogation of molecular vibrations in crystalline and amorphous solids by Raman and infrared spectroscopy methods can provide a wealth of revealing information concerning the composition, morphology, and spatial distribution of the extant phases. When these measurements are made in situ, such as during processes taking place in extreme environments (e.g., elevated temperature and pressure, oxidizing or reducing), where phases are evolving and/or dissipating, it is also possible to derive kinetic and mechanistic parameters. This paper summarizes the possibilities and limitations involved in using various types of Raman and infrared measurement methods to study metal dusting corrosion. Applications of conventional, microprobe, and imaging molecular spectroscopy approaches are discussed, with examples taken directly from metal dusting investigations. Some perspective is offered concerning the origin of observable condensed matter phonons emanating from the surface films and the carbon particles that accompany carbon dusting on various types of metals and alloys. Concepts for the systematic investigation of carbon dusting chemistry using molecular spectroscopy methods are presented.

INTRODUCTION

The application of molecular spectroscopy methods to problems in materials science is receiving increased emphasis. The molecular vibrations or, in the case of solid materials, the phonons that are detectable by molecular spectroscopy measurement techniques are characteristic/indicatory features of molecular and crystalline materials. Since the issues involved in the examination of carbon dusting corrosion deal primarily with solid phases, the remainder of the discussion will summarily describe the measurement and interpretation of the molecular spectra of solids, using examples taken from Raman studies of the carbon dusting corrosion of iron.

The most commonly used methods for measuring molecular spectra are based on Raman scattering and on the absorption, transmission, or reflection of infrared radiation. Laser-excited Raman spectroscopy, dispersive infrared spectroscopy, and Fourier transform infrared (FTIR) spectroscopy are well-developed methods and the associated instrumentation can be found in virtually all laboratories where comprehensive materials analyses are performed. Informative discussions of the general methodologies and their application to solid materials can be found, e.g., in Suëtaka (1995) and Ferraro and Krishnan (1990). Two features of the Raman and infrared instrumentation methodologies that make them especially useful for the study of corrosion processes and corroded specimens are (1) their adaptability to in situ investigations (including conditions of elevated temperature and wide ranging pressure) and (2) the effective use that can be made of their integration with conventional optical and confocal microscopes.

* *Corresponding author address:* V. A. Maroni, Argonne National Laboratory, 9700 South Cass Ave., Argonne, IL 60439; e-mail: Maroni@cmt.anl.gov.

ESSENTIAL ELEMENTS OF MOLECULAR SPECTROSCOPY

A detailed explanation of the origin of molecular vibrations is beyond the scope of this paper. A sufficient view can be gained by considering the simplest case of all—the diatomic oscillatory. For the diatomic molecule

A-----B

where the masses of atoms **A** and **B** are given by $\mathbf{m_A}$ and $\mathbf{m_B}$, we can assume that the bond between **A** and **B** is a spring with spring constant **k** (analogous to a bond force constant). In the limit where the frequency of oscillation, **ν**, can be described in the harmonic oscillator approximation, we obtain (from application of simple two body kinematics) the expression

$$\nu = (1 / 2\pi c)\,(k / m_r)^{1/2}$$

where $\mathbf{m_r}$, the reduced mass of the harmonic oscillator, is given by

$$m_r = (m_A m_B) / (m_A + m_B)$$

The treatment of larger molecules and crystalline lattices is a straightforward extension of this simplified case (see Nakamoto 1986 and Decius and Hexter 1977), and the basic interplay between force constants and atomic masses remains the same, i.e., vibrational frequencies generally increase with increasing bond force constant value and decrease with increasing atomic mass.

Values of **ν** are usually reported in wavenumbers (cm^{-1}), but occasionally in meV (1 meV = 8 cm^{-1}). The first order (normal mode) vibrational bands of most molecular systems appear between a few tens of cm^{-1} and 4000 cm^{-1}. But for molecules/crystals containing elements other than hydrogen, 2500 cm^{-1} defines the upper end of the frequency range. The characteristic normal mode frequencies of the various forms of carbon, for example, lie between 1000 and 2000 cm^{-1}, whereas, the frequencies of the transition metal oxides and carbides that might be observed for carbon dusting specimens lie below 1000 cm^{-1} (Nakamoto 1986).

From statistical analysis considerations of molecular vibrations, we learn that the populations of vibrational states are governed by Boltzmann statistics, but in almost all instances one is measuring transitions between the ground vibrational state and the first excited state as depicted in Figure 1. Infrared spectroscopy involves the measurement of absorption of discreet quanta of radiation from a white beam of radiation in the infrared portion of the frequency spectrum (10 cm^{-1} to 4000 cm^{-1} for the far- through mid-infrared region). In Figure 1, this would correspond to a transition from state "g" to state "e". The absorptions occur at frequencies (energies) corresponding to specific vibrational modes of the molecule or crystal being measured.

In Raman spectroscopy, one uses a monochromatic excitation source (usually a laser) having a frequency (energy) well above that of the range of typical molecular vibrations/phonons. Lasers with energies that range from 10,000 to 50,000 cm^{-1} can be used, the choice of energy being somewhat dependant on the optical absorption properties of the sample. During Raman scattering, a molecule or crystal absorbs a full quantum of the laser energy (ν_{ex} in Figure 1), rises in energy to a virtual state, then re-emits the quantum of absorbed laser energy. It

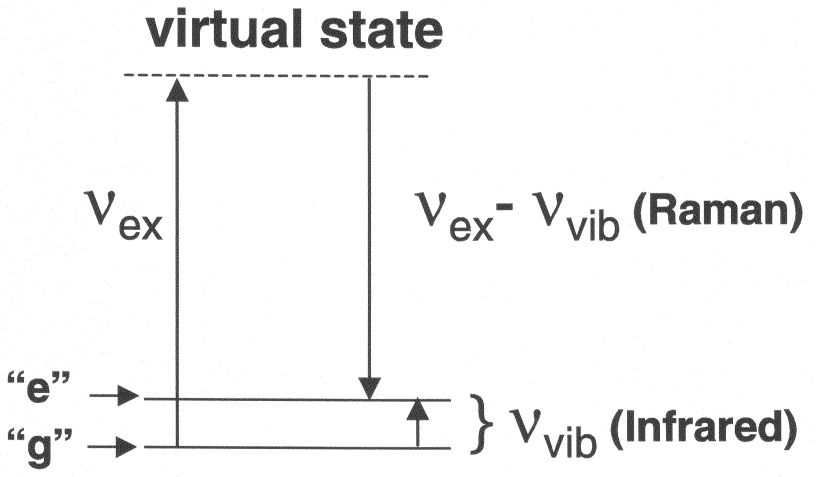

FIGURE 1 Energy Level Diagram for Raman and Infrared Processes

will usually re-emit the same quantum of energy (ν_{ex}) and thus return to the original ground state (Rayleigh scattering), but if the molecule undergoes a transition to one of its vibrationally excited states (ν_{vib} in Figure 1) while in the virtual electronic statethe emitted quantum of radiation will have an energy $\nu_{ex} - \nu_{vib}$ (Stokes scattering). In the much less likely event that the molecule is in a vibrationally excited state (e.g., state "e" in Figure 1) when it absorbs the quantum of laser energy and returns to the vibrational ground state prior to re-emiting the absorbed laser energy, the emitted radiation will have an energy equal to $\nu_{ex} + \nu_{vib}$ (anti-Stokes scattering). Raman spectroscopy almost always involves the measurement of Stokes scattering.

RAMAN AND INFRARED MODE ACTIVITY AND INTENSITY

The number of degrees of freedom of a molecule or a crystal lattice is equal to three times the number of atoms, **N**, in the molecule or in the unit cell of the crystal. The number of vibrational degrees of freedom for a molecule is determined by subtracting the translational and rotational degrees of freedom (5 for linear and 6 for nonlinear molecules) from 3**N**. For a crystal lattice only the three translational degrees of freedom are subtracted from 3**N**. The number of vibrational degrees of freedom that are observable by either Raman or infrared spectroscopy is determined by analysis of the symmetry properties of the molecule or crystal. The details of such analyses are beyond the scope of this paper, but it is important to note that for isolated molecules, point group symmetry is important (Nakamoto 1986), whereas for crystalline solids, the analysis involves space group algebra (Decius and Hexter 1977 and Fateley et al. 1971). In the case of crystalline solids, the space group symmetry of the crystal lattice and the site symmetries of the individual atoms in the lattice must be known to solve the vibrational secular equation. Once the number and symmetry type of the vibrational degrees of freedom for a molecule or a crystal have been determined, it is possible to predict the number and symmetry type of the ones that are Raman and/or infrared active. One important aspect of this determination occurs for molecules or crystal lattices that possess a center of inversion. For such molecules or crystals, there will be mutual exclusion of the Raman and infrared active modes, i.e., Raman active modes will be infrared inactive and infrared active modes will be Raman inactive. Part I of Nakamoto (1986) covers all these principals in sufficient detail for most interested readers.

The Raman activity and Raman intensity of a particular normal mode are determined from the polarizability tensors for that mode, whereas infrared activity/intensity are determined from dipole moment tensors. These relationships are shown diagrammatically in Figure 2, where α is the polarizability, μ is the dipole moment, and q is the motional coordinate associated with a particular normal mode. Note that the intensity, **I**, is proportional to $(d\alpha / dq)_0$ and $(d\mu / dq)_0$ for Raman and infrared activity, respectively. The zero subscript indicates that the derivative is evaluated at the equilibrium (ground state) condition of the motional coordinate. Using the carbon dioxide molecule (a molecule with a center of inversion) as an example, the diagrams in Figure 2 show that the symmetric stretching mode of CO_2 has a non-zero $(d\alpha / dq)_0$ but a zero value for $(d\mu / dq)_0$, while the antisymmetric stretching mode has a non-zero $(d\mu / dq)_0$ but a zero value for $(d\alpha / dq)_0$. In the actual spectra of CO_2, the symmetric stretch appears in the Raman spectrum but not in the infrared spectrum, and the antisymmetric stretch appears in the infrared but not the Raman. In a qualitative sense one can see that the polarizability ellipsoids in the stretched and compressed states of the symmetric stretch are not equivalent (in shape and volume), whereas they are for the antisymmetric stretch.

In a crystalline lattice, it is often the case that the lattice contains imperfections. These imperfections can be atomic site vacancies, impurity atoms on lattice sites, misoriented grain boundaries, and interstitial atoms to name a few. Such imperfections destroy the natural symmetry of the perfect crystal and also compromise the selection rules for Raman and infrared activity. If the imperfections prevail over a significant atomic percentage of the lattice, modes that are normally inactive in the Raman or infrared spectrum can become active. As will be shown further on, lattice disorder influences the observed Raman spectra of carbon dusting deposits.

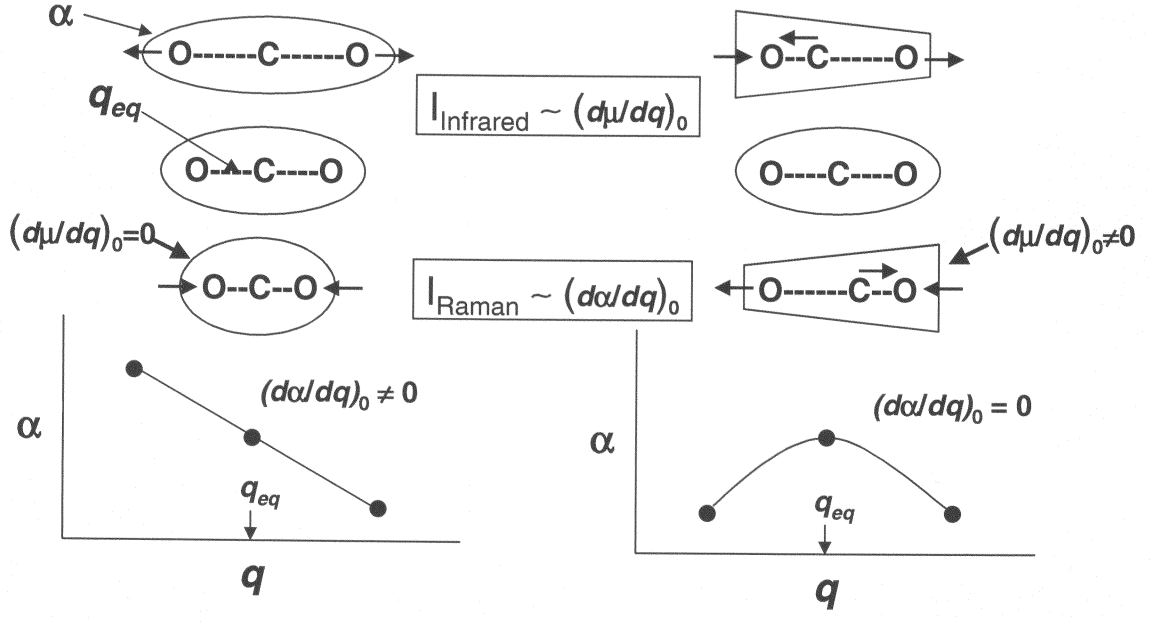

FIGURE 2 Relationship of Symmetry, Dipole Moment (μ), AND Polarizability (α) to Raman and Infrared Mode Activity and Intensity

MEASUREMENT OF RAMAN AND INFRARED SPECTRA

Measurement methodologies for Raman and infrared spectra are at a highly developed state. The nature of the basic components for both types of spectroscopies are categorically the same: a source of radiation (monochromatic for Raman, polychromatic for infrared), optics for radiation steering/focusing, a monchromator- or interferometer-based frequency spectrum analyzer (FSA), a detector, and a computer to operate the system and collect/process/store the spectra. While there are still some advantages to dispersive FSAs, most infrared spectroscopy and a fair amount of Raman spectroscopy (particularly on organic materials) are done using instruments that employ interferometric FSAs.

In our experience with the investigation of carbon dusting corrosion, Raman spectroscopy is proving to be more useful than infrared because of the opacity of various forms of carbon to infrared radiation and the relatively strong Raman scattering inherent to most morphological forms of carbon. There are two basic optical configurations for the measurement of laser-induced Raman spectra: the conventional configuration and the microprobe configuration, as diagrammed in Figure 3. In the conventional configuration, the excitation laser is typically brought in at a non-perpendicular angle with respect to the sample surface and the isotropically scattered Raman radiation is collected with a wide-angle optic over an angular range that excludes any specularly reflected laser radiation. In the microprobe configuration, the laser is introduced to the sample through a short focal length lens that also serves as the collection optic. Specially designed optics block backscattered laser radiation so that only the Raman scattering enters the monochromater. The advantage of this configuration is that the short focal length lens can be made part of a microscope, such that the region of the sample being struck by the excitation laser can be viewed and even imaged. With commercially available Raman microprobe instruments, submicron resolution of surface domains on samples is possible (Williams et al. 1996). The Raman results reported in this paper were obtained using a Renishaw System 2000 Imaging Raman Microscope equipped with a He-Ne laser (633 nm).

RAMAN MICROSCOPY OF CARBON DUSTING SPECIMENS

An extensive series of Raman measurements on loose carbon dusts and on metal coupons from carbon dusting experiments has been made at the Argonne National Laboratory over then past year. Selected examples of the types of results obtained in these measurements will be presented in this section. Additional descriptions of the results and their implications with respect to the mechanism(s) of carbon dusting are presented in a companion publication (Zeng et al. 2001). It has turned out in these measurements that informative spectral features can be found over a wide frequency range (200 to 3400 cm^{-1}).

Raman spectra of carbon dust from experiments wherein iron coupons were subjected to two different dusting environments are shown in Figures 4 through 6; the test conditions are tabulated in Table 1. In these experiments the exposure environment was flowing gaseous CO + H_2 + CO_2 and the exposure conditions were 100 hours at 1300°F for Tests 4 and 5 and 5 hours at 1100°F for Test 7. The difference between Test 4 and Test 5 was that H_2O was also present in the gas mix in the case of Test 5. Let us first consider the spectra in the 200 to 1000 cm^{-1} region (Figure 4). There are no Raman bands in this spectral region for the dusts from the longer-duration/higher-temperature exposure tests (the spectrum labeled Test 4&5 in Figure 4 is representative of all such exposures). This is also the case for the Raman spectra of the two types of graphite included in Figure 4 and is consistent with expectation for graphitic carbons (Knight and White 1989). The bands that appear with varying intensity in the Raman spectra of two samples of the dust from Test 7 (the spectra labeled Test 7 and Test 7a in Figure 4) are due to

iron oxide particles commingled with the carbon dust. This observation will be discussed in more detail further on.

TABLE 1 **CONDITIONS FOR CARBON DUSTING TESTS**

TEST NO.	TEST ATMOSPHERE	TEMPERATURE (^{O}F)	TIME (HOURS)
3	**$CO + H_2 + CO_2 + H_2O$**	**1100**	**5**
4	**$CO + H_2 + CO_2$**	**1300**	**100**
5	**$CO + H_2 + CO_2 + H_2O$**	**1300**	**100**
6	**$CO + H_2 + CO_2 + H_2O$**	**1100**	**5**
7	**$CO + H_2 + CO_2$**	**1100**	**5**

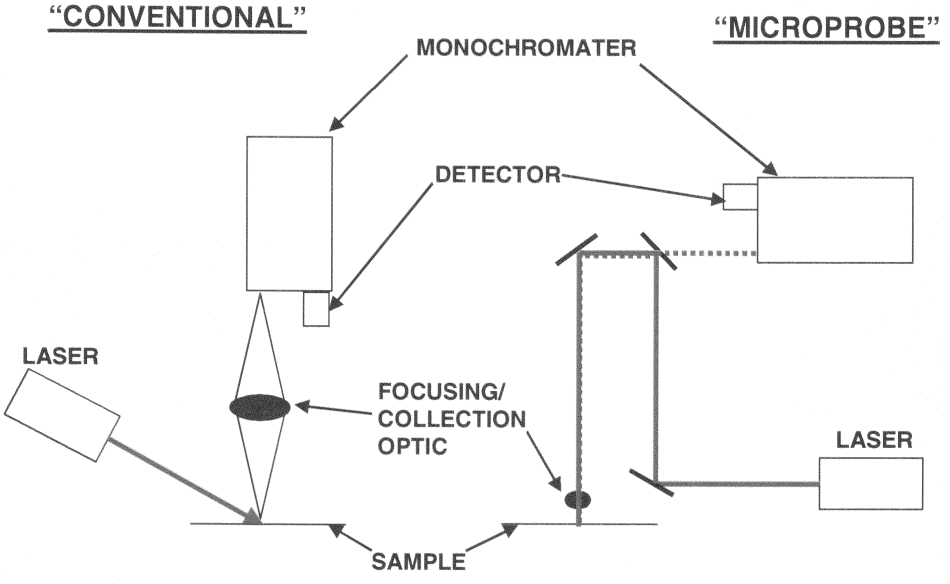

FIGURE 3 Schematic layouts for "conventional" and "microprobe" type raman spectroscopy measurements

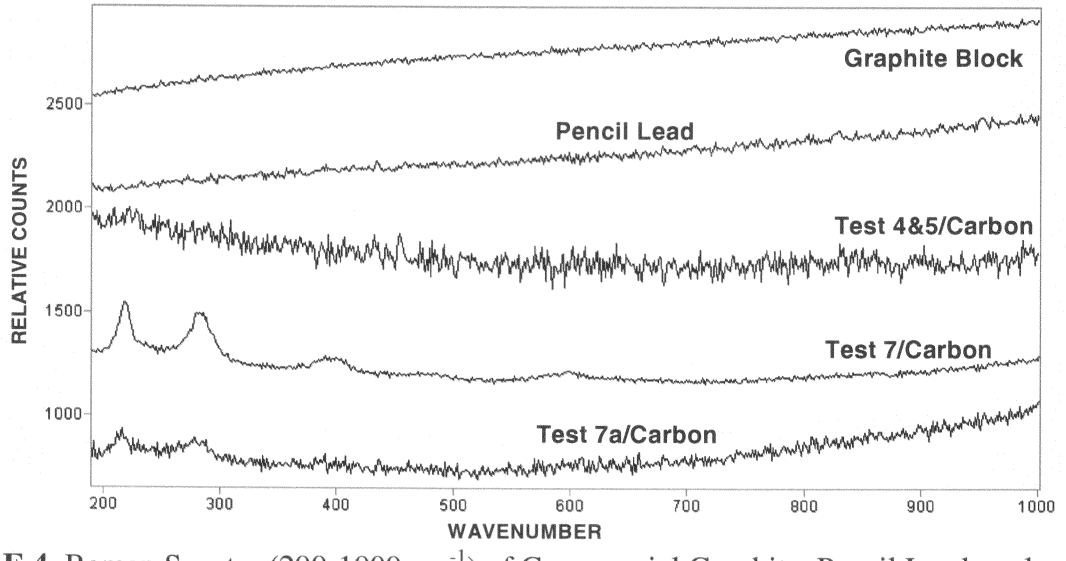

FIGURE 4 Raman Spectra (200-1000 cm^{-1}) of Commercial Graphite, Pencil Lead, and Specimens of Carbon Particles from Carbon Dusting Corrosion Tests

Raman spectra of the same set of samples in the 1000 to 2000 cm^{-1} are shown in Figure 5. This spectral region contains the characteristic first order phonons of all forms of carbon. The spectra of the two graphite samples are typical of medium- to high-density graphitic materials. The mode nominally at 1580 cm^{-1} is the Raman active E_{2g} phonon of graphite (Knight and White 1989). The other prominent band at ca. 1360 cm^{-1} is due to a mode of graphite that would be inactive in a perfect (defect free) graphite crystal and will hereinafter be referred to as the D band per the nomenclature of Mernagh et al. (1984). Its appearance and intensity relative to the 1580 cm^{-1} band is a measure of the extent of disorder in the graphitic material (Lespade et al. 1982). The appearance of the 1360 cm^{-1} band is often accompanied by the observation of a shoulder on the high frequency side of the E_{2g} phonon (ca. 1620 cm^{-1}) as noted by Nakamizo et al. (1978). The graphite block and the pencil lead exhibit all three of these spectral features to some extent (Figure 5), as do most commercially available forms of graphite (Nakamizo et al. 1974); but the carbon dusts from Tests 4, 5, and 7 showed even greater amounts of disorder. The lower test temperature (1100°F) and shorter exposure time (5 hours) of Test 7 produced a slightly more disordered carbon dust in a CO + H_2 + CO_2 atmosphere than did the higher-temperature (1300°F)/longer-term (100 hours) conditions of Test 4. The addition of water to the sweep gas mix (Test 5) appeared to reduce the disorder level in the dust relative to the result for Test 4.

Raman spectra in the 2000 to 4000 cm^{-1} region for this same series of samples (see Figure 6) contain mainly broad weak bands that are attributed to the overtones and combinations of the D and E_{2g} modes (i.e., 2D, D+E_{2g}, and 2 E_{2g}) per Sato et al. (1978). The most intense feature in this spectral region is 2D, but the factor(s) influencing the variations of its relative intensity in the case of the liberated carbon particles from these particular carbon dusting experiments needs further investigation.

Now let us consider the results of Raman microprobe examinations of the surfaces of the iron coupons from the tests listed in Table 1. As the results for the 200 to 1000 cm^{-1} region (Figure 7) show, the spectra of specimens from the 1100°F/five-hour exposures (Tests 3, 6, and 7) all contain the Raman active phonons of Fe_2O_3 (Thibeau et al. 1978). Note (1) that the Fe_2O_3 phonons are more intense for the tests with H_2O in the exposure atmosphere and (2) that they do not appear on the surface of specimens exposed for 100 hours at 1300°F (Test 4 and Test 5),

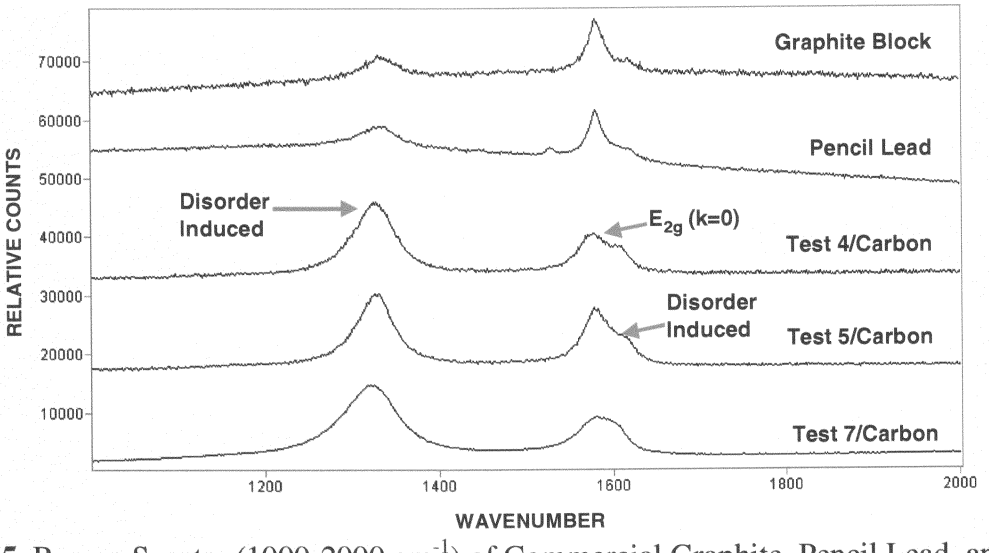

FIGURE 5 Raman Spectra (1000-2000 cm^{-1}) of Commercial Graphite, Pencil Lead, and Specimens of Carbon Particles from Carbon Dusting Corrosion Tests

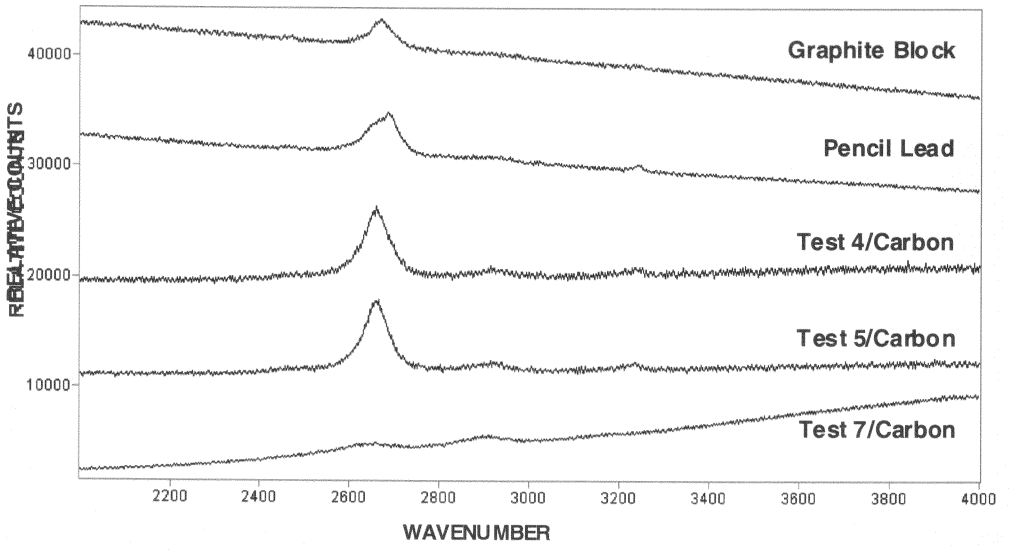

FIGURE 6 Raman Spectra (2000-4000 cm^{-1}) of Commercial Graphite, Pencil Lead, and Specimens of Carbon Particles from Carbon Dusting Corrosion Tests

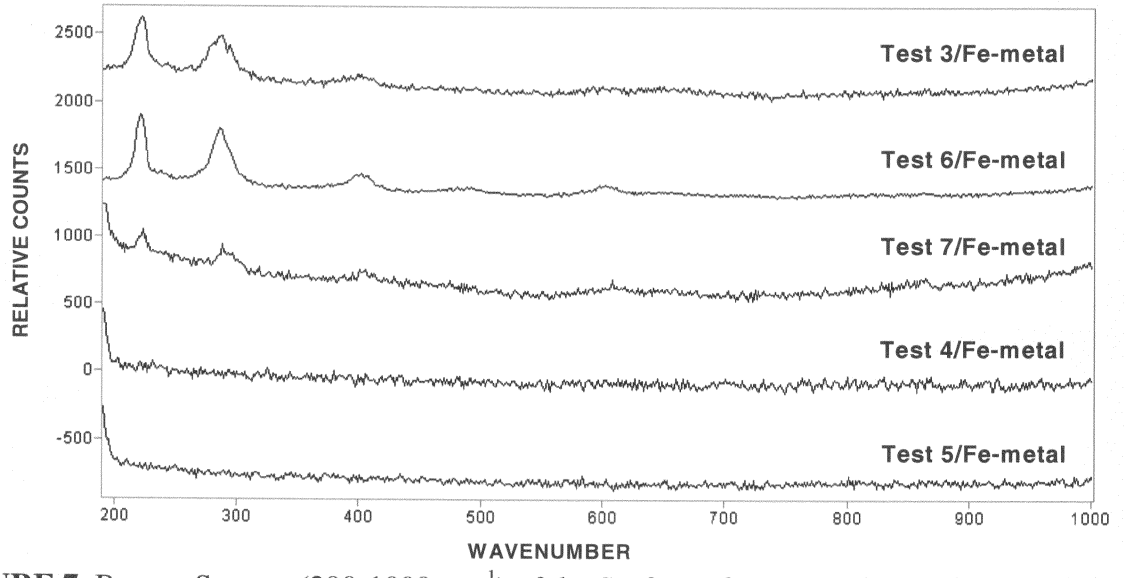

FIGURE 7 Raman Spectra (200-1000 cm^{-1}) of the Surface of Iron Specimens from Carbon Dusting Corrosion Tests

whether or not H_2O was present in the exposure atmosphere. In the 1000 to 2000 cm^{-1} region (Figure 8), we observe the D and E_{2g} phonons in an intensity ratio that gives evidence of a highly disordered surface-bound graphite. And again, as was seen in Figure 5, the carbon dust produced at the lower-temperature/shorter-time conditions exhibits the greatest disorder. The 2D, D+E_{2g}, and 2 E_{2g} overtone and combination bands for the residual carbon on the specimen surfaces are more pronounced (Figure 9) than for the dusts (i.e., Figure 6) but the relative intensities for the different exposure conditions appear to be the same.

The results in Figures 4 through 9 illustrate the type of information that can be gained from the study of carbon dusting using Raman spectroscopy methods. For example, we find that the carbon dusting of iron exhibits a measurable sensitivity to exposure conditions. Five hours at

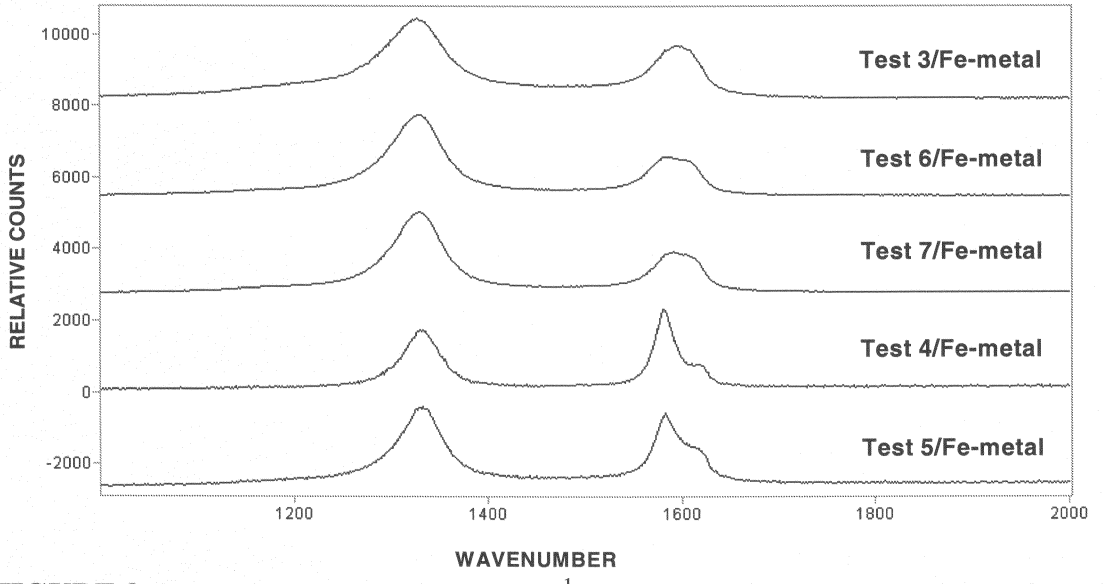

FIGURE 8 Raman Spectra (1000-2000 cm^{-1}) of the Surface of Iron Specimens from Carbon Dusting Corrosion Tests

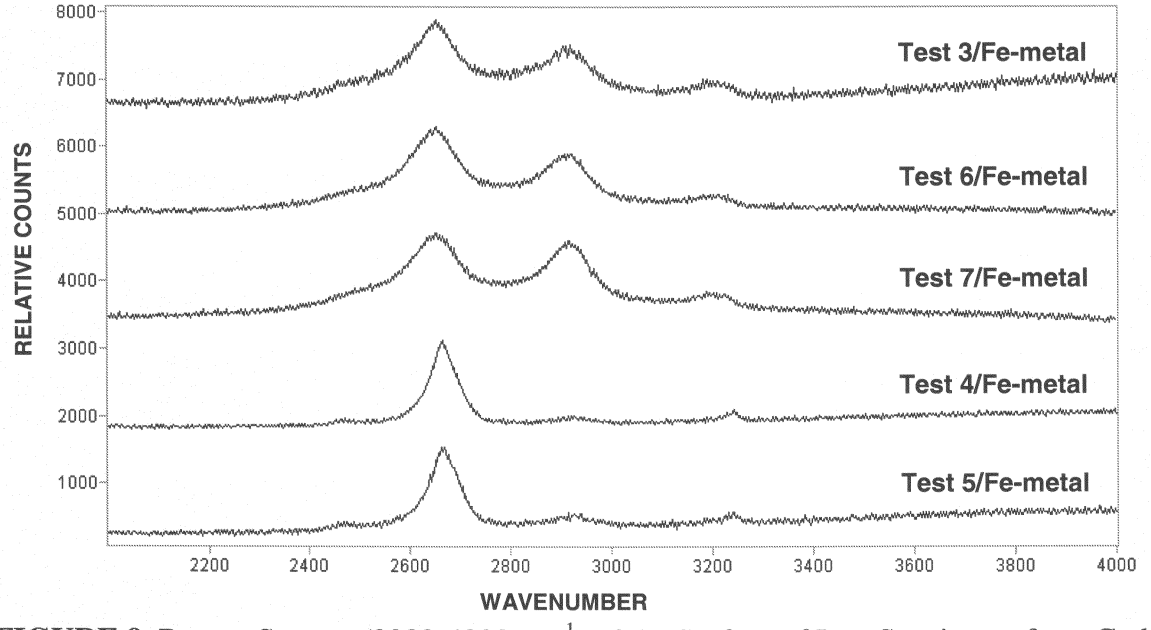

FIGURE 9 Raman Spectra (2000-4000 cm^{-1}) of the Surface of Iron Specimens from Carbon Dusting Corrosion Tests

1100°F in a flowing CO + H_2 + CO_2 atmosphere produces as much dusting as 100 hours at 1300°F in the same atmosphere; but the lower temperature seems to induce the formation of Fe_2O_3 which dislodges from the iron surface and mingles with the loose carbon dust. The presence of H_2O in the sweep gas enhances the formation of Fe_2O_3. The relative intensities and full-width at half-maximum (FWHM) of the D and E_{2g} modes for the surface-bound carbon (and the loose dust as well) reveal that the 1100°F exposure conditions produce a more disordered graphitic dust than the 1300°F conditions. It is most likely the case that the dust formed at lower temperature has a smaller average particle size (Lespade et al. 1982). Manifestations of the effect

of the presence of H_2O on the spectral features of the graphitic carbon phonons are not as obvious—the most critical factor appears to be temperature.

Our collective interpretation of these results is that the dominant factor affecting the Raman observations for the carbon dusts (both the liberated dusts and the surface-bound carbon) is the graphite grain size. Using the work of Lespade et al. (1982) as a guide, we would conclude from Figures 4 and 7 that the grain size is <10 nm for the higher temperature exposures and <5 nm for the lower temperature exposures. With such small grain sizes, it is not surprising that the D band and the 1620 cm^{-1} band (sometimes referred to as the D′ band) appear with considerable intensity. These bands arise from the loss of local inversion symmetry experienced by the carbon atoms near grain boundaries, the preponderance of surface carbon atoms, and quite possibly randomization of the ordering of successive carbon layers (turbostatic stacking) as discussed by Knight and White (1989). The appearance of Fe_2O_3 commingled with the liberated carbon dust is surely an indicator and a manifestation of the erosive nature of carbon dusting. The reader is referred to the companion paper by Zeng et al. (2001) for a fuller discussion of the mechanistic aspects of carbon dusting in relation to the experiments described in this paper.

PERSPECTIVE ON FUTURE MOLECULAR SPECTROSCOPY STUDIES OF CARBON DUSTING CORROSION

The next logical step in such studies is to perform the Raman and infrared measurements in situ. In the case of Raman measurements, this would probably have to be done using the conventional methodology diagrammed in Figure 3. Because of the likely need to have the collection optic close to the specimen surface, applications of the microprobe method will require the use of an optical element that can withstand the exposure conditions (particularly the temperature). The possibility for developing such optics is currently under investigation in our laboratory as is the in situ study of carbon dusting using conventional Raman microscopy.

Infrared spectroscopy can be used in at least two ways for the study of metal dusting. One is to use transmission methods to monitor the gas phase species during carbon dusting. This could be done in the elevated temperature environment with a fiber-optically-coupled immersion probe or in a specially designed cell outfitted with multi-pass infrared optics; but it could also be done downstream of the exposure zone using a flow-through gas cell. Most vendors of infrared sampling accessories provide products that are suitable for these types of measurements.

For direct in situ measurements of metal dusting corrosion we are looking into the possible application of diffuse reflectance infrared Fourier transform (DRIFT) methods. The type of accessory we have used successfully in the past to obtain real-time in situ infrared spectra of solid samples in flowing-gas environments at elevated temperature is shown in Figure 10. The operational details for this accessory (as used in our work) have been described in papers by Johnson et al. (1988) and Maroni and Epperson (2001). In brief, process gas introduced at the *gas entrance port* flows upwards along the cal-rod-heated *sample post*. The heated process gas passes over the sample resting atop the *sample post* inside the *sample cup*, into a labyrinth at the base of the *sample cup*, and out of the cell via the *gas exit port*. The infrared beam is focused onto the sample by an external parabolic mirror and the diffuse scattering is collected with a second external parabolic mirror. The focused incoming beam and the diffuse scattering pass through the *windows* in the dome above the *sample cup*. In past work with this cell we were able

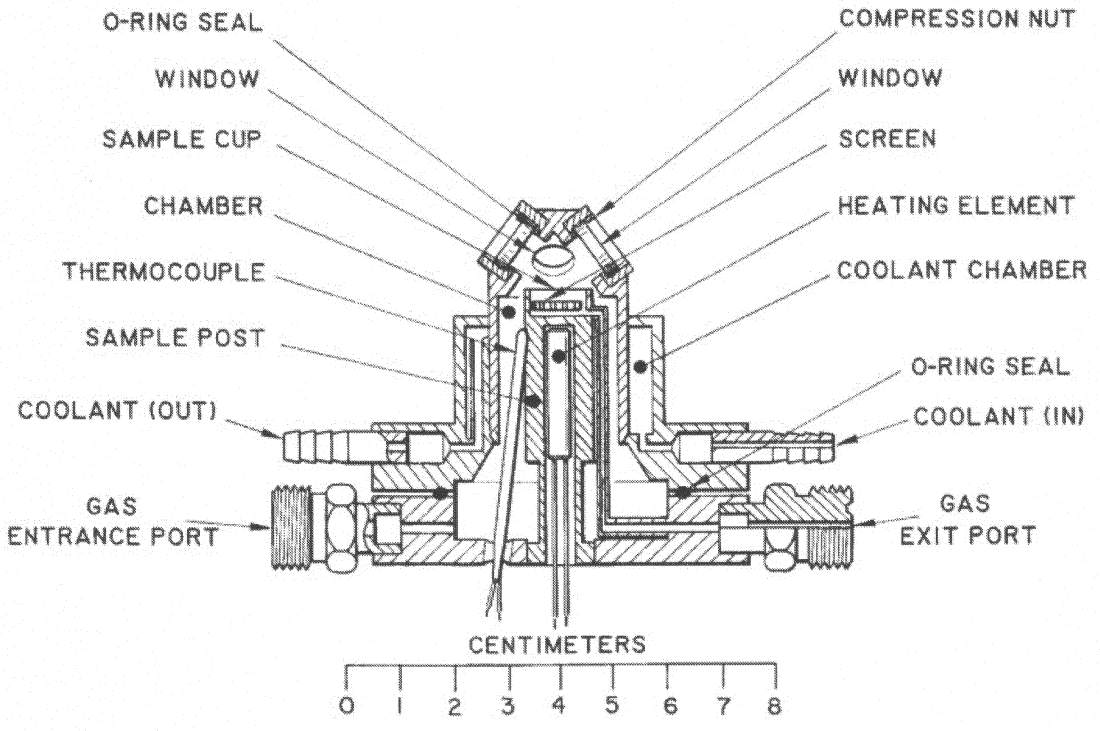

FIGURE 10 Controlled Environment Diffuse Reflectance Cell

to record interpretable DRIFT spectra of samples at temperatures as high as 1100°F. It should be possible to conduct carbon dusting experiments comparable to Tests 3, 6, and 7 in Table 1 using this cell.

Another potentially useful infrared technique that may be applicable to the study of carbon dusting corrosion is attenuated total reflection (ATR) spectroscopy. An ATR-based approach that has been used successfully to study particulate matter is diagrammed in Figure 11. In this approach, particulate matter in a flowing gas stream is size segregated using a nozzle-type particle impactor. Particles of a specific size range are impacted onto ATR plates. By stacking the ATR plates and moving them through the nozzle gap, it is possible to study the evolution of the particulate matter as a function of time. The integration of the ATR approach into an instrument with a built in FTIR measurement capability has been done in our laboratory. This device, called the infrared aerosol analyzer (IAA), has been used to study the chemistry of atmospheric particulate matter (Johnson et al. 1983, Novick et al. 1999). Its adaptation to the study of carbon particles in the gaseous environments downstream of carbon dusting exposures should be straightforward. Specifically, in addition to observing the infrared active phonons of the various chemical and morphological forms of carbon that are created during dusting, it should be possible to detect molecular species adsorbed on the carbon particles.

Finally, it is noteworthy in closing to mention that in the field of materials science, molecular spectroscopy results often couple very informatively with the results of other types of analytical measurements, such as electron microscopy and x-ray diffraction, as well as with measurement methods that probe surface area, particle size distributions, and stress/strain fields.

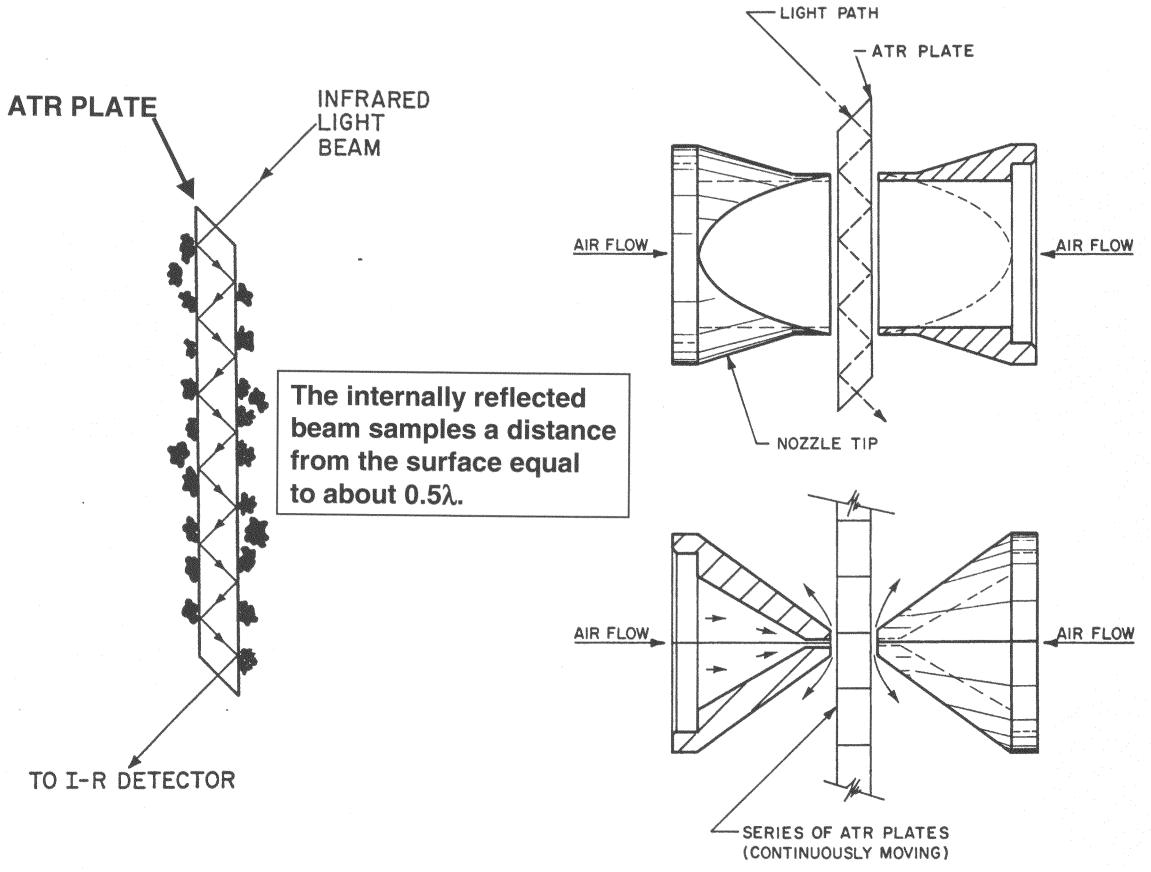

FIGURE 11 Features of the ATR Impactor Method for Investigating the Infrared Spectra of Fine Particles in Gas Streams

ACKNOWLEDGEMENT

This research was sponsored by the Office of Industrial Technologies, U.S. Department of Energy, under Contract W-31-109-ENG-38.

REFERENCES

Decius J.C., and R.M. Hexter, 1977, *Molecular Vibrations in Crystals*, McGraw-Hill.

Fateley, W.G., N.T. McDevitt, and F.F. Bently, 1971, "Infrared and Raman Selection Rules for Lattice Vibrations," *Applied Spectroscopy* 25:155-173.

Ferraro, J.R., and K. Krishnan, 1990, *Practical Fourier Transform Infrared Spectroscopy*, Academic Press

Johnson, S.A., R. Kumar, and P.T. Cunningham, 1983, "Airborne Detection of Acidic Sulfate Aerosol Using an ATR Impactor," *Aerosol Sci. Technol.* 2:401

Johnson, S.A., R.-M. Rinkus, T.C. Diebold, and V.A. Maroni, 1988, "The Use of Diffuse Reflectance Infrared Spectroscopy for Studies of Molecular Sieve Catalysis," *Applied Spectroscopy* 42:1369-1375.

Knight, D.S., and W.B. White, 1989, "Characterization of Diamond Films by Raman Spectroscopy," *Journal of Materials Research* 4:385-393.

Lespade, P., R. Al-Jishi, and M.S. Dresselhaus, 1982, "Model for Raman Scattering from Incompletely Graphitized Carbons," *Carbon* 20:427-431.

Maroni, V.A., and S.J. Epperson, 2001, "An In Situ Spectroscopic Investigation of the Pyrolysis of Ethylene Glycol Encapsulated in Silica Sodalite," *Vibrational Spectroscopy* 27:43-51.

Mernagh, T.P., R.P. Cooney, and R.A. Johnson, 1984, "Raman Spectra of Graphon Carbon Black," *Carbon* 22:39-42.

Nakamizo, M., H. Honda, and M. Inagaki, 1978, "Raman Spectra of Ground Natural Graphite," *Carbon* 16:281-283.

Nakamizo, M., R. Kammereck, and P.L. Walker, Jr., 1974, "Laser Raman Studies of Carbons," *Carbon* 12:259-267

Nakamoto, K., 1986, *Infrared and Raman Spectra of Inorganic and Coordination Compounds,* 4th Edition, John Wiley & Sons.

Novick, V.J., S.A. Johnson, H.A. Hisgen, and V.J. Reyes, 1999, "Real Time Chemical Vapor Detection and Enhancement Utilizing Aerosol Adsorption," *Rev. Sci. Instrumen.* 70:1829

Sato, Y, M. Kamo, and N. Sekata, 1978, "Raman Spectra of Carbons at 2600-3300 cm^{-1} Region," *Carbon* 16:279-280.

Suëtaka, W., 1995, *Surface Infrared and Raman Spectroscopy: Methods and Applications*, Plenum Press.

Thibeau, D., C.W. Brown, and R.H. Heidersbach, 1978, "Raman Spectra of Possible Corrosion Products of Iron," *Applied Spectroscopy* 32:532-535.

Williams, K.P.J., I.C. Wilcock, I.P. Hayward, and A. Whitely, 1996, "Applications of State-of-the-Art Raman Microscopy and Direct Raman Imaging," *Spectroscopy* 11:45-50.

Zeng, Z., K. Natasan, and V.A. Maroni, 2001, "Study of Metal Dusting Mechanism in Iron Using Raman Spectroscopy and X-Ray Diffraction," this proceedings.

METAL DUSTING OF STEEL ALLOYS: RAMAN, FT-IR, AND XPS RESULTS

G.L. JOHNSON, K.L. BAUMERT*, T. MEBRAHTU, and G. XIAOPING
Air Products and Chemicals, Inc.
Allentown, PA 18195

ABSTRACT

Laboratory tests were conducted in an attempt to observe the presence of carbon monoxide bound to iron atoms on the surface of a bulk, polycrystalline sample. The results were inconclusive, however it was shown that an oxide is produced on the metal surface when exposed to carbon monoxide. Carbon was also deposited on the surface during the test. This indicates that the Boudrard reaction does not fully explain the gas-metal surface reaction.

INTRODUCTION

In syngas production, metal dusting results in high metal wastage rates in certain pieces of equipment. To understand the mechanisms, laboratory tests were conducted. Initially, the focus was to determine if CO was adsorbed on metal surfaces. Samples were exposed to CO and the reactions/deposits were measured.

BACKGROUND

Improved understanding of the mechanisms of metal dusting/high temperature corrosion is important for many industrial processes. In reforming or syngas applications, where gaseous CO, CO_2, H_2, and H_2O are present, metal dusting occurs by degradation of the surface into particles of metal oxides, metal carbides, and carbon. Despite the wealth of information available in the literature, there is a lack of consensus on a molecular-level description of metal dusting reaction mechanisms. There is an ongoing debate in the literature (Grabke 1995; Dean 2001; Grabke and Muller-Lorenz 2001; Jones and Baumert 2001; Kirchheiner and Jimenez Soler 2001) on the relative significance of the following broad aspects of metal dusting: (i) carbon deposition/saturation of surface region, (ii) carbon diffusion into the bulk of metal alloys, (iii) formation of stable and metastable metal carbides, (iv) decomposition of metal carbides to carbon and metal particles, and (v) formation and stability of a protective surface oxide.

Macroscopic measurements, obtained by monitoring changes in weight, physical properties and elemental composition, have proved useful to test the corrosion resistance of a given material (Fabiszewski et al. 2000). In this study, we apply spectroscopic and surface analysis methods, including Polarization Modulated Infrared Reflection-Absorption Spectroscopy (PM-IRRAS), Raman spectroscopy, and X-ray photoelectron spectroscopy, to investigate corrosion mechanisms at the onset of metal dusting. This work seeks to provide insight into the resistance or susceptibility of a given material to metal dusting, thereby complementing studies in the metal dusting fundamentals program (Fabiszewski et al. 2000).

*Corresponding author address: K. L. Baumert, Air Products and Chemicals, 7201 Hamilton Blvd., Allentown, PA 18195; e-mail: baumerk@apci.com.

ANALYTICAL PROCEDURES

1. **Apparatus:** The primary device for this investigation is a Refractor Reactor™ cell from Harrick Scientific, shown schematically in Figure 1. The cell is constructed from 316 stainless steel and uses Viton O-ring seals. The IR windows in the cell are zinc selenide wedges with anti-reflection coatings for the mid-IR. The cell contains a heated sample mounting platform to accept 2" x 3" metal coupon samples for study by reflectance spectroscopy (PM-IRRAS). The cell body is constructed with a jacket for circulating cooling water to protect the elastomer seals during high temperature operation. The temperature of the sample mounting platform is monitored by an attached thermocouple and a controller unit that also provides over-temperature protection. Another controller and a thermocouple attached to the heater block control the temperature. In addition, an emergency stop button is located on the front of the controller housing. Cooling water for the cell is provided by a circulating bath while the cell is operated. The bath reservoir contains a low water level sensor that will shut off the pump in case of a leak and an over-temperature control that shuts down the unit if the bath temperature exceeds a preset level. If the flow of water to the cell cooling jacket stops, a separate flow sensor will also shut off the power to the temperature controller for the cell heaters. The cell is located in the accessory purge cabinet attached to the Nicolet Magna 860 FT-IR interferometer at the West wall in B-208.

2. **Samples:** Three lap-finished 2" x 3" x 1/8" coupons each of Iron, Ni 200, Carbon Steel (C1008), and Stainless Steel (316L) were obtained from the Metal Samples division of Alabama Specialty Products, Inc. Each coupon was stamped on one side with its

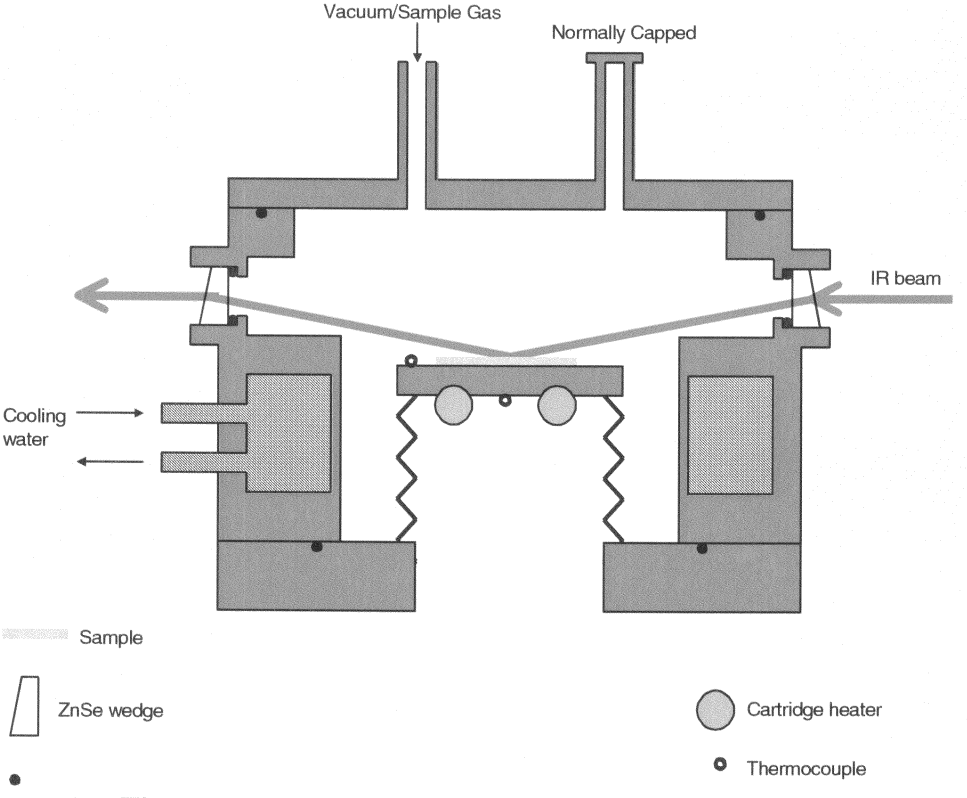

Figure 1 Refractor Reactor™ from Harrick Scientific.

composition, Fe, Ni 200, C1008, or 316L and an index number, 001-003. One corner was cut off of each coupon to allow room for the thermocouple that was mounted on the sample platform. In addition, the mounting bars that clamp the coupons to the sample platform in the Refractor Reactor™ cell had to be modified by welding on additional metal because the coupons were slightly under the specified thickness. The coupons were polished on a Buhler Vibramet polishing machine with alumina slurries down to 0.3 micron. Before mounting in the cell, each polished sample was rinsed with methylene chloride (Aldrich, Spectrophotometric grade) and cleaned in an argon plasma discharge with a Harrick plasma cleaner, catalog number PDC-32G.

3. **Operation:** A polished and plasma cleaned sample coupon was attached to the sample stage in the cell with three screw-down clamping bars. Making sure the Viton O-ring was in place and free of debris, the cell cover was closed with the Allen bolts. The gas line from the fume hood was attached to the VCO fitting on the cell cover. The electrical connections to the temperature controller and the cooling water lines to the circulating bath were checked. The valve on the gas line was opened to evacuate the cell with the molecular drag pumping station in the fume hood. The system was leak checked by closing the valve to the vacuum pumps and watching the thermocouple gauge for a rapid rise in pressure. If there was no leak, the valve to the molecular drag pumping station was re-opened. The circulating bath was started and the temperature control was set to 60°C and its over-temperature safety was set to 70°C. The temperature controller for the cell heater block was set to the desired experimental temperature, between 400-750°C, and the over-temperature shut off controller was set to 20 degrees higher. Once the system reached equilibrium, a control PM-IRRAS spectrum of the sample surface was obtained. The valve between the vacuum pump and the gas manifold was closed and the necessary pressure of CO, up to 20 Torr, was delivered to the cell. Spectra of the sample surface were obtained as necessary.

4. **PM-IRRAS**: The collimated infrared beam from a Nicolet Magna 860 interferometer with dual input channels was focused with a 170 mm plano-convex BaF_2 lens. The sample was mounted horizontally at the focal point of the lens on the sample plate of the Refractor Reactor™ cell. The first wedged window in the cell refracted the IR beam approximately 75° from normal to the sample. The IR beam between the lens and cell was linear polarized in the horizontal direction by a wire grid polarizer on a KRS-5 substrate. A Hinds PEM-90 Photoelastic Modulator with an octagonal ZnSe element then modulated the linear polarization with an optical retardation of 0.5λ at 73.9 kHz. The frequency of the maximum efficiency of the modulator was selected at 1600 cm^{-1} (6250 nm). The interferometer was operated with a mirror velocity of 0.6329 cm/sec (1.26 kHz at 2000 cm^{-1}) to supply the IR beam to the photoelastic modulator. The reflected infrared beam was refracted back to the horizontal plane by the second wedged window in the Refractor Reactor™ cell and focused with a 75 mm f.l. BaF_2 lens onto a liquid nitrogen cooled MCT-A photoelectric detector. The detector signal was split into the A channel of the Magna 860 and a Stanford Research Systems model SR650 active high pass filter set to reject <50 kHz. The high pass filter was necessary to block the Fourier amplitude modulation signal from the interferometer. The output of the filter was fed to a Stanford Research Systems model SR830 DSP lock-in amplifier that was referenced to the Hinds controller for the photoelastic modulator. The time constant for the lock-in was 300 μsec and the input attenuation was 12 dB. The lock-in output was sent to the B channel of the Magna 860. The A channel signal is the raw output of the detector and therefore represents the sum of

all the polarization states. The B channel signal is the frequency locked difference between the p and s linear polarization output of the photoelastic modulator. The ratio of the difference signal (B channel) to the sum signal (A channel) is the reflectance spectrum of the sample surface. Spectra were obtained by co-adding 128 scans from each channel at 2 cm^{-1} resolution. The ratio of the single beam scans obtained from the A and B channels (B/A) produces a reflectance spectrum of the sample surface.

5. **Gas Phase IR Absorption:** The ratio of an A channel signal obtained while the sample is exposed to the gas to an A channel signal obtained from the sample under vacuum produces a gas phase infrared absorbance spectrum.

6. **Raman Spectroscopy**: Raman spectra of the sample surfaces after high temperature exposure to CO were obtained with a Kaiser Holoprobe® spectrograph coupled with a multimode optical fiber to an Olympus BX-60 optical microscope. A Coherent continuous wave Nd:YAG laser with a frequency doubling crystal was used to provide 10 mW of 532 nm illumination at the sample through a second multimode optical fiber. The laser was focused onto the sample and the Raman signal was collected (180° backscatter orientation) with an Olympus MS-Plan 80X ultra-long working distance microscope objective. The spectrograph output was focused onto a TEM-cooled (-40°C) CCD camera detector and the signal was integrated for 60 seconds and averaged for 4 acquisitions. The spectrograph was frequency calibrated with emission lines from a neon lamp and intensity calibrated with a NIST-traceable tungsten lamp. Both calibration lamps were mounted in a single housing supplied by Kaiser Optical Systems. Raman spectra of various features visible on the surfaces of the samples were obtained and images noting the measured features were saved.

7. **In Situ Raman Spectroscopy:** A replacement cover was fabricated for the Refractor Reactor™ cell with modifications to accept a Kaiser Raman probe head that was coupled with optical fibers to the Holoprobe® spectrograph and laser. The modified cell diagram is shown in Figure 2. The window (20 mm diameter x 2 mm thick) and plano-convex lens (10 mm diameter x 10 mm f.l.) were UV-grade silica. Optical glass and sapphire optics were found to produce artifacts in the regions of interest in the spectra. Originally, the lens was mounted above the window, but the necessary focal length was too long to observe spectra from test samples. The lens was mounted on a plate inside a threaded cylinder underneath the window. The cylinder had holes drilled in it to speed evacuation of gas from the cell.

8. **X-ray Photoelectron Spectroscopy:** X-ray photoelectron spectra of the as-received and exposed metal samples were acquired on the PHI 5000LS ESCA spectrometer, with a base operating pressure of 1 X 10^{-9} Torr. A standard Mg K_{α} (1253.6 eV) x-ray source was used under the following experimental conditions: 15 keV accelerating voltage, 400 W, 800 μm spot-size, and 45° take-off angle. Survey and high-resolution multiplex spectra were collected using pass energies of 117.40 eV and 23.50 eV, respectively.

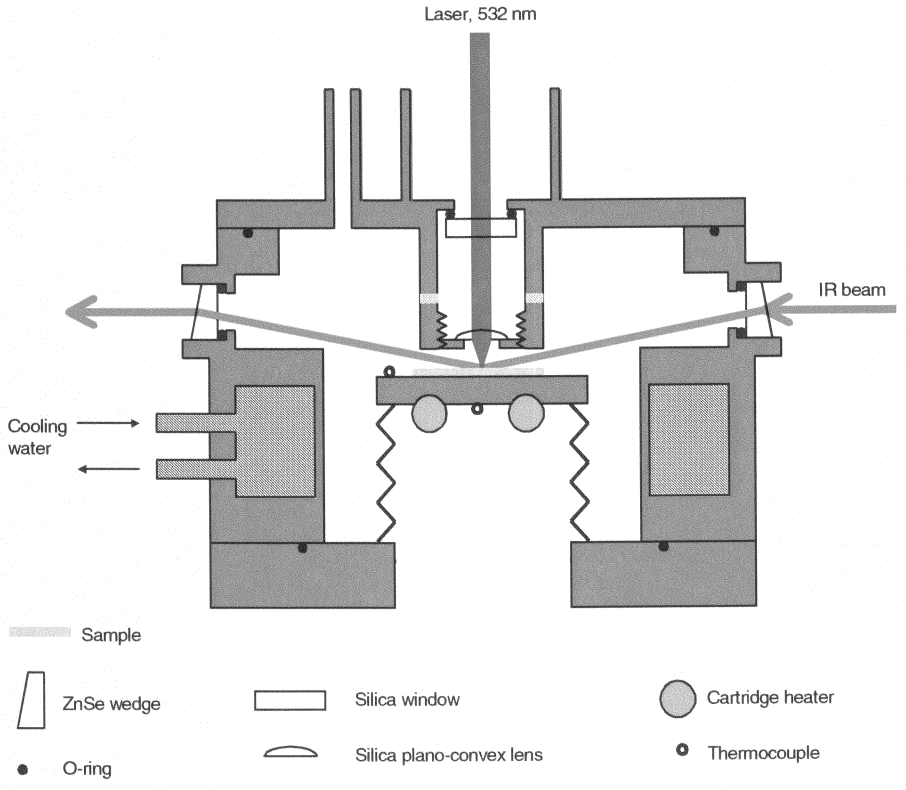

Figure 2 Refractor Reactor™ with Top Cover Modified for In Situ Raman Spectroscopy.

RESULTS AND DISCUSSION

1. **PM-IRRAS:** The initial purpose of this study was to attempt to observe the presence of carbon monoxide bound to iron atoms on the surface of a bulk, polycrystalline sample. The frequency shift of the C-O stretching vibration would have been used to confirm calculations of the binding strength of the complex. The system was tested with a 1" x 1.5" x 0.125" sample of platinum. The Pt sample was annealed in a H_2/O_2 flame and quenched in Milli-Q deionized water that had been purged with nitrogen. The sample was then transferred to the cell and evacuated to 10^{-2} Torr. Carbon monoxide was introduced into the cell and then evacuated. The PM-IRRAS spectrum of the Pt surface showed an absorbance band at 2075 cm^{-1} that is assigned to the C-O stretching of the carbon monoxide/platinum complex. The temperature of the sample was ramped from 30°C to 116°C while obtaining PM-IRRAS spectra. Between 65°C and 70°C the C-O stretching band began to broaden and lose intensity and by 90°C the band dropped below the noise level of the PM-IRRAS signal.

2. While an essentially monolayer coverage of CO could be observed on the Pt sample, there were no indications in the PM-IRRAS spectra of a stable, room temperature carbon monoxide complex with the Fe, C1008, Ni 200, or 316L samples. Another possible use of the PM-IRRAS system would be detecting product species formed on the sample surface during high temperature exposure to CO. One result that will be discussed later was that Raman spectra of the Fe sample after exposure to CO above 400 °C indicated the presence of magnetite (Fe_3O_4) on the surface. It would be desirable to observe the in situ formation of surface oxides but instrument limitations currently prevent using PM-IRRAS to do this.

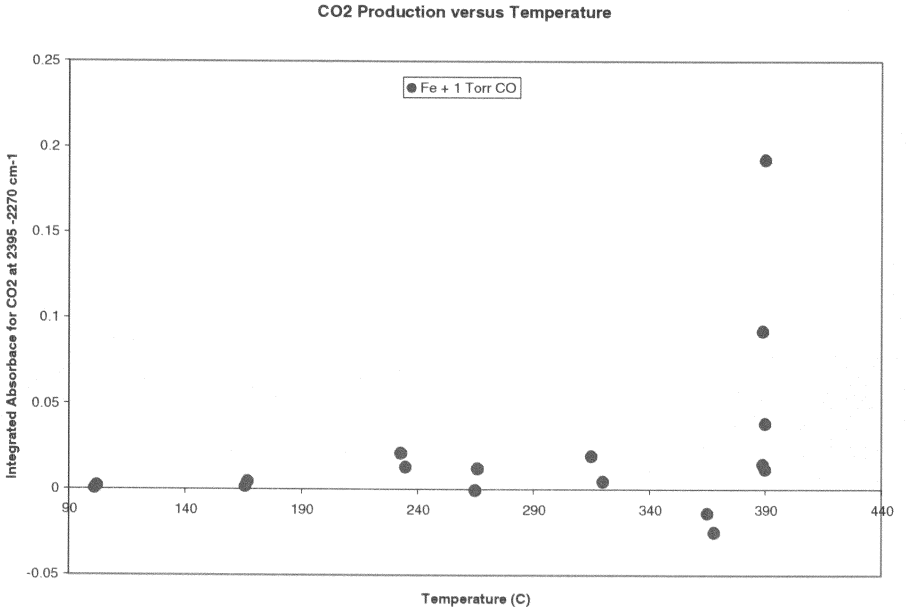

Figure 3 Infrared Spectrum for CO_2 as a Function of Temperature.

The frequency cutoff of the detector is 850 cm^{-1}, which is well above the infrared absorbance bands of magnetite at 725 cm^{-1} and 570 cm^{-1}. The frequency cutoff of the photoelastic modulator (PEM) is 560 cm^{-1} which places it in the middle of the region where magnetite and other metal oxides exhibit their strongest infrared absorbances.

Gas Phase IR Absorption: The temperature of an iron sample under 1 Torr of CO was ramped up from 100 °C to 390 °C while monitoring the gas phase infrared spectrum. No significant changes in the gas phase spectra were observed until 390 °C, where the spectrum of CO_2 was observed. Moreover, the intensity of the CO_2 spectrum increased with time when the temperature was held constant at 390 °C, as shown in Figure 3. One of the reactions known to occur during metal dusting (CO disproportionation or Boudouard reaction) in the presence of carbon monoxide is:

(1) $2CO = C + CO_2$

Further evidence for this reaction, the observed Raman spectrum of carbon on the samples after exposure to CO above 400 °C, will be discussed later.

In order to make some determination of relative production of carbon dioxide, spectra of a 27 ppm (by volume) standard of CO_2 in helium at 30, 125, 250, 500, and 1200 Torr in the cell were obtained at room temperature. A fresh polished sample of Ni 200 was used to provide a reflective surface for the grazing angle IR beam. The integrated absorbance of the CO_2 feature (2395–2272 cm^{-1}, baseline: 2417–2269 cm^{-1}) versus the partial pressure of CO_2 in the cell is plotted in Figure 4. The data were least-squares fit to a line with a slope of 14.68 and intercept at 0.0253 (A). The relevant statistics, prob>F, prob>|t|, and R^2, indicated that the linear fit model and its coefficients are statistically significant within 0.5% and the model accounts for 99.94% of the variability in the data. Because the calibration spectra were measured at room temperature the accuracy of the predicted pressures CO_2 pressures at significantly higher temperatures will be degraded.

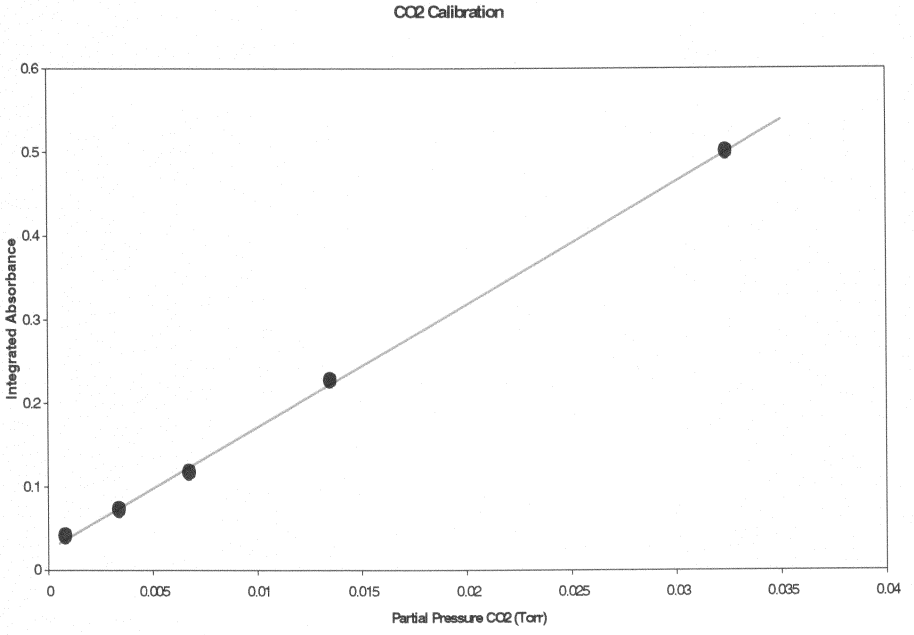

Figure 4 Variation in Absorbance with Partial Pressure of CO_2.

The calibration spectra were not measured at the higher temperatures because the total pressure of the gas standard overloads the capacity of the cell heaters, introducing further variability. The calculated partial pressures of carbon dioxide produced with an iron sample exposed to CO at different temperatures and pressures of 1 or 2 Torr are shown versus time in Figure 5. The rate of CO_2 production showed some correlation with increasing temperature and a dramatic shift when the initial pressure of carbon monoxide was doubled. Calculated partial pressures of carbon dioxide from sample material at various temperatures and initial CO pressures are shown in Figure 6. One conclusion from the data in Figure 6 is that near 450°C carbon dioxide was produced more efficiently over the Fe sample at lower pressures than the C1008, Ni 200, or 316L. Further examination of the data led to the conclusion that if the CO_2 production was increased by raising either the temperature or initial carbon monoxide pressure, it would eventually reach a plateau, indicating that an equilibrium process was occurring.

3. **Raman Spectroscopy**: Raman spectroscopy is recognized as a useful tool for characterizing metal corrosion products. The advent of instruments with microscope attachments in the 1980's increased the utility of the technique by allowing the analyst to view and select specific features in a sample. With the addition of computer-controlled motorized microscope stages, surface features are now routinely mapped according to their compositions. The image in Figure 7 shows the surface of a polished Fe sample after exposure to 1 Torr of carbon monoxide at 450°C to 500°C. The grain boundaries had become visible and circular black features about 2- 5 microns in diameter were observed at spots on the surface. The red squares on the image indicate where the laser was focused to obtain Raman spectra, shown in Figure 7 (Spectra 1 – 4) and Figure 8 (Spectra 5 – 8). The spectra near the black spot were dominated by the two overlapping bands at 1595 cm^{-1} and 1350 cm^{-1} that are assigned to amorphous carbon. In addition to the carbon features a sharp band at 668 cm^{-1} and weak bands near 550 cm^{-1} and 310 cm^{-1} are assigned to magnetite(Fe_3O_4).

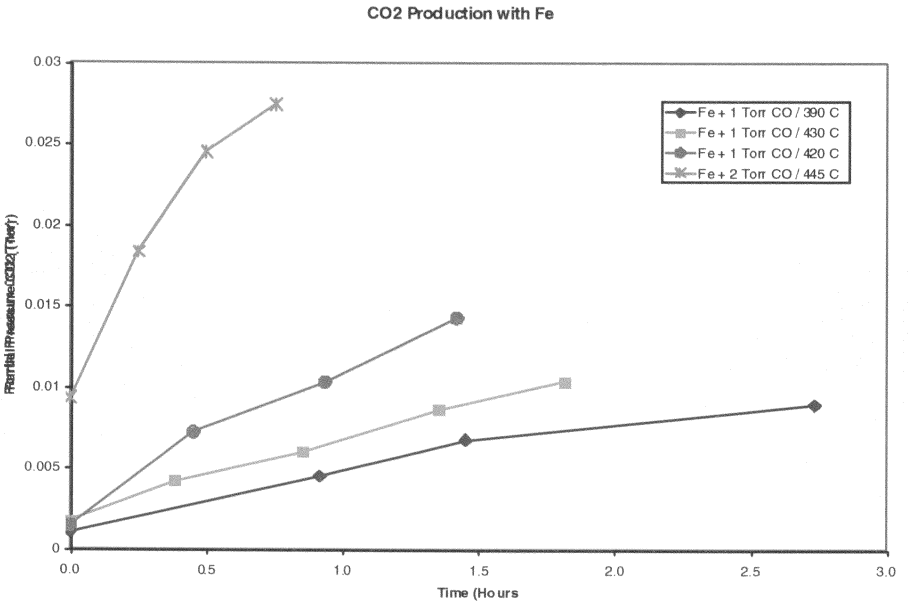

Figure 5 Calculated CO_2 Pressure on Iron Surface as a Function of Temperature.

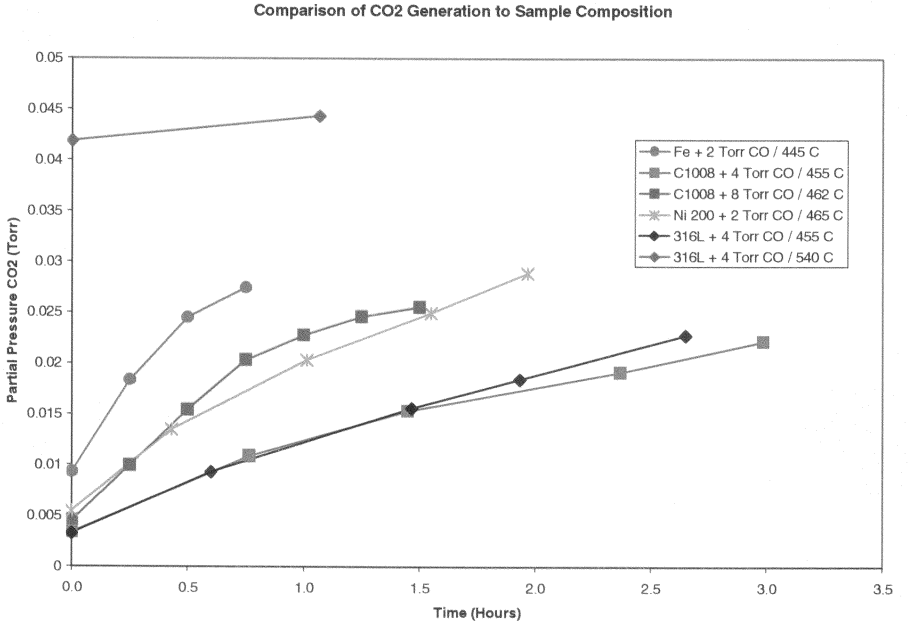

Figure 6 Calculated CO_2 Pressures on Iron Surface at Various Initial CO Pressures.

The spectra obtained farther away from the black spot were dominated by the magnetite bands while the carbon spectrum dropped in intensity.

Figure 9 shows an image obtained from a sample of low carbon steel, C1008, that had been exposed to 4 Torr of carbon monoxide at 450°C to 470°C. Once again, the grain boundaries had become visible with a slight darkening of the surface. The red squares on the image indicate where the laser was focused to obtain the Raman spectra in Figure 9.

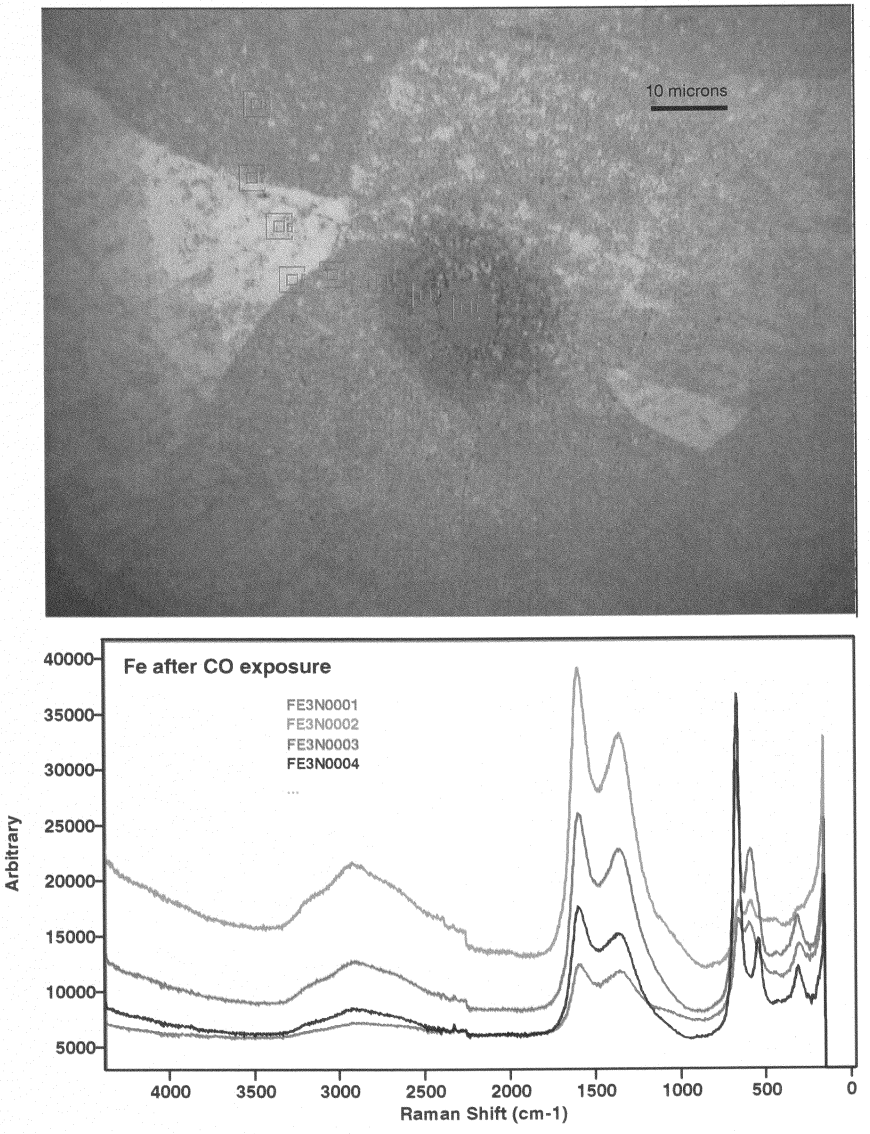

Figure 7 A Photograph of Fe surface exposed to 1 Torr CO (top) and Raman Spectra obtained at locations 1 through 4.

The Raman spectrum of amorphous carbon at all the sampling points while the presence of magnetite was indicated at points 3 and 5 by a weak, broad feature near 650 cm^{-1}. The sample was exposed to 4 Torr of CO at 430°C for 3 hours, followed by two exposures to 8 Torr of CO at 460 °C for 2 hours each. The image of the sample after the second series of carbon monoxide exposures is shown in Figure10, and the red squares on the image indicate where the laser was focused to obtain the Raman spectra shown in the same figure. The ordinate scale is the same in Figures 9 and 10 for the Raman spectra, and comparison shows that after the second exposure there was significantly more amorphous carbon present on the sample surface and magnetite was also formed. The data indicate that surface carbonization occurs ahead of oxidation evenly across carbon steel, as opposed to iron where spots of nearly pure carbon occur infrequently on a film of mixed carbon and magnetite.

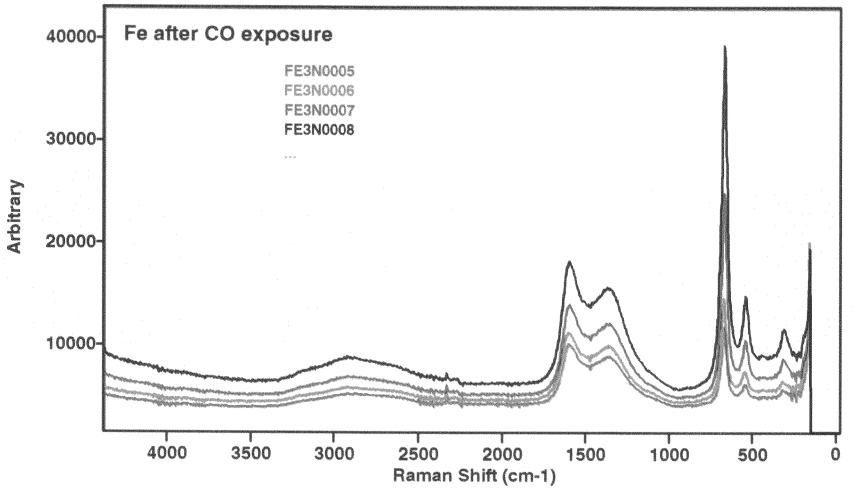

Figure 8 Raman Spectra obtained at locations 5 through 8, indicated in the Photograph in Figure 7.

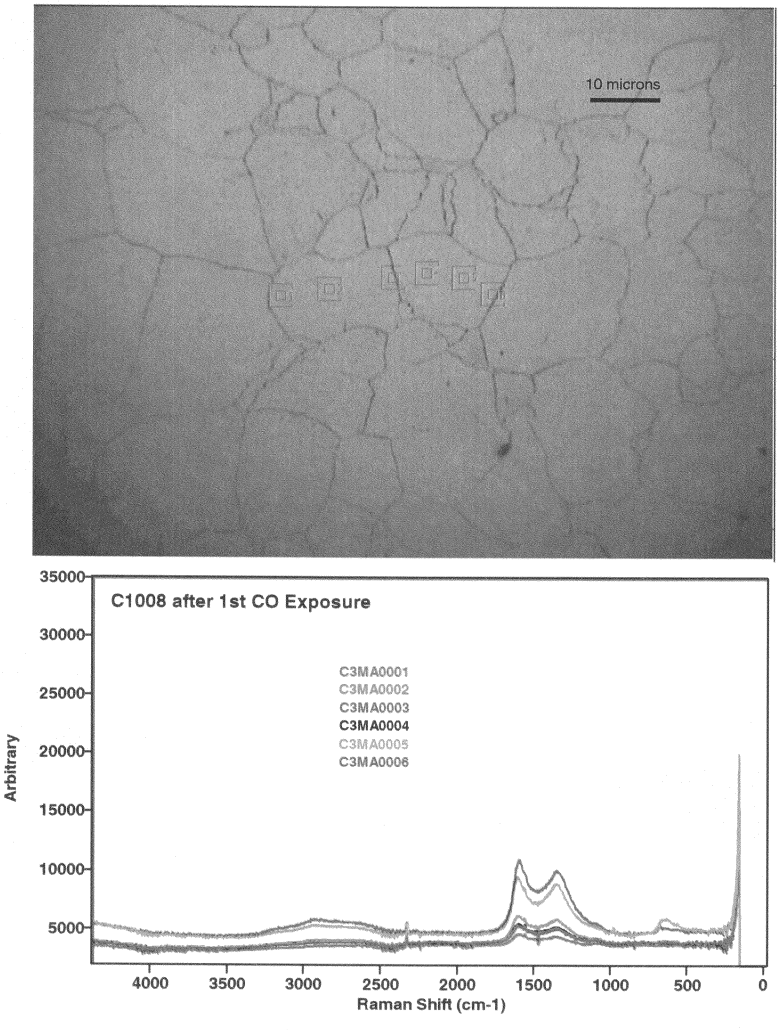

Figure 9 An image of low carbon steel that was exposed to 4 Torr of CO at 450°C to 470°C.

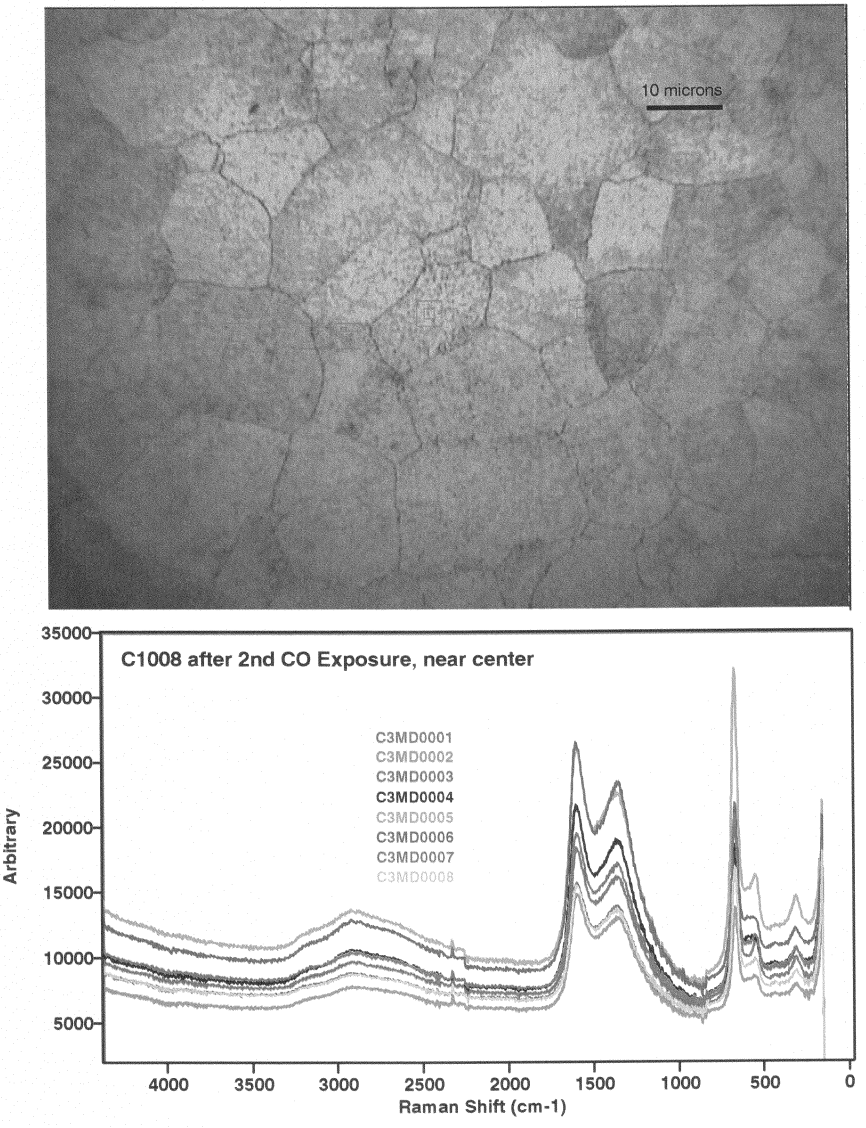

Figure 10 Image and Raman Spectra for Carbon Steel after Second Exposure to CO.

The image in Figure 11 shows the surface of a Ni 200 sample after exposure to 1.5 Torr of carbon monoxide at 400°C for 2 hours and another exposure to 1.5 Torr of carbon monoxide at 470°C for 2 hours. The grain structure was visible mainly through surface darkening of individual grains interspaced between what appeared to be clean metal. The red squares on the image indicate where the laser was focused to obtain the Raman spectra shown in the same figure. The spectra were characteristic of graphitic carbon and the intensities show that the carbon was concentrated at the grain boundaries. Diffusion of carbon in Ni 200 to the surface at elevated temperatures is a known process, so a duplicate sample of Ni 200 was subjected to the same temperature schedule under vacuum for a control. The image of the control after heating is shown in Figure 12 with the Raman spectra that correspond to the red squares in the image. The spectra were again characteristic of graphitic carbon, although the intensities were significantly lower than observed in Figure 11. These results suggest that future samples should be low-carbon nickel, such as Ni 201.

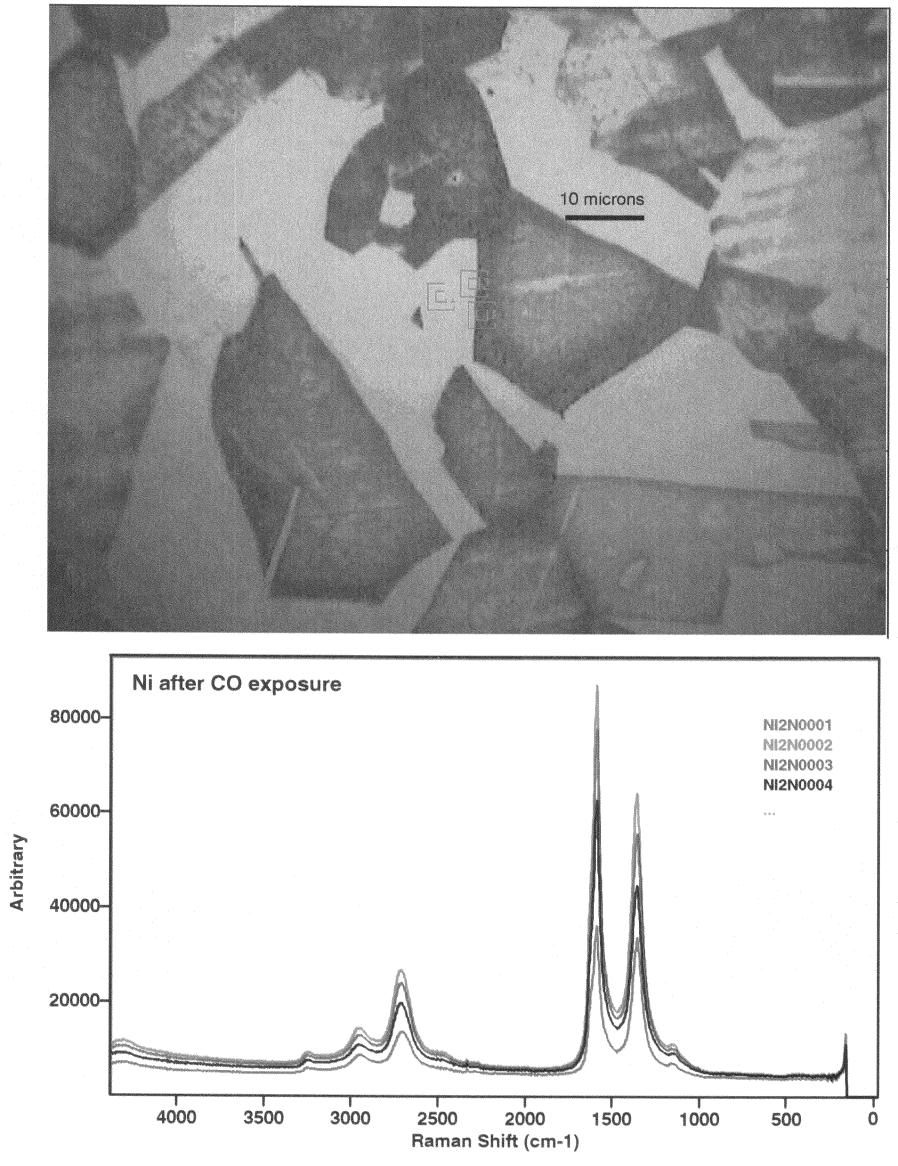

Figure 11 Surface of a Ni 200 Sample after Exposure to 1.5 Torr of CO at 400°C for 2 h and Another Exposure to 1.5 Torr of CO at 470°C for 2 h.

The image in Figure 13 shows the surface of a sample of 316L stainless steel after exposure to 4 Torr of CO at 455°C for 3 hours and 4 Torr of CO at 540°C for 1 hour. The grain structure was visible with a red surface discoloration and small black spots were scattered on the sample. The red squares on the image indicate where the laser was focused to obtain the Raman spectra shown in the same Figure. The spectra exhibited two overlapping bands at 1595 cm^{-1} and 1350 cm^{-1} that are assigned to amorphous carbon and a sharp band at 675 cm^{-1} that is assigned to a spinel mixed $(Fe_x, Cr_y)_3O_4$ oxide. The mixed oxides show a hypsochromic frequency shift from the magnetite band near 667 cm^{-1}, as shown in Figure 14. The sample was replaced in the cell and exposed twice to 4 Torr of CO at 455 °C for 2 hours. The image of the surface after the second series of CO exposures is shown in Figure 15. The blue discoloration was also visible in the center of the sample surface without

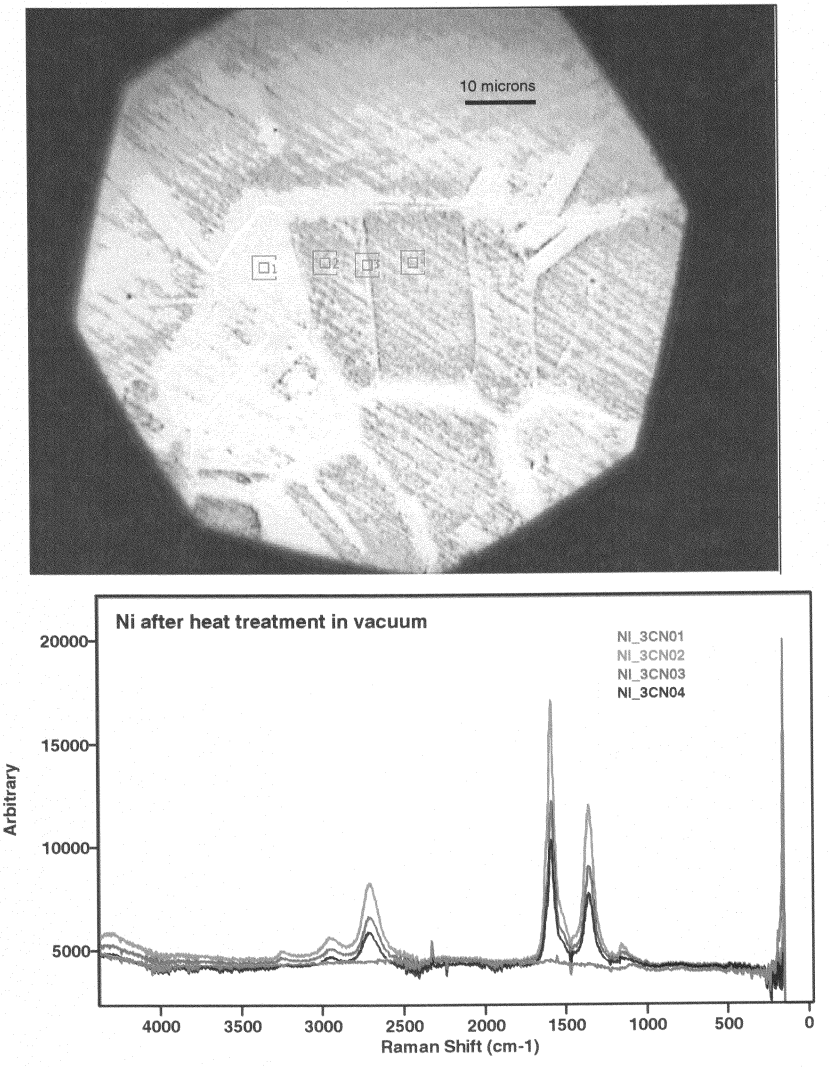

Figure 12 Image of Ni200 after Heating in Vacuum and Raman spectra that correspond to the red squares in the image.

magnification. The red squares on the image indicate where the laser was focused to obtain the Raman spectra shown in the Figure. The intensities of the amorphous carbon and spinel oxide bands were nearly doubled compared to after the first CO exposures.

4. Mounted and polished cross sections of 304 stainless steel that had been exposed to 50% CO, 50% H_2 at 565°C and 732°C under flow in a tube furnace for extended times were received from J. Hoffman for Raman analysis. The image in Figure 16 is from the sample exposed at 565 °C. The red squares on the image indicate where the laser was focused to obtain the Raman spectra shown in the same Figure. The two sharp bands at 1583 cm^{-1} and 1349 cm^{-1} are assigned to graphitic carbon and the strong, sharp band at 681 cm^{-1} is assigned to a spinel mixed $(Fe_x, Cr_y)_3O_4$ oxide. The frequency shift of the spinel may indicate the relative proportions of iron and chromium in the mixed oxide. Figure 17 shows the image obtained from the 304 stainless that was exposed at 732°C. Note that in this case there is a samples showed that there was more metal wastage at the lower temperature, 565 °C, as per APCI/CRS/00-003. The difference in the oxide structures

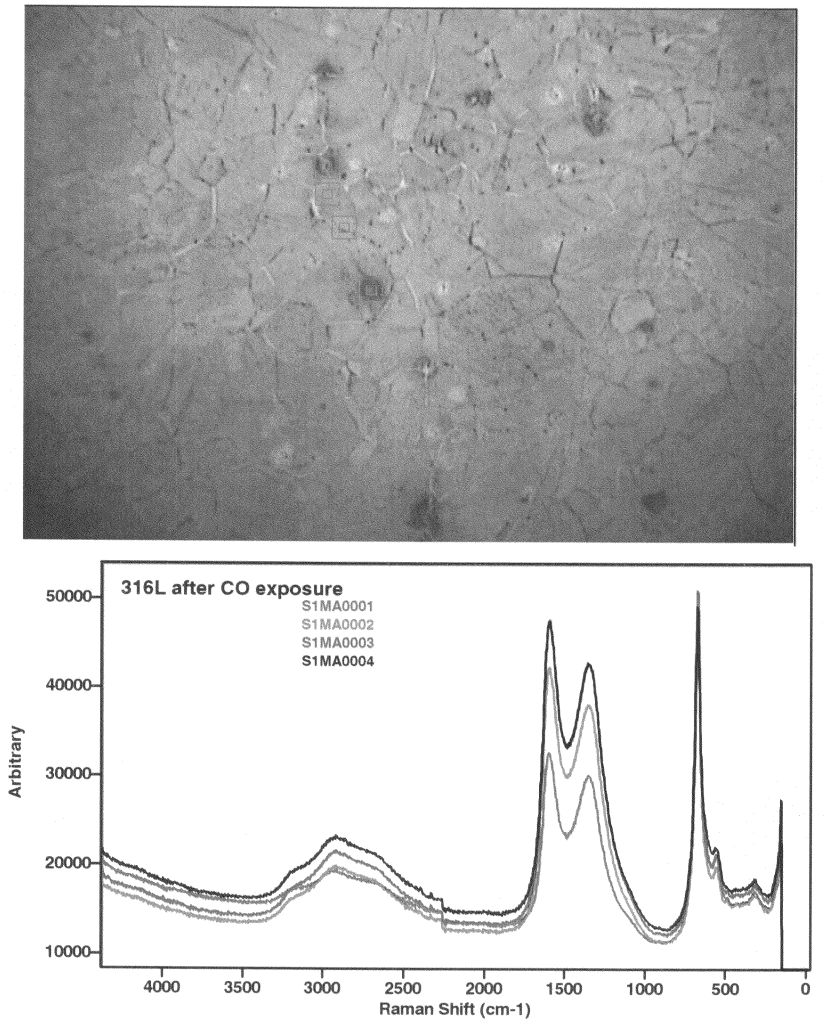

Figure 13 Surface of 316L Stainless Steel after Exposure to 4 Torr of CO at 455°C for 3 h and 4 Torr of CO at 540°C for 1 h.

between the high and low temperature samples suggests the chromia coating may provide some degree of protection to the metal from metal dusting.

In Situ Raman Spectroscopy: The first attempt to monitor the sample in the cell under reaction conditions was when the Ni 200 sample was exposed to 1.5 Torr of carbon monoxide at 470 °C for 2 hours. The Raman spectra obtained at 30 minute intervals are shown in Figure 18. The spectrum of graphitic carbon was observed to increase with time. The values for the partial pressure of carbon dioxide calculated from the gas phase infrared spectrum and the integrated Raman intensity of the graphitic carbon bands at 1580 cm^{-1} and 1350 cm^{-1} were normalized and plotted in Figure 19.

Further attempts to monitor the Raman spectrum at high temperature did not prove successful. Figure 20 shows the Raman spectra obtained while raising the temperature, under vacuum, of an iron sample that had amorphous carbon and magnetite on its surface from previous CO exposure

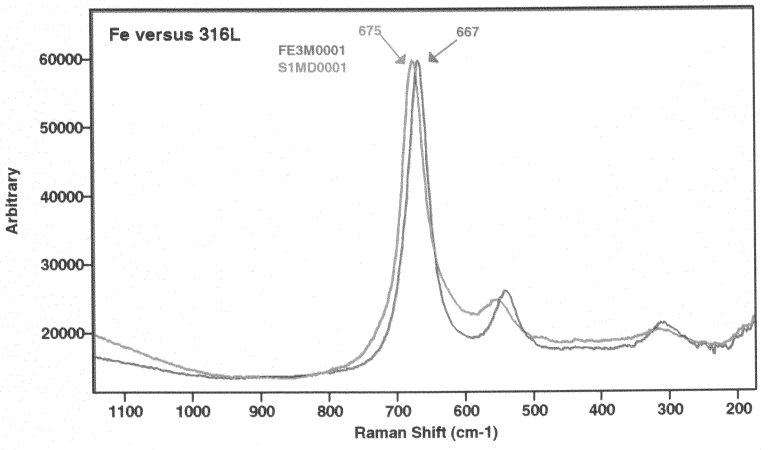

Figure 14 Raman Spectra for magnetite and mixed oxide.

at elevated temperature. Once the sample temperature exceeded 422 °C, the characteristic 667 cm^{-1} magnetite band was lost in the artifacts from the system optics. The intensity loss with temperature probably reflects the shift of vibrational energy distribution away from the ground state. Since Stokes Raman shifts occur from the ground state the intensity of the spectrum will drop concurrently. It may be possible to obtain in situ data by monitoring the anti-Stokes Raman shifts that begin at higher energy states but we currently don't possess a grating for the Holoprobe® spectrometer that would allow us to observe the anti-Stokes signal.

5. **X-ray Photoelectron Spectroscopy:** Table 1 summarizes the surface composition data for all as-rcvd and CO-exposed metal samples. Carbon deposition on CO-exposed Fe, C1008 and Ni 200 was confirmed by the higher surface carbon content as measured by XPS. The relative increase was highest for Ni 200; this result may be partly due to segregation of bulk carbon since Ni 200 contains ~ 0.15 wt% carbon. The most interesting part of the XPS results was in the metal oxidation state comparisons before and after CO exposures. Figure 21 presents the Fe 2p photoelectron spectrum for as-rcvd and CO-exposed C1008. The shoulder at ~707 ev in the as-rcvd sample is due to the metallic form of iron that is covered by a thin oxide/passivation layer (< 50 Angstroms). Upon CO-exposure, the C/M surface ratio was shown to increase; at the same time, iron became fully oxidized. Both these findings are consistent with Raman spectroscopy data. The spectra for pure Fe were essentially identical to those displayed in Figure 21. XPS spectra for as-rcvd and CO-exposed Ni 200 confirm the higher surface carbon content and lack of nickel oxidation upon CO-exposure under the following experimental conditions: 400 – 480 °C, 2 Torr CO. Future experiments will include Ni 201 (~ 0.02 wt% carbon) to unambiguously decouple the effect of bulk carbon on metal dusting reactions.

Similarly, XPS analyses were performed on as-rcvd and CO-exposed SS316L. Results for the Fe 2p region are presented in Figure 22. The oxidation behavior of iron in SS316L is analogous to pure iron and C1008, i.e. the metallic component is readily oxidized upon CO-exposure. Figure 23 shows Cr 2p photoelectron spectra for a dark region on the sample that was exposed to more aggressive conditions (i.e. higher temperature). Based on relative peak intensities and calculated atomic concentrations, it is clear that chromium is enriched in the surface region

TABLE 1 XPS Compositional Data for As-received and CO-exposed Metal Samples

Sample	Description	C/M (XPS)	Fe (at %)	C (at %)	O (at %)	N (at %)	Cr (at %)	Ni (at %)	Ca (at %)	Oxidation states (XPS)
Fe	As received	2.7 - 3.0	17.3	49.2	32.7	0.8	-	-	-	metal (w); oxide (s)
	CO-exposed, 0.5-1 Torr, 450°C	6.0 - 7.8	8.9	64.0	26.5	0.6	-	-	-	all oxide
C1008	As received	2.8 - 3.0	17.0	48.9	33.3	0.8	-	-	-	metal (w); oxide (s)
	CO-exposed, 460°C, 8 Torr, dark	6.0 - 6.3	9.7	59.7	30.1	0.4	-	-	-	all oxide
	CO-exposed, 460°C, 8 Torr, light	8.7 - 9.7	7.0	64.7	27.9	0.4	-	-	-	all oxide
Ni 200	As received	4.1 - 4.2	-	63.8	20.8	-	-	15.3	-	metal (s); oxide (m)
	CO-exposed, 451-483°C	18.1 - 23.1	-	85.4	10.5	-	-	4.1	-	metal (s); oxide (w)
SS316L	As received	4.9 - 5.0	7.8	59.9	26.8	0.4	3.2	1.1	0.8	Fe: M+O; Cr: O; Ni: M+O
	CO-exposed, 540°C 1h, dark	3.5 - 3.7	7.6	53.9	30.3	0.8	7.2	0.3	-	Fe: O; Cr: O; Ni (trace)
	CO-exposed, 540°C 1h, light	4.0 - 4.1	8.7	55.1	30.7	0.7	4.5	0.3	-	Fe: O; Cr: O; Ni (trace)

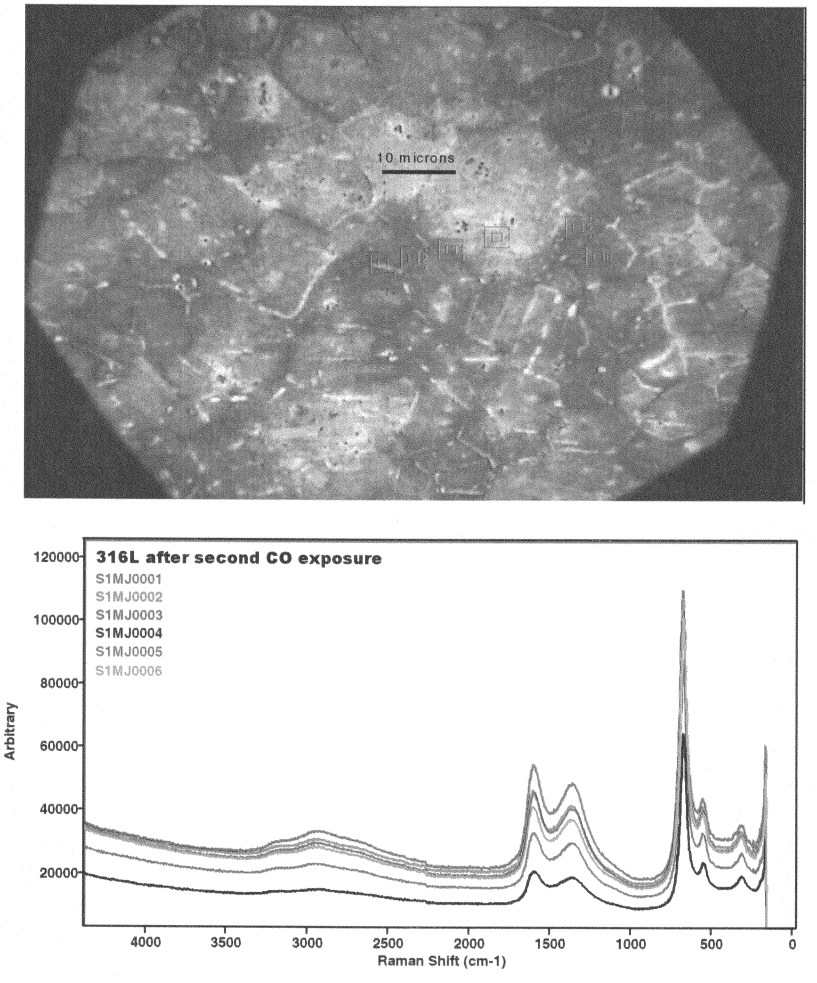

FIGURE 15 Image of Surface after a Second Series of Exposures to 4 Torr of CO at 455 °C for 2 h and Raman Spectra.

(approx. two-fold increase in Cr/Fe ratio). In this region of the sample, the surface Cr:Fe stoichiometry is approximately 1:1. Additional studies (e.g. grazing angle x-ray diffraction) are being performed to verify the form of mixed oxide spinels that are present in the near surface region.

SUMMARY

Metal dusting, a form of corrosion in high temperature syngas, contributes to increased maintenance costs to the industry. This investigation applies vibrational and surface spectroscopic methods to study the surface chemistry during the initiation of metal dusting reactions. Samples of Fe, Ni 200, Carbon Steel (C1008) and Stainless Steel (316L) were exposed to low pressures of CO (< 20 Torr) between 300 °C to 600 °C while infrared spectra of the gas phase were obtained *in-situ*. Exposed metal surfaces were examined *ex-situ* by Raman spectroscopy and X-ray photoelectron spectroscopy. Preliminary results obtained to-date lead to the following conclusions:

- CO disproportionation (i.e., Boudouard reaction), as evidenced by the formation of gaseous CO_2, is observed on all CO-exposed samples at the onset of metal dusting conditions (>390°C). The relative rate of CO_2 formation is dependent on several variables, including CO pressure, temperature, exposure time, and metal composition. CO exposures also lead to amorphous carbon deposition on Fe, C1008, and SS316L.

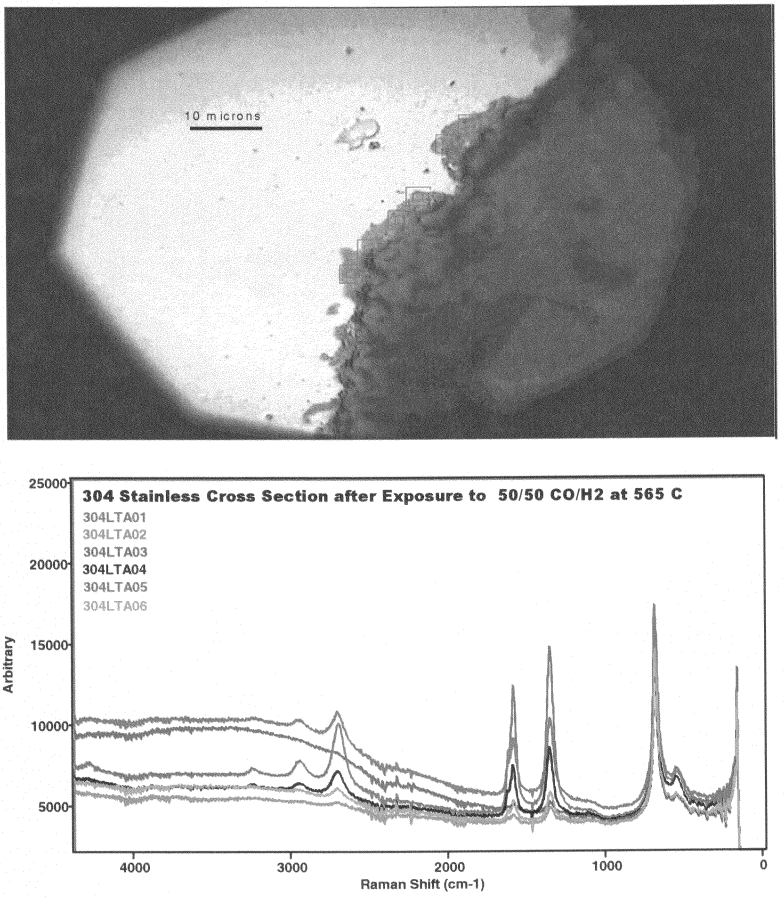

FIGURE 16 Image of 304 Stainless Steel Exposed to 50% CO, 50% H_2 at 565°C and Raman Spectra.

- Metal oxidation, generally concurrent with carbon deposition, is an integral component of CO-initiated metal dusting reactions on Fe, C1008, and SS316L. Continued CO exposures lead to the formation of an ordered form of Fe_3O_4 (magnetite) on Fe and C1008, while a mixed-oxide spinel, $(Fe_xCr_y)_3O_4$, was indicated on SS316L. The relative amounts of amorphous carbon and metal oxide were non-uniform across the resulting heterogeneous surfaces, which exhibited irregular pitting and clearly defined grains and grain boundaries.

- In contrast to Fe-based samples, CO-exposure of Ni 200 (0.15 wt% carbon) resulted in growth of a more ordered/graphitic form of carbon. Ni 200 did not undergo oxidation under these experimental conditions: 400–480°C, 2 Torr CO. Future experiments will include Ni 201 (~ 0.02 wt% carbon) to unambiguously decouple the effect of bulk carbon on metal dusting reactions.

- Mounted and polished cross sections of Stainless Steel 304 that had been exposed to 50% CO, 50% H_2 at 565°C and 732°C under flow in a tube furnace for extended times were also analyzed. The difference in the oxide structures between high and low temperature exposures suggests the chromia coating may provide some degree of protection to the alloy from metal dusting.

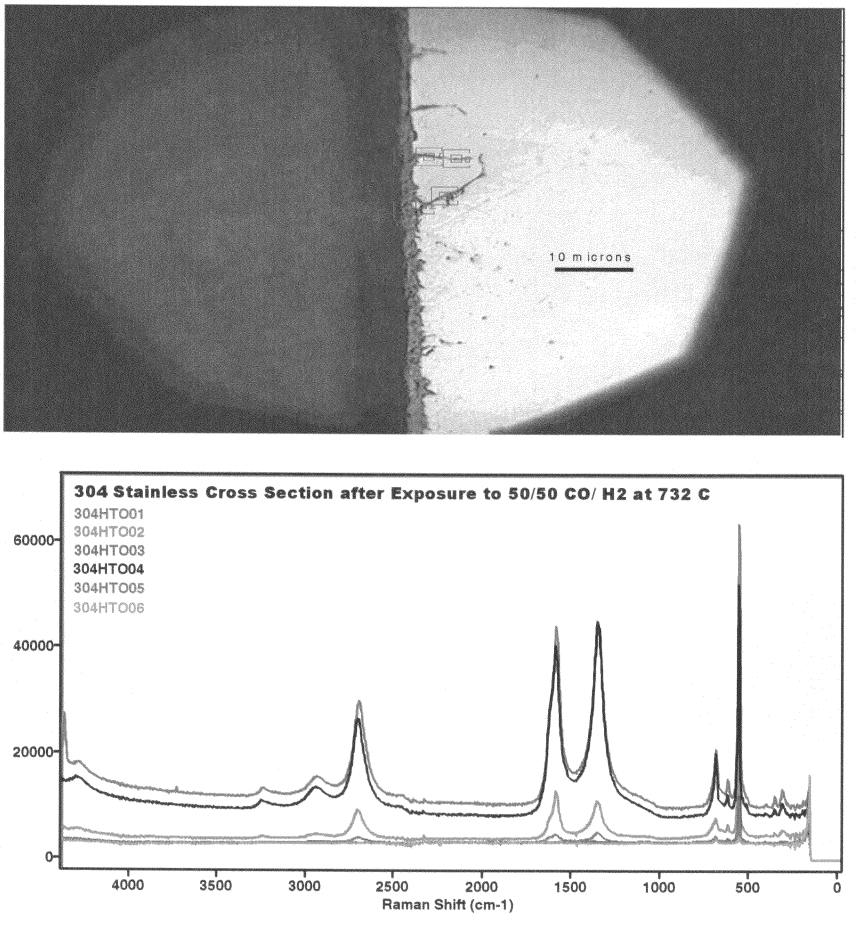

FIGURE 17 Image of 304 Stainless Steel Exposed to 50% CO, 50% H_2 at 732°C and Raman Spectra.

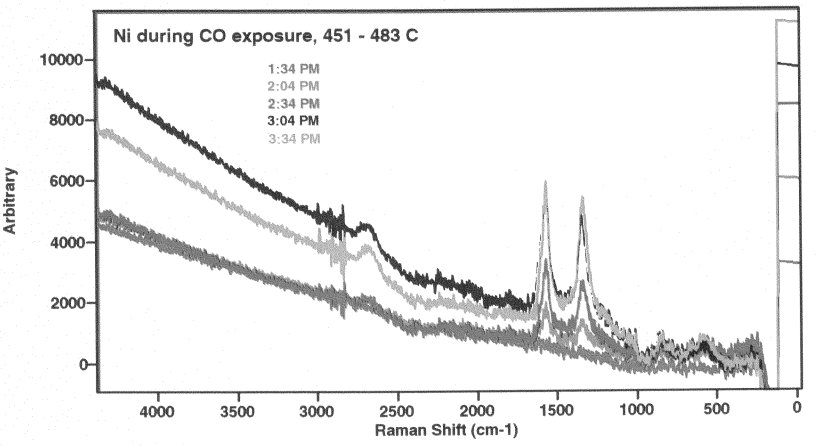

FIGURE 18 Raman Spectra of Surface of Ni 200 Exposed to 1.5 Torr of CO at 470 °C for 2 h.

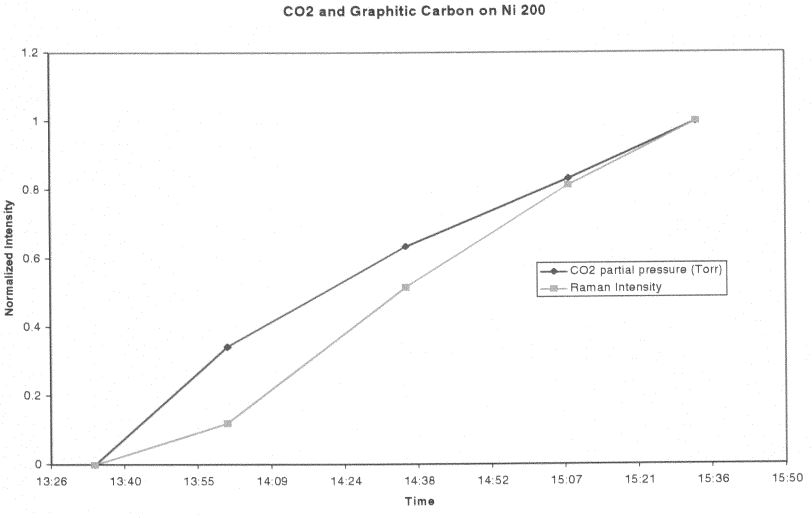

FIGURE 19 Calculated Values of CO_2 Pressure and Integrated Raman Intensity for Ni200.

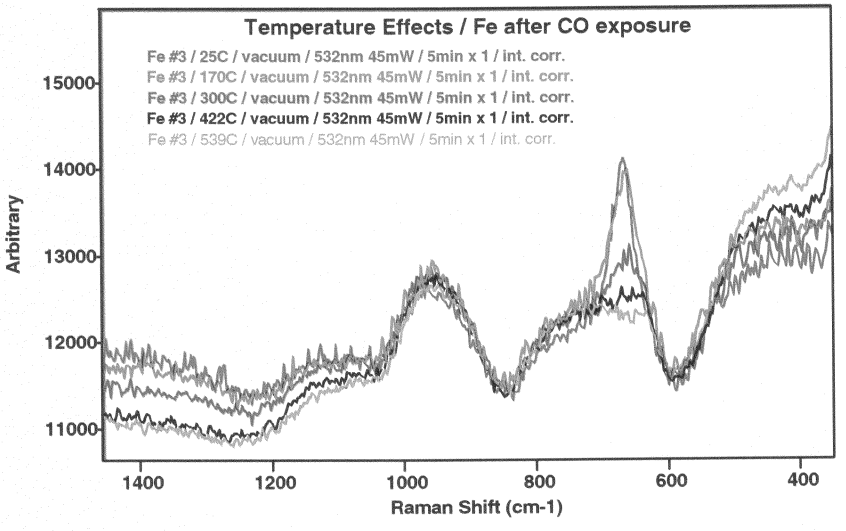

FIGURE 20 Raman Spectra Obtained While Raising the Temperature, Under Vacuum, of an Fe Sample with Amorphous Carbon and Magnetite on its Surface from Previous CO Exposure.

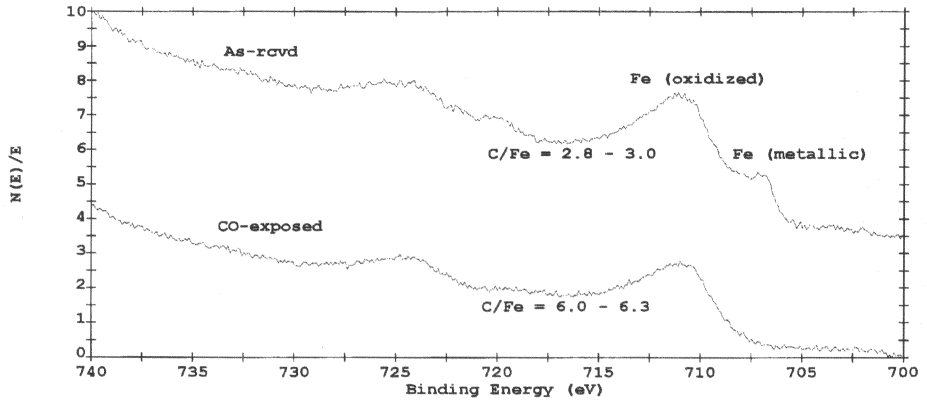

FIGURE 21 Fe 2p Photoelectron Spectra of As-received and CO-exposed Carbon Steel; dark region

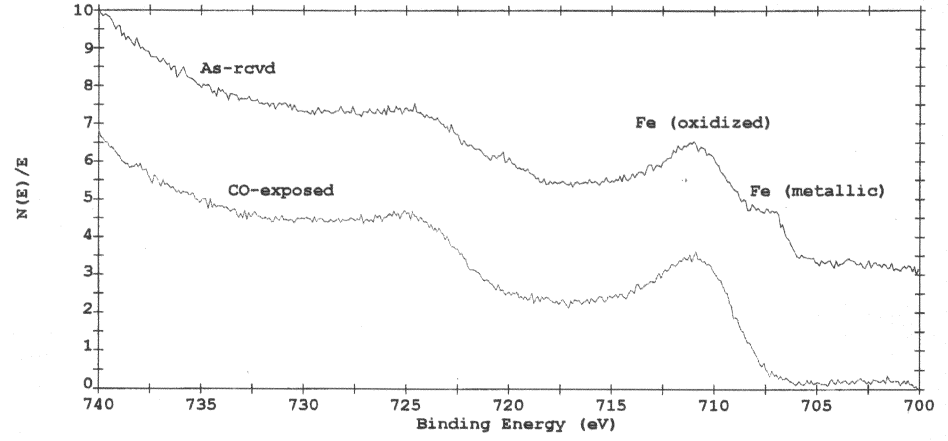

FIGURE 22 Fe 2p Photoelectron Spectra of As-received and CO-exposed 316L; dark region

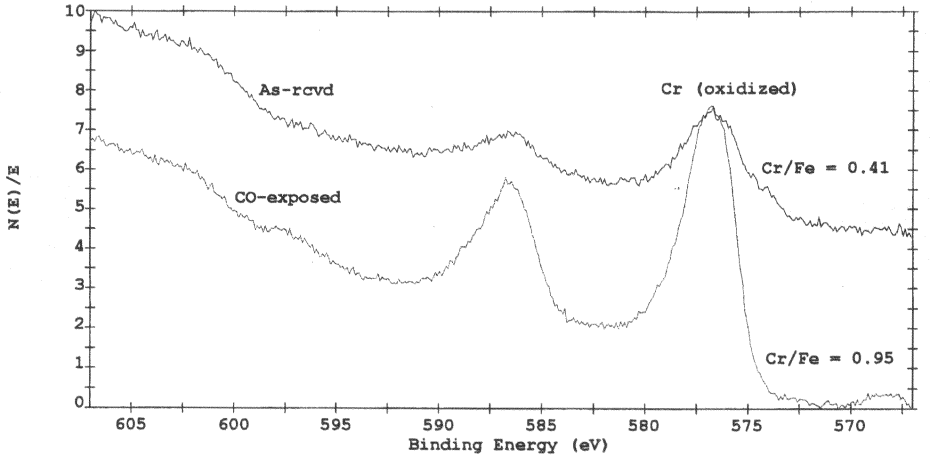

FIGURE 23 Cr 2P Photoelectron Spectra of As-received and CO-exposed 316L; dark region

REFERENCES

Dean, Jr., S. W., "Estimating Metal Dusting Attack on Stainless Steel Alloys in Syngas Environments", Paper No. 01384, NACE 2001.

Fabiszewski, A. S., W. R. Watkins, J. J. Hoffman and S. W. Dean, Jr., "The Effect of Temperature and Gas Composition on the Metal Dusting Susceptibility of Various Alloys", Paper No. 00532, NACE 2000; A. S. Fabiszewski, W. R. Watkins, J. J. Hoffman and S. W. Dean, Jr., RRRS document APCI/CRS/00-003.

Grabke, H. J., "Metal Dusting of Low- and High-Alloy Steels", Corrosion, Vol. 51 (9), p. 711-720, 1995.

Grabke, H. J. and E. M. Muller-Lorenz, "Occurrence and Prevention of Metal Dusting on Stainless Steels", Paper 01373, NACE 2001.

Jones, R. T. and K. L. Baumert, "Metal Dusting – An Overview of Current Literature", Paper No. 01372, NACE 2001.

Kirchheiner, R. and J. L. Jimenez Soler, "Correlation of Oxidation, Carburization and Metal Dusting: Controlling Corrosion by Corrosion", Paper 01374, NACE 2001.

MECHANISMS OF METAL DUSTING CORROSION OF PURE METALS

C.M. CHUN, ExxonMobil Research and Engineering, Annandale, New Jersey*
T.A. RAMANARAYANAN, ExxonMobil Research and Engineering, Annandale, New Jersey
L. CLAVENNA, ExxonMobil Process Research, Baton Rouge, Louisiana

ABSTRACT

Metal dusting is a severe form of corrosive degradation of metals and alloys at high temperatures (300-850°C) in carbon-supersaturated gaseous environments. Fe, Ni and Co, as well as alloys based on these metals are all susceptible. The corrosion manifests itself as a break-up of bulk metal to metal powder - hence the term, metal dusting. The present work is a study of the metal dusting corrosion of pure metals, Fe, Ni and Co in high carbon activity environments. The main goal of the study was to advance the atomic level understanding of metal dusting. Investigations covered a temperature range from 350 to 1050°C. Four regimes of corrosion were identified for Fe as a function of temperature. In regime I the corrosion rate gradually increases with temperature, in regime II the corrosion rate undergoes a rapid rise, in regime III the corrosion rate decreases with temperature and in regime IV, the rate is more or less constant. Formation of metastable Fe_3C resulting from carbon supersaturation at the surface, followed by its dissociation triggered by interfacial graphite, are phenomena associated with regimes I, II and III. Intercalation and diffusion of iron atoms in graphite are the mechanisms whereby metal particles are carried away from the corrosion interface. In regime IV no metastable M_3C forms: there occurs direct intercalation of iron into graphite. For Ni and for Co, where no metastable carbide forms over the entire temperature range, the metal dusting mechanism is similar to regime IV for iron.

INTRODUCTION

Metal dusting involves the disintegration of bulk metals and alloys into metal particles at high temperatures in environments that are supersaturated with carbon. It is generally believed that the phenomenon is most wide-spread in the temperature range, 400~700°C. Hochman (Hochman and Burson 1966; Hochman 1972 and 1977) did early research on metal dusting. Since then Grabke and co-workers (Grabke, Krajak and Nava Paz 1993; Grabke 1998; Klower, Grabke and Muller-Lorenz 1998; Nava Paz and Grabke 1993; Strauss and Grabke 1998) have carried out some detailed studies on the subject. The micro-mechanistic aspects of metal dusting have been investigated by transmission electron microscopy (TEM) as reported by others (Pippel, Woltersdorf and Schneider 1998; Chun, Mumford and Ramanarayanan 1999 and 2000). In most of the above work carbon monoxide has been used as the main carbon providing molecule. Metal dusting in the presence of methane and at higher temperatures has been addressed (Forseth and Kofstad 1995).

It appears that CO is the most potent metal dusting molecule and the presence of hydrogen in carbon monoxide tends to accelerate metal dusting corrosion. When considering metal dusting corrosion in CO or CH_4-containing environments, the following reactions can lead to the transfer of carbon to the metal surface.

*Corresponding author address: C. Chun, ExxonMobil Research and Engineering, 1545 Route 22 East, Annandale, NJ 08801; e-mail: changmin.chun@exxonmobil.com.

$$CO + H_2 = C + H_2O \quad [1]$$
$$2CO = C + CO_2 \quad [2]$$
$$CH_4 = C + 2\,H_2 \quad [3]$$

As reported by others (Grabke and Tauber 1975; Shatynski and Grabke 1978), reaction [1] has the fastest kinetics: this would explain the higher metal dusting rates encountered in CO-H_2 environments. Hochman (Hochman 1972 and 1977) has proposed the following scheme to explain the metal dusting corrosion of iron. Initially, the metastable carbide, Fe_3C, forms on the iron surface in the carbon-supersaturated gaseous environment. Subsequently, carbon deposits on the iron carbide surface. The deposition of carbon destabilizes the iron carbide whereupon it dissociates into carbon and metal particles, resulting in metal dusting. Grabke (Grabke 1998) has further refined this general mechanism: a schematic representation is shown in figure 1. The gradient of carbon activity at various stages of the corrosion process is also indicated in figure 1. Also included in figure 1 are cross sectional scanning electron microscopy (SEM) images of the different stages taken from our present study. In figure 1a, carbon is being transferred to the iron surface by reaction between CO and H_2. Figure 1b shows the precipitation of metastable Fe_3C on the surface. The subsequent decomposition of iron carbide upon carbon deposition is shown in figure 1c. Iron carbide dissociation is triggered by graphite deposition, which decreases the carbon activity at the Fe_3C/graphite interface to 1. The carbon atoms resulting from subsequent Fe_3C dissociation attach themselves to the graphite. Metal atoms arising from iron carbide dissociation can migrate away from the Fe_3C/graphite interface via the space between adjacent graphite planes (Pippel, Woltersdorf and Schneider 1998).

Our investigation is in agreement with this mechanism in an overall sense. However, studying the corrosion interface at the nano level using cross sectional TEM raises several interesting questions. In the present fundamental study, based on the microstructure of metal-dusted

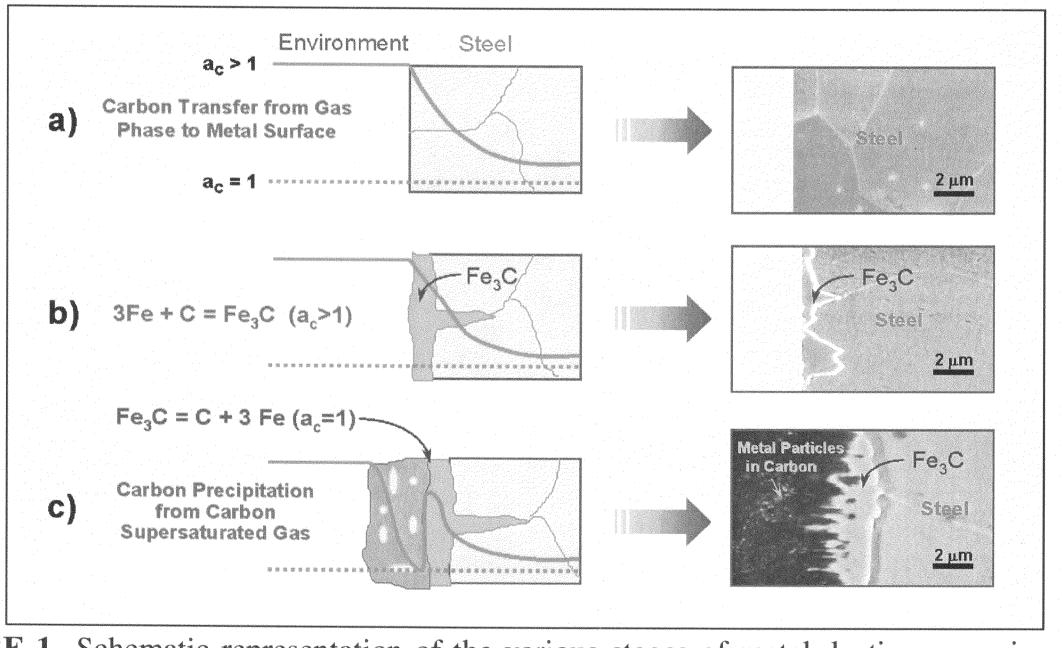

FIGURE 1 Schematic representation of the various stages of metal dusting corrosion of iron (Grabke 1998).

Fe, Ni and Co samples, the influence of temperature and gas chemistry on the corrosion process has been further explored. The atomic level mechanistic picture also attempts to explain the influence of reaction layers and forms of carbon on the corrosion process.

EXPERIMENTAL APPROACH

Polycrystalline Fe, Ni and Co foils were used in the experiments. Foils of 99.99 % purity were obtained from Alfa Co. and had thickness of ~100 μm and ~250 μm. Foils of rectangular geometry with approximate dimensions of 1 cm × 0.5 cm were investigated without further surface preparation. The metal dusting gas mixture consisted of CO and H_2, the CO:H_2 ratio ranging from 98:2 to 5:95. Corrosion kinetics were investigated thermogravimetrically using a Cahn 1000 electrobalance and also by timed exposure to a gas mixture in a tubular reactor followed by microscopic measurement of the recession of the metal surface from its initial location. The temperature of corrosion ranged from 350°C to 1050°C. In the thermogravimetric measurements, the carbon pick up by the metal sample is used as a measure of metal dusting corrosion while the microscopic approach involves a direct measurement of metal loss. The latter is thus considered more accurate. After corrosion, selected samples were mounted vertically in an EpoFix embedding medium. The cross-sectional morphology of the corrosion interface was examined by JEOL 840A SEM. Cross sectional TEM combined with microdiffraction and microchemical analysis was used to investigate the reaction interfaces at the nano level. A sandwich structure with the specimen in the middle was created using Gatan G1 epoxy glue and dummy glass pieces. Discs of 100 mm thickness were then cut and polished from the sandwich. These were dimpled and ion-milled to generate electron transparent areas. Micrographs were taken using a Philips CM200/FEG TEM.

RESULTS

Effect of Gas Chemistry (CO/H_2) in Metal Dusting Corrosion of Fe

Shown in figure 2a are results for the general corrosion rate of iron (in mils per year or mpy) measured at 550°C after 7 hours of reaction as a function of the composition of the metal dusting gas mixture. These results were obtained from microscopic measurement of the metal recession with respect to an inert metal coating. Two distinct regions were observed. In region A, the corrosion rate is more or less independent of the gas composition. In region B, the general corrosion rate is seen to go through a maximum, which occurs at the 50CO:50H_2 composition. These results are consistent with the observation by other researchers (Grabke and Tauber 1975) that reaction [1] has the maximum rate of carbon transfer. The forward rate of reaction [1] should be proportional to the product of the concentrations of CO and H_2. This product is a maximum at equal concentrations of CO and H_2 in the gas mixture. Thus it appears that for short duration of corrosion (~7 hours) at 550°C, surface reaction transferring carbon is the rate-limiting step.

The cross sectional SEM micrograph in figure 2b shows the typical microstructure of polycrystalline Fe foil having an average grain size of 10 μm. After reaction at 550°C for 7 hours at the 50CO:50H_2 composition, the cross sectional microstructure reveals the regions of general corrosion and localized corrosion of iron: the arrows indicate the recession of the metal surface with respect to a coated region free of metal dusting. A typical expanded view of the general corrosion region is presented in figure 2c. An Fe_3C surface layer and a carbon deposit consisting of metal particles and iron carbides can be readily observed. Most surfaces of Fe_3C grains at the interface with carbon deposit are serrated. Some regions have become encased in graphite forming relatively large Fe_3C particles (>5 μm) within the carbon deposit. These particles are

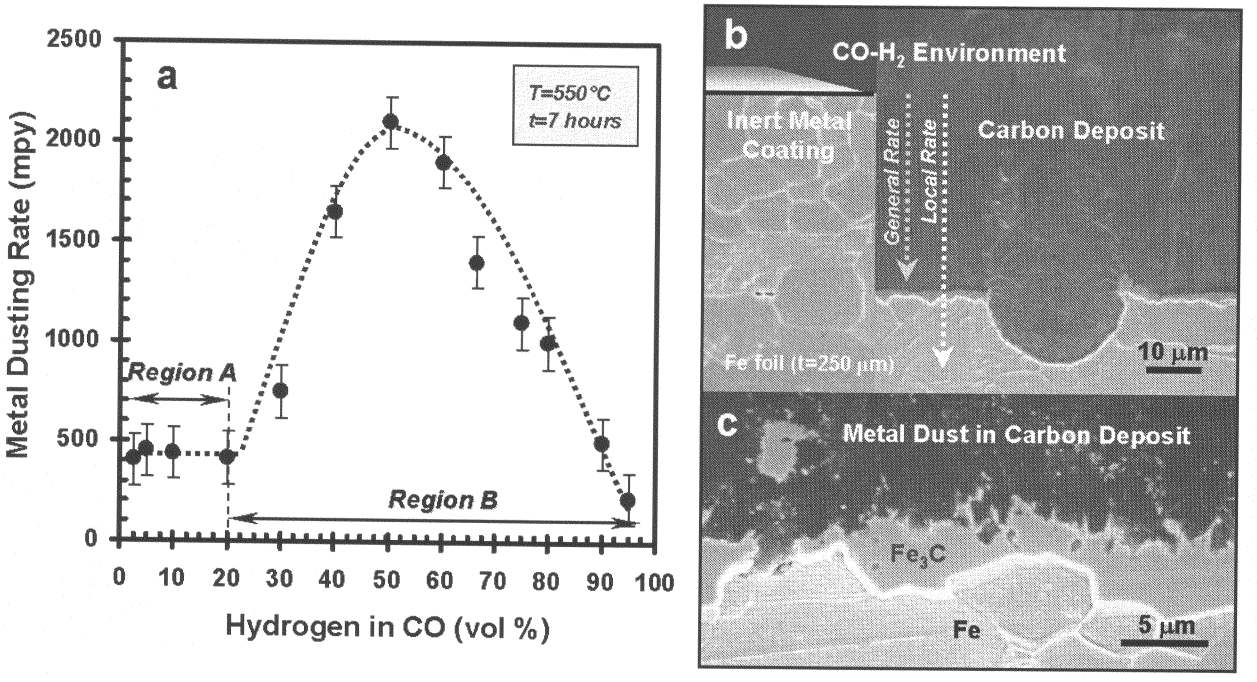

FIGURE 2 (a) Metal dusting corrosion rate of iron (250 μm thick foil) as a function of H_2 content in CO after reaction at 550°C for 7 hours. Cross sectional SEM images showing regions of (b) general and localized corrosion of iron foil and (c) expanded view of the Fe/Fe_3C/C interface after reaction at 550°C for 7 hours at 50CO:50H_2.

probably dislocated from the surface Fe_3C layer and undergo further disintegration with continued carbon transfer.

Effect of Temperature on Metal Dusting Corrosion of Fe

The temperature dependence of the general corrosion rate of iron measured after 48 hours of reaction in a 50CO:50H_2 gas mixture is shown in figure 3a. The effect of temperature on the metal dusting rate can be divided into four regimes – these regimes are marked in figure 3a. In regime I which extends from 350°C to 500°C, there is a gradual increase in corrosion rate with temperature with a very small slope. Between 500°C and 575°C, regime II, the corrosion rate undergoes a rapid rise, reaching a maximum at 575°C. In regime III, which extends from 575°C to 775°C, the corrosion rate gradually decreases with temperature. Finally in regime IV, which occurs above ~775°C, the corrosion rate is more or less independent of temperature. Each of these regimes is described below.

Regime I (350 ℃~500 ℃) – This regime is characterized by the formation of a surface Fe_3C layer on iron and deposited carbon on the surface. Figure 3b, which is a cross sectional BF TEM image of a sample of Fe foil subjected to metal dusting at 350°C for 72 hours in a 98CO:2H_2 gas mixture, shows fracturing of surface Fe_3C, characteristic of regime I. Shown in the inset is the selected area electron diffraction (SAED) pattern taken at Fe_3C/Fe interfacial area at a beam orientation of B=[031] Fe_3C and B=[011] Fe. In figure 3c, the cross sectional SEM image of a sample after reaction at 450°C for 7 hours at the 98CO:2H_2 composition again shows a region with a characteristic appearance of "volcanic eruption" of surface Fe_3C. Thus stresses generated during the formation and growth of Fe_3C appear to be rather large in regime I. Above a critical stress level,

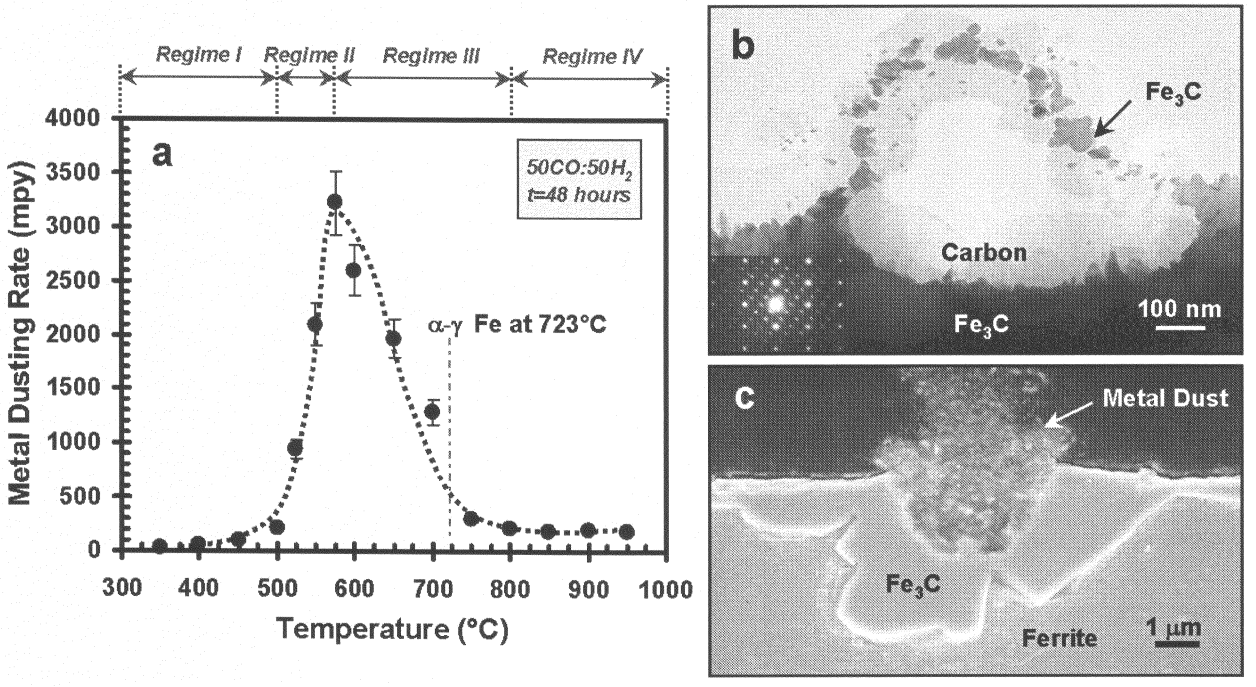

FIGURE 3 (a) Temperature dependence of the metal dusting corrosion rate of iron in $50CO:50H_2$ gas mixture. (b) C/S BF TEM image showing fracture of surface Fe_3C and SAED pattern at Fe_3C/Fe interface after reaction at 350°C for 72 hrs at $98CO:2H_2$. (c) C/S SEM image showing "volcanic eruption" of surface Fe_3C after reaction at 450°C for 7 hrs at $98CO:2H_2$.

the surface Fe_3C layer breaks up: ripples of fractured Fe_3C, migrating upward through the carbon deposit, can be seen in figure 4a. Figure 4b, a high resolution TEM image of the Fe_3C/carbon interface shown in figure 3b, indicates that the nature of carbon deposit on the surface of Fe_3C is mostly amorphous in this region. Amorphous carbon does not provide a pathway for iron atoms from dissociated Fe_3C to escape. Therefore, stress relief by continuous fracturing of Fe_3C is characteristic of regime I. It is also evident from figure 4a that corrosion preferentially continues in the region where initial fracture of Fe_3C has occurred. This is probably due to increased stress build-up in the Fe_3C layer on the concave metal surface resulting from the break-up of first-formed Fe_3C. The sequence of Fe_3C formation and fracture leads to localized corrosion.

Regime II (500℃~575℃) – Figure 2b is characteristic of regime II. Both general corrosion, characterized by the growth and dissociation of Fe_3C, and localized corrosion resulting from the rupture of Fe_3C, occur in regime II. A magnified SEM image of the general corrosion region is shown in figure 2c. The competition between Fe_3C growth at the metal/Fe_3C interface and Fe_3C dissociation at the carbide/carbon deposit interface characterizes general corrosion. The carbon deposit next to Fe_3C has a substantial amount of graphite in addition to amorphous carbon; the proportion of graphitic carbon increases with temperature. At the same time, general corrosion is favored since graphitic carbon offers a pathway for the migration of metal atoms arising from Fe_3C dissociation.

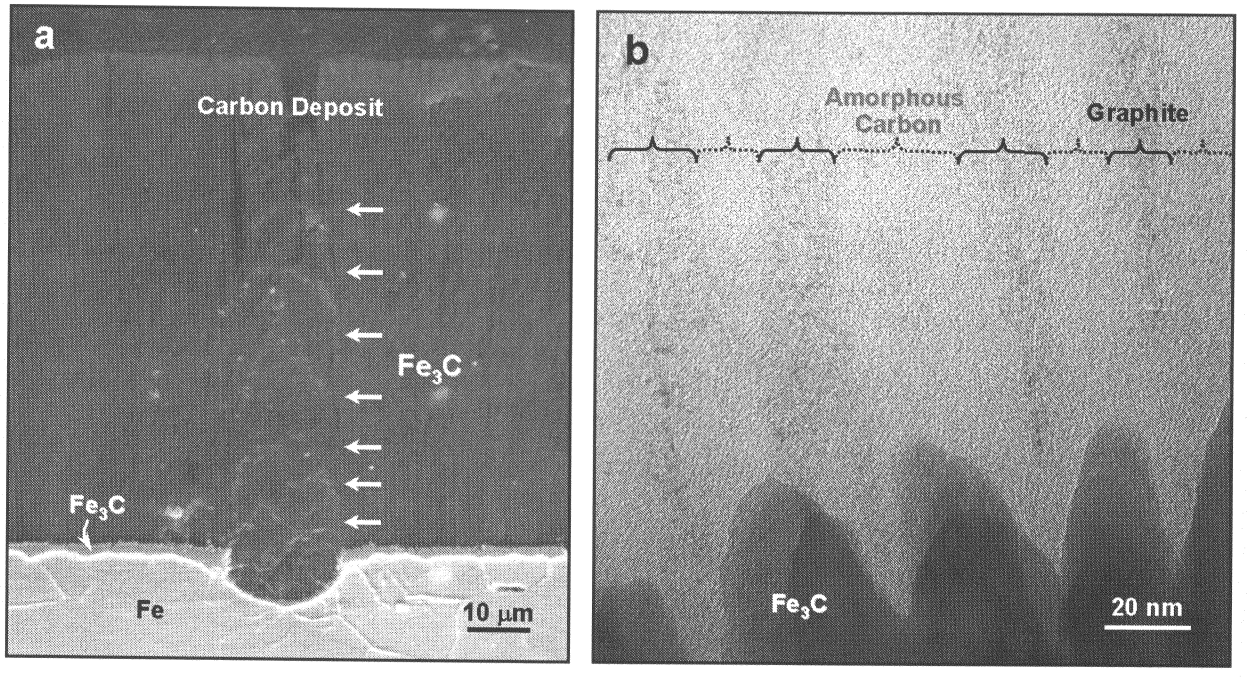

FIGURE 4 (a) Cross sectional SEM image showing ripples of fractured Fe_3C after reaction at 500°C for 7 hours at $50CO:50H_2$. (b) High resolution TEM image of the Fe_3C/carbon interface after reaction at 350°C for 72 hours at $98CO:2H_2$.

Regime III (575°C~775°C) – The typical microstructure in the falling part of the curve (figure 3a) is shown in figure 5a. This image was obtained by Secondary Ion Mass Spectroscopy (SIMS) of a metal dusted Fe foil, which was corroded at 650°C for 7 hours at the $50CO:50H_2$ composition. Fe_3C growth and its dissociation are the principal corrosion processes in this regime. The SEM micrograph in figure 5b shows a cross sectional image of a metal-dusted Fe foil after reaction at 750°C for 7 hours at the $50CO:50H_2$ composition. The average Fe_3C layer thickness in this regime is about 3 times higher as compared to the 650°C case. This suggests a slowing down in the Fe_3C dissociation rate. The room temperature microstructure below the Fe_3C layer shows a pearlitic structure typical of the transformation of carbon-saturated gFe (fcc) to pearlite (aFe + Fe_3C) on cooling.

Regime IV (775°C~1050°C) – This regime is characterized by the absence of surface Fe_3C carbide. A typical high temperature microstructure is shown in figure 6a. This image was obtained after corrosion at 800°C for 7 hours at the $50CO:50H_2$ composition. The absence of surface carbide is because of the rapid dissolution and diffusion of carbon in the austenite phase (gFe) at this high temperature. The room temperature microstructure is fully pearlitic (aFe + cementite), arising from the dissociation of carbon-saturated austenite upon cooling (figure 11d). Figure 6b shows the Fe/carbon interface after metal dusting at 950°C for 7 hours at the $50CO:50H_2$ composition. Most grains of Fe are serrated by the intrusion of carbon. The localized corrosion of iron is profuse primarily in the grain boundary regions. Some locations of the carbon/Fe interface appear to be smooth; basal planes of graphite are oriented parallel to the surface in such regions as confirmed by cross sectional TEM.

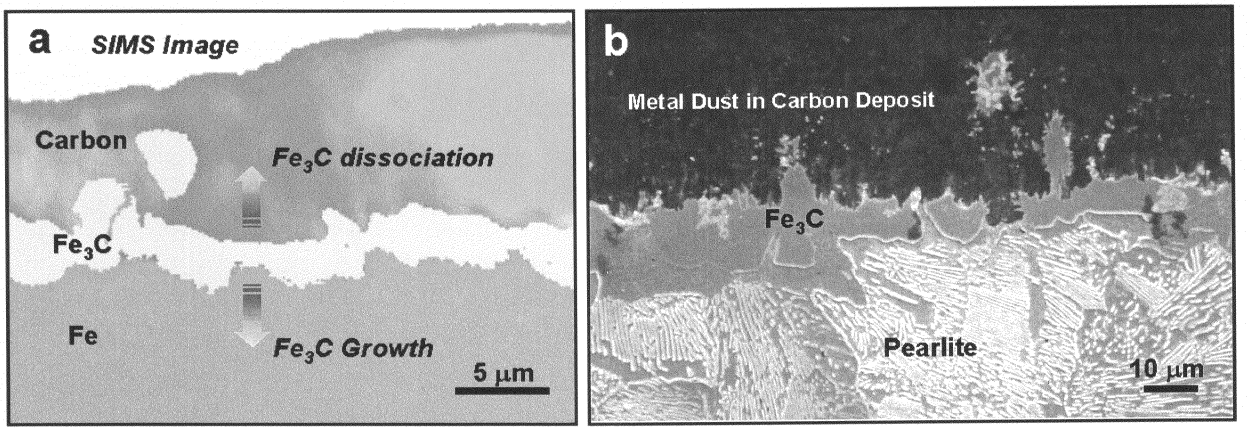

FIGURE 5 (a) SIMS image of metal-dusted interface showing the competition between Fe_3C growth and dissociation after reaction at 650°C for 7 hours at $50CO:50H_2$. (b) Cross sectional SEM image of metal-dusted iron after reaction at 750°C for 7 hours at $50CO:50H_2$.

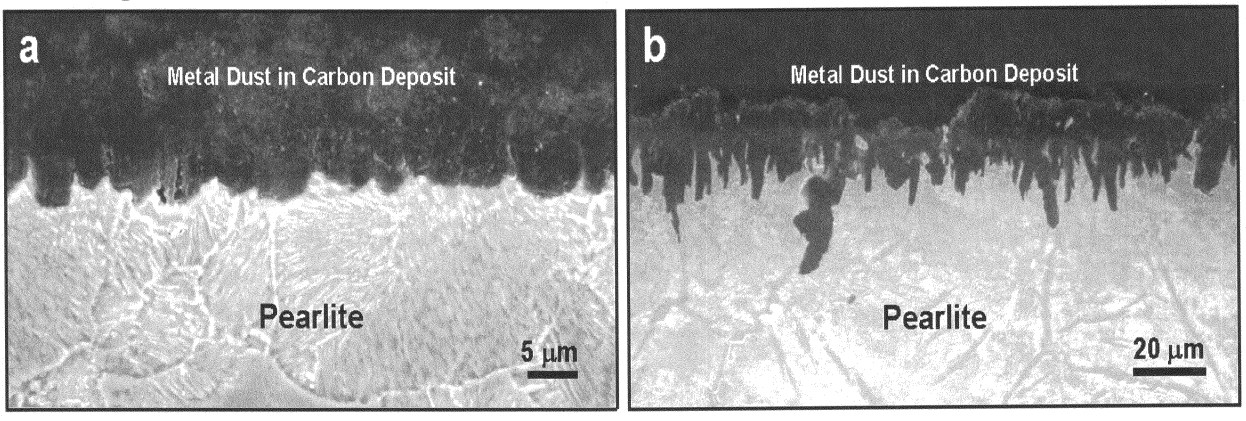

FIGURE 6 Cross sectional SEM image of metal-dusted iron after reaction (a) at 800°C, and (b) at 950°C for 7 hours at $50CO:50H_2$.

Temperature Dependence of Metal Dusting Corrosion of Ni and Co

Over the temperature range of corrosion investigated in the present study both Ni and Co do not form a carbide. Nevertheless, Ni and Co do undergo metal dusting corrosion. Shown in figure 7a is the corrosion rate of Ni and Co as a function of temperature at a CO/H_2 ratio of 25.The effect of temperature on the metal-dusting rate can be divided into two regimes – these regimes are marked in figure 7a. In regime A, which extends from 350 and 750°C, the corrosion rate gradually increases with temperature (cf., regime I for Fe). In regime B, which occurs above 750°C, the corrosion rate is more or less independent of temperature (cf., regime IV for Fe). Regime A is characterized by amorphous carbon deposit on Ni surface. Figure 7b, a cross sectional TEM image of the carbon/Ni interface after reaction at 400°C for 7 hours at CO/H_2 = 25, indicates that the nature of carbon deposit on the surface is mostly amorphous with some graphite also present. The graphitic carbon is oriented randomly within amorphous carbon matrix. The proportion of graphitic carbon increases with temperature in regime A. Regime B is typified by the predominance of graphitic carbon deposit on the Ni surface. Figure 7c, a cross sectional TEM image of the carbon/Ni interface after reaction at 650°C for 7 hours at CO/H_2 = 25, shows that the carbon deposit next to the Ni surface has a substantial amount of graphite, whose basal planes are oriented perpendicularly to the surface.

DISCUSSION

Temperature Dependence of Metal Dusting Corrosion Rate

The temperature dependence of general corrosion rate can be correlated with forms of carbon on the corrosion process. For iron, the rate of general corrosion in regime I is rather low (figure 3a), increasing slowly with temperature. High resolution TEM images of the Fe_3C/carbon interface at temperatures from 400°C to 500°C are very similar to the one at 350°C (figure 4b). The nature of carbon layer next to Fe_3C is substantially amorphous. The proportion of graphitic carbon increases slightly with temperature in regime I. Since iron atoms from dissociated Fe_3C can not migrate away through amorphous carbon, the corrosion rate is suppressed, leading to fracturing of surface Fe_3C. However, there is a very rapid increase in the rate of corrosion in regime II. This is due to a substantial increase in the content of graphitic carbon in the carbon deposit with temperature, which leads to a rapid rise in corrosion rate as a function of temperature in this regime. The decrease in corrosion rate in regime III can be explained by the schematic carbon activity profile at various interfaces as indicated in figure 8. The decomposition of cementite is triggered by carbon deposition whereby the carbon activity at the Fe_3C/carbon interface becomes unity. Meanwhile, the carbon activity of carbon in Fe_3C decreases with increasing temperatures. The nucleation rate of metal particles by cementite decomposition should be related to the chemical potential difference of carbon in cementite and graphite, namely $(\square_c-\square_c^*)$, where $\square_c$ is the chemical potential of carbon in cementite and $\square_c^*$ is that in graphite, respectively. Since this difference decreases sharply with temperature in regime III, it qualitatively provides an explanation for the decrease in corrosion rate with temperature. Because of the slower decomposition rate of Fe_3C, one would expect a thicker Fe_3C layer in this regime as temperature increases. This is confirmed by the cross sectional SEM micrograph in figure 5.

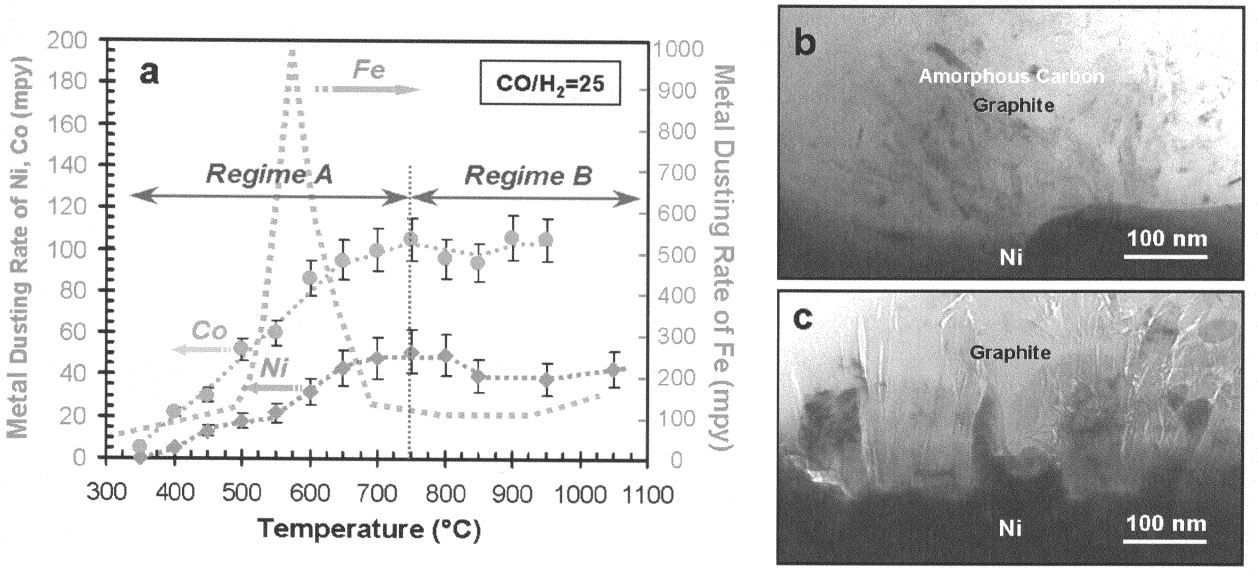

FIGURE 7 (a) Temperature dependence of the general rate of metal dusting corrosion of nickel and cobalt at a CO/H_2 ratio of 25. Also plotted is the metal dusting rate of iron at the same gas composition for comparison. Cross sectional TEM images at the Ni/carbon interfaces after reaction (b) at 400°C for 7 hours and (b) at 650°C for 7 hours at a CO/H_2 ratio of 25.

The temperature dependence of general corrosion rate of Ni and Co also can be correlated with the nature of carbon on the metal surface. Raman spectroscopy, in addition to TEM, was used to investigate the nature of carbon as a function of temperature. Carbonaceous deposits produced by the decomposition of CO and H_2 at 400, 600, 750, and 850°C on Co foil substrates were studied. Raman spectra were excited at a wavelength of 514.5 nm from an Ar^+ laser operating at 50 mW. The laser power was attenuated resulting in about 5 mW incident on the sample. The measurements represent the structure of the carbon layer adjacent to the Co substrate since the filamentous carbon overlayer was removed. The predominant features in the first order Raman spectrum excited at 514.5 nm are bands at 1581 cm^{-1} (G band) and 1355 cm^{-1} (D band). Weaker features at 1620 cm^{-1} (D' band) and 1500 cm^{-1} (D" band) have also been reported.

The G band is the only feature in the first-order spectrum of graphite. For imperfect material with shorter range order the D, D', and D" bands appear. The relative intensity of the D to G bands depends both on the degree of disorder and the angle between the incident laser and the graphitic planes. For this study, the fraction of the G band intensity to the total intensity of the (G+D) bands was taken to represent the degree of order in the deposits. Figure 9a shows the increase in this fraction with temperature. For the 400°C and 600°C temperatures, the fraction for the three positions (left, center, and right, shown as diamond data points) shows good sample homogeneity. For the 750 and 850°C samples, additional measurements were made since the samples were found to be structurally more inhomogeneous, due primarily to the growth of highly ordered graphitic grains. The single square data point for the 850°C sample is representative of scattering from a single large graphite grain. These results suggest that the amorphous carbon becomes more highly ordered and graphitic as the temperature increases. The gradual increase in corrosion rate with temperature if figure 7a is consistent with this finding.

Similar to the behavior of Fe in regime IV, the corrosion rates of Ni and Co in regime B are nearly independent of temperature above approximately 750°C. This would mean that the activation energy for the rate-limiting step in corrosion is negligible. The most likely rate-limiting step is the diffusion of metals through graphite. The atomic diameters of Fe, Ni and Co are 2.52 Å, 2.60 Å and 2.77 Å, respectively. On the other hand, the distance between basal planes in graphite is 3.35 Å. Thus it is not unresonable to expect that the diffusion of metals through graphite would be rather unrestricted accounting for the very low activation energy.

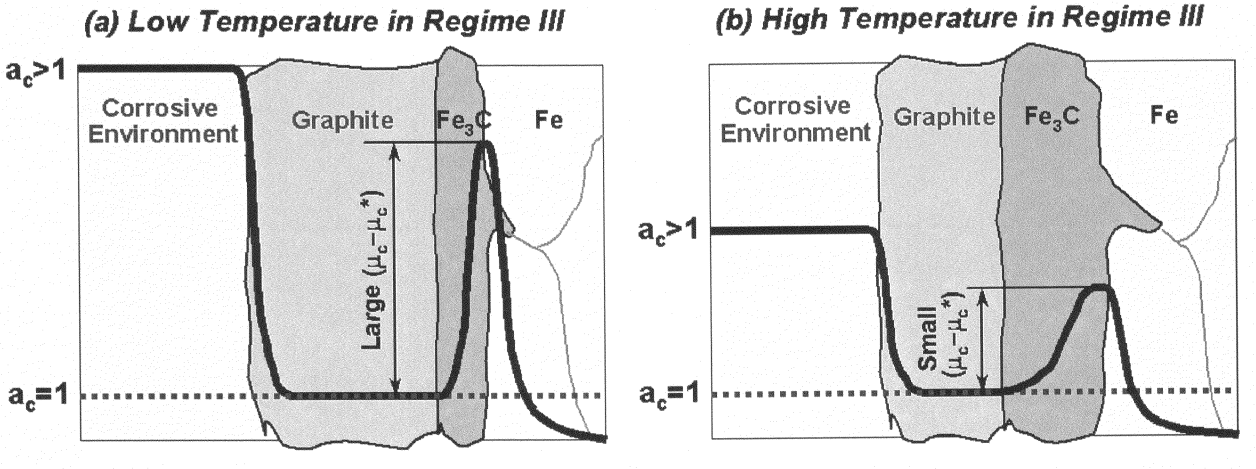

FIGURE 8 Schematic carbon activity profile at various interfaces during metal dusting corrosion of Fe in regime III.

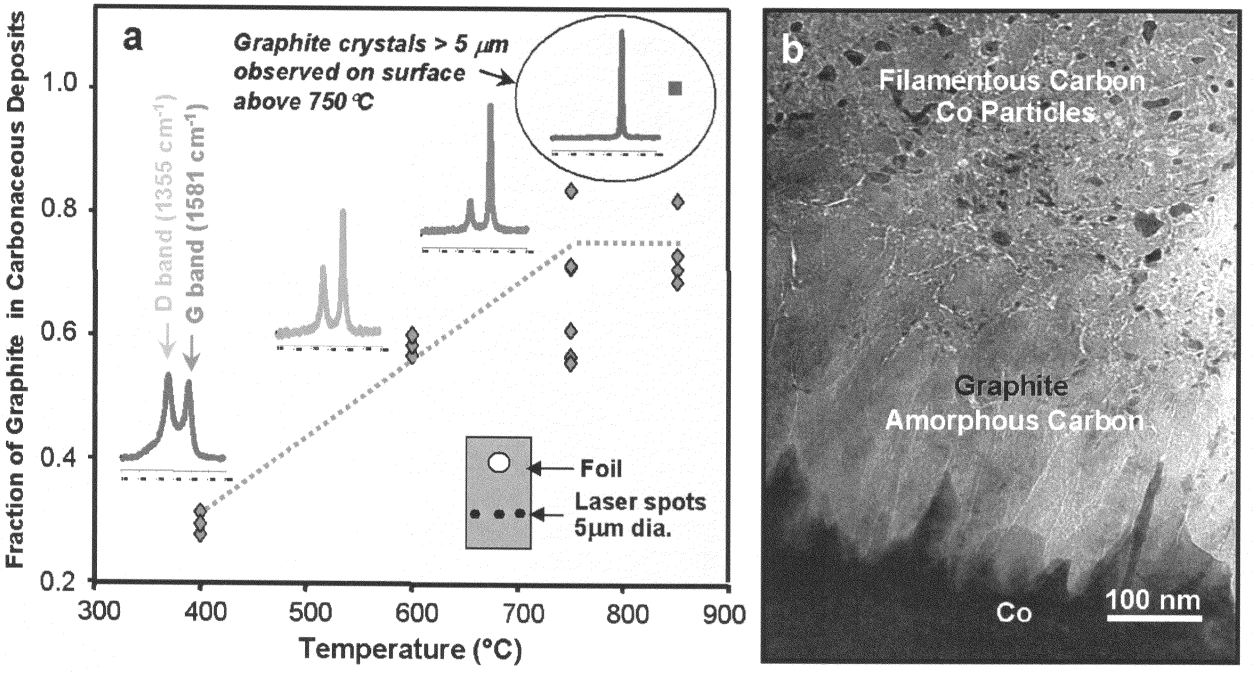

FIGURE 9 (a) Fraction of graphite in carbonaceous deposits on the surface of cobalt foils as a function of temperature. (b) Cross sectional TEM image showing the carbon/Co interface after reaction at 600°C for 7 hours at $50CO:50H_2$.

Nanomechanism of Metal Dusting Corrosion of Fe

In the Presence of Surface Fe_3C Carbide (Regimes I, II and III) – In order to examine the metal dusting mechanism of Fe at the nano level, cross sectional TEM investigations were carried out. Shown in figure 10 are TEM images of the different interfaces and electron diffraction pattern from the carbon deposit. The TEM image in figure 10a is a cross-section of a sample after reaction at 450°C for 7 hours at the $98CO:2H_2$ composition showing Fe metal, a surface layer of cementite and carbon deposit on the cementite. The carbon deposit is a mixture of amorphous and graphitic carbon. A magnified TEM image of the cementite/carbon deposit interface after corrosion at 650°C for 7 hours at the $98CO:2H_2$ composition is shown in figure 10b. The iron carbide at the interface is seen to be highly serrated. The nature of carbon layer next to Fe_3C is predominantly graphitic (~80 %), the rest being amorphous. In general, proportionately more amorphous carbon was observed at the lower temperatures next to the Fe_3C surface. A selected area electron diffraction (SAED) pattern from the carbon deposit next to the cementite, shown in figure 10c, confirms that the carbon in this region is predominantly graphitic. The reflections from graphite (002) planes are highly oriented. The graphite is aligned perpendicular to the cementite for the most part as is evident from the SAED pattern. Fe particles have been identified within the graphite phase as indicated by the diffraction rings for Fe (110) in figure 10c. A high resolution TEM image at the graphite/Fe_3C interface, figure 10d, reveals graphite fringes with an interplanar spacing of ~3.35 Å. At the Fe_3C/Fe interface, a high resolution TEM image shown in figure 7e reveals continuous lattice fringes throughout the interface, suggesting the epitaxial relationship of (031) Fe_3C // (011) Fe. The interplanar spacing of the Fe_3C (031) plane is 2.01 Å and the spacing of the Fe (011) is 2.03 Å. The cross-sectional TEM image of the filamentous carbon/graphite interface after corrosion at 650°C for 7 hours at the $98CO:2H_2$ composition is shown in figure 10f. The outer surface of the carbon deposit which is in contact with the gas phase is profuse with filamentous carbon, whose growth has been

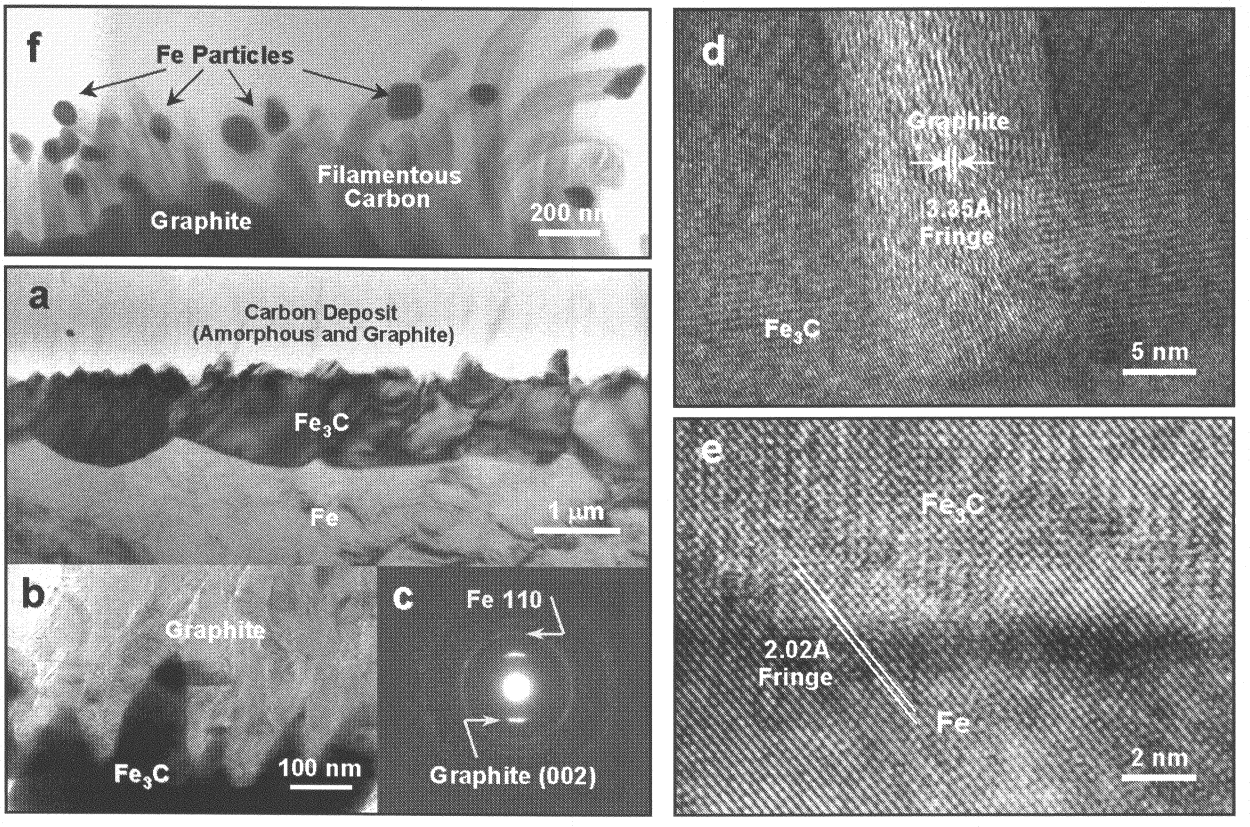

FIGURE 10 Cross sectional TEM images showing (a) Fe/Fe_3C/C interface (b) expanded view at Fe_3C/Carbon interface. (c) SAED pattern from graphite region. High Resolution TEM images showing (d) graphite fringes at Fe_3C/graphite interface and (e) lattice fringes at Fe/Fe_3C interface. (f) BF TEM image showing filamentous carbon at the outer surface of carbon deposit.

catalyzed by metal particles. The coke may have different shapes and is composed often of fine carbon filaments growing behind the catalytic metal particles which are located at the top.

The above observations are consistent with the following mechanism shown schematically in figure 12a. After formation of an Fe_3C surface layer on Fe in the carbon supersaturated environment, graphitic carbon deposits on the Fe_3C layer in more or less perpendicular orientation to Fe_3C. Graphite deposition triggers Fe_3C dissociation with iron atoms intercalating and diffusing outward through the interspace between adjacent graphite planes. At the outer surface of the graphite, the metal atoms coalesce to metal particles, which catalyze filamentous carbon formation and are carried away. This detailed mechanism is consistent with recent findings of other investigators (Pippel, Woltersdorf and Schneider 1998).

In the Absence of Surface Fe_3C Carbide (Regime IV) – The question now arises as to the mechanism of metal dusting of iron at temperatures above ~775°C where a continuous surface carbide layer does not form. For an iron foil after reaction at 850°C for 7 hours at the 98CO:2H_2 composition, the cross sectional TEM of the iron/graphite interface shows many regions where graphite has deposited with basal planes in perpendicular orientation to the iron substrate as evident from the SAED pattern. An example is shown in figure 11a. Figure 11b shows a region where the graphite planes are oriented parallel to the surface of iron. The parallel alignment of graphite planes suppresses metal transport through graphite by shutting off the

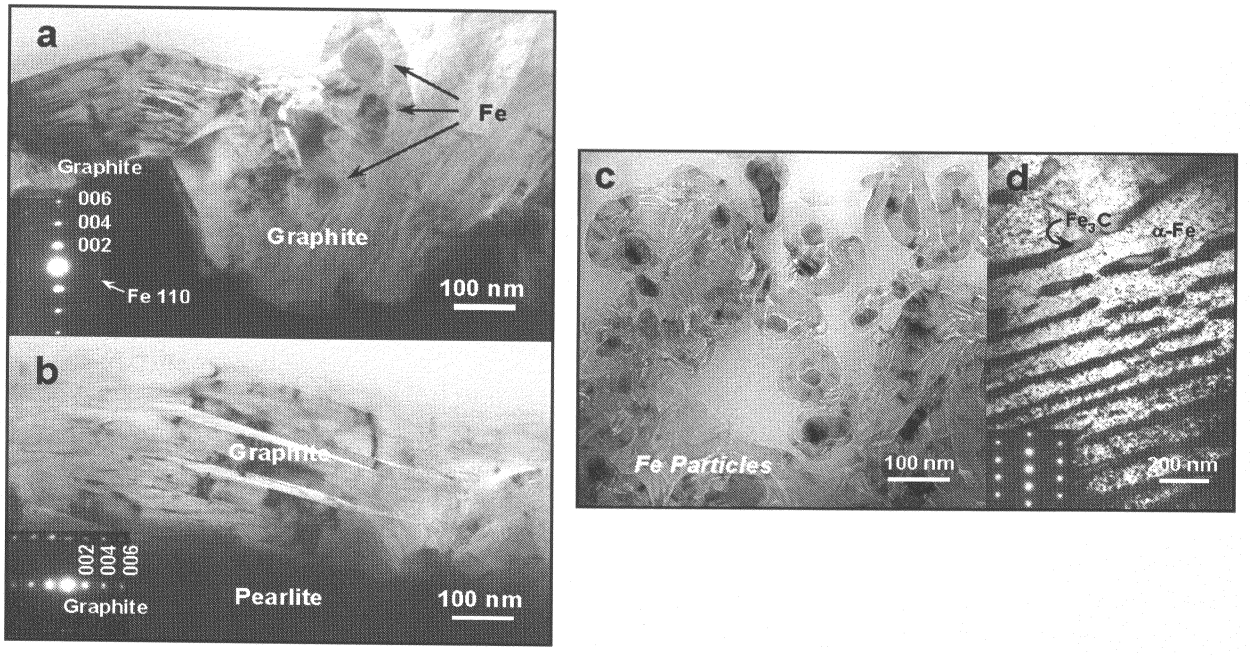

FIGURE 11 Cross sectional TEM images at Fe/carbon interfaces showing graphite basal planes in (a) perpendicular orientation and (b) parallel orientation (insets are SAED patterns for graphite). (c) TEM image showing filamentous carbon at the outer surface of carbon deposit. (d) Cross sectional TEM image and SAED pattern at B=[113] showing pearlitic structure after corrosion at 850°C for 7 hours at $98CO:2H_2$, followed by cooling to room temperature.

metal migration path. Corrosion predominantly occurs in those regions where the graphite planes have perpendicular orientation with respect to the metal surface. Metal atoms directly intercalate into graphite, diffuse outward and catalyze filamentous carbon formation at the outer surface of graphite. Details of the filamentous coke region of the same specimen are shown in figure 11c, which reveals relatively small graphite encapsulated Fe particles (5~50 nm) in the outer reaction zone. Mainly controlled by gas chemistry and temperature, the coke may have different morphologies, growing as cones, tentacles, and leeches and is composed often of closed forms of carbon shells growing outside the catalytic particle which is situated at its core. The above observations are consistent with a mechanism involving direct intercalation of Fe atoms into graphite deposited on the metal surface (figure 12b).

Nanomechanism of Metal Dusting Corrosion of Ni and Co

Bright field TEM image reveals, in addition to metal particles, a mixture of graphitic carbon, amorphous carbon and filamentous carbon in the corrosion product. The detail of the metal dusting attack on a Ni grain is shown in figure 13. A cross sectional TEM bright field image, a high resolution TEM image, and a corresponding selected area electron diffraction (SAED) pattern at a beam orientation of B= [111] are presented. The Ni foil was metal dusted at 550°C for 7 hours at CO/H_2=25. Figure 13a shows details of the filamentous coke region of the same specimen, which reveals relatively small Ni particles (5 to 80 nm) in the outer reaction zone. The carbon layer next to Ni is predominantly graphitic (about 80%), the rest being amorphous (figure 13b). Figure 13c shows 3.35 Å lattice fringes of graphite (002) basal planes at the Ni/carbon interface. Similar observations were made in a cross sectional TEM image of the

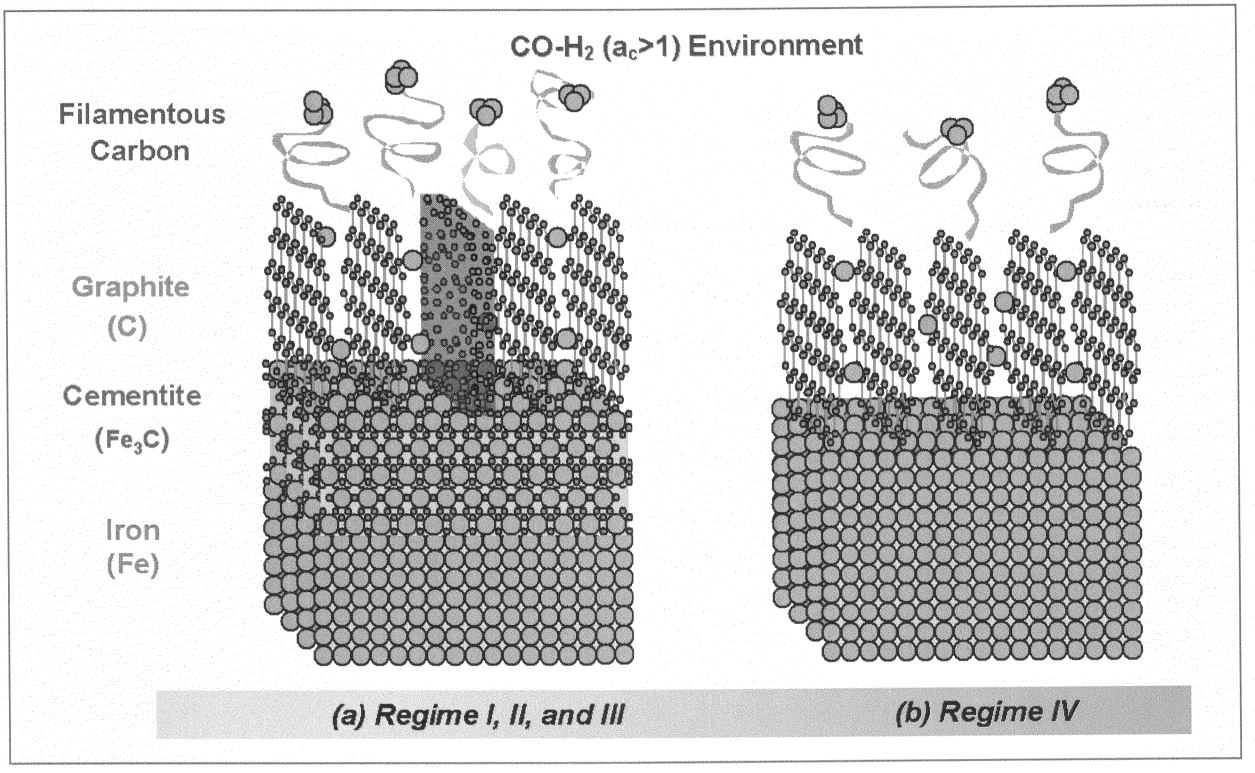

FIGURE 12 Schematic representation of the mechanism of metal dusting corrosion of iron.

carbon/Co interface after reaction at 600°C for 7 hours at 50CO:50H_2 as shown in figure 9b. The development of a serrated metal surface, i.e. the irregular disintegration, is mainly caused by intrusions of graphite into the metal phase. The structure of graphite region observable under diffraction contrast conditions indicates an oriented growth of the atomic planes perpendicular to the original metal surface. This observation corresponds to the features occurring in the zone of cementite decomposition reported in previous studies of metal dusting of iron (Pippel, Woltersdorf and Schneider 1998), thus suggesting a similar disintegration mechanism. However, in the case of Ni, there is no carbide phase detectable at the reaction front, indicating that Ni corrodes without the formation of a compound phase. In the area of graphite layer, energy dispersive X-ray spectroscopy (EDXS) reveals Ni with mass content of about 1.8%, thus indicating a partial dissolution of the metal in graphite similar to suggestions for iron. Thus, nickel atoms can intercalate into graphite and thus diffuse outward to the interface with gas phase where they coalesce to minute nickel particles. These particles catalyze the formation filamentous coke, which transports the particles away during its growth. The mechanism by which Ni corrodes depends on the composition of the gas phase (Chun, Mumford and Ramanarayanan 2000). At a CO/H_2 ratio of 1, in addition to the above mechanism, an additional corrosion mechanism is operative which involves the diffusion of carbon into the nickel lattice followed by graphite precipitation within the bulk. When such precipitation is profuse enough, complete disintegration of the nickel specimen results.

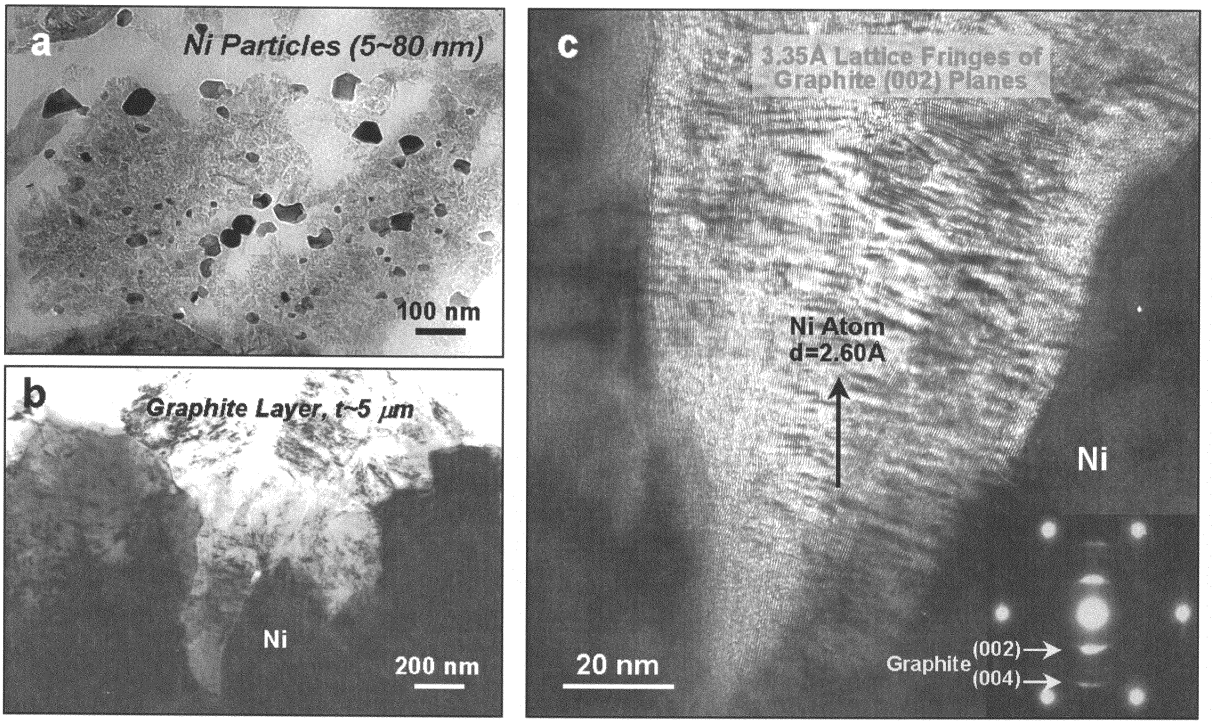

FIGURE 13 Cross sectional TEM images showing (a) the filamentous coke at the outer surface of carbon deposit and (b) the carbon/Ni interface after reaction at 550°C for 7 hours at CO/H_2=25. (c) High resolution TEM image of lattice fringes of graphite (002) planes and SAED pattern at the graphite/Ni interface.

SUMMARY

In carbon-supersaturated gaseous environments, Fe, Ni, and Co can disintegrate by a corrosion process known as metal dusting at temperatures ranging from 350 to 1050°C. Four temperature regimes have been identified in the metal dusting corrosion of Fe. In regime I, which extends from 350~500°C, the formation of metastable Fe_3C surface layer and its subsequent rupture and reformation are the main corrosion mechanisms. Predominantly amorphous carbon is present on the surface of Fe_3C in this temperature regime. Between 500°C and 575°C, regime II, there is a very rapid increase in the rate of corrosion. The growth of metastable Fe_3C followed by its dissociation is the main corrosion mechanism. Graphitic carbon deposit is predominant on the Fe_3C surface with the graphite planes oriented perpendicular to the Fe_3C surface. Iron atoms arising from Fe_3C dissociation intercalate into graphite and diffuse outward to the carbon-supersaturated environment where they coalesce and catalyze filamentous carbon formation. Between 575°C and 775°C, regime III, the corrosion rate decreases with temperature, but the corrosion mechanism still involves the growth and dissociation of metastable Fe_3C. The decrease in the chemical potential of carbon in Fe_3C with temperature and the consequent decrease in the nucleation rate of Fe particles from Fe_3C are suggested as explanations for the decrease in corrosion rate in this regime. Above 775°C, regime IV, a surface Fe_3C layer is absent primarily because of the rapid dissolution and diffusion of carbon in Fe at these high temperatures. Direct intercalation of Fe atoms into graphite deposited on the metal surface is the mechanism of corrosion in this regime. For Ni and for Co, where no metastable carbide forms over the entire temperature range, the metal dusting mechanism is similar to regime IV for Fe. Surface graphite deposition followed by intercalation of metal atoms into the graphite is the main corrosion

mechanism. Metal atoms can coalesce at the outer surface of graphite to form Metal particles, which catalyze the formation of filamentous carbon and are carried away.

ACKNOWLEDGMENTS

The authors express their appreciation to J. Mumford for his technical efforts throughout this experimental study. They gratefully acknowledge the efforts of W. Lamberti for performing the SIMS work and R.J.L. Chimenti and P. Kalamaras for carrying out the micro Raman spectroscopy.

REFERENCES

Chun, C.M., J.D. Mumford, and T.A. Ramanarayanan, 1999, "Relationship between Coking and Metal Dusting," *Materials and Corrosion*, 50:634-639.

Chun, C.M., J.D. Mumford, and T.A. Ramanarayanan, 2000, "Carbon-Induced Corrosion of Nickel Anode," *Journal of the Electrochemical Society*, 147:3680-3686.

Forseth, S., and P. Kofstad, 1995, "Metal Dusting Phenomenon during Carburization of FeNiCr-alloys at 850-1000°C," *Materials and Corrosion*, 46:201-206.

Grabke, H.J., R. Krajak, and J.C. Nava Paz, 1993, "On the Mechanism of Catastrophic Carburization: Metal Dusting," *Corrosion Science* 35:1141-1150.

Grabke, H.J., R. Krajak, and E.M. Muller-Lorenz, 1993, "Metal Dusting of High Temperature Alloys," *Materials and Corrosion* 44:89-97.

Grabke, H.J., and E.M. Muller-Lorenz, 1998, "Protection of High Alloy Steels against Metal Dusting by Oxide Scales," *Materials and Corrosion* 49:317-320.

Grabke, H.J., 1998, "Thermodynamics, Mechanisms and Kinetics of Metal Dusting," *Materials and Corrosion* 49:303-308.

Grabke, H.J., and G. Tauber, 1975, *Arch. Eisenhuttenwes*, 46:215.

Hochman, R.F., and J.H. Burson, 1966, "The Fundamentals of Metal Dusting," pp.331-342 in *Proc. of API Division of Refining*, 46, American Petroleum Institute, Washington, DC.

Hochman, R.F., 1972, "Basic Studies of Metal Deterioration (Metal Dusting) in carbonaceous Environments at Elevated Temperatures," pp. 260-263 in *Proceedings of the Fourth International Congress on Metallic Corrosion*, NACE, Houston, Texas.

Hochman, R.F., 1977, "Catastrophic Deterioration of High Temperature Alloys in Carbonaceous Atmospheres," pp. 715-732 in *Proceeding of the Symposium on Properties of High Temperature Alloys with Emphasis on Environmental Effects*, Z.A. Foroulis and F.S. Pettit, Editors, The Electrochemical Society, Pennington, New Jersey.

Klower, J., H.J. Grabke, and E.M. Muller-Lorenz, 1998, "Metal Dusting of Nickel-base Alloys," *Materials and Corrosion* 49:328-329.

Nava Paz J.C., and H.J. Grabke, 1993, "Metal Dusting," *Oxidation of Metals* 39:437-456.

Pippel, E., J. Woltersdorf, and R. Schneider, 1998, "Micromechanisms of Metal Dusting on Fe-base and Ni-base Alloys," *Materials and Corrosion* 49:309-316.

Shatynski S.R., and H.J. Grabke, 1978, *Arch. Eisenhuttenwes*, 49:129.

Strauss, S., and H.J. Grabke, 1998, "Role of Alloying Elements in Steels on Metal Dusting," *Materials and Corrosion*, 49:321-327.

STUDY OF METAL DUSTING MECHANISM IN IRON USING RAMAN SPECTROSCOPY AND X-RAY DIFFRACTION

Z. ZENG*, K. NATESAN, and V. A. MARONI
Argonne National Laboratory
Argonne, IL 60439, USA

ABSTRACT

The metal dusting phenomenon, which is a metal loss process that occurs in hot reactive gases, was investigated in iron and certain iron-base alloys by Raman scattering, X-ray diffraction (XRD), and scanning electron microscopy. Coke from metal dusting exhibits six Raman bands at 1330 (D band), 1580 (G band), 1617, 2685, 2920, and 3235 cm^{-1}. The bandwidths and the relative intensities of the 1330 and 1580 cm^{-1} bands are related to the crystallinity and defect structure of the coke. Both Raman and XRD analyses suggest that the metal dusting process influences the catalytic crystallization of carbon. A new mechanism of metal dusting is therefore proposed, based on the premise that coke cannot crystallize well by deposition from carburizing gases at low temperature without catalytic activation because of its strong C-C bonds and high melting temperature. Cementite or iron participates in the coke crystallizing process in a manner that tends to improve the crystallinity of the coke. At the same time, fine iron or cementite particles are liberated from the pure metal or alloys.

INTRODUCTION

Metal dusting is a high temperature corrosion phenomenon that occurs in Fe-, Co-, or Ni-base alloys in strongly carburizing gas atmospheres at carbon activities (a_C) >1 in the temperature range of 400 to 900°C. During the metal dusting process, corrosion of the metals and alloys occurs, accompanied by the formation of fine metal carbide or pure metal and carbon dust. Dusting-related failures have occurred most often in the petroleum and petrochemical industries. This deterioration has been studied for more than 50 years, but its mechanism and driving force are still not clear.

Hochman (Hochman 1977) proposed the following mechanism for the metal dusting of iron: (a) Carbon deposited on the metal surface and is dissolved in the metal; (b) cementite (Fe_3C) forms as carbon diffuses into the iron and the metal becomes oversaturated; and (c) metastable Fe_3C decomposes to Fe and graphite. Grabke and his coworkers carried out detailed studies on this mechanism (Grabke et al. 1998; Pippel et al. 1995). According to Hochman's mechanism, the final products are graphite and iron. However, there is no conclusive evidence that the iron phase is present in every case of metal dusting. It is not clear what drives the formation and decomposition of cementite under the same conditions of temperature, pressure, and composition. It is easy to understand that graphite crystallizes from a supersaturated solution, but it is doubtful that this crystallization also causes Fe_3C to decompose.

*Corresponding author address: Z. Zeng, Argonne National Laboratory, 9700 S. Cass Avenue, Argonne, IL 60439; e-mail: zeng@anl.gov

The formation and decomposition of chemical bonds require a sizeable free energy change. There is no question that cementite is a product of metal dusting. However, it is arguable whether this compound is essential to metal dusting or is only a by-product of that process.

To investigate the metal dusting phenomenon, scanning electron microscopy (SEM), transmission electron microscopy, Auger electron spectroscopy, and X-ray diffraction(XRD) analyses have been used to study the microstructure, electron binding, and phase chemistry of the metal dusting products. Thus far, investigations have focused on defects in the metals. Defects in the carbon dust have hardly been studied, even though carbon is an integral part of the metal dusting process.

Graphite has a layered structure with the space group $P6_3/mmc$ (see Fig. 1). Carbon atoms within the layers bond strongly through sp^2 hybridization and arrange in a two-dimensional honeycomb network. The layers are stacked in a hexagonal crystal structure and are bound together by van der Waals forces. Because the van der Waals forces are weak, the C-C distance between layers is large (335.4 pm). For this reason, graphite crystals readily disorder along the c-axis (Krebs, 1968).

Raman scattering from various forms of carbon is sensitive to structural disorder of the material (Dillon and Woollam 1984; Tuinstra and Koenig 1970; Nakamizo et al. 1978). As a result, Raman spectroscopy provides a useful nondestructive technique for structural characterization of carbon materials. Lattice defects in graphite break down the hexagonal symmetry of the graphite lattice and modify the optical selection rules for the lattice vibrational modes that are observable in Raman scattering. A single Raman line, the E_{2g2} vibration mode, is theoretically expected for the hexagonal lattice of graphite and has been observed at 1575 cm^{-1} in natural graphite. In glassy carbon, the layers are perfectly parallel but their mutual orientation in the direction of the planes is random (due to the weak link between the layers). A band at 1355 cm^{-1} observed for glassy carbon has been assigned to a defect-activated vibrational mode originating from the distorted hexagonal lattice of graphite near the crystal boundary. The two bands at 1355 and 1575 cm^{-1} are designated as the D (distorted) band and the G (graphite) band, respectively.

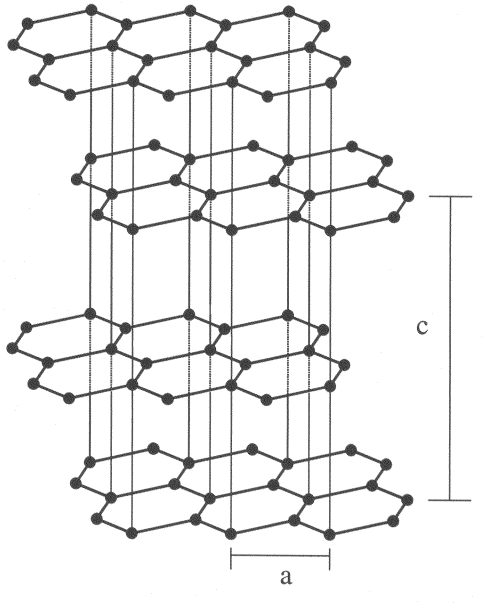

FIGURE 1 Structure of graphite. Carbon atoms within layers are arranged in a two-dimensional honeycomb network; layers are stacked in a hexagonal crystal structure.

It has been reported that the relative intensity ratio I_D/I_G and the relative bandwidths increase in progression from single-crystal graphite through polycrystalline graphite up to glassy carbon; hence, their values can be used as a measure of imperfection of the graphite layer planes (Dillon and Woollam 1984; Tuinstra and Koenig 1970; Nakamizo et al. 1978). These parameters are more defect-sensitive than are the XRD parameters that define crystalline size. Therefore, Raman spectroscopy represents a useful tool for investigating the defects in carbon structures and their relationships to the metal dusting phenomenon. In this paper, we present results of Raman spectroscopy measurements that are pertinent to metal dusting.

EXPERIMENTAL

Pure iron and 78Fe-22Al alloy were used for metal dusting experiments. Specimens were polished with 400 grit SiC paper, and experiments were conducted in a horizontal furnace with a quartz tube (1.5 inch in diameter). One set of specimens was hung in an alumina boat and exposed to a flowing carburizing atmosphere of 72.4% H_2-8.1% CO_2-17.2% CO-2.3% H_2O at 593 and 704°C. The specimens were then cooled in the furnace to room temperature in the same atmosphere after exposure.

After each exposure period, specimen weight change was determined after removal of adhering coke in an ultrasonic bath with acetone. Phases present in the coke and metal samples were analyzed by X-ray powder diffraction. Microstructure was examined with a JSM-6400 scanning electron microscope. To study the metallographic cross section, the samples were electrolytically etched with 10% acetic acid at 10 V for 30 seconds.

Raman spectra were obtained with a Renishaw System 2000 imaging Raman microscope equipped with an He-Ne laser that delivered ≈5 mW to thespecimen. The spectra were recorded between 190 and 4000 cm^{-1} with the laserpartially defocused to a diameter of ≈5 μm to avoid burning or otherwise transforming the carbon deposits. Spectra were taken at three to six locations on a given specimen to verify that the observed surface deposits were uniform in composition. Magnetization of the samples was measured by a vibrational sample magnetometer under 1 Tesla in an Ar atmosphere.

RESULTS AND DISCUSION

Metal dusting rates of the iron and the Fe-Al alloys are shown in Table 1. The pure iron was corroded severely. At 593°C, the metal dusting rate of the Fe-Al alloy is close to that of the pure iron, which indicates that an Al_2O_3 protecting layer had not formed to protect the alloy from metal dusting. However, the Fe-Al alloy gained weight at 704°C because it took oxygen from the atmosphere and formed an oxide layer on the surface to stop metal dusting.

TABLE 1 Metal loss of iron and alloys (mg/cm^2)

Metal	Exposure Temperature (°C)	
	593	704
Fe	-55.1	-13.7
Fe-Al	-45.7	0.45

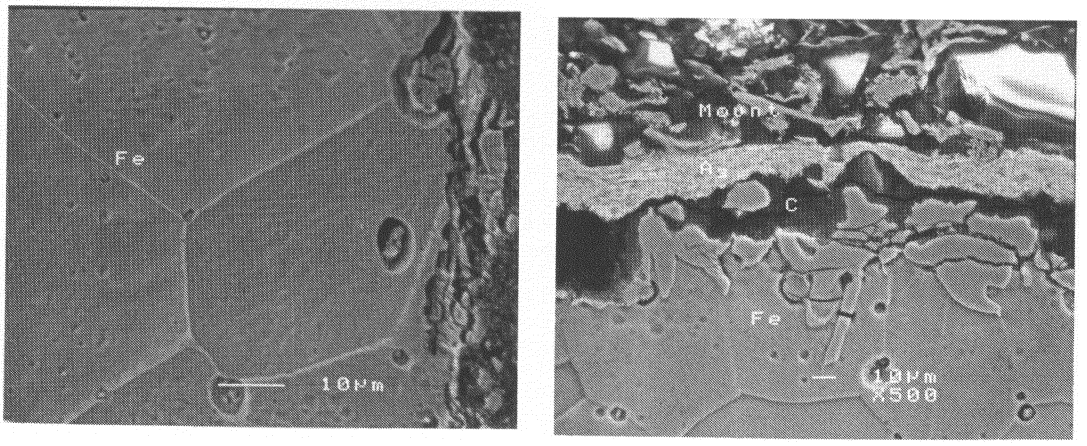

FIGURE 2 (a) SEM photomicrograph of metallographic cross section of iron, showing tightly bound carbon layer on iron surface after ultrasonic cleaning. Iron particles are separated into small particles and move away from the metal surface, (b) Grain boundaries that were attacked more severely.

There is a tightly adhering carbon layer on the surface of the iron and the Fe-Al alloy (Fig. 2a). It cannot be removed by ultrasonic cleaning followed by acetone washing with a cotton tip. Metallographic cross section shows that the iron is separated into small islands on the surface of the specimen. The overall volume increase is ~10% when the carbon diffuses into the iron and forms cementite. This volume expansion must create many defects. The metal dusting process causes the metal particles to further separate into nanometer size particles that become embedded in the coke. The metal appears to have been attacked more severely at grain boundaries and dislocation points (Fig. 2b). Therefore, defects in the metal seem to initiate and propagate the metal dusting process.

The major phases in the metal dusting product are graphite and Fe_3C (Fig. 3a). There may be a small amount of Fe_3O_4, which presents a weak diffraction peak at $2\theta = 35.4°$. According to the mechanism proposed by Hochman (Hochman 1977), Fe_3C decomposes to Fe and C at the final step, in which case the final products should be Fe and C. However, there is no iron diffraction peak in the product of metal dusting. Because XRD may not be able to find the iron when its content is < 5%; a magnetic measurement method was used. Iron is a strong ferromagnetic material with a Curie temperature (Tc) of 770°C (Lide 1999). A huge magnetization increase would be observed at 770°C if there were iron in the product of metal dusting. Figure 4 shows the magnetization of metal dusting product as a function of temperature. The large transition of magnetization at 210°C is due to Fe_3C (Lide 1999). The small magnetization increase at 582°C may be due to a small amount of ferromagnetic Fe_3O_4 with a Tc of 585°C (Lide 1999). However, there is no obviously transition of magnetization near 770°C. The very small magnetic moment near 700°C indicates that the concentration of regular α-iron in the product of metal dusting is < 0.1%. It is possible that some iron particles are too small for XRD and magnetic measurement to observe. However, both XRD and magnetic measurement show that the major phase in coke is obviously Fe_3C rather than Fe. The Fe_3C is the final product of metal dusting, not merely the intermediate compound predicted by Hochman's mechanism. Therefore, further investigation is needed to establish metal dusting causes and mitigation for the metal dusting corrosion observed under our experimental conditions.

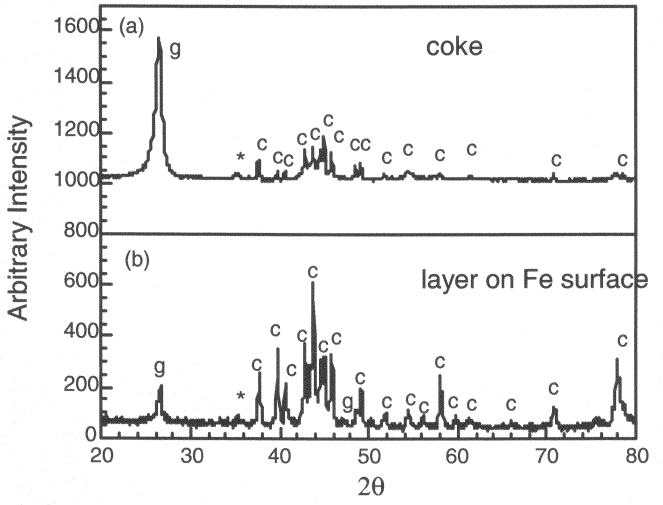

FIGURE 3 X-ray diffraction pattern of coke and surface layer on iron sample after exposure to carburizing gas at 593°C for 100 h; major phases are graphite (g) and cementite (c); there may also be a small amount of Fe_3O_4 (aesterisk) which presents only its strongest peak.

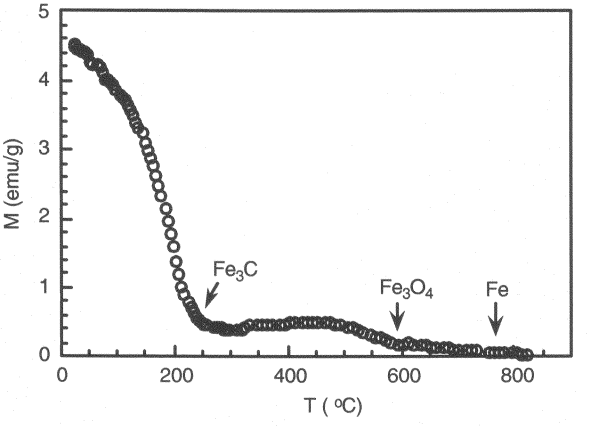

FIGURE 4 Magnetization (M) of metal dusting product made at 593°C as a function of temperature.

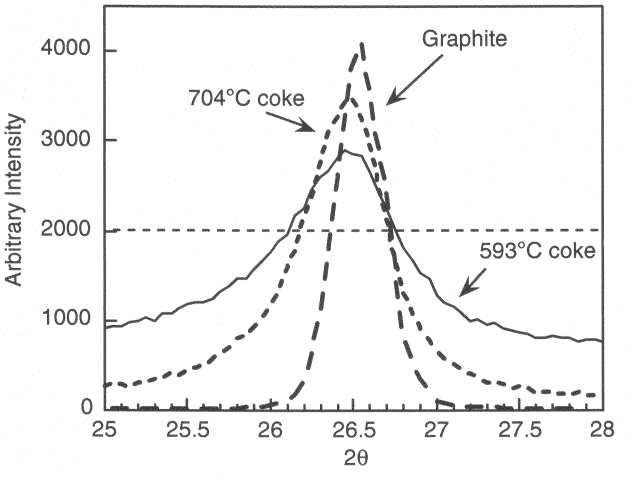

FIGURE 5 Peak widths of [002] diffraction increase from graphite to coke made at 704°C to coke made at 593°C; narrower peak width indicates better crystallinity.

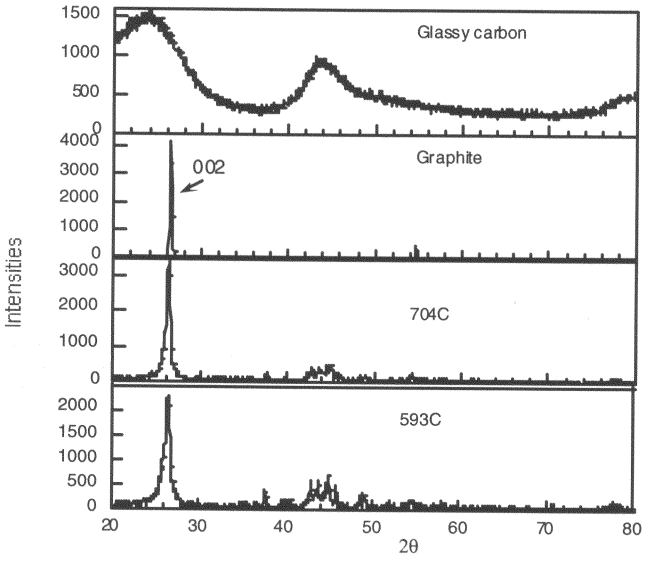

FIGURE 6 X-ray diffraction pattern of glassy carbon, well-crystallized graphite, and coke made at 593°C and 704°C. Major phases in coke samples are graphite and cementite.

TABLE 2 Crystallite dimensions and interlayer plane distances of graphite, coke made at 704°C, coke made at 593°C, and glassy carbon; Δ is difference of interlayer plane distance of carbon from single-crystal graphite (with interlayer plane distance 3.354 Å).

Carbon materials	Interlayer plane distance (Å)	Δ (Å)	Crystallite size (Å)		Mean number of layers per particle
			c-axis	a-axis	
Graphite	3.356	0.002	220	299	65.7
Coke made at 704°C	3.362	0.006	145	151	43.3
Coke made at 593°C	3.365	0.011	110	127	32.8
Glassy carbon	3.736	0.382	12	15	3.4

The [002] X-ray diffraction peak widths of the carbon dust are broader than that of the well-crystallized graphite (Fig. 5), which we interpret as indicating that the crystallinity of carbon dust is poorer than that of graphite. However, the [002] peak widths of the coke are much narrower than those of glassy carbon (see Fig. 6). Table 2 shows that the crystallite sizes of cokes are much larger than that of glassy carbon. To the authors' knowledge, the crystallite sizes of cokes are also considerably larger than those reported for other carbonaceous materials made at a similar temperature (Blayden et al. 1940; Schaeffer et al. 1953; Kinney 1956).

The interlayer distances of the carbon plane are related to the degree of disorder (Blayden et al. 1940; Schaeffer et al. 1953). The layers are not parallel in the disoriented graphite structure. Average interlayer plane distance increases when the layers are disoriented, as shown in Fig. 7. The interlayer plane distance is 3.354 Å for single-crystal graphite (Franklin 1951). The interlayer plane distance of coke is very close to that of the well-crystallized graphite.

Franklin (Franklin 1951) proposed the following relationship of the proportion of disorientated layers (p) as a function of interlayer plane distance (d):

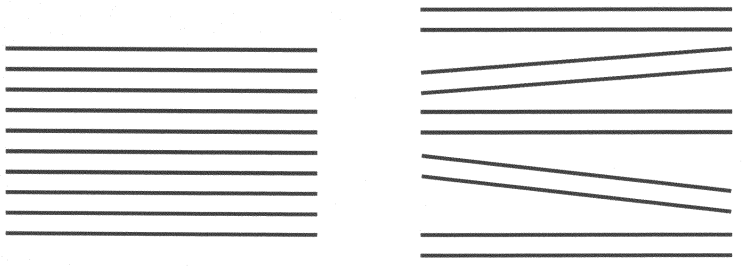

Single crystal graphite Disoriented graphite

FIGURE 7 Average interlayer plane distance of disoriented graphite is greater than that of single-crystal graphite

$$d = 3.44 - 0.086(1-p^2).$$

According to this relationship, the interlayer plane distances of coke made at 704°C seen in Table 2 (3.362 Å) are indicative of a carbon having ~70% three-dimensional ordering. For the carbons produced by conventional treatment of carbon-containing raw materials, a heat treatment temperature >2000°C for thermal recrystallization is necessary before this high degree of three-dimensional ordering is achieved (Blayden et al. 1940; Schaeffer et al. 1953).

Raman spectra of coke, glassy carbon, and graphite are presented in Fig. 8. The well-crystallized graphite shows two peaks: the sharp band at 1580 cm^{-1} (G band) can be assigned to the E_{2g} C-C stretching mode (Tuinstra and Koenig 1970; Nemanich and Solin 1977; Al-Jishi 1982). The other peak at 2685 cm^{-1} is a two-phonon band taken to be 2 x 1330 cm^{-1}. The first-order phonon band at 1330 cm^{-1} (D band) is not observed for well-crystallized graphite because of the k = 0 selection rule (Tuinstra and Koenig 1970). However, disorder in the lattice can cause a breakdown of this selection rule, which is why the 1330 band is observed in the Raman spectra of glassy carbon. Symmetry may also be affected by a high degree of disorder that could, for example, cause the second-order phonon at 2685 cm^{-1} to disappear in the Raman spectra of glassy carbon. The 2685 cm^{-1} band is designated as the G' band because its character is similar to that of the G band. The highly disordered carbons have very broad Raman bands, and the intensity of the 1330 cm^{-1} band increases when carbon becomes more disordered. Intensities of the D band are considered to depend on in-plane displacements, which lead to a loss of hexagonal symmetry of the two-dimensional graphite lattice within the planes (Nakamizo et al. 1978). A shoulder at 1617 cm^{-1} in the cokes formed at 704°C is also dependent on structural disorder and is therefore designated as the D' band. Its behavior is qualitatively similar to that of the D band (Vadano and Fischbach 1978; Knight and White 1989). The 2920 cm^{-1} feature arises from a combination of the strong density of states at ≈1330 and 1617 cm^{-1} (Nemanich and Solin 1979). The 3235 cm^{-1} band is the first overtone of the G band (Nemanich and Solin 1977).

The widths of Raman bands for the coke from the dusting process are between those of well-crystallized graphite and glassy carbon. The D/G intensity ratio of coke made at 704°C is lower than that of coke made at 593°C, and the D band for coke made at 704°C is obviously

narrower (Fig. 9). The G band at 1583 cm^{-1} and the D' band at 1617 cm^{-1} are separated in the coke made at 704°C, whereas the G and D' band of the coke made at 593°C are merged in one broad band. The bandwidths and the D/G intensity ratio are related to the crystallinity of the carbon dust (Dillon and Woollam 1984; Tuinstra and Koenig 1970; Nakamizo et al. 1977, 1978). Therefore, the coke made at 704°C is better crystallized than the coke made at 593°C. The intensity of the G' band at 2685 cm^{-1} is reported to be highly sensitive to the structure (Sato et al. 1978). For coke made at 704°C, the G' band is much stronger than for coke made at 593°C, and the G' bandwidth (71 cm^{-1} at half height) of coke made at 704°C is also narrower than the G' bandwidth (112 cm^{-1} at half height) of coke made at 593°C, which also indicates that the coke made at 704°C is better crystallized than that made at 593°C.

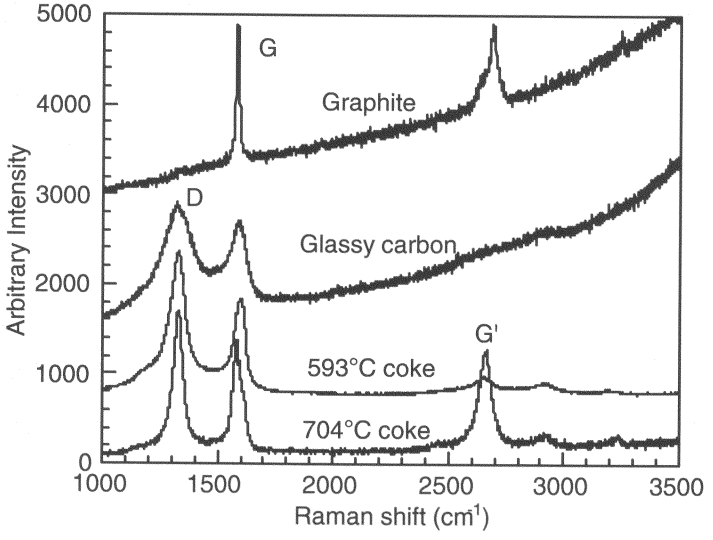

FIGURE 8 Raman spectra of graphite, glassy carbon, and coke made at 593°C and 704°C. 1330 cm^{-1} band is designated as D (disorder) band because its character is related to disorder of the graphite phase, whereas 1580 and 2680 cm^{-1} bands are assigned to G and G' bands, respectively.

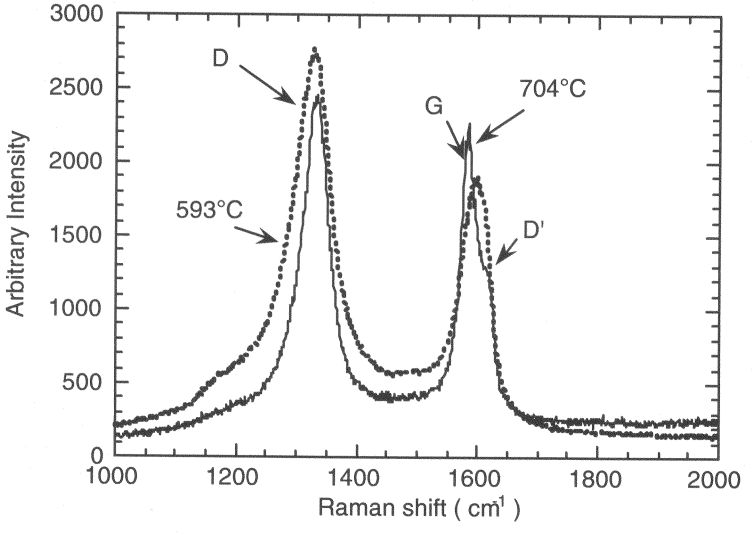

FIGURE 9 Raman spectra of coke made at 593°C and 704°C. Raman bandwidth for coke made at 704°C is narrower than that for coke made at 593°C. D/G intensity ratio for coke made at 593°C is 1.5, whereas that for coke made at 593°C is only 1.1.

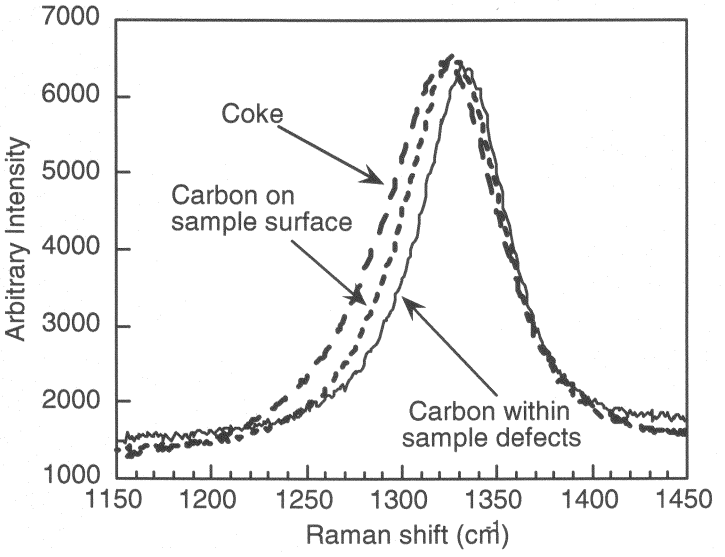

FIGURE 10 Raman spectra of coke, carbon on alloy sample surface, and carbon in sample defects.

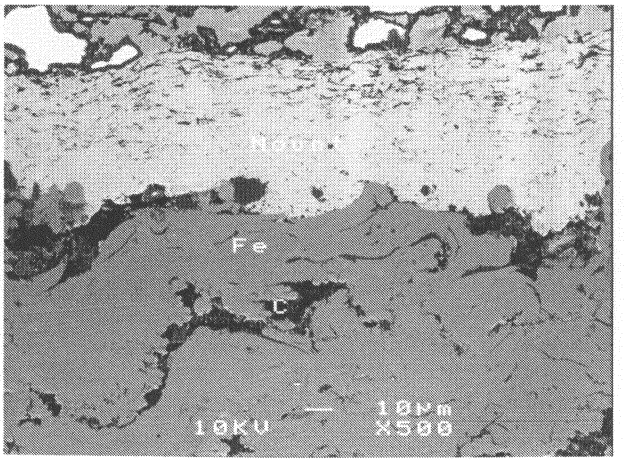

FIGURE 11 SEM cross section of Fe-Al alloy after metal dusting experiment at 593°C. Carbon has diffused into and precipitated within the alloy. EDX analysis indicates that dark areas are filled with carbon.

As mentioned, there is a closely adhering layer of carbon on the surface of the alloys. The Raman spectra in Fig. 10 show that the Raman band for the carbon on the surface of the iron is narrower than that for coke at some distance from the surface. This may indicate that carbon in the tightly adhering layer of the iron surface has better crystallinity.

Figure 11 is a cross section of the Fe-Al alloy layer after a metal dusting experiment. Carbon has diffused and precipitated inside the alloy. Energy dispersive X-ray analysis reveals that the dark areas are filled with carbon. Raman spectra were obtained by spotting the laser on the carbon deposits in the Fe-Al coating layer. Figure 8 shows that the line width of the Raman band for the carbon in the alloy is narrower than that for the coke and the surface carbon. The band position is shifted to a slightly higher frequency (10 cm^{-1}) for the carbon in iron. Therefore,

crystallinity of the carbon increases progressively from coke through surface carbon to carbon in the metal after metal dusting.

Experimental results from the Raman, XRD, and SEM measurements shed some light on the mechanism of metal dusting. There appears to be a relationship between metal dusting and the degree of crystallization of the carbon dust.

Our interpretation of the crystallizing process for carbon during dusting is shown in Fig. 12. In the initial stage, single carbon atoms are deposited on the surface of the iron; they then either dissolve in the iron or accumulate to form small carbon particles. There are dangling bonds on the particle surfaces as well as many defects such as vacancies and distorted bonds in the particles. All of these surface and internal defects cause an increase in the free energy of these particles compared to the free energy of well-crystallized graphite. At higher temperature, where the carbon atoms have enough energy to migrate, the carbon recrystallizes from small distorted particles to large well-crystallized graphite. However, because the C-C bond is very strong (the melting temperature of carbon is 4492°C), the recrystallization process requires a higher temperature. Therefore, achieving good crystallinity below 1000°C is difficult for two : first, carbon layers in the graphite structure are easily disoriented because the van der Waals forces between the layers are very weak, and second, recrystallization below 1000°C is difficult because the bond in the layers is too strong.

The rate of carbon recrystallization could be dramatically increased by the catalysts of iron or cementite. The cementite structure has been described as a framework of almost close-packed iron atoms held together by metallic bonding to the small carbon atoms in the largest interstices. Because carbon occupies only one-sixth of the interstices, it can dissolve in and move though those interstices. When carbon dissolves in the iron or cementite, the Fe-C bond is much weaker than the

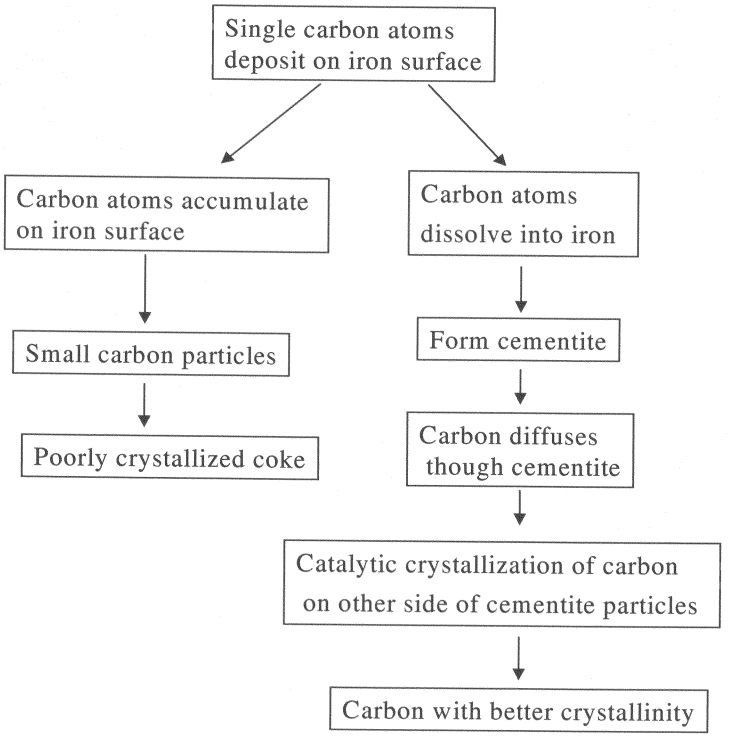

FIGURE 12. Proposed process for carbon crystallization after deposition from carburizing gas.

C-C bond, and transportation of carbon atoms is greatly facilitated. Therefore, the poorly crystallized coke can transfer though iron and eventually achieve improved crystallinity. The carbon free energy is then reduced by reducing the number of dangling bonds on the surface and the number of internal defects in the carbon particles.

Figure 13 shows the catalytic recrystallization process. Carbon atoms are deposited on the surface of Fe_3C. As mentioned above, the carbon layers in the graphite structure are easily disoriented because the van der Waals forces between the layers are weak. Carbon cannot grow with good crystallinity if the lattice planes of Fe_3C do not match the graphite lattice planes to help the crystallization of carbon (up position of Fig. 13). However, when carbon atoms diffuse through the cementite and precipitate from a favorable lattice plane, the lattice of cementite provides an excellent orientation for the epitaxial growth of graphite. Graphite was reported to grow perpendicular to the lattice plane of Fe_3C with its layer plane (Chun et al. 1999). Cementite has an orthorhombic lattice with cell parameters a = 5.091, b = 6.743, c = 4.526 Å; its b axis is almost the same as the c axis of graphite (6.724 Å). This is helpful for the crystallization of graphite. Such a catalytic crystallization process causes the coke produced from metal dusting to have a much larger crystallite size and a smaller interlayer plane distance than those carbons made by other methods at a similar temperature (Franklin 1951; Blayden et al. 1940; Schaeffer et al. 1953).

The catalytic crystallization effect by iron was proven by Nakamizo et al (Nakamizo et al. 1974; Kammereck et al. 1974). They investigated the effect of iron on the crystallization of glassy carbon made from furfuryl alcohol. Addition of only 3% iron led to a dramatic decrease in the widths of the D and G bands and the D/G intensity ratio. The line widths of carbon with iron annealed at 600°C were narrower than those of the carbon without iron annealed at 2000°C (Nakamizo et al. 1974). X-ray diffraction showed that addition of iron narrows the graphite [002] peak dramatically (Kammereck et al. 1974). These experiments show that the crystallization rate of carbon is dramatically increased by iron or cementite catalysts.

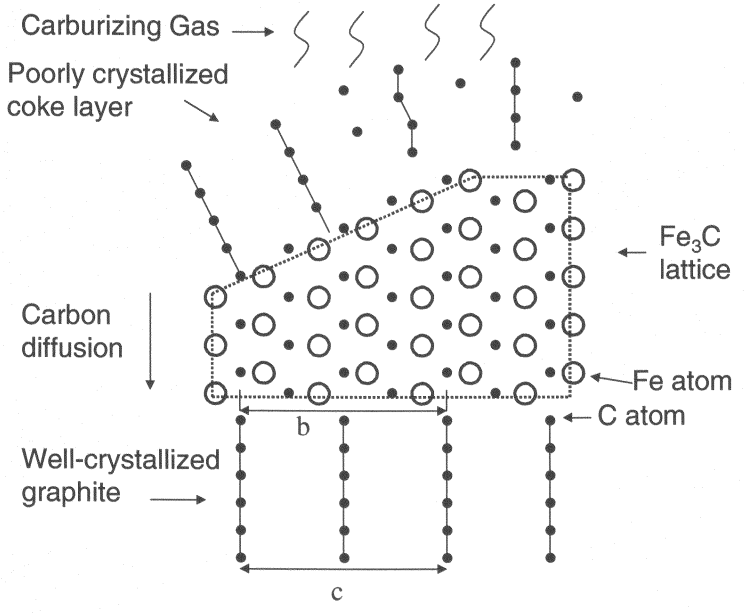

FIGURE 13 Poorly crystallized carbon dissolves in and diffuses through cementite, whose lattice provides excellent orientation for crystallization of graphite; b dimension of cementite (6.743 Å) is very close to c dimension of graphite (6.724 Å).

In our proposed catalytic crystallization process, carbon dissolves on the surface of the iron and crystallizes out in the bulk iron. Because the free energy of coke is probably higher than that of well-crystallized graphite, the saturating concentrations for coke and graphite will be different. High free energy coke should have a slightly higher saturating concentration than that of graphite ($a_C = 1$); then the saturating concentration of coke will be oversaturating for graphite. Therefore, poorly crystalline coke could dissolve in iron or cementite and crystallize out as well-crystallized graphite. In this process, carbon transfers from the cementite surface and grows inward via the defects or grain boundary of cementite or iron. The accumulation of carbon in alloy causes the metal particles to disintegrate, as seen in Figs. 2a and 11. Fig. 14 shows how cementite particles separate into small particles as carbon particles accumulate at the defects. Such a transport process will continue until the cementite particles become too small to provide a template for carbon growth to 10nm-size crystals (Table 2). The metal finally becomes nanometer-size dust in this process. X-ray diffraction shows that the average size of the cementite particles in the coke is only 27 nm.

Our proposed metal dusting mechanism of iron can be described as follows:

1. Carbon deposits on iron surface and supersaturates the iron.

2. Cementite forms on the surface of iron, and the accompanying volume expansion creates defects.

3. Carbon diffuses through the cementite and precipitates at cementite defects.

4. Accumulation of carbon at cementite defects causes the cementite particles to separate into small particles and move away from the metal.

5. Gas penetrates into cracks in the metal and continues further carbon deposition and metal dusting.

At high temperature, cementite decomposes quickly (Chun et al. 1999). Iron may work directly as a catalyst to help the crystallization of carbon because the iron lattice can also provide a good orientation for the growth of graphite. Carbon diffuses through the iron and precipitates at the defects, which also cause iron particles to separate. Cementite is a phase that forms when carbon diffuses into iron. However, in our mechanism, the decomposition of cementite is not a necessary condition to initiate the metal dusting. In the metal dusting process, cementite works as a solvent and catalyst for the diffusion and crystallization of carbon. XRD shows that cementite and carbon are the major phases in the products of metal dusting, whereas according to Hochman's mechanism, the final product should be iron and carbon.

The effect of carbon on the metal dusting of iron is the focus of Hochman's mechanism. In our proposed mechanism, however, iron plays a major role in the crystallization of carbon, and the metal dusting phenomenon is only a by-product of the catalytic crystallization process.

As mentioned above, carbon crystallinity increases from coke to surface carbon to carbon inside the alloy after metal dusting. This phenomenon can be explained if we assume that there are two types of carbon in the carbon deposition and metal dusting process. According to Fig. 12, the carbon that participates during the metal dusting process will have better crystallinity. This carbon should have already diffused through the metal, whereas the carbon that is not involved in

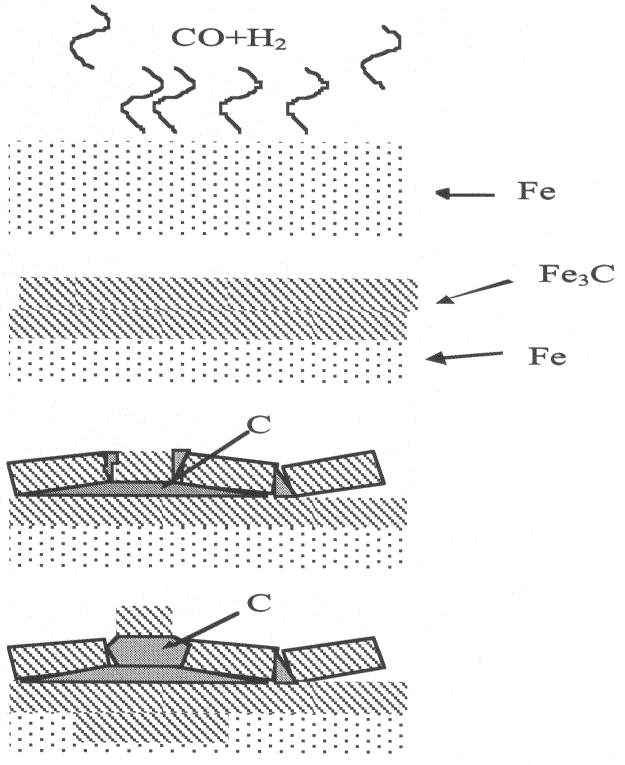

FIGURE 14. Process of cementite particle separation by the accumulation of carbon particles in defects. First step: carbon is deposited on the surface of iron. Second step: carbon dissolves the iron and forms cementite, creating many defects as the volume increases ~10% when cementite forms. Third step: carbon diffuses though cementite and precipitates at the defects; the accumulation of carbon at the defects causes the cementite particles separate. Fourth step: gas penetrates into cracked areas and deposits carbon. More cementite forms, and the metal dusting corrosion proceeds further.

the catalytic reaction is poorly crystallized and does not diffuse into the metals. Carbon inside the alloy (Fig. 11) may have already diffused through the iron and participated in the metal dusting process; at that point, it should be well crystallized, while the coke and surface carbon may contain carbon entities that accumulated on the iron surface without participating in metal dusting. The average size of cementite particles in the coke is only 27 nm; these particles may function as a catalyst for carbon deposition, but some may be too small to help the carbon grow to large crystals. Carbon deposited on these small cementite particles may not crystallize well and thus will remain small and have little growth. Coke at some distance from the metal surface is more likely to contain such poorly crystalline carbon. Therefore, the crystallinity of this coke is the poorest of all the carbon that formed during metal dusting.

CONCLUSIONS

Information on crystallinity of coke formed by metal dusting can be derived from the line width and the D/G intensity ratio in the Raman spectra of dust residues. Raman and XRD experiments show that coke deposited at high temperature has better crystallinity than that deposited at low temperature, while the metal dusting rate is lower at 704°C than that at 593°C. Crystallinity of the participating carbon that diffuses into the iron is better than that of the non-participating carbon far away from the iron surface. These results could be explained if the mechanism for metal dusting in iron is considered to be a process of catalytic crystallization of carbon with participation by iron. The difference in the free energies of poorly crystallized coke and well-crystallized graphite causes a driving force for recrystallization of coke. However, this process cannot occur at low temperature because the C-C bonds are too strong to allow movement of carbon atoms. Cementite and iron help the crystallization process, and their particles are moved in the process of carbon transportation that leads to metal dusting. Although the driving force is very small, it results in severe corrosion in the long term. It is not necessary to invoke the decomposition of cemenitite in this metal dusting mechanism.

ACKNOWLEDGMENTS

This work is supported by the U.S. Department of Energy, Office of Industrial Technologies, under Contract W-31-109-Eng-38. Special thanks to D. L. Rink for his assistance in conducting the metal dusting experiments.

REFERENCES

Al-Jishi R., 1982, "Lattice-dynamical Model for Graphite," Phys. Rev. B, 26: 4514-4522.

Blayden H. E., H. L. Riley, and A. Taylor, 1940, "Crystallite Growth DuringCarbonization," J. Am. Chem. Soc., 62:180-186.

Chun C. M., T. A. Ramanarayannan, and J. D. Murnford, 1999, "Relationshipbetween Coking and Metal Dusting," Materials And Corrosion, 50: 634-639.

Dillon R. O. and J. A. Woollam, 1984, "Use Raman Scattering to InvestigateDisorder and Crystallite Formation in as-deposited and Annealed Carbon Film," Physical Review B, 29:3482-3489.

Franklin R. E., 1951, "The Structure of Graphite Carbons," Acta Cryst., 4: 253-261.

Grabke H. J., 1998, "Thermodynamics, Mechanisms and Kinetics of MetalDusting," Materials and Corrosion, 49:303-308.

Hochman R. F., 1977, " Catastrophic Deterioration of High Temperature Alloys inCarbonaceous Atmospheres," pp. 715-732 in Proc. Symp. on Properties of High-Temperature Alloys with Emphasis on Environmental Effects, Z. A. Foroulis and F. S. Pettit, eds., The Electrochemical Society, 1977.

Kammereck R., M. Nakamizo, and P. L. Walker, 1974, "Stucture and Propertiesof Iron Containing Glassy Carbons," Carbon, 12, 281-289.

Knight D. S., and W. B. White, 1989, " Characterization of Diamond Films by Raman Spectroscopy," J. Mater. Res., 4: 385-393.

Krebs H., 1968, *Fundamentals of Inorganic Crystal Chemistry*, McGraw-Hill, p. 150.

Lide D. R., 1999, CRC Handbook of Chemistry and Physics, (CRC Press), P12-119 to P12-123

Nakamizo M., R. Kammereck, and P. L. Walker, 1974, "Laser Raman Studies on Carbons," Carbon, 12:259-267.

Nakamizo M., H. Honda, M. Inagaki, and Y. Hishiyama, 1977, "Raman Spectra, Effective Debye Parameter and Magnetoresistance of Graphitized Cokes," Carbon, 15:295-298.

Nakamizo M., H. Honda, and M. Inagaki, 1978, "Raman Spectra of Ground Natural Graphite," Carbon, 16:281-283.

Nemanich R. J. and S. A. Solin, 1977, "Observation of an Anomalously Sharp Feature in the 2nd Order Raman Spectrum of Graphite," Solid State Comm. 23:417-419.

Nemanich R. J. and S. A. Solin, 1979, "First-and Second-order Raman Scatterring from Finite-size Crystals of Graphite," Phys. Rev. B, 20:392-401.

Pippel E., J. Woltersdorf, H.J. Grabke, and S. Strauss, 1995, "Microprocesses of Metal Dusting on Iron," Steel Research, 66: 217-221.

Sato Y., M. Kamo, and N. Setaka, 1978, "Raman Spectra of Carbons at 2600-3300 cm^{-1} Region," Carbon, 16:279-280.

Schaeffer W. D., W. R. Smith, and M. H. Polley, 1953, Ind. Eng. Chem., 45, 1721 Tuinstra F. and J. L. Koenig, 1970, "Raman Spectrum of Graphite," J. Chem. Physics, 53:1126-1130.

Vidano R. and D. B. Fischbach, 1978, "New Lines in the Raman Spectra of Carbons and Graphite," J. Amer. Ceram. Soc. 61:13-17.

A NEW CORROSION MECHANISM FOR METAL DUSTING ON 304L STAINLESS STEEL

P. SZAKALOS*, R. PETTERSSON, S. HERTZMAN
Swedish Institute for Metals Research (SIMR), Stockholm, Sweden.

ABSTRACT

Metal dusting has been induced in laboratory experiments on 304L stainless steel in synthesis gas (25%CO+3%H_2O+H_2) at 650°C. Detailed metallographic studies in combination with thermodynamic modelling have formed the basis of a proposed new mechanism for metal dusting of chromia-forming stainless steels. The role of carbides and oxygen is considered central to the mechanism and to the description of the metal dusting phenomenon as it appears in engineering alloys.

1. INTRODUCTION

Metal dusting or catastrophic carburisation is a widespread high temperature corrosion problem, but the complex mechanisms behind the phenomenon are not fully understood. Metal dusting is a disintegration of metals and alloys into a dust of metal particles and graphite (coke). This occurs in carburising atmospheres or, more commonly, in carburising and selectively oxidising atmospheres, such as synthesis gas. Temperatures are typically in the range between 400-900°C (Grabke 1995, 1998; Schneider et al. 1997; Perkins et al. 1976; Hochman 1976). It is believed that a dense layer of chromia or alumina (Grabke 1995, 1998) prevents carburisation and metal dusting on engineering alloys, at least for a certain period. In an industrial plant there is often an influence of thermal- and mechanical-load or erosion that speeds up the breakdown of the more or less protective oxide layers. The corroded metal shows either pitting or general attack. Several studies of metal dusting have been published and a number of mechanisms to explain metal dusting have been proposed. The most accepted mechanisms are those proposed by Grabke (1995, 1998) and Hochman (1976) involving decomposition of metastable carbides. In nickel and Ni-base alloys another mechanism is proposed by Pippel et al (1998), Grabke (1998) and Schneider et al. (1997) in which graphite forms into and inside the Ni-matrix which leads to small Ni-particles embedded in graphite. Recently, Norwegian research groups with Schmid et al. (1999) and de Bruyn et al. (2001) have emphasised that oxygen plays an important role in the mechanisms of metal dusting in CO-containing gas mixtures. In the present work the mechanisms of metal dusting will be described in general and an active corrosion mechanism involving both carbon and oxygen is proposed. The mechanism is based on results from laboratory exposures in a CO-containing gas mixture on 304L type of steel at 650°C.

2. EXPERIMENTAL

The material studied was a 304L stainless steel with a composition (in wt.%) of 18.35Cr 10.15Ni 1.26Mn, 0.42Si, 0.39Mo, 0.043N and 0.013C. Specimens were cut from 25mm bar stock, giving a semicircle shape with dimensions 25×12× 2 mm. The laboratory exposure was conducted at 650°C/1000h in a quartz tube furnace with a diameter of 25 mm. Four temperature cycles down to 100-200°C and back to 650°C, each with a duration time of about 4-5 h, were

*Corresponding author address: Peter Szakalos, Swedish Institute for Metals Research (SIMR), Drottning Kristinas väg 48, S-114 28 Stockholm, Sweden. Fax: +46-8-4404535. E-mail: SZAKALOS@SIMR.SE

conducted in order to raise the carbon activity and promote initiation of metal dusting. Samples were prepared by grinding to 600 mesh followed by a standard pickling operation in 1.8M HNO_3 + 1.6M HF at 50°C for 80 sec, then cleaned in acetone prior to being tested in the cold furnace. To reach a low oxygen partial pressure, pure hydrogen was flushed through the furnace for three hours at 650°C. The reaction gas was then introduced, with an initial composition of 25%CO+3%H_2O+H_2 According to the thermodynamic calculations employed this gives an equilibrium gas composition when graphite has formed of 11%CO+12%H_2O+4%CO_2+H_2 and an oxygen partial pressure pO_2 of $1.6x10^{-24}$. The flow rate was 250 ml/min, which corresponds to a gas velocity over the specimen of 9 mm/s.

The post exposure metallographic examination was made with JEOL JSM-6400 scanning electron microscope (SEM) and the analyses were made with a Link-Inca Energy Dispersive Spectrometer (EDS). Micrographs were also taken with a Field Emission Gun-SEM Leo-1530.

3. RESULTS AND DISCUSSION

3.1. The initiation of a metal dusting pit

SEM investigations of the surface showed the presence of surface oxides, particularly adjacent to the grain boundaries. However, none of the metal dusting pits start in the grain boundaries but initiate instead in the middle of larger grains. In Fig. 1 SEM image of a metal dusting attack in early stages is shown, together with SEM-EDX line scan analyses that show the relative amounts of carbon, oxygen and chromium.

The simultaneous processes of oxidation and carburisation are apparent in that there is a Cr-rich oxide border around the coke-filled pit. It thus appears that when CO dissociates on the steel surface, or on the thin non-protective oxide, carbon diffuses into the steel and forms carbides while oxygen reacts with the metal and forms oxides. The grain boundary diffusionof chromium appears to be fast enough at 650°C to support a more protective chromia layer at grain boundaries.

3.2 The reaction front in a metal dusting pit

When a metal dusting pit has initiated, an extensive carbon ingress occurs, especially at the grain boundaries, and may result in degenerated eutectoidic carbide structures, i.e. discontinuously precipitated carbides see Figs 2a and 2b.

The dominating precipitate is probably $M_{23}C_6$-carbides but close to the reaction front M_7C_3-carbides, which have a higher carbon content, may also form as discussed later in this paper. The former austenitic grain bulk has also largely transformed to carbides as shown in the etched cross-section from a pit, Fig. 3a. The carbon ingress declines rapidly with distance away from the metal dusting pit, and at a distance of 60µm from the pit there are only a few carbides visible in the grain bulk, as shown in Fig 3b. Below the pit, the carbides extends some hundred microns in depth, indicating that the conditions are more favourable for carbon ingress at the bottom of the pit, see Fig. 3c.

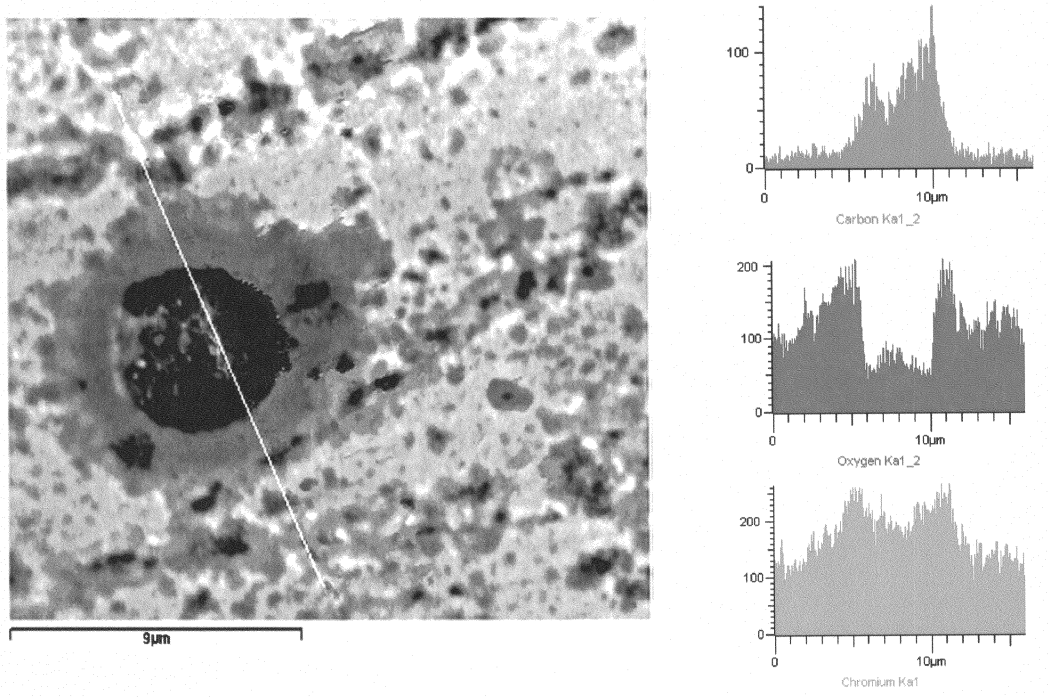

FIGURE 1 Early stages of a metal dusting pit are shown with SEM-EDX analyses. The simultaneous processes of oxidation and carburization are apparent with a Cr-rich oxide border around the coke filled pit.

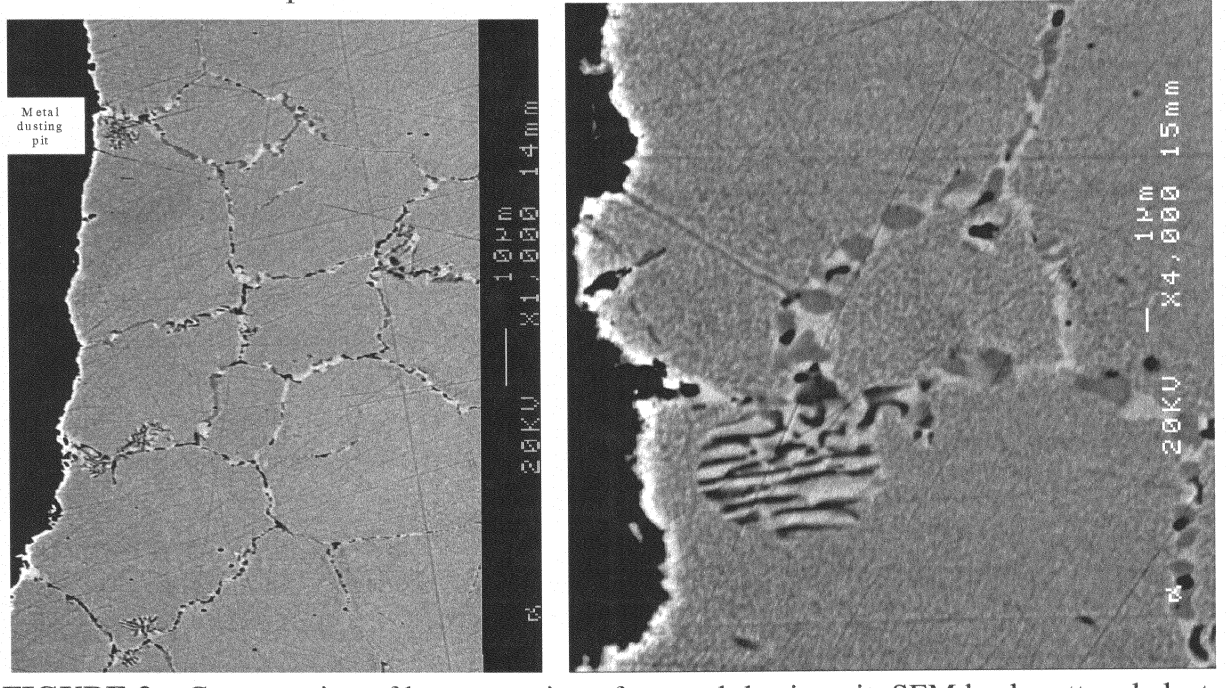

FIGURE 2a Cross-section of bottom region of a metal dusting pit. SEM backscattered electron image, unetched. Showing heavily carburised grain boundaries. A close up is shown in Figure 2b.

FIGURE 2b Cross-section of the bottom region of metal dusting pit. SEM backscattered electron image, unetched. The former austenitic grain boundaries show a degenerated eutectoidic carbide structure, i.e. discontinuous precipitation. The carbides showing black contrast are probably M_7C_3 and those giving dark grey contrast $M_{23}C_6$.

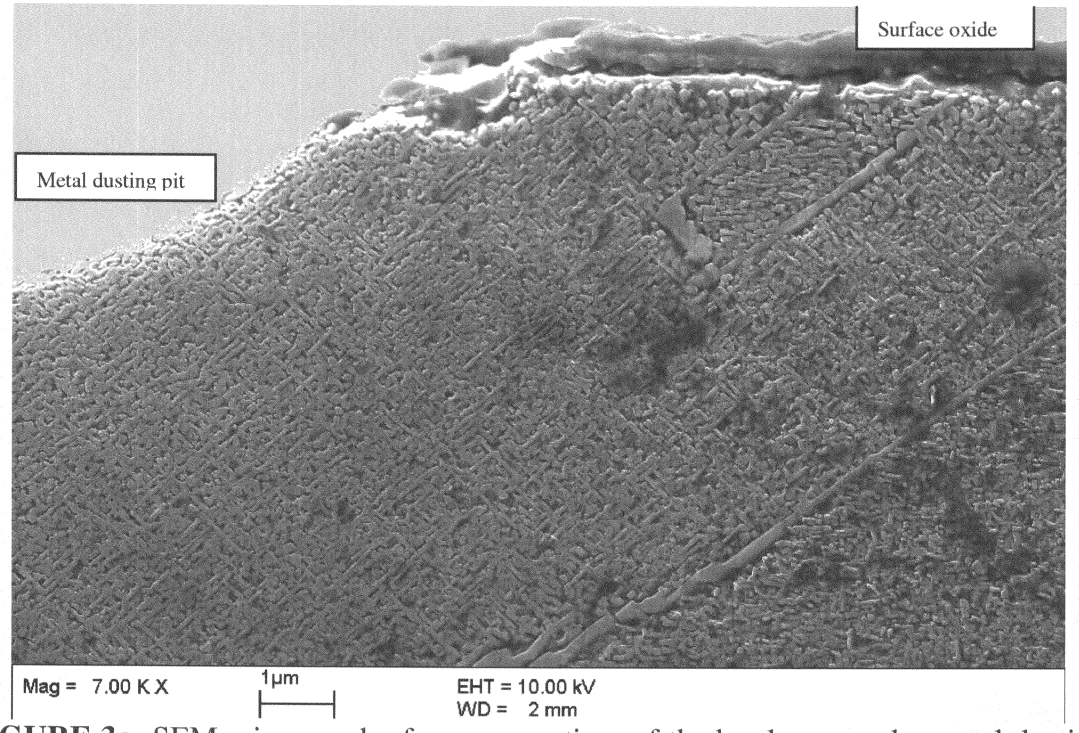

FIGURE 3a SEM micrograph of a cross-section, of the border around a metal dusting pit, electrolytically etched to show the carbide structure. An oxide scale is present on the unattacked surface.

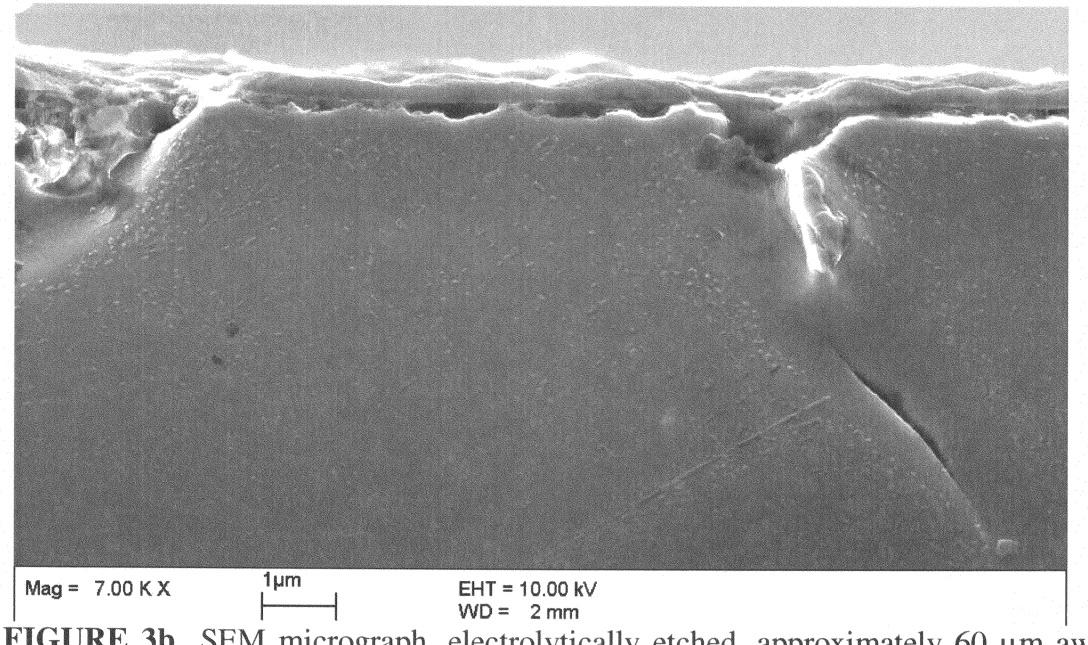

FIGURE 3b SEM micrograph, electrolytically etched, approximately 60 µm away from the metal dusting pit. A semi protective chromia layer is present on the surface and only very slight carbide formation has occurred in the austenitic matrix (compare with Fig. 3a).

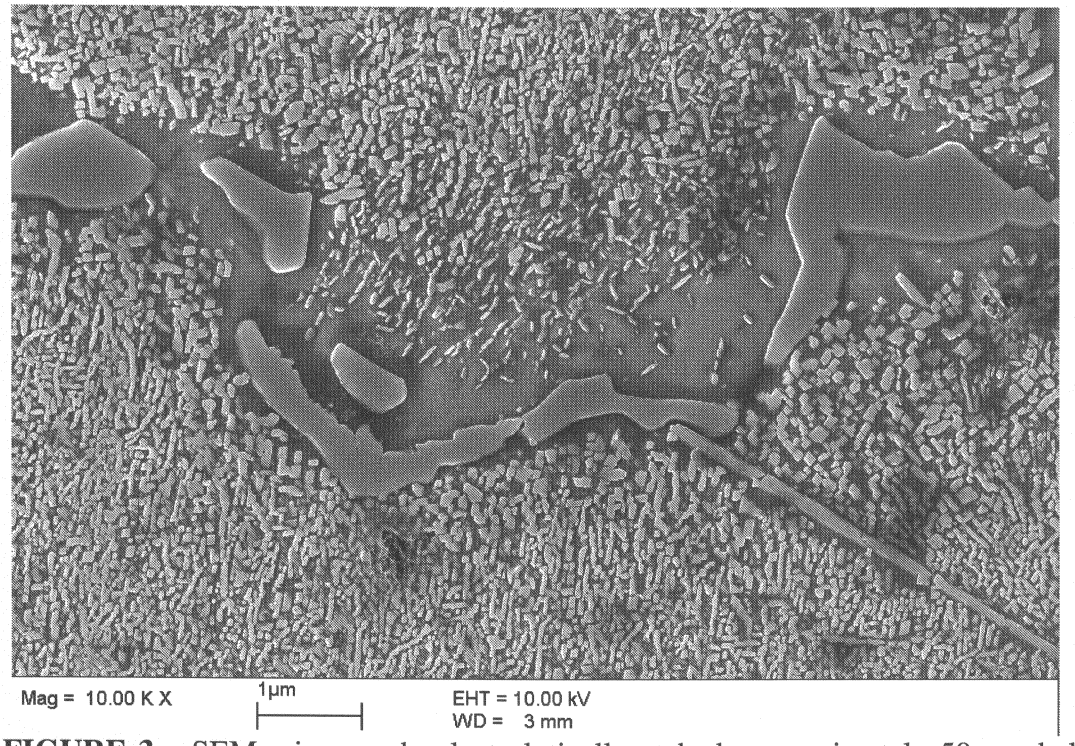

FIGURE 3c SEM micrograph, electrolytically etched, approximately 50 µm below the base of the metal dusting pit. The austenitic structure is strongly carburised and contains at least 50% carbides.

To study the thin metal dusting corrosion front it is important that the sample is in the unetched condition. SEM images of a prepared cross-section for studying the outermost metal dusting reaction front are presented in Figs. 4a-4c and SEM-EDX analysis are included in Fig. 4c.

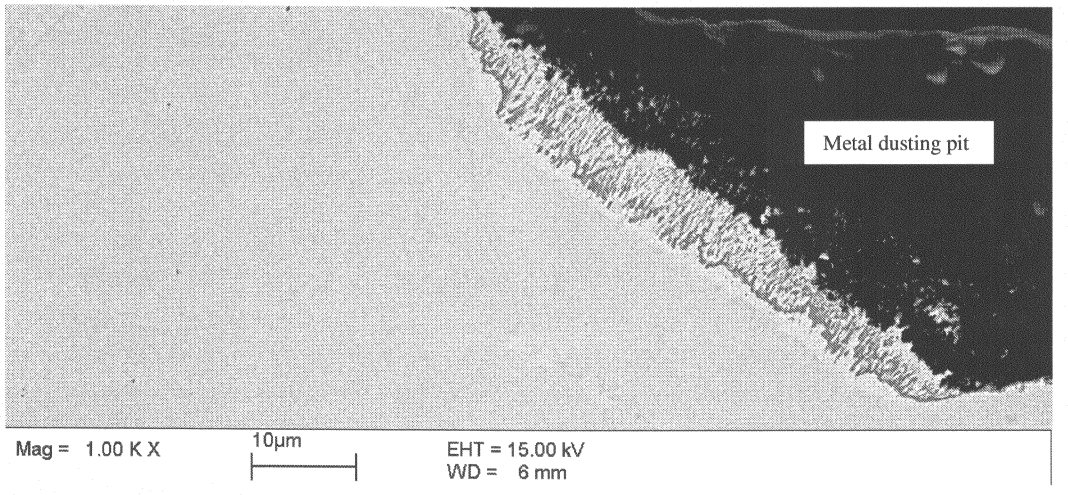

FIGURE 4a An unetched cross-section of a metal dusting pit showing the active reaction front with a mixture of a more or less carbide free and Cr-depleted austenite decorated with Cr-rich oxides. Detailed micrographs are shown in Figs. 4b and 4c respectively.

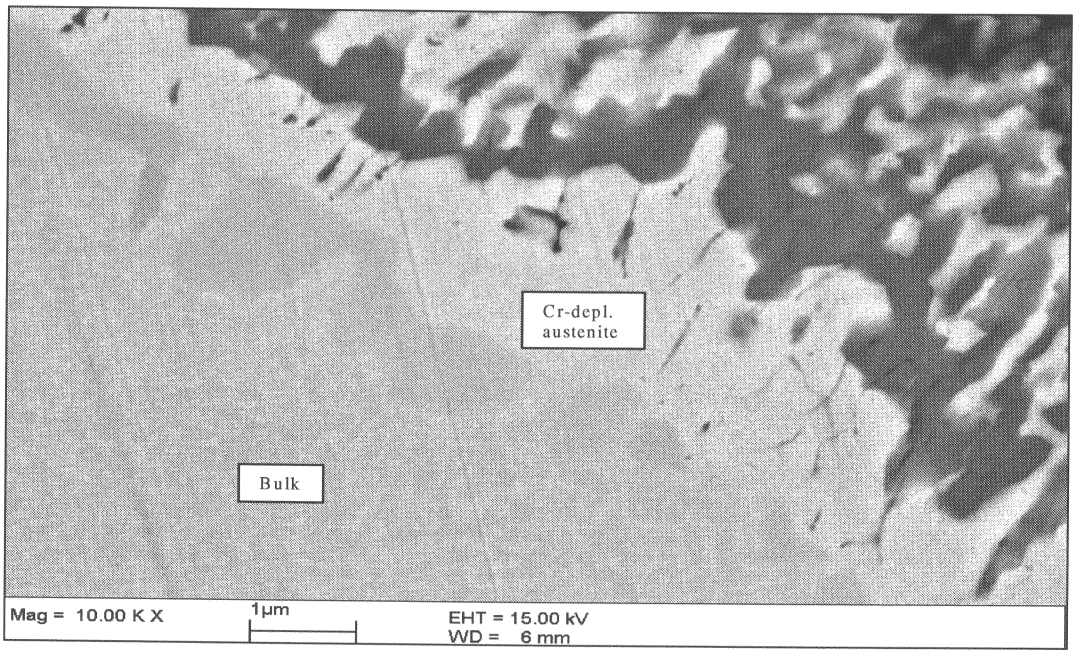

FIGURE 4b SEM backscattered electron image, unetched. A close up from the reaction front in Fig. 4a. The strongly carburised bulk structure corresponds to the etched bulk structure in Figs. 3a and 3c. The same region is shown in Fig. 4c with EDX-analyses. Thin black graphite channels are observed which extend through the Cr-depleted austenite border into the oxide.

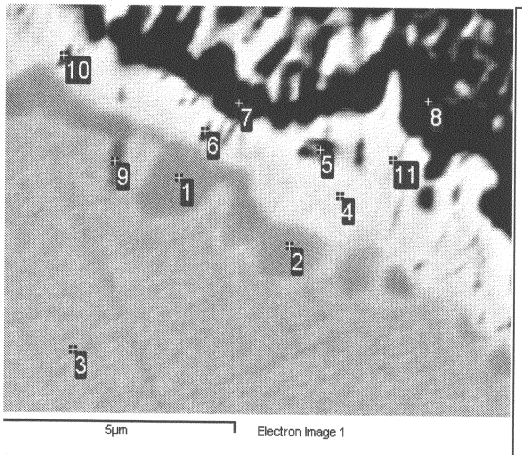

Spectrum	C	O	Si	Cr	Mn	Fe	Ni	Mo	Total
1 Carbide	16	0	0,0	14	0,0	68	2	0,4	100
2 "	22	0	0,0	12	0,0	63	3	0,3	100
9 "	15	0	0,0	19	0,0	61	5	0,3	100
3 Carburised bulk	11	0	0,8	18	1,5	60	8	0,3	100
4 Cr-depleted γ	3	0	0,0	3	0,0	82	12	0,0	100
11 "	6	0	0,4	4	0,0	79	11	0,0	100
5 Cr-depleted γ with graphite	11	0	2,5	4	0,0	72	11	0,0	100
6 "	12	0	0,7	6	0,0	71	10	0,0	100
10 "	8	0	0,4	5	0,0	77	10	0,2	100
7 Oxide	0	40	0,7	24	2,2	31	2	0,0	100
8 "	0	48	0,5	18	1,8	29	3	0,0	100

All results in Atomic Percent

FIGURE 4c SEM-EDX analysis from the same region of the active corrosion front as in Fig 4b. The metal dusting reaction front may be divided into four zones: a strongly carburised bulk structure (Sp. 3), a carbide zone low in Cr (Sp.1 and 2), a light contrast region with dissolving carbides, i.e. a Cr-depleted austenite with graphite channels (Sp. 4,11,5,6 and 10). The outermost zone consists of the corrosion products, a mixture of oxides (Sp.7-8, dark contrast) and austenite particles or flakes, all penetrated by graphite channels (black in contrast). Compare also with the schematic illustration of the active corrosion front in Fig. 9.

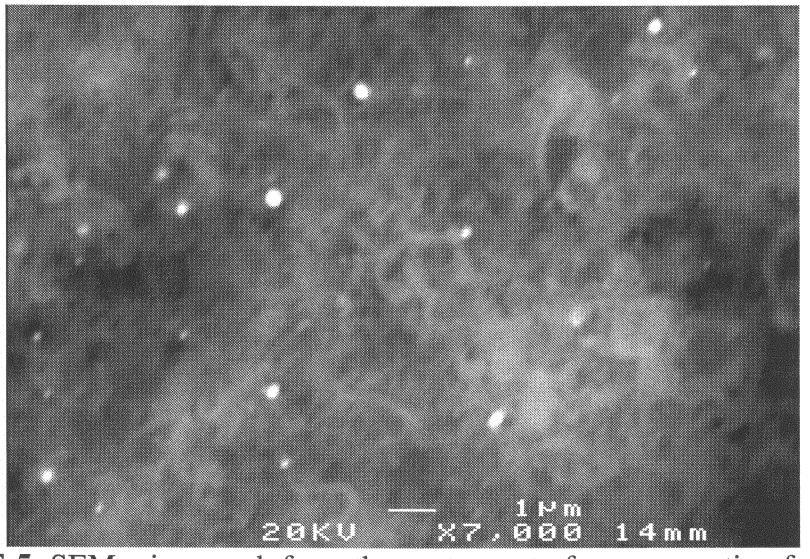

FIGURE 5 SEM micrograph from the centre part of a cross-section from an outgrowing coke protrusion from a metal dusting pit, approximately 2 mm perpendicular from the reaction front. Note the very small austenite metal particles compared with the large metal fragments released at the reaction front, see Figs 4a and 4b. The metal particles, influenced by signals from the coke, having a typical analysis in weight-% of 56C-38Fe-5.2Ni, which gives a Fe/Ni ratio of about 7. These Fe-Ni particles disintegrates continuously under simultaneous production of filamentous carbon.

A more or less carbide free and Cr-depleted austenite, frequently denoted "white phase" (Grabke 1995), decorated by a Cr-rich oxide is evident. The measured Fe/Ni ratio in the Cr-depleted austenite is around 6.8. A network of filaments showing black contrast and a high carbon content is observed inside the Cr-depleted austenite and extends into the oxides, see Fig. 4b. Both the structure and composition suggests that these filaments are graphite. The rather large metal particles or fragments released in the reaction front cannot be detected in the outgrowing coke. In fact, a few millimetres from the dusting pit reaction front, only very small austenitic metal particles are observed, see Fig. 5.

3.3. Thermodynamic modelling with ThermoCalc

The two most important findings described above, the existence of a more or less carbide-free and Cr-depleted austenite in the reaction front and the presence of a Cr-rich oxide, provide information of central importance to understanding the metal dusting mechanism. The ThermoCalc (TC) (Sundman et al. 1985) modelling describes 304L type of stainless steel at 650°C and at normal atmospheric pressure. Two databases are combined for the calculations, the SSOL database for the phases in the steel and the SSUB database for the gas phases and oxides. The major equilibrium gas components are H_2, CO, H_2O, CO_2 and CH_4.

The diagram in Fig. 6 shows the mole fraction of stable solid phases as a function of oxygen partial pressure with a fixed carbon activity a_c=1 and graphite phase suppressed. The graphite phase has to be suppressed in order to have carbides present in the calculation. Schematically, the diagram in Fig. 6 can be regarded as a section across the metal dusting reaction front from the metal interface (at low oxygen partial pressure) towards the gas phase (high oxygen partial pressure). According to TC, the equilibrated oxygen partial pressure in the

exposure is $pO_2=10^{-24}$, which means that the stable phases are austenite and Cr-Fe spinel oxide with no carbides. In reality, the corrosion products also contain graphite but the graphite phase was suppressed in the calculation. According to the TC-calculations, the carbide-free austenite consists of 86%Fe-14%Ni and 0.06%Cr at $a_c=1$, which gives a Fe/Ni ratio of about 6.1. This findings corresponds well with the SEM-EDX results which gave a Fe/Ni ratio of 6.8, albeit with some Cr-present.

Fig. 7 shows the calculated mole fraction of phases as a function of carbon activity with graphite phase suppressed and a fixed oxygen partial pressure of $pO_2=10^{-24}$. This shows that the spinel oxide is stable even at carbon activities above 100. Fig. 8 gives the mole fraction of phases as a function of carbon content in 304L steel. From this it is seen that a 304L steel will contain almost 50% M_7C_3 carbides when the carbon activity is $a_c=1$.

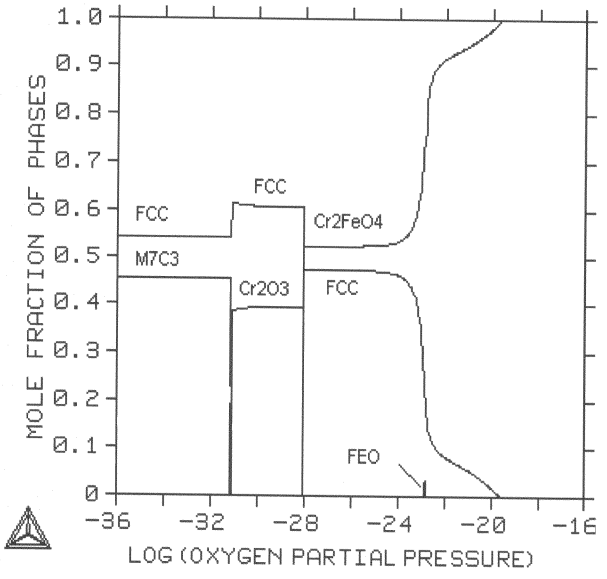

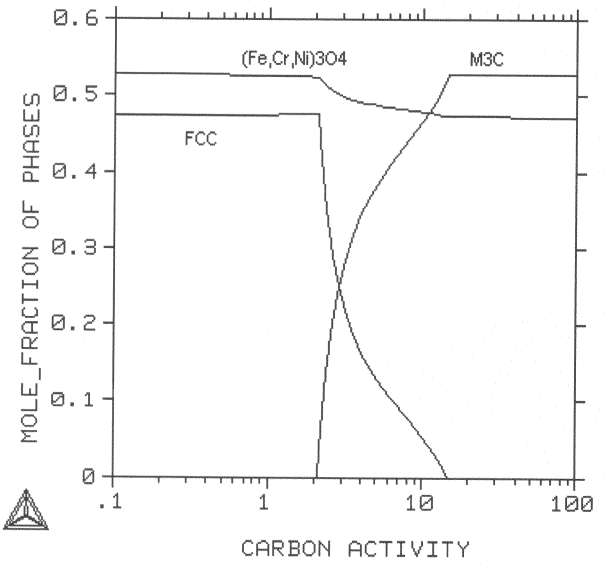

FIGURE 6 (Left) Mole fraction of stable phases in the 304L-C-O-H system as a function of oxygen partial pressure with a fixed carbon activity $a_c=1$ and graphite phase suppressed. For the equilibrated gas composition used in this study, with $pO_2=1.6x10^{-24}$, the stable phases will be FCC-austenite and a Cr-Fe spinel oxide. Schematically, the diagram can be seen as a cross section of the thin metal dusting front from the metal interface (at low pO_2) towards the gas phase (high pO_2).

FIGURE 7 (Right) Mole fraction of stable phases as a function of carbon activity with the graphite phase suppressed and a fixed oxygen partial pressure of $pO_2=1.6x10^{-24}$. The spinel oxide is stable, even at carbon activities above 100.

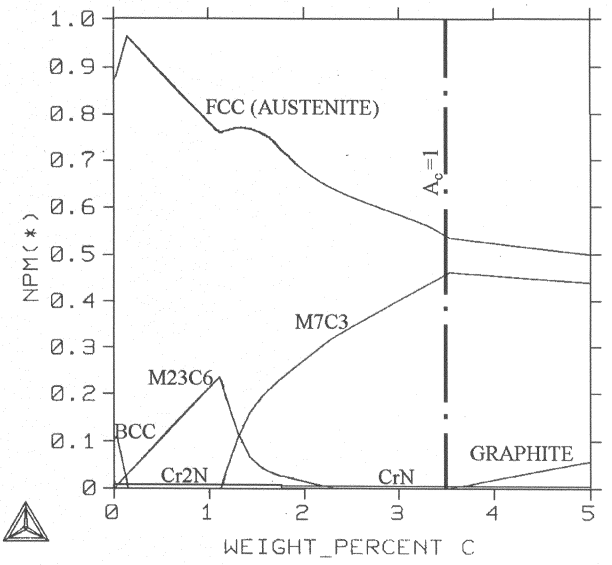

FIGURE 8 Mole fraction of stable phases as a function of carbon content in 304L steel. At carbon activity a_c=1, carbon content in steel reaches approximately 3.6w% with a carbide content close to 50%.

3.4. The mechanisms of metal dusting

Three main mechanisms have been used to describe the corrosion phenomenon called metal dusting.

Type I: Decomposition of metastable carbides.

The first mechanism is well understood and described exhaustively by Grabke (1995, 1998) and Hochman (1976). The mechanism may be summarised as decomposition of previously formed metastable cementite into graphite and iron during metal dusting conditions. However, the thermodynamic calculations discussed later in this paper suggest that this mechanism is restricted to iron and low alloyed steels and may not be extended to include commercial stainless steels and nickel base alloys, since the alloyed cementite, M_3C as well as M_7C_3- and $M_{23}C_6$-carbides are more stable. However, according to TC these carbides will dissolve *if the oxygen partial pressure is high enough* and they may be subjected to the type III mechanism during metal dusting conditions.

Type II: Graphite formation into and inside thermodynamically stable phases.

The type II mechanism has been described on nickel by Pippel et al. (1998), Grabke (1998), and Schneider et al. (1997). In more general terms this mechanism seems to be valid for both pure nickel and binary iron nickel compositions. This mechanism is thus also relevant to the Cr depleted austenite described above. Thermodynamically, neither carbides nor oxides are stable in Ni or Fe-Ni austenites under metal dusting conditions, only metal and graphite are stable. This degradation mechanism may be described as graphite formation into and inside the carbon-saturated metal matrix, which leads to very small metal fragments surrounded by graphite. This mechanism seems to continue so the metal particle decreases in size with time. It is suggested by Pippel et al. (1998) that the process may continue to an atomic scale.

The type II mechanism may also appear in conjunction with the type III mechanism described below and operates on the Cr-depleted austenite border at the reaction front as well as the austenitic dust embedded in the coke.

Type III: The proposed mechanism: Active corrosion by carbon and oxygen

The type III mechanism put forward here has not previously been described in detail, although several researchers have discussed the possible active role of oxygen during metal dusting conditions in combination with high steam contents of 30-50% (Perkins et al. 1976; Eberle and Wylie 1959). In gas atmospheres with low steam content (2-3%) the phenomenon was first mentioned by Schmid et al. (1999). M. Lundberg (2001) has also pointed out that oxygen seems to have an active role during metal dusting. H.J. de Bruyn et al. (2001) took the idea further and drew attention to the occurrence of internal oxidation during metal dusting, at least in reformer gas with high water vapour content, and suggests that the phenomenon may also occur with low water vapour content.

The active corrosion by carbon and oxygen is probably the major degradation mechanism in chromia-forming engineering alloys exposed in CO-containing atmospheres with or without water vapour. It is possible that this mechanism may also be operative for Cr-containing alumina formers. Metal dusting in a CO-containing environment may be seen as an active corrosion by carbon, comparable with chlorine-induced active corrosion. In the case of metal dusting, carbon reacts with metal and metal carbides are formed. The carbides oxidise and free carbon is released which forms carbides and so forth. This process is similar to chlorine-induced active corrosion where metal chlorides are formed which oxidises and chlorine is released to form more metal chlorides (Reese and Grabke 1992).

3.5 Principal reactions of the type III mechanism

The reactions are presented in detail below. Consider ten atoms of 304L steel of composition 18Cr-10Ni-72Fe in wt.%, i.e. an approximate atomic ratio of 2Cr-1Ni-7Fe. The following reactions show the steps involved in fully equilibrated carburization and metal dusting process in a CO/H_2 containing gas (a_c=1) at 650°C. Schematically, the corrosion mechanism may be divided into two stages:

The carburisation reaction (1):

$$(2Cr\text{-}Ni\text{-}7Fe)\gamma_{304L}+1.29CO(g) \rightarrow (6Fe\text{-}Ni)\gamma_{matrix}+0.43[(Cr_{14/3}Fe_{7/3})C_3]+1.29O(ad)$$

Since CO is the carbon source, oxygen will be released when the dissociation process takes place on the metal surface. Some of the adsorbed oxygen may react with hydrogen and form water vapour but the microstructural evidence presented in this paper indicates that a considerable amount of the oxygen forms a Cr-oxide on the steel surface. The ThermoCalc modelling predicts formation of M_7C_3-type carbide if the carbon activity is unity, but as the carbon activity is decreased in the steel, $M_{23}C_6$-carbides constitutes the majority of the total carbide formed. The Cr-depleted austenite matrix (γ_{matrix}) containing fine carbide precipitates now reacts with CO according to the fully equilibrated metal dusting reaction:

Carbide dissolution followed by selective oxidation and metal dust formation (2):

$$(6Fe\text{-}Ni)\gamma_{matrix}+0.43[(Cr_{14/3}Fe_{7/3})C_3]+4CO(g) \rightarrow (6Fe\text{-}Ni)\gamma_{dust}+(Cr_2Fe)O_4 + 5.29C(s)$$

where γ_{dust} is austenitic particles, i.e. metal dust. The equilibrium corrosion products are thus, austenitic metal particles, Cr-Fe spinel oxides and elementary carbon. The carbide is a necessary reaction intermediate and the overall reaction simplifies to:

Summary reaction of the active corrosion (3):

$(2Cr\text{-}Ni\text{-}7Fe)\gamma_{304L}+4CO \rightarrow (6Fe\text{-}Ni)\gamma_{dust}+(Cr_2Fe)O_4+4C(s)$

The summary reaction will be identical in case of oxidation of $M_{23}C_6$-carbides instead of M_7C_3-carbides; it is only the carbon and CO content in the reaction (1) and (2) that differs. However, the carbide content close to the reaction front is at least 50%, see Fig. 3, which is the maximum amount of carbide precipitates, as M_7C_3, at 650°C according to ThermoCalc, see Fig. 8. When studying the overall reaction one could suspect that metal dusting of stainless steels by CO is basically degradation by oxidation but as discussed above, a more correct description would be to see metal dusting active corrosion by carbon. There is one major difference between the two active corrosion processes, in case of chlorine-induced corrosion, virtually all metal atoms react chemically to form corrosion products. In case of metal dusting, according to the above reactions, only three of ten metal atoms, i.e 30 atomic-% of the steel reacts chemically to form corrosion products and the remaining 70% metal forms metal particles or dust without any chemical reaction. These proportions corresponds surprisingly well with the SEM observations in the active reaction front in a metal dusting pit, see Figs. 4a-4b.

3.6. Diffusion processes in the Type III mechanism

The whole process with C, O and Cr diffusion is illustrated in Fig. 9. It appears that Cr-diffusion is the rate-limiting factor of the type III mechanism, since this is necessary for Cr-depletion of the austenite boundary layer. Cr bulk diffusion is too slow to explain the rather fast kinetics of metal dusting, instead it is required that Cr diffuses with a rate more consistent with that of grain boundary diffusion.

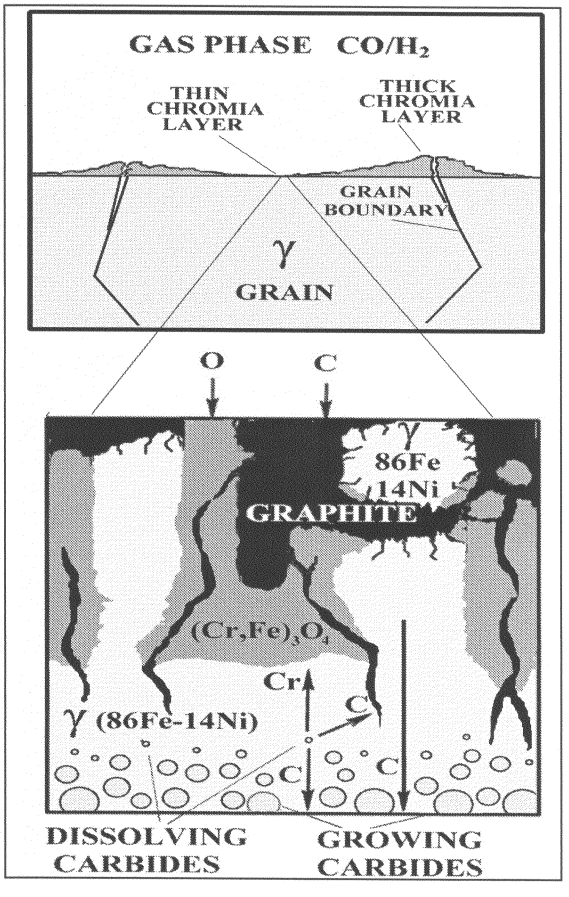

FIGURE 9 The upper part shows a (large) austenite grain in cross-section with internal oxidation of the grain boundaries. The metal dusting pit is however initiated on the grain bulk surface. The lower detail summarises the diffusion paths, included in the active corrosion process with carbon and oxygen (type III mechanism), in combination with formation of graphite channels (type II mechanism). The graphite substructure promotes the Cr-diffusion and subsequently the oxide formation. The corrosion products consist of Fe-Ni austenitic metal dust, spinel oxides and elementary carbon, but no carbides.

A possible mechanism for enhanced diffusion is provided by the presence of a network of graphite filaments, as seen in Fig. 4b, which suggests that the type II mechanism with inward growth of graphite is operating in the active corrosion front. This network of graphite channels will enhance Cr-diffusion and thus also the carbide dissolution and oxide formation. Using these findings, it is possible to calculate the metal dusting kinetics based on the Cr-diffusion through the austenite boundary layer (Szakalos, to be published).

4. CONCLUSIONS

Metal dusting has been induced in a 304L stainless steel by laboratory testing in a synthesis gas atmosphere. Detailed metallographic observations and thermodynamic calculations have formed the basis of a proposed new mechanism for metal dusting applicable to chromia-forming stainless steels in CO-containing environments. The mechanism involves carbides as reaction intermediates but not as stable end products. The equilibrated corrosion end products are instead carbon (graphite and filamentous carbon), spinel oxides and Cr-depleted austenite particles in the case of a 304L steel. This mechanism of metal dusting as well as the type of corrosion products is consistent with the thermodynamic conditions of the material under the influence of a carbon and oxygen gradient.

-Schematically, the corrosion mechanism may be divided into two stages:

i) Carburisation:

304L → Cr-depleted austenite + carbide

ii) Carbide dissolution followed by selective oxidation and metal dust formation:

Cr-depleted austenite + carbide → Cr-depleted metal dust + oxide +carbon

The carbide is a necessary reaction intermediate and the overall reaction is;

304L → Cr-depleted metal dust + oxide + carbon

For the stainless steel investigated, a second complementary mechanism was also found to be operative. This has previously only been described in pure nickel and Ni-base alloys, and involves graphite formation into and inside the Ni-enriched and Cr-depleted austenite. This contributes to the proposed new mechanism by enhancing chromium diffusion in the surface austenite.

ACKNOWLEDGEMENTS

Thanks are expressed to Libin Liu for help with the thermodynamic calculations and to Ulla Gustavsson and Jacek Komenda for help with the SEM-EDX analysis and FEG-SEM analysis respectively. Thanks are also expressed to Mats Lundberg, Sandvik Steel, for valuable discussions and critical reading of the manuscript. The work was financed by High Temperature Corrosion Centre (HTC) and financial support for writing this paper was provided by Professor Christoffer Leygraf, Division of Corrosion Science, Royal Institute of Technology, Stockholm.

REFERENCES

de Bruyn, H. J., E. H. Edwin and S. Brendryen, 2001,"Apparent influence of steam on metal dusting" Corrosion, NACE, Paper No. 01383.

Eberle, F., and R.D. Wylie, 1959, "Attack on metals by synthesis gas from methane-oxygen combustion," Corrosion 15, 12 p. 622t-626t.

Grabke, H. J., 1995, "Metal dusting of low- and high-alloy steels" Corrosion 51, 9, p.711-720.

Grabke, H. J., 1998, "Thermodynamics, mechanisms and kinetics of metal dusting" Materials and Corrosion 49, p.303-308.

Hochman, R. F., 1976, "Catastrophic deterioration of high temperature alloys in carbonaceous atmospheres," Electrochemical Society Inc. Proc., vol. 77-1, pp 715-732.

Lundberg, M., 2001, Sandvik steel AB, Personal communication.

Perkins, R. A., W.C Coons, F.J. Radd, 1976, "Metal Dusting corrosion in coal gasification environments," Electrochemical society Inc. Proc., 77-1, p. 733-749.

Pippel, E., J.Woltersdorf, R. Schneider, 1998, "Micromechanisms of metal dusting on Fe-base and Ni-base alloys," Materials and Corrosion, Vol. 49, No 5, pp. 309-316.

Reese, E., and H.J. Grabke, 1992, "Effects of chlorides on the oxidation of the 2.25Cr-1Mo Steel," Materials and Corrosion 43, p.547-557.

Schmid, B., Ø. Grong, R. Ødegård, 1999, "Coke formation in metal dusting experiments," Materials and Corrosion 50 (11), pp. 647-653.

Schneider, R., E., Pippel, J.Woltersdorf, S. Strauss and H.J. Grabke, 1997, "Microprocesses of metal dusting on nickel and Ni-base alloys. Steel Research," Vol. 68, No 7, pp326-332.

Sundman, B., B. Jansson, J-O. Andersson, 1985, CALPHAD 9, pp 153-190.

Szakalos, P., R. Pettersson, S. Hertzman, "An active corrosion mechanism for metal dusting on 304L stainless steel," to be published.

APPLICATION OF ESEM FOR IN-SITU STUDY OF HIGH TEMPERATURE CORROSION PROCESSES

H. J. de Bruyn* and N. Aas
Statoil ASA, Trondheim, Norway
B. Schmid
Hydro Aluminium, Holmestrand, Norway

ABSTRACT

The development of environmental scanning electron microscopes (ESEM) has made the in-situ study of high temperature corrosion processes possible. Several in-situ oxidation and metal dusting studies were conducted, demonstrating the value of ESEM in high temperature corrosion research.

Oxidation studies have been conducted on T-91 steel, type 304 stainless steel, alloy 800H, and alloy 601. Samples of these materials were exposed to water vapor and pure oxygen at 973 K while investigating the effect of surface finish and oxidation procedure. Differences in oxide scale growth and morphology were observed in the two different environments.

The paper provides an overview of the in-situ study technique illustrated with results from the oxidation studies.

INTRODUCTION

Development of the environmental scanning electron microscope (ESEM) is generally associated with the work of Danilatos (1997). The instrument, which has been on the market now for more than 10 years, was initially designed to be able to image wet specimens. The numerous applications in the literature prove that this aim has been achieved (Microscopy and Research, 1993).

During the development of the instrument, it was realized that the gaseous atmosphere in the specimen chamber served several purposes. Firstly, the relatively high chamber pressure ensures that wet specimens do not dry out, thus remaining in their original state. Secondly, the gas can be used to enhance the secondary electron signal from the sample surface, becoming an integral part of the environmental secondary detection (ESD) mechanism. The other advantage of this ESD detector is the ability of the ionized gas to dissipate charge. This means that any sample, including non-conductors, can be imaged in the ESEM. The gas can finally also be used to induce in-situ surface reactions for direct observation.

One of the first in-situ studies of high temperature oxidation in a scanning electron microscope was performed by Rapp and others (Rapp 1994; Verma et al. 1981). Their investigations were undertaken in a modified scanning electron microscope, fitted with a hot stage. This set-up could establish a gas pressure of 30 Pa right over the sample surface. Secondary electron images were collected using a conventional Everhart-Thornley detector. Important results were obtained but the system had some limitations (Lee and Rapp 1988).

*Corresponding author address: H. de Bruyn, Research & Technology, Statoil ASA, Postuttak N-7005 Trondheim, Norway; e-mail: hdb@statoil.com.

There are only few studies in the literature that demonstrate the use of the ESEM in high temperature studies, and even fewer on high temperature corrosion. Recently a thesis on metal dusting research has been published (Schmid 2000) that includes the development and use of the ESEM as a high temperature corrosion research tool. Some of the oxidation studies conducted for this thesis will be shown here to illustrate the use of the ESEM in high temperature corrosion research.

EXPERIMENTAL

All experiments referred to in this paper were carried out in an ElectroScan ESEM 2020 equipped with a hot stage. Initial studies were carried out to establish the limitations of the ESEM and to optimize the instrument set-up as far as possible.

Hot stage set-up

The ESEM hot stage is shown in figure 1. It consists of a heating element embedded in a thermal insulator. The sample to be studied is placed in a small alumina crucible on top of this element. Water-cooling of the whole device ensures that no overheating takes place, and that cooling to room temperature at the end of experiments is done efficiently. The supplier recommended that a heat shield be used when temperatures are to exceed 873K in order to minimize heat loss through convection.

During preliminary experiments it was found that the heat shield reduced the signal intensity quite drastically and increased the noise level. Increasing the gas pressure in the chamber could not compensate for this loss of signal intensity. The small hole in the heat shield also limited the accessible sample area. During extended experiments this in combination with drift of the image, often made it impossible to return to an area of interest. The possibility of conducting the experiments without the heat shield was therefore investigated.

A 0,5 mm thick iron sheet sample was oxidized in ambient air with the hot stage at 973K. The surface temperature of the iron oxide scale that formed was measured pyrometrically and compared to the temperature measured by a thermo-element below the sample. The temperature difference of approximately 10K was considered acceptable. Further experiments were therefore conducted without the heat shield.

The working principle of the hot stage is resistive heating, regulated by a feedback mechanism in which the measured temperature is compared with a set temperature, and any discrepancy between these two is compensated for by a current supply. When holding a set temperature, it was often found that the controller would reduce the current level. This then lead to a temperature drop, which again requires the controller to increase the current supply. The overall effect was a slightly fluctuating temperature (±5K), which was acceptable in terms of the experimental conditions. However, the effect this had on image quality was unacceptable. Every time the hot stage drew current the image drifted and the image contrast changed. This worsened at higher magnification to the effect that the acquisition of good quality images was impossible. The use of a platinum crucible instead of the alumina crucible improved the situation. Likewise did temporary switching off of the cooling water to the hot stage reduce vibrations during the acquisition of images.

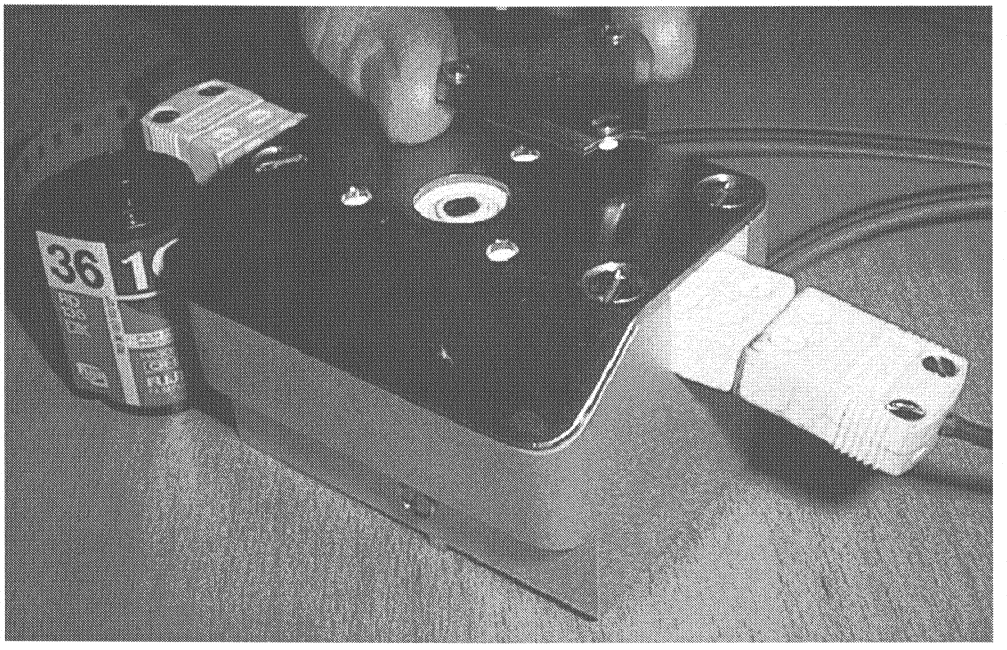

FIGURE 1 ESEM hot stage used for oxidation studies described in this paper. The heat shield is lifted for a better view.

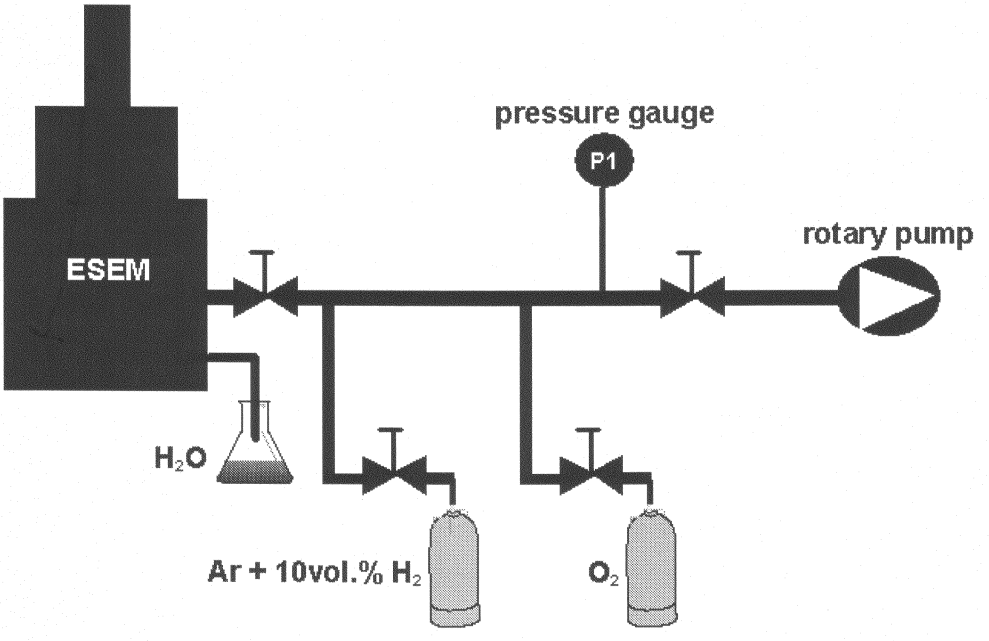

FIGURE 2 Gas inlet system dedicated to supply water vapor, oxygen, or a hydrogen-argon mixture to the ESEM chamber.

Gas supply system

The ESEM was supplied with a flask from which water can be introduced into the chamber. There is also an auxiliary gas inlet at the back of the console for allowing different gases into the ESEM chamber.

It was required to switch between different gases during the experiments. A dedicated gas inlet system (see figure 2) was therefore installed. This allowed purging of the gas lines and the ability to rapidly switch between different gas mixtures without exposing the experiment to air.

Experimental conditions

Samples were cleaned in acetone before exposure in the ESEM. The temperature was then raised at a rate of 60 K/min to the required test temperature while maintaining an Ar-10%H_2 gas mixture at a pressure of 1333 Pa in the chamber. The gas environment was replaced at least every other minute to ensure a reducing atmosphere. At the target temperature, the reducing gas was quickly pumped out and replaced with the reactive gas for a specific experiment. During the course of the experiments, the reactive gas was partially evacuated and refreshed in a batch-wise manner, i.e. the ESEM chamber was partially evacuated and refilled every 15 minutes. A chamber pressure of 667 Pa was maintained throughout the experiments.

ESEM conditions

Most of the experiments were run at 15 kV beam energy, 20 – 40 μA beam current (LaB_6 filament), a condenser setting of 50% and the hot stage ESD detector. A working distance ranging between 8,8 – 10,0 mm was used. The Statoil ESEM is also equipped with a Link ISIS microanalysis system. This was used for identification of corrosion species after the experiments.

OXIDATION STUDIES

The formation of protective oxide scales on an alloy surface is a critical requirement for its performance in corrosive high temperature environments. Alloys exposed to metal dusting environments require the formation of dense protective oxide scales that will resist carbon diffusion into the alloy. Understanding the type and nature of oxides that form in metal dusting environments therefore becomes a key requirement in explaining the performance of different alloys.

Following the exposure of the pure metals, iron, chromium, and nickel (Schmid, 2000), a series of engineering materials, T-91 steel, austenitic stainless steel type 304, alloy 800H and alloy 601, was oxidized in the ESEM in two different environments, pure oxygen and water vapor. These exposures were performed at 973K in order to have reasonably short experiments. Photographs were only taken when changes were observed and not at fixed time intervals. The nominal composition of the exposed materials is presented in table 1.

Identification of different oxides was performed by a combination of elemental analysis by EDX and by morphological comparison with oxides obtained on the oxidation of pure metals.

Table 1 Nominal composition of engineering materials in oxidation experiments.

Material	%Cr	%Ni	%Fe	%C	%Al	%Mo
T91-steel	8.00 – 9.50	0.40 max	Bal.	0.08 – 0.12	0.04 max	0.85 – 1.05
Type 304 stainless	18.0 – 20.0	8.0 – 10.5	Bal.	0.08 max	-	-
Alloy 800H	19.0 – 21.0	30.0 – 32.0	Bal.	0.06 – 0.08	0.20 – 0.40	-
Alloy 601	22.0 – 24.0	Bal.	9.0 – 11.0	0.03 – 0.08	1.1 – 1.6	-

Predicted oxide stability

Prediction of oxide stability at equilibrium from available thermodynamic data is limited to pure metals and relatively simple environments. Stability diagrams constructed from such data (HSC Chemistry, version 4.0) can nonetheless be used to obtain an approximate prediction of oxide species likely to form.

Equilibrium oxide stabilities for iron, chromium and nickel have been constructed as a function of temperature and oxygen partial pressure. These are presented in figures 3 – 5. The two experimental environments in the ESEM experiments, pure oxygen (A) and water vapor (B), are indicated on these. In a 100% oxygen environment, the p_{O2} value is equal to the total pressure of the environment. A $log\ p_{O2}$ value of –2,17 was calculated for the exposures in pure oxygen at 973K.

For exposures in water vapor, the oxygen partial pressures were calculated from the following reaction:

$$2H_2O \rightarrow 2H_2 + O_2$$

From this it can be shown that:

$$\log p_{O_2} = 2\log p_{H_2O} - \log K_p - 2\log p_{H_2}$$

Likewise, a $log\ p_{O2}$ value of –8,07 was calculated for exposures in water vapor at 973K.

From the stability diagrams it can be predicted that both environments are likely to produce the same chromium and nickel oxide species (Cr_2O_3 & NiO). In the case of iron, however, it is likely that oxidation in pure oxygen will produce hematite (Fe_2O_3), while oxidation at the same temperatures in water vapor is likely to produce magnetite (Fe_3O_4) as the stable oxide.

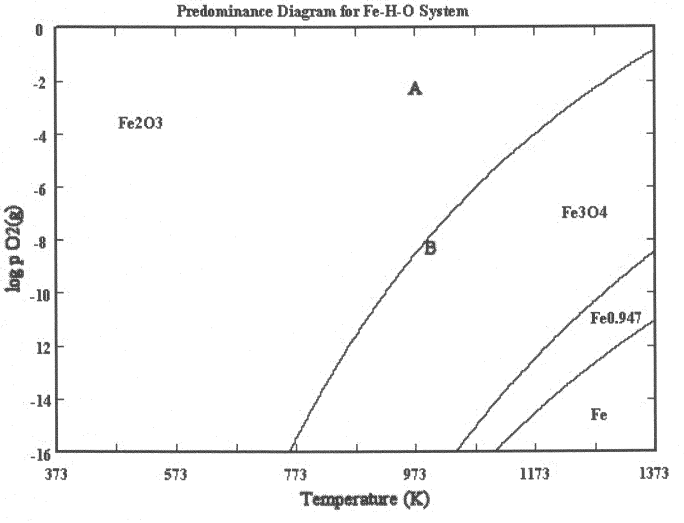

Figure 3 Predominance diagram for the Fe-H-O system. Conditions for oxidation in pure oxygen is indicated as A and for water vapor as B.

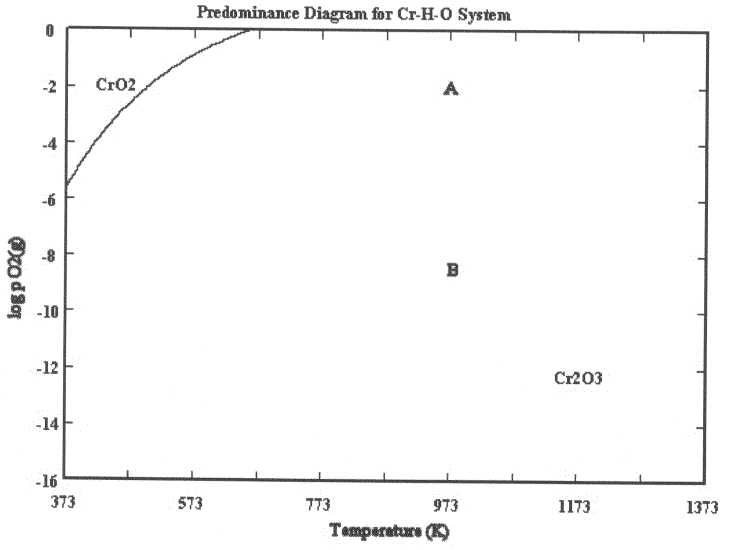

Figure 4 Predominance diagram for the Cr-H-O system. Conditions for oxidation in pure oxygen is indicated as A and for water vapor as B.

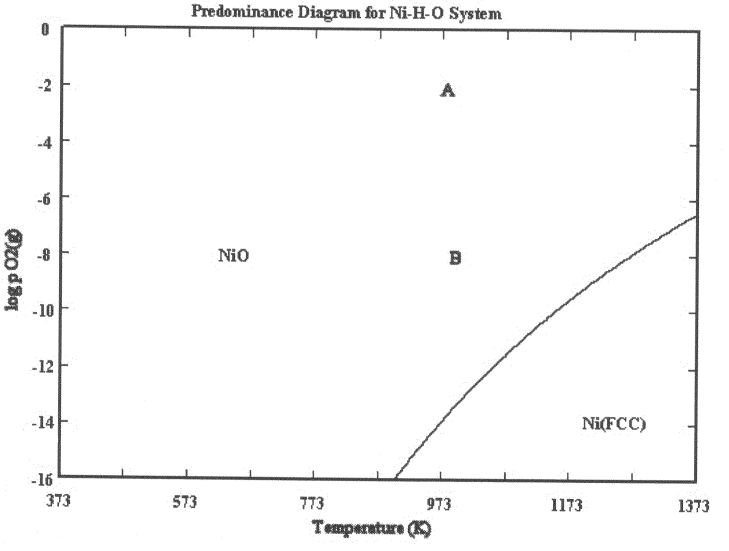

Figure 5 Predominance diagram for the Ni-H-O system. Conditions for oxidation in pure oxygen is indicated as A and for water vapor as B.

Although the oxide composition for each engineering material could not be accurately predicted, it was expected that mixed oxides (Cr-Fe-Ni) would form during oxidation, with the ratio between these elements changing with the composition of the material.

Oxidation experiments

T91-steel

Oxidation of this steel in pure oxygen resulted in relatively featureless changes on the surface. An oxide layer with smooth and rounded features could be detected on the surface after approximately 15 minutes. With time this developed further, but remained the same in

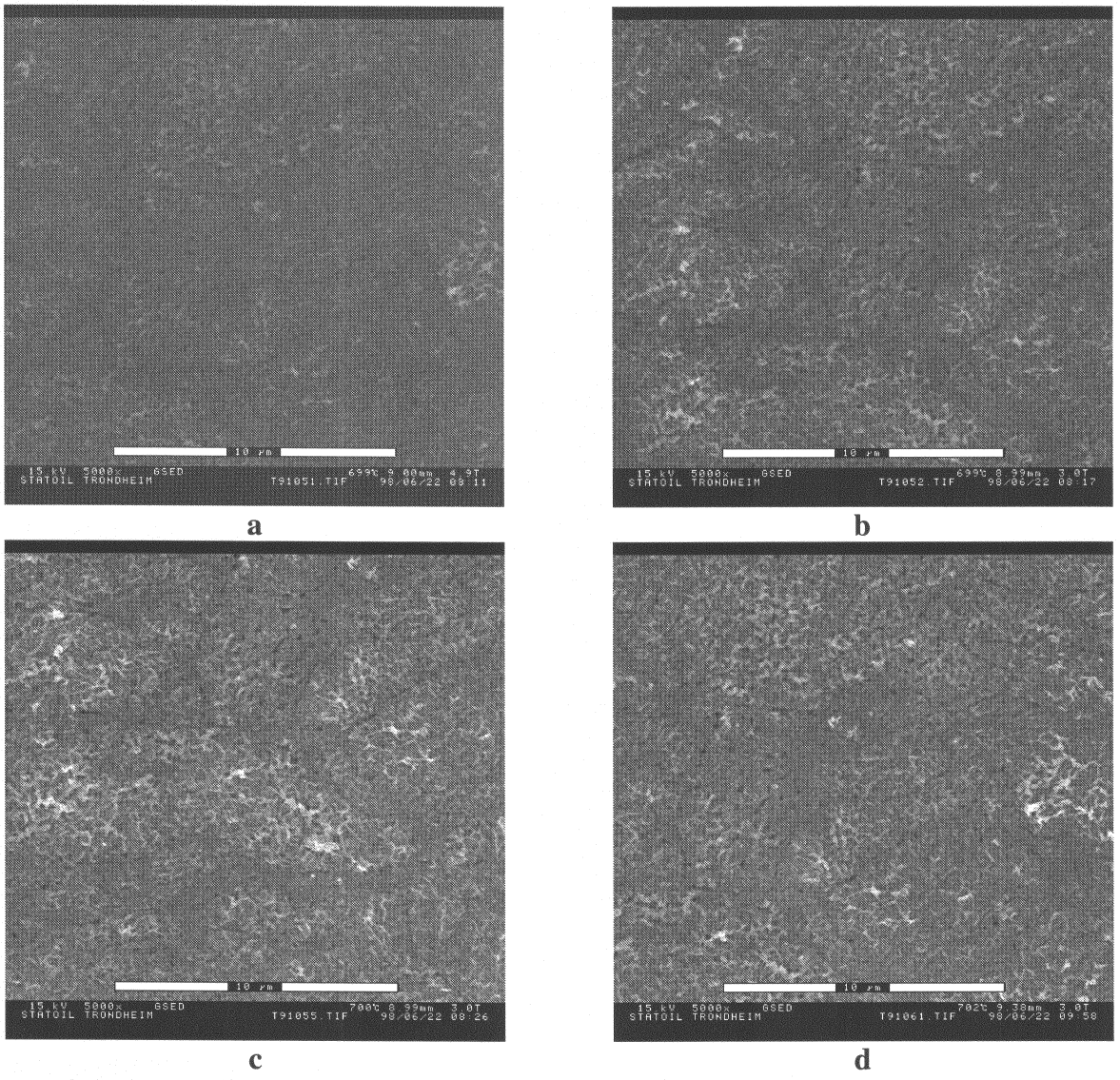

Figure 6 Oxidation of T91-steel in pure oxygen at 973 K. ESEM images taken after 15 minutes (a), 21 minutes (b), 31 minutes (c), & 122 minutes (d). Scale marker for all images is 10 µm.

appearance (see figure 6a–d). The developed oxide layer was mostly iron-rich, possibly representing a hematite (Fe_2O_3) layer.

In water vapor, the steel started oxidizing rapidly, and after 2 minutes distinct surface changes could be observed. The surface oxides rapidly appeared as angular crystals that grew with time (see figure 7a – d). The morphology of the oxide growing on the surface appeared to be comparable to wüstite ($FeO_{0,9470}$), later transforming to magnetite (Fe_3O_4). This was thought to be due to kinetic reasons and not due to thermodynamic equilibrium.

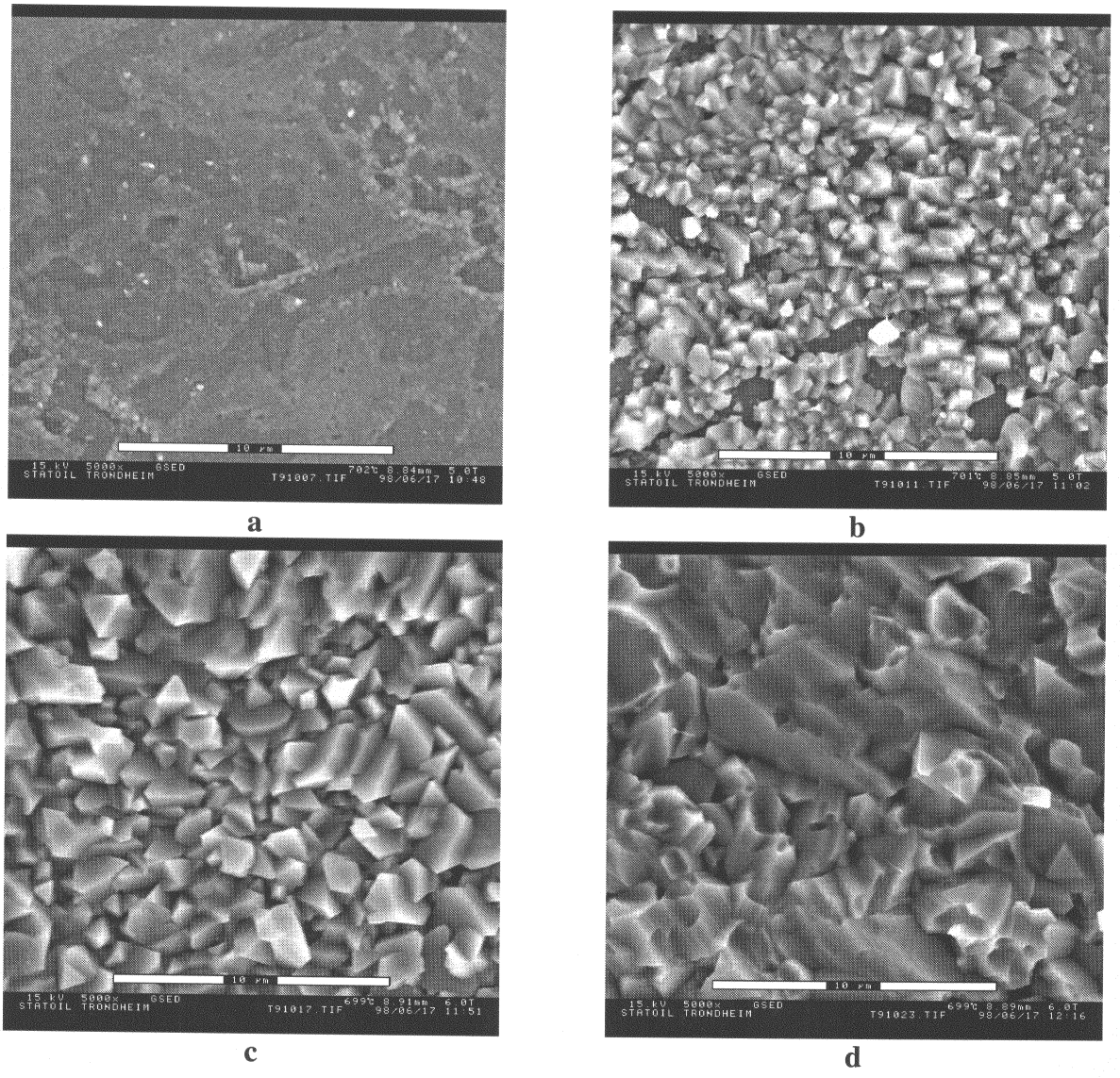

Figure 7 Oxidation of T91-steel in water vapor at 973 K. ESEM images taken after 2 minutes (a), 15 minutes (b), 65 minutes (c), & 90 minutes (d). Scale marker for all images is 10 μm.

Austenitic stainless steel – type 304

A fine-grained mixed oxide structure could be seen developing on the austenitic stainless steel during oxidation in pure oxygen (see figure 8a – d). This developed rapidly, covering all the grains in the field of view. Iron-rich nodules, probably hematite, appeared on top of the fine-grained oxide layer during the latter stages of the experiment.

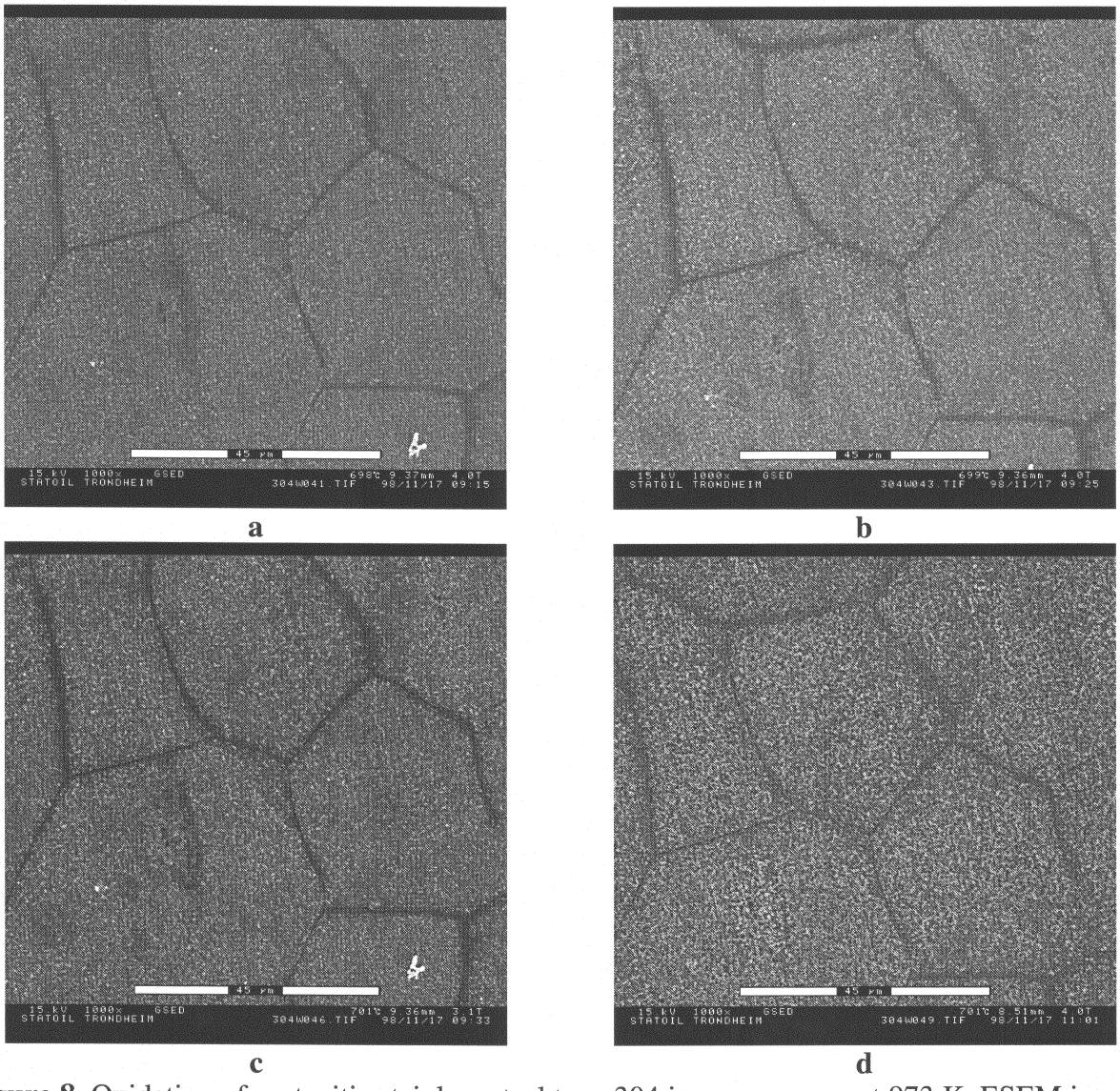

Figure 8 Oxidation of austenitic stainless steel type 304 in pure oxygen at 973 K. ESEM images taken after 5 minutes (a), 15 minutes (b), 23 minutes (c), & 107 minutes (d). Scale marker for all images is 45 μm.

In water vapor, oxidation of the surface occurred slower and the developing oxide layer was not present on all the grains. However, where an oxide layer developed, it appeared to be associated with deformation and slip planes in each grain (see figure 9a – d). This again appeared to be a mixed oxide. Angular crystals, probably wüstite (similar to the water vapor oxidation of the T91-steel), could also be identified during the latter stages of the experiment.

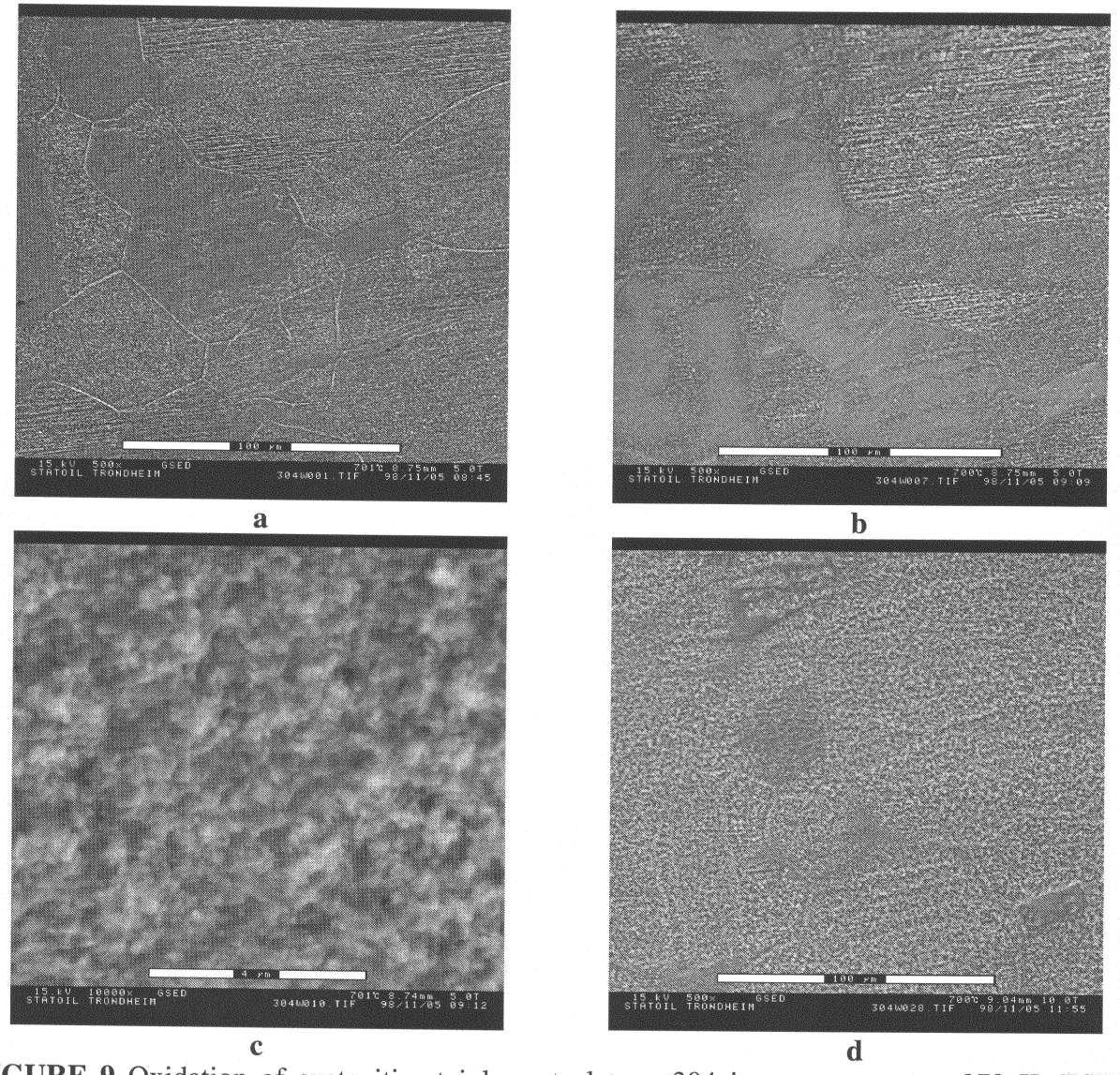

FIGURE 9 Oxidation of austenitic stainless steel type 304 in water vapor at 973 K. ESEM images taken after 5 minutes (a), 29 minutes (b), 134 minutes (c), & 197 minutes (d). Scale marker for images a, b, & d is 100 μm, and 4 μm for image c.

Alloy 800H

Alloy 800H exhibited slow growth of a mixed oxide layer, covering the entire surface in pure oxygen (see figure 10a – d). In the latter stages of the experiment this again appeared globular.

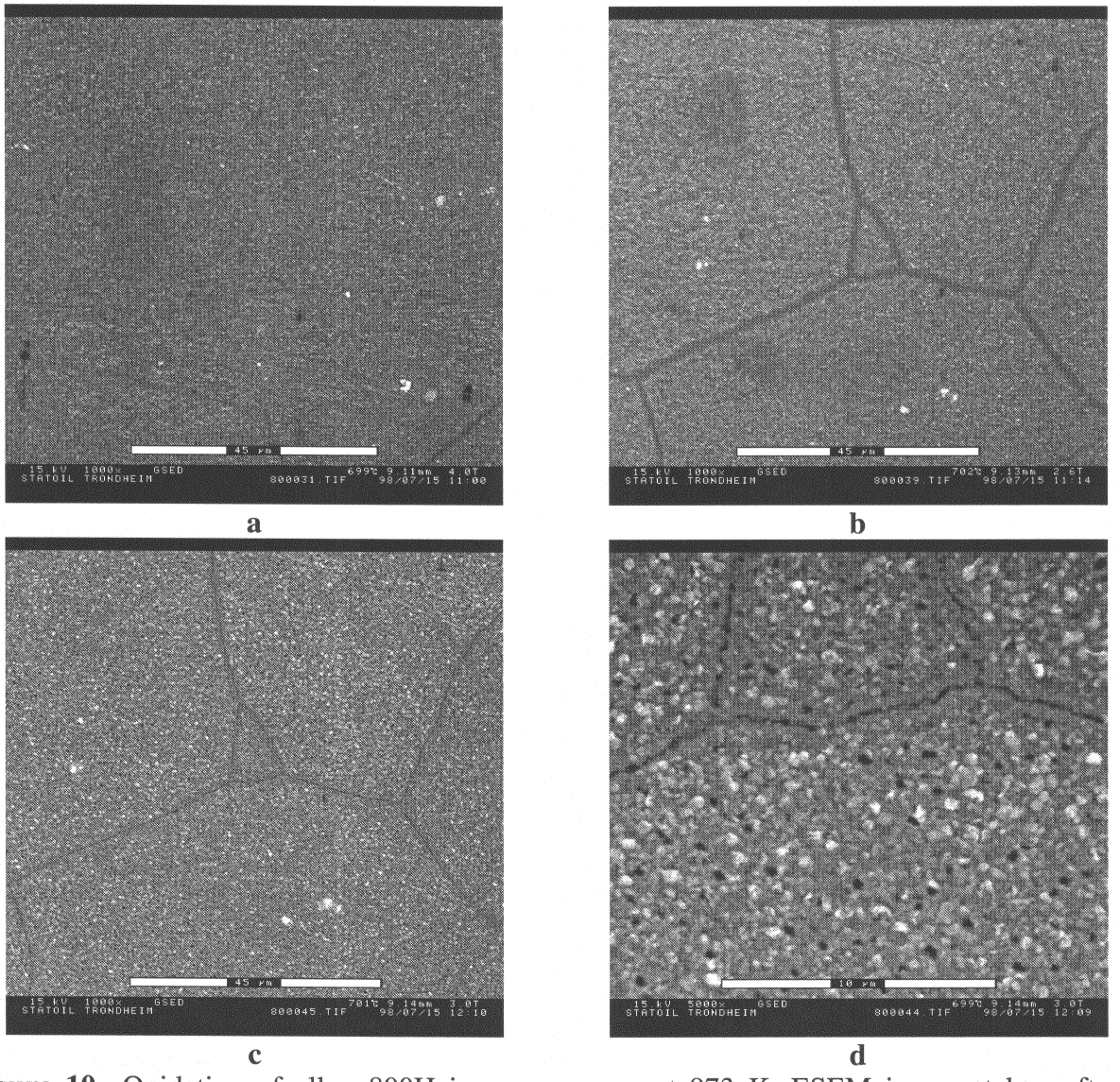

Figure 10 Oxidation of alloy 800H in pure oxygen at 973 K. ESEM images taken after 5 minutes (a), 19 minutes (b), 74 minutes (c), & 75 minutes (d). Scale marker for images a to c is 45 μm, and for image d 10 μm.

Oxidation in water vapor occurred slower. A mixed oxide formed preferentially on some grains and appeared to be associated with deformation and slip planes in the material. The austenite grain boundaries could be distinctly observed throughout the experiment (see figure 11a–d). Angular oxide crystals were seen during the latter stages of the experiment. These appeared to be iron-rich grains (typical wüstite structure) on top of a chromia layer. However, no decomposition of the iron-rich grains occurred during cooling.

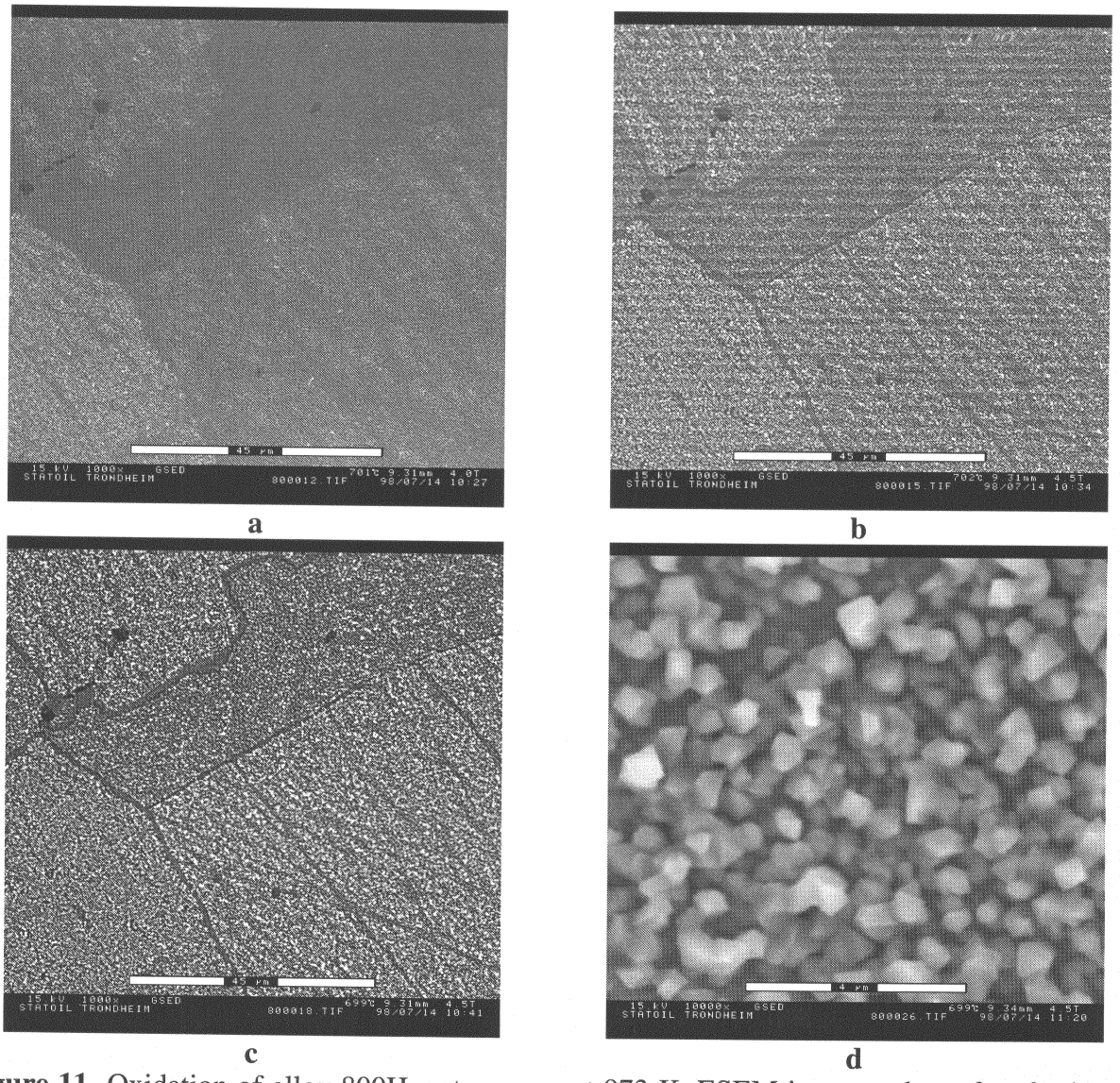

Figure 11 Oxidation of alloy 800H water vapor at 973 K. ESEM images taken after 6 minutes (a), 13 minutes (b), 21 minutes (c), & 59 minutes (d). Scale marker for images (a) to (c) is 45 μm, and for image (d) 4 μm.

Alloy 601

This high chromium nickel-based alloy exhibited dramatically different behavior during oxidation in pure oxygen. A fine-grained oxide layer developed rapidly and appeared to cover most of the surface. In isolated areas globular iron-rich oxides appeared on top of the chromium-rich oxide layer (see figure 12a – d).

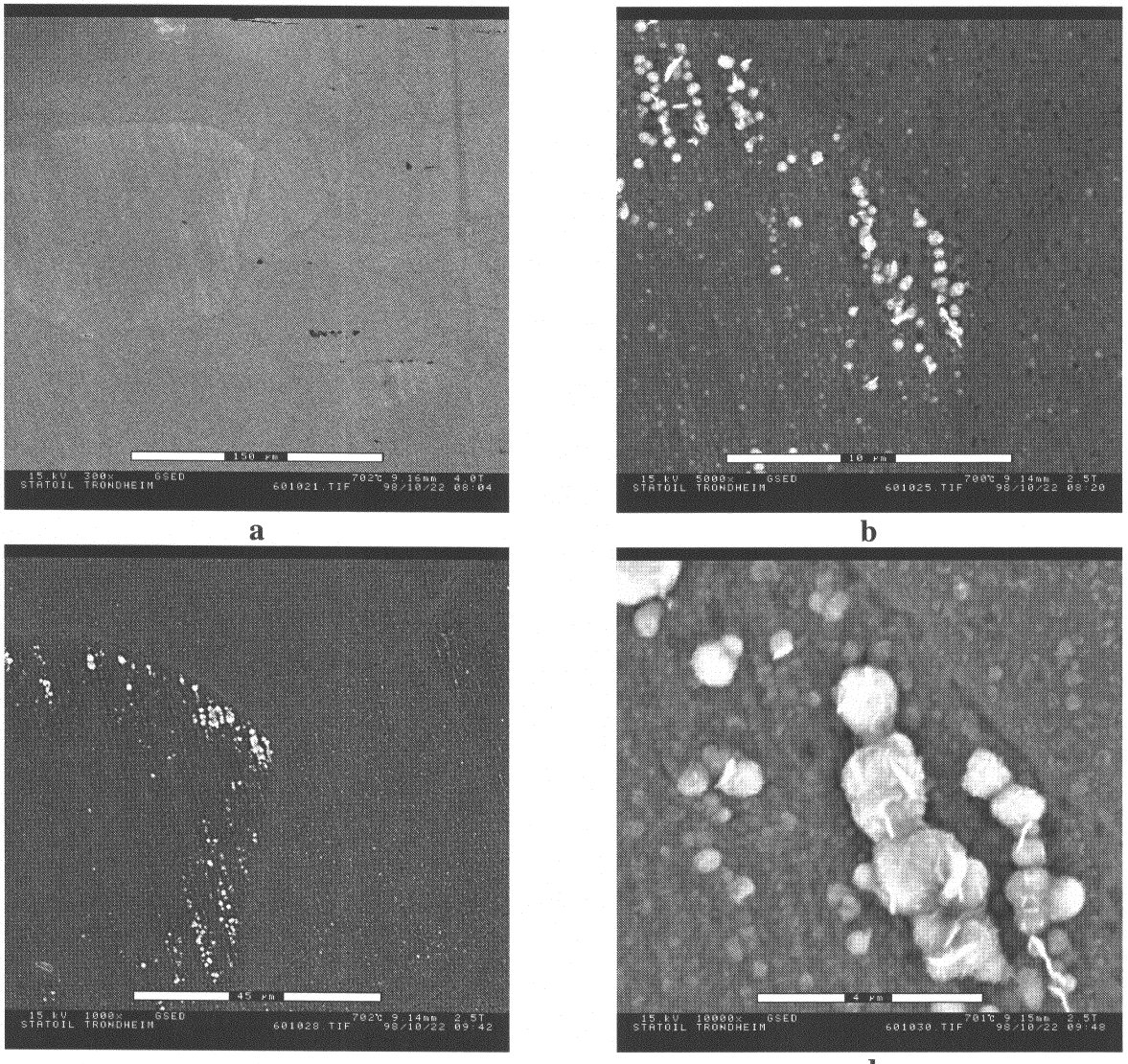

Figure 12 Oxidation of alloy 601 in pure oxygen at 973 K. ESEM images taken after 4 minutes (a), 20 minutes (b), 107 minutes (c), & 108 minutes (d). Scale marker for image (a) is 150 μm, for image (b) 10 μm, for image (c) 45 μm, and for image (d) 4 μm.

Islands of angular iron-rich oxides appeared on the alloy surface during the early stages of oxidation in water vapor. This occurred only on random grains but again showed some association with previous deformation and slip planes in the material (see figure 13a – d). With time, the angular iron-rich oxides grew in size and number and were eventually laying on top of a fine-grained chromium-rich oxide layer.

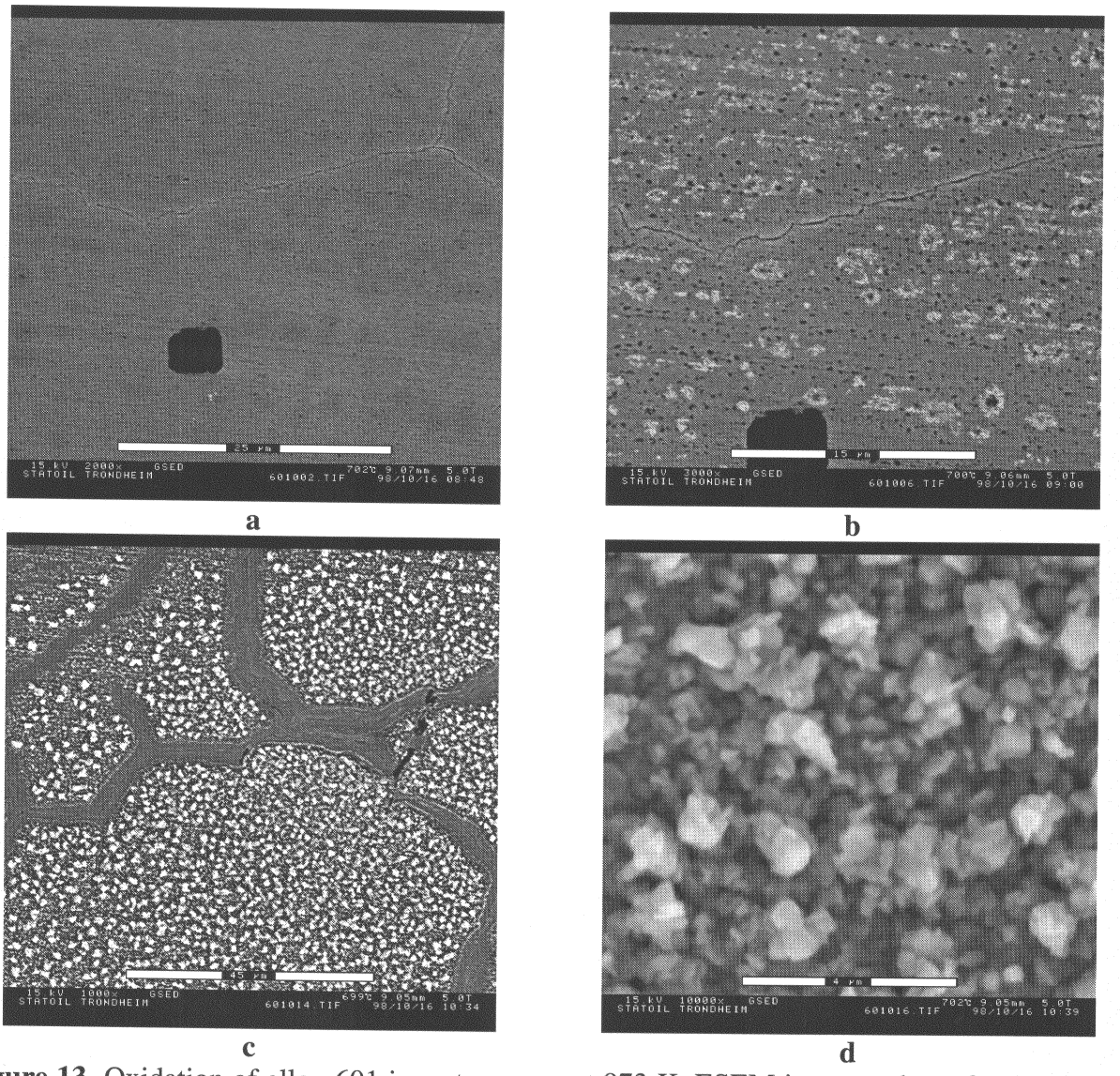

Figure 13 Oxidation of alloy 601 in water vapor at 973 K. ESEM images taken after 7 minutes (a), 18 minutes (b), 113 minutes (c), & 117 minutes (d). Scale marker for image (a) is 25 μm, for image (b) 15 μm, for image (c) 45 μm, and for image (d) 4 μm.

DISCUSSION

Microscopic examination of corrosion processes often relies on "before" and "after" examination of exposed materials. This approach relies on a range of assumptions the most important for high temperature corrosion being that a surface structure developed during exposure in a certain environment is retained when the material is cooled down and exposed to atmospheric conditions. This has repeatedly been shown not to be the case and the need for in-situ studies has been shown. In-situ microscopy techniques, of which the ESEM is one, have advanced the understanding of corrosion phenomena tremendously, simply because they provide an in-situ view of the materials during exposure (Danilatos, 1997). However, these techniques all suffer a common drawback in that they generally function under conditions that are far from "real" conditions. The heating procedure used for the oxidation studies in this paper is comparable to the "hot-bare oxidation" method described by Graham and coworkers (1972).

This is in contrast to "furnace-raised oxidation", where the sample is heated in an oxidizing atmosphere as described by Nicholls (1995). All this has to be taken into account when relating observations to actual material performance.

The main limitations of the ESEM are linked to the working requirements of the instrument. These are the static gas atmosphere and the pressure range of 133–2666 Pa required for recording quality images. Although these conditions differ significantly from those encountered in "real" operations or even other laboratory experiments, the in-situ ESEM exposures provide data more valuable than most other in-situ microscopy techniques.

A limitation of the ESEM is its resolution, which is not only determined by the technical standard of the instrument, but also by a range of other variables. A water vapor atmosphere in the ESEM gave best results. Oxygen was slightly poorer, and hydrogen in argon had a very short contrast range. Images were often better when taken at high temperature, compared to post-exposure examination at room temperature using the same instrument set-up. Although imaging of non-conducting samples is possible in the ESEM, a marked difference was observed between the various oxide scales, attributed to electronic conductivity of the oxide scales. This was found to be in agreement with the influence of temperature and the fact that image quality generally decreased with an increase in scale thickness, i.e. with extended oxidation time.

This work has illustrated not only the use of ESEM as a high temperature research tool, but also the value of thoroughly understanding oxidation before attempting to understand complex corrosion processes such as metal dusting. The formation of iron-rich oxide scales on engineering materials illustrated how inhomogeneous oxides scales on these materials are. The influence of oxygen partial pressure on the oxidation of different alloys was also illustrated. Some of the reasons why these materials are failing in metal dusting environments, where islands of iron-rich oxides would provide both sites for catalytic carbon formation and diffusion paths into the base alloy, were shown.

Following the work described in this paper, Schmid (2000) exposed pure iron and nickel samples to methanol vapor and hydrogen-carbon monoxide gas mixtures (773 & 1073 K). On the iron sample, carbon filaments were formed at 773 K, and the extent of corrosion was found to depend upon the gaseous environment. The precipitation of surface carbides and the catalytic gasification of carbon filaments on iron were followed in the ESEM. Nickel appeared catalytically inert at 773 K but showed heavy surface restructuring at 1073 K. Grain boundary grooving, grain growth, surface rearrangement, and the nucleation of embedded particles were observed in-situ. This again illustrated the versatility of the ESEM in high temperature corrosion research.

CONCLUSIONS

The development of techniques for the in-situ study of oxidation in different environments in an environmental scanning electron microscope (ESEM) has proved to contribute significantly to further the understanding of metal dusting corrosion. This has made it possible to see the growth of oxide layers on engineering materials in real time, showing the existence of unstable, non-protective iron-oxide species at high temperature. It also demonstrated the inhomogeneous nature of oxides on complex alloys. This provides an understanding that in a metal dusting environment, this would provide the ideal sites to catalyze carbon from the process environment. It also provides the entry points for carbon diffusion into the alloy matrix, ultimately causing severe damage.

The value of the environmental scanning electron microscope (ESEM) in high temperature corrosion research has been illustrated.

REFERENCES

Danilatos, G.D., 1997, "Environmental Scanning Electron Microscopy," pp 13 – 14 in *In-situ Microscopy in Materials Research: Leading International Research in Electron and Scanning Probe Microscopies.* P.L. Gai (ed.), Kluwer Academic Publishers, Boston.

"Environmental Scanning Electron Microscopy," 1993, special issue of *Microscopy and Research*, 25(5/6):353 – 534.

Rapp, R.A., 1994, "The high-temperature oxidation of metals forming cation-diffusing scales," Metal. Trans. A, 15A(12):765 – 782.

Verma, S.K., Raynaud, G.M. & Rapp, R.A. 1981, "Hot-stage scanning electron microscope for high-temperature in-situ oxidation studies," Oxidat. Metals, 15(5/6):471 – 483.

Lee, M. & Rapp, R.A., 1988, "Development of scale morphology during wüstite growth on iron at high temperature," Oxidat. Metals, 30(1/2):125 – 138.

Schmid, B., 2000, "Microscale examination of metal dusting in steels and in-situ observations of high temperature oxidation of metals," Ph.D Thesis 2000:57, Norwegian University of Science and Technology.

HSC Chemistry, Version 4.0. Outokumpu Research Oy, Pori, Finland.

Graham, M.J., Sproule, G.I., Caplan, D. & Cohen, M., 1972, "The effect of surface preparation on the oxidation of nickel," J. Electrochem. Soc., 119 (7):883 – 887.

Nicholls, J.R., 1995, "Discontinuous measurements of high temperature corrosion," in *A Working Party Report on Guidelines for Methods of Testing and Research in High Temperature Corrosion*, Grabke, H.J. & Meadowcroft, D.B. (eds.), The Institute of Materials, London.

Schmid, B., Aas, N., Grong, O. and Odegård, R., 2001, "In situ environmental scanning electron microscope observations of catalytic processes encountered in metal dusting corrosion on iron and nickel," Applied Catalysis, A: General, 215:257-270.

METAL DUSTING AND PRESSURE – IS THERE A RELATIONSHIP?

T. P. LEVI,* C. W. THOMAS, N. BRIGGS AND I. E. MINCHINGTON
Industrial Research Limited, Materials performance Technologies,
Lower Hutt, New Zealand

ABSTRACT

The results presented in this paper describe the initial findings from studies on the effect of pressure on metal dusting. The pressures and temperatures chosen reflected a variety of actual plant conditions and were between 0.15 and 3 MPa and 450 and 650°C, respectively. It was shown that the conditions and atmosphere were capable of producing metal dusting on 316 and other selected materials. The initial results indicate that generally the observed attack increases with increasing pressure and temperature.

INTRODUCTION

Metal dusting is a high temperature damage process that can occur suddenly and unpredictably. The susceptibility of materials to metal dusting is dependent on several parameters: the activity of the carburizing environment, temperature, surface finish, alloy composition and pressure. Changes in process conditions leading to higher carbon activities are responsible for the increase in reported incidences of metal dusting. A variety of plants are affected including: steam reformers, direct reduction of iron, ethylene, methanol, ammonia and hydrogen (Lin 1994, Yoshimoto 1991, Stahl 1995, Lant 2001, Holland 2001, Bairamov 2001).

Un-scheduled plant outages cause production losses, these in combination with repair and refurbishment costs, on a global scale add up to many millions of dollars. To achieve high economic efficiency it is essential that a solution to this maverick phenomenon is found.

This challenge has been accepted by the materials science community and there have been extensive studies on metal dusting that have concentrated on elucidating the mechanisms and models (Grabke 1998, Schneider 1997, Klöwer 1998, Forseth 1995, Pippel 1998), causes (Van der Biest 1980, Norton 1981, Maier 1999) and prevention (Barnes 1986, Bater 2001, Kirchheiner 2001, Grabke 2001). It is, however, believed that process variables, such as pressure (Maier 1998, Maier 1999, Levi 2001, Levi, 2001), temperature, velocity and turbulence, influence metal dusting and their effects are not fully understood.

The results presented in this paper look at the effect of pressure and temperature on metal dusting. Work has been carried out in the temperature range of 450 to 650°C and at pressures between 0.15 and 3 MPa. Some experiments also examined the effect of etching.

*Corresponding author address: T. P. Levi, Industrial Research Limited, Materials Performance Technologies, Lower Hutt, New Zealand; e-mail: t.levi@matperf.com

EXPERIMENTAL

Experimental Test Parameters

A material that was known to suffer from metal dusting was selected for this work. The nominal composition of Type 316SS is given in Table 1. The pressures at which the experiments were conducted nominally 0.15, 1, 2, and 3 MPa, and the test temperatures were between 450 and 650°C.

The gaseous atmosphere chosen for the trials was a 75%H_2 – 25%CO mixture, a fairly common "syngas" for which the carbon activity, a_c, can be calculated from the following reaction:

$$CO + H_2 = H_2O + C \quad a_c = pCO * pH_2/pH_2O * K_1 \qquad [1]$$

where pCO, pH_2 and pH_2O are the partial pressures of carbon monoxide, hydrogen and water vapour respectively and K_1 is the equilibrium constant.

TABLE 1 The nominal composition of Type 316SS

Element	Nickel	Chromium	Iron	Molybdenum	Manganese
Wt%	10-14	16-18	Balance	2-3	2-2.5

Testing at less than 1 MPa

For the tests at pressures less than 0.5 MPa a vertical top-loading autoclave consisting of an inner reaction tube externally heated by a 3-zone kanthal-wound furnace was used (Guttman 1983). The reaction tube, specimen support tubes and thermowell were all made from pure Al_2O_3.

The specimens were ground on 180-grade SiC paper under controlled conditions of pressure, rotational speed and lubricant flow. Each coupon was then accurately measured (+/- 0.01 mm), uniquely identified, ultrasonically degreased in acetone and stored in a desiccator. Prior to insertion in the reaction chamber of the corrosion rig the specimens were weighed to constant weight (+/- 0.01 mg).

Five replicate samples of each alloy were loaded into the reaction vessel and, after establishing the correct gas quality and flow rate, heated up to the test temperature of 600°C. CoMParatively high flow rates of 30-35 1/h were used and the system pressure was 0.15 MPa.

Testing was interrupted after periods of 150, 600, 700 and 750 hours and selected specimens were discontinued for detailed structural analysis using optical and scanning electron microscopy (SEM) for microstructural studies, and energy dispersive X-ray analysis (EDX) for semiquantitative micro-compositional analysis.

Testing at pressures greater than 1 MPa

The design of the experimental equipment meant each sample was tested individually. Once the sample had been prepared it was placed in a special test assembly, connected into the

gas feed system and purged with cold "active" gas. The system was then brought to pressure and temperature and left to run for a pre-determined time.

Due to the nature of the gas reactions, namely the condensation of water in colder parts of the circuit, the actual pressure to which specimens were exposed was "cyclic". The system was filled to pressure, however as the gaseous reactions occurred it fell rapidly and when it was 25% below the desired pressure the system was cleared of the reacted gas and re-pressurized with fresh gas. Table 2 details the target nominal experimental conditions.

TABLE 2 Specimen exposure conditions and average and maximum pit depths observed

Specimen pre treatment	Exposure time (h)	Pressure (MPa)	Temperature (°C)	Average pit depth (mm)	Maximum pit depth (mm)
Polished	150	0.15	650	0.05	-
Cleaned	48	1	450	n/a	n/a
Cleaned	48	1	580	0.010	0.010
Cleaned	48	1	651	0.067	0.160
Cleaned	48	2	447	0.008	0.010
Cleaned	48	2	576	0.014	0.030
Cleaned	48	2	647	0.181	0.335
Cleaned	48	3	550	0.081	0.125
Cleaned	48	3	451	0.046	0.072
Cleaned	48	3	651	0.2226	0.383
Treated 25% HNO_3	48	1	651	0.069	0.140
Treated 25% HNO_3	48	2	647	0.202	0.355

The test samples were cut from bar stock material. The machined surface of the sample was cleaned by degreasing. In some cases the test samples were exposed for 3 minutes to aqueous 25% nitric acid. Next several thermocouples were attached to the specimen to monitor the temperature distribution.

After exposure the specimens were removed, photographed and prepared for analytical examination again using conventional techniques. In an attempt to maintain any deposition product on the specimen, epoxy resin was poured on the surface and allowed to set overnight prior to sectioning.

RESULTS AND DISCUSSION

The specimens exposed at 0.15 MPa at 650°C for 150 hours exhibited metal dusting. The results from the other temperatures at this pressure will not be reported here. It should also be remembered that these low pressure specimens were exposed for three times as long as the 1, 2 and 3 MPa specimens. The surface of the specimens were almost completely covered with coke.

Where this had been removed blowing with air it was possible to see the extensively pitted surface, Figure 1. Examination in cross-section showed relatively smooth pits of approximately 0.05 mm in depth.

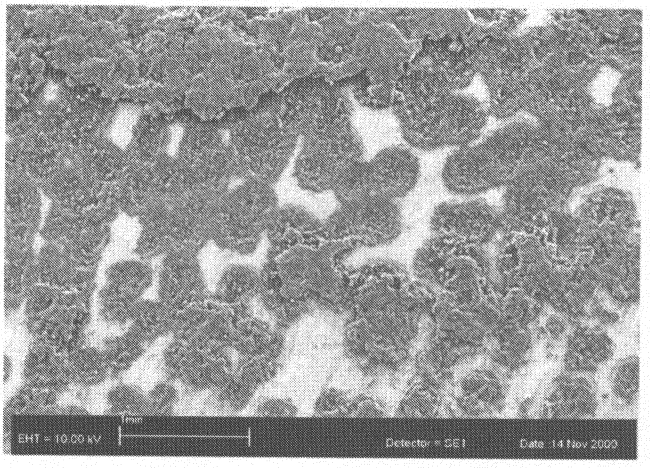

FIGURE 1 SEM of surface of 316 after exposure at 0.15 MPa at 650°C for 150 h

None of the specimens exposed at 1 MPa exhibited metal dusting attack until the temperature had reached 580°C, even then only very slight attack was observed. Smooth, hemispherical pits were distributed over the surface of the specimen in a random fashion. Increasing the temperature to above 600°C initiated pitting within the pits and the numbers of these small pits increased with increasing temperature until at 650°C the original pit took on a "chewed" aspect. The pit "contents were analyzed using EDX and found to contain metallic particles together with coke and quite significant amounts of oxygen. In several regions at the base of the pits, oxide rich areas were detected.

The specimens exposed at 2 MPa showed a progressive increase in attack with increasing temperature. At or below 500°C almost no attack was observed. As the temperature increased slight pitting damage became visible. At 600°C, hemispherical pits developed and started to coalesce and this behavior increased with temperature. EDX analysis of the material within the pits showed it to be rich in iron, chromium and carbon, with some oxygen present.

All the specimens exposed at 3 MPa exhibited metal dusting and at this higher pressure there was significantly more attack at the lower temperatures. Again, as the temperature increased the apparently random development of large hemispherical pits was noted and the coalescence followed by the pitting within the pits was also apparent, Figure 2.

Two samples were exposed at approximately 600°C at 1 and 2 MPa to determine if etching the surface in a 25% HNO_3 solution would have any effect on the rate of attack. For 316 SS in these conditions and with this surface treatment no significant increase in attack was observed.

Table 2 details exposure times, pressures and temperatures for the specimens. It also gives the average depth and maximum depth of the pits observed on all the specimens examined in this study.

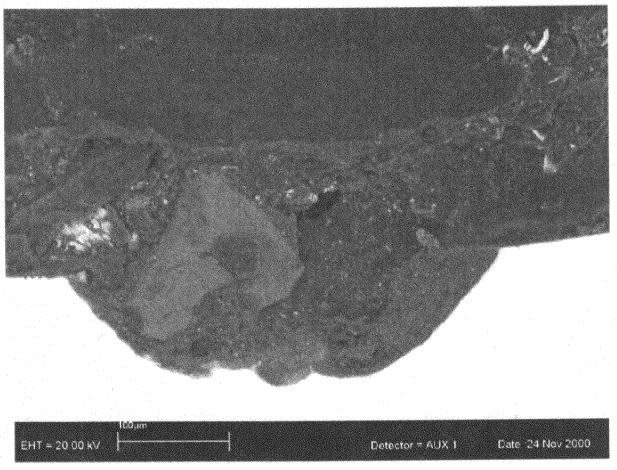

FIGURE 2 SEM cross section after exposure at 3 MPa at 650°C for 48 h

A graphical representation for the average pit depth results for the different pressures is shown in Figure 3. The number of pits generally increased with temperature. Both the average and maximum depth of the pits increased with increasing temperature and increasing pressure. It should be noted that the specimen exposed at 0.15 MPa was exposed for 150 hours (i.e., just over three times as long as the other specimens.

During the dusting process at pressure, a build up of coke/metal particles across the surface of pits was observed. This "pillar" like development has also been observed by other authors (Maier 1998, Maier 1999). Past studies have described the concept of incubation periods, prior to the onset of metal dusting. It is believed that an incubation period has been identified in the present studies. During each of the high pressure tests an interesting feature was the speed at which the gas reactions proceeded. Initially they were extremely sluggish. However, once the actual reaction started the apparent rate of the gas reaction sped up considerably as shown in Figure 4.

At several intervals gas samples were taken for analysis, typical results are given in Table 3. Sample 1 was taken just after the start of an experiment, sample 2 was taken about 15 minutes into the experiment, interestingly methane has already started to form. Sample 3 as taken just prior to the gas being refreshed and sample 4 was taken as the pressure was dropping to 1 MPa at the end of the experiment.

Several specimens exhibited chromium depleted regions. In general these areas were more frequently located at the base of pits rather than at the original metal surface. For this material these areas are probably connected with the increased amount of carburization observed at the base of pits when coMPared to original metal surface areas. In contrast however the depth of carburization into the metal matrix was greater at the metal surface than the base of the pits The penetration into the metal matrix generally increased with increasing pressure and temperature.

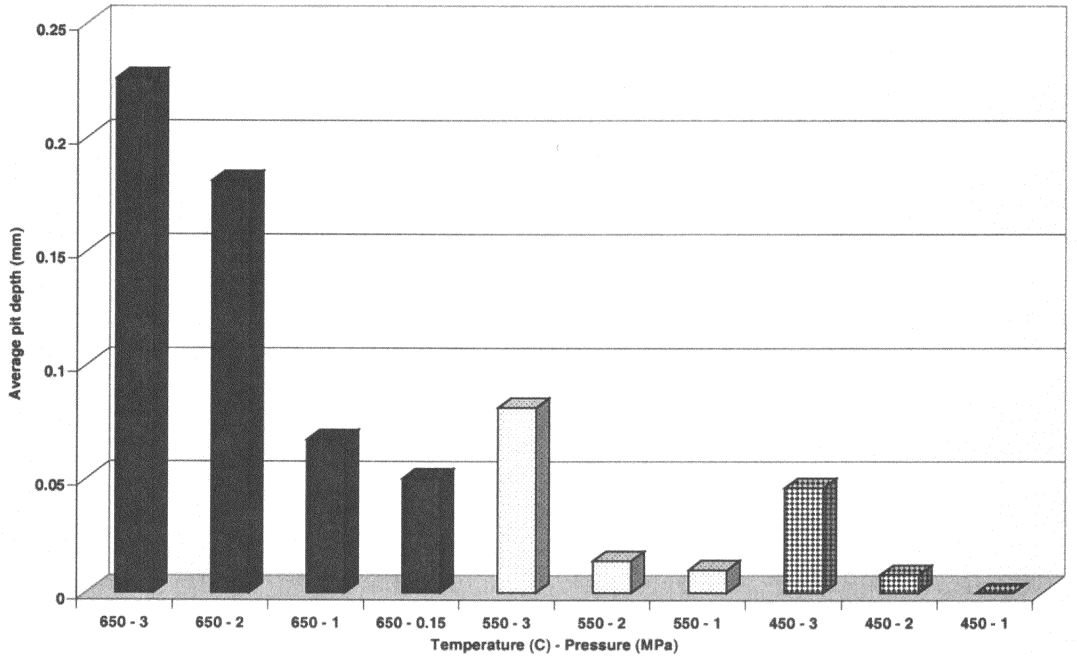

FIGURE 3 Graphical representation of the average pit depths measured for the specimens

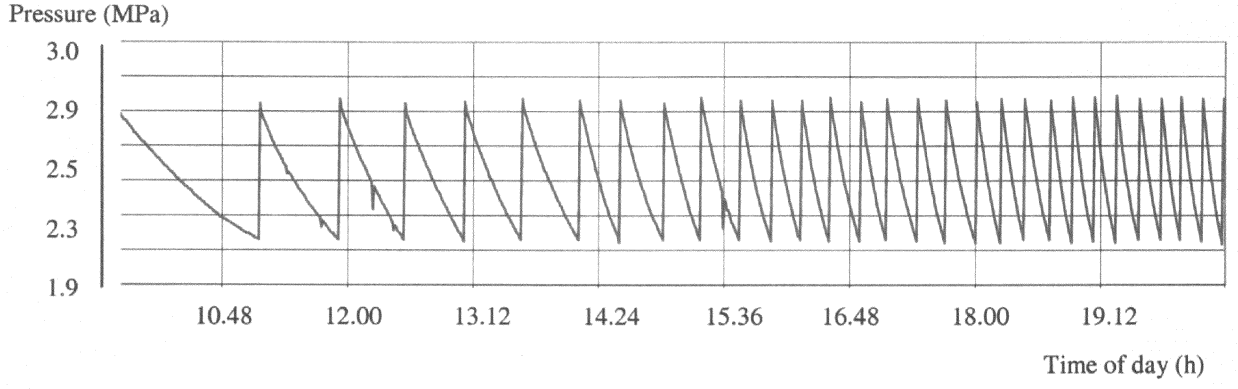

FIGURE 4 Detail of pressure against time for a typical high pressure run. Shows increase in the gas consumption with increasing time

TABLE 3 Exit gas analysis from a typical 2 MPa experiment at 650°C (volume %)

	CO	CO_2	N_2	CH_4	C_2H_6	H_2	Total
Sample 1	22.4	<0.1	4.7	<0.1	<0,.01	69.7	96.8
Sample 2	20.8	0.8	2.7	4.0	0.06	68.6	97.0
Sample 3	13.6	2.3	0.8	24.1	0.43	55.7	96.9
Sample 4	4.5	0.6	1.4	59.6	0.33	33.4	99.8

CONCLUSIONS

The effect of pressure at 0.15, 1, 2 and 3 MPa, at temperatures between 450°C and 650°C, has been studied for Type 316 SS. From the work to date the following conclusions can be drawn:

- Increasing the pressure from 0.15 to 1 to 2 to 3 MPa caused an increase in the metal dusting attack on the specimens.
- At 1, 2 and 3 MPa an increase in attack with increasing temperature was observed.
- The rate of the gaseous reaction increased with time of exposure.
- Generally, the specimens etched in 25% HNO_3 exhibited similar amounts of attack as the unetched specimens.
- Morphologies of attack vary from smooth hemispherical to "chewed", with increasing temperature.
- Oxide development was detected at the base of several pits indicating an attempt at healing.
- Chromium depleted regions were detected.

These initial results from this preliminary test program indicate that pressure does contribute to metal dusting attack. More in-depth, systematic studies are in progress to try to elucidate the mechanisms and extent of the effect. It is postulated that there will be a steady increase in severity of attack with pressure until a plateau is reached after which attack remains constant. Additionally, experiments are underway to ascertain if the nature of the pressure effect is most strongly linked to the incubation period or to the rate of attack.

ACKNOWELDGEMENTS

Contributions of several colleagues within Materials Performance Technologies and Industrial Research Limited are acknowledged, namely; Kay Cared (SEM/EDX) and Helen White (metallographic preparation). Additionally contributions of several colleagues within the Institute of Advanced Materials, Pennen, NL are gratefully acknowledged, namely; S. Canetoli, M. Maier and K. Schuster. This work and preparation of this manuscript was supported under New Zealand Foundation of Research and Technology Funding.

REFERENCES

Bairamov, A.Kh. and Bradley, R., 2001, *Proc NACE Conf. "Corrosion/01",* Paper No 01389, Texas, USA.

Barnes, J., Corish, J. and Norton, J.F., 1986, *Oxid. Of Mets.,* 26 (No. 5/6), 333.

Bater, G.T., 2001, *Proc. NACE Conf. "Corrosion/01",* Paper No. 01387, Texas, USA.
Forseth, S. and Kofstad, P. 1995, *Materials and Corrosion*, 46, 201.

Forseth, S. and Kofstad, P., 1995, *Materials and Corrosion,* 46, 201.

Grabke, H.J., 1998, *Materials and Corrosion,* 49, 303.

Grabke, H.J. and Müller-Lorenz, E.M., 2001, Grabke, H.J., Krajak, R., Müller-Lorenz, E.M. and Strauβ, S., 1996, *Werkstoffe und Korrosion*, 47, 495.

Grabke, H.J. and Müller-Lorenz, E.M., 2001, *Proc NACE Conf. "Corrosion/01"*, Paper No. 01389, Texas, USA.

Guttmann, V., Hurst, R.C., Norton, J.F., Van der Biest, O. and Van de Voorde, M., 1983, *Proc. Symp. "Corrosion in fossil Fuel Systems"*, The Electrochem. Soc., Pennington, USA, 83/5, 147.

Holland, M.L., 2001, *Proc. NACE Conf. "Corrosion/01"*, Paper No. 01385, Texas, USA.

Kirchheiner, R. and Jimenez-Soler, 2001, *Proc NACE Conf. "Corrosion/01"*, Paper No 01374, Texas, USA.

Klöwer, J., Grabke, H.J. and Müller-Lorenz, E.M., 1998, *Materials and Corrosion,* 49, 328.

Lant, T. and Tomkings, A.B., 2001, *Proc NACE Conf. "Corrosion/01"*, Paper No. 01378, Texas, USA.

Levi, T.P., Briggs, N., Minchington, I. and Thomas, C.W., 2001, *Proc NACE Conf. "Corrosion/01"*, Paper No 01375, Texas, USA.

Levi, T.P., Briggs, N., Minchington, E. and Thomas, C.W., August 2001, Submitted to *Werkstoffe und Korrosion.*

Lin, J.Y., Chiang, F.C., Chang, H. and Su, C.C., 1994, *Proc. Conf. Corrosion '94*, Paper No 184.

Maier, M. and Norton, J.F., May 1999, *Proc. of the EFC Workshop "Coking and Decoking"*, Porto, Portugal.

Maier, M. and Norton, J.F., 1999, *Prof. NACE Conf. "Corrosion/99"*, San Antonio, USA.

Maier, M. Norton, J.F. and Frampton, P.d., 1998, *Materials and Corrosion,* 49, 331.

Norton, J.F., Blidegn, L., Canetoli, S. and Frampton, P.D., 1981, *Werkstoffe und Korrosion,* 32, 467.

Pippel, E., Woltersdorf, J. and Schneider, R., 1998, *Materials and Corrosion,* 49, 309.

Schneider, R., Pippel, E., Woltersdorf, J., Strauβ, S. and Grabke, H.J., 1997, *Steel Research,* 68(7), 326.

Stahl, H. and Thomsen, S.G., 1995, *AIChE Ammonia Safety Symp.*, Paper No. 3g, 18-20 Sept., Arizona, USA.

Van der Biest, O. Harrison, J.A. and Norton, J.F., *Book266/EUR 6814,* The Metals Soc., London, 681.

Yoshimoto, T. and Takahashi, M., 1991, *Proc. 1st Internat. Conf. On Heat Resistant Materials*, 461, 23-26 Sept. Wisconsin, USA.

ROLE OF ALLOYING ELEMENTS IN Fe-BASE AND IN Ni-BASE ALLOYS ON METAL DUSTING

H.J. GRABKE*, E.M. MÜLLER-LORENZ, S. STRAUSS
Max-Planck-Institut für Eisenforschung GmbH, Düsseldorf, Germany

ABSTRACT

Most important for protection of high alloy steels and Ni-base alloys is the formation of a protective scale, i.e. a chromia or spinel/chromia scale in the temperature range of interest. Thus, a high Cr-content is important and some wt% of Si or Al are helpful in the oxide formation. Contents of carbide forming elements M = Ti, Zr, V, Nb, Mo and W may retard the start of metal dusting, since upon carbon ingress they must be tied up by internal carbide formation, before oversaturation occurs and metal dusting can start. Presence of large M-carbides or –nitrides, however, can lead to local failure of the oxide scale by outgrowth of their voluminous oxides.

High Ni-contents retard the carbon ingress and lead to a metal dusting mechanism which is much slower than that for steels, also the coke formation is less on Ni-base alloys. Accordingly, Ni-base alloys with high Cr-content > 25 wt% and some Al/or Si are most resistant against metal dusting (Alloys 602, 690, 230), also NiCr 50 50 is metal dusting resistant and some Cr-base alloys.

INTRODUCTION

In the temperature range 400 – 800°C, critical concerning occurrence of metal dusting, generally chromium steels are applied in process industry. Low alloy steels such as 1%CrMo, 2 1/4%CrMo etc. are heat resistant and oxidation resistant up to about 600 °C but in metal dusting conditions ($a_C > 1$) they may be used only in atmospheres with high enough H_2O- and/or CO_2-content so that magnetite can be formed. However, mostly the process conditions are more severe, and metal dusting starts on these steels immediately and uniformly, so that after a few hours the metal wastage rate is constant (Grabke et al. 1994). Cr-rich oxide scales are necessary for protection against metal dusting which are formed on ferritic steels with >11%Cr and austenitic steels with >17%Cr (Grabke et al. 1993), the difference in chromium needed, is caused by the higher Cr-diffusivity in the ferritic lattice. A rapid Cr-supply to the surface is necessary to form the protective scale which is composed of an outer layer of the spinel $(Mn,Fe)Cr_2O_4$ and an inner layer of chromia Cr_2O_3, and it was found advantageous to enhance the Cr-diffusion by providing fast-diffusion paths, grain boundaries and dislocations, by a fine grain microstructure and/or surface working (Grabke et al. 1997, 1998; Grabke and Müller-Lorenz 1998; Grabke et al. 2000).

But even high alloy steels with sufficient Cr-content have shown attack by metal dusting after more or less long periods of exposure under metal dusting conditions. In principle, the same

*Corresponding author address: H. .J. Grabke, Max-Planck-Institut für Eisenforschung GmbH, Max-Planck-Str. 1, 40237 Düsseldorf; e-mail: grabke@mpie.de

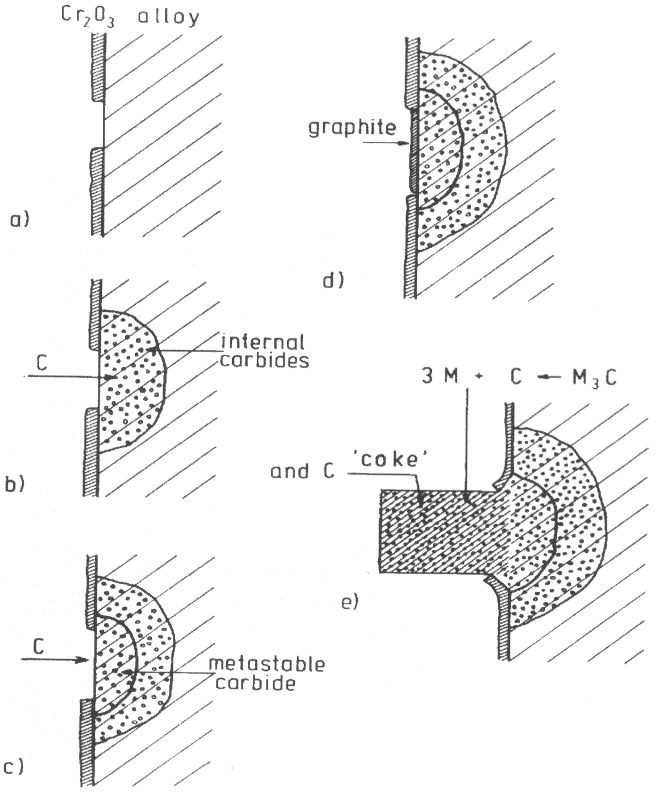

FIGURE 1 Schematics of the metal dusting mechanism for high alloy steels (see text).

mechanism applies for high alloy steels as for iron (Grabke 2001), but some additional steps must be considered, see Fig. 1.

i. the protective oxide scale fails at some weak point in the surface (the character of such weak points will be discussed later),

ii. carbon is transferred into the metal phase at this spot where the gas has access to bare metal surface,

iii. carbon diffuses inward and at first reacts with the alloying elements which form stable carbides, $M_{23}C_6$ and M_7C_3 with Cr as main component and MC with M = Ti, Zr, V, Nb, W, and Mo_2C,

iv. after oversaturation the remaining Fe-Ni matrix is transformed to instable M_3C, this decomposes after graphite nucleation to graphite and fine Fe-Ni particles:

$$(Fe,Ni)_3C = 3Fe\text{-}Ni + C(graphitic) \quad (1)$$

v. The fine metal particles cause vast carbon deposition and outgrowth of coke from the pit, which is starting to grow from the 'weak point'. If the oxide scale is rather weak, wide and flat pits arise and in the case of a rather stable oxide scale the pits may be nearly hemispherical. In practice the coke is carried away by the gas flow, in the laboratory experiment different coke and pit morphologies were observed (Grabke et al. 1993),

vi. Due to formation of H_2O and CO_2, upon carburization and carbon deposition the oxygen pressure rises in a surface-near gas film and oxygen is dissolved in the metal phase following the carbon. This oxygen ingress may cause internal oxidation of the internal carbides $M_{23}C_6$ and M_7C_3, formed in reaction step (iii).

So, in metal dusting of high alloy steels and Ni-base alloys often internal chromia and spinel formation is observed (Szakalos et al. 2001). However, this is not a process which is characteristic and general in metal dusting, and the Cr in the steels and alloys will end up in oxides anyway, since the oxygen pressure needed for Cr_2O_3 formation is very low.

ROLE OF ALLOYING ELEMENTS IN HIGH ALLOY STEELS

Certainly a high Cr-content is important for the metal dusting resistance of any alloys, and ferritic steels with 12–28wt.% Cr have proven to be rather resistant (Grabke et al. 1993, 2000). In contrast, austenitic steels with similar Cr-contents are less resistant, as mentioned already, due to the lower Cr-diffusivity in the austenitic matrix (Grabke et al. 1993, 2000). Especially the widely used Alloy 800 proved to be very susceptible and many failure cases were reported of this alloy. In a series of exposures with model alloys on the base of Alloy 800, i.e. Fe-20%Cr-32%Ni, the role of several alloying elements was tested, concerning metal dusting resistance (Strauß and Grabke 1998). The base alloy showed strong attack and severe mass loss after short time, (Fig. 2a). The presence of the carbide forming elements Nb, W and Mo delayed the start of metal dusting up to >500 hours. This effect does not clearly enhance the metal dusting resistance, it easily can be explained by the formation of the stable carbides of these elements which somewhat delays the oversaturation of the matrix.

The kinetics of internal carbide is described by the equation for the penetration depth x of internal carbide formation (Schnaas and Grabke 1978).

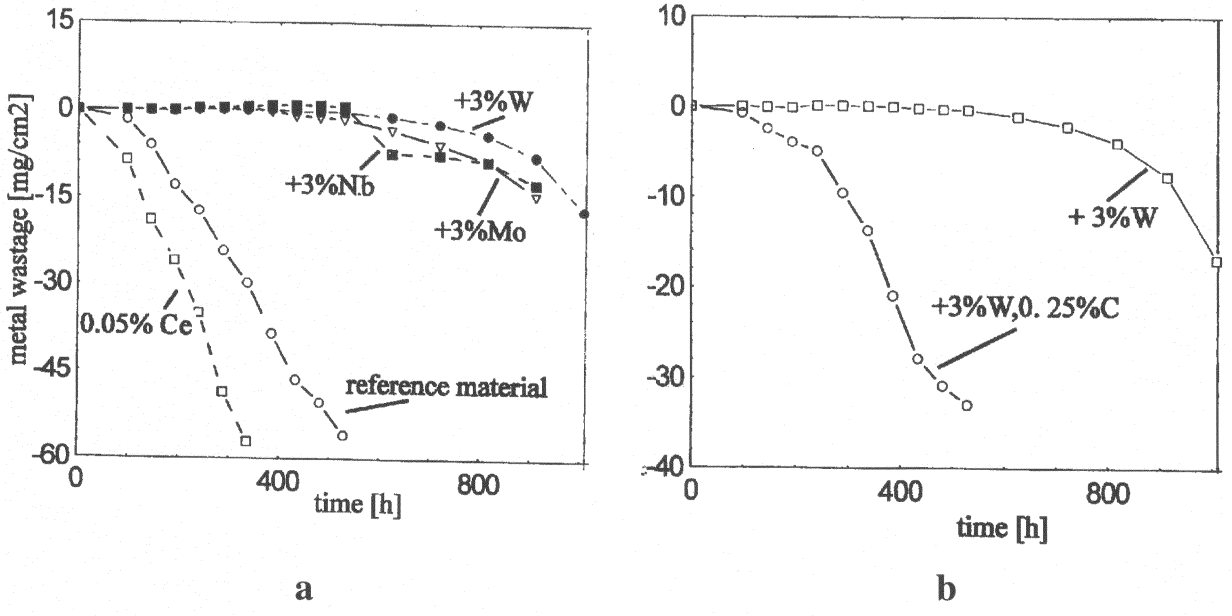

FIGURE 2 Mass losses by metal dusting of model alloys based on Fe-32Ni-20Cr(Alloy 800) with different alloying additions: a) Nb, W, Mo, Ce, b) W + C.

$$x^2 = 2 \cdot \frac{D_C \cdot c_C}{\nu \cdot c_M} \cdot t \qquad (2)$$

where D_C and c_C are the diffusivity and solubility of carbon (in the Fe-Ni matrix after carbide precipitation), c_M the concentration of carbide forming elements, and ν an average stoichiometric number for all precipitated carbides MC. So the start of metal dusting is delayed with increasing concentration c_M of elements forming stable carbides. This interpretation for the role of Nb, W, Mo etc. was confirmed by exposures of model alloys in which the carbide forming element was tied up with carbon, e.g. the model alloy with 3%W plus 0.25%C (Fig. 2b) for such alloys metal dusting started much earlier.

Precipitates of the carbides and nitrides of Ti, Zr, Nb, Mo and W may play a deleterious role in initiating metal dusting. If such precipitate lies at the surface and is oxidized, the growth of the voluminous oxides of these elements disturbs the formation and growth of a protective scale (Litz et al. 1988). The negative effect of Ce shown in Fig. 2 a may be caused by a similar effect, by oxidation of intermetallic phases precipitated in the alloy with 0.05%Ce. The beneficial effects of Ce on chromia formation and adherence are exerted only at higher temperatures and generally at lower Ce concentration. It may be noted that the 27%Cr-32%Ni-steel AC 66 with 0.05 %Ce also proved to be very susceptible to metal dusting.

Clearly beneficial effects of Si and Al additions were observed (Fig. 2). The samples with 2.5% Si and 4.5% Al showed no mass loss by metal dusting up to 1500 hours, but small spots of attack were detected. At the low temperature no protective SiO_2 and Al_2O_3 layers are formed. But Si and Al are selectively oxidized in the very first hours of exposure, forming nuclei and islands of oxide which inhibit carbon ingress and allow time for Cr-diffusion to the surface and formation of a Cr-rich protective oxide.

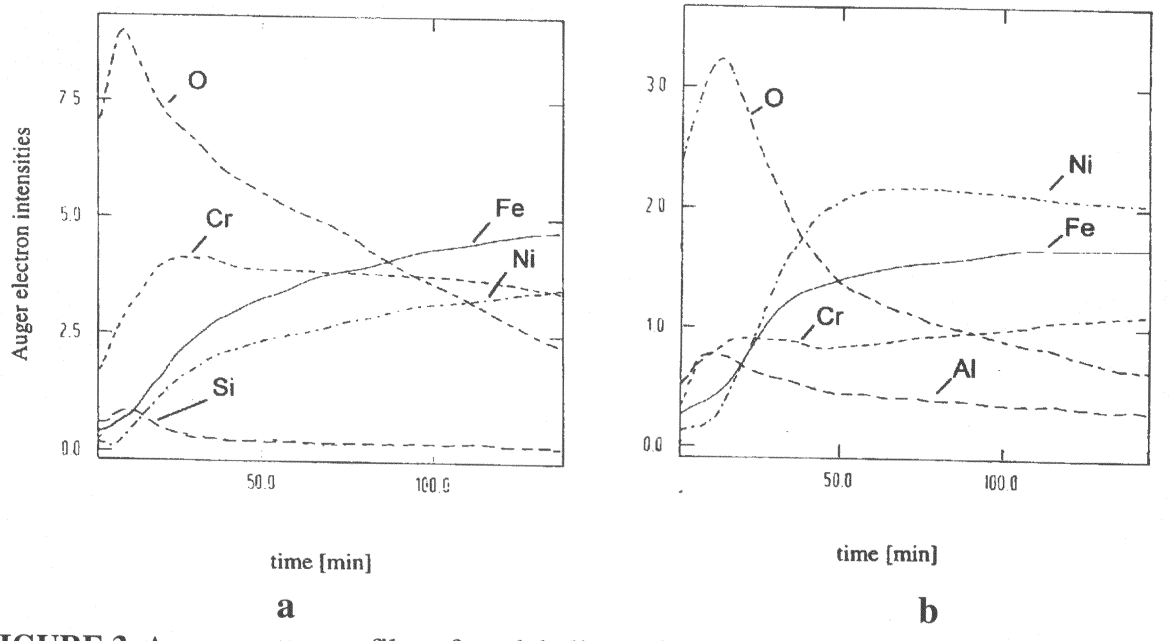

FIGURE 3 Auger sputter profiles of model alloys after 1500 hours exposure under metal dusting conditions. a) Fe-32Ni-20Cr + 2.5% Si; b) Fe-32Ni-20Cr + 4.5 % Al.

This was observed in in-situ studies (Grabke et al. 1997; Tökei et al. 2000) by Auger electron spectroscopy (AES) and can be seen also from AES sputter profiles (Fig. 3) taken on the Si- and Al-doped 20Cr-32Ni-alloys after 3 hours exposure. These profiles indicate SiO_2 and Al_2O_3 on top of a Cr-rich oxide scale, obviously formed in the initial 'transient state' of oxidation, since in long-term oxidation SiO_2 and Al_2O_3 should form below Cr_2O_3 according to thermodynamic rules.

NICKEL-BASED ALLOYS

If the mechanism of metal dusting described for Fe and steels would apply for Ni-based alloys, $(Ni,Fe)_3C$ should be formed as an intermediate. This would need increasing carbon activities with increasing Ni-content (Grabke et al. 1993, 1996), but in fact metal dusting starts for any Ni-Fe alloy at a carbon activity about $a_C > 1$, as was shown in experiments with binary alloys at 650 °C and carbon activities a_C = 1.8, 3.0, 5.0, 7.5, see Fig. 4a.

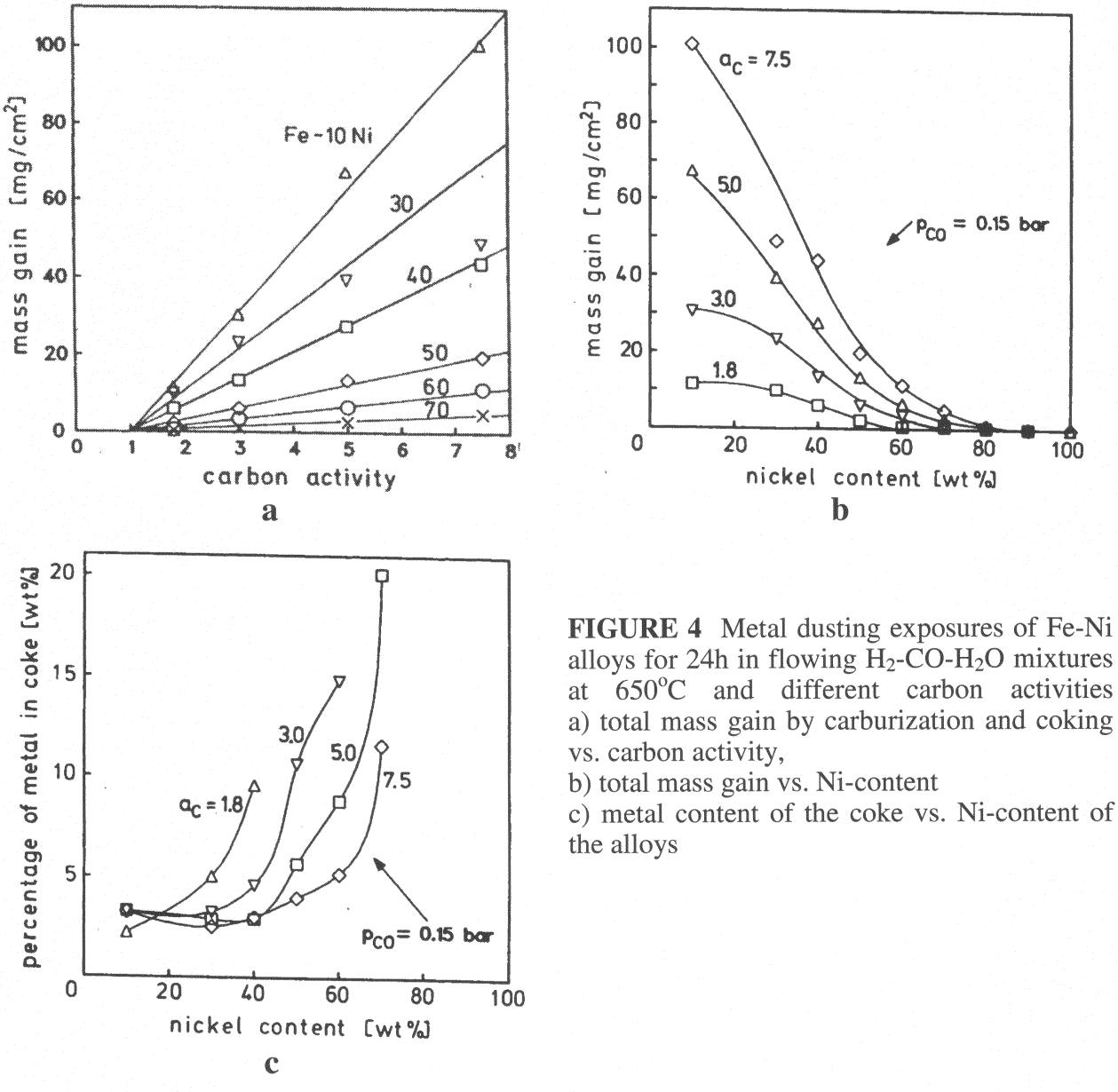

FIGURE 4 Metal dusting exposures of Fe-Ni alloys for 24h in flowing H_2-CO-H_2O mixtures at 650°C and different carbon activities
a) total mass gain by carburization and coking vs. carbon activity,
b) total mass gain vs. Ni-content
c) metal content of the coke vs. Ni-content of the alloys

The results clearly indicate a change of mechanism for Ni-Fe alloys with more than 40% Ni, on which no M_3C was found after metal dusting exposures. Obviously the alloys with a higher Ni content are destroyed by the mechanism valid for pure Ni, i.e. direct ingress of graphite. This change in mechanism also results in a decrease of carbon dissolved and deposited on the alloys and an increase of the metal content in the coke with the Ni-content in the alloys (Figs. 4b, c). The relatively big metal particles, released by metal dusting from Ni-base alloys are less catalytically active for carbon deposition (Strauß et al. 1999) than the fine particles (≈20 nm) from metal dusting of steels.

So in principle, resistance against metal dusting is better for Ni-based alloys (Grabke et al. 1993; Grabke et al. 1996; Klöwer et al. 1998; Klarström et al. 2001) than for steels, since

- the mechanism is different and much slower,
- coke formation is considerably less,
- carbon solubility and diffusivity are lower.

The latter point is important for decreasing the risk of metal dusting initiation on Ni-Cr alloys. As in the case of high alloy steels there will be a run of C-diffusion inward and Cr-diffusion outward, to start either metal dusting or protective scale formation. Cr-diffusion is relatively fast and increases with the Ni-content of the alloys. However,the widely used Alloy 600 with only 15-16% Cr is not resistant, many failure cases have been reported. On Alloy 600 sometimes general attack was observed, but mostly relatively flat pits are spreading gradually over the surface. In laboratory exposures at 650 °C (Fig. 5a) the whole surface was affected after about 3000 h and a wastage rate was observed of 0.033 mg/cm^{2}h corresponding to 0,36 mm/year, this rate is nearly 2 orders of magnitude slower than that on steels.

Better resistant is Alloy 602 with about 23%Cr and 1.4%Al, but this alloy is susceptible to local pitting. In several laboratory exposures some pits started to grow on Alloy 601 from the beginning (Klöwer et al. 1998; Grabke et al. 2001), and grew to nice hemispherical shape and about same depth. Since the wastage rate 0.7 mm/year calculated from the depth of the pits is even higher than that determined for Alloy 600, perforation of tube or sheet walls would occur even earlier for this material. But the metal dusting behaviour of Alloy 601 can be improved by surface working, as shown by exposures of as-delivered (black), polished and ground samples (Fig. 5b). The ground surface state proved to be most resistant, after 10 000 hours the metal wastage rate was 5.8×10^{-4} mg/cm^{2}h (Klöwer et al. 1998).

Similar and lower wastage rates were observed for the alloys 160 with 28% Cr and 2.8% Si, 45-TM with 27 % Cr and 2.7 % Si, 617 with 22% Cr and 1 % Al, 602 CA with 25% Cr and 2.3 % Al, and 690 with 28% Cr. So the important roles of Cr, Si and Al for resistance against metal dusting were confirmed for Ni-base alloys. For these most resistant alloys the formation of a protective scale is strongly favored, compared to initiation of metal dusting, and in fact, after exposures the metallographic cross sections generally showed thin oxide scales. Spurious local carburization was detected, but overgrown by the oxide scale so that metal dusting did not start. Later series of exposures with Alloys 600, 601 and 602CA confirmed the superior resistance of 602CA (Grabke et al. 2001). This material was recommended for the construction of several plants with severe metal dusting conditions, and now after 2-3 years no failures were reported.

Certainly also NiCr 5050 is very metal dusting as shown by application as a coating for components strongly endangered by metal dusting (Holland 2001) and laboratory tests up to 10.000 hours (Grabke et al. unpublished study). In the latter series of exposures also some high Cr-alloys were tested:

Cr-44Fe-5Al-0.3Ti-0.5Y_2O_3, Cr-5Fe-1Y_2O_3, pure Cr and proved to be resistant. For such alloys the chromia formation is strongly favored and carbon ingress is nearly impossible since dissolved carbon is gettered by internal carbide formation.

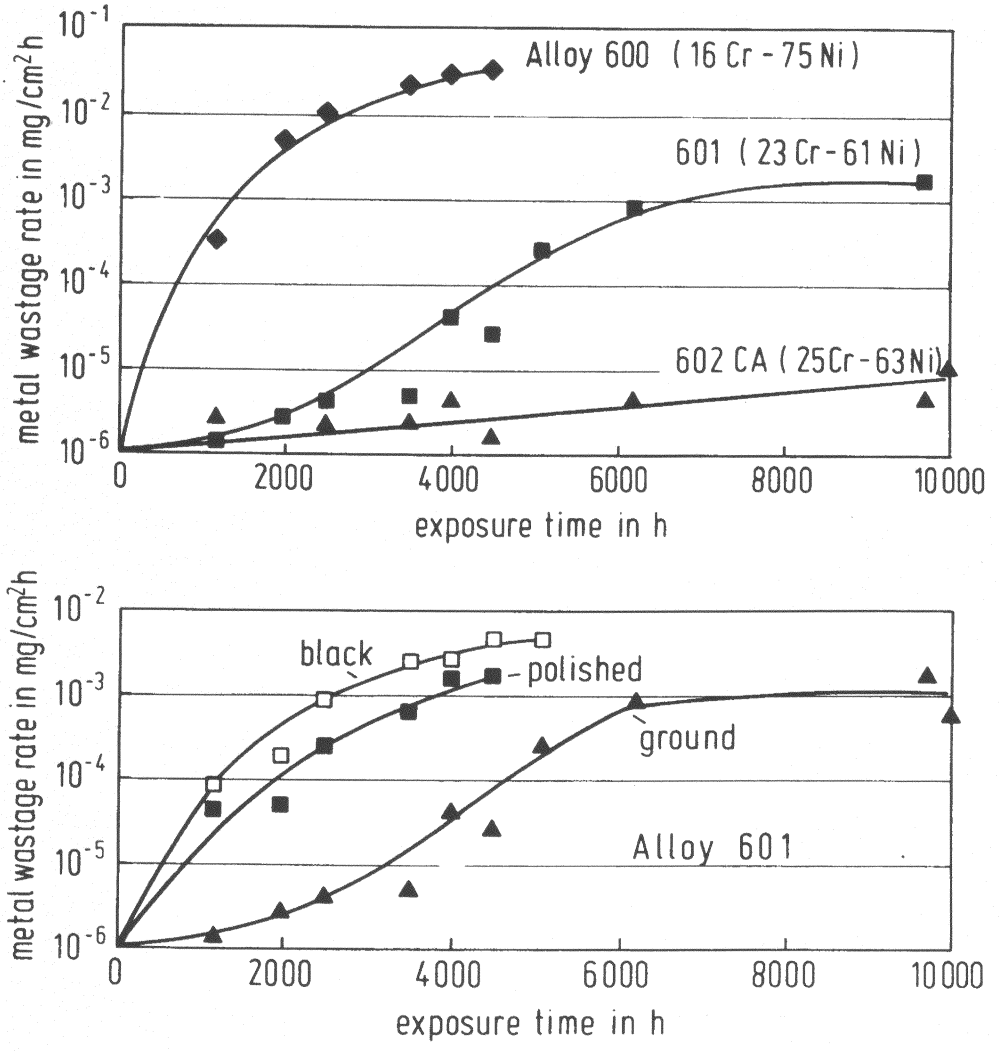

FIGURE 5 Exposures of Ni-based alloys in CO-H_2-H_2O at 650°C. Increase of metal wastage rate with time a) for three different alloys, b) for Alloy 601 in different surface states.

REFERENCES

Grabke, H.J., R. Krajak, J.C. Nava Paz, 1993, "On the Mechanism of Catastrophic Carburization, metal dusting", *Corros. Sci.*, 1993, 35:1141-1150

Grabke, H.J., R. Krajak and E.M. Müller-Lorenz, 1993, "Metal Dusting of High Temperature Alloys", *Werkst. und Korr.* 44:89-97

Grabke, H.J., C.B. Bracho-Troconis and E.M. Müller-Lorenz, 1994, "Metal Dusting of Low Alloy Steels", *Werkst. u. Korr.* 45:215-221

Grabke, H.J., R. Krajak, E.M. Müller-Lorenz and S. Strauss, 1996, "Metal Dusting of Nickel-Base Alloys", *Werkst. u. Korr.* **47**:495-504

Grabke, H.J., E.M. Müller-Lorenz, B. Eltester, M. Lucas and D. Monceau, 1997, "Resistance of 9-20%Cr-Steels against Metal Dusting ", Steel Research 68:179-185

Grabke, H.J., E.M. Müller-Lorenz, S. Strauß, E. Pippel and J. Woltersdorf, 1998, "Effects of Grain Size, Cold Working, and Surface Finish on the Metal Dusting Resistance of Steels", *Oxid. Metals* 50:2241-2254

Grabke, H.J. and E.M. Müller-Lorenz, 1998, "Mechanisms of Metal Dusting and Ways of Protection", *Mat. Corr.* 49:317-320

Grabke, H.J., E.M. Müller-Lorenz, J. Klöwer and D.C. Agarwal, 1998, "Metal Dusting of Ni-Base Alloys", *Mat. Performance (NACE)* **37**:58

Grabke, H.J., 2000, "Nickel-Based Alloys in Carbonaceous Gases", *Corrosion* 56, No. 8, 801-808

Grabke, H.J., E.M. Müller-Lorenz, B. Eltester and M. Lucas, 2000, "Formation of Chromium Rich Oxide Scales for Protection against Metal Dusting", Proceed. "Microscopy of Oxidation 4", Cambridge 1999, *Mat. at High Temp.* 17:339-346

Grabke, H.J., E.M. Müller-Lorenz and H.P. Martienz, unpublished study, "Metal Dusting Resistance of Chromium and High Cr-Alloys"

Grabke, H.J., E.M. Müller-Lorenz and M. Zinke, 2001, "Metal Dusting Resistance of Welded Ni-based Alloys", CD ROM Congress Proceedings EUROCORR 2001, Riva del Garda

Holland, M., 2001, "Practical Experience with Countering Metal Dusting in a Methane Reforming Unit", *Corrosion NACE 2001*, paper 1379 Klöwer

Klarström, D.L., L.D. Paul and H.J. Grabke, 2001,"The Metal Dusting Behaviour of Several High Temperature Nickel Based Alloys", *Corrosion NACE 2001,* paper 1379

Klöwer, J., H.J. Grabke, E.M. Müller-Lorenz, 1998, "Metal Dusting of Ni-Base Alloys", *Mat. Corr.* 49:328-329

Litz, J., A. Rahmel and M. Schorr, 1988, "Selective Oxidation and Internal Nitridation of the Ni-Base Superalloys", IN 738 LC and IN 939 in Air, *Oxid. Metals* 30:95

Schnaas, A. and H.J. Grabke, 1978, "High Temperature Corrosion and Creep of NiCrFe-Alloys in Carburizing and Oxidizing Environments", *Oxidation of Metals* 12:387-404

Strauss, S., H.J. Grabke, 1998, "Role of Alloying Elements on Metal Dusting", *Mat. Corr.* 49:321-327

Strauss, S., R. Krajak, H.J. Grabke, 1999, "Coking by Metal Dusting of Nickel-Base Alloys", *Mat. Corr.* 50:622-627

Szakalos, P., R. Petterson and S. Hertzman, 2001, "A New Corrosion Mechanism for Metal Dusting on 304L Stainless Steel", *Corrosion Sci. in press*

Tökei, Zs., H. Viefhaus and H.J. Grabke, 2000, "Initial Stages of Oxidation of a 9%CrMoV-Steel: Role of Segregation and Martensite Laths", *Applied Surface Sci.* 165:23-33.

METAL DUSTING FAILURES ON Fe-Cr-Ni ALLOYS IN PETROCHEMICAL PLANTS

T. KISO*, H. MOCHIZUKI, and K. HOSOYA
JGC Corporation
Ibaraki, Japan

ABSTRACT

Fe-Cr-Ni alloys, like alloy 800, type 310 and HP (Fe-25Cr-35Ni centrifugal cast alloy), have been widely used in hydrocarbon environments above 600°C. It is sometimes the case that carburization (and oxidation in some cases) combined with metal loss on these alloys occurs. This phenomenon which has been observed in petrochemical plants is known as "metal dusting" and is discussed in terms of operating conditions, such as fluid gas compositions, metal surface temperatures and alloying elements.

INTRODUCTION

Fe-Cr-Ni heat resistant alloys have been used where temperatures exceed 600°C. The alloys used in process areas where synthesis gas (H_2-CO-CO_2-H_2O) or hydrocarbon gas, which contains hydrogen (H.C.-H_2), flows have sometimes caused carburizaton (and oxidation in some cases) with metal wastage in the temperature range of 450-850°C. This phenomenon is commonly known as "metal dusting". The failures usually possess the typical appearance of uniform wastage for low alloys and pitting for high alloys, as reported by Grabke (1995). The correlation between the environment and alloying element, however, is not still clear. For that reason, no comprehensive method of predicting when and where metal dusting will occur has been developed, as reported by Fabiszewski (2000).

This paper presents several failures which were thought to comprise the metal dusting phenomenon experienced in operating plants. Of these failures, discussion was focused on two failures with Fe-Cr-Ni alloys, such as alloy 800H and HP-Mod (Fe-25Cr-35Ni-Nb centrifugal cast alloy), to consider the correlation between environments and the alloying elements.

FIELD EXPERIENCE

Alloying Element and Temperature

The failures which were considered to be "metal dusting" are summarized in Table 1. Failures were experienced not only on Fe-Cr-Ni alloys but also on Cr-Mo low alloy steels from the viewpoint of plant materials in petrochemical plants in the temperature range of 450-830°C. The failures occurred in two types of environments, namely, synthesis gas environment (H_2-CO-CO_2-H_2O) and hydrocarbon gas environment which contained hydrogen (H.C.-H_2).

The materials listed in Table 1 were arranged according to chromium equivalents (Cr_{eq}) to examine the correlation between materials and temperature, as shown in Figure 1. The Cr_{eq}

*Corresponding author address: Tomoaki Kiso, JGC Corporation, Research Center, 2205, Narita-cho, Oarai-machi, Ibaraki Pref., 311-1313, Japan; e-mail: kiso.tomoaki@jgc.co.jp

TABLE 1 Summary of Failures Experienced in Operating Plants

Plant	Damaged Portion	Materials	Operation (years)	Temp. (°C)	Press. (MPa)	Typical Gas Composition
Styrene Monomer	Reinforcing pad of pipe support	type 316	ND	800	ND	ND
	Combined feed heat exchanger	1.1/4Cr-1/2Mo	3	620	0.15	EB/Styrene/Steam/H_2
	Inner bore of heat exchanger	2.1/4Cr-1Mo	ND	510	ND	ND
Catalytic Reforming	Furnace tube	9Cr-1Mo	1.75	665	0.75	H.C./ H_2
	Furnace tube	alloy 800	1	650	0.87	H.C./ H_2
Ammonia	Sampling nozzle of reformer tube	alloy 800	2.25	750	2.6	$H_2/CO/CO_2/ H_2O$
Methanol	Reformer tube	type 310	3.5	700	0.39	$H_2/CO/CO_2/CH_4/H_2O/N_2$
	Boiler tube	5Cr-1Mo	ND	450	ND	$H_2/CO/CO_2/CH_4/H_2O$
Oxosynthesis Gas	Ferrule of WHB	alloy 800	ND	760	ND	$H_2/CO/CO_2/CH_4/H_2O$
	Ferrule of WHB	type 310	2	800	1.28	$H_2/CO/CO_2/CH_4/H_2O$
	Bypass valve shaft	alloy 800	ND	ND	1.76	$H_2/CO/CO_2/CH_4/H_2O$
	Ferrule of WHB	alloy 800	2	820	2.35	$H_2/CO/CO_2/CH_4/H_2O$
	Reformer tube	HP	12	830	1.47	$H_2/CO/CO_2/CH_4/H_2O$

ND: No data.

equation, Cr_{eq}= Cr% + 3(Si%+Al%), as reported by Parks (1997), was applied to the Cr_{eq} calculation. Fe-Cr-Ni alloys having the higher Cr_{eq} of over 24, which is considered to be a minimum limit for metal dusting resistance as reported by Schillmoller (1986), experienced damage. It is apparent from Figure 1 that Cr-Mo low alloy steels experienced metal dusting in the lower temperature range (450-650°C), while the Fe-Cr-Ni alloy experienced it in the higher temperature range (above 650°C). These facts, however, do not indicate a temperature effect for metal dusting on each material because the materials were selected based on their mechanical properties (allowable stress) for high temperature environments.

The failures of alloy 800 and type 310 occurred in various temperatures as shown in Table 1 and Figure 1. It can be considered from the facts that the metal dusting temperature on each material varies depending upon the fluid gas composition.

Effect of Gas Compositions in Steam Reforming Process

With regard to Fe-Cr-Ni alloys, Table 1 shows that components, such as reformer tubes and waste heat boilers, exposed to a synthesis gas environment in steam reforming processes, have the highest susceptibility to metal dusting. Steam reforming processes for making synthesis gas are widely applied for methanol, ammonia, oxo alcohol and hydrogen, as shown in Table 1.

A H_2 to CO ratio was applied in the environment to assess carbon deposition. Figure 2 shows carbon deposition boundaries of the H_2/CO ratio, as reported by Lefrancois (1963). The

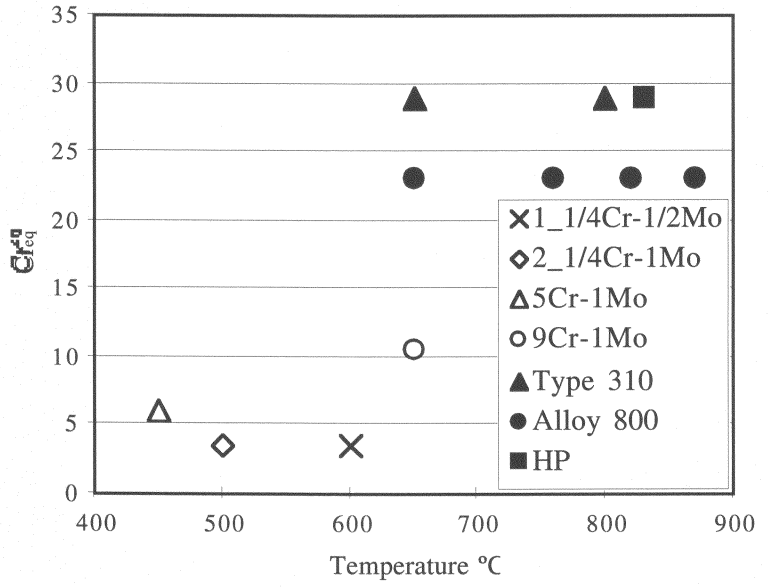

FIGURE 1 Chromium Equivalents and Operating Temperature of Failures Experienced.

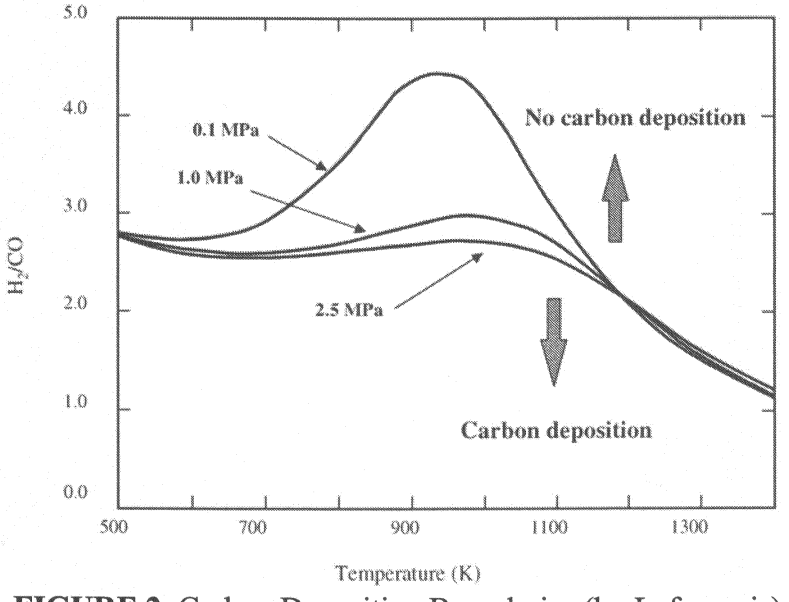

FIGURE 2 Carbon Deposition Boundaries (by Lafrancois).

H_2/CO ratios of steam reforming processes vary depending upon subsequent processes and products. Typical H_2/CO ratios of process gas at the steam reformer outlet in several plants are as follows:

Hydrogen plant	3~6
Ammonia plant	2~4
Methanol plant	2~3
Oxo alcohol plant	1~2

According to Figure 2 and the typical gas composition shown above, it is considered that the steam reforming unit of a hydrogen plant has less susceptibility to metal dusting than units

used in ammonia, methanol and oxo alcohol plants, though all of them have similar steam reforming processes. This is considered to be the reason why failures have not been experienced in hydrogen plants.

INVESTIGATION OF TWO FAILURES

Most failures of Fe-Cr-Ni alloys have been experienced in synthesis gas environments as described above. Therefore, further investigation was carried out on two failures to consider the effects of alloying elements and environments.

Case 1 - Ferrule of Waste Heat Boiler Tube in Oxosynthesis Gas Plant

Thinning damage on alloy 800H ferrules in several waste heat boiler tubes were observed in the steam reforming section of an oxosynthesis gas plant (for making isocyanate). The thinning occurred only on the tip of the ferrules and small pits were observed on the outside surface near thinning portion. The surfaces of thinning portion and pits were covered with black scale, as shown in Figure 3. No damage was observed on other areas of the ferrule or boiler tube itself.

Operating conditions of waste heat boiler were as follows.

Temperature : 820°C (tube inlet) – 400°C (tube outlet)
Pressure : 2.3 Mpa
Operation : 2 years
Gas composition (in %): $30.9H_2+14.6CO+15.7CO_2+35.6H_2O+3.2CH_4$; $H_2/CO = 2.1$

Case 2 - Reformer Tube in Oxo Alcohol Plant

Leakage due to thinning damage was observed on a HP-Mod reformer tube near the outlet, in the steam reforming section of an oxo alcohol plant. Figure 4 shows the damaged portion on the internal surface of a reformer tube.

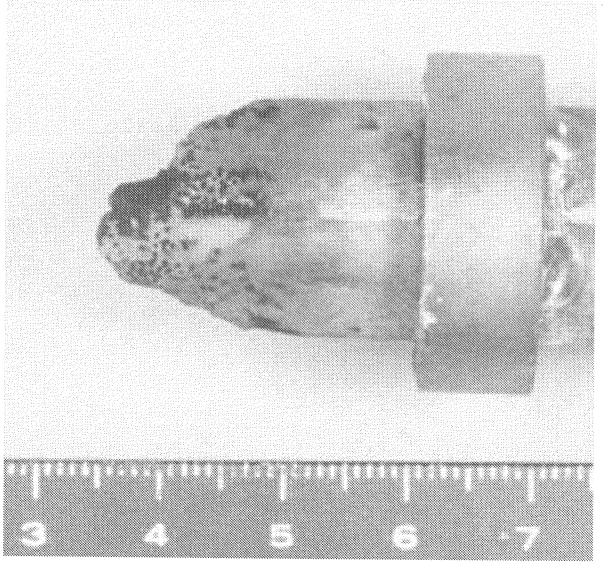

FIGURE 3 Thinning Portion of the Ferrule (alloy 800H) with Small Pitting on the Outside Surface.

Figure 5 shows a schematic illustration of the reformer tube near the outlet. An internal accessory of alloy 800H, comprised of a catalyst support tray and short piece of tube, was inside the reformer tube. Fluid gas flowed through the internal accessory and the space between the reformer tube and the internal accessory was a stagnant area where fluid gas couldn't flow. The thinning damage was found only on the inside surface of the reformer tube outside the furnace. On the other hand, no thinning or pitting was found on the internal accessory.

Operating conditions of reformer tube were as follows.

Temperature: 830°C (tube outlet)
Pressure: 1.4Mpa
Operation: 102,000 hours
Gas composition (in %): $24.6H_2+23.4CO+24.1CO_2+27.1H_2O+0.8CH_4$; $H_2/CO=1.1$

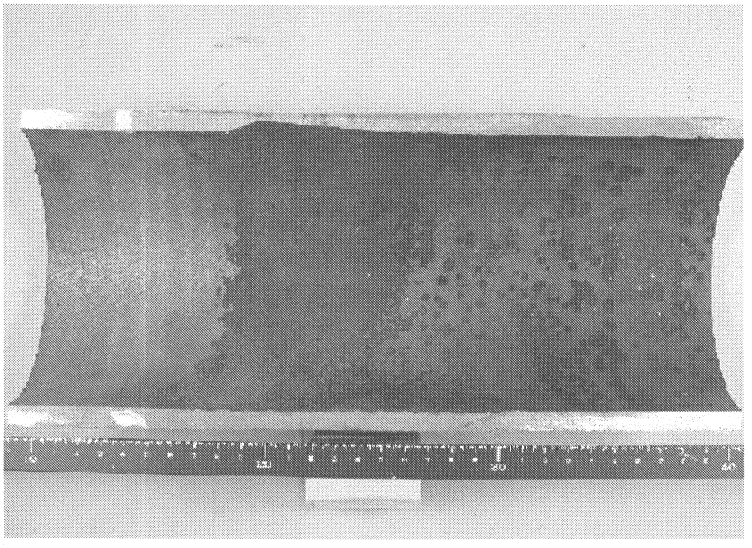

FIGURE 4 Damaged Portion of Reformer Tube (HP-Mod) Inside Surface near Outlet.

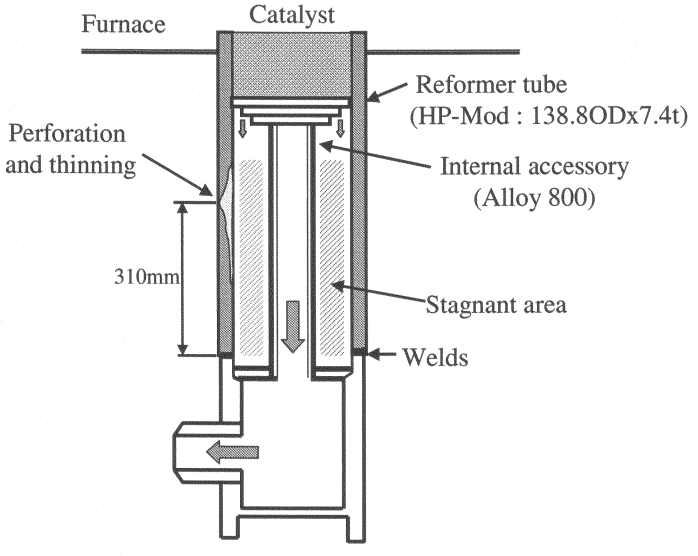

FIGURE 5 Schematic Illustration of Reformer Tube Outlet.

Effect of Temperature

The fact that metal dusting had occurred only in a limited area indicates that a very narrow temperature range has the highest susceptibility to metal dusting. The metal dusting temperature would be affected by the fluid gas composition.

A metal temperature profile around the damaged portion of the reformer tube (Case 2) was estimated to examine the reason why the HP-Mod (Cr_{eq}=29) reformer tube experienced metal dusting while the internal accessory of alloy 800H (Cr_{eq}=23) did not. The actual metal temperature of an adjacent reformer tube was measured by thermocouples during operation after the failed reformer tube was removed, and the measurement results were combined with the damage profile of failed reformer tube, as shown in Figure 6. Because the space between the internal accessory and reformer tube was a stagnant area, the metal temperature of the reformer tube outside the furnace was more likely to decrease than that of the internal accessory where high temperature fluid gas was in direct contact. Regarding this failure, the insulation covering the damaged portion accidentally failed causing the metal temperature to drop as estimated in Figure 6. Consequently, only a slight temperature difference would lead to metal dusting even on HP-Mod (Cr_{eq}=29) where alloy 800H (Cr_{eq}=23) had not suffered metal dusting. Therefore, the slight difference in Cr_{eq} would not be very effective in preventing metal dusting.

Metallurgical Investigation

Corrosion products adhering to the thinned portion of the alloy 800H ferrule (Case 1) were investigated using an EPMA (Electron Probe Micro Analyzer). The result of the microscopic examination is shown in Figure 7 as a COMP image. The COMP image shows the heavier

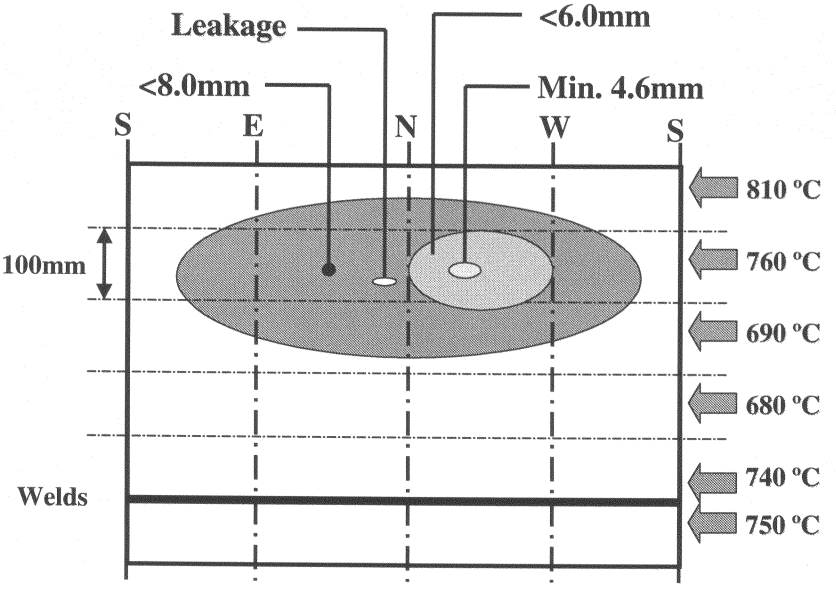

FIGURE 6 Estimated Metal Temperature Profile of Damaged Reformer Tube (Reformer Tube : 138.8OD x 7.4t).

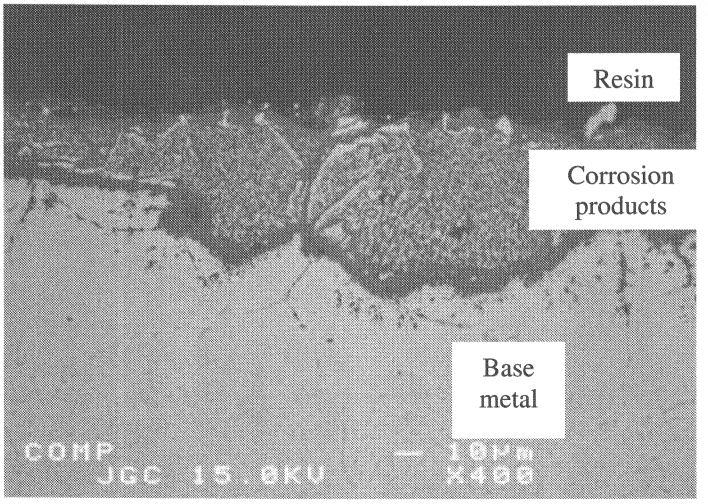

FIGURE 7 COMP Image of Corrosion Products Adhering to the Metal Surface of Thinning Portion.

elements (in this case, metal elements) in bright shades and the other lighter elements in dark shades. According to Figure 7, corrosion products on the metal surface contained widely-dispersed small metal particles.

The corrosion products were identified with oxide by quantitative analysis though carbon ingress, and were observed about 100μm from the base metal surface. The fluid gas in Case 1 contained a large amount of H_2O (35.6%), so there is a possibility of oxidation. An ordinary oxide scale, however, does not contain such metal particles, hence, the metal particles dispersed in the corrosion products gave the signature of metal dusting.

Furthermore, quantitative analysis (map analysis) by EPMA was performed on a cross section of the thinned HP-Mod reformer tube (Case 2) to confirm the surface state. Figure 8 shows the results of map analysis. Carbon ingress was found about 100μm from the surface around the thinned portion. (The high carbon level observed on the outside of the metal surface as a white color was due to a resin.) A chromium oxide film about 20μm in thickness was detected on the surface of the sound portion, while no distinct chromium oxide film was detected on the surface of thinned portion. These phenomena support the metal dusting mechanism, that is, (a) occurrence of a defect in the oxide scale, (b) internal carbide formation, (c) formation of a metastable carbide, (d) decomposition of the now unstable carbide to carbon and metal particles, as reported by Grabke (1995).

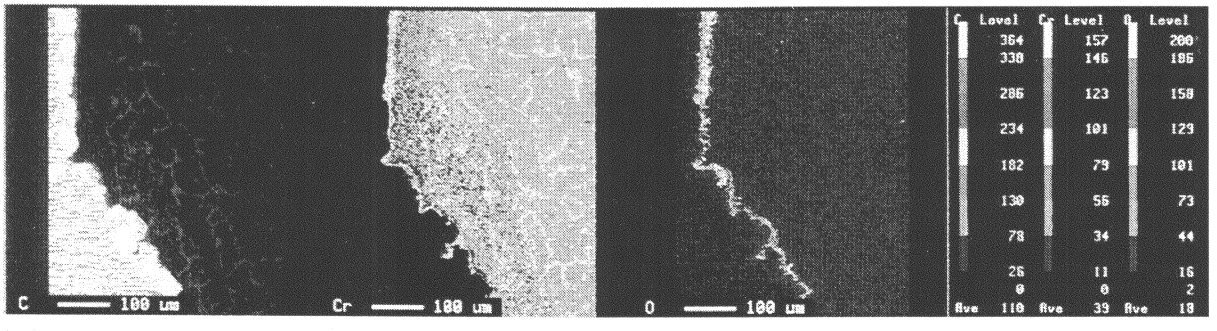

Figure 8 Quantitative Analysis (Map Analysis) on the Thinned HP-Mod Reformer Tube

CONCLUSIONS

From the failures in operating plants described here, the following were obtained.

- Fe-Cr-Ni alloys applied in the steam reforming units where the H_2 to CO ratio of fluid gas is less than around three have a high susceptibility to metal dusting.
- Metal dusting temperatures are very narrow and vary depending upon fluid gas compositions. Further, stagnant areas are susceptible to metal dusting.
- Slight differences in Cr_{eq} are not very effective in preventing metal dusting.
- The results of metallurgical investigation on the experienced failures support the published mechanism of metal dusting derived from experimental data.

Recently, technologies to prevent metal dusting have been developed from the metallurgical point of view, such as the application of high alloys. An estimating method for metal dusting using environmental factors, however, will be highly required from the economic point of view.

REFERENCES

Fabiszewski, A.S., 2000, "The Effect of Temperature and Gas Composition on the Metal Dusting Susceptibility of Various Alloys," Paper No.00532 in CORROSION 2000.

Grabke, H.J., 1995, "Metal Dusting of Low- and High-Alloy Steels," CORROSION, Vol.51: 711-720.

Lefrancois, P.A., and W.B. Hoyt, 1963, "Chemical Thermodynamics of High Temperature Reactions in Metal Dusting Corrosion," CORROSION, Vol.19: 360t-368t.

Parks, S.B., and C.M. Schillmoller, 1997, "Improve Alloy Selection for Ammonia Furnaces," Hydrocarbon Processing Oct.: 93-98

Schillmoller, C.M., 1986, "Solving High-Temperature Problems in Oil Refineries and Petrochemical Plants," Chemical engineering, 93, 1:83-87.

METAL DUSTING IN A LABORATORY ENVIRONMENT – ALLOYING ADDITION EFFECTS

B. A. BAKER* and G. D. SMITH
Special Metals Corporation
Huntington, West Virginia

ABSTRACT

Long-term testing of a wide variety of nickel-base and iron-base alloys has been conducted in an environment generated by an inlet gas composition of CO-20% H_2 at 621°C. Some degree of metal dusting attack has been observed for all alloys tested. Multivariate analysis has been performed, in order to determine the effects of various alloying additions upon the mass loss rate and the pitting progression rate. The results indicate the beneficial effects of a nickel-base alloy matrix, scale-forming element additions, and the presence of certain carbide-forming elements upon alloy performance.

INTRODUCTION

Metal dusting has been responsible for considerable losses in equipment and production time across numerous industries including petrochemical processing, direct iron-ore reduction and heat treating. The phenomenon termed "metal dusting" can be described as a catastrophic form of carburization which occurs under conditions where the carbon activity of the gaseous atmosphere is greater than one and can result in rapid metal wastage, producing pits and grooves as the affected metal disintegrates into a mixture of powdery carbon and metal particles.

CAUSES AND THERMODYNAMIC CONSIDERATIONS

Consider stream reforming as an example of a process in which metal dusting can occur. The combination of natural gas, or methane, with steam at high temperature produces a mixture of gases commonly referred to as 'syngas' which contains mostly H_2, CO, CO_2, H_2O and some CH_4. When such gas mixtures are present in the process stream in the critical temperature range of about 450° to 800°C, metal dusting can be a severe corrosion problem (Jones and Baumert, 2001). Figure 1 shows equilibrium constants versus temperature for a few reactions which are capable of producing carbon in such a gas mixture. The reaction for cracking of butane, while not predicted to have significance in the typical syngas environment, has been included in Figure 1 for the purpose of illustrating the likelihood for the occurrence of metal dusting within a solely hydrocarbon-based environment. Within the syngas environment, the two reactions contributing most to carbon deposition are: 1.) the reduction of CO by hydrogen and 2.) The decomposition of CO_2 (the Boudouard reaction). The fact that the equilibrium constant for each of these reactions dips below one at about 750°C helps to explain why metal dusting activity within syngas environments is typically observed in the temperature range of about 450°C to about 800°C (the lower temperature boundary being determined by reaction kinetics).

Correspondng author address: B. Baker, Special Metals Corporation, 3200 Riverside Drive, Huntington, WV 25705; e-mail: bbaker@smcwv.com

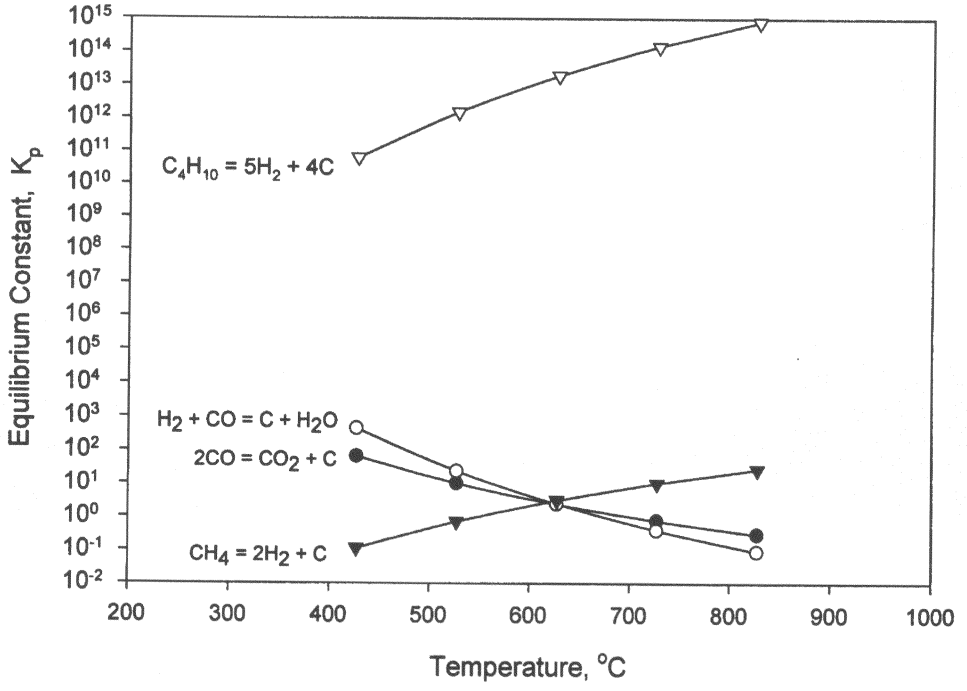

Figure 1 Equilibrium constants for reactions which may produce carbon in metal dusting environments.

The need for greater efficiency has reduced the quantity of steam used for the reforming process, resulting in lower steam-to-hydrogen ratios. Higher front-end pressures have also increased the CO content of the syngas. Lower H_2O/H_2 ratios in combination with higher CO/CO_2 ratios result in lower oxygen partial pressures and higher carbon activities, respectively, and serve to increase the severity of metal dusting attack. In addition, the use of advanced catalysts which are not tolerant to sulfur in the process stream, has necessitated the use of alloys which are more resistant to metal dusting, as sulfur-containing species can be added to the process stream in order to mitigate the problem. Avoidance of metal dusting is often accomplished in industry by designing around the critical temperature range. Syngas is produced at temperatures above the critical range (>800°C) and transferred to a boiler via a short transfer line where it is rapidly quenched to temperatures below the critical metal dusting range (<450°C). Alloy ferrules that are used in the transfer line do often experience metal dusting and are periodically replaced. The need to maximize the efficiency of steam reforming technology has led to the development of equipment which must be capable of operating within the range of temperature and carbon activity which can promote metal dusting. This necessitates the use of materials which exhibit excellent resistance to metal dusting attack.

An adherent, protective, healable oxide surface layer is required for protection of an alloy against metal dusting attack. Although oxide formation may be stable, the oxide layer may still be susceptible to disruption. Higher levels of the scale forming element will then make the scale healing process more rapid and complete. Figure 2 illustrates the pO_2 required to form various metal oxides at 627°C. Additions of particular interest obviously include silicon, aluminum and chromium. Ultimate resistance to metal dusting may involve complex interactions of scale characteristics, diffusivity of scale-forming elements and carbon through the alloy matrix and carbon saturation limits.

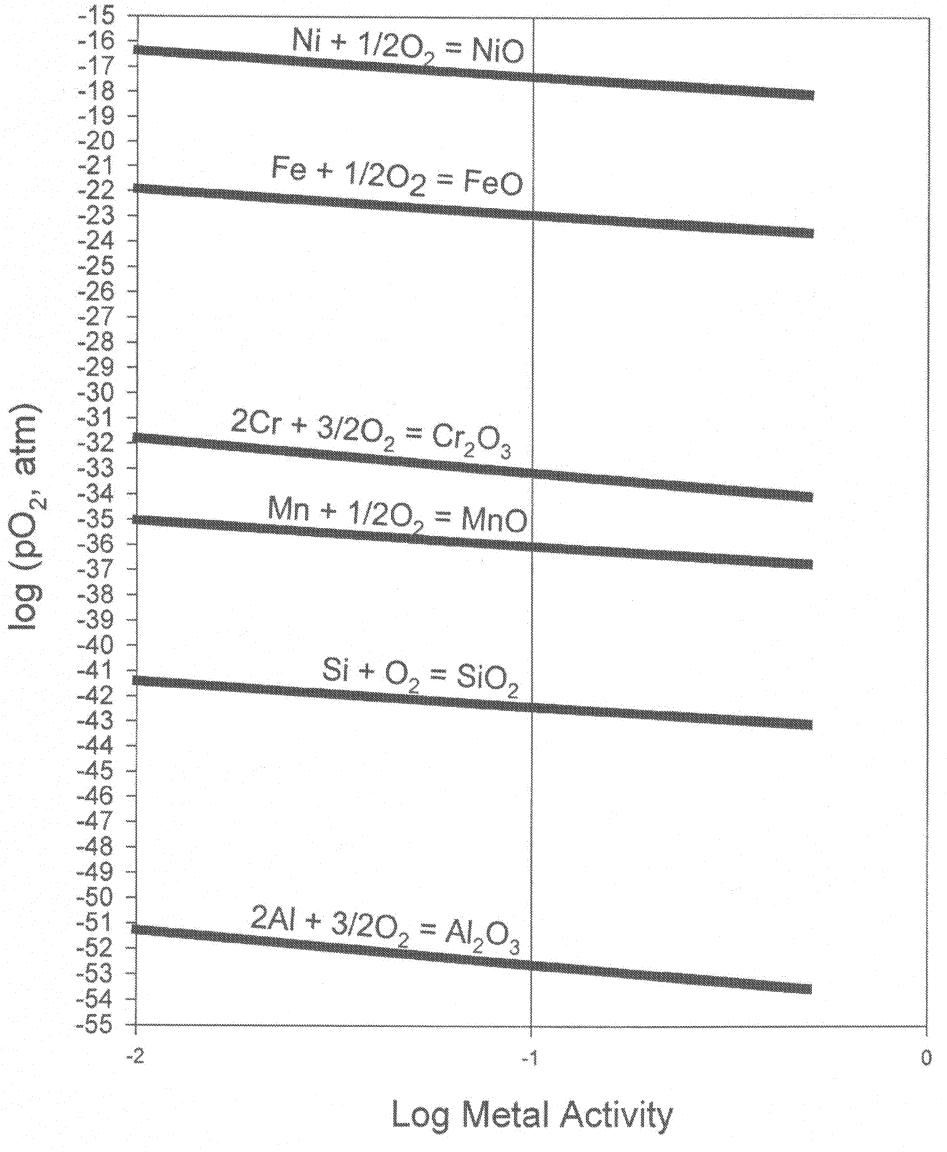

Figure 2 The log of oxygen partial pressure required for the formation of the most stable oxides of aluminum, chromium, nickel, manganese, and silicon as a function of metal activity at 627°C.

EXPERIMENTAL

Table 1 shows the chemical composition for each alloy tested. Test specimens were prepared from commercially available material; sample dimensions were approximately 2.5cm X 2.5cm X thickness. Samples were ground to a 120-grit finish for standardization purposes.

Samples were exposed at 621°C in a horizontal electrically heated furnace having a mullite tube, in an atmosphere generated from an inlet gas mixture of CO-20% H_2. Samples were cycled, lightly brushed, ultrasonically cleaned in methanol and weighed at two-week intervals. In addition to mass change, pitting depth was also determined for each sample using an optical microscope having a calibrated fine focus knob.

RESULTS

Figure 3 illustrates the mass loss rate as a function of time. The maximum pit depth as a function of time is plotted in Figure 4. Table 2 shows the pit progression rate for each alloy tested. Figure 5 shows the result of multiple regression analysis of the log of the pit progression rate, calculated by averaging the pit depth over the total testing duration, versus a summation of the weight percentage of various alloying additions. The summation coefficients were based upon the regression results. Only the austentic nickel-base alloys and Fe-Ni-Cr alloys were included in this calculation; the ferritic alloy, MA956, and also alloy 400 were excluded. The best fit was produced using the following summation (multiples of weight percentage):

$$(Ni + Co) + 2Cr + 5Mo + 9Ti + 11Si + 23Al - 1Fe.$$

This same regression technique was used to characterize the variation in the log of the mass loss rate with the percentage of certain alloying additions (Figure 6). Again, only the austenitic nickel-base and Fe-Ni-Cr alloys were included in the calculation. The best fit was obtained using the following summation:

$$(Ni + Co) + 5Mo + 11Cr + 15W + 52Ti + 54Al + 83Si - 1.5Fe.$$

As a general trend, nickel-base alloys exhibited lower mass loss rates and pitting progression rates than iron-base alloys. Alloys 600 and MA754, which contain only 15% and 20% chromium, respectively, were exceptions and had a fairly high mass loss rate resulting from numerous, albeit fairly shallow, pits. Neither of these alloys other significant additions of scale-forming or carbide-forming elements. Alloy 690 (Ni-29Cr-9Fe), commonly used as heat-exchanger tubing in the nuclear industry, exhibits much lower mass loss and pit progression rates than those for alloy 601, which is increasingly used as an upgrade from iron-base materials such as Cr-Mo steels, austenitic stainless steels and Fe-Ni-Cr heat-resistant alloys such alloy 800. Figure 7 shows photomicrographs of a pit in the alloy 690 sample in cross section after 14160 hours of testing. Etching the sample electrolytically in methanol-5% HNO_3 revealed the characteristic 'white layer' near the pit surface, presumed saturated with carbide, in addition to the intergranular carbides extending beneath the white layer. The mechanically alloyed corollary to alloy 690, alloy MA758, also exhibits good performance. Alloy MA956, a ferritic alumina former, also exhibited good performance for a considerable incubation period of almost 12,000 hours after which pitting initiated and progressed quite rapidly.

Figure 8 shows photomicrographs of a pit in the alloy MA956 after the total testing duration of 15,926 hours. Large carbides are evident after etching. The pitting progression also appears to

TABLE 1 Nominal composition of commercial alloys (in weight percent)

Alloy	Ni	Cr	Fe	Mn	Si	Al	Ti	C	Other
INCONEL® alloy MA754	78	20	-	-	-	0.3	0.5	0.05	0.5 Y_2O_3
INCOTHERM™ alloy TD	73	22	-	-	1.4	-	-	0.01	3.0 Mo
INCONEL® alloy 600	72	15.5	8	0.3	0.3	0.3	0.3	0.08	-
INCONEL® alloy MA758	67	30	-	-	-	0.4	0.5	0.05	0.5 Y_2O_3
MONEL® alloy 400	64	0.1	1.6	0.7	0.1	0.02	0.4	0.15	32.2 Cu
INCONEL® alloy 693	62	29	4	-	-	3.1	-	-	Nb, Zr
INCONEL® alloy 625LCF®	61	21.5	2.5	-	0.1	0.2	0.2	0.02	9 Mo, 3.6 Nb
INCONEL® alloy 601	60.5	23	13	0.2	0.2	1.4	0.4	0.05	-
INCONEL® alloy 690	59	29	9	0.2	0.1	0.3	0.3	0.02	-
INCONEL® alloy C-276	57	15.5	5.5	-	-	0.1	0.2	-	16 Mo, 3.8W
INCONEL® alloy 671	53	46	-	-	-	0.3	0.3	0.03	-
INCONEL® alloy 617	55	22	1	-	0.1	1.2	0.4	0.08	12.5 Co, 9 Mo
NIMONIC® alloy 263	51	20	39	0.3	0.1	0.5	2.2	0.06	20 Co, 5.9 Mo
INCOLOY® alloy 825	42	21.5	28	0.4	0.1	0.1	1	0.02	3 Mo, 2Cu
INCOLOY® alloy DS	37	16	41	1.0	2.3	-	-	0.08	-
INCOLOY® alloy 330	35	19	44	1.0	1.3	-	-	0.07	-
INCOLOY® alloy 803	34	27	36	1.0	0.8	0.4	0.4	0.08	-
INCOLOY® alloy 864	34	21	39	0.4	0.8	0.3	0.6	0.03	4.2 Mo
INCOLOY® alloy 800	32	21	45	0.9	0.1	0.4	0.4	0.07	-
INCOLOY® alloy MA956	-	20	75	-	-	4.5	0.5	0.05	0.5 Y_2O_3

TABLE 2 Pitting Progression Rate after Exposure in CO-20% H_2 at 621°C

Alloy	Pit Depth		Exposure Time	Pit Progression Rate	Pit Progression Rate
	Mils	µm	Hours	Mils per Hour	µm/h
800	25.0	635	1056	2.37E-02	9.32E-04
330	17.0	432	1056	1.61E-02	6.34E-04
DS	24.0	610	2400	1.00E-02	3.94E-04
803	21.5	546	2400	8.96E-03	3.53E-04
825	7.0	178	1662	4.21E-03	1.66E-04
864	9.1	231	2184	4.17E-03	1.64E-04
601	19.8	503	6600	3.00E-03	1.18E-04
600	1.8	46	1392	1.29E-03	5.09E-05
MA956	18.6	472	15936	1.17E-03	4.60E-05
MA754	3.3	84	2936	1.12E-03	4.43E-05
TD	7.3	185	6728	1.09E-03	4.27E-05
263	17.0	432	15936	1.07E-03	4.20E-05
625LCF	6.3	160	6397	9.85E-04	3.88E-05
MA758	7.0	178	8023	8.72E-04	3.44E-05
690	12.1	307	14160	8.55E-04	3.36E-05
C-276	4.0	102	6397	6.25E-04	2.46E-05
671	3.6	91	8686	4.14E-04	1.63E-05
617	1.6	41	14160	1.13E-04	4.45E-06
693	1.7	43	15816	1.07E-04	4.23E-06

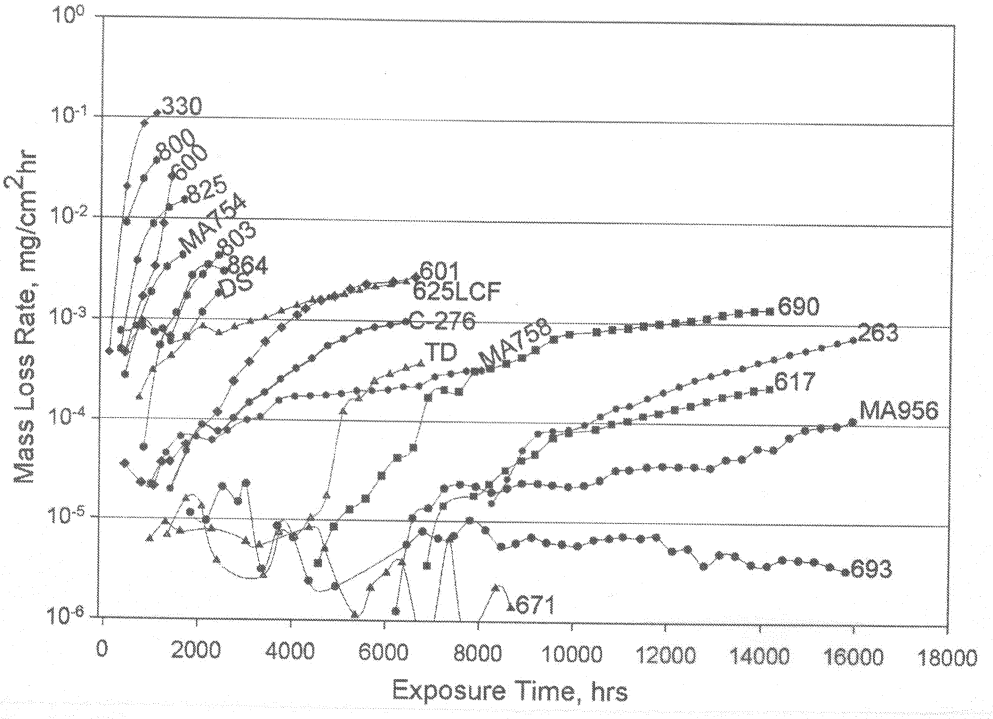

Figure 3 Mass loss rate versus exposure time for alloy samples exposed to CO-20% H_2 at 621°C.

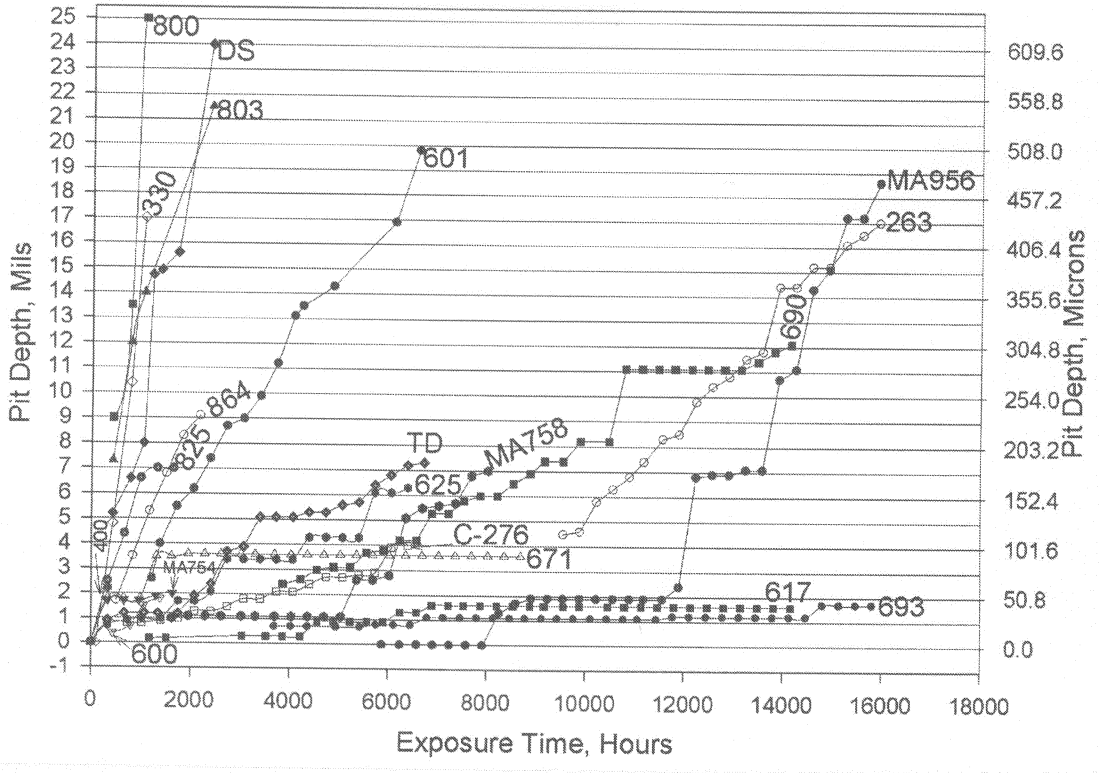

Figure 4 Maximum pit depth measurements for alloy samples exposed to CO-20% H_2 at 621°C.

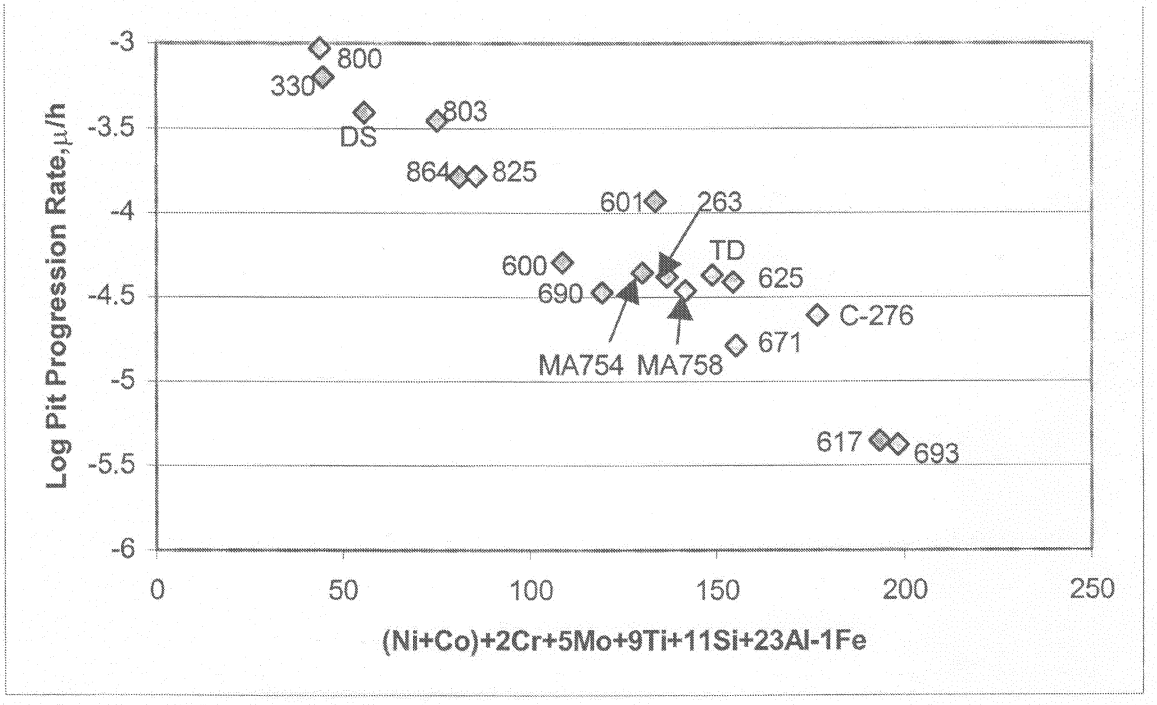

Figure 5 Results of multiple linear regression for pit progression rate versus composition.

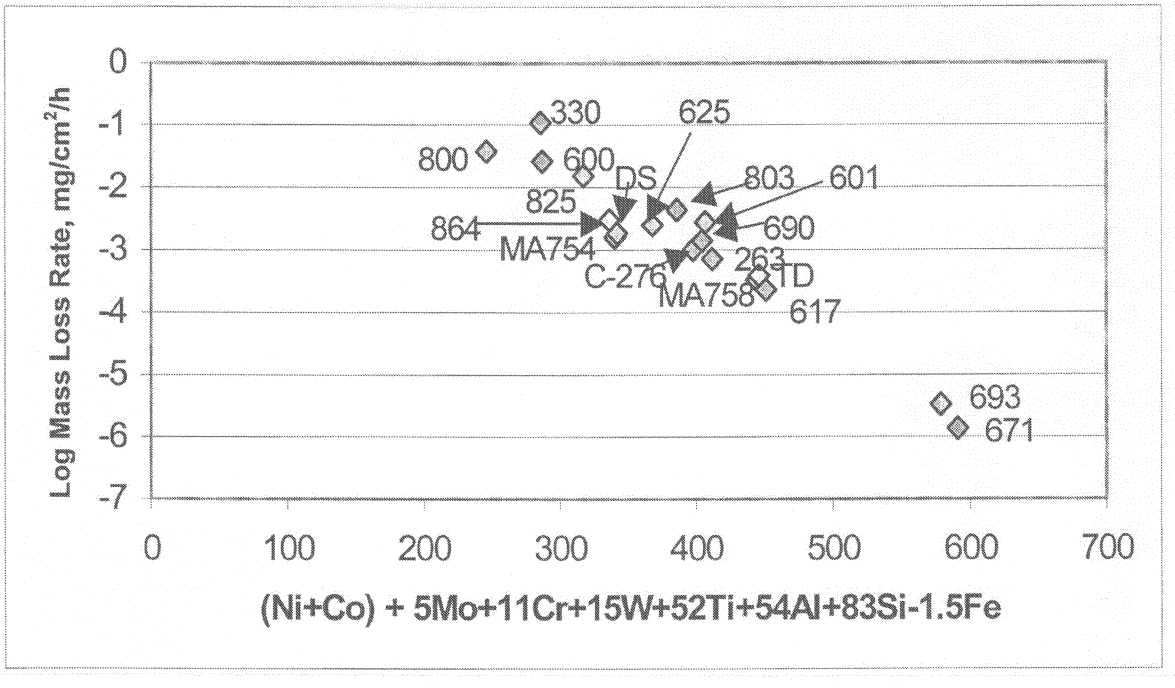

Figure 6 Results of multiple linear regression for log mass loss rate versus composition.

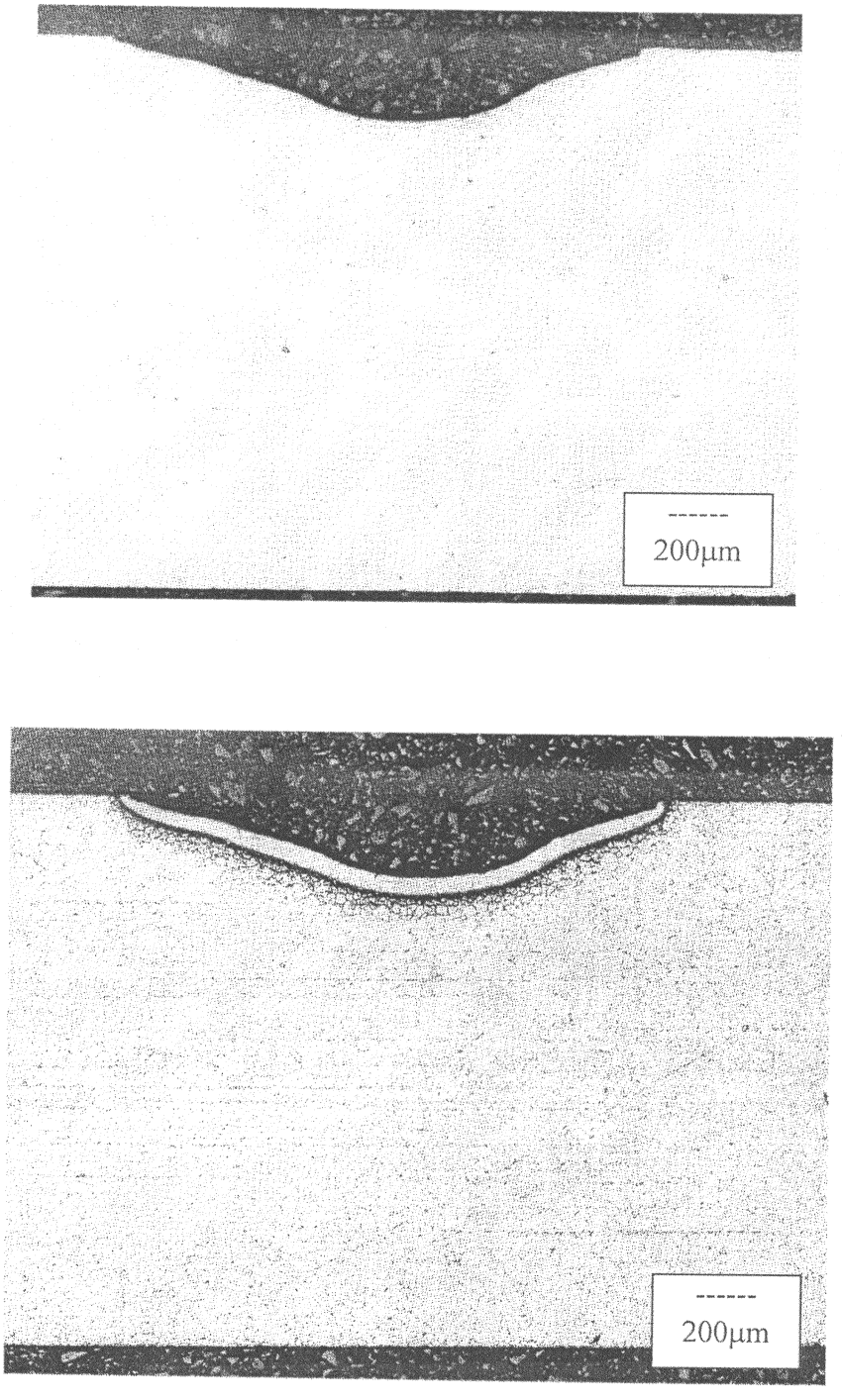

Figure 7 Photomicrographs showing a cross section of an alloy 690 sample exposed in CO-20% H_2 at 621°C for 14,160 hours. The top photo shows a pit in the unetched condition. The bottom photo shows the same are after electrolytically etching in methanol - 5% HNO_3.

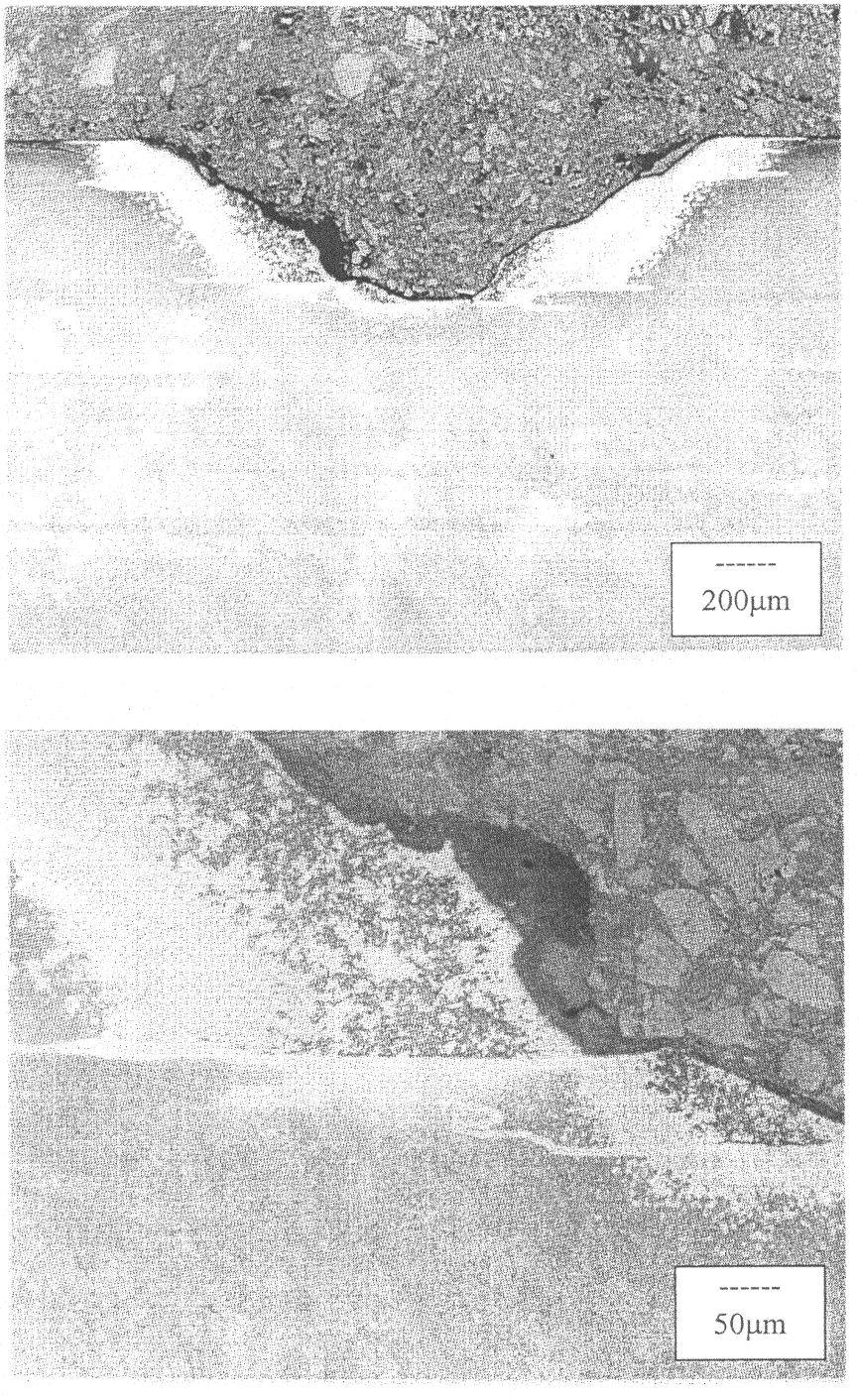

Figure 8 Photomicrographs showing alloy MA956 after 15, 936 hours of exposure in CO-20% H_2 at 621°C. The sample was electrolytically etched in methanol - 5% HNO_3.

be possible related to the orientation of the large grains. Alloy 263 performed well despite its modest chromium level of 20% and 39% iron content, and appears to possibly gain protection from its substantial titanium addition and possibly its molybdenum addition, which may promote early carbide formation and provide diffusional blocking of the carbon flux (Müller-Lorentz 1999). Figure 9 shows photomicrographs of the surface of the alloy 263 sample after 15, 936 hours of exposure. A thin layer of what is presumed to be carbide is evident at the surface, away from the pitted region. Alloy 617, having 22% chromium and 1.2% aluminum, may also gain the same benefit from its molybdenum addition. Figure 10 shows photomicrographs of the alloy 617 sample after 14,160 hours of exposure. As with the alloy 263, what is presumed to be a thin layer of carbide is present of the surface of the alloy 617 as well. Alloy 625LCF, a refined version of alloy 625, has performed reasonably well and contains 21.5% chromium, 9% molybdenum and 3.6% niobium and probably benefits from its fine grain structure. The high silicon content of alloy TD may have afforded some enhancement in performance, in addition to its 3% molybdenum content. Alloy 671, with its substantial chromium addition, is performing admirably, despite pitting activity initially to a depth of about 75 microns.

The best performer overall in the laboratory test was alloy 693, which possesses very high chromium and aluminum contents in combination with a high nickel alloy matrix. In-situ field exposures under metal dusting conditions have confirmed this alloy's superior performance. Figure 11 shows a photomicrograph of a sample sectioned after 15,816 hours of testing.

CONCLUSIONS

Due to efforts to increase the efficiency of processes involving the production of syngas and development of advanced catalysts, metal dusting corrosion has become more prevalent. Failures of iron-base alloys as well as nickel-base alloys which contain insufficient levels of key alloying elements have prompted equipment designers to seek materials that are more resistant to metal dusting. Field and laboratory data confirm the desirability of addition of certain scale-forming and possibly carbide-forming elements in conjunction with a nickel-base alloy matrix to limit pit progression rates. Based upon the results of this study, the newly-developed alloy 693 offers the most promising potential for metal-dusting limited applications.

ACKNOWLEDGEMENTS

The authors would like to thank Chad Clary for testing and evaluation of the materials in this study. INCONEL®, INCOLOY®, INCOTHERM™, MONEL®, NIMONIC®, and 625LCF® are trademarks of the Special Metals group of companies.

REFERENCES

Jones, R. T. and Baumert, K. L., 2001, Paper Number 1372, CORROSION/2001, Houston, Texas.

Müller-Lorentz, E. M., 1999, Proc. EUROCORR 1999, Aachen, Germany, September.

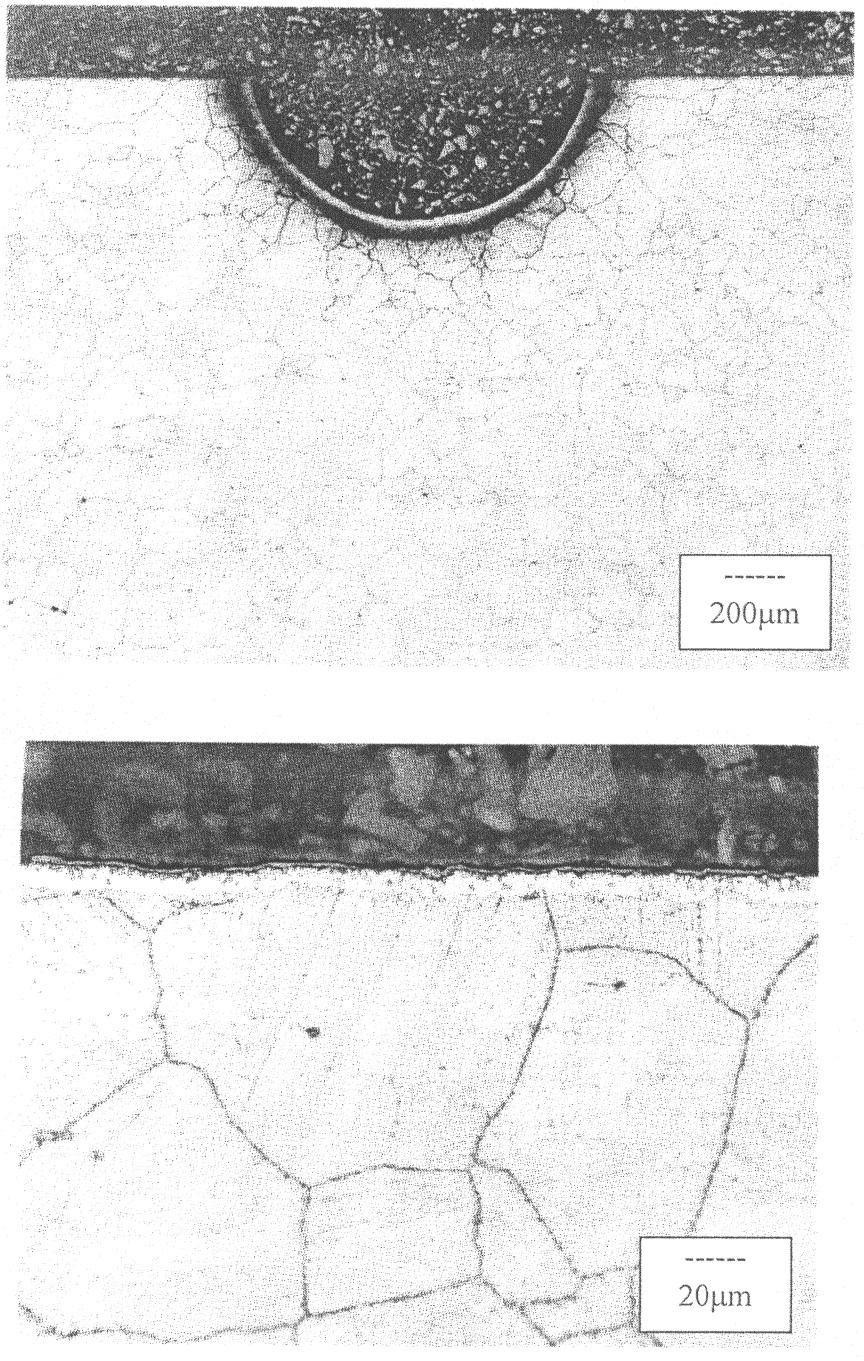

Figure 9 Photomicrographs showing alloy 263 after 15, 936 hours of exposure in CO-20% H_2 at 621°C. The sample was electrolytically etched in methanol - 5% HNO_3. The top photo shows the microstructure of a typical pit. In areas not affected by pitting, a distinct, thin surface layer is present.

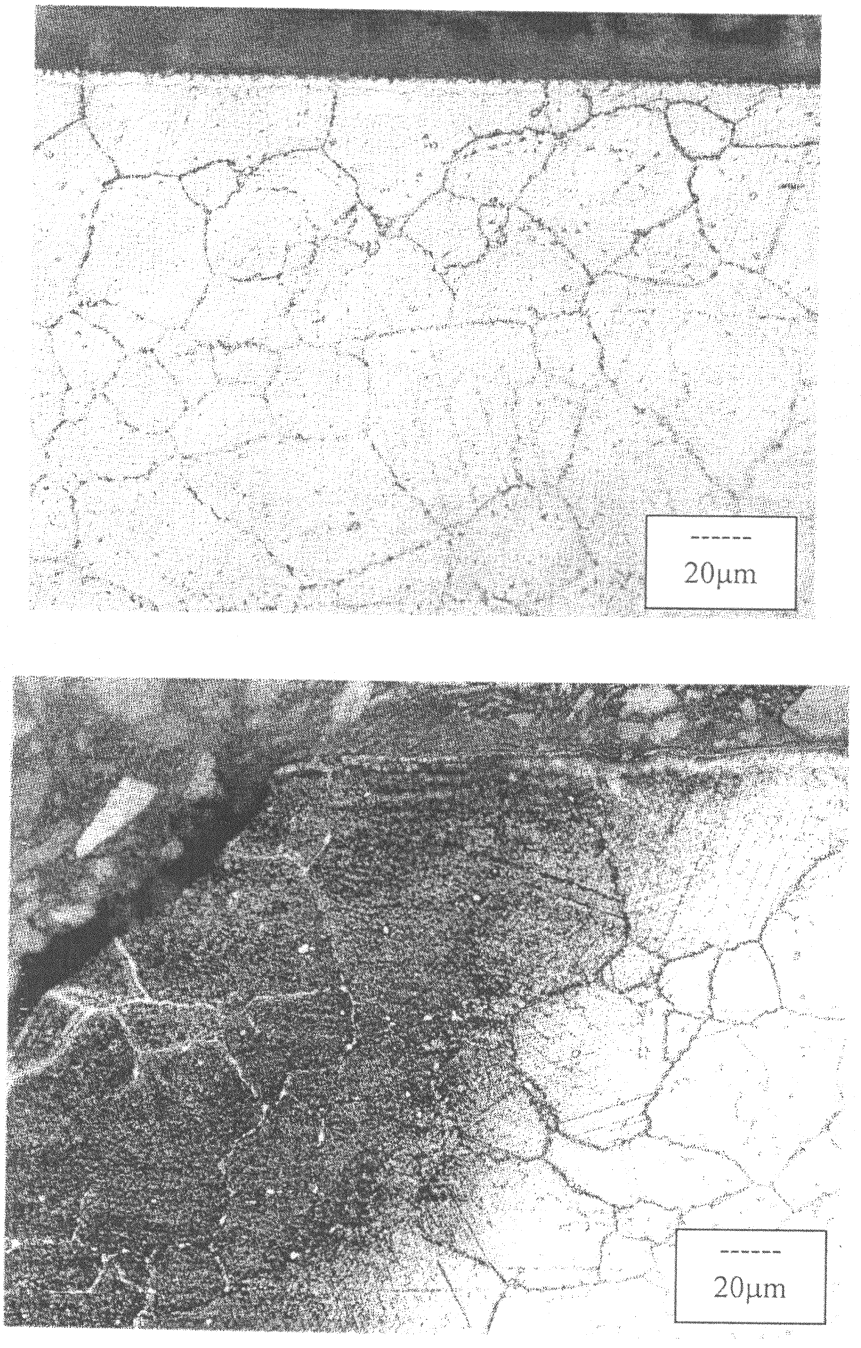

Figure 10 Photomicrographs showing alloy 617 after 14,160 hours of exposure in CO-20% H_2 at 621°C. The sample was electrolytically etched in methanol - 5% HNO_3. The top photo shows the microstructure of the general surface, which exhibited a thin layer presumed to be carbide. While only shallow pitting (less than 50 microns) was observed on the general surface, the corners of the sample were attacked (bottom photo).

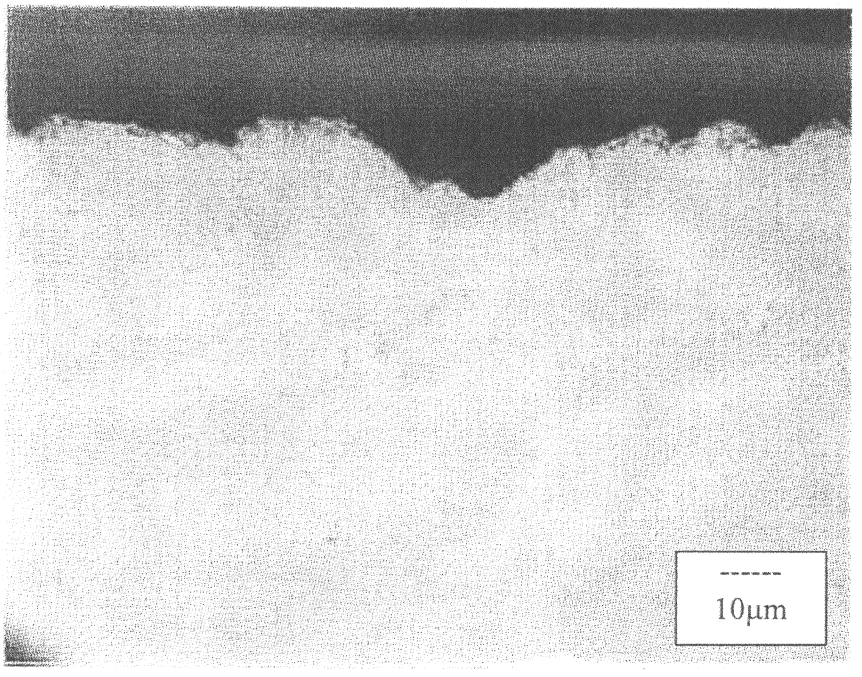

Figure 11 Photomicrograph showing the surface of alloy 693 after 15, 816 hours of exposure in CO-20% H_2 at 621°C.

THE METAL DUSTING BEHAVIOR OF SEVERAL HIGH TEMPERATURE ALLOYS

D. L. KLARSTROM, Haynes International, Inc.,Kokomo, IN*
H. J. GRABKE, Max-Planck Institut für Eisenforshung, Düsseldorf, Germany

ABSTRACT

The metal dusting behavior of several nickel based, high temperature alloys was investigated in a gaseous environment composed of 49% CO-49% H_2-2% H_2O having a carbon activity of 18.9. Samples of the alloys were exposed in the test environment at a temperature of 650°C for periods up to 10,000 hours. Periodically, the samples were removed from test to determine metal wastage and to examine them for pitting attack. The materials tested included alloys that form chromia, alumina and silica type scales. Results of the exposures are interpreted in terms of the compositional variations of the alloys tested.

INTRODUCTION

Metal dusting is a form of material degradation that occurs in a strongly carburizing environment mainly in the temperature range of 450°-750°C (Grabke, et al. 1996). The attack generally occurs in Fe-, Ni- and Co-based alloys and results in the formation of a dust composed of metal particles and carbon. Sometimes oxides and carbide particles are included as well. This high temperature corrosion phenomenon is a particular problem in industrial processes such as ethylene pyrolysis, hydrogen reforming, ammonia synthesis and steel surface carburization in which the conditions required for metal dusting are met. The present study was developed in order to gain information on the resistance to metal dusting of some commercially important high temperature, nickel based alloys. In addition, due to the compositional variations of the alloys studied, it was believed that some insight might be obtained on the effects of the various alloying elements in resisting metal dusting attack.

EXPERIMENTAL PROCEDURES

The alloys used in the study are listed in Table 1. HAYNES® 214™, 230® , HR-120®, and HR-160® alloys were manufactured by Haynes International, Inc., while INCONEL® 601 alloy and INCOLOY® 800H alloy were manufactured by Special Metals Corporation. HAYNES, 230, HR-120 and HR-160 are registered trademarks and 214 is a trademark of Haynes International, Inc., INCONEL and INCOLOY are registered trademarks of Special Metals Corporation. Duplicate test samples were prepared from bright annealed sheet approximately 3 mm thick from each alloy with the exception of 601 and 800H alloys which had been black annealed andpickled. The samples were exposed in a flowing gas mixture composed of 49% CO-49% H_2-2% H_2O with a_c= 18.9 at a temperature of 650°C. The gas composition corresponded to a syngas such as might obtained from methane conversion for use in ammonia or methanol synthesis, or for the direct reduction of iron ore. The test was interrupted periodically to examine the samples for metal wastage. Any coke deposits formed were scraped from the sample surface and analyzed for metal content. A metal wastage rate was then calculated based on the values obtained. When too much coke was formed on a sample or if its outgrowth interfered with the wastage determinations of other samples, the sample was removed from the test. The test was

*Corresponding author address: Dwaine L. Klarstrom, Haynes International, Inc., P.O. Box 9013, Kokomo, IN 46904-9013; e-mail: dklarstrom@haynesintl.com

TABLE 1 Nominal Composition of Alloys Investigated

Commercial Designation	UNS No.	Nominal Composition (Weight %)										
		Ni	Co	Cr	Fe	Al	Si	Mn	Mo	W	C	Other
214	N07214	75	-	16	3	4.5	0.2*	0.5*	-	-	0.05	0.01 Y
230	N06230	57	5*	22	3*	0.3	0.4	0.5	2	14	0.10	0.02 La
HR-120	N08120	37	3*	25	35.7	0.1	0.6	0.7	2.5*	2.5*	0.05	0.7 Nb, 0.2 N
HR-160	N12160	37	30	28	3.5*	-	2.75	0.5	1*	1*	0.05	0.5 Ti
601	N06601	61	-	23	14.6	1.4	0.5*	1*	-	-	0.1*	
800H	N08810	33	-	21	45.1	0.4	1.0*	1.5*	-	-	0.08	0.4 Ti

* Maximum

TABLE 2 Final metal wastage rates obtained for exposures in $49CO\text{-}49H_2\text{-}2H_2O$ at 650°C

Alloy Designation	UNS No.	Total Exposure Time, h	Final Metal Wastage Rate, mg/cm^2h
HR-120	N08120	190	4.1×10^{-2}
800H	N08810	925	2.7×10^{-3}
214	N07214	5,707	1.0×10^{-3}
601	N06601	10,000	2.5×10^{-3}
230	N06230	10,000	3.2×10^{-4}
HR-160	N12160	10,000	0.0*

*Attack Too Small for Analysis

carried out for a maximum exposure time of 10,000 h. At the conclusion of the test exposure, all samples were examined metallographically.

RESULTS

Metal Wastage Rates

The final metal wastage rates and the total exposure times for the alloys tested are summarized in Table 2. It can be seen that both HR-120 and 800H alloys with high iron content underwent significant metal dusting after relatively short exposures of 190 and 925 h, respectively. The susceptibility was not directly proportional to the iron content since HR-120 had the lower iron level, but experienced metal dusting sooner. The final metal wastage rate of HR-120 alloy was also almost an order of magnitude higher than for 800H alloy. The time for the onset of severe metal dusting was much longer for 214 alloy at 5707 h, but signs of metal wastage were evident after 2840 h as illustrated in Figure 1. After 4000 h, the metal wastage rates of the alloy increased markedly. Samples of 601 and 230 alloys lasted the full 10,000 h exposure with much higher final metal wastage rates noted for 601 alloy. As shown in Figure 1, both alloys exhibited evidence of metal wastage after 6689 h, but the increase in the metal wastage rates was higher for 601 alloy. At the conclusion of the test, the metal wastage rate for 601 alloy was almost an order of magnitude greater than that observed for 230 alloy. Both samples of HR-160 alloy endured the full 10,000 h exposure with metal wastage rates too low to determine.

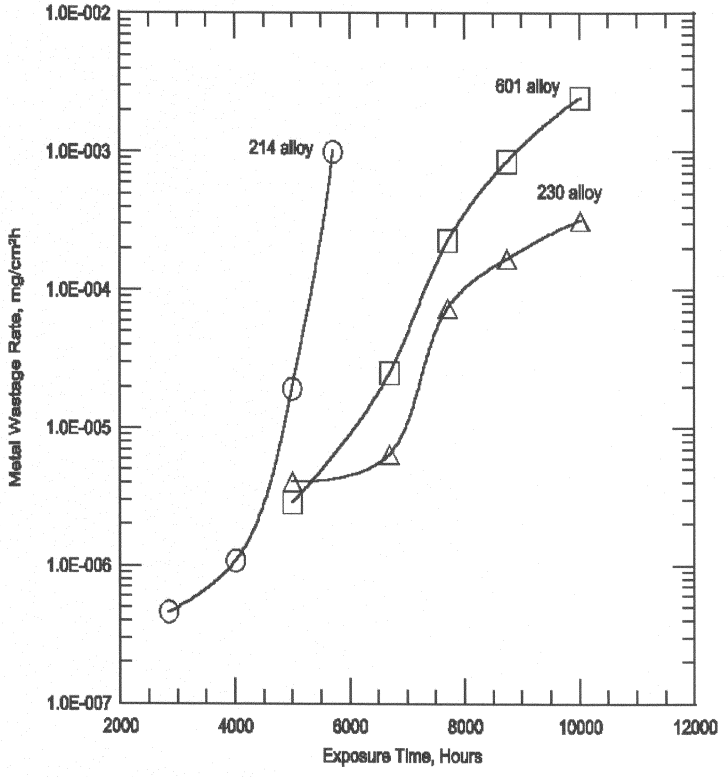

FIGURE 1. Metal Wastage Rates Obtained as a Function of Time in 49% CO-49% H_2-2% H_2O at 650°C for Selected Alloys.

Surface Examinations and Metallographic Analyses

The nature of the metal dusting attack observed in HR-120, 800H and 214 alloys after various periods of exposure is presented in Figure 2. A region of carburization can be noted near the surface for samples of HR-120 and 800H alloys shown in Figures 2(a) and (b). Wide surface attack and extensive coke formation was noted for the samples of HR-120 alloy. Pitting and general wastage were noted on the 800H samples. However, it was estimated that only about 1% of the total surface had been attacked. Extensive coke formation was also noted on these samples. For the 214 alloy samples, a thin layer of coke was noted. Some pitting was also evident on 1-2% of the surface area. As shown in Figure 2(c), the pits had a carburized zone and were filled with coke.

The metal dusting attack observed in the samples of 601, 230 and HR-160 is summarized in Figure 3. The attack observed for 601 alloy is shown in Figure 3(a). Numerous round pits with a diameter of approximately 1.2 mm were evident. This behavior has also been reported in other studies (Grabke et al. 1996; Grabke et al. 1998). For 230 alloy, a few spots 1-2 mm in diameter were noted on both sides of the samples. A cross section of the attack shown in Figure 3(b) indicated a carburized region approximately 0.1 mm deep with coke formation on the top surface. The samples of HR-160 alloy showed no evidence of metal dusting as illustrated in Figure 3(c). There was evidence of extensive carbide precipitation which was due to the long thermal exposure at 650°C rather than to carburization attack since no carburization zone was present. Such carbide precipitation was natural and unrelated to any form of metal dusting attack.

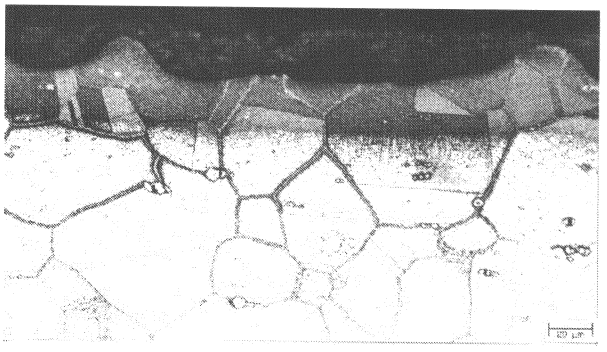

(a) HR-120 alloy, 190 h

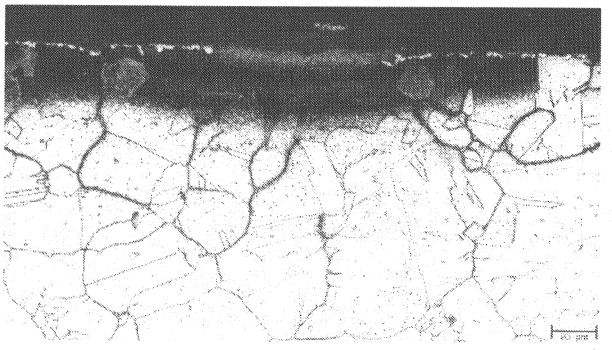

(b) 800H alloy, 925 h

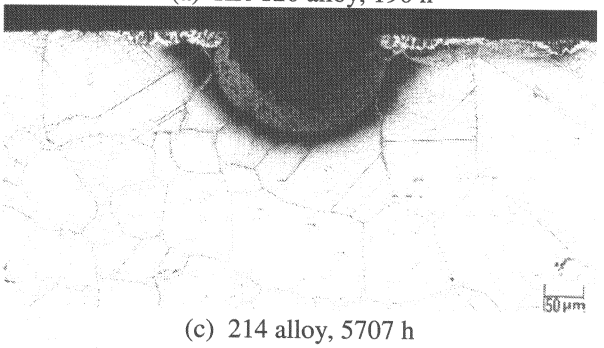

(c) 214 alloy, 5707 h

FIGURE 2. Metal Dusting Attack Observed in HR-120, 800H and 214 alloys After Various Periods of Exposure.

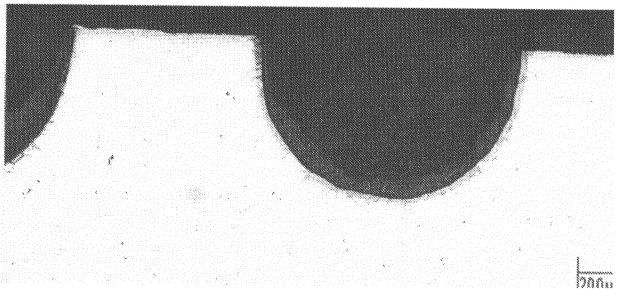

(a) 601 alloy

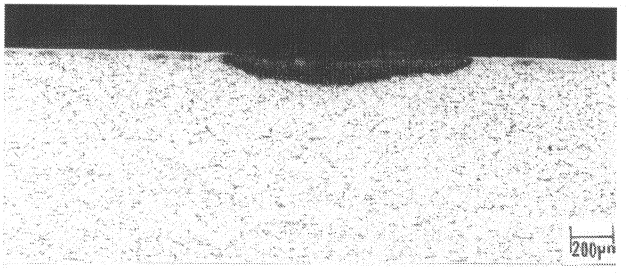

(b) 230 alloy

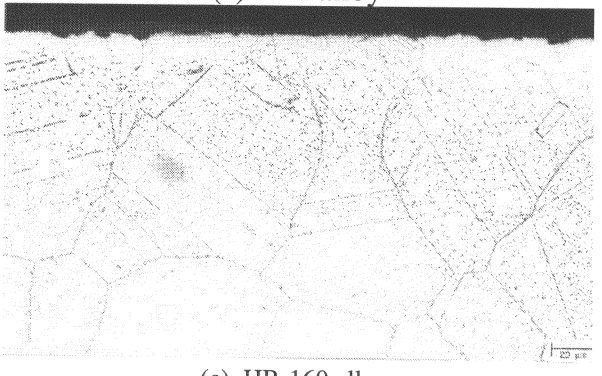

(c) HR-160 alloy

FIGURE 3. Metal Dusting Attack Observed in 601, 230 and HR-160 alloys After 10,000 h exposure.

DISCUSSION

Table 2 provides a ranking of the materials studied with respect to their resistance to metal dusting. Alloys with high iron contents such as HR-120 and 800H provide poor resistance because of their increased solubility of carbon. The fact that the susceptibility to metal dusting was not directly proportional to the iron content is interesting to note, and it indicates that minor

element effects can be important. The behavior exhibited by 214 alloy is also of note. Under the test conditions imposed of low oxygen partial pressure and low temperature, the formation of a protective aluminum oxide film on the alloy was inhibited by very low kinetics. Therefore, its improved performance over HR-120 and 800H alloys was the result of its much higher nickel content. A higher chromium content was also beneficial which can be seen if one compares the resistance of 214 alloy to that of 601 and 230 alloys which have higher chromium levels, but lower nickel contents. The better resistance of 230 alloy over 601 alloy, is interesting to ponder. The major difference between the two alloys was the presence or absence of molybdenum and tungsten. This can be explained on the basis of the type of carbide formed during the carburization process. Without these elements, only chromium-rich $M_{23}C_6$, M_7C_3 or Cr_3C_2 carbides would form. The subsequent depletion of chromium reduces the capability of the alloy to form a protective chromium oxide film to resist carbon ingress. With the addition of molybdenum and tungsten, a displacement of chromium becomes possible, e.g. $Cr_{21}Mo_2C_6$, and molybdenum- or tungsten-rich carbides can also form. This would be beneficial in terms of reducing the depletion of chromium so that a protective chromium oxide film can be formed. Such behavior has been observed previously in iron-based alloys (Strauss and Grabke 1998). In the case of HR-160 alloy, the effect of silicon in decreasing carburization attack is well known (Lai 1990). Its combination of nickel, chromium and silicon levels apparently make it an alloy very resistant to metal dusting.

CONCLUSIONS

1. HR-120 and 800H alloys, which contain high levels of iron, suffered severe metal dusting within the first 1000 hours exposure in the test environment.

2. Resistance to metal dusting increased with nickel content. However, chromium levels on the order of 22-23% at the expense of nickel were found to be extremely beneficial.

3. The presence of molybdenum and tungsten in 230 alloy was found to enhance metal dusting resistance.

4. The best resistance to metal dusting was found in the combination of nickel, chromium and silicon as represented by HR-160 alloy.

REFERENCES

Grabke, H. J., R. Krajak, E. M. Muller-Lorenz and S. Strauss, 1996, Materials and Corrosion, 47, p 495.

Grabke, H. J., E. M. Muller-Lorenz, J. Klower and D. C. Agarwal, 1998, Mat. Performance, 37, p. 58.

Lai, G. Y., 1990, High-Temperature Corrosion of Engineering Alloys, ASM International, Materials Park, OH, p. 58.

Strauss, S. and H. J. Grabke, 1998, Materials and Corrosion, 49, p 321.

EFFECTS OF CHLORINE CONTAMINATION ON THE KINETICS OF OXIDATION/CARBURIZATION OF CHROMIUM CONTAINING AUSTENITIC ALLOYS

M. MCNALLAN*, S. THONGTEM, Y.S. PARK, and J. TOMEI
University of Illinois at Chicago
Chicago, IL

ABSTRACT

Chromium containing austenitic alloys such as 310 stainless steel and 800H are very resistant to oxidation by either O_2 or CO_2 because they form a protective Cr_2O_3 layer. When they are exposed to CO_2 in the presence of chlorine contamination at temperatures between 1100 and 1200 K, the alloys are subject to rapid attack with formation of a porous oxide layer and an internally carburized zone. The attack in CO_2 is much more rapid than in O_2 containing the same level of chlorine contamination. The microstructure and kinetics of this attack are discussed in the context of metal dusting.

INTRODUCTION

Iron based alloys such as 310 Stainless steel and Alloy 800 are used in many applications where the oxidation resistance of low alloy steels is inadequate but cost considerations do not justify the use of nickel based alloys (Lai, 1990). These alloys contain sufficient nickel to stabilize the austenite phase, and obtain their oxidation resistance from the formation of protective Cr_2O_3 scales, which form by selective oxidation of the chromium that they contain (Kofstad, 1988). While the alloys have adequate resistance to oxidation in clean air, they may be attacked much more rapidly in environments that are contaminated with other species such as chlorine, and these alloys have been particularly susceptible to metal dusting.

Metal dusting is generally observed in environments with high activities of carbon. The mechanism of accelerated attack in metal dusting involves the penetration of carbon into the alloy where it forms internal carbides, disrupts the formation of a protective oxide layer and catalyzes formation of carbon deposits (Grabke et. al, 1998, Chun et. al, 1999,). A key step in metal dusting is the penetration of the carbon through any pre-existing oxide or other protective layer on the metal (Petkovic-Luton and Ramanarayan 1990). Chlorine forms volatile reaction products with most metals (Daniel and Rapp 1976). In mixed environments where oxygen is also present, the condensed corrosion products are generally oxides, but the morphology of the corrosion products is affected by the presence of volatile species during the oxidation (Maloney and McNallan 1985, Lee and McNallan 1990, Zahs et. al. 1999). Chlorine contamination during oxidation can lead to the formation of porous, non-protective oxides which grow at much higher rates than the dense protective oxide layers which form in clean oxygen (Lee and McNallan 1987).

Internal carburization of chromium containing alloys can be prevented if a protective oxide layer is present, as is usually the case when the oxygen potential is high and carbon potential is low. In the presence of chlorine, however, the non-protective morphology of the oxide may

*Corresponding author address: M. J. McNallan, CME Department, University of Illinois-Chicago, Chicago, IL 60607; e-mail: mcnallan@uic.edu.

permit carbon to penetrate to the scale-metal interface and affect the kinetics of corrosion in ways that are not observed in uncontaminated oxygen-carbon gas mixtures (McNallan et.al., 1993). This paper describes the results of experiments performed in gas mixtures containing oxygen, carbon, and chlorine in which alloy 800H is subject to accelerated attack.

APPARATUS AND PROCEDURE

The apparatus used in these experiments is shown schematically in Figure 1. It consists of a fused silica reaction tube closed at the top by a gas-tight water cooled cap. A fused silica tube in the center of the reaction tube serves both as a gas inlet line and a specimen holder. Metal coupons, in the form of rectangular sections of rolled sheet approximately 15mm x 15mm x 1.5 mm thick were suspended from fused silica hooks welded to the sides of the central tube. The alloy compositions are given in Table I. The specimens were all suspended at the same level in the tube to prevent cross contamination from volatile species.

Table I Alloy Compositions (weight %)

Alloy	Fe	C	Cr	Mn	Ni	Si	Ti
310 SS	Bal.	0.06	24.87	1.94	19.72	0.68	-
Alloy 800H	Bal.	0.01	20.90	0.92	30.74	0.38	0.43

The system was heated in a resistance heated furnace. Reactive gases of Ar, O_2, CO_2, and Cl_2, were prepared by blending gases from reagent grade cylinders. The gases flowed downward through the central tube and were reflected back upward past the test coupons before being exhausted from the furnace through a fume hood. In a typical experiment, four test coupons were exposed to an environment and were removed from the furnace a geometrically increasing intervals of time for characterization by mass change and evaluation of internal attack by optical or electron microscopy.

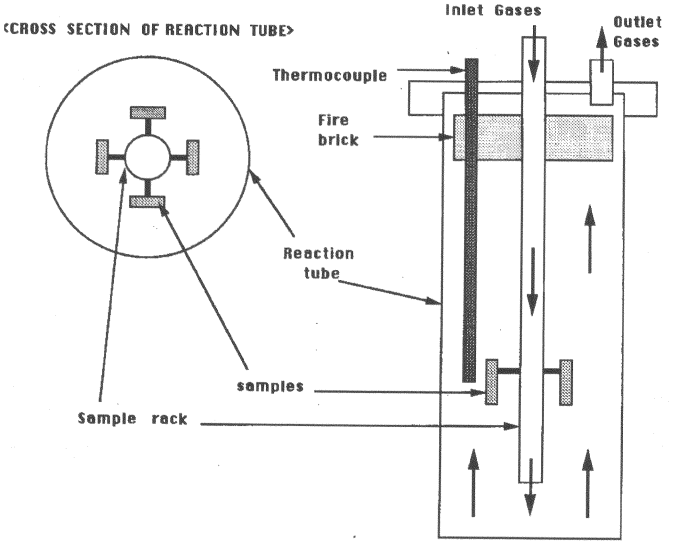

SCHEMATIC DIAGRAM OF THE HIGH TEMPERATURE REACTION TUBE.

Figure 1 Schematic diagram of the fused silica reaction tube for metal exposure to Ar-CO_2-Cl_2 gas mixtures.

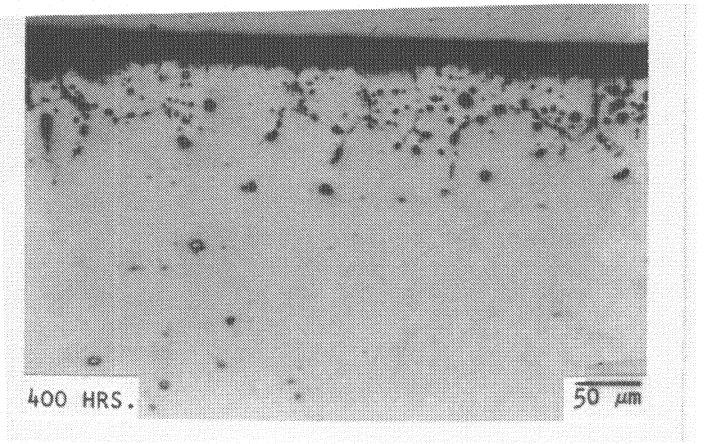

Figure 2 Optical micrograph of Internal attack in Alloy 800H after 400 hours exposure to Ar-20% O_2-0.25%Cl_2 by volume at 1200 K.

RESULTS AND DISCUSSION

Ar-O_2-Cl_2 Mixture

When austenitic alloys are exposed to gas mixtures containing both oxygen and chlorine, they are subject to both external attack and internal attack. The majority of the corrosion damage in such environments is due to internal attack occurring by formation of pores along grain boundaries near the exposed surface. Figure 2 shows an example of internal attack in Alloy 800H after 400 hours of exposure at 1200 K to a gas mixture of Ar-20% O_2-0.25%Cl_2 by volume. The average depth of internal attack after this period is approximately 60 micrometers.

Ar-CO_2-Cl_2 Mixture

Although the oxygen potential in CO_2 is high enough that a protective oxide scale is normally formed and replacement of O_2 by CO_2 would not be expected to result in accelerated oxidation of these alloys, very rapid internal attack occurs when the O_2 in the previous environment is replaced by CO_2. Figure 3 shows a micrograph of Alloy 800H after 200 hours of exposure to gas mixture of Ar-20% CO_2-0.25%Cl_2 by volume at 1200K. Although the general features of the corrosion are the same, with the internal attack characterized by pore formation along grain boundaries, the depth of the attack is much greater than in Figure 2, penetrating approximately 400 micrometers from the exposed surface. After 400 hours of exposure, the test specimen had been penetrated to the centerline in several locations. This acceleration of internal corrosion was attributable only to the addition of carbon to the gas mixture.

Further examination of the specimen exposed to this environment for 400 hours using scanning electron microscopy verified that the form of the internal attack was pore formation along grain boundaries as shown in Figure 4. Energy dispersive X-ray microanalysis showed that the composition of the metal in the vicinity of the pores was substantially altered due to selective removal of chromium. Figure 5 shows the relative intensity of Cr Kα radiation (Intensity of Cr Kα radiation/ (Fe Kα radiation + Ni Kα radiation + Cr Kα radiation)) as a function of distance from a pore located approximately 200 micrometers from the surface of Figure 4 along the points indicated by E, F, G, and H in Figure 4. There is a steep gradient in chromium content in the alloy as a function of distance from the pore. Farther from the metal surface, the chromium gradients were steeper and confined to smaller distances from the pores,

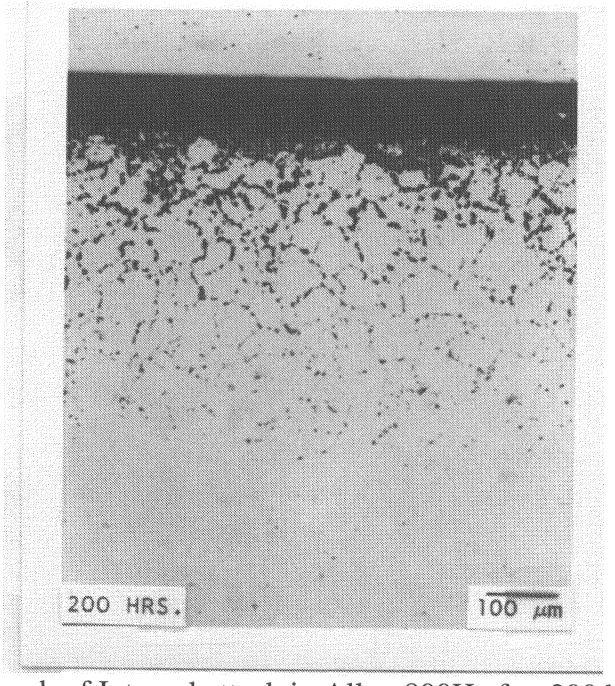

Figure 3 Optical micrograph of Internal attack in Alloy 800H after 200 hours exposure to Ar-20% CO_2-0.25%Cl_2 by volume at 1200 K.

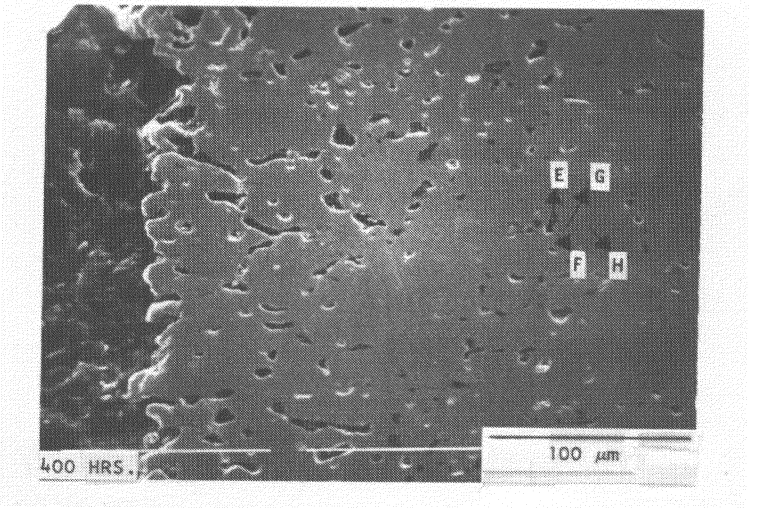

Figure 4 Scanning electron micrograph of Internal attack in Alloy 800H after 400 hours exposure to Ar-20% CO_2-0.25%Cl_2 by volume at 1200 K showing internal porosity.

while nearer the surface the gradients were shallower and there was a general depletion of chromium from the alloy.

Beyond the maximum depth of the internal attack, there was a decoration of grain boundary which was visible in scanning electron microscopy. Figure 6 is a high-resolution micrograph showing a grain boundary just beyond the maximum depth of penetration of the pores. The sample was lightly etched to bring out the features of the microstructure. The particles arrayed along the grain boundary are carbides, and energy dispersive X-ray

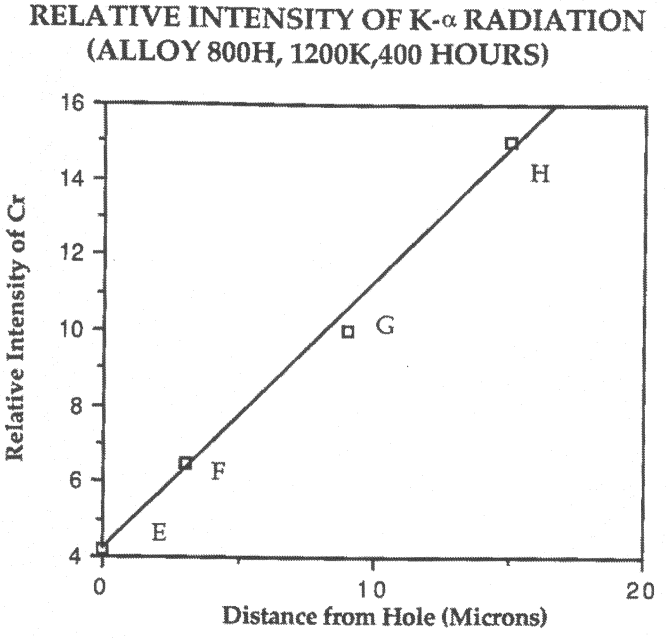

Figure 5 Relative intensity of Cr K□ radiation (Cr/(Cr+Fe+Ni)) determined by EDS at positions E, F, G, and H on Figure 4, demonstrating gradient in chromium content of metal as a function of distance from pore.

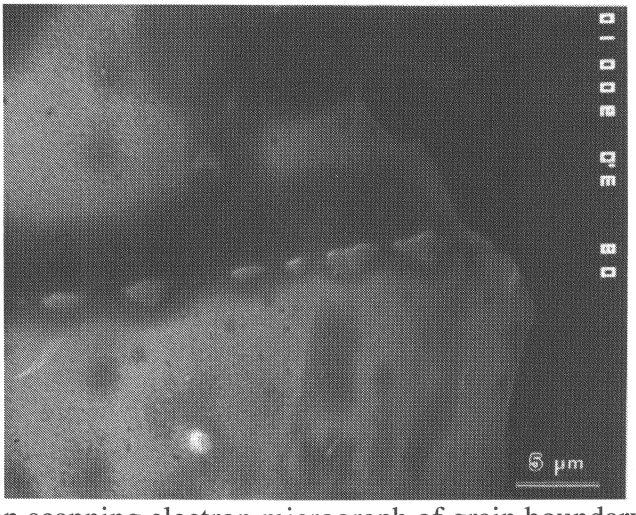

Figure 6 High resolution scanning electron micrograph of grain boundary just beyond the penetration depth of the deepest pores, showing precipitation of carbides along grain boundary ahead of internal attack.

spectroscopy indicated that they are enriched in chromium and titanium, the most stable carbide forming elements in the alloy.

The kinetic and microstructural features of the attack are consistent with a general mechanism of corrosion in which the chlorine and carbon act synergistically to accelerate the internal corrosion of the alloy. First, chlorine attacks and penetrates the normally protective Cr_2O_3 scale on the alloy allowing CO_2 to penetrate through pores from the gas-scale interface to the region of low oxygen potential at the scale-metal interface. CO_2 in this location reacts with

the metal, locally lowering the oxygen potential and raising the carbon potential. The carbon then dissolves into the metal phase, where it diffuses into the alloy, and reacts with chromium and titanium which precipitate as carbides on the grain boundaries. Subsequently, these carbides are selectively attacked by chlorine to form volatile chromium and titanium chlorides and redissolve the carbon in the metal. The volatilization of the chromium and titanium leaves pores along the grain boundaries which penetrate into the alloy.

The kinetics of the internal attack in both Ar-20% O_2-0.25%Cl_2 and Ar-20% CO_2-0.25%Cl_2 obey a parabolic rate equation as shown in Figure 7. The change from O_2 to CO_2 as the oxidizing species leads to an approximately 10 fold increase in the rate of penetration.

In general, a parabolic rate equation is associated with a corrosion process in which the rate is controlled by transport through a growing reaction product layer. For internal attack in chlorine containing environments, possible transport processes include diffusion of volatile chromium chlorides through the pores or diffusion of chromium metal in the alloy to the pore surfaces or the grain boundaries ahead of the pores. Gas phase and solid state diffusion processes can usually be distinguished as rate controlling steps because the apparent activation energy for diffusion in the gas phase is much lower than that for solid state diffusion. Therefore, if the experiment is repeated at a lower temperature, a larger decrease in the rate of corrosion would be expected if the rate is controlled by solid state diffusion than if it is controlled by gas phase diffusion.

When the experiment was repeated at 1100 K instead of 1200 K, the rate of penetration increased by approximately an additional factor of 10 as shown in Figure 7. The is contrary to the expectations for an activation controlled process, and indicates that there has been a change in reaction mechanism as temperature decreased. The phenomenon is explained by the microstructure shown in Figure 8, which demonstrates that the morphology of the internal attack

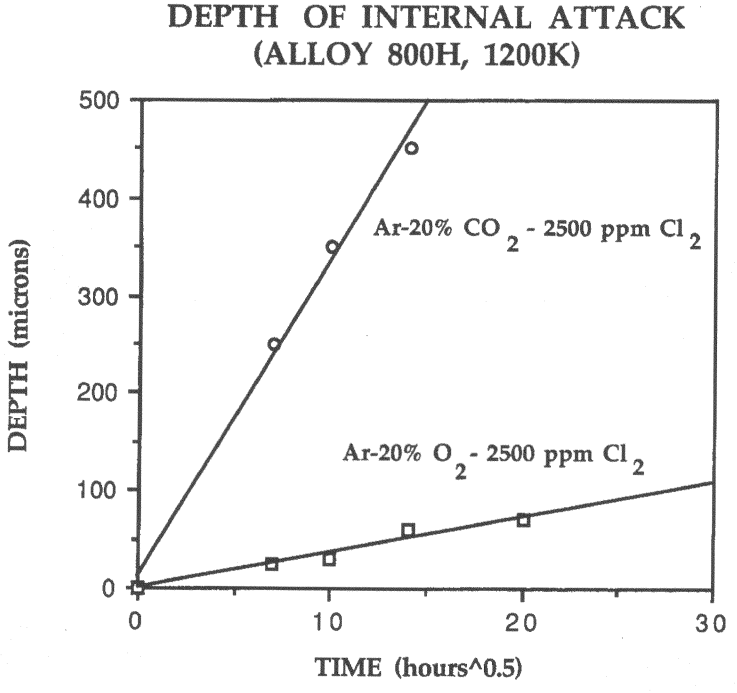

Figure 7 Parabolic plot of internal penetration in Alloy 800H exposed to gas mixtures containing Cl_2.

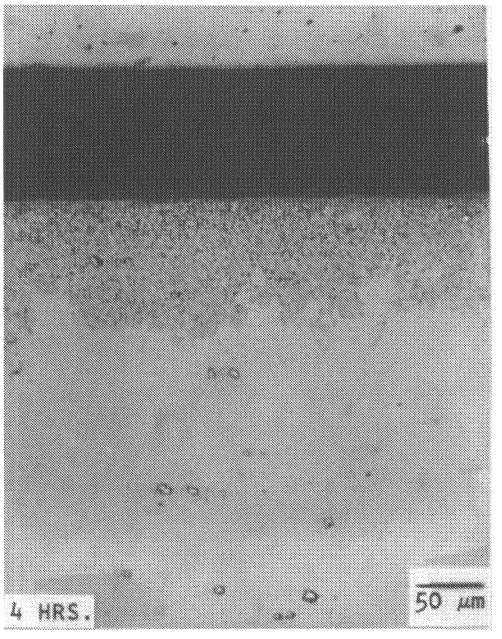

Figure 8 Optical micrograph of Internal attack in Alloy 800H after 4-hour exposure to Ar-20% CO_2-0.25%Cl_2 by volume at 1100 K.

has changed drastically when the temperature was reduced. The internal attack observed at 1100 K is on a much finer scale than that at 1200 K and is not confined to the grain boundaries. Because of the finer scale of the corrosion products, the diffusion times are reduced and the attack proceeds much more rapidly.

CONCLUSIONS

Chlorine contamination produces a strong acceleration in the rate of attack of austenitic chromia forming alloys in oxidizing and mixed oxidizing/carburizing environments. There is a strong synergistic effect when both chlorine and carbon are present. Chlorine accelerates internal carburization in CO_2 containing gases by leading to the formation of a porous, non-protective scale, which is penetrated by carbon containing gases. Carbon, as CO_2 in the gas mixture, accelerates the chlorination attack by concentrating the chromium as chromium carbides, where it is selectively chloridated. At the higher temperature investigated (1200 K), the carbides are concentrated along grain boundaries and the attack leads to deep pores penetrating along the grain boundaries. At the lower temperature investigated (1100K), the carbides are finer and distributed throughout the grains. This leads to rapid, general attack at the lower temperature.

REFERENCES

Chun, C.M., Mumford, J.D., Ramanarayan, T.A., 1999, "Mechanisms of Metal Dusting Corrosion of Iron," in *High Temperature Corrosion and Materials Chemistry, the Per Kofstad Memorial Symposium*, M. McNallan, E. Opila, T. Maruyama, T. Narita, Eds., Eletrochemical Society, Inc., Pennington NJ.

Daniel, P.L., Rapp, R.A. "High Temperature Corrosion by Halogens," in *Advances in Corrosion Science and Technology*, M.G. Fontana and R.W. Staehle, Eds., 5, 55-176.

Grabke, H.J., Muller-Lorenz, E.M., Klower, J., Agarwal, D.C., 1998, "Metal Dusting of Nickel-Based Alloys, *Materials Performance*, 37, No 7, 58-63.

Kofstad, P., 1988, *High Temperature Corrosion*, Elsevier Applied Science, Essex, UK.

Lai, G.Y., 1990, *High Temperature Corrosion of Engineering Alloys*, ASM International, Materials Park, OH.

Lee, S.Y., McNallan, M.J., 1990. "Inhibition of Oxidation of Iron in Chlorine Containing Environments at 1100 K and 1200 K," *Journal of the Electrochemical Society*, 137, 472-479.

Lee, Y.Y., McNallan, M.J., 1987, "Ignition of Nickel in Environments Containing Oxygen and Chlorine," *Metallurgical Transactions*, 18A, 1099-1107.

Maloney, M.J., McNallan, M.J., 1985, "The Effect of Chlorine on the Kinetics of Oxidation of Cobalt in Environments Containing 0.5 Atmosphere of Oxygen Between 900 and 1200 K," *Metallurgical Transactions*, 16B, 751-761.

McNallan, M.J., Thongtem, S., Liu, J.C., Park, Y.S., Shyu, P., 1993, "Corrosion of Chromium Containing Alloys in Non-Steady State Environments Containing Oxygen, Carbon, and Chlorine," *Journal de Physique IV*, 3, 143-150.

Petkovic-Luton, R., Ramanarayanan, T.A., 1990, "Mixed Oxidant Attack of High Temperature Alloys in Carbon and Oxygen-Containing Environments," *Oxidation of Metals*, 34, 381-400.

Zahs, A., Spiegel, M., Grabke, H.J., 1999, "The Influence of Alloying Elements on the Chlorine Induced High Temperature Corrosion of Fe-Cr Alloys in Oxidizing Atmospheres," *Materials and Corrosion*, 50, 561-578.

ANALYSIS OF METAL DUSTING IN WASTE HEAT BOILER

K. NATESAN*, A. PUROHIT and D. L. RINK
Argonne National Laboratory
Argonne, IL
and
W. J. SALOT
Honeywell International
Hopewell, VA

ABSTRACT

Severe metal dusting has been observed in ammonia plant primary waste heat boilers (WHBs), which are located at the secondary reformer outlet. These WHBs typically operated at a pressure of 31 atm with CO/CO_2 and H_2/H_2O ratios of 1.75 and 1.02, respectively. After service lives of more than 9 years, portions of both the 800HT shroud, covering the refractory shell liner, and of the RA-330 tube bundle baffle support rods, in one WHB were missing completely. At that time, the shroud was replaced with Alloy 800HT, except Inconel alloy 601 in the top two courses, and the tube bundle was replaced with a rebuilt spare, identical to the original.

INTRODUCTION AND BACKGROUND

The phenomenon of severe metal dusting – through the full thickness of affected components – was observed in the two primary waste heat boilers (WHBs) of an ammonia-producing plant (Hopewell, VA). This plant is owned and operated by Honeywell International. Its capacity now exceeds 1350 mt/d of ammonia, a 50% increase over its original design capacity. The plant was designed and constructed by M. W. Kellogg Company, and was commissioned in 1967.

For the Hopewell ammonia plant, observed metal dusting has been limited to the process outlet end (top end) of the primary waste heat boilers, and appears to have increased with production rates. The Hopewell primary WHB shell liners and tube bundles have always been replaced in less than 10 years and 9 years, respectively, usually based on scheduled inspections rather than shutdown-forcing shell or tube ruptures. At the end of these periods, portions of the 800HT shrouds were no longer capable of retaining the refractory liner, resulting in a risk of shell rupture.

This paper describes observations and analysis of metal dusting of an 800HT shroud after 9 years and 2 months of service at Hopewell. The RA-330 baffle support rods in the associated 9 year old tube bundle suffered equally severe metal dusting, but the corresponding 1.25 Cr-0.5 Mo ferritic steel tubes did not suffer any metal dusting. The tubes, cooled by boiler feed water, operate at much lower metal temperatures. The present paper discusses the results obtained from the failure analyses of the shroud only.

*Corresponding author address: K. Natesan, Argonne National Laboratory, 9700 South Cass Avenue, Argonne, IL 60439; e-mail: natesan@anl.gov

DESCRIPTION OF THE OPERATING CONDITIONS

The WHB of the Hopewell plant is schematically shown on Figure 1. The relevant operational parameters are stated in Table 1. The incoming gas was at a nominal pressure of 31 atm (455 psig) and a temperature of about 1,790 ± 40°F (978 ± 22°C), while the gas outlet temperature was 890 ± 30°F (477 ±17°C). The composition of the input gas was (in vol.%) 8.5 CO-4.8 CO_2-36.3 H_2-0.14 CH_4-14.5N_2-35.6H_2O.

The phenomenon of metal dusting was observed in all regions of the shroud operating in the temperature range between about 477°C and 642°C. The temperature where the most severe metal dusting occurred was about 477°C in and near the outlet nozzle. Calculated thermodynamic equilibrium values, based on the aforementioned gas composition and temperature, for Cr-C-O and Fe-C-O at 477°C are shown in Figures 2 and 3, respectively. The calculated equilibrium values for 677°C, where no metal dusting was noted, are shown in Figures 4 and 5. The operating envelopes for Cr and Fe are outlined by the heavy lines in Figures 2 through 5.

SPECIMEN HISTORY AND ORIENTATION

Specimen sections from the shroud were obtained after 9 years and 2 months of service in the Hopewell ammonia plant. Some of these sections came from locations near the occurrence of maximum metal dusting. Average operational temperature at this location was estimated to be about 500°C. In this paper we report the findings of the metal dusting of the shroud material only because metal dusting could have resulted in a breach of the shell at the outlet nozzle.

The shroud was made of 800HT plate of nominal 0.25-in. (6.35-mm) thickness. The weld material for the shroud construction was Inconel 625 alloy. The nominal composition of 800HT is (in wt%) 20Cr-32Ni-0.3 Si-0.3 Al-0.4 Ti-Bal Fe. 800HT was chosen many years before because of its high temperature strength and resistance to oxidation. Metal dusting had not been anticipated. However, in recent years at high operating rates, unexpectedly severe metal dusting of 9+ year old 800HT was found in both primary WHBs. Fortunately, it was detected in time to prevent a serious shell failure.

The condition of the baffle support rods above the top baffle in the tube bundle is shown in the photomacrograph of Figure 6. Metal dusting almost completely destroyed the rods in this location.

Optical macrographs of the as-received and as-sectioned specimens from the shroud are shown in Figures 7 and 8. The locations marked "A" and "C" in Figure 7 show where the metal dusting was the severest for the shroud. Figure 8 shows the same locations in side/elevation view. The razor sharp section ("C" in Figure 7) is quite apparent in Figure 8. The specimen sections in Figures 7 and 8 were investigated through a variety of analytical techniques, and the results obtained from this investigation are reported in the next section.

The shroud was fabricated using Inconel 625 as the weldment filler material. It is not known whether the welds were made by the tungsten inert-gas or the shielded metal arc process. The welds and the heat-affected zone were also analyzed during this investigation. The nomenclature adapted for the orientation of individual metallographic sub-sections is shown in Figure 9. "Inside" surface refers to the inside of the WHB. The design and the construction of

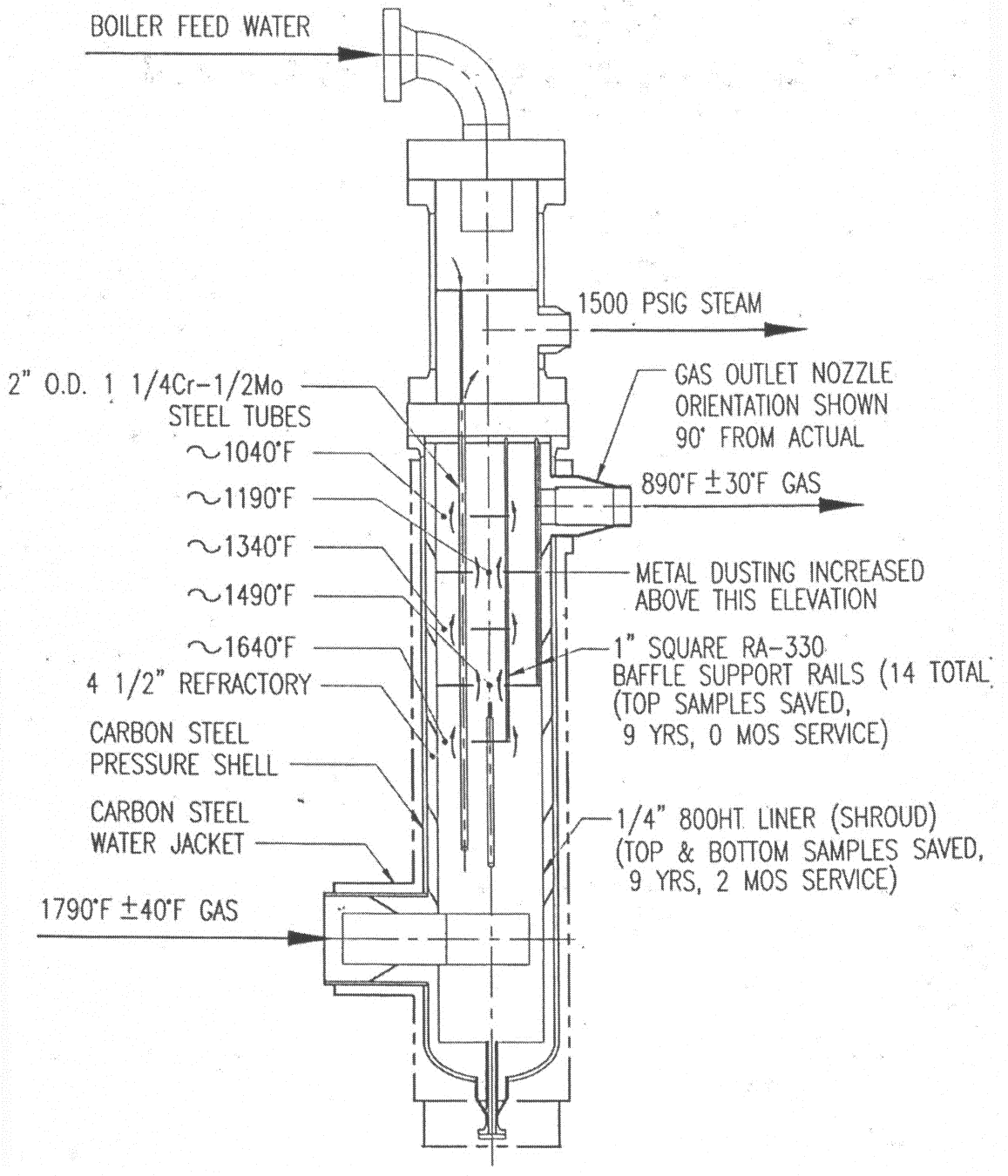

FIGURE 1 Schematic of WHB waste heat boiler of the ammonia generating plant located at Hopewell, VA.

the WHB are such that the full impact of the flowing gas is felt on the "inside" surface. The boundary layer on the as seen in Figure 10(a), the inside and outside surfaces were found to have four distinct regions, marked A, B, C, D and E, F, G, H, respectively. The chemical details inside surface is minimal, and therefore, supply of carbon is unlimited. On the other hand, for the "outside" surface, the gas is nearly stagnant, reducing the availability of carbon and oxygen.

Table 1 Operational parametres for the waste-heat boiler

Waste Heat Boiler Gas Parameters
Inlet Gas T = 1790 ± 40°F (≈ 975°C)
Outlet Gas T = 890 ± 30°F (≈ 475°C)
Steam Outlet at 1500 psig, 890°F
Metal Dusting Temperature Range
890°F > T <1200°F (475°C >T < 650°C)
System Overall Pressure 455 psig (26 atm)

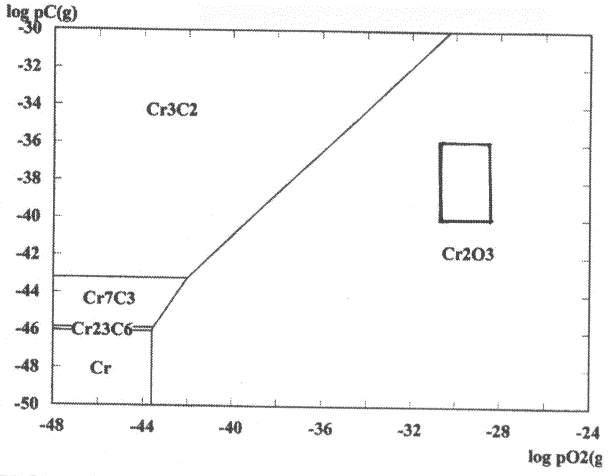

FIGURE 2 Equilibrium for Cr-C-O system at 477°C. The heavy lines indicate the operating envelope for the plant.

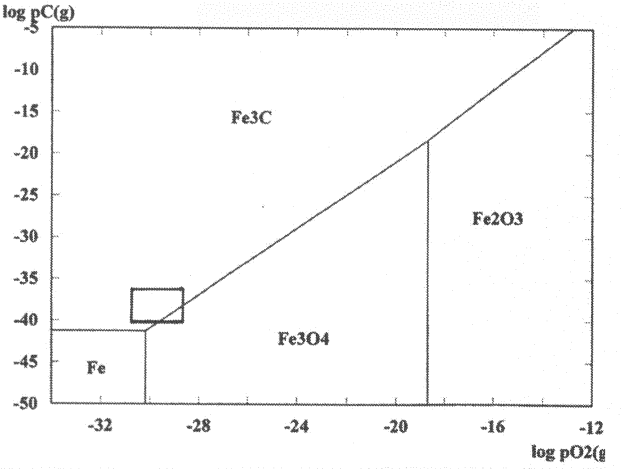

FIGURE 3 Equilibrium for Fe-C-O system at 477°C. The heavy lines indicate the operating envelope for the plant.

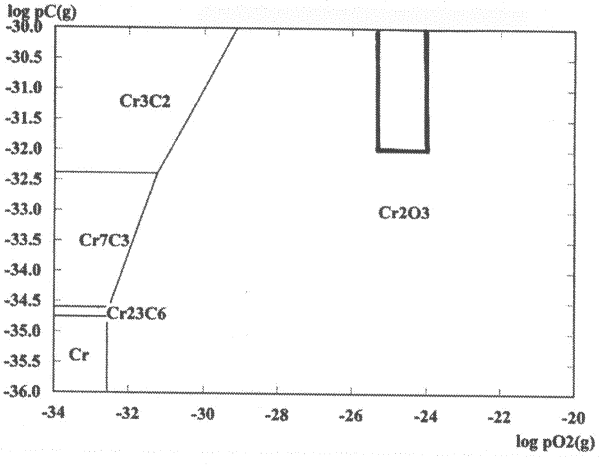

FIGURE 4 Equilibrium for Cr-C-O system at 677°C. The heavy lines indicate the operating envelope for the plant.

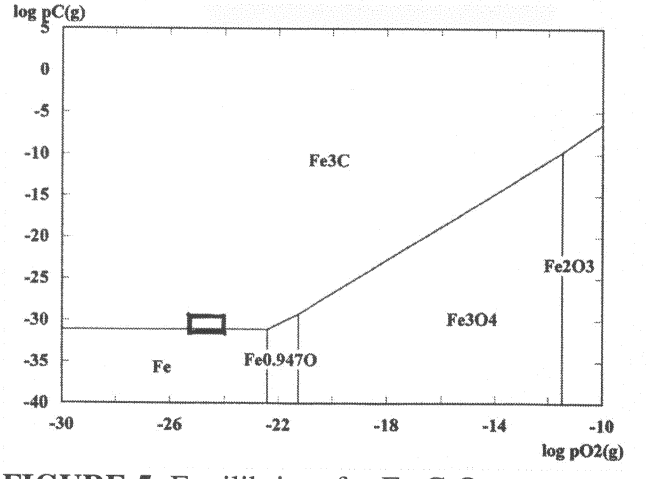

FIGURE 5 Equilibrium for Fe-C-O system at 677°C. The heavy lines indicate the operating envelope for the plant.

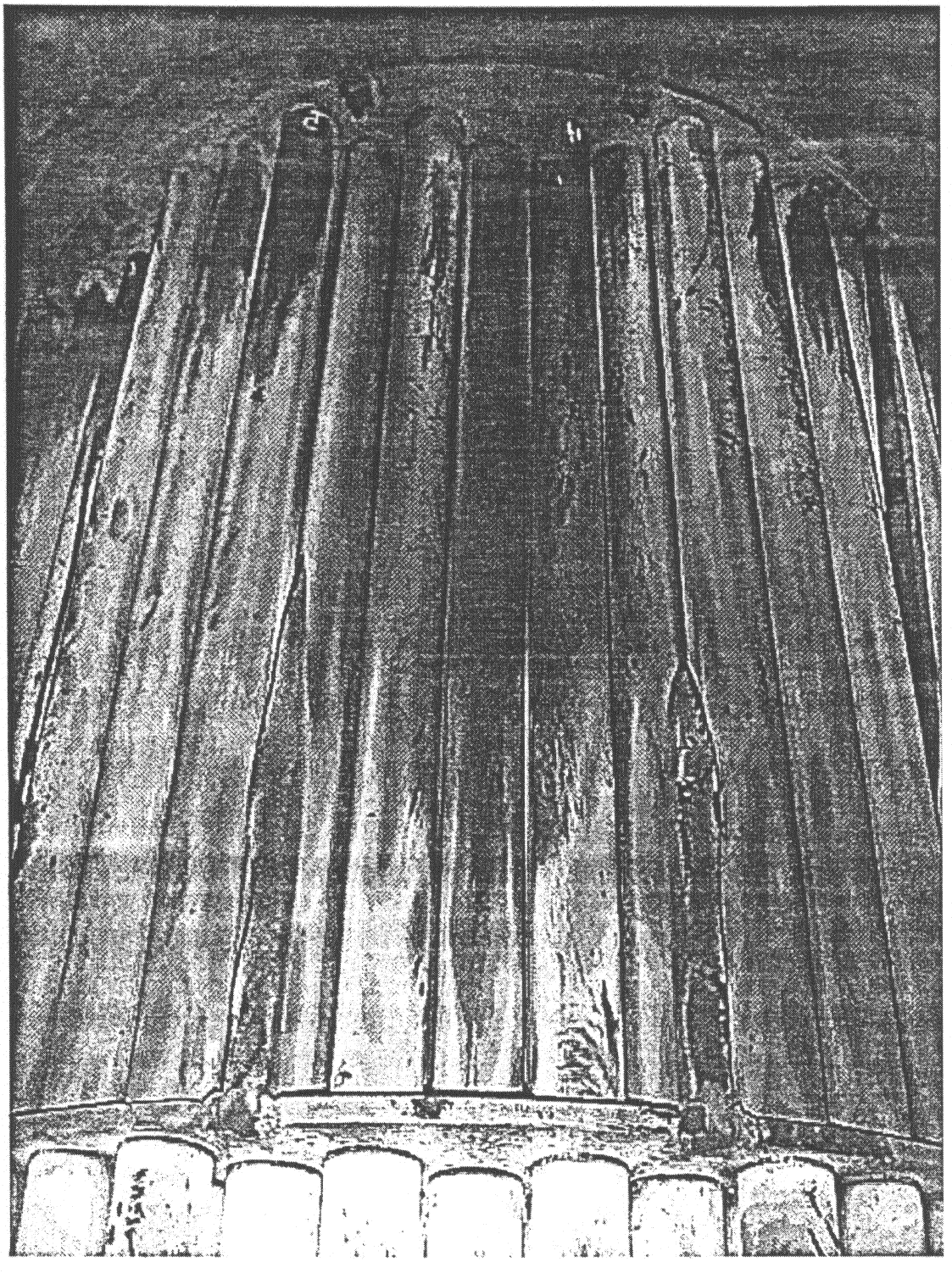

FIGURE 6 Photomacrograph of WHB tubes. The tube alloy is 1 1/4 Cr-1/2 Mo Ferritic steel. The location of severe metal dusting is indicated by letters MD.

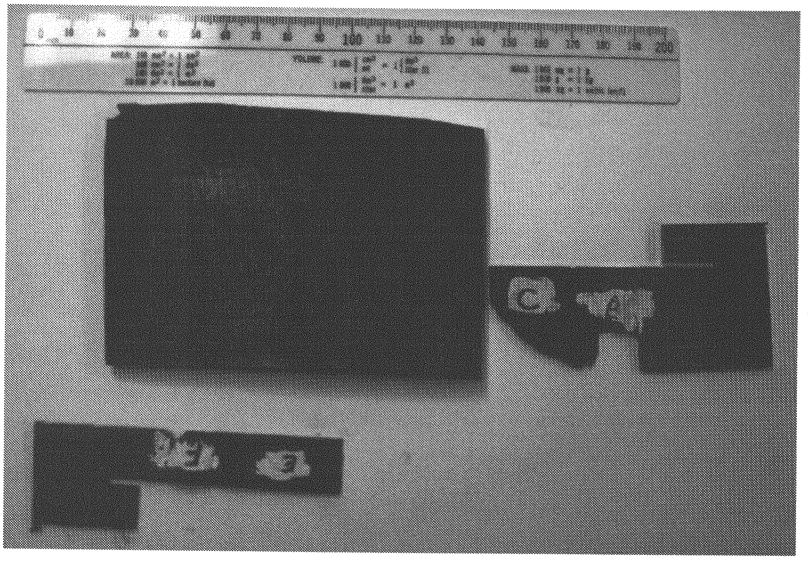

FIGURE 7. Photomacrograph (plan view) of the WHB shroud section where the severest level of metal dusting was observed. WHB shroud material: Alloy 800HT. Locations marked "C" and "A" are the spots where the 0.25-in. metal was wasted away in 9 years and 2 months of service. Location "A" and "F" are at the weldment region. Weld metal: Alloy Inconel 625.

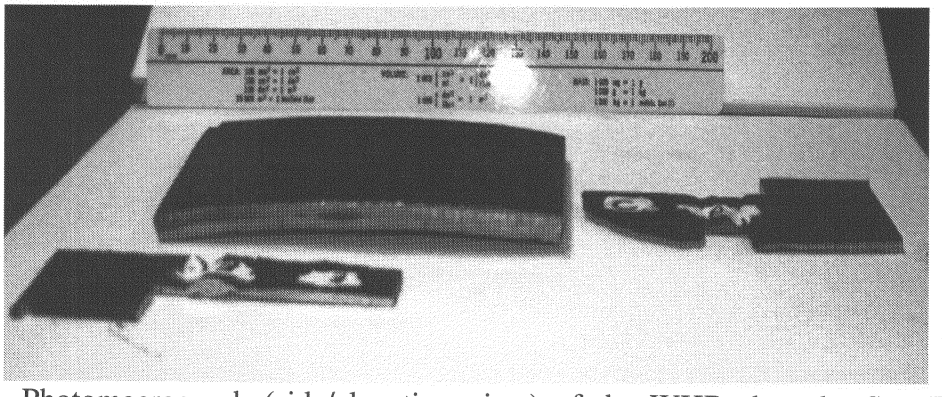

FIGURE 8 Photomacrograph (side/elevation view) of the WHB shroud. See Figure 7 for additional details.

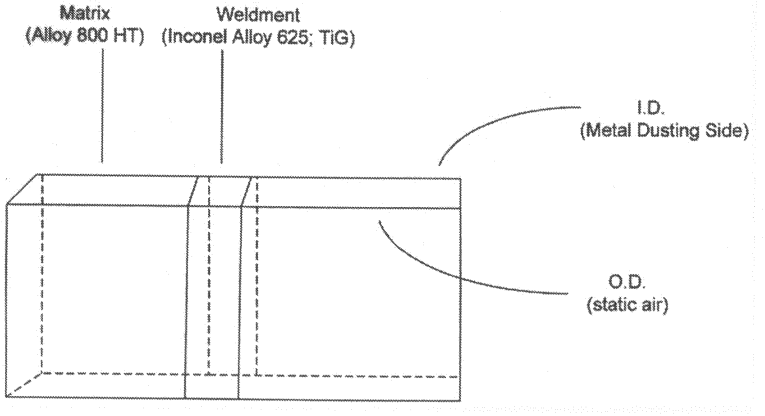

FIGURE 9 Nomenclature for metallographic sections.

RESULTS

Optical Microscopy

Typical and representative optical micrographs of the specimens are presented in this section. Optical microscopy was performed using the standard Nomarski interference contrast technique.

Figure 10 presents typical low-magnification micrographs for a cross section of the shroud (800HT). The inside surface is at the bottom of both figures, while the outside surface is at the top. Even in these low-magnification photomicrographs, the different morphology of the corrosion layer is apparent. The outermost layer on the inside surface is dark/black, and it is about an order of magnitude thicker than the corresponding bright/white layer on the outside surface. The section shown in Figure 10 is from an area near where the corrosion/metal wastage was maximal. The section thickness in these figures is about 1.3 mm, which is 20% of the original thickness of 6.35 mm. As noted earlier, the inside surface is quite different from the outside surface, despite the temperature being nearly the same. The reason is the gas composition/environment. On the outside, the gas is nearly stagnant, while the inside surface is exposed to the full impact of the process gas; the results are presented in Sec. 5.3.

The thin bright layer on the outside surface - ≈50 μm in thickness – has many vertical cracks. These vertical cracks are more clearly seen in slightly higher magnification micrographs [Figures 11 and 12]. Figures 13 through 16 are from the same region, at a yet higher magnification and under "false color contrast." This false color illumination/contrast technique is quite useful in identifying various phases and layers that might not be apparent under the standard grey/black contrast. Similar micrographs of the inside surface region are shown in Figures 17(a) - (c) and 18(a) - (d). Interestingly, Figures 17 and 18 show two distinct layers within the outermost layer. The black and white contrast technique would not be able to reveal such potentially important differences. The layers marked "D" (for the inside surface) and "H" (for the outside surface) are the grain boundary penetration region.

The oxide morphology of the outside surface of the weld region is shown in Figures 19 through 22, while that on the inside surface is shown in Figures 23 through 25. As noted earlier and as seen in these photomicrographs, the corrosion/oxidation/carburization rate for the weld is greatly reduced – by more than an order of magnitude, on the corresponding surface – as compared with the basic corrosion rate of 800HT. The inside oxide layer thickness is about 100 μm, while that on the outside surface is less than 20 μm.

Scanning Electron Microscopy

Detailed analyses using scanning electron microscopy (SEM) and energy dispersive x-ray analyses (EDAX) were performed on many sub-sections of the samples. These samples were selected from the location where metal dusting was most pronounced – where T = about 500C – as well as from samples located at a lower elevation, where metal dusting was not so pronounced.

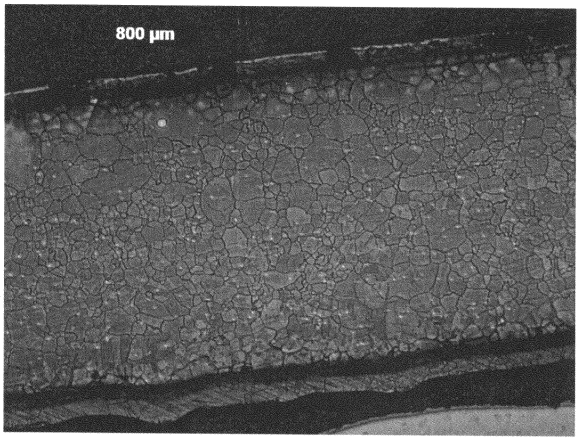

FIGURE 10(a) Low magnification photomicrograph showing the entire cross section of the WHB shroud (Alloy 800HT). Inside surface is at the bottom of the micrograph.

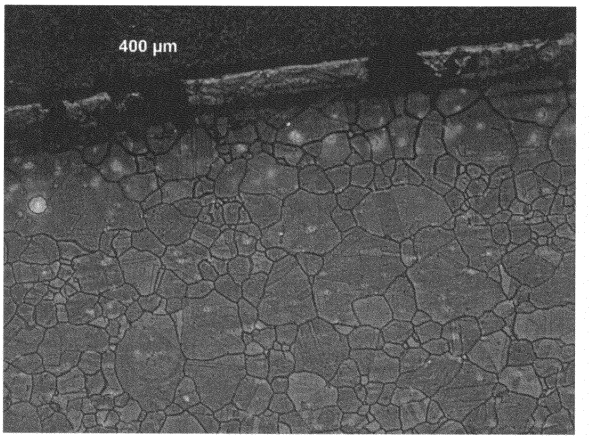

FIGURE 10(b) Detail of the outer surface [from Figure 10(a)].

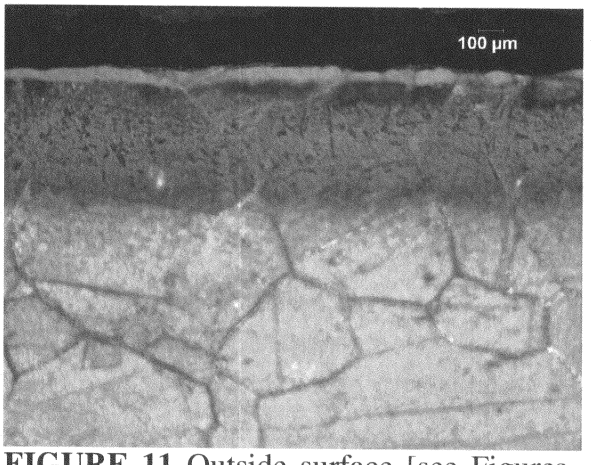

FIGURE 11 Outside surface [see Figures 10(a) and 10(b)].

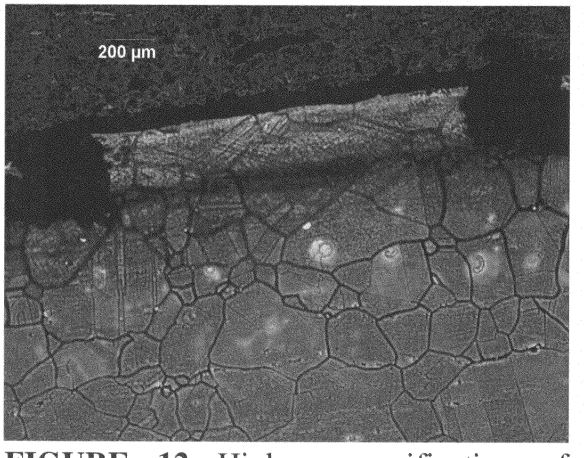

FIGURE 12 Higher magnification of Figure 10(b).

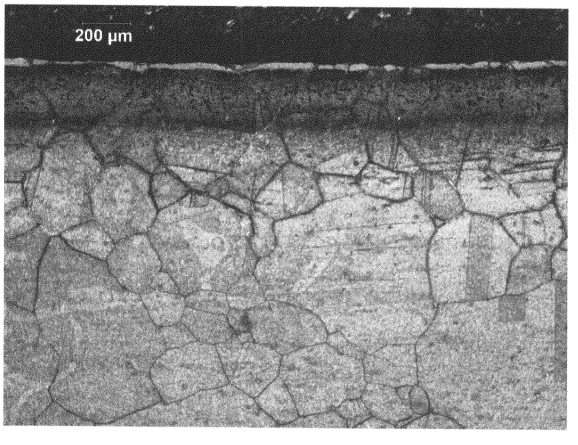

FIGURE 13 Outside surface.

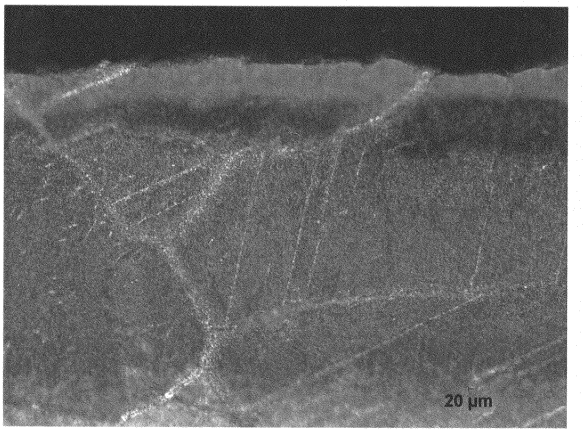

FIGURE 14 Outside surface; higher magnification in false color contrast.

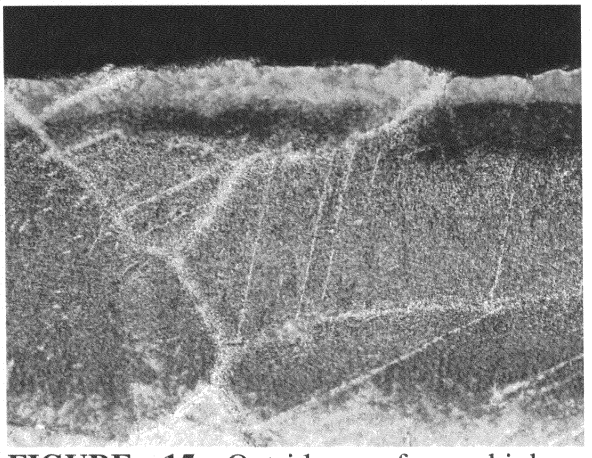

FIGURE 15 Outside surface; higher magnification in false color contrast.

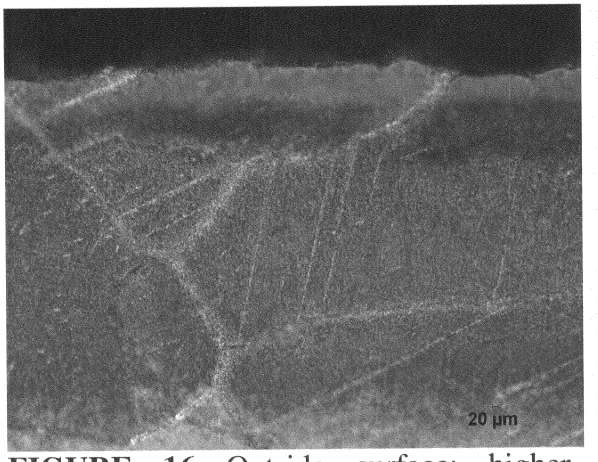

FIGURE 16 Outside surface; higher magnification in false color contrast.

FIGURE 17(a) Outside surface; false color contrast.

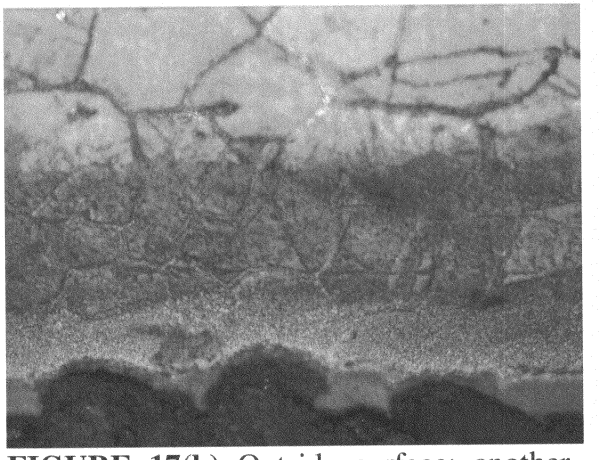

FIGURE 17(b) Outside surface; another false color contrast.

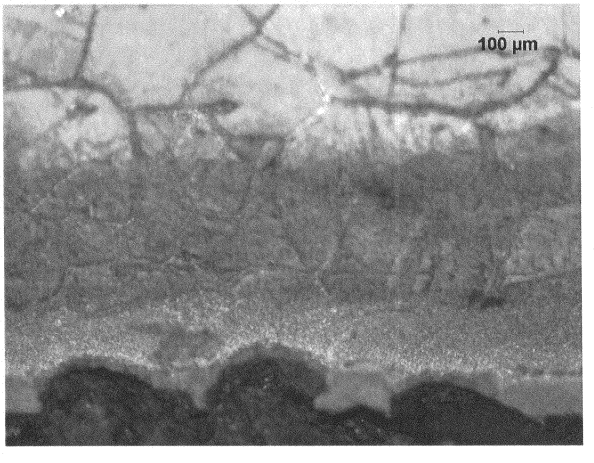

FIGURE 17(c) Outside surface; third false color contrast.

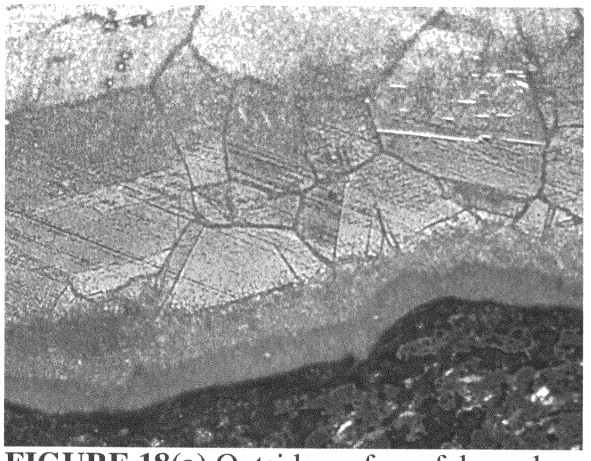

FIGURE 18(a) Outside surface; false color contrast.

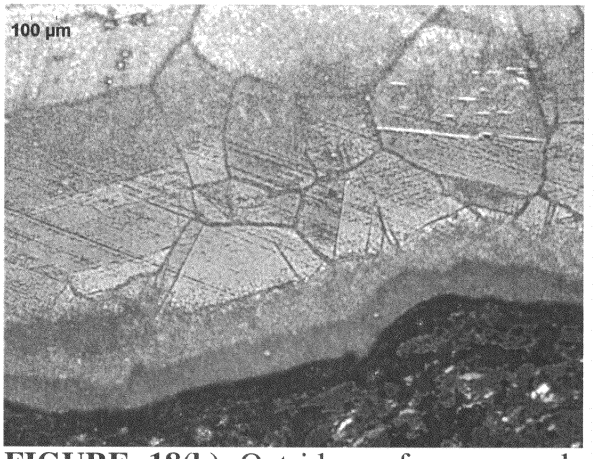

FIGURE 18(b) Outside surface; second false color contrast.

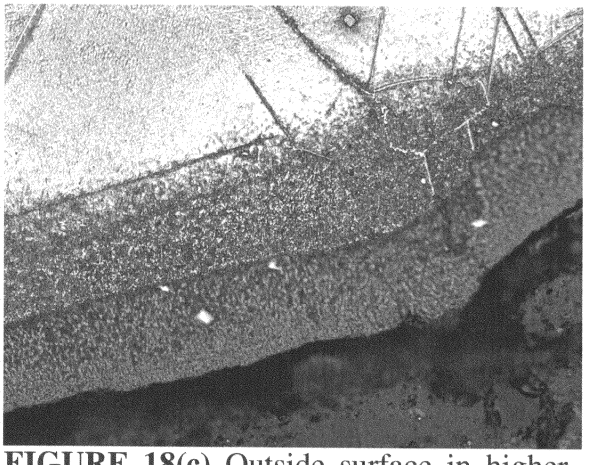

FIGURE 18(c) Outside surface in higher magnification; false color contrast.

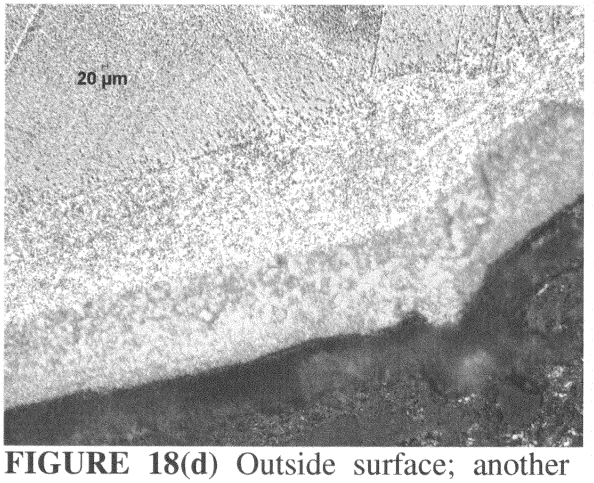

FIGURE 18(d) Outside surface; another false color contrast.

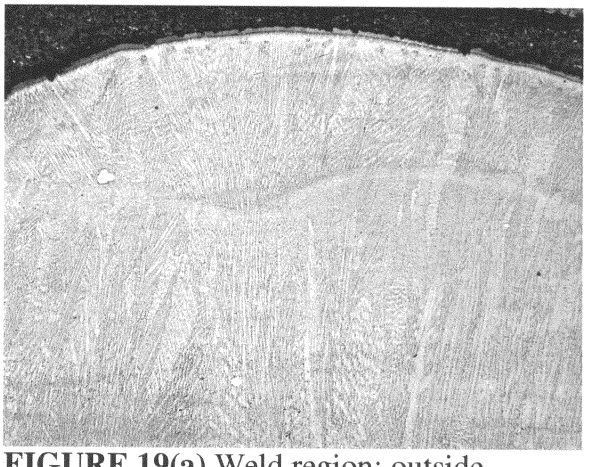

FIGURE 19(a) Weld region; outside surface.

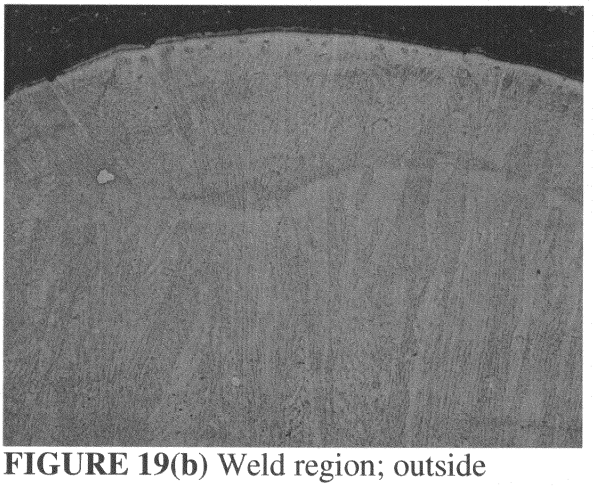

FIGURE 19(b) Weld region; outside surface; false color contrast.

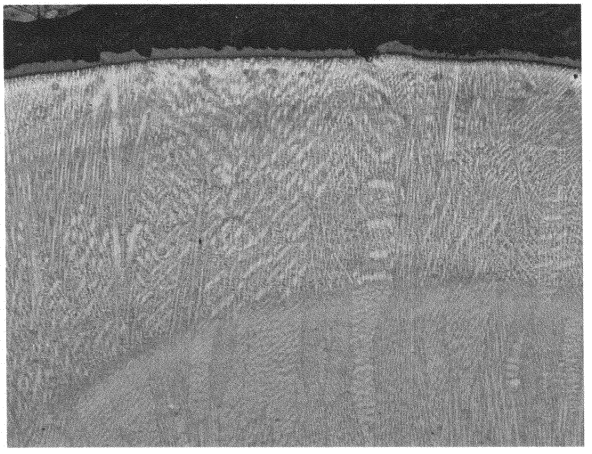

FIGURE 20(a) Weld region; outside surface.

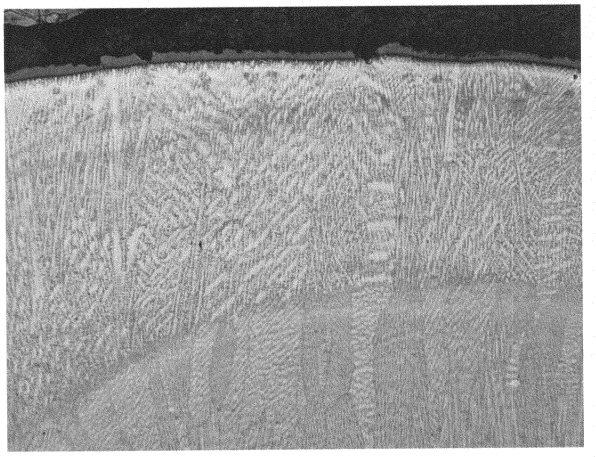

FIGURE 20(b) Weld region; outside surface; false color contrast.

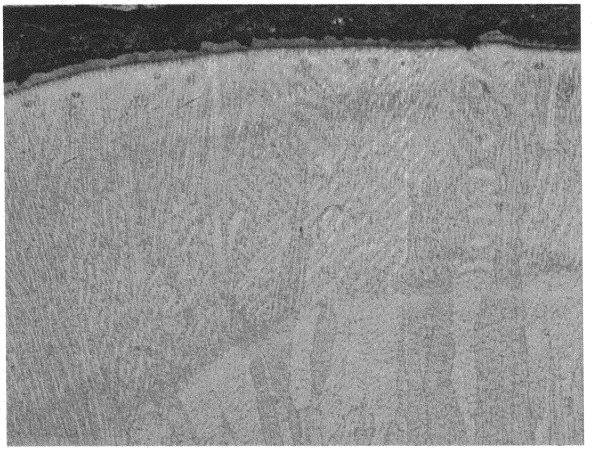

FIGURE 20(c) Weld region; outside surface; another false color contrast.

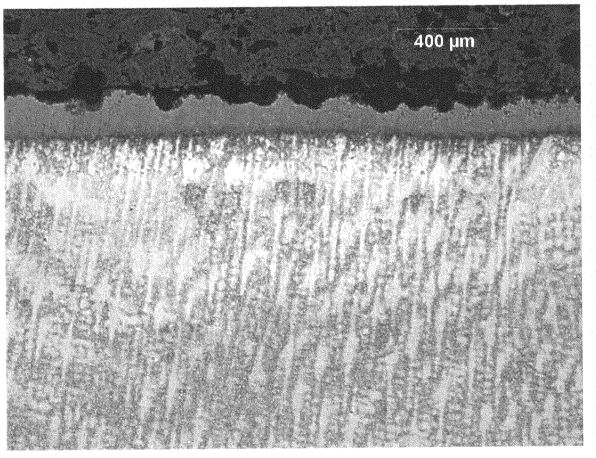

FIGURE 21(a) Weld region in higher magnification; outside surface.

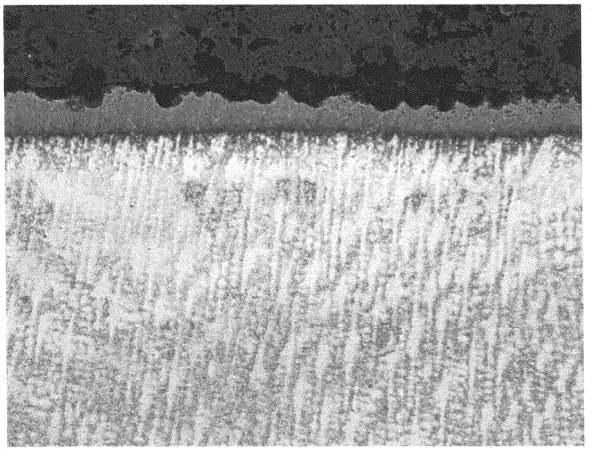

FIGURE 21(b) Weld region; outside surface; false color contrast.

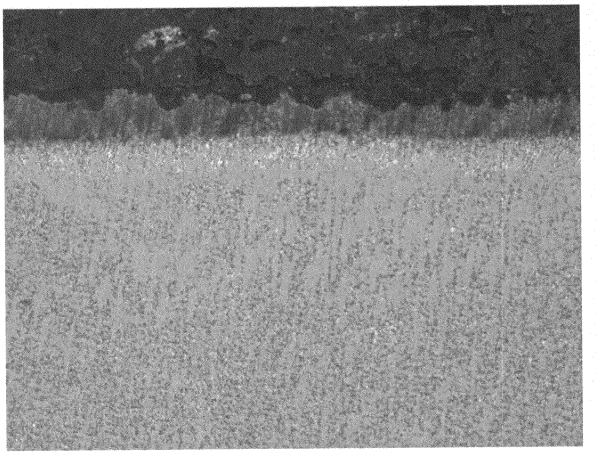

FIGURE 21(c) Weld region; outside surface; another false color contrast.

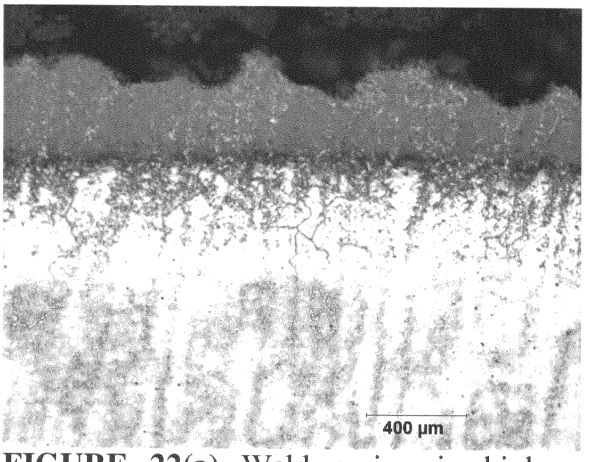

FIGURE 22(a) Weld region in higher magnification; outside surface.

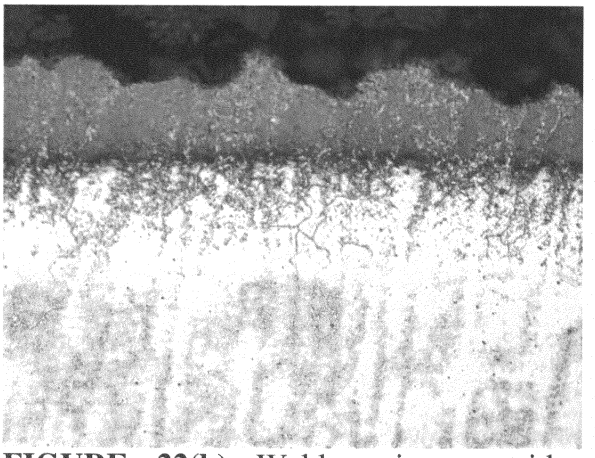

FIGURE 22(b) Weld region; outside surface; false color contrast.

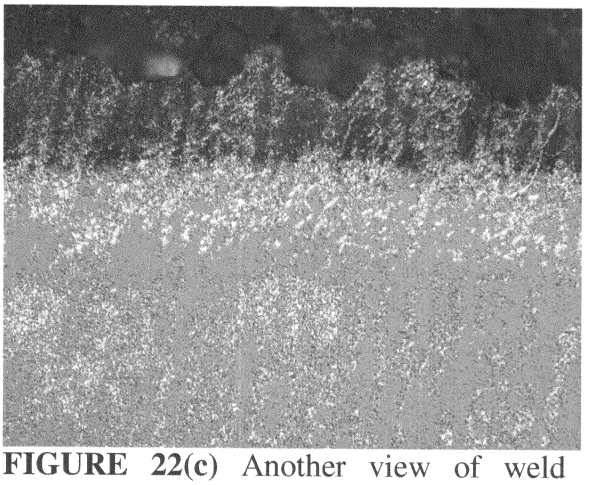

FIGURE 22(c) Another view of weld region; outside surface; false color contrast.

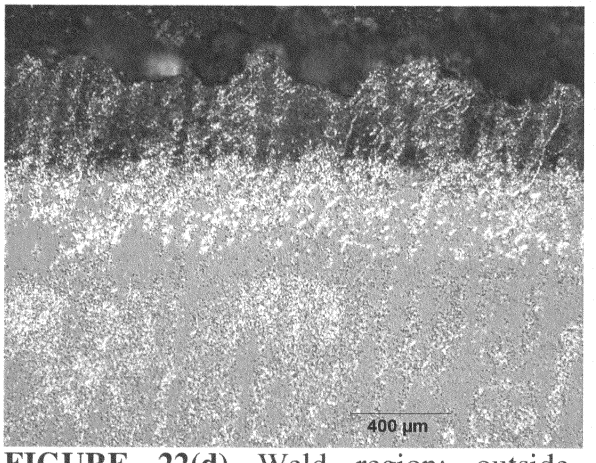

FIGURE 22(d) Weld region; outside surface; another false color contrast

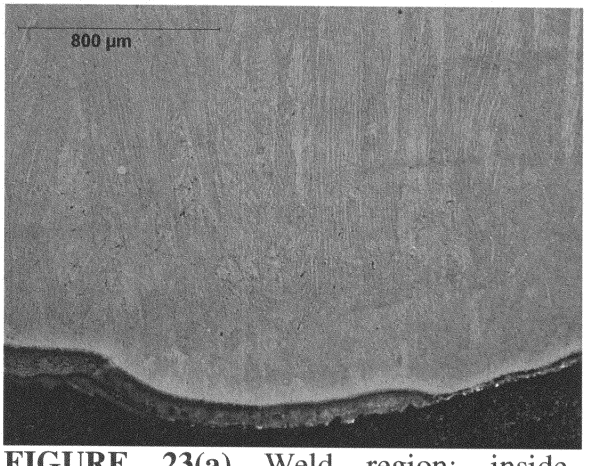

FIGURE 23(a) Weld region; inside surface.

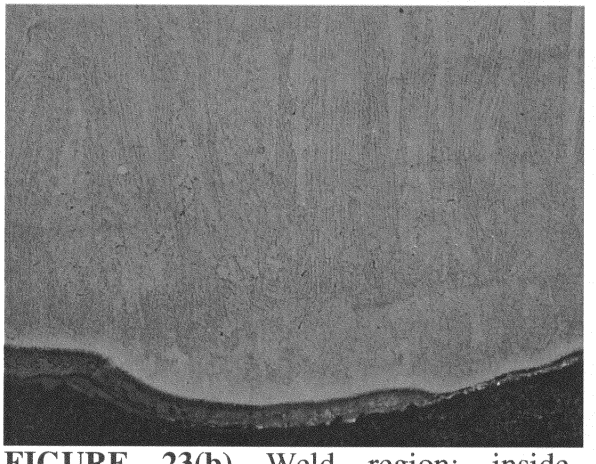

FIGURE 23(b) Weld region; inside surface; false color contrast.

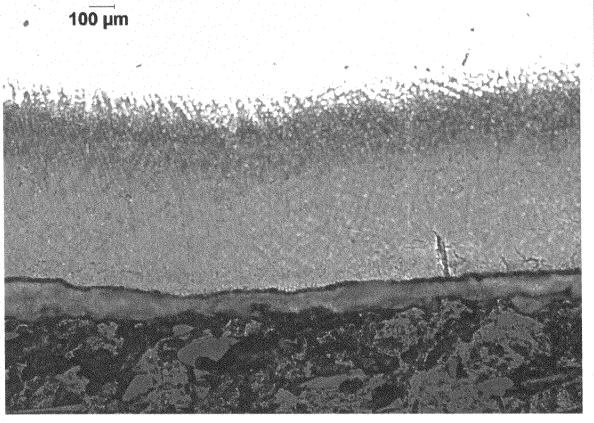

FIGURE 24(a) Weld region; inside surface.

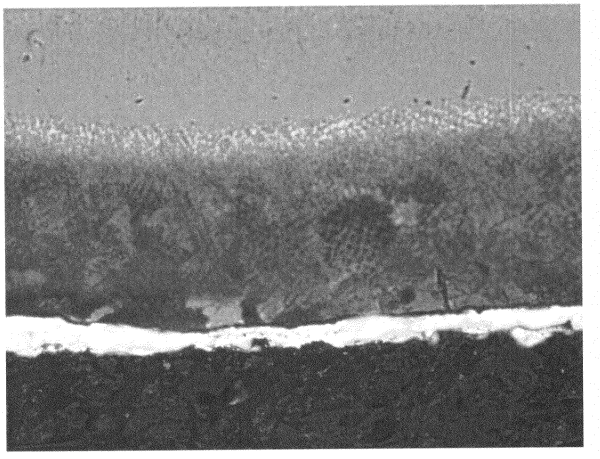

FIGURE 24(b) Weld region; inside surface; false color contrast.

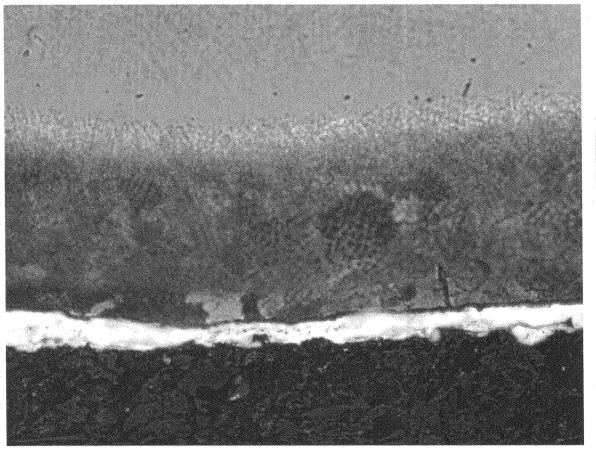

FIGURE 24(c) Weld region; inside surface; second false color contrast.

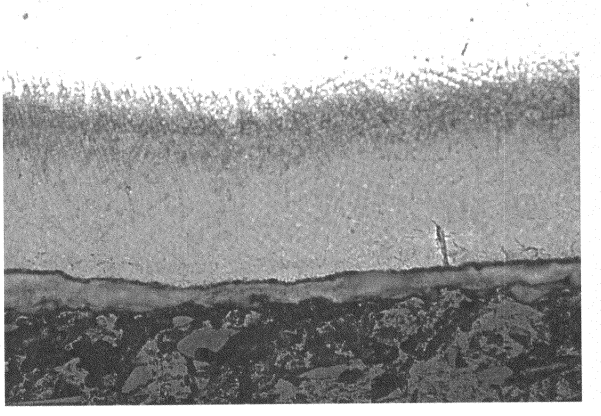

FIGURE 24(d) Weld region; inside surface; third false color contrast.

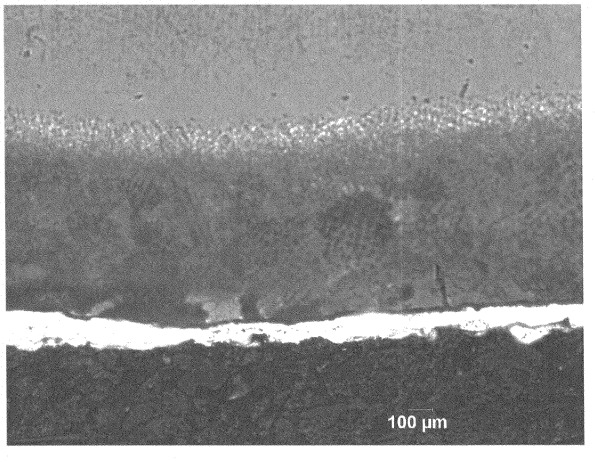

FIGURE 24(e) Weld region; inside surface; fourth false color contrast.

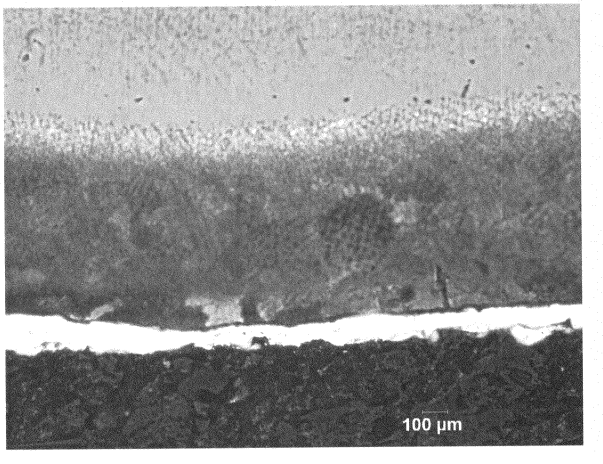

FIGURE 24(f) Weld region; inside surface; fifth false color contrast.

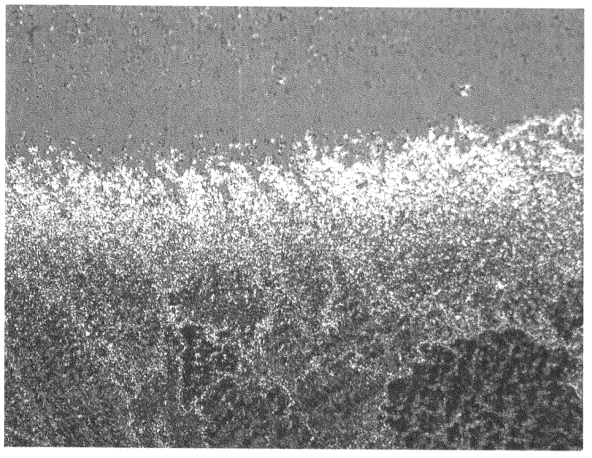

FIGURE 25(a) Weld region; inside surface.

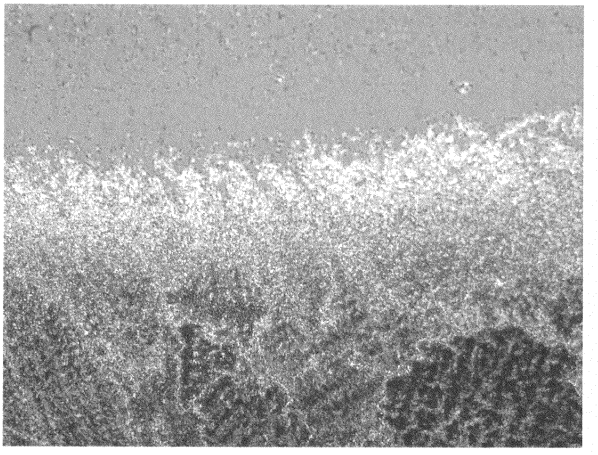

FIGURE 25(b) Weld region; inside surface; false color contrast.

FIGURE 26 Low magnification SEM image of the weldment region. Shroud material (800HT) is on the left side.

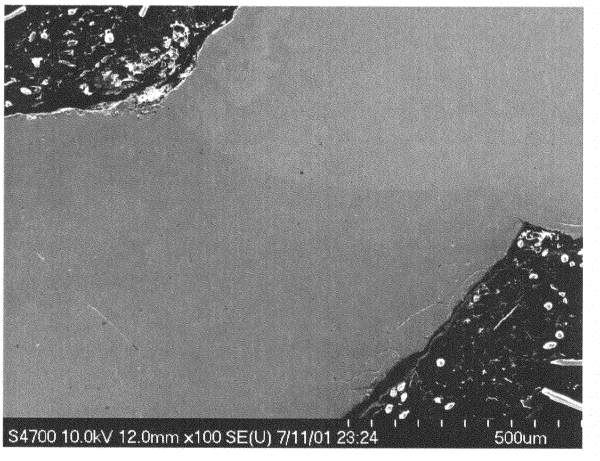

FIGURE 27 Higher magnification SEM image of Figure 26; at the junction of weldment and base alloy.

Typical micrographs collected from the SEM studies are shown in Figures 26 through 44. Figure 26 is from a location near a weld region. It shows both the 800HT and the 625 weld. In this micrograph, the inside surface is at the bottom, while the outside surface is at the top. The weld is the smooth half of the micrograph (i.e. the right hand section of Figure 26). The grain boundaries of 800HT are clearly visible in the left part of the micrograph. The difference between the inside and outside surfaces is apparent and clearly visible. The corrosion layer on the inside surface of the 800HT is highly porous and fragmented, while that on the outside surface is fairly uniform and smooth. Figure 27 is from the other side of the weld. Again, the inside surface is severely affected as compared to the outside surface. Additional details of this area are shown in Figures 28 and 29.

The condition of a region close to that shown in Figure 27 is given in Figure 30. The details of the inside surface region at this location are shown in Figures 31 and 32. Similarly, the morphology of the outside surface is shown in Figures 33 through 43.

FIGURE 28 Inside surface region of the base alloy (Alloy 800HT).

FIGURE 29 Inside surface region of the base alloy (Alloy 800HT); magnified view.

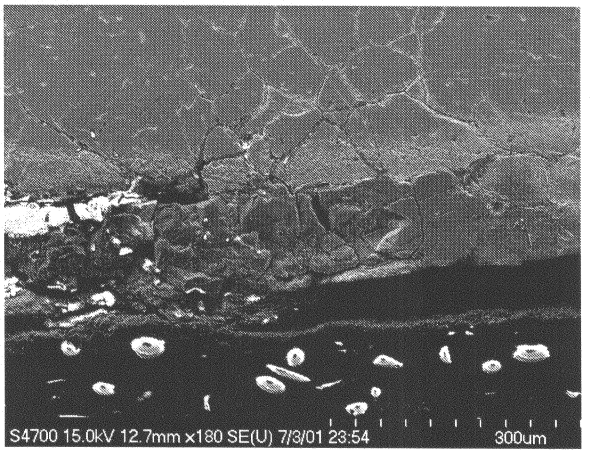

FIGURE 30 Inside surface region of the base alloy (Alloy 800HT).

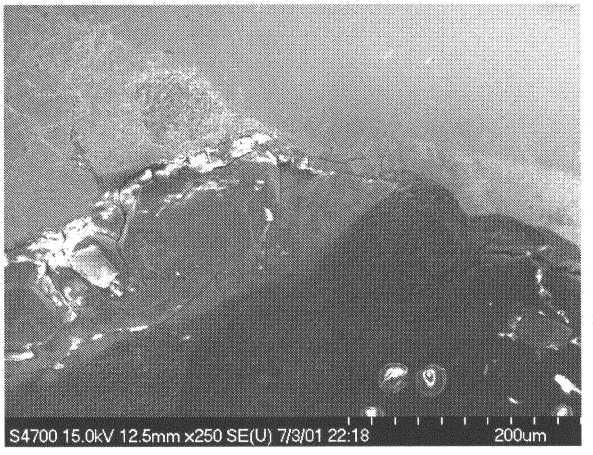

FIGURE 31 Another view of the inside surface region of the base alloy (Alloy 800HT).

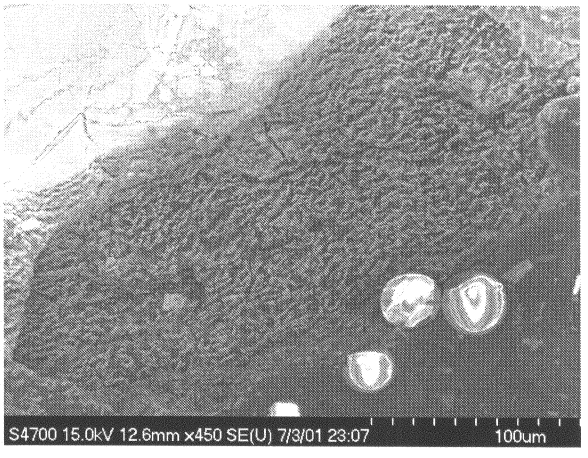

FIGURE 32 Inside surface region of the base alloy (Alloy 800HT).

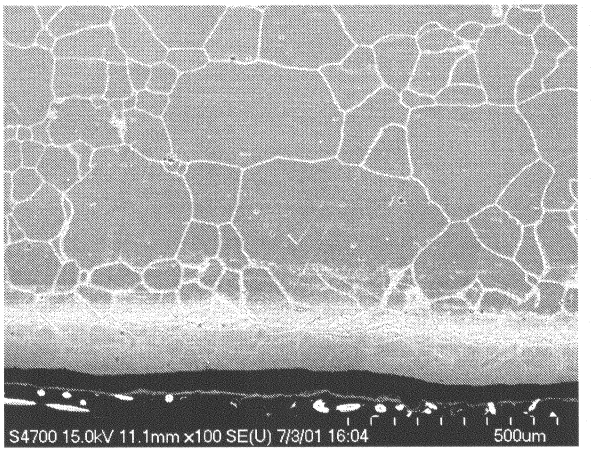

FIGURE 33 Outside surface region of the base alloy.

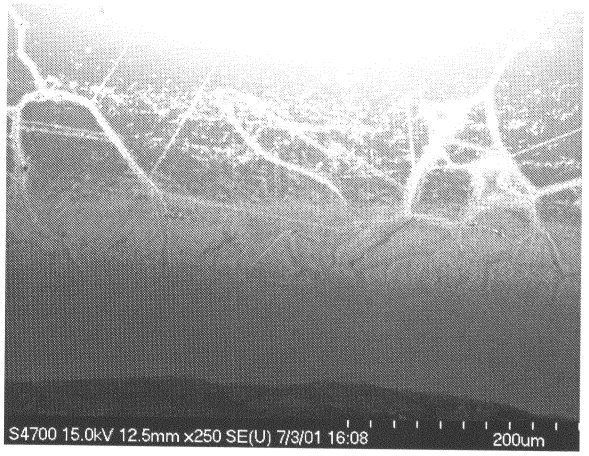

FIGURE 34 Outside surface region of the base alloy; magnified view.

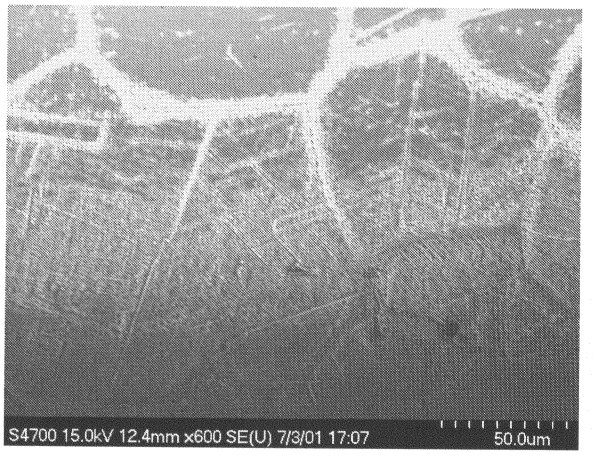

FIGURE 35 Outside surface region of the base alloy; another magnified view.

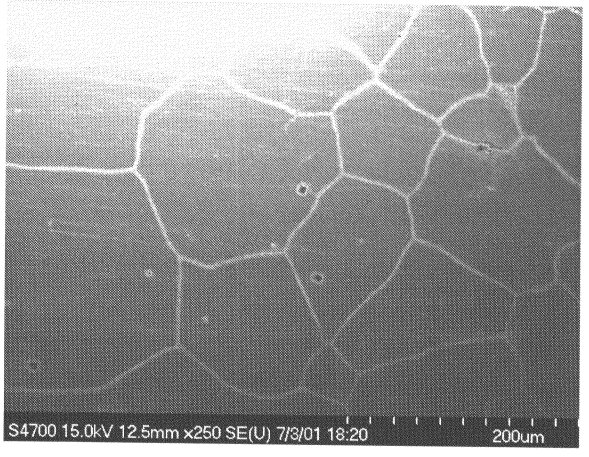

FIGURE 36 Outside surface region of the base alloy.

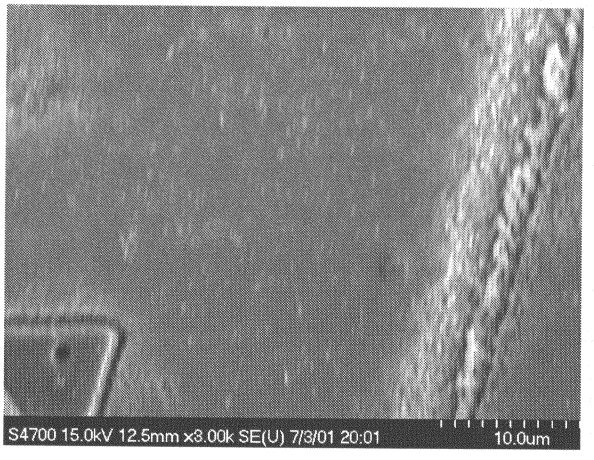

FIGURE 37 Outside surface region of the base alloy; magnified view.

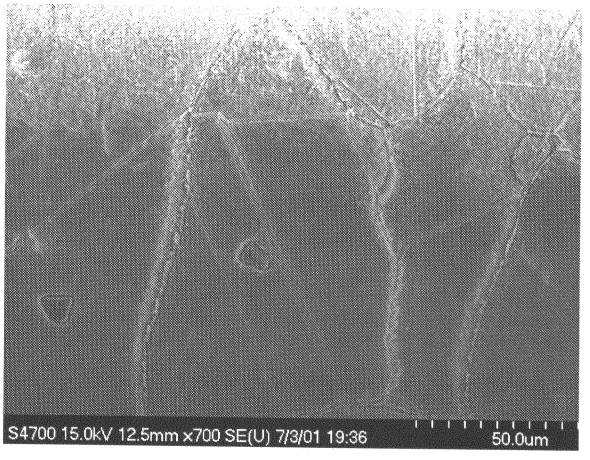

FIGURE 38 Outside surface region of the base alloy, showing grain boundaries.

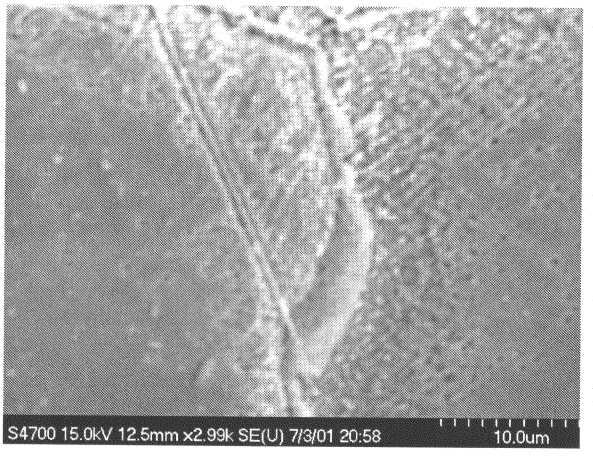

FIGURE 39 Outside surface region of the base alloy, showing precipitates.

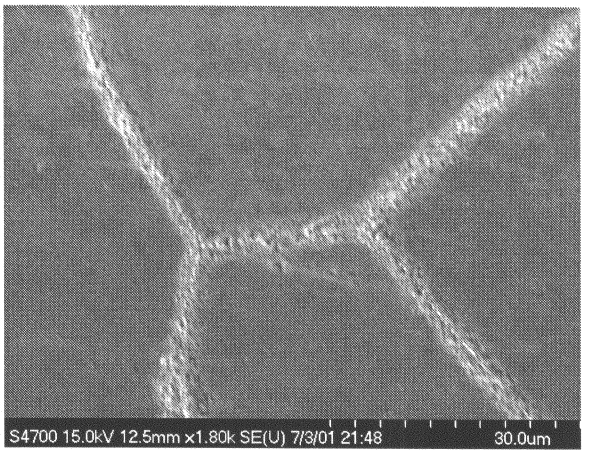

FIGURE 40 Outside surface region of the base alloy; grain boundaries.

FIGURE 41 Outside surface region of the base alloy; grain boundaries magnified.

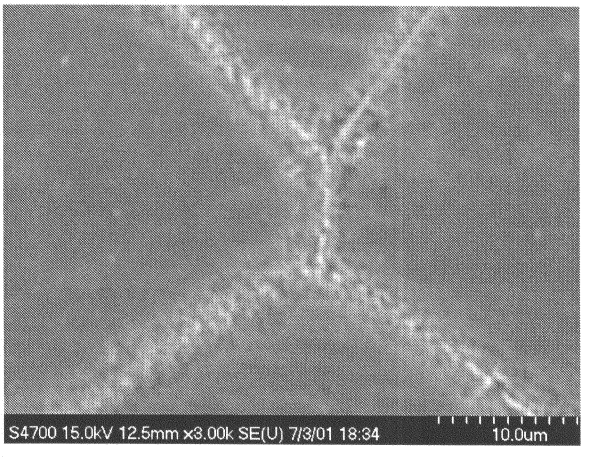

FIGURE 42 Outside surface region of the base alloy; magnified view.

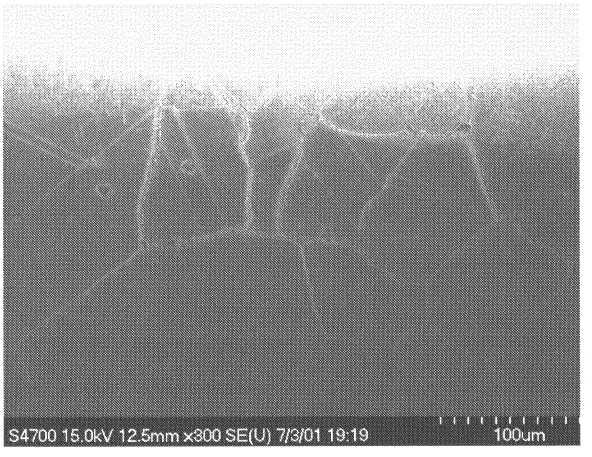

FIGURE 43 Another view of the outside surface region of the base alloy.

Figure 44 represents an interesting area. It is from an inside surface region where the bulk of the corrosion layer seems to have flaked off. Such a region is also visible in Figure 30.

Chemical Analyses

Chemical analyses of the corrosion process/products were performed using three independent methods. The first method was the standard EDAX, which was used in conjunction with the SEM investigation. This method reveals elemental compositions – within the well known limitations of EDAX. The second method is the standard wet chemistry-inductively coupled plasma (ICP) combination technique. In this method, the substance to be investigated is dissolved in a suitable solvent (usually an inorganic acid), and the resultant solution is investigated via ICP analysis. Here too, only the elemental concentrations are obtained. The final technique is the standard x-ray diffraction method. Through this method, one can determine the distribution of the various compounds and, under ideal conditions, phases present in the specimen.

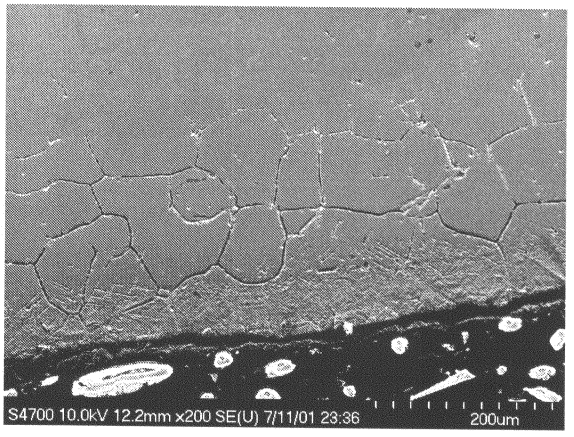

FIGURE 44 Inside surface region of the base alloy.

Energy Dispersive X-ray Analysis

In this section typical EDAX data are presented. The inside surface corrosion layer for alloy 800HT, as seen earlier from the optical and SEM investigation, was found to consist of five distinct layers. These layers are schematically shown in Figure 45 and summarized in Table 2. As noted in Table 2, the corrosion layers decrease in carbon and increase in chromium from the outer edge of the layer to the alloy base. The outermost layer, on the inside surface ["a" in Table 2 and "A" in Figure 10(a)] consists of pure graphite. The next layer, going inwards, consists of a mixture of pure graphite and chromium carbide. The next layer ("b" in Table 2) consists of chromium oxide and chromium carbide, in a 50-50 mixture. The next layer, "c", consists of chromium and iron carbides and traces of chromium oxide. The outermost layer on the alloy side is, as expected, depleted in chromium. The chromium depletion or migration followed two directions: one is toward the nearest grain boundary – where it forms a carbide – and the other is toward the outer surface, as noted above. Thus, although the zone marked as "d" in Table 2 is nominally referred to as the grain-boundary penetration zone, it is also the chromium depletion zone. Carbon is the penetrant in this grain-boundary penetration zone.

The corrosion layer on the outside surface is similar to that of the inside surface, with two major exceptions. The first concerns the absence of a graphite/carbon-rich layer, and the second, the total thickness of the layer. The outside layer, for most part, was an order of magnitude less in thickness. Schematically, the outside corrosion layer is shown in Figure 46. The morphology is also quite different. The outermost sub-layer ("a", Figure 46) is mostly chromium oxide. The next sub-layer ("b", Figure 46) is chromium-rich oxide and carbide; this is followed by another sub-layer ("c" in Figure 46), which is the grain-boundary affected zone. The absence of a graphite or carbon layer clearly indicates that supply of carbon is limited. In other words, the available carbon is transported/diffused inwards – through the oxide and the oxide-carbide region. The rate-limiting step appears to be the availability of the carbon. This hypothesis seems to be reasonable, given the near stagnant nature of the gas flow on the outside surface.

Wet Chemistry and ICP Analysis

A typical portion of the inside corrosion layer was analyzed using the standard wet chemistry technique coupled with ICP. The corrosion sample was physically removed from the inside surface by using a sharp scalpel blade. The sample was dissolved in nitric acid and

subsequently analyzed with the standard ICP method. The results of this analysis are given in Table 3. These results are consistent with the expected constituents of the corrosion layer.

X-Ray Diffraction (XRD) Analysis

Similar to the wet chemistry analysis noted above, XRD analysis was performed on the corrosion layer from the inside surface. The results are presented in Figure 47 and Table 4. The phases and compounds that were detected include: Cr_2O_3 (chromium oxide); $FeCr_2O_4$ (chromite/spinel); Fe_3Ni_3 (awaruite); and C (graphite). Cementite (Fe_3C) was not detected.

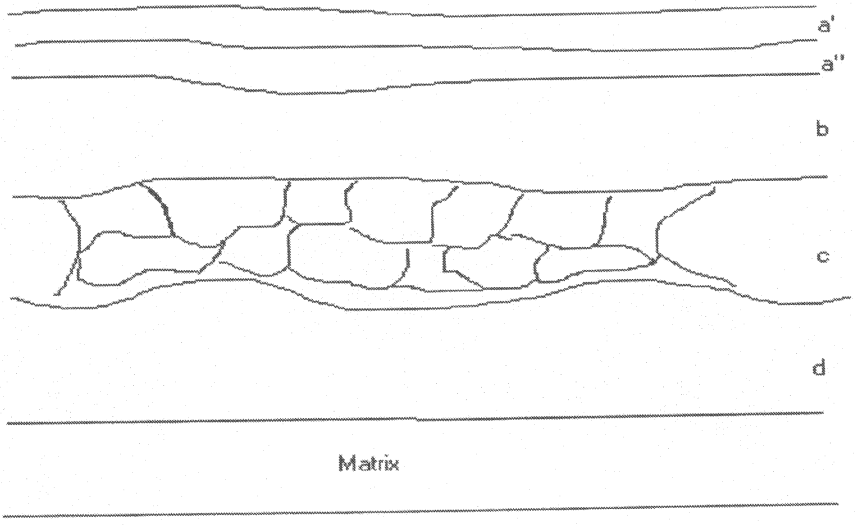

FIGURE 45 Schematic of corrosion layer development.

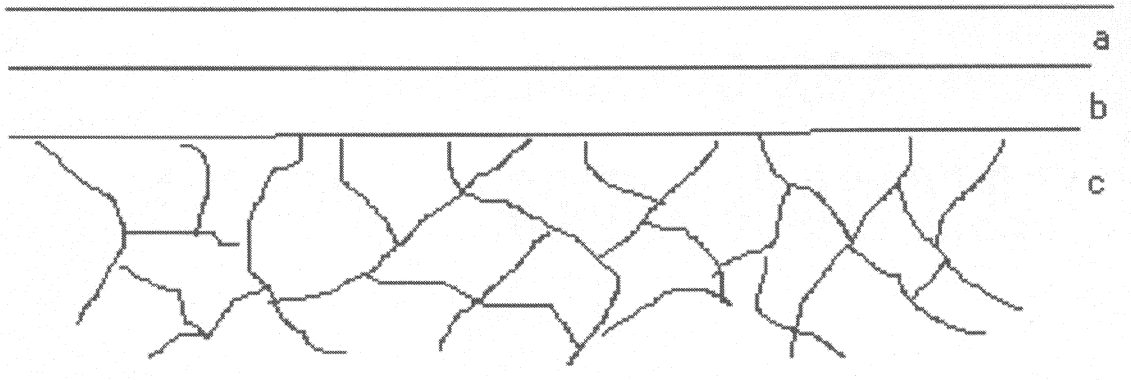

FIGURE 46 Schematic of outer corrosion layer.

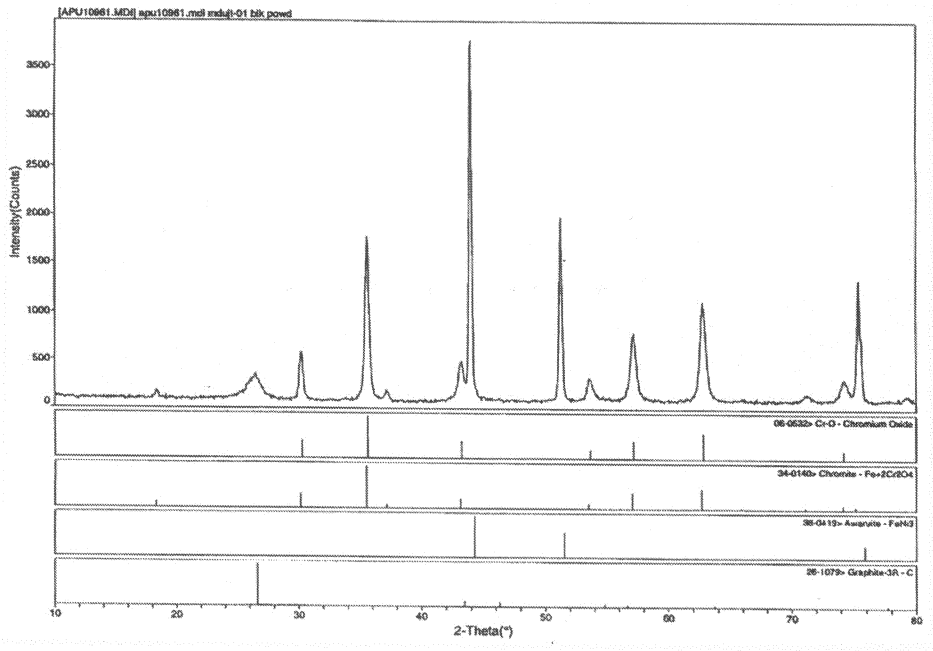

FIGURE 47 XRD Analysis of the corrosion layer on the inside surface of the shroud of the WHB: Intensity vs. 2θ angle.

DISCUSSION

The particular WHB that we have examined was in service for about 9 years and 2 months, and was taken out of service after this time because of imminent probability of failure. The walls of the shroud were thinned out to (near) zero thickness.

The metal wastage rate (for Alloy 800 HT) is calculated to be equal to about 27.5 mils per year (27.5 mpy). The weld metal wastage rate is one order of magnitude less than this rate. The weld metal (Inconel 625) corrodes at a rate of about 2.5 mpy. The maximum metal wastage rate was found to occur at a temperature of about 677°C.

The optical and SEM photomicrographs indicate a complex metal wastage process. Chemical analyses revealed that the corrosion layer consists of five distinct regions. The outermost region is nearly pure graphite followed by a mixture of graphite and chromium-rich oxides and carbides. This region is followed by a mixture of chromium and iron oxides and carbides. The final region is the alloy layer, which is depleted in chromium and mostly composed of carbide growth in the grain boundary region. However, based on this observation and coupled with general knowledge of the progression of metallic corrosion, it is reasonable to assume that the metal wastage process consists of periodic growth of the above-noted five part corrosion layer, followed by mechanical breaking/flaking caused by cyclical thermal and mechanical stresses. Once the total corrosion layer reaches a thickness of about 150 μm, it becomes mechanically unstable and breaks off. A fresh layer then begins to form. It too breaks off after reaching about 150 μm in thickness. The value of 150 μm is reasonable because we did not find any region with corrosion layer greater than 150 μm anywhere on the failed shroud piece, even though the total metal wastage after 9 years and 2 months amounted to about 6.35 mm (6,350 μm).

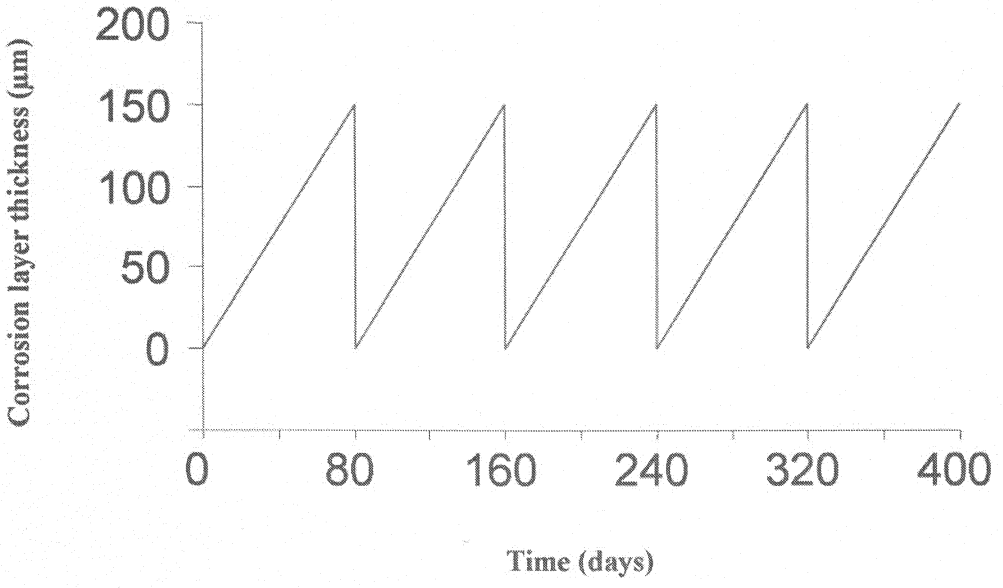

FIGURE 48 Schematic of metal dusting progression.

One further refinement of the aforementioned progression is worth noting. The first corrosion layer, clearly, forms on the virgin 800HT. The second and all subsequent layers begin to form on a chromium-depleted and grain-boundary penetrated surface.

Schematically, the progression of metal wastage is shown in Figure 48. As noted earlier, the maximum formation of metal dusting or the corrosion rate for Alloy 800HT in this ammonia-producing plant was determined to be 27.5 mpy. This is about 700 µm per year. Therefore, it takes about 80 days – in round numbers – to form a corrosion layer of 150 µm. This is what is depicted in Figure 48. Assuming continuous operation, figure 48 indicates that after about 80 days, the old oxide/corrosion layer flakes off and a new layer begins to form. This process is repeated until all metal is consumed.

CONCLUSIONS

The following conclusions were reached

- Simultaneous oxidation/carburization phenomena are operating during "metal dusting" of alloy 800 HT as used in the ammonia plant.
- Alloy 800 HT is susceptible to metal dusting. Discontinuous chromium oxide and carbide layers are partly responsible for metal dusting.
- The high nickel-chrome weldment alloy, Inconel 625, is not (significantly) susceptible to metal dusting (for the conditions of the ammonia plant).
- Cementite was not present within the "metal dusting" (i.e., corrosion) layer.
- The availability of carbon (i.e. carbon potential/activity) and gas velocity have a profound impact on the kinetics of the metal dusting. The inside surface, wherein the carbon availability is significantly more than that on the outside surface, corrodes at an order of magnitude higher rate.

DEVELOPMENT OF COATINGS AGAINST METAL DUSTING ATTACK

C. ROSADO, Dechema e.V., Frankfurt am Main, Germany
F. DETTENWANGER, Dechema e.V., Frankfurt am Main, Germany
M. SCHÜTZE, Dechema e.V., Frankfurt am Main, Germany*

ABSTRACT

The present work deals with the development and testing of coating systems against metal dusting attack. The recently developed coatings are based on high amounts of strong oxide formers, like Si, Al and Ti, which are able to form protective oxide layers even under the highly reducing metal dusting atmospheres. The coatings were applied on ferritic and austenitic steel substrates by either high velocity oxygen fuel spraying (HVOF) or by (co)diffusion of one or two elements via a pack cementation process respectively. The process parameters of the diffusion coatings were optimized with respect to the different substrate materials and diffusing species.

Isothermal tests at 400 and 700 °C under metal dusting atmosphere were carried out for up to 1000 h for coated and uncoated specimens. Discontinuous mass change measurements were performed in order to determine the kinetics of the attack. After the corrosion tests the metallographic cross sections of the specimens were investigated by light and electron microscopy (SEM, EPMA). Especially the interdiffusion of substrate and coating and the formation of potentially protective oxide layers on top of the coatings was studied using elemental mapping and concentration profiles. The results obtained so far indicate that coatings have a high potential for significantly increasing the life-time of components under metal dusting conditions. The different systems investigated will be classified, evaluated, and discussed with respect to their protection potential and the responsible protection mechanisms. In addition, new data were obtained regarding the metal dusting attack on uncoated steel substrates giving further insight into the metal dusting phenomena in general.

INTRODUCTION

Metal Dusting is a catastrophic form of high-temperature corrosion generally occurring for "reducing" and strongly carburizing atmospheres with carbon activities greater than one (a_c>1) in the temperature range from 400 °C to 800 °C. The corrosion attack leads to a powder composed of graphite and fine metal particles as the reaction product. Grabke and Wolf 1987; Hochman 1977). Metal dusting is a serious problem for several industries such as petrochemical plants, coal gasification plants, heat treating industries and there is a strong demand for a technical solution.

Based on the classical paper by Hochman (1977) and the work by Grabke and coworkers (1998, 1993) the principal steps of metal dusting attack on iron based alloys can be summarised as follows:

- Adsorption and decomposition of carbon on the metal surface

*Corresponding author address: M. Schütze, Karl-Winnacker-Institut der DECHEMA e.V., Theodor-Heuss- Allee 25; Frankfurt am Main; D-60486; e-mail: schuetze@dechema.de.

- Absorption of carbon from the surface into the bulk
- Carbon oversaturation of the substrate
- Carbide formation ($M_{23}C_6$, M_7C_3) followed by the formation of an intermediate metastable carbide (M_3C)
- Carbon deposition resulting in destabilisation of M_3C according to the reaction:

$$M_3C \rightarrow 3M + C \quad (1)$$

- The fine metal particles resulting from this reaction act further as catalyst for carbon deposition from the atmosphere.

One critical parameter for metal dusting is the reactivity of the alloy surface with the gas atmosphere and, therefore the modification of the metal surface offers one possibility of metal protection. The aim of the present work is the development of metal dusting resistant coatings for industrially important high-temperature alloys.

EXPERIMENTAL

Two different coating methods have been applied: diffusion and overlay coatings. The diffusion coatings are produced by the "pack cementation method" and consist of Al, Ti, Si plus Cr as a diffusion barrier (see Table 1). The overlay coatings based on the intermetallic γ-TiAl phase are produced by HVOF. Five different alloys have been selected as substrates (German Designation 10CrMo9 10, X10CrAl18, X18CrN28, Alloy 800H and Alloy P91). The composition of these materials is given in Table 2.

In the pack cementation process the samples are introduced in a powder pack containing a mixture of a master alloy, which is a powder of the elements to be enriched in the surface of the material, an activator (generally a halide salt) and an inert filler material. The pack is heated under an Ar/H_2 atmosphere in a furnace for a certain period of time and temperature which varies depending on the coating applied, and the substrate composition. Changing the parameters of the test, different coating thicknesses and phases are obtained.

The carburizing-reducing test atmosphere consists of a mixture of CO, H_2 and H_2O, with carbon activities greater than one. Some alloys have been also tested in an "industrial" metal dusting atmosphere with CO_2, CO, CH_4, H_2, H_2S, N_2, HCl as main components.

Assuming that the formation of carbon solely takes place by the reaction:

$$CO + H_2 = C + H_2O \quad (2)$$

the carbon activity of the test gas can be calculated by using the following equations:

$$a_c = \frac{PCO \cdot PH_2}{k \cdot PH_2O} \quad (3)$$

$$\log k = -(7100/T + 7.496) \quad (4)$$

Table 1 Experimental parameters and powder compositions of the pack process

Substrate	Process	Temp (°C)	Time (h)	% Al	% Si	%Ti	%Cr	% Al2O3	%NH4Cl
10CrMo9 10	Aluminizing	850	6	5	-	-	-	94.5	0.5
	Siliconizing	1000	7	1	7	-	-	90	2
	Chromizing	1120	24	-	-	-	21	75	4
	Co-diffusion	1000	7	3	9	-	-	86	2
X10CrAl18	Aluminizing	800	6	12	-	-	-	86.5	1.5
	Siliconizing	1000	7	1	7	-	-	90	2
X18CrN28	Aluminizing	800	6	12	-	-	-	86.5	1.5
	Siliconizing	1000	7	1	7	-	-	90	2
Alloy 800	Aluminizing	800	6	12	-	-	-	86.5	1.5
	Siliconizing	1000	7	1	7	-	-	90	2
	Co-diffusion	1000	10	1.7	-	5.2	-	89.1	4
Alloy P91	Aluminizing	800	6	12	-	-	-	86.5	1.5
	Siliconizing	1000	7	1	7	-	-	90	2

Table 2 Composition of the Alloys

Alloy	%C	%Si	%Cr	%Al	%Ni
X18CrN28	0,15-0,20	≤1	26-29	-	-
X10CrAl18	≤ 0,12	0,70-1,40	17-19	0,70-1,20	-
10CrMo9 10	0,08-0,15	≤0,5	2-2,5	-	-
Alloy 800	≤0,12	≤1,00	19-23	0,15-0,60	30,0-34,0
Alloy P91	0,08-0,12	0,20-0,50	8,0-9,5	<0,040	<0,40
Alloy	%Mn max.	%Mo max.	%P max.	%S max.	Others
X18CrN28	1	-	0,045	0,03	N 0,15-0,20
X10CrAl18	1	-	0,04	0,03	-
10CrMo9 10	0,40-0,70	0,90-1,20	≤0,030	≤0,025	Cu ≤0,30
Alloy 800	2	-	0,03	0,02	Ti 0,15-0,60
Alloy P91	0,30-0,60	0,85-1,05	0,02	0,01	V 0,20 - Nb 0,08

$$\log a_c = \log\left(\frac{PH_2 \cdot PCO}{PH_2O}\right) + \frac{7100}{T} + 7.496 \qquad (5)$$

The resulting carbon activities are a_c = 9904 for T = 400 °C and a_c = 5.68 for T = 700°C.

The coated samples were isothermally tested under metal dusting conditions (25% CO, 73% H_2, 2% H_2O) for different periods of time at 400 °C and 700 °C. Uncoated samples were also tested for comparison. The samples were ultrasonically cleaned in ethanol and acetone and weighed before inserting them into the furnace. After each exposure, the samples where brushed for coke removal (if present) and weighed to register the mass change. Measurements of the thickness of the specimens were carried out as well. At the end of the test the samples were cross-sectioned for metallographic examination.

RESULTS

Table 3 shows a summary of the general behaviour of the different samples tested under metal dusting conditions.

Table 3 General Classification of the Attack for the Alloys Tested at 400 and 700 °C.

Test Data at 400°C				Diffusion coatings					Overlay coat.	
Alloy	Type of attack*	Without coating		Chromizing + Aluminizing	Aluminizing		Siliconizing	Co-diffusion Al + Ti	HVOF TiAl	
Test duration		1012 h	336 h	336 h	168 h	840 h	168 h	168 h	336 h	504 h
10CrMo9 10	MD	-	1	0	-	-	1	-	-	-
(1.7380)	CF	-	2	0	-	-	1	-	-	-
X10CrAl18	MD	0	-	-	(504h)0	-	0	-	-	0
(1.4742)	CF	1	-	-	(504h)0	-	0	-	-	0
X18CrN28	MD	-	0	-	-	0	0	-	-	-
(1.4749)	CF	-	1	-	-	0	0	-	-	-
X10NiCrAlTi32 20	MD	(676h)0		-	0	-	0	0	0	-
Alloy 800 (1.4876)	CF	(676h)0		-	0	-	0	0	0	-
X10CrMoVNb9 1	MD	-	1	-	0	-	1	-	-	-
Alloy P91 (1.4903)	CF	-	2	-	0	-	2	-	-	-

Test Data at 700°C			Diffusion coatings				Overlay coat.
Alloy	Type of attack*	Without Coating	Chromizing + Aluminizing	Aluminizing	Siliconizing	Co-diffusion Al + Ti	HVOF TiAl
Test duration		(393 h)	(561 h)	(561 h)	(168 h)	(393 h)	(168 h)
10CrMo9 10	MD	1	0	-	1	-	-
(1.7380)	CF	2	0	-	2	-	-
X10CrAl18	MD	0	-	0	0	-	0
(1.4742)	CF	0	-	0	1	-	0
X18CrN28	MD	0	-	0	0	-	-
(1.4749)	CF	1	-	0	1	-	-
X10NiCrAlTi32 20	MD	(225h)1	-	0	0	0	-
Alloy 800 (1.4876)	CF	(225h)1	-	0	1	0	-
X10CrMoVNb9 1	MD	1	-	0	2	-	-
Alloy P91 (1.4903)	CF	2	-	0	2	-	-

*Abbreviations: MD: metal dusting, CF: coke formation, 2: heavily attacked, 1: slightly attacked, 0: no attack.

Alloy 10CrMo9 10

Alloy 10CrMo9 10 was tested under metal dusting conditions for 561 h. Samples of this material with and without coating were tested at 400 and 700 °C revealing that the material without coating showed coke deposition already after 5 h. The coke deposits grew homogeneously on the surface of the sample during the exposure and at the end of the test weight loss kinetics were higher than at the beginning.

At the end of the test, cross sections were prepared for metallographic examination and microprobe analyses (EPMA) were performed as well. After etching the samples with Nital, it was possible to observe the formation of a cementite layer (Fig. 1) on the surface of the uncoated sample at both temperatures. This is in agreement with the mechanism of metal dusting in which a metastable carbide (in this case cementite) forms and decomposes later leading to graphite and metal particles. EPMA analyses revealed the penetration of carbon into the substrate of about 30 μm in depth (Fig. 1).

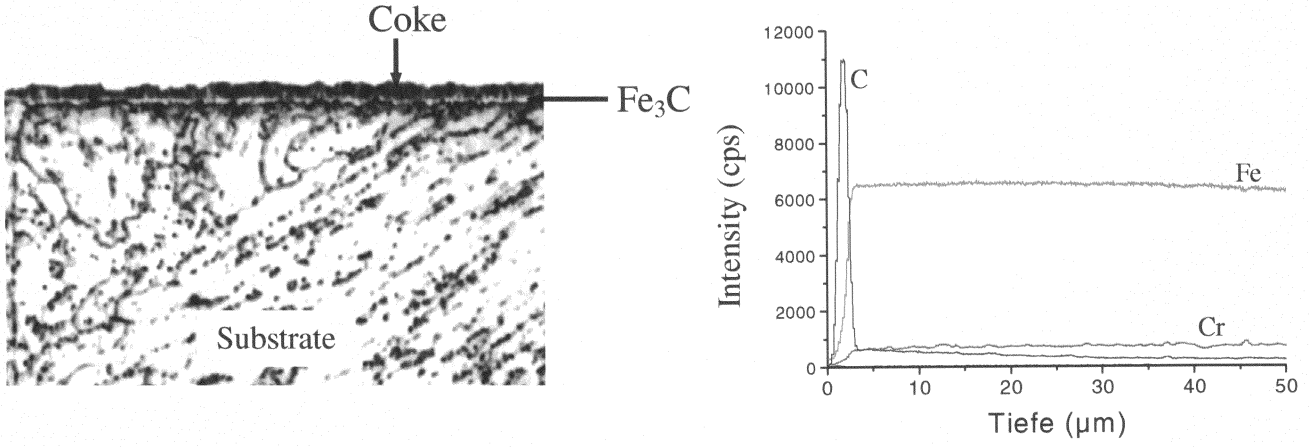

Figure 1 Alloy 10CrMo9 10 without coating tested under metal dusting conditions for 336 h at 400 °C. Left: Cross-section shows formation of cementite. Right: EPMA concentration profile. Penetration of carbon into the substrate.

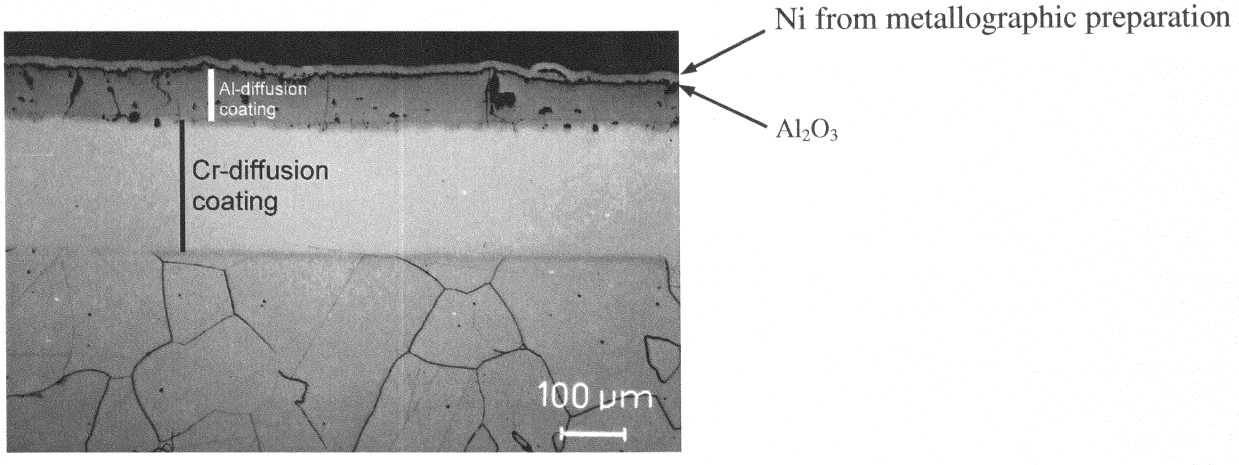

Figure 2 Alloy 10CrMo9 10 tested under metal dusting conditions for 336 h at 400 °C. The diffusion coating applied protects the sample due to the formation of an alumina scale.

Before the exposure, one sample was also coated by the pack cementation method in two steps. Chromizing was performed first to enrich the surface with chromium in order to create a diffusion barrier for the subsequent aluminizing step which was performed to create an Al-diffusion coating (Fig. 2). A Si-diffusion coating as well as a Si-Al-codiffusion coating were also produce for this alloy.

For the material coated with an Al-diffusion coating, also in the metallographic investigations no attack by metal dusting was observed nor was there any coke formation on the surface for both temperatures. EPMA analyses showed neither carbon penetration nor carbide formation in the sample and the weight change measurements revealed an increase in weight.

For the material coated with a Si-diffusion coating, coke deposits were already seen from the beginning of the test for both temperatures and the loss of weight was higher for 400 °C than

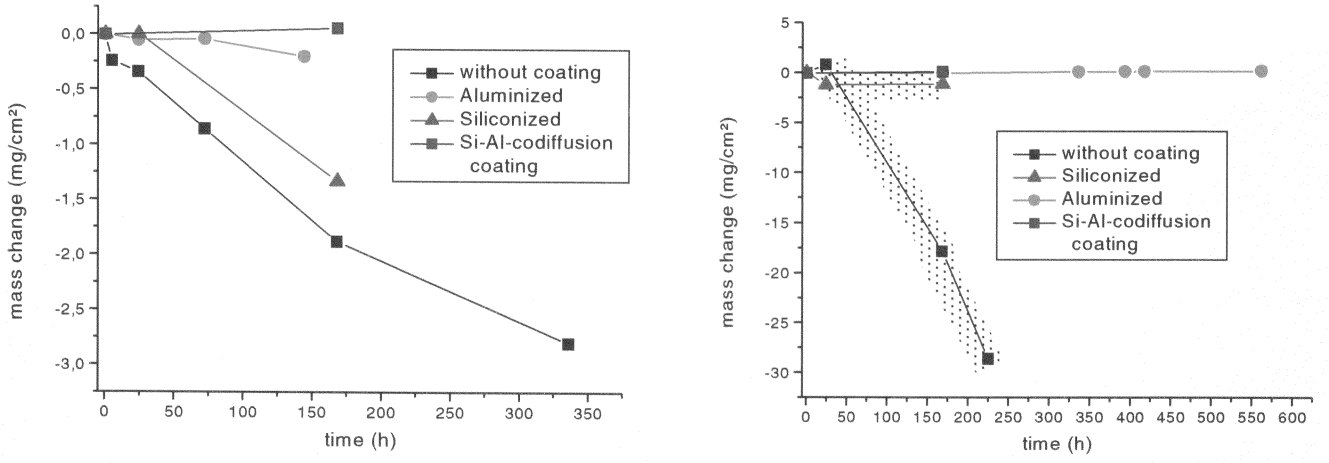

Figure 3 Mass change masurements for Alloy 10CrMo9 10 with different coatings. The dotted area indicates coke deposition. Left: 400 °C, Right: 700 °C.

for 700 °C (Fig.3). The Si-Al-codiffusion coating showed neither coke deposition nor metal dusting attack. However the experiment has only run up to 168 h so far.

Alloy X18CrN28

This material was coated by the aluminizing process. Since in this case the substrate contains a sufficient amount of chromium to act as a barrier against the diffusion of aluminum, no chromizing step was performed. Samples of this material were tested with and without coating at 400 °C and 700 °C for up to 840 h. For the sample without coating, there was a very fine and adherent coke layer on the surface after 72 h and at the end of the test for both temperatures. However no attack was apparently present on the sample despite of the thin layer of coke.

The uncoated samples were tested only for 336 h at 400 °C and for 393 h at 700 °C during which mass changes were measured showing first an increase in weight. However after 24 h a weight decrease was observed (Fig.4). Under these experimental conditions, an oxide scale starts to form but the oxygen partial pressure is not high enough and it is not possible to form an adherent, homogeneous and protective oxide scale on the sample before coke deposition takes place.

For the sample with the Al-diffusion coating neither coke formation nor metal dusting occurred during the time of exposure and there was also a mass increase. The coating prevented any carbon penetration into the substrate and protected the material against this atmosphere by the formation of a protective alumina scale.

The Al-coated substrate was also tested under an industrial atmosphere (CO-CO_2-CH_4-H_2-H_2S-HCl-H_2O) at 620 °C for 1176 h in which the results were positive as well. There were no carbon penetration, coke deposits or metal dusting. Samples with a Si-diffusion coating were tested at both temperatures and only at 700 °C a very thin coke layer was found on the surface of the substrate but no attack occurred.

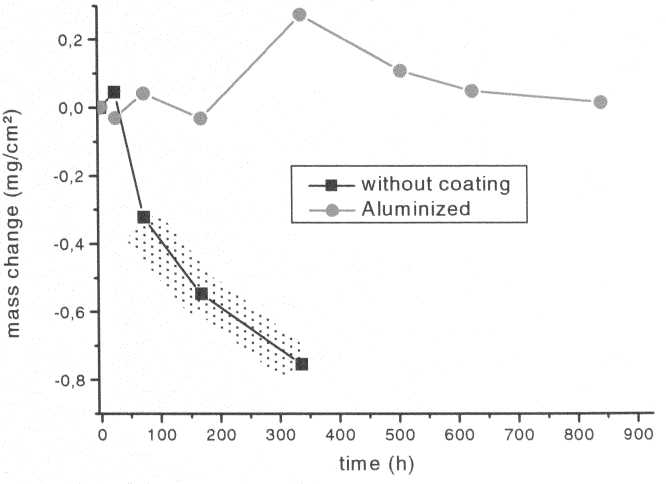

Figure 4 Mass change measurements on Alloy 18CrN28 under metal dusting conditions at 400 °C. The dotted area indicates coke deposition.

Alloy X10CrAl18

This material was coated by two different techniques. A TiAl coating was applied by the HVOF method and an Al-diffusion coating as well as a Si-diffusion coating were applied by the pack cementation method. At 400 °C no attack by metal dusting nor coke formation were observed. Similar results were obtained at 700 °C revealing no attack. However the siliconized sample presented a thin coke layer at the end of the test.

One sample without coating was tested at each temperature in order to compare the behavior of the base material with the coatings and it was found that for the time of exposure the material itself is not sensitive to metal dusting under the experimental conditions due to the development of a protective oxide scale which was stable during the whole test and protected the sample by preventing the penetration of carbon into the substrate from the gas atmosphere. However, at 400 °C and after 336 h a very thin and adherent layer of coke had formed on the surface of the specimen although no attack was present. This layer of coke stopped to form after 800 h and no further coke deposition was observed after this time.

This material was also tested under the industrial atmosphere (CO-CO_2-CH_4-H_2-H_2S-HCl-H_2O) at 620 °C with the Al-diffusion coating applied and the result was the same as for alloy X18CrN28. No attack was observed for up to 1176 h.

Alloy 800H

Using the HVOF technique, a TiAl coating was applied to this material and tested under metal dusting conditions at 400 °C up to 336 h. During this time, no attack was visible on the sample and there was no coke formation either. Mass changes were also measured and an increase of weight of the specimen was found during the exposure time. However, the coefficients of thermal expansion of the material and the coating are different so that after heating and cooling a delamination crack had developed (Fig.5) although no through cracking occurred. Thus, the gas atmosphere could not reach the substrate and any kind of attack in the sample was prevented. However, at this temperature, an uncoated sample was also tested up to 676 h and no attack or coke deposition were found due to the formation of a protective chromia scale.

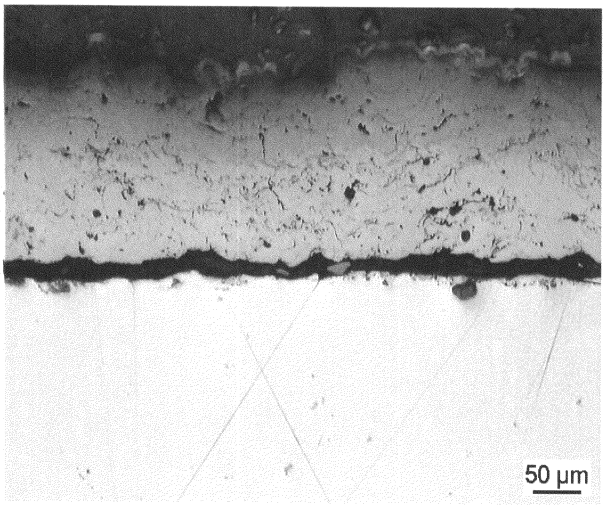

FIGURE 5 Delamination crack due to thermal expansion mismach for Alloy 800 coated with a TiAl intermetallic by HVOF.

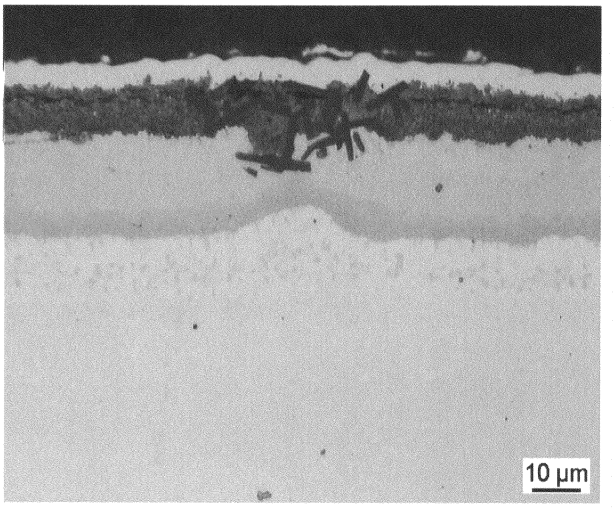

FIGURE 6. Cross section of a Ti-Al-codiffusion coating on Alloy 800. From top to bottom: Ni coating from metallographic preparation, Ti-Al rich oxide scale, Al-Ti-Ni rich phase, Ti-carbide and the small precipitates are Ni-Al intermetallic.

Three different diffusion coatings were applied to this material by the pack cementation method. An Al-diffusion coating, a Si-diffusion coating and a co-diffusion Ti-Al-coating. All of them were tested under metal dusting conditions at 400 °C and at 700 °C at which the most critical conditions are supposed to be present. The Al-diffusion coating turned out to be protective. No attack was present during the time of exposure up to 561 h. The co-diffusion coating showed coke deposition after only one week of exposure, however no more coke formation was observed for the rest of exposure, i. e. up to 393 h. After the test, the sample was cross sectioned revealing an oxide layer which was rich in Ti and Al (Fig. 6). EPMA analyses were made as well and it was found that the oxide provides protection to the sample and no carbon penetration occurred during the test. The siliconized sample showed coke deposition at 700 °C but no attack was found after one week of exposure. The coke was then removed and no attack or coke formation were observed after further exposure. At the end of the test, no attack or coke deposition were present in the sample. The sample without coating showed at 700 °C coke deposits and at the end of the test after 225 h some pits were observed at one of the edges of the specimen as well as a decrease in weight of the specimen.

Alloy P91

At 400 °C, this material was tested for 168h with an Al-diffusion and a Si-diffusion coating and up to 336 h without coating. The aluminized sample was not attacked and there was no coke formation on the sample. However, there was some spallation of the aluminizing coating causing a decrease in the weight of the sample (Fig. 7) but this does not lead to coke deposition or metal dusting attack. For the siliconized sample both, metal dusting attack and coke formation, were present in the sample and a decrease in the weight of the specimen had occurred (Fig. 8). For the sample without coating there was coke deposition on the sample and homogeneous attack.

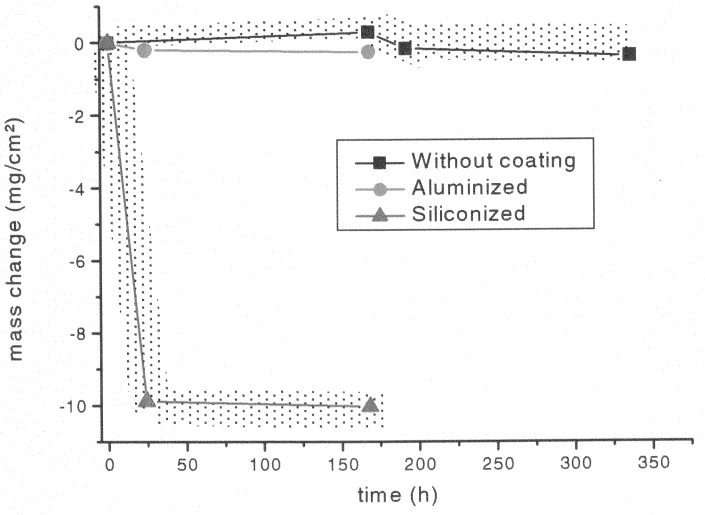

Figure 7 Mass change measurements on Alloy P91 under metal dusting conditions at 400 °C. The dotted area indicates coke deposition.

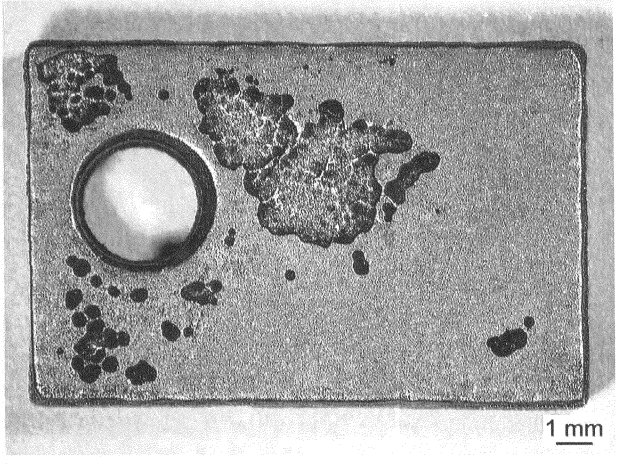

Figure 8 Surface of a siliconized sample of Alloy P91 after 393 h of exposure under metal dusting conditions at 700 °C. Attack by pitting.

At 700 °C, the aluminized sample tested for 561 h did not show coke deposition or metal dusting attack. On the contrary, the siliconized sample was heavily attacked showing pitting after 168 h of exposure. The sample without a coating was tested as well showing coke formation and metal dusting attack.

DISCUSSION

First of all it has to be kept in mind that the testing times presented in this paper are relatively short since the project is still in progress. Furthermore not all temperatures and not all coating types planned have been covered yet which will, however, be the subject of the remaining time in the project where testing times of at least up to 1000 hrs are aimed at. Nevertheless the results obtained so far reveal some interesting aspects.

The first is the very good resistance of the aluminizing/chromizing coating on the low alloy steel 10CrMo9 10. While without coating this steel showed heavy coke formation and severe metal dusting attack, it was absolutely free of these features when the coating had been

applied. Coatings of this type have been produced commercially and are widely used for protection in petrochemical equipment. The combination of a low cost steel and a coating which can be applied by a relatively simple process can be regarded as a cost effective solution which may be a serious competitor to high alloy steels if the positive behavior is maintained at long exposure times. The chromizing step is necessary in the production of this coating since a barrier of increased chromium content in the metal subsurface zone prevents further inward diffusion of aluminum during service which can be rather rapid (especially at 700°C) in a ferritic or ferritic/martensitic matrix. Aluminium, however, is the key protective alloying element since chromia formation is impeded at low oxygen partial pressures as encountered in metal dusting atmospheres. Furthermore chromium outward diffusion to the metal surface can often be too slow in this temperature region, thus, resulting in impeded chromia scale formation and therefore insufficient protection of the metal.

The results for the siliconizing coating on the low alloy steel were somewhat disappointing. Silicon should also lead to a very stable oxide similar to aluminum. Evidently silicon was not able to form a continuous silica layer as the pitting type of attack showed. Locally there must have been protection since the attack without coating was uniform. Siliconizing showed a positive effect only for Alloy 800. The diffusion of Silicon into the substrate during the pack cementation process is not as easy as the diffusion of aluminium. Thus, the possible amount of Silicon in the substrate is very low and insufficient to develop a protective oxide scale. Only for alloy 800, the amount of Silicon diffused into the substrate is higher, therefore alloy 800 coated with the Si-diffusion coating showed a better behavior. Possibly the coating did not yet have the optimum composition and structure since it had turned out that the fabrication steps are not as easy as for the aluminum type coating. However, Silicon makes the Al-diffusion coating less brittle and the addition of this element to the aluminizing coating can provide a better mechanical behavior as well as a better corrosion resistance to the material (Wynns and Bayer 1998). Taking these facts into account, a Si-Al-codiffusion coating was produced obtaining very satisfactory results, although the testing times of this coating were very short but longer exposure times as well as the development of this coating on other substrates will be carried out.

The aluminizing coating also had a very beneficial effect on all high alloy steels. In no case coke formation or metal dusting were found. A chromizing step was not necessary for these materials since inward diffusion of Al in the pack cementation process led to the build-up of a Cr enriched barrier in the metal subsurface zone based simply on the original content of Cr in these steels. Without protective coating Alloy 800, P91 and X18CrN28 had shown coke formation at 700°C while X10CrAl18 had a clean surface. Alloy 800 furthermore exhibited some limited metal dusting attack. All in all it can, therefore, be expected that the aluminizing coating can offer significant protection for these materials also for longer testing times since coke deposition evidently is avoided. This seems to be true also at 400°C where unprotected X10CrAl18 tended to show coke formation. Interestingly this material was the only one which was free of coke deposits at 700°C even in the uncoated state. It can be suspected that an aluminum content of as low as about 1% in this material can stimulate the formation of a protective oxide scale possibly by facilitating nucleation of a chromia layer.

The TiAl-codiffusion coating so far had only been applied to Alloy 800. The coating prevented coke deposition and metal dusting attack. The idea behind this co-diffusion coating was that alumina scale formation usually is impeded at lower temperature whereas the formation of extremely stable titania may help as a stimulator for alumina scale formation or as a protective oxide itself. Especially in highly sulfidizing reducing environments this concept had led to a

massive improvement of material resistance by the respective coating which could not be achieved by any other treatment (Weber and Schütze 2001). The production of this coating so far is still in an experimental stage and some fine-tuning may be necessary. In how far this coating can have some advantages over a simple aluminizing coating has to be investigated in tests of longer duration.

The same TiAl alloy basis had been applied as an overlay coating (HVOF) to two of the high alloy steels (X10CrAl18 and Alloy 800). In both cases protection was achieved which illustrates the potential of the TiAl basis. It should, however, be pointed out that the coating should be maintained physically intact during service as otherwise the underlying material would be in an unprotected state, or even worse, if cracks or crevices are formed an atmosphere may be present in these defects with a decreased oxygen partial pressure and possibly an even further increased carbon activity. Furthermore, carbon deposition in crevices may result in high deposition stresses choking off parts of the coating. As a consequence diffusion coatings should be preferred for the components which can be manufactured off-site while overlay coatings may help to cover the joining areas on-site.

CONCLUSIONS

Different coatings were applied on ferritic and austenitic steel substrates and they were tested under metal dusting conditions in order to evaluate their protection behavior against metal dusting attack at 400 and 700 °C. The test results obtained so far indicate:

- Al-diffusion coatings were protective for all alloys at both temperatures and no coke deposition or metal dusting occurred.
- Si-diffusion coatings were tested at both temperatures obtaining good results only for alloy X10CrAl18, alloy X18CrN28 and Alloy 800 at 400 °C.
- Ti-Al-codiffusion coatings showed good results for Alloy 800 and coke deposition or metal dusting did not take place.
- TiAl-coatings applied by the HVOF technique were protective for all alloys on which this coating was applied (X10CrAl18 and Alloy 800).
- Si-Al-codiffusion coating showed good results. However the testing time was only of 168 h.

The results presented in this paper have of course been obtained for relatively short testing times. The tests will be continued to at least 1000 h and different temperatures which will reveal whether the trends observed so far remain or which changes of behaviour will take place. At the end of the programme it is hoped to have a clearer picture of the potential of protective coatings against metal dusting for low and high alloy steels.

ACKNOWLEDGEMENTS

The present work is funded by the German Ministry for Economy and Technology via Arbeitsgemeinschaft industrieller Forschungsvereinigungen (AiF) under the auspices of the AiF-member society GfKORR e. V. under contract no. 12121 N/1. The authors also want to thank Mr. Aumüller from ATZ/Evus for producing the thermal spray coatings.

REFERENCES

Grabke, H. J., 1998, "Carburization: A High Temperature Corrosion Phenomenon", MIT Publications No. 52.

Grabke, H. J., R. Krajak and E. M. Müller-Lorenz, 1993, "Metal Dusting of High Temperature Alloys", Werkstoffe und Korrosion 44, 89-97.

Grabke, H. J. and I. Wolf, 1987, "Carburization and oxidation", Materials Sciences and Engineering 87, 23-33.

Hochman, R. F., 1977, in "Properties of High-Temperature Alloys", ed. By A. Foroulis and F.S. Pettit. The Electrochemical Society, Princeton, 715-723.

Weber, T., M. Schütze, 2001, "Coatings against High Temperature H_2S-Corrosion", Proc. Eurocorr 2001, in press.

Wynns K. A., G. T. Bayer, 1998, "Aluminium-Silicon Diffusion Coating", US Patent, patent n°: WO9820182.

METAL DUSTING AND COKING – WAYS AND MEANS OF PROTECTION

H.J. GRABKE*, E.M. MÜLLER-LORENZ, A. SCHNEIDER
Max-Planck-Institut für Eisenforschung GmbH, Düsseldorf, Germany

ABSTRACT

Presence of sulfur in the carburizing atmosphere can retard or even suppress metal dusting of Fe and steels. Sulfur is adsorbed strongly on metallic surfaces, blocking the reaction sites for carbon transfer from the atmosphere. The adsorbed sulfur also hems nucleation of graphite on Fe and Fe_3C surfaces, interrupting the mechanism of metal dusting on Fe and steels. Thus in CO-H_2-H_2O-H_2S or CH_4-H_2-H_2S atmospheres prolonged growth of cementite or even Hägg carbide was observed. The contents of H_2S needed to suppress metal dusting have been determined to increase with temperature and carbon activity.

On high alloy steels, ferritic steels with >11% Cr and austenitic steels with >17% Cr, protective Cr-rich oxide scales may be formed. But at temperatures <600°C it is not for sure that Cr-diffusion in the steel is fast enough for protective scale formation, before fatal carbon ingress. The Cr-diffusion can be enhanced by providing fast diffusion paths, by using fine-grain steels and even more effectively, by introducing surface-near deformation, i.e. dislocations by grinding, sandblasting etc. Metal dusting exposures at 500–600°C showed that ground specimens of 9–20% Cr steels are more resistant than etched specimens without surface deformation. Chemically etching or pickling is deleterious for metal dusting resistance of all materials.

Joint application of sulfur dosing and of favoring the oxide scale formation by an appropriate alloy composition and a deforming surface finish are the well-studied ways and means, available for combating metal dusting.

INTRODUCTION

To obtain protection of metals and alloys against metal dusting their surface must be blocked by adsorbed sulfur or sealed by a protective oxide scale. On a sulfur-covered surface or on the surface of oxides such as Cr_2O_3, Al_2O_3 and spinels the adsorption and dissociation of CO, CH_4 and other hydrocarbons generally does not take place. Such surface reaction is necessary for carbon transfer into the metal, i.e. the first step of the metal dusting mechanism. Sulfur in addition interrupts this mechanism and oxides are impermeable for carbon, if they have no pores or cracks. How to achieve the protection by sulfur and/or oxides will be described here.

*Corresponding author address: Prof Dr. H.J. Grabke, Max-Planck-Institut für Eisenforschung GmbH, Max-Planck-Str. 1, 40237 Düsseldorf; e-mail: grabke@mpie.de

PROTECTION BY SULFUR

The effect of sulfur on occurrence of metal dusting was studied in detail in CO-H_2-H_2O-H_2S mixtures on iron. The samples were exposed for about 200 h in the gas mixtures and examined afterwards for occurrence of metal dusting. This study (Grabke and Müller-Lorenz 1995; Schneider et al. 1998) yielded dots for attack (black) or no attack (open) in a diagram log pH_2S/pH_2 vs. 1/T (Fig. 1). These data could be well correlated to knowledge about sulfur adsorption on iron from previous studies. The adsorption isotherm for the reaction

$$H_2S = H_2 + S \text{ (adsorbed)} \qquad (1)$$

had been derived from measurements of the kinetics of nitrogenation in N_2 and carburization in CH_4-H_2 on iron foils (Grabke et al. 1977; Grabke 1980). These reactions are retarded with increasing coverage of adsorbed sulfur and the degree of sulfur coverage in dependence on pH_2S/pH_2 was derived from the dependence of reaction rates on pH_2S/pH_2.

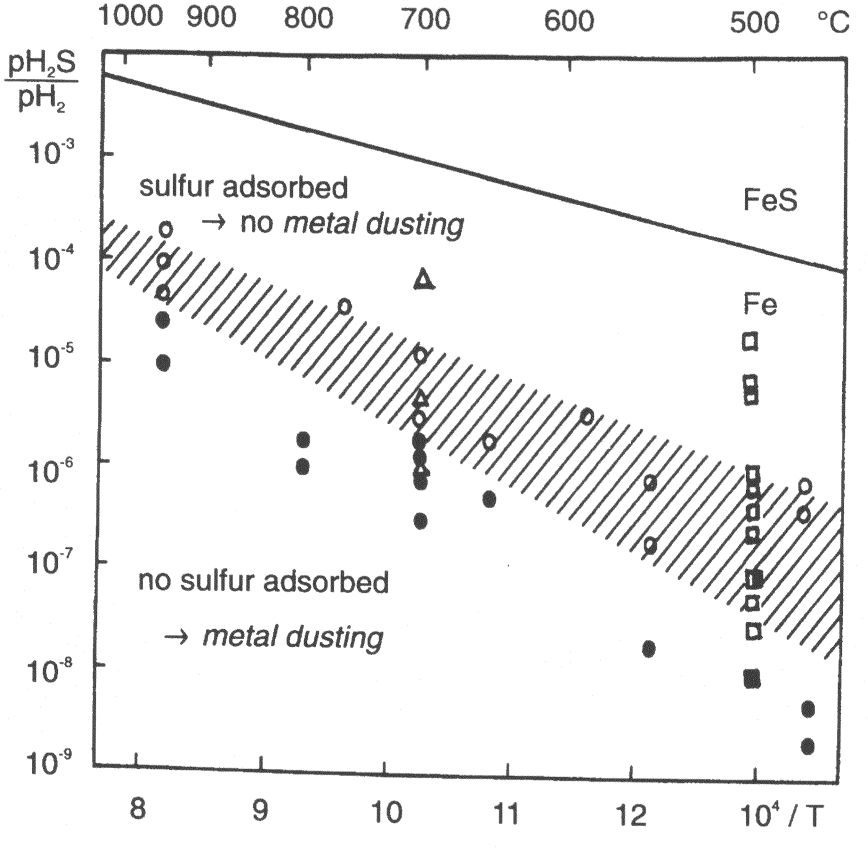

FIGURE 1 Effect of sulfur activity in the atmosphere on sulfur adsorption and metal dusting, in the plot of log pH_2S/pH_2 vs 1/T regions are indicated, where nearly no sulfur is adsorbed and metal dusting occurs, where sulfur coverage approaches saturation and metal dusting is increasing increasingly suppressed (hatched area) and region where a sulfur monolayer prevents metal dusting.

The hatched area in Fig. 1 corresponds to the approach of sulfur coverage from $\theta_S \approx 0.9$ to a monolayer, and divides the regions of metal dusting attack and no attack. At low temperatures rather low values of pH_2S/pH_2 are sufficient to provide protection, at higher temperatures this value increases. It may be noted that the data correspond well to values known from studies of the carburization of high temperature alloys at 900 and 1000°C, for ratios pH_2S/pH_2 necessary for suppressing internal carbide formation largely (Grabke et al. 1979).

Adsorbed sulfur blocks the surface for the adsorption of CO or CH_4 and other hydrocarbons, the molecules cannot adsorb and dissociate if their adsorption sites are occupied by sulfur. But even at high pH_2S/pH_2 some sites will be free in adsorption equilibrium such as reaction (1) at high temperatures. So carbon can be transferred through such vacancies and the carbon transfer is not suppressed completely but retarded. So after oversaturation, cementite nucleation and growth occur at the iron surface, beneath the adsorbed sulfur. Now the sulfur has an additional effect, it hinders the nucleation of graphite, which would initiate the cementite decomposition. So cementite is stabilized and in fact, cementite could be grown in $CO-H_2-H_2O-H_2S$ mixtures up to considerable thicknesses (Grabke and Müller-Lorenz 1995; Schneider et al. 1998). On such layers, thermodynamics, disorder and carbon diffusion in cementite could be studied and data were obtained which were not available for this instable compound as yet (Schneider et al. 1998, 2000).

The action of sulfur on the metal dusting of three steels 2 1/4% Cr, Alloy 800 and HK 40 was demonstrated in an exposure at 600°C in H_2-24%CO-2%H_2O. The samples were exposed at first without H_2S addition, until after some days they showed nearly constant metal wastage rate (Fig. 2). When 10 vppm H_2S were added and immediately the corrosion was retarded. Interruption of H_2S addition resulted in acceleration of attack, and a new addition of H_2S in

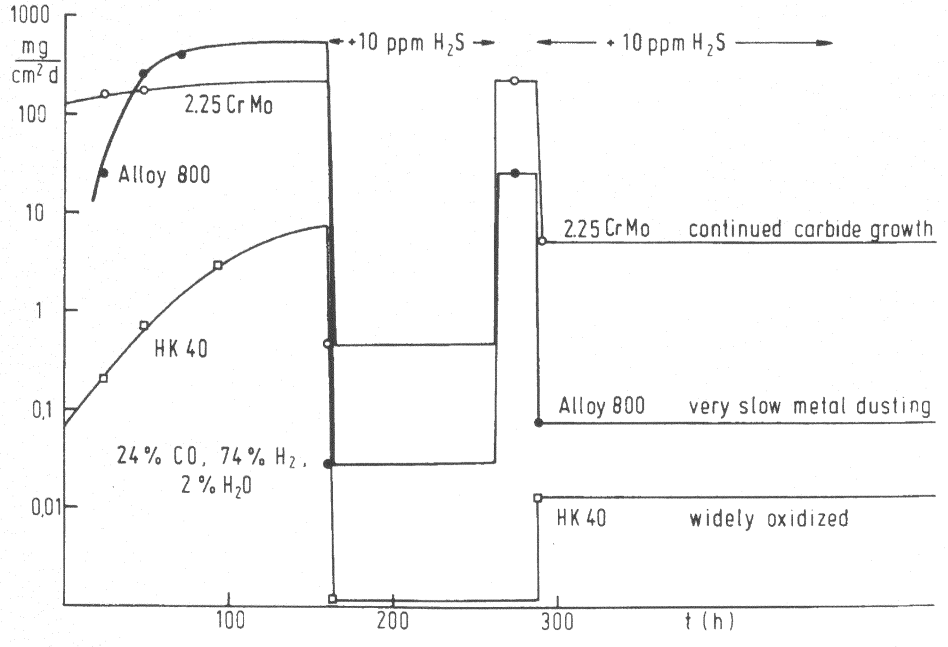

FIGURE 2 Logarithmic plot of metal wastage rates vs time, in a metal dusting exposure at 600°C, of a low alloy 2.25CrMo-steel, a high alloy 20Cr-32Ni-stel (Alloy 800) and a cast 25Cr-20Ni-steel(HK40), - changes of rate without and with H_2S addition.

retardation. So one can switch off and switch on metal dusting very abruptly by presence or absence of H_2S in the atmosphere, the adsorption equilibrium (1) is established rapidly. But, for the three alloys, the sulfur effect is different. As described for iron on the low alloy steel, continued cementite growth is observed. On Alloy 800 continued metal dusting is going on, but strongly retarded in the presence of H_2S. For HK40 (cast 25%Cr-20%Ni steel) during the periods with H_2S oxide growth is possible as indicated by the metallographic cross section, and the metal dusting attack is reduced effectively. One may conclude that for low alloy steels the protection is limited, corrosion by cementite growth continues. On the very susceptible Alloy 800 the metal dusting is not fully suppressed. Only by the joint effect of sulfur and oxide formation on HK40 a sufficient protection is achieved.

PROTECTION BY AN OXIDE SCALE

The protection by a dense uniform oxide scale is more effective than by the monoatomic sulfur adsorption layer. But the scale must be composed of chromium rich oxides, i.e. on Ni-base chromia alloys Cr_2O_3 and on steels generally an outer spinel $(Mn,Fe)Cr_2O_4$ and inner chromia layer. Such Cr-rich scales are not easily formed in the temperature range most critical concerning metal dusting about 600°C, since Cr-diffusivities are low. The Cr-supply to the surface upon exposure to the corrosive atmosphere must be rapid, so that the protective oxide is dense, before too much carbon enters the metal phase and ties up the Cr by formation of stable carbides $M_{23}C_6$ and M_7C_3. Therefore fast-diffusion paths must be supplied for Cr-transport to the surface, which is possible by application of fine-grained steels and alloys and/or surface working by grinding, sandblasting, shot-peening etc. Certainly also a high Cr-content is useful, and possibly the use of ferritic steels, in which Cr-diffusion is faster by about 2 orders of magnitude compared to austenitic steels (Grabke et al. 1997, 1998, Grabke and Müller-Lorenz 1998).

Effect of Microstructure

The effect of fine grain size was clearly demonstrated by a failure case, of a heat exchanger made of Alloy 800, which served for cooling syngas from 575 to 350°C (Grabke et al. 1998). In the same regions where Alloy 800 was wasted from 10 mm to zero, some sheets made of stainless steel 304 were not attacked at all. Surface analysis of the fine-grained steel 304 showed the presence of a thin protective Cr- and Si -rich oxide film. Obviously, the stainless steel had a good chance to form such film, whereas on the large-grained Alloy 800, Cr-rich oxide grows only above the grain boundaries and on the wide grain surfaces Fe-rich unprotective oxide is formed (Grabke et al. 1998). So the Alloy 800 most probably was attacked beginning with the start of operation.

The positive effect of cold rolling and of fine grain size was further confirmed by exposures of the steels 304, 310 and 800 in different states, but in the same exposures grinding proved to be even more favorable for prolonging the protection (Grabke et al. 1998).

Effect of Grinding

In exposures of four ferritic steels and two austenitic steels the effects of grinding and of etching (in H_3PO_4-H_2SO_4) were studied, by determining the metal mass transferred into the coke after each period. Such studies were performed at 500, 525, 560 and 600°C (Grabke et al. 1998; Grabke et al. 1997), the increase of wastage rate with time is shown for the exposures at 600°C in Fig. 3. In the etched state the 2 1/4%Cr, 9%Cr-steel, and 12CrMoV-steel(lo) with 10.4%Cr were attacked by metal dusting all over their surface and more or less constant wastage rates observed

already after short time. This is valid also for the austenitic steels 304 and 800, for which the wastage rate attained is somewhat less. Only the 12CrMoV-steel(hi) with 11.2% Cr is more resistant. In the ground state all steels show better resistance, except the 2 1/4% Cr-steel which would not form an oxide in both states. In the ground state the steels 12CrMoV(hi) and 304 proved to be rather resistant, better than the Alloy 800 with its higher Cr-content. Similar results were obtained at the other temperatures.

The effect of grinding on the oxide composition was clearly demonstrated by Auger sputter profiles, taken after the 240 h exposure at 600°C (Fig. 4). On the most resistant steels relatively thin scales had grown, 110 nm on the 12CrMoV-steel and 45 nm on steel 304, composed of Mn- and Cr-oxide, nearly free of iron. This kind of scale is impermeable for carbon, the carbon signal decreases to zero from the surface into the oxide.

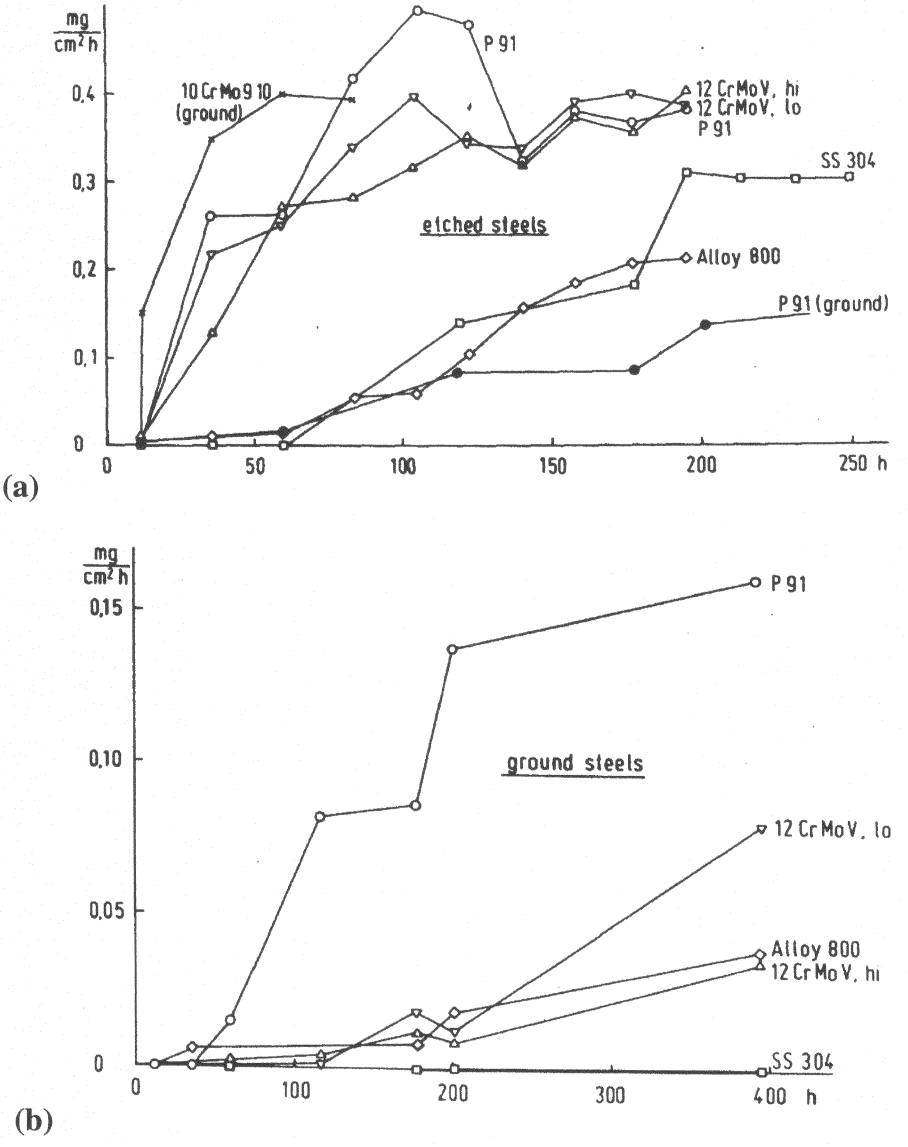

FIGURE 3 Increase of wastage rates with time in metal dusting exposures of various steels at 600°C; a) etched steels b) ground steels.

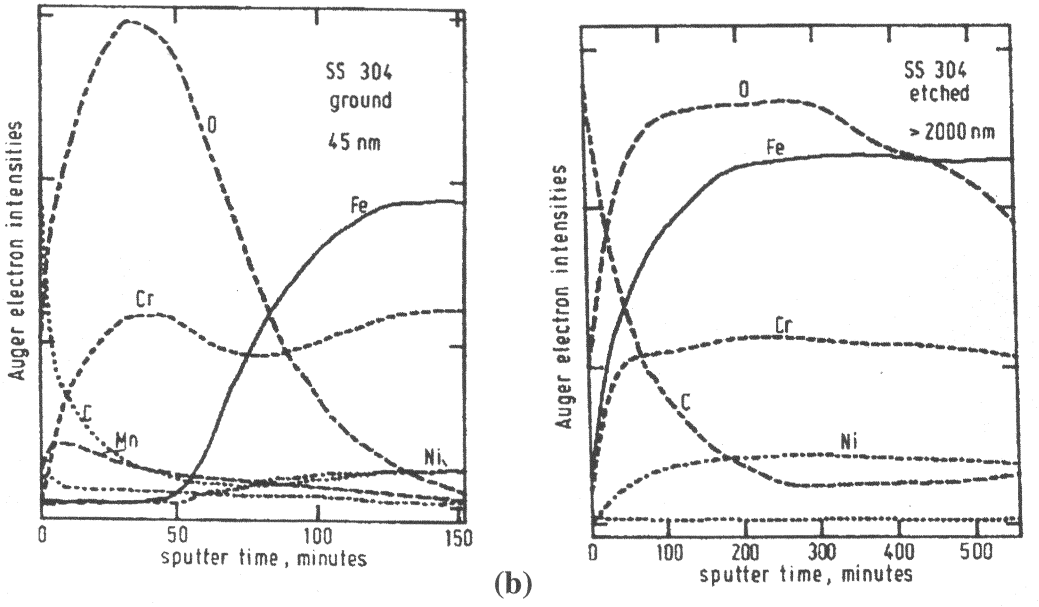

FIGURE 4 Auger sputter profiles of SS304 after metal dusting exposures at 600°C for 300 h a) thin protective Mn- and Cr-rich scale on the ground sample b) thick unprotective Fe-rich scale on the etched sample.

For the etched specimens, the oxide scale is thicker and is composed of Fe- and Cr-oxide in the case of steel 304, even Ni is in the oxide, which is most probably a $(Fe,Cr,Ni)_3O_4$ spinel. Such spinel appears to be permeable for carbon since the carbon signal stays high throughout the oxide into the metal phase. Such spinel also is permeable for sulfur (Lobnig and Grabke 1990) as shown by tracer studies, probably due to pores and channels.

CONCLUSIONS

Protection against metal dusting is possible by preventing ingress of carbon into the metal phase by adsorbed sulfur and/or dense oxide scales. Adsorption of sulfur from H_2S in the atmosphere can protect low alloy steels up to limited temperatures <600°C, the content of H_2S necessary is rather low but it must be always present. Only at high rations H_2O/H_2 and CO_2/CO protective scales (magnetite) are formed on low alloy steels.

High alloy steels can form protective Cr-rich scales, but for their formation Cr-diffusion in the steels should be enhanced by a fine grained microstructure and/or a surface near deformation by grinding, sandblasting etc. Additional presence of sulfur from the atmosphere is very advantageous, for mending spots where the scale has either cracked or spalled – the sulfur adsorption on the bare metal surface impedes carbon ingress and start of metal dusting, until the oxide layer heals again. So, for high alloy steels one should aim at protection by controlled sulfur in the atmosphere and generation of a protective Cr-rich scale.

If process conditions do not allow the presence of sulfur, Ni-based alloys with high Cr- and Al- or Si-addition are the only choice to attain resistance against metal dusting.

REFERENCES

Grabke, H.J., 1980, "Adsorption, Segregation and Reactions of Nonmetal Atoms on Iron Surfaces", *Materials Sci. & Eng.* 42:91-99.

Grabke, H.J., R. Möller and A. Schnaas, 1979, "Effect of Sulfur on the Carburization of a CrNiFe-Alloy at High Temperatures", *Werkstoffe u. Korrosion* 30:794-799.

Grabke, H.J. and E.M. Müller-Lorenz, 1995, "Effect of Sulfur on the Stability of Cementite", *Steel Research* 66**:** 252-258.

Grabke, H.J. and E.M. Müller-Lorenz, 1998, "Mechanisms of Metal Dusting and Ways of Protection", *Mat. Corr.* 49: 317-320.

Grabke, H.J., E.M. Müller-Lorenz, B. Eltester, M. Lucas and D. Monceau, 1997, "Resistance of 9-20%Cr-Steels Against Metal Dusting", *Steel Research* 68:179-185.

Grabke, H.J., E. Müller-Lorenz, S. Strauss, E. Pippel and J. Woltersdorf, 1998, "Effects of Grain Size, Cold Working, and Surface Finish on the Metal Dusting Resistance of Steels", *Oxid. Metals* 50:2241-254.

Grabke, H.J., E. M. Petersen and S.R. Srinivasan, 1977, "Influence of Adsorbed Sulfur on Surface Reaction Kinetics and Surface Self-Diffusion on Iron", *Surface Sci.* 67:501-516

Lobnig, R. and H.J. Grabke, 1990, "Mechanisms of Oxide Scale Failure in Simultaneous Oxidation and Sulfidation ", *Corrosion Sci.* 30:1045-1071.

Schneider, A., G. Inden and H.J. Grabke, 2000, "Growth Kinetics of Iron Carbide Layers During Gas Carburization", EUROMAT 99, Vol. 9 *Interface Controlled Materials*, M. Rühle, H. Gleiter (EDS), Wiley-VCH, 30-37.

Schneider, A., H. Viefhaus, G. Inden, H.J. Grabke and E.M. Müller-Lorenz, 1998, "Effect of H_2S on Metal Dusting and on the Stability of Cementite", *Mat. Corr.* 49: 330-335.

METAL DUSTING BEHAVIOR OF COATINGS

K. Natesan*, Z. Zeng, W. K. Soppet, and D. L. Rink
Argonne National Laboratory
Argonne, IL 60439

ABSTRACT

Surface modification by preoxidation and/or by coatings and alternative materials are being examined at ANL to alleviate the metal dusting problem. Oxide coatings have the advantage that they can minimize carbon-producing reactions (by reducing the availability of catalytic surface) and can also act as a barrier to minimize carbon ingress and pitting of the substrate alloy. We have selected in-situ development of oxide scales, pack diffusion of Al or Cr/Si, and thermal spray of FeAl as avenues for further study. Preliminary tests showed virtually no carbon in pre-oxidized layers of Al-, Cr-, and Si-enriched layers that were subjected to metal dusting environments.

INTRODUCTION

Metal dusting is a catastrophic corrosion phenomenon that leads to the disintegration of structural metals and alloys into dust composed of fine particles of the metal/alloy, carbides, and carbon (Natesan et al. 2002). Metal dusting occurs at intermediate temperatures of 400-800°C, but this type of corrosion is possible at any temperature at which the carbon activity (a_C) in the gas phase is >>1. There are two major issues of importance in metal dusting. First is formation of carbon and subsequent deposition of carbon on metallic materials. Second is the initiation of metal dusting degradation of the alloy. The first is influenced by a_C in the gas mixture and the availability of the catalytic surface for carbon-producing reactions to proceed. There may be a threshold in a_C (>>1) for carbon deposition. Metal dusting of the alloy in the reformer environments is determined by a competition between the oxide scale development and access of the virgin metal surface to the carbon deposit. The presence of an oxide scale may not prevent metal dusting but can delay its initiation, thereby slowing the overall attack.

Coatings can minimize gas phase reactions by lack of availability of metal surfaces for catalysis. This, in turn, can minimize or eliminate coking and carbon deposition. Furthermore, coatings can act as barriers to carbon ingress into the substrate alloy since carbon diffusion through oxide scales is generally orders of magnitude lower than through the alloys. Among the oxides as coatings, the potential candidates are chromia, alumina, and silica. Iron oxide may not be a viable candidate unless the Fe-oxide to Fe-carbide reaction is slow enough that oxide can be maintained for the desired service life. The present paper discusses the application of oxide scales developed in-situ on metallic surfaces or oxide coatings applied by external methods to mitigate metal dusting degradation.

*Corresponding author address: K. Natesan, Argonne National Laboratory, 9700 South Cass Avenue, Argonne, IL 60439; e-mail: ntesan@anl.gov

EXPERIMENTAL PROGRAM

Three approaches are being examined for the development of oxide surface layers for evaluation in metal dusting environments. The first approach is to develop the oxide layer on the structural alloys by a preoxidation treatment. In this case, the specimens are exposed to either air or a low-pO_2 (established by H_2/H_2O or CO/CO_2 gas mixtures) environment at temperatures between 750 and 900°C. Generally, depending on the Cr content of the alloy and pO_2 in the exposure environment, the alloys develop (Fe,Cr) or (Ni,Cr) spinels or "pure" Cr oxide on the surface. Regulating the exposure time and temperature can control the thickness of the oxide layer.

The second approach involves a pack diffusion process in which the alloy surface is enriched in oxide-forming elements such as Al, Cr, and/or Si. Subsequently, the surface-enriched alloy is oxidized in air to develop the oxide scale of choice. Pack diffusion is widely used to confer oxidation resistance on ferrous alloys. Pack diffusion processes include aluminizing, chromizing, and siliconizing. Specimens/components are packed in metal powders in sealed heat-resistant retorts and heated inside a furnace to precisely controlled temperature-time profiles. In the aluminizing process, a source of Al reacts with a chemical activator on heating to form a gaseous compound (e.g., pure Al with NaF to form AlF). This gas is the transfer medium that carries aluminum to the component surface. The gas decomposes at the substrate surface, depositing Al and releasing the halogen activator. The halogen activator returns to the pack and reacts with the Al again. Thus, the transfer process continues until all of the aluminum in the pack is used or until the process is stopped. The coating forms at temperatures ranging from 700 to 1100°C over a period of several hours.

The third is thermal spray approach in which the surface treatment involves energizing the surface of the workpiece in order for adhesion to take place. Conventional surface finishing methods involve heating an entire component, but the thermal spray technique usually adds energy and material into the surface, keeping the bulk of the object relatively cool and unchanged. This allows surface properties to be modified with minimal effect on the structure and properties of the underlying material. Coatings can be sprayed from rod or wire stock or from powdered materials. The material (e.g., wire) is fed into a flame where it is melted. The molten stock is then stripped from the end of the wire and atomized by a high velocity stream of compressed air or other gas, which propels the material onto a prepared substrate or workpiece. The basic steps involved in any thermal coating process are substrate preparation, masking and fixturing, coating, finishing, inspection, and stripping (if necessary). Roughening is also necessary for most of the thermal spray processes to ensure adequate bonding of the coating to the substrate. Specimens with a thermal spray coating of FeAl are included for evaluation in metal dusting environments.

Materials for In-situ Scale Development

The test materials for in-situ scale development include a number of Fe- and Ni-base alloys, predominantly those commercially available. In the present paper discussions pertain only to Fe-base alloys whose nominal compositions are listed in Table 1. The specimens were preoxidized by exposing them in an H_2-2 vol.% H_2O gas mixture at 900°C for 200 h. The gas mixture established a pO_2 of 2.1×10^{-20} atm at 900°C.

Pack-Diffusion Coatings

Specimens with Al (termed "alonizing") and Cr,Si (termed "ChromePlexing") enrichment were obtained from Alon Surfaces for evaluation in metal dusting environments. Substrates

selected for Al enrichment included three Fe-base alloys (T22, 800, and 321 stainless steel) and three Ni-base alloys (601, 625, and HR160). Substrates selected for ChromePlexing included only the three Fe-base alloys since it was not feasible to enrich Cr/Si on Ni-base alloys.

TABLE 1 Nominal chemical compositions (wt.%) of alloys selected for the experimental program.

Material	C	Cr	Ni	Mn	Si	Mo	Al	Fe	Other
T22	0.20	2.3	–	0.6	0.5	1.0	-	Bal	–
T91	0.08	8.6	0.1	0.5	0.4	1.0	-	Bal	N 0.05, Nb 0.07, V 0.2
153MA	0.05	18.4	9.5	0.6	1.4	0.2	-	Bal	N 0.15, Ce 0.04
253MA	0.09	20.9	10.9	0.6	1.6	0.3	-	Bal	N 0.19, Ce 0.04
353MA	0.05	24.4	34.7	1.4	1.3	0.1	-	Bal	N 0.18, V 0.06
321L	0.02	17.4	9.3	1.8	0.5	-	-	Bal	N 0.02, Ti 0.3
310	0.03	25.5	19.5	1.7	0.7	-	-	Bal	-
800	0.08	20.1	31.7	1.0	0.2	0.3	0.4	Bal	Ti 0.31
803	0.08	25.6	36.6	0.9	0.7	0.2	0.5	34.6	Ti 0.6
38815	0.01	13.9	15.3	0.6	5.8	1.0	0.13	Bal	-
MA956	-	20.0	-	-	-	-	4.5	Bal	Ti 0.5, Y_2O_3 0.6
321	0.04	17.3	10.3	1.2	0.4	-	-	Bal	Ti 0.4, N 0.01
APMT	0.04	21.7	-	0.1	0.6	2.8	4.9	Bal	-
4C54	0.17	26.7	0.3	0.7	0.5	-	-	Bal	N 0.19

Figures 1-3 show scanning electron microscopy (SEM) micrographs of cross sections of alonized Fe-base alloys (T22, 321 stainless steel, and Alloy 800) along with elemental profiles as a function of coating thickness obtained by energy dispersive X-ray spectroscopy (EDX). Aluminum concentration at the surface of all three alloys in the as-coated condition was in a range of 35-45 wt.%. The depth profile in T22 shows a gradual decrease in Al concentration to a depth of ≈300 μm. The aluminum concentration profile for 321 stainless steel (which contains ≈10.3 wt% Ni) is less gradual, but the depth of the Al-enriched layer is ≈200 μm. In Alloy 800 (which contains 31.7 wt.% Ni) a layer of Ni_3Al intermetallic forms on the interface between the Al enriched layer and the alloy substrate. This layer seems to slow the diffusion of Al into the substrate. As a result, the Al concentration profile is much flatter (28-36 wt.% Al) over a distance of 140 μm, after which there is a sharp drop in Al concentration.

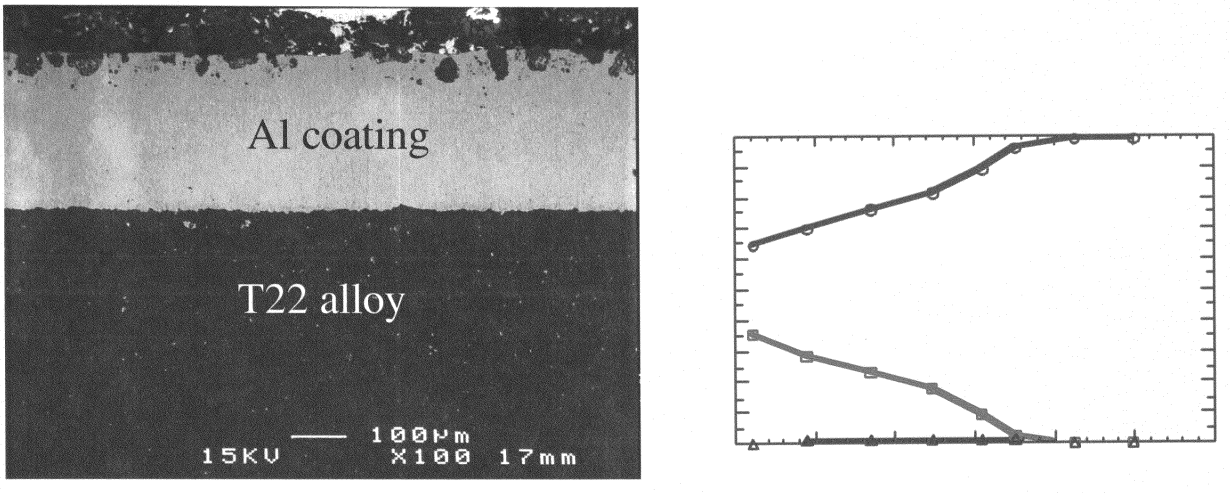

FIGURE 1 SEM photomicrograph of cross section of alonized T22 steel and EDX elemental depth profiles of Al and Fe for the specimen in the as-coated condition.

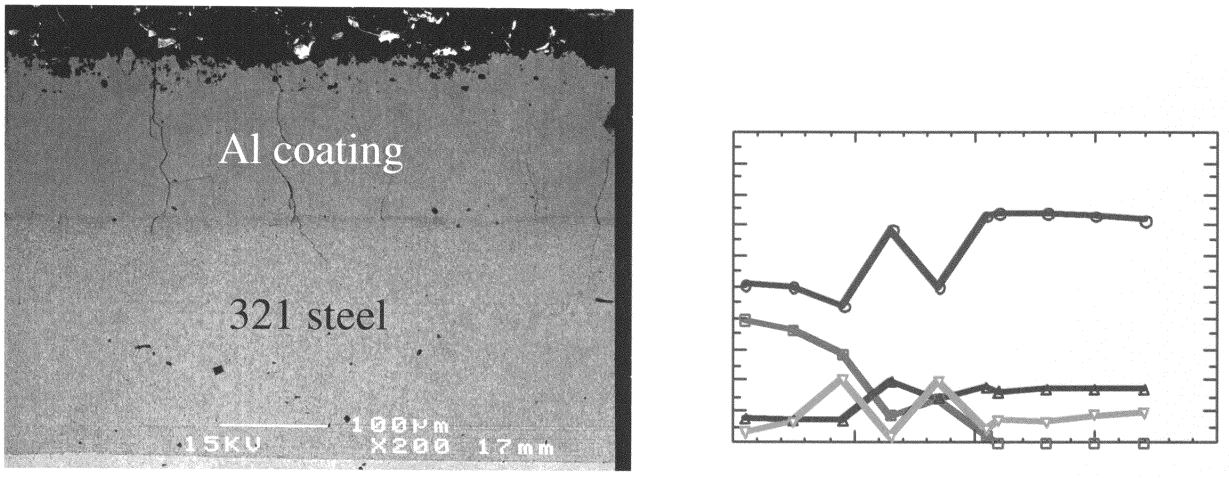

FIGURE 2 SEM photomicrograph of cross section of alonized 321 stainless steel and EDX elemental depth profiles of Al, Fe, Cr, and Ni for the specimen in the as-coated condition.

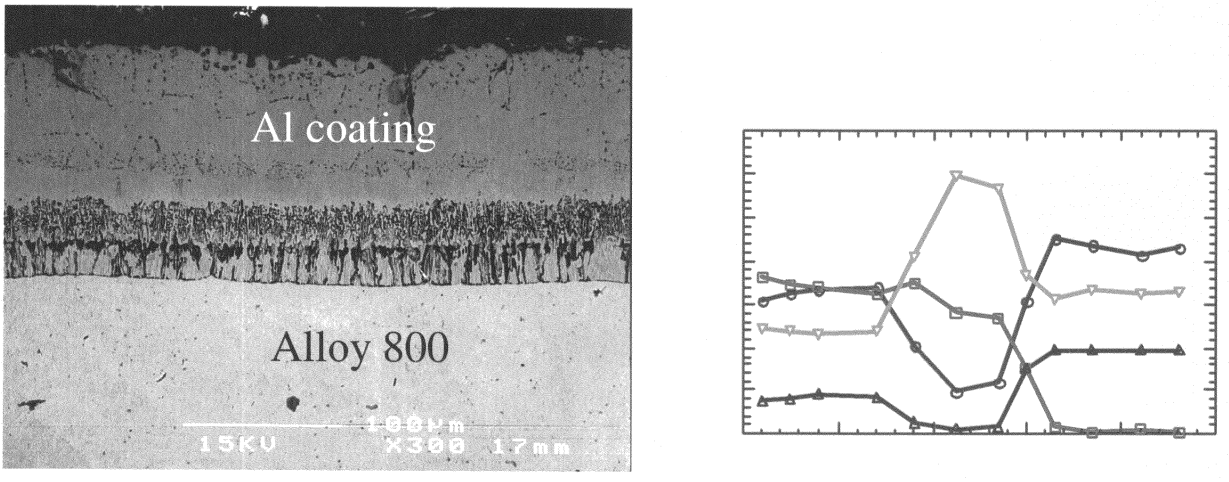

FIGURE 3 SEM photomicrograph of cross section of alonized Alloy 800 and EDX elemental depth profiles of Al, Fe, Cr, and Ni for the specimen in the as-coated condition.

Figures 4-6 show SEM photomicrographs of cross sections of ChromePlexed Fe-base alloys (T22, 321 stainless steel, and Alloy 800) along with elemental profiles as a function of coating thickness obtained by EDX analysis. Chromium and silicon concentrations at the surface of T22 steel were 12 and 2.5 wt.%, respectively. The elemental profiles shows that these concentrations remain fairly constant up to a depth of ≈250 µm. In the case of 321 stainless steel the Cr and Si concentrations were ≈20-25 and ≈5 wt.%, respectively, to a depth of 250 µm. The Cr concentration in Alloy 800 was in the range of 20-30 wt.%, while the Si content was similar to that of 321 stainless steel.

Specimens with pack-diffusion coatings were oxidized in air for 200 h at 900°C to develop the oxide scales.

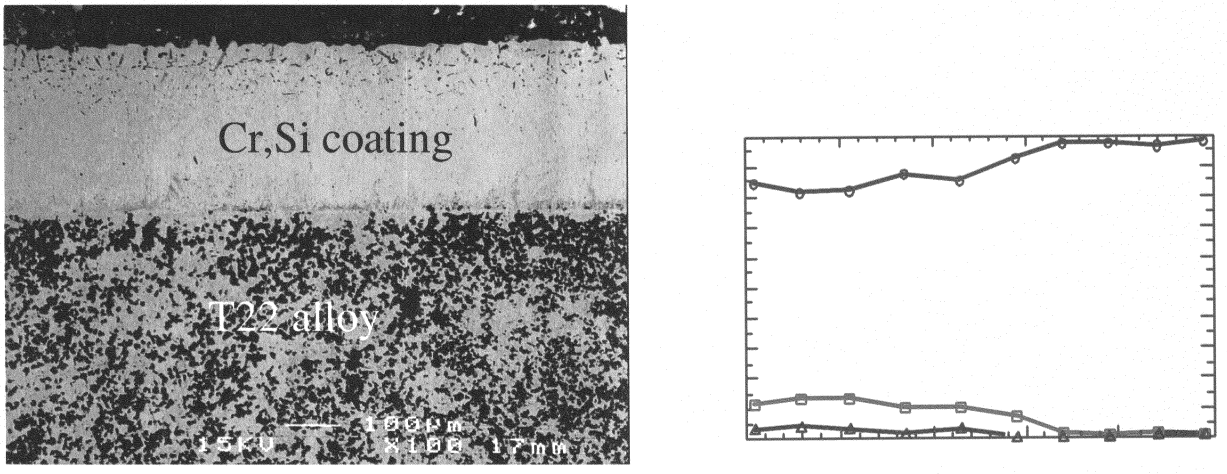

FIGURE 4 SEM photomicrograph of cross section of ChromePlexed T22 steel and EDX elemental depth profiles of Si, Fe, and Cr for the specimen in the as-coated condition.

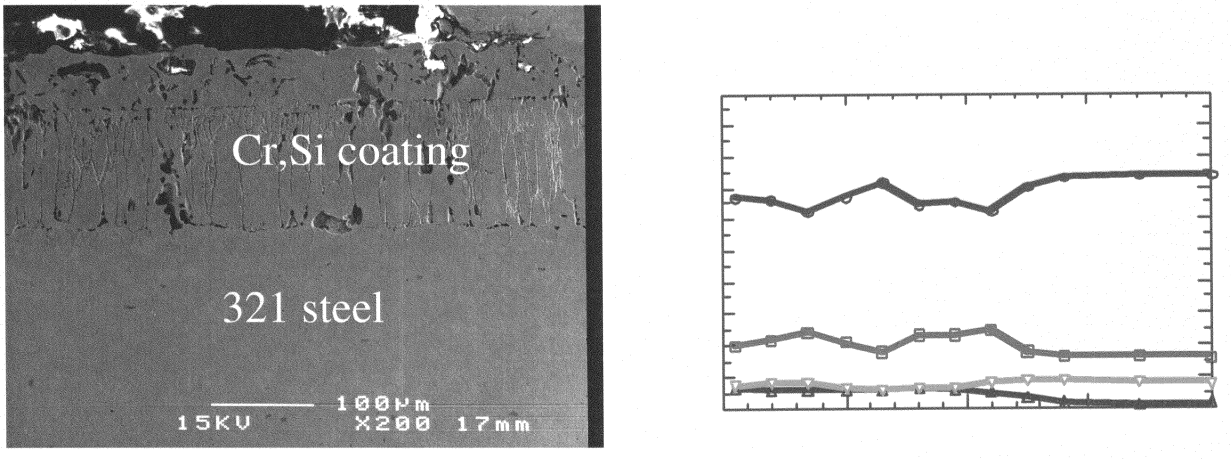

FIGURE 5 SEM photomicrograph of cross section of ChromePlexed 321 stainless steel and EDX elemental depth profiles of Si, Fe, Cr, and Ni for the specimen in the as-coated condition.

Metal Dusting Exposures

The metal dusting exposures of preoxidized Fe-base alloy specimens and oxidized pack-diffusion coated specimens were conducted in test systems that were described in another paper in this proceedings. The preoxidized Fe-base alloy specimens were exposed for 311 h at 593°C in a gas mixture with a composition (in vol.%): 66.2 H_2, 23 CO, 7.1 CO_2, 1.4 CH_4, and 2.3 H_2O. The carbon activity established by the gas mixture [based on the reaction: $CO(g) + H_2(g) = C + H_2O(g)$] at 593°C is 33. The oxidized pack-diffusion coatings were exposed for 142 h at 593°C to a gas mixture of composition (in vol.%): 52 H_2, 18 CO, 5.6 CO_2, 1.1 CH_4, and 23 H_2O. This gas mixture simulates the effluent of a H_2 reformer, and the carbon activity (based on the same reaction as above) established by this gas mixture at 593°C is 2.0.

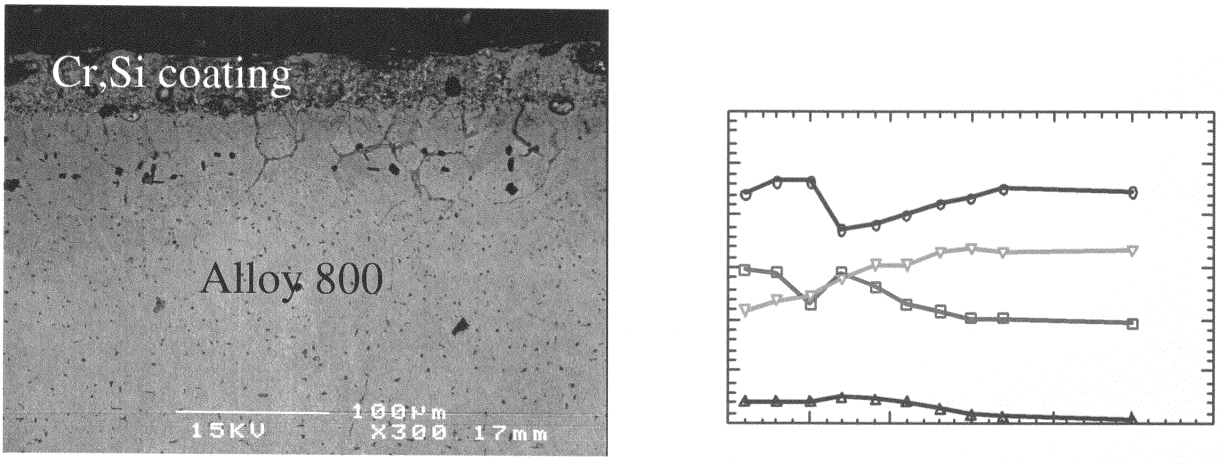

FIGURE 6 SEM photomicrograph of cross section of ChromePlexed Alloy 800 and EDX elemental depth profiles of Si, Fe, Cr, and Ni for the specimen in the as-coated condition.

TEST RESULTS AND DISCUSSION

Specimens with In-situ Oxide Scales

Weight changes were determined for the preoxidized Fe-base alloy specimens after exposure in the metal dusting environment for 311 h at 593°C. The microstructure of each specimen was examined with a JOEL-6400 scanning electron microscope. The samples were electrolytically etched in 10% acetic acid solution at 10 V for 30 s. Raman spectra were obtained with 60 mW of 476-nm radiation from a Kr-ion laser. The incident beam impinged on the specimen at a ≈45° angle from the normal. Scattered light was collected with a f/1.4 lens and analyzed with a triple Jobin-Yvon grating spectrometer and a CCD detector. All of our spectra were acquired for 300 s at room temperature.

Table 2 shows the weight change data for specimens tested in the metal dusting environment. A comparison of the data on these specimens with earlier-developed information on specimens without preoxidation showed that preoxidation in the H_2-H_2O environment had no significant benefit from the standpoint of either carbon deposition (indicting no reduction in catalytic activity) or pitting/metal dusting attack.

The raman spectroscope is an excellent tool to study the phases in thin oxide layers. Possible phases such as Cr_2O_3, $FeCr_2O_4$, and Fe_3O_4 spinels in the oxide scales have been studied by Raman scattering (Thibeau et al. 1978; Farrow et al. 1980; Thierry et al. 1988; Renusch et al. 1996;). Major Raman bands for Cr_2O_3 and Fe_3O_4 spinel are at 550 cm^{-1} and 670 cm^{-1}, respectively. In this work, we used Raman spectroscopy to study the phase composition of oxide scales and the relationship between phase composition and metal dusting.

For example, the Raman spectra showed that the ratios of the intensity of the 550 cm^{-1} band (Cr_2O_3) over the 684 cm^{-1} band (Fe,Cr spinel) for pre-oxidized specimens are less than those without the pre-treatment (see Fig. 7). High spinel content in oxide scales is not good to resist metal dusting corrosion. The oxygen pressure in our preoxidation step may be too high to

TABLE 2 Weight loss data for preoxidized* alloys after exposure at 593°C for 311 h in a gas mixture of composition (in vol.%) 66.2% H_2-7.1% CO_2-23% CO-1.4% CH_4-2.3% H_2O.

Alloys	Mass loss ($mg/cm^2 \cdot h$)	Visual examination
T22	0.7	Heavy carbon deposition
T91	0.032	Pits, carbon deposition
153MA	$5.3x10^{-3}$	Pits
253MA	$4.3x10^{-3}$	Dark spots
321L	~0	Pits
310	~0	Light carbon deposition
800	~0	Pits
803	~0	Light carbon deposition
38815	~0	Clean surface
MA956	~0	Dark surface
321	$9.3x10^{-4}$	Pits
APMT	~0	Dark surface
4C54	~0	Dark surface

* Specimens were pre-oxidized in a H_2O/H_2 atmosphere at 900°C for 200 h.

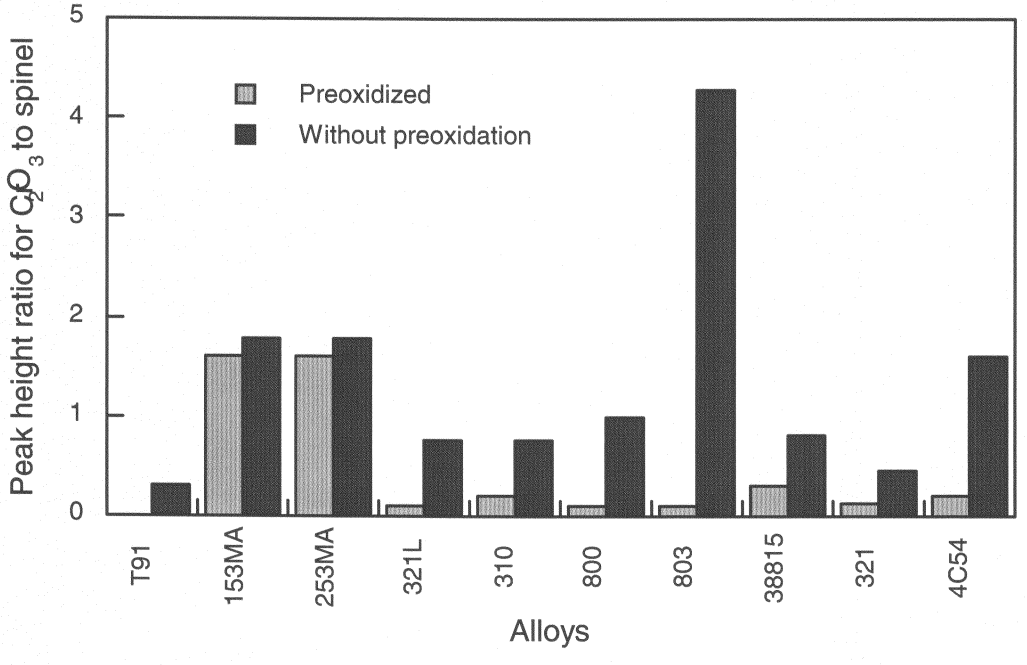

FIGURE 7 The intensity ratio of band 550 cm^{-1} (Cr_2O_3) over band 684 cm^{-1} (spinel) after exposure in a metal dusting environment for specimens with and without preoxidation in 2.3 vol.%H_2O-H_2 gas mixture for 200 h at 900°C.

oxidize iron and to form a spinel phase. If the oxidation condition results in only Cr_2O_3 phase in the scale, the scale will be resistant to coking and to subsequent metal dusting of the underlying alloy. Additional long-term tests with and without preoxidation treatments are in progress to establish the optimum oxide composition/phase to obtain adequate resistance to metal dusting.

Pack-Diffusion Coatings

Specimens with pack-diffusion coatings were oxidized in air for 200 h at 900°C to develop the oxide scales and, subsequently, were exposed to the gas with 23 vol.% H_2O at 593°C for 142 h. Figures 8-10 show SEM photomicrographs of surfaces of alonized specimens after oxidation and oxidation/metal dusting treatments. Similar photomicrographs for the ChromePlexed specimens are shown in Figs. 11-13. In general, the oxidized surface layers were intact after exposure in the metal dusting environment. There was some discoloration of the air-oxidized specimens after exposure to the carbonaceous atmosphere, but detailed Raman analysis of the specimen surfaces showed almost no carbon. The preliminary results clearly showed that the oxide layers developed on pack-diffusion coated specimens minimize the catalytic reactions that can lead to carbon generation and deposition. Additional long-term experiments are in progress with several of the surface-modified alloys to establish the integrity of these preformed oxide layers in resisting metal dusting degradation.

SUMMARY

Effort is underway at Argonne National Laboratory to mitigate metal dusting degradation of alloys by forming oxide scales either in-situ or by the pack-diffusion technique. Experiments were conducted to examine the viability of oxide scales preformed in a low oxygen environment established by a H_2-H_2O gas mixture. A detailed analysis of the Raman spectra on various specimens with and without preoxidation showed that the relative amounts of (Fe,Cr) spinel and chromia in the oxide scale determine the susceptibility of the scale to metal dusting. The higher the

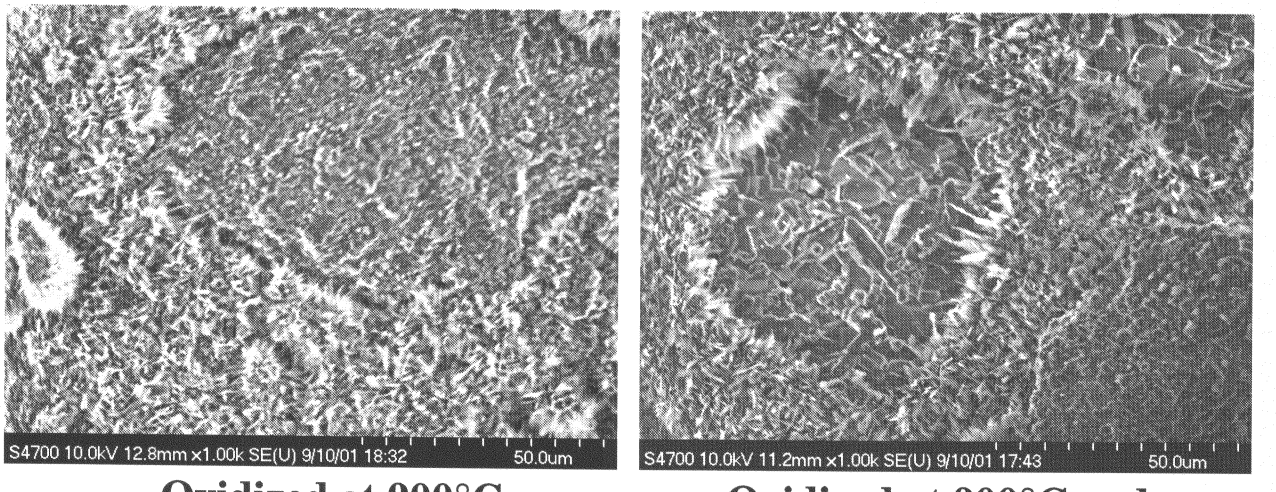

FIGURE 8 SEM photomicrograph of surface of alonized T22 steel after (left) oxidation at 900°C in air and (right) oxidation at 900°C followed by metal dusting exposure for 142 h at 593°C.

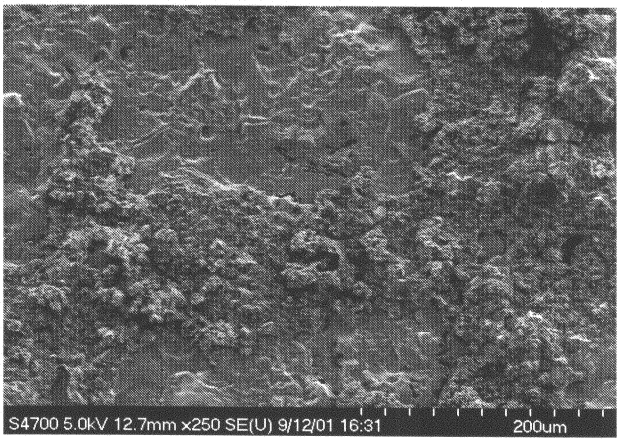

Oxidized at 900°C

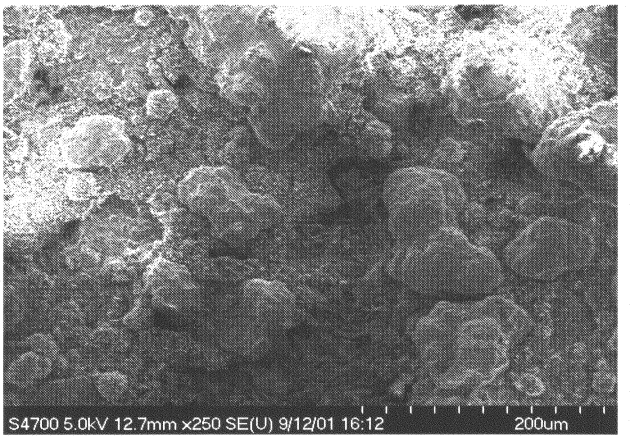

Oxidized at 900°C and metal dusted at 593°C (1100°F)

FIGURE 9 SEM photomicrograph of surface of alonized 321 stainless steel after (left) oxidation at 900°C in air and (right) oxidation at 900°C followed by metal dusting exposure for 142 h at 593°C.

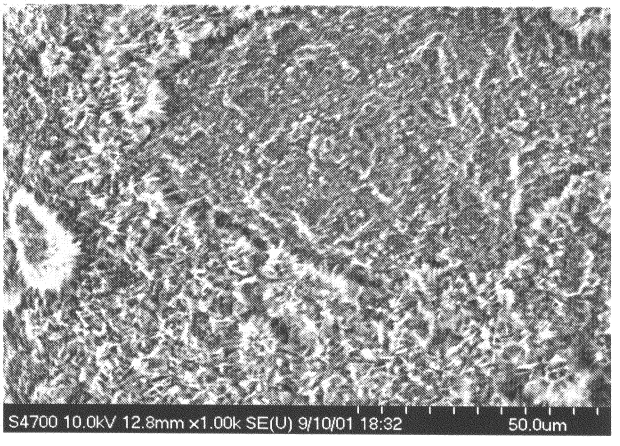

Oxidized at 900°C

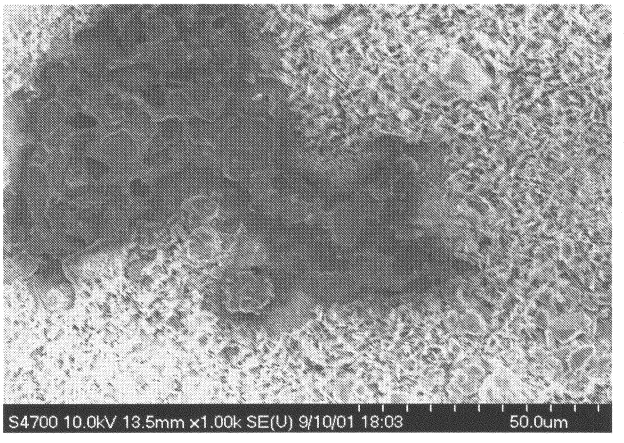

Oxidized at 900°C and metal dusted at 593°C (1100°F)

FIGURE 10 SEM photomicrograph of surface of alonized Alloy 800 after (left) oxidation at 900°C in air and (right) oxidation at 900°C followed by metal dusting exposure for 142 h at 593°C.

amount of spinel, the greater the chance that it will be reduced in the metal dusting environment, with the resultant Fe leading to carbon-forming reactions and subsequent metal dusting attack. A "pure" chromia can enhance the resistance to metal dusting since this oxide will be stable in the low pO_2 atmosphere prevalent in process environments. Preliminary results showed that the oxide coatings formed by the pack-diffusion approach can definitely retard the catalytic reactions that can lead to carbon formation and deposition. Additional experiments are in progress to assess the role of oxide scale composition and microstructure in the mitigation of metal dusting degradation.

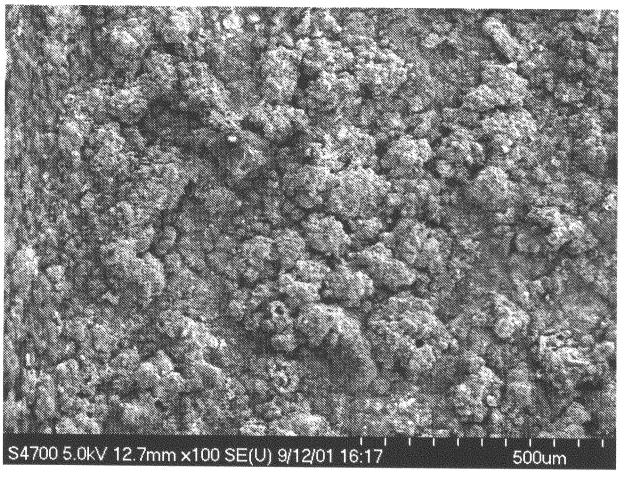

Oxidized at 900°C

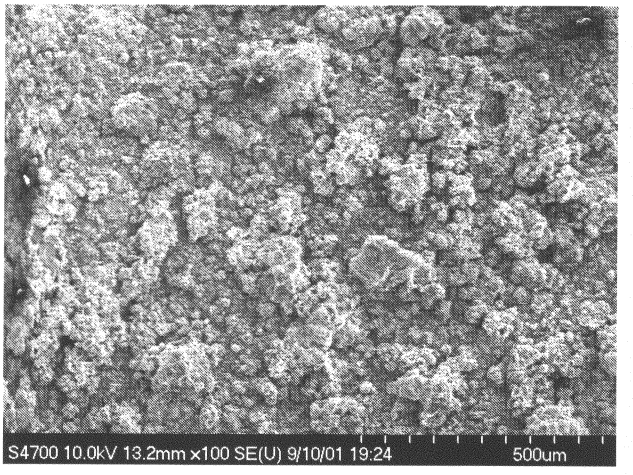

Oxidized at 900°C and metal dusted at 593°C (1100°F)

FIGURE 11 SEM photomicrograph of surface of ChromePlexed T22 steel after (left) oxidation at 900°C in air and (right) oxidation at 900°C followed by metal dusting exposure for 142 h at 593°C.

Oxidized at 900°C

Oxidized at 900°C and metal dusted at 593°C (1100°F)

FIGURE 12 SEM photomicrograph of surface of ChromePlexed 321 stainless steel after (left) oxidation at 900°C in air and (right) oxidation at 900°C followed by metal dusting exposure for 142 h at 593°C.

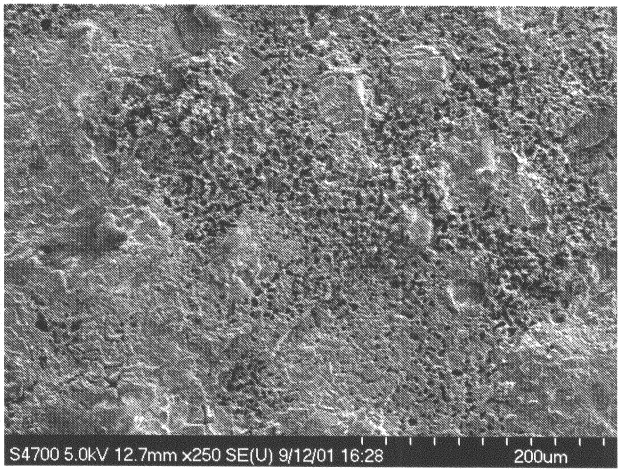

Oxidized at 900°C

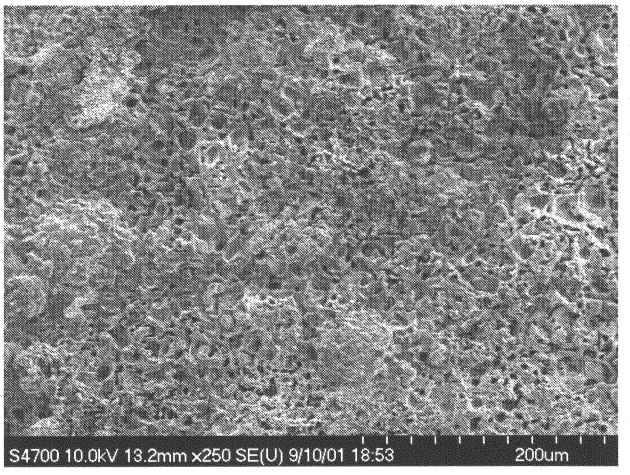

Oxidized at 900°C and metal dusted at 593°C (1100°F)

FIGURE 13 SEM photomicrograph of surface of ChromePlexed Alloy 800 after (left) oxidation at 900°C in air and (right) oxidation at 900°C followed by metal dusting exposure for 142 h at 593°C.

ACKNOWLEDGEMENT

This work was sponsored by the U.S. Department of Energy, Office of Industrial Technologies, and Dr. Charles Sorrell was the Program Manager for the project. Coated specimens of various alloys were supplied by Alon Surface Technologies, Inc.

REFERENCES

Farrow, R. L., R. E. Benner, A. S. Nagelberg, and P. L. Mattern, 1980, Thin Solid Film, 73, 353.

Natesan, K., 2002, Study of Metal Dusting Phenomenon and Development of Materials Resistant to Metal Dusting: Annual report, Argonne National Laboratory Report, ANL-02/05, 2002.

Renusch, D., B. Veal, K. Natesan, and M. Grimsditch, 1966, Oxid. Met., 46, 365.

Thibeau, R. J., C. W. Brown, and R. H. Heidersbach, 1978, Appl. Spec., 32, 532.

Thierry, D., D. Persson, C. Leygraf, D. Delichere, S. Joiret, C. Pallotta, and A. Hugot-Le Goff, 1988, J. Electrochem. Soc. 135, 305.

CONTROLLING/MITIGATING METAL DUSTING PROBLEMS WITH A NEW NICKEL BASE NI-CR-AL-Y HIGH CARBON ALLOY 602CA (N06025)

D. C. Agarwal, Krupp VDM Technologies, Houston, Texas*
U. Brill, Krupp VDM GmbH, Altena, Germany

ABSTRACT

In the high temperature corrosion, besides oxygen attack, alloys frequently encounter attack by carbon species. This attack can take two forms namely carburization and metal dusting (some times referred to as catastrophic carburization). Carburization generally occurs at carbon activities <1 and at temperatures >800°C and results in alloy embrittlement due to formation of internal carbides. Metal dusting on the other hand leads to rapid wastage, thinning and disintegration of alloys into graphite and metal particles and occurs in environments with carbon activities significantly greater than 1 and temperatures in lower range of 430 to 900°C. Metal dusting has been encountered in many industries such as in production of hydrogen, syngas, chemical plants for the synthesis of hydrocarbons, methanol, ammonia, in refineries, petrochemical plants, heat treating and reduction of iron ore plant. Attempts to inhibit metal dusting can take many forms such as using better alloy metallurgy, surface engineering modifications and/or pre-treatments of the alloy surfaces, use of coatings and using gas inhibitors such as addition of sulfide compounds (H_2S), which causes other problems. This paper presents some laboratory data, field data and some applications of a new nickel base chromia-alumina forming alloy 602CA (UNS N06025) along with its physical metallurgy characteristics, in providing solutions to this mode of high temperature degradation.

INTRODUCTION

Metal dusting, a phenomenon which was first documented in the 1950's has been extensively studied in the last 30 years with various theories as to its mechanistic behavior in both iron base and nickel base alloys. These are well documented in the literature (Hochman 1972, 1977; Grabke et al. 1993, 1996; Grabke 1998, 1999; Pippel et al. 1998; Mueller-Lorenz 1999). Production of syngas, a mixture of CO, H_2, CO_2, and H_2O from natural gas via steam reforming technology is a common starting step in production of hydrogen, ammonia, methanol, and liquid hydrocarbons, which are used in production of many intermediates and consumer end products. To increase production efficiency the trend to use less steam has resulted in lower steam to hydrogen ratios and higher pressures led to higher CO content (higher CO/CO_2 ratio). Both of these result in lower oxygen partial pressures and higher carbon activities. This combination synergistically accelerates the severity and propensity for metal dusting attack to occur. Metal dusting can cause unscheduled shutdowns and has been encountered in the following systems of many industries:

- In ammonia synthesis, need for increased heat recovery has caused metal dusting in the heat recovery section as well as the reformer itself.

*Corresponding author address: D. C. Agarwal, Krupp VDM Technologies, 11210 Steeplecrest Drive #120, Houston, TX 77065; e-mail: dcagarwal@pdq.net

- In direct reduction of iron ore technology where, depending on the process, coal gasification is encountered and/or reformed methane is dried and reheated to increase production efficiency.
- In heat-treat industry that utilizes gas mixtures for carburizing. Other gases used in heat-treating may combine with oil residues on parts to form gases chemically favorable for melt dusting.
- In refineries in processes involving hydro-dealkylation and catalyst re-generation systems.
- In nuclear plants which employ carbon dioxide for cooling.
- In the recycle-gas loop components of coal gasification units.
- In fired heaters in petrochemical industries handling hydrocarbons at elevated temperatures.
- In fuel cells using molten salts and hydrocarbons.
- In methanol production plants.

The common compound in every one of the above industries is the presence of carbon dioxide.

Other than the postulated theories regarding thermodynamics and mechanisms of metal dusting which are well documented in the open literature, what is known about metal dusting today can be summarized as follows:

- Stagnant condition (low gas velocity) areas tend to favor metal dusting.
- Nickel alloys with higher nickel content and chromia-alumina-forming elements tend to resist metal dusting better than iron alloys.
- Alloys high in Cr, Al, and Si may form protective oxide layers, which prevent ingress of carbonaceous corrosive species thus enhancing metal dusting resistance.
- Temperature ranges where metal dusting is more pronounced are generally between 450 and 900°C.
- Gas constituents and the various ratios of these constituents can either promote or inhibit metal dusting.
- Surface oxide stability is necessary to resist metal dusting.
- Surface modifications and coatings, which provide added stability to protective oxide layers, will enhance metal dusting resistance.
- Factors that degrade surface-oxide stability, i.e., mechanical and thermal stresses and strains may cause accelerated degradation.

Protection of an alloy against metal dusting attack requires the formation of an adherent, protective, capable of sustaining some strain, thermally stable and more importantly self repairing oxide surface layer. A nickel base alloy 602CA (UNS N06025) appears to fulfill these requirements and has shown promising results in both laboratory and field tests in combating metal dusting. Developed in the early 1990's, the alloy has found some very successful applications in various industries. The typical chemical composition of the alloy in weight % is given below:

Ni	Cr	Fe	Al	C	Ti	Zr	Y
Bal	25	9.5	2.2	0.18	0.15	0.06	0.08

This alloy is covered in ASTM and other international specifications. Data for coverage in ASME Boiler and Pressure Vessel Code was submitted for allowable stress calculations up to 1650°F for use in Section VIII, Div. 1 & SCI and was approved in a code case #2359 by the ASME Board in August 2001.

The major properties of interest in this alloy are:

- Excellent oxidation resistance up to 1200°C, superior to other nickel base alloys currently available in the market.
- Good high temperature strength (stress rupture and stress to produce 1% creep at temperatures up to 1200°C), superior to many other Ni-base alloys over 1000°C.
- Excellent carburization resistance.
- Excellent metal dusting resistance.

ALLOY 602CA DEVELOPMENT GOALS AND PROPERTIES

This alloy was originally developed to fulfill the needs of those industrial applications where good oxidation resistance and mechanical strength properties up to 1200°C were needed such as in the heat-treat industry. Since then the alloy due to its unique combination of high temperature corrosion resistance properties and creep/stress rupture properties has found many applications in a variety of industries (Grabke et al. 1998). Table 1 presents the typical composition of some of the common high temperature alloys used in the industry.

Alloy 602CA employs the beneficial effects of high chromium, high aluminum, high carbon and microalloying with titanium, zirconium and yttrium in a nickel matrix. The relatively high carbon content of approximately 0.18-0.20% in conjunction with 25% chromium ensures the precipitation of bulky homogeneously distributed carbides, typically 5-10 microns in size. Transmission and scanning electron microscopy suggest these bulky carbides to be of M23C6 type primary precipitates. Microalloying with titanium and zirconium allows for the formation of finely distributed carbides and carbonitrides. Solution annealing even up to 1230°C does not lead to complete dissolution of these stable carbides and thus the alloy resists grain growth and maintains relatively high creep strength due to a combination of solid solution hardening and carbide strengthening. This phenomenon of grain growth resistance is responsible for maintaining good ductility; high creep strength up to 1200°C and superior low cycle fatigue strength. Repair and reconditioning of exposed parts is thus easily achieved. The presence of approximately 2.2% aluminum in this alloy allows for the formation of a continuous homogeneous self-repairing Al_2O_3 sub-layer beneath the Cr_2O_3 layer, which synergistically imparts excellent oxidation as well as carburization and metal dusting resistance. " Reactive elements" like yttrium significantly increase the adhesion and spalling resistance of the oxide layers, thereby further enhancing the high temperature corrosion resistant behavior. Also, because of its relatively low aluminum content, this alloy does not embrittle due to gamma prime formation, as is the case with higher aluminum containing nickel alloys.

METAL DUSTING STUDIES (LAB. TESTS)

In a recent study on metal dusting behavior of nine nickel base alloys and four Fe-Ni-Cr alloys (Grabke 1997; Klower et al. 1997) tested in a carburizing H_2-CO-CO_2 gas with carbon activity >>1 at 650°C, alloy 602CA was one of the most resistant materials. Figure 1 shows the metal wastage rate of three nickel base alloys due to metal dusting; alloys 600 and 601 were in the "ground" condition whereas alloy 602CA was in the "black" condition. Table 2 gives the tabular data for the various materials tested. Note that only alloy 45TM and alloy 602CA were in the "black" condition," the rest were in the "ground" condition, except alloy 601 which was tested in three different conditions 1.e., "black," "polished" and "ground."

Table 1 Metallurgical Optimization of Alloy 602CA Nominal Chemistry Comparison to Some Other High Temperature Alloys Used in Industry.

Alloy	Fe	Ni	Cr	Si	C	Others
309	Bal	13	25	0.5	0.15	-
310	Bal	20	25	0.5	0.08	-
253	Bal	11	21	1.7	-	N, Ce
DS	Bal	36	18	2.2	0.06	-
800/800H	Bal	31	20	0.4	0.08	At, Al0.4
45TM	23	Bal	27	2.7	0.08	RE
600	9	Bal	16	-	0.07	-
601	14	Bal	23	-	0.06	Al 1.4
690	9	Bal	28	-	0.02	-
602CA	9.5	Bal	25	-	0.18	Y, Zr, Ti, Al 2.2
C-4*	2	Bal	16	0.04	0.005	Mo 16
X	18	Bal	22	-	0.10	W, Co, Mo 9
625	3	Bal	22	-	0.03	Cb, Mo 9
617	1.5	Bal	22	-	0.06	Co 12, Mo 9, Al 1.2
214	3	Bal	16	-	0.04	Al 4.5, Y
160	2	Bal	28	2.75	0.05	Co 29

*Alloy C-4 is not considered a high temperature alloy and was included to study the effects of high Mo.

From Table 2 data, it is interesting to note that the alloys like 800H and HK-40/HP-40, lower chromium and silicon containing DS alloy, alloy 600 and the three surface conditions of alloy 601, a Ni-Cr-Mo alloy C-4, lower chromium high aluminum alloy 214 and lower nickel high chromium high silicon low iron high cobalt alloy 160, all exhibited high metal dusting attack. Alloy 800H was the worst. Alloy 602CA, a high nickel-high carbon (typically 0.1%), moderately high aluminum (2.2%) and high chromium (25%) with micro-alloying elments of Ti, Zr, and Y have one of the best results. Alloy 45TM, a high chromium- high silicon-moderately high nickel and iron alloy also performed well as did the high nickel and high chromium alloy 690. One very important point to note is that these results were obtained on unstressed coupons. In the real world the components exposed to metal-dusting type environments are stressed and hence have a certain amount of strain. This strain may damage the protective oxide layer and thus cause accelerated attack.

Another important observation from the data in Figures 1 and 2 is the behavior of the 3 different surface conditions of alloys 601 and 602CA. Per Figure 2, the worst condition as far as metal dusting attack in alloy 601, was the "black" condition, followed by the "polished" condition with the best result obtained with the "ground" condition. In Figure 1, the curves for the alloys 600 and 601 are in the "ground" condition whereas the curve for alloy 602CA in the "black" condition. This indicates that the surface effects in alloy 602CA are minimal and no de-chromization of the alloy surface took place. In comparison with alloy 601, some de-chromization may have occurred during the annealing and/or hot rolling process (black condition). It also indicates that the surface oxide layer in alloy 602CA is very stable in contrast to alloy 601.

Table 2 Total Exposure Times and Final Wastage Rates after Exposure in Carburizing CO-H_2-H_2O Gas at 650°C

Alloy	Surface condition	Total exposure time (h)	Final metal wastage rate ($mg/cm^2 \cdot h$)
800H	ground	95	0.21
HK-40	-	190	0.04
HP-40	-	190	0.038
DS	ground	1988	4.3×10^{-3}
600H	ground	5000	0.033
601	black	6697	7.3×10^{-3}
601	polished	1988	4.9×10^{-3}
601	ground	10000	5.8×10^{-4}
C-4	ground	10000	1.1×10^{-3}
214	ground	9665[1]	1.2×10^{-3}
160	ground	9665[1]	6.3×10^{-4}
45TM	black	10000	1.0×10^{-5}
602CA	black	10000	1.1×10^{-5}
617[2]	ground	7000[1]	3.7×10^{-6}
690	ground	10000	2.0×10^{-6}

[1]The total exposure time of these specimens was less than 10,0000 h because they were inserted later than the other alloys.
[2]Alloy 617 showed evidence of metal dusting after 7000 h.

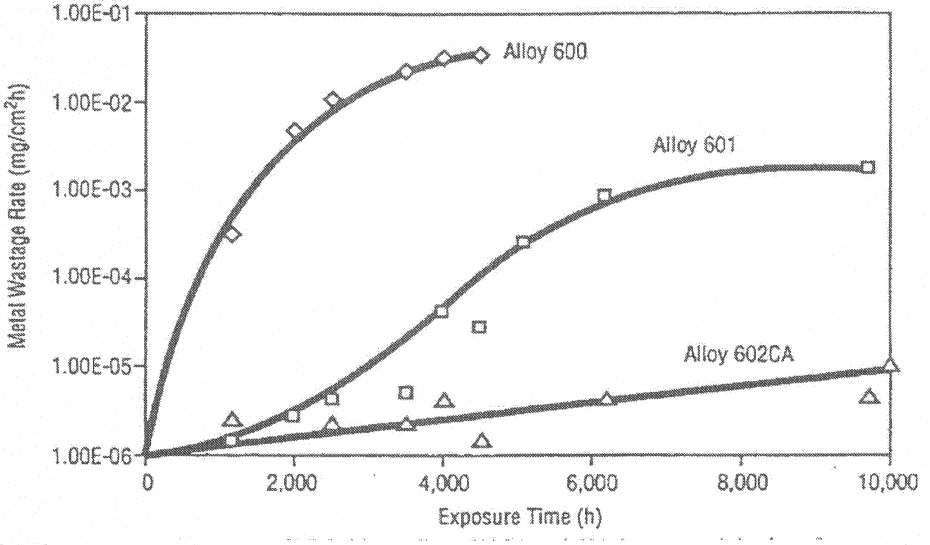

Figure 1 Metal wastage of Ni-base alloys 602CA and 601 due to metal dusting after exposure in strongly carburizing CO-H_2-H_2O gas at 650°C.

The fact that alloy 601 gave better performance in the ground condition (Figure 2) can be explained by a high density of dislocations introduced during grinding which serves as fast diffusion paths for chromium to the surface allowing a good chromia scale to form more readily. Also, grinding removes the de-chromized layer due to either hot rolling or annealing. Other researchers (Grabke et al. 1996; Mueller-Lorenz 1999; Baker and Smith 2000) have also confirmed this phenomenon.

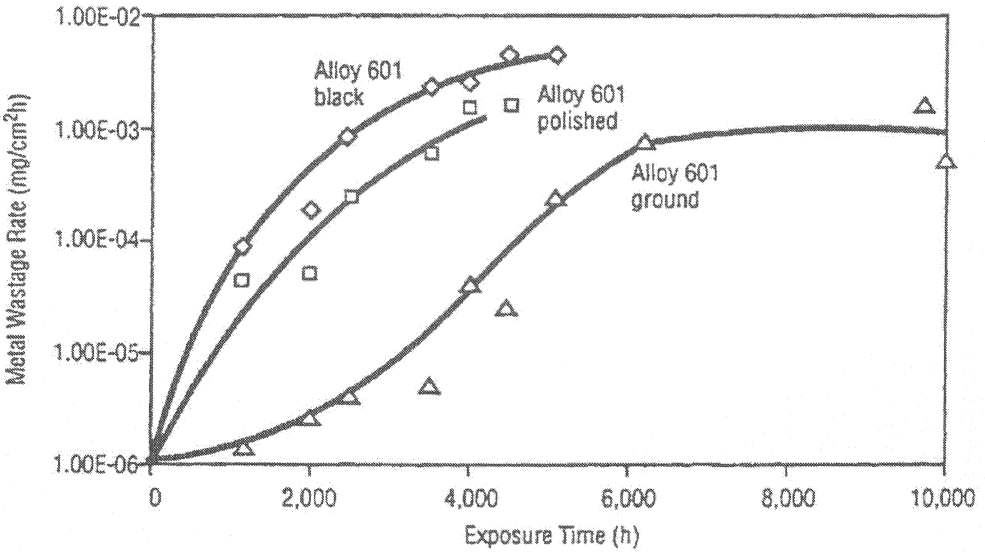

Figure 2 Metal wastage rate of alloy 601 with three surface conditions after exposure in strongly carburizing CO-H_2-H_2O gas at 650°C.

OTHER DATA ON ALLOY 602CA

The high temperature mechanical properties and oxidation resistance of this alloy are adequately covered in the open literature (Agarwal and Brill 1994, 2000). To briefly recap, Table 3 shows the cyclic oxidation data from 750 to 1200°C in air and Table 4 shows the cyclic carburization behavior in methane/hydrogen environment. As is evident, this alloy possesses excellent combination of oxidation and carburization resistance. However besides oxygen attack, high-temperature alloys are frequently subjected to attack by carbon. The degradation of metallic systems in carburizing environments can take two forms, namely carburization and metal dusting, which has already been discussed in the previous section. Due to the very low solubility of carbon in nickel, materials with high nickel content are considered beneficial for imparting carburization resistance. Alloys high in chromium, aluminum, and silicon may form protective oxide layers, which prevents the ingress of carbonaceous corrosive species thus providing improved resistance. However, if alternating exposure to carburizing and oxidizing environments is experienced, the precipitated carbides are converted to oxides and the liberated CO widens the grain boundaries thus loosening the oxide layer, whereby causing accelerated deterioration. The higher nickel plus chromium coupled with high aluminum content of alloy 602CA results in lowest carbon weight gain in the temperature range tested as shown in Table 4. The reason for improved carburization behavior is due to the formation of an alumina sub-layer rather than via the nickel content alone as exhibited by the oxidation data in Table 3 at 1200°C for 602CA and alloy 601. This alumina sub-layer is also responsible for preventing internal oxidation in this alloy. In comparison, alloy 601 suffers internal oxidation when exposed to 1200°C as shown in Figure 3. The higher thermodynamic stability of the alumina sub-layer even under very low partial pressures of oxygen and more than 5 orders of magnitude lower dissociation pressure are the primary reasons for the formation of the protective alumina sub-layer. Alloy 602CA follows a parabolic oxidation rate in isothermal tests conducted in air and the rate constant lies well inside the area of Al_2O_3 forming alloys and hence is one order of magnitude lower when compared with chromia forming alloys (Figure 4).

Table 3 Cyclic oxidation data -1200 hours – 24 cycles

	Weight change inmg/cm2 h				
Alloy	750°C	850°C	1000°C	1100°C	1200°C
602CA	+0.4	+3	+12	+7	-310
X	+1	+8	+5	-5	-
800H	+7	+8	-24	-162	-
625	+1	+6	-100	-1410	-
601	+1	+10	+7	-24	-820
188	+1	+4	+7	-302	-
617	+4	+12	+19	-19	-

Table 4 Cyclic carburization behavior in CH_4/H_2 environment ($a_C = 0.8$)

	Weight change inmg/cm^2·h		
Alloy	750°C	850°C	1000°C
310	2	130	305
800H	4	143	339
625	4	105	204
617	2	50	64
X	2	93	204
601	2	69	152
602CA	0	44	58

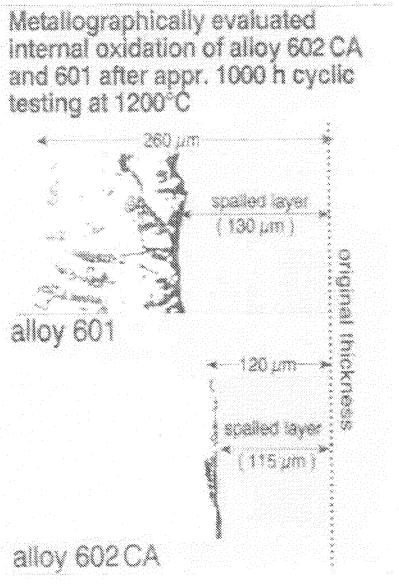

Figure 3 Internal oxidation attack on alloy 601 after cyclic testing in air at 1200°C for 1000 hours; alloy 602CA free from any internal oxidation attack.

APPLICATIONS OF ALLOY 602CA

Due to the unique combination of its oxidation resistance, carburizing and metal dusting resistance behavior and good high temperature mechanical characteristics, alloy 602CA has been extensively used in a variety of diverse applications as shown below:

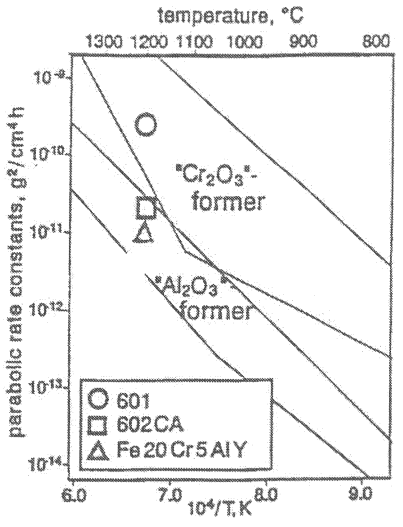

Figure 4 Areas of parabolic rate constants for alumina and chromia forming alloys.

- Heat Treat Industry: Furnace rolls, bell furnaces, bright annealing furnaces, accessories and transport hooks for enameling furnaces, transport rollers for ceramic kilns, wire conveyor belts, anchor pins for refractories, tubes for bright annealing wires, and other furnace accessories.
- Calciners: Rotary kilns for calcining and production of high purity alumina, calcining of chromic iron ores to produce ferro-chrome and reclamation of spent nickel catalysts from petrochemical industries
- Chemical/Petrochemical -Production of hydrogen via a new steam reformer technology
- -Production of phenol from benzene via a new and cheaper process
- Automotive - catalytic support systems, glow plugs
- Vitrification of nuclear waste
- Direct reduction of iron ore technology to produce sponge iron.

A brief description of some of these applications is documented elsewhere (Agarwal and Brill 2000; Krupp VDM 2001, Brill and Rockel 2000).

METAL DUSTING APPLICATIONS

In many of the applications, the industries are very reluctant to divulge any of the usage information and the various parameters used in their processes. Hence some of the applications described below may lack the details of these applications.

Direct Reduction of Iron Ore Technology: The COREX® process is a direct smelting reduction process where coal is used directly in a melter gasifier as a reducing agent, thus eliminating the need of a blast furnace and coke oven. The metallurgical reactions in producing the sponge iron are carried out in two separate process reactors – the reduction shaft and the melter gasifier. In the melter gasifier coal is converted to char at the temperature range of 1050°C. Oxygen blown in the base of the melter gasifier creates a reduction gas by coal gasification comprised of 95%CO plus hydrogen and approximately 3% carbon dioxide. After exiting, the gas is cooled to required reduction gas temperature of 800-850°C. This gas, after removing the dust, is fed to the reduction shaft where the ore is reduced to sponge iron. The sponge iron is sent to the melter gasifier by specially designed screws where the melting takes

place. The tapping procedures of the molten sponge iron are similar to blast furnace technology. Greater details of this process are described elsewhere. Due to the extreme carburiztion and metal dusting conditions existing in this technology, alloy 602CA was tested and selected. Pre-fabricated components made from alloy 602CA-plate thickness up to 50 mm were used in this technology. The components have performed as per design. Greater details on this process are described elsewhere (Eberle et al. 1996).

Refinery: Pilot tests with alloy 602CA were conducted in refinery pig tail applications where metal dusting resistance is needed. The environment consisted of CH4, CO, CO2, propylene and H2. Alloy 310 SS, 800H and the high silicon containing alloy 85H did not perform well due to either embrittlement or severe metal dusting wastage. Alloy 310 failed by sigma phase formation. After 10,000 hours of operation, alloy 602CA had the lowest metal wastage of <0.005" compared to some other nickel alloys having wastage rates varying between 0.009 and 0.047". Alloy 600 had a wastage rate of 0.022", Haynes alloy 556 with a wastage of 0.036", Haynes 230 at 0.022", alloy RA333 with a rate of 0.047" and RA85H at 0.009". After 15,000 h alloy 602CA continues to give excellent service. This alloy is also specified for a project in Australia/New Zealand in steam reforming units as used in methanol, ammonia and hydrogen production, where metal dusting is a serious problem.

Phenol Production: In another test program for a new technology to produce phenol from benzene, where carburization/metal dusting is a serious problem, alloy 602CA is being tested along with other alloys. Preliminary results showed alloy 602CA to perform well.

Ammonia Plant (Europe): In a three year test program at temperatures of 450-850C, alloy 602CA had no metal dusting attack whereas alloy 601 had some attack and alloy 800H severe attack. This again confirms the laboratory tests conducted by several researchers (Grabke et al. 1998; Baker and Smith 2000; Agarwal and Brill 2000). The plant selected alloy 602CA for the various components. In another plant in Western Europe, alloy 602CA showed no metal dusting (temperature and exposure time were not revealed).

Methanol Plant (Europe): Testing and usage with alloy 602CA and alloy 601 showed alloy 602CA to perform significantly better than alloy 601. No other details were given. Other companies as well as in the ammonia and methanol plants in Europe and U.S.A have confirmed the metal dusting results of Grabke et al. (1998). It has been postulated that increased efficiency of ammonia and methanol plants can only be achieved by decreasing the steam/carbon ratio, thus increasing the carbon activity and consequently higher tendency to material wastage by metal dusting phenomenon.

Based on the success of alloy 602CA, many other test programs with this alloy are underway in industry. Unfortunately, details are not available due to the confidentiality aspects of these tests being conducted by the various companies. One important emerging technology in the pilot R&D stage is the reforming of natural gas and other hydrocarbon fuels to produce hydrogen for use in fuel cells. Many companies are involved in testing and proving this technology and the produced hydrogen will then be used in fuel cells to power individual households with distributive power. In some of the initial testing, alloy 602CA has performed very well. However, the details of these test programs are proprietary and confidential.

Many times questions from the end users on fabrication, weldability and post weld heat-treatments of this alloy arise. A brief recap of this specific aspect is presented below.

FABRICABILITY/WELDABILITY OF ALLOY 602CA

Welding of alloy 602CA follows the same general rules established for welding other highly alloyed nickel base materials, where cleanliness is very important and critical (Krupp VDM 2001). Heat input should be kept low with inner-pass temperatures not exceeding 150C, preferably 120C. The use of GTAW (TIG) process and matching filler metal is recommended. Submerged arc welding (SAW) with a GTAW top layer has also been successfully used. The reason for using a GTAW top layer is to restore part of the aluminum, which is lost during the submerged arc process. Neither preheating nor any post-weld treatment is required. The shielding gas for GTAW is argon plus 2% nitrogen. Addition of nitrogen in the shielding gas is very critical in preventing any hot cracking during welding.

Other welding processes such as plasma arc welding, SMAW as also referred to sometimes in Europe as MMA (manual metal arc), GMAW (MIG/MAG-metal active gas) have also been used successfully. For GMAW-MAG, the shielding gas is argon with additions of helium, nitrogen, and carbon dioxide. For shielded metal arc welding matching electrodes are available. There are many applications of this alloy in the industry requiring various fabrication processes and these are well documented in the open literature (Agarwal and Brill 2000; Krupp VDM 2001; Brill and Rockel 2000).

CONCLUSIONS

- Metal dusting phenomenon is still not fully understood although great progress has been made its basic understanding over the last 50 years.
- Data generated by many researchers point to the fact that nickel alloys, high in nickel, chromium, and aluminum or silicon provide better resistance to metal dusting attack.
- Alloy 602CA is one such high nickel alloy with high chromium and high aluminum, which has shown promise in combating this mode of metal degradation.
- Quite a few successful applications have already been achieved by alloy 602CA in combating metal dusting and other modes of high temperature attack. Many other tests are being run at various companies to produce hydrogen by reforming of natural gas and/or other hydrocarbons, and the initial feedback is that alloy 602CA has performed exceedingly well.

ACKNOWLEDGEMENT

Parts of this paper were originally presented at NACE International Conference "Corrosion/2001,"and NACE International is gratefully acknowledged.

REFERENCES

Agarwal, D.C. and U. Brill, 2000, Corrosion/2000 paper #521, NACE International, Houston, TX.

Agarwal, D.C. and U. Brill, 1994, Materials Degradation Problems in High Temperature Environments: Alloys – Alloying Effects – Solutions, Industrial Heating, pp. 55-60.

Baker, B. A. and G. smith, 2000, Corrosion/2000 paper #257, NACE International, Houston, TX.

Brill, U. and M. Rockel, 2000, High temperature Alloys from Krupp VDM for Industrial Engineering Applications up to 1200C, VDM Report #25.

Eberle, A., et al., 1996, Recent Developments In COREX Technology, 13th Annual International Pittsburgh Coal Conference, Pittsburgh, PA, USA.

Grabke, H. J. and E. M. Mueller-Lorenz, 1993, Materials and Corrosion, 44, pp.89-97.

Grabke, H. J, et al., 1996, Materials and Corrosion, 47, pp. 495-504.

Grabke, H. J, 1998, Materials and Corrosion, 49, pp. 303-308.

Grabke, H. J, 1999, Proc. EUROCORR 1999, Aachen, Germany.

Hochman, R. F., 1972, Proceedings 4th International Congress on Metal Corrosion, NACE, p. 258.

Hochman, R. F., 1977, Proceedings Symposium on Properties of High Temperature Alloys with Emphasis on Environmental Effects, Z. A. Foroulis and F. S. Pettit, eds. The Electrochemical Society, p 715.

Klower, J., et al., 1997, Metal Dusting and Carburization Resistance of Nickel base Alloys, Corrsion/97, paper #139, NACE International, Houston, TX.

Krupp VDM, 2001, Materials Data Sheet Nicrofer 6025HT-alloy 602CA, Materials Data Sheet No. 4037, Werdohl, Germany.

Mueller-Lorenz, E. M., 1999, Proc. EUROCORR 1999, Aachen, Germany.

Pippel, E., R. Schneider, and J. Woltersdorf, 1998, Materials and Corrosion, 49, pp. 309-316.

DEVELOPMENT OF METAL DUSTING RESISTANT MATERIALS FOR GTL PRODUCTION

B. J. Crewdson and P. W. Farnell*
Synetix, Cleveland, United Kingdom

ABSTRACT

The incorporation of Gas Heated Reforming technology into ATR based GTL processes offers the combined benefits of significantly higher efficiency and lower capital cost. Under conditions that can be designed with confidence today, significant efficiency benefits can be realized at the same capital cost as an ATR based flowsheet. Synetix, together with Methanes are constructing a Materials Demonstration Unit to prove materials of construction under more aggressive process conditions which will maximize efficiency and, at the same time, provide substantial reductions in capital cost.

INTRODUCTION

Current commercial scale GTL production is based on gasification of coal or steam reforming or partial oxidation of natural gas (POX) and facilities based on these technologies have been in operation in South Africa and Malaysia for many years. The large scale plants now being planned by the major oil companies will be based on the use of large, remote reserves of natural or associated gas which are difficult to bring to market in more established ways such as pipelining or LNG. While POX will continue to be important, catalytic processes for the generation of synthesis gas for large Fischer-Tropsch plants have gained favor in recent years and have been adopted as the preferred technologies for most future GTL facilities.

Currently, the most widely proposed technology for GTL production is autothermal reforming (ATR). There are a number of variants of this basic process, some incorporating proprietary technology, but all comprise the catalytic partial oxidation of natural gas with steam and oxygen or air. These catalytic processes offer benefits compared to POX, both in respect of a more ideal stoichiometry of the synthesis gas for Fischer-Tropsch synthesis and lower capital cost of the facilities.

The performance of ATR based GTL plants can be substantially improved by incorporating a Gas Heated Reformer (GHR) coupled with a secondary reformer in place of the ATR as reported by Chang (2000). The GHR allows the recycle of high grade heat from the reformed gas directly back into the reforming process as illustrated in Figure 1 and eliminates the need to generate large quatities of high pressure steam for the process train.

*Corresponding author address: P. W. Farnell, Synetix, P.O. Bax 1, Belasis Avenue, Billingham, Cleveland, TS23 1LB, United Kingdom; e-mail: peter_farnell@ici.com.

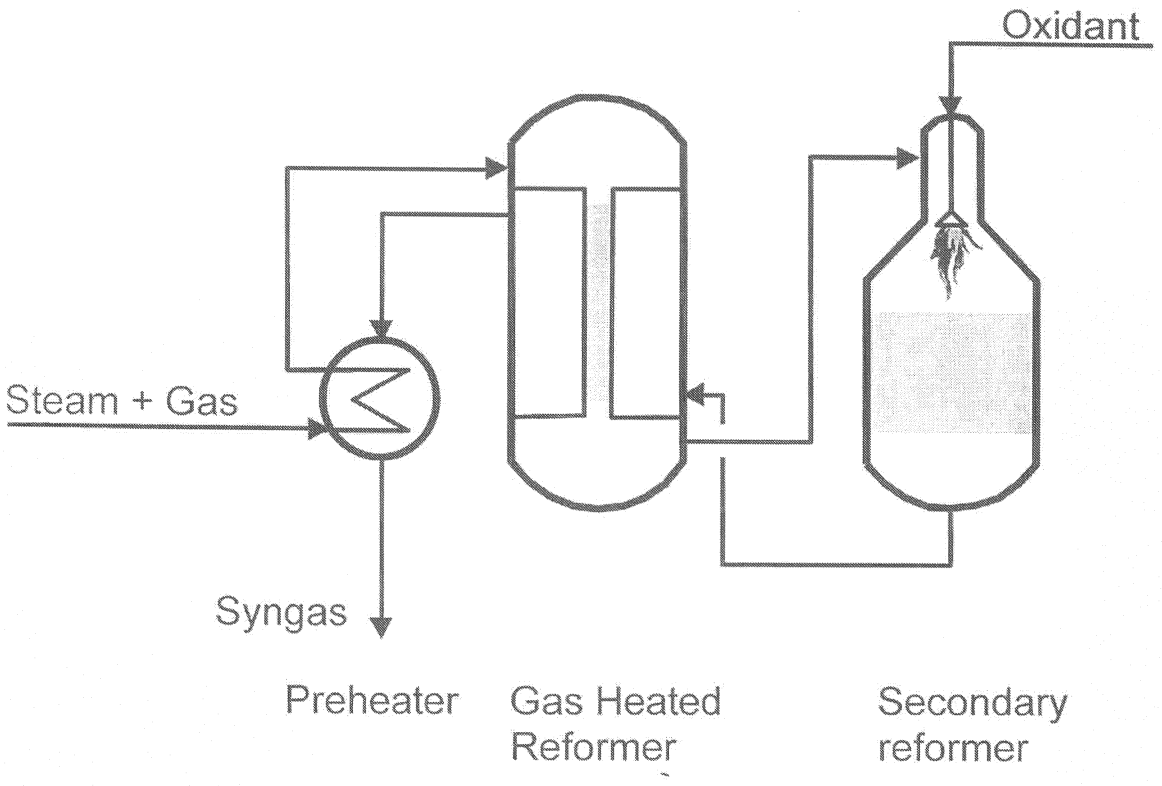

Figure 1 GHR Reforming System Flowscheme.

This combination results in thermal efficiencies some 10% higher than for a typical ATR based plant and the elimination of the high-pressure steam systems and simplification of the power generation equipment delivers a lower capital cost for the plant. GTL plants will normally need to be self sufficient in energy and most cases, there will be no local market for export power owing to the remote location of these units. The recovery of heat back into the reforming process greatly simplifies the design of a power-balanced flowsheet. In addition, the higher thermal efficiency results directly in a reduction in CO_2 emissions of 30-50% as reported by Statoil et al. (2000), the exact figure depending mainly on the composition of the natural gas feedstock. Key comparative data are reported in Table 1 below.

Table 1 Comparative Data for ATR and GHR Reforming Schemes

	ATR (steam:carbon ratio=0.6)	GHR (Steam:carbon ratio=0.9)
Total energy GJ/bbl	9.59	8.74
CO_2 emissions kg/bbl	163	113
Relative capital cost	100	93

DEVELOPMENT OF GAS HEATED REFORMING

Synetix first developed its Leading Concept Ammonia Process (LCA) incorporating gas heated reforming in the 1980s and this was applied to ammonia production with plants being

commissioned near Bristol in the UK in 1988 and later at Yazoo City, USA in 1998. In the early 1990s, Synetix adapted the technology for methanol production as the Leading Concept Methanol Process (LCM) and a demonstartion methanol unit has been opearting near Melbourne in Australia since 1994. In the latest extension to this family of processes, Synetix's Leading Concept Liquids Process (LCL) applies GHR technology to the production of synthesis gas for Fischer-Tropsch based GTL plants.

THE ADVANCED GAS HEATED REFORMER

The early applications of Synetix's gas heated reforming technology proved successful and all plants continue to operate. Development of the technology continued during the 1990s and it became apparent that there were some features of the first generation GHR that could be improved. For example, catalyst loading was more difficult and time consuming than in a conventional steam reformer and some aspects of the design of these bayonet tube units were complex adding to cost and limiting the maximum size which could be constructed.

By 1998 an improved and simplified design of Gas Heated Reformer known as the Advanced Gas Heated Reformer (AGHR) had been developed and a demonstration unit was installed in the methanol plant now operated by Coogee Energy in Melbourne in order to test and prove features of the new design. The AGHR has a simplified internal design incorporating a sliding seal system that accommodates tube expansion without the need to use bayonet tubes.

These changes simplify design and fabrication and rsult in a substantial reduction in the fabrication cost of the uit. Catalyst loading and removal is also much easier and is carried out in the same way as a conventional steam refoirmer using traditionsl sock loading or Synetix's Unidense™ loading system. In addition, detailed engineering studies carried out this year have shown that the AGHR can be confidently scaled up to a capacity of 25-30,000 bpd ina single train. Figure 2 illustrates the outline layout of the AGHR. The AGHR as shwn in Figure 3 has now been in operation for over three years and has fully proved the new design features of the unit.

METAL DUSTING CORROSION

Over the last fifteen years, through its experience of designing and operating gas heated reformers in ammonia and methanol duties Synetix has developed the leading position in the understanding and application of materials in reforming and synthesis gas environments.

The AGHR reforming conditions used for methanol and ammonia have now been fully proven over many years of operation and materials as well as the process and mechanical design of both the GHR and AGHR are fully established. For GTL production, although an AGHR operating under similar process conditions to those used for methanol offers significant benefits in terms of overall efficiency, achieving the maximum efficiency gains and capital cost benefits require a change in reforming conditions and, specifically, a lower steam:carbon ratio. This is preferably in the range of 0.6-1.0, the exact optimum depending on the details of the specific project.

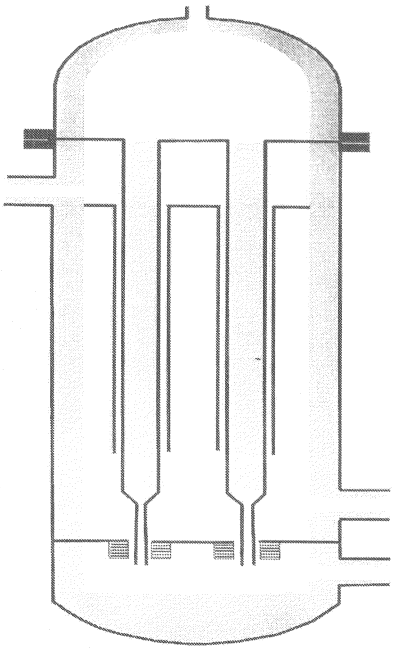

Figure 2 AGHR Layout.

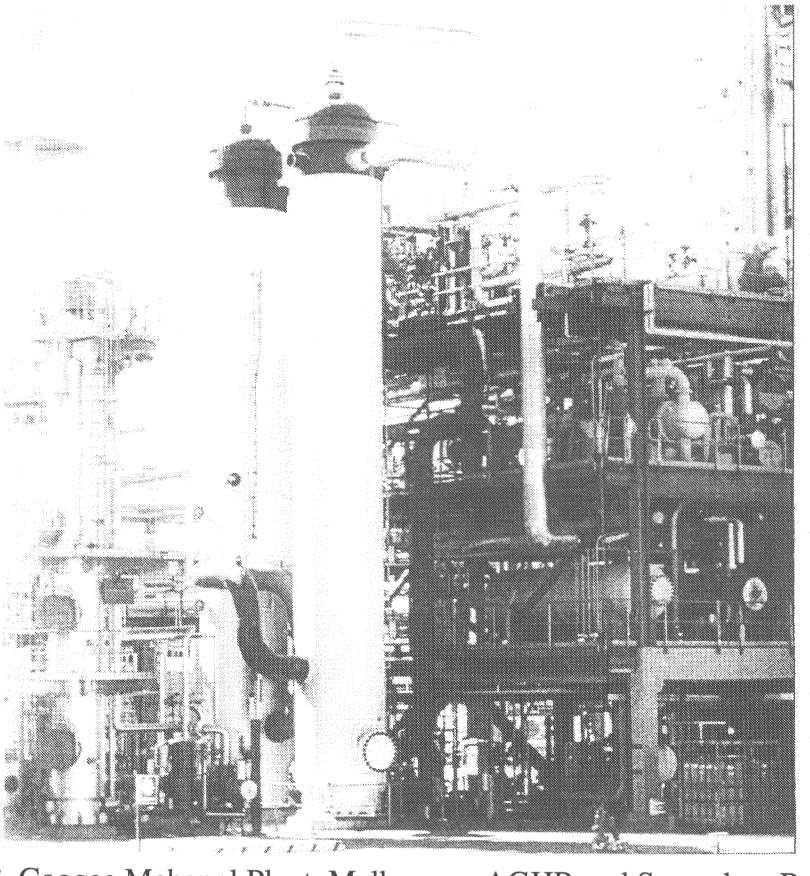

Figure 3 Coogee Mehanol Plant, Melbourne, AGHR and Secondary Reformer.

Metal dusting corrosion has been an unpleasant feature of synthesis gas plants for many years. As early as the 1970s localized corrosion was routinely discovered in the ferrules protecting the refractory linings in the boilers of ammonia and methanol plants. This localized damage in non-critical components was generally manageable but the problem intensified during the 1980s as the development of more efficient plants resulted in increasingly severe process conditions. Today, as process conditions are changed to suit different situations many incidents of metal dusting continue to occur as reported by others (Agarwal et al. 2001; Baumert et al. 1998).

Metal dusting is a result of attack by components of synthesis gas on the metal surfaces of the plant. The phenomenon is complex, and attack can be localized or general, at low rates that can be accommodated in the design of the equipment or catastrophic with materials disappearing within weeks. In addition, there can be a lengthy incubation period before the onset of corrosion, which makes materials testing difficult and uncertain. As well as being dependent on process gas composition, corrosion rates are affected by other parameters such as temperature, pressure and fluid flow parameters and, of course, by the nature of the metal components in question.

MATERIALS DEVELOPMENT

When GHR technology was first developed for ammonia duty in the 1980s, there were no known materials of construction for use in metal dusting environments at the temperatures of 500-750°C which might be experienced in a GHR. Prior to designing the first GHRs, Synetix initiated a development program to identify suitable materials of construction. The development program was long and difficult and provided only a starting point for materials selection. Development work has continued since the first plants were commissioned with the commercial operation of the units now providing on-going confirmation of the current choice of materials. Synetix now has well over 10 years proven commercial experience in the design and operation of equipment for this duty and has a world leading technical position in this field.

No materials of construction have yet been demonstarted to operate successfully at the lower steam ratio conditions required for the optimum use of GHR technology in GTL plants. Long, and sometimes painful, experience has shown that while laboratory and other small scale testing may have a place in providing some limited initial screening of materials it cannot provide reliable data on the performance of an alloy under plant conditions. To address this problem Synetix, in partnership with Methanex, the world's largest producer of methanol is constructing a Materials Demonstration Unit (MDU) in New Zealand. The design of the AGHRs in the MDU will draw upon the knowledge and experience of Synetix combined with the operating experience in synthesis gas processes of Methanex.

THE MATERIALS DEMONSTRATION UNIT

The MDU comprises 2 Gas Heated Reformer trains as illustrated in Figure 4 with full size tubes, each coupled to a secondary reformer and associated equipment. The two trains will operate under different conditions in order to demonstrate metallurgy suitable for both GTL and further enhanced methanol process conditions. In an experimental program initially lasting 18 months the MDU will test several different alloys simultaneously under conditions closely replicating those of a full-scale commercial unit. The unit will provide long-term data under commercial plant conditions thus providing a high level of confidence in the results of the work.

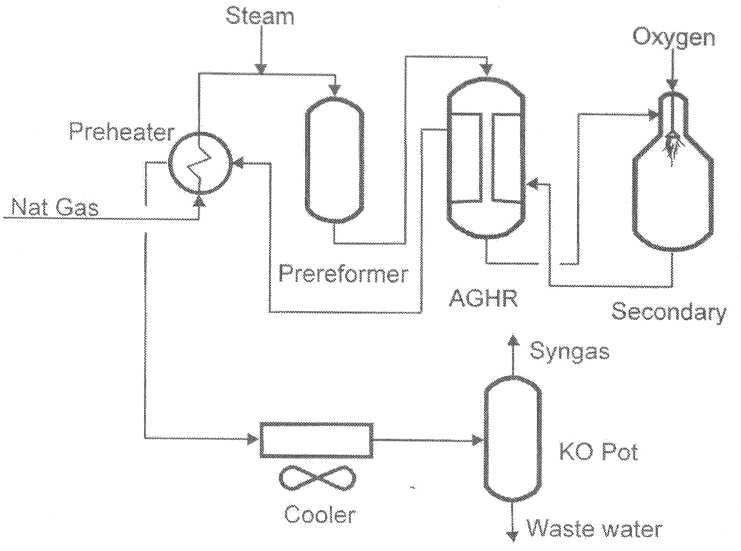

Figure 4 Materials Demonstration Unit Flowsheet for One Train.

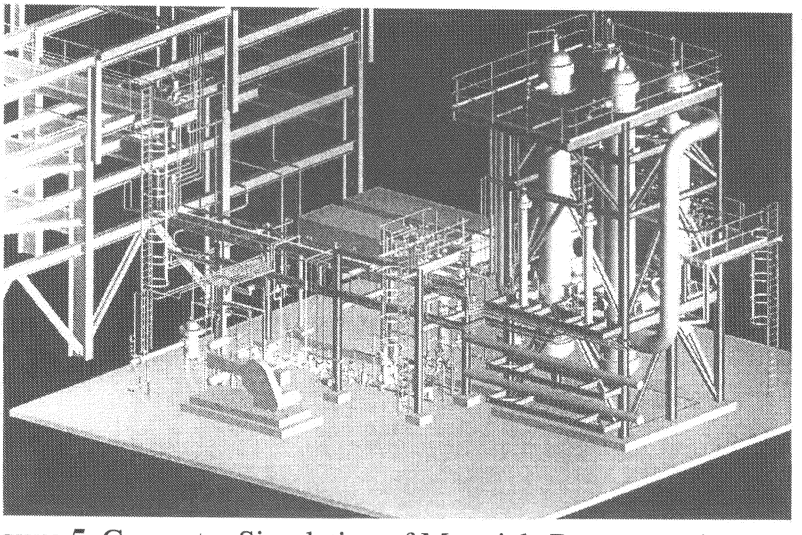

Figure 5 Computer Simulation of Materials Demonstration Unit.

Engineering work on the project started in mid 2000, construction is now well advanced and the units will be commissioned in October 2001. Preliminary results will be available in 2002 with final results coming in during 2003 and will provide an important demonstration of the materials selection for the construction of large-scale GTL facilities. Figure 5 illustrates the Materials Demonstration Unit reforming section.

SYNETIX LCL PROCESS

Today, the Synetix LCL process incorporating the AGHR operating at a steam ratio of 2 offers significant efficiency and operating cost benefits at a capital cost equal to an ATR process at a steam ratio of 0.6. At these process conditions the materials of construction are well established and are within Synetix's envelope of commercially proven experience. The results of the MDU test program will be incorporated as they become available during 2002-2003 and will

enable Synetix to offer substantial capital and operating cost benefits compared to other GTL processes.

REFERENCES

Agarwal, D. C., U. Brill and J. Klower, 2001, "Recent Results on Metal Dusting of Nickel Base Alloys and Some Applications," NACE Corrosion 2001 Conference, Paper 01382.

Baumert, K. L.and J. J. Hoffmann, 1998, "Materials Performance in Maethanol Reforming Units," Materials Performance, 37 (5), pp. 60-64.

Chang, T., 2000,Oil and Gas Journal, 98, p. 49.

Statoil/Synetix GTL SynGas Study, 2000, unpublished.

Panel Discussion

The panelists were K. Baumert (air Products and chemicals, USA), H. J. de Bruyn (Statoil ASA, Norway), P. W. Farnell (Synetix, United Kingdom), H. J. Grabke (Max-Planck Institut, Germany), C. W. Thomas (Industrial Research ltd., New Zealand), and H. Van Wortel (TNO Institute of Industrial Technology, The Netherlands). K. Natesan (Argonne National Laboratory, USA) was the moderator.

Each of the panelists was asked to present their views on the metal dusting issue and what they think should be done in the future to mitigate this type material degradation.

P. W. Farnell

I am quite amazed over the last couple of days. I am an engineer and work on the macro scale and in this Workshop, I have seen some of the micro scale effort that has been going on to address the metal dusting. It is certainly an eye opener, something that has been quite outside my experience.

Regardless of that I believe one of the key issues that we must appreciate within the industry is that simple tests can be flawed. I don't claim to understand why, but from my perspective of trying to specify materials, I know that this is the case. Really, from my point of view, one of the worst things that supports this attitude is when you spend $2-3M on a new heat exchanger, and 18 months later it is full of holes while the laboratory tests say that the material should not metal dust. There is obviously some fact that is not coming about in these tests.

Even when you do get good tests, and this is part of my experience in ICI, short-term tests are often misleading. Even if you get them under realistic conditions, incubation is a big issue. So the question is how we can try and do these tests in a reasonable amount of time with meaningful results. One of the other fact6ors that we have been quite substantially is by the time you have been operating it hourly for three years r so, through a whole range of operations – startup, shutdown, leaving the system on hot standby, overheating, all the normal things that get on a plant trip – the alloy you got in there is not the alloy that you started with. And degradation of the alloy by other mechanism may make the alloy susceptible to metal dusting, even though the starting alloy was eminently suitable for metal dusting environment. The bottom line is that the operating history is a key factor.

With the background of a big industrial user of these materials we ask whether a realistic economic tests can actually be developed to address metal dusting. Also could we develop a predictive theory? Could we come up with a little Excel spreadsheet in which you insert your gas composition and it gives results on materials performance. If we cannot do this, then we are left with empiricism looking at behavior of various alloys for the selection and application.

Finally, I want to mention that the chemical industry is very conservative. Unless you can prove that something has been running for a good number of years, nobody is really interested. Catch 22, how do you prove it without actually using it? That is difficult.

K. L. Baumert

My view is somewhat similar to that of Farnell. I have been looking at metal dusting degradation in our plants for the last two years or so. During that time, with MTI sponsorship, we reviewed the literature in this area and came up with a report on available information, but nothing conclusive. From what I heard for the last couple of days in this Workshop, in my own way of looking at it, I can say that we have a reasonable understanding of what happens in the metal. There also have been a lot of laboratory investigations using laboratory mixtures. As yet I can't use them to alter the design of reformers, install a big heat exchanger up front, and capture the high energy from the high-temperature outlet.

What these laboratory investigations have shown is that the laboratory-selected gas mixtures are very much different from what we have in reformers. But they are used because they can initiate metal dusting. The plant environments also produce metal dusting but these environments are difficult to reproduce in the laboratory, especially at high pressures.

Another parameter of interest in metal dusting is carbon activity. We cannot measure it but we can calculate it from inlet gas chemistry. But we don't know what it means especially under non-equilibrium conditions. We can also calculate oxygen potential. The two reactions that are of interest are steam-carbon and Boudouard. Some of the work that we have done suggests that it is not the whole picture.

The laboratory investigations indicate that they can produce metal dusting using mixtures of different gas chemistry. The results also show that sulfur additions inhibit the process. How it does it doesn't really matter. It might poison the catalytic activity on metal surface or it might repair the oxide. But in general, we are producing hydrogen and CO and there is a catalyst downstream to convert that to something else. Any hint of sulfur destroys these catalysts and therefore, we take great pains to take the sulfur out.

We have found aluminum coatings to be resistant to metal dusting. We have had them in our plants for over 20 years. But there are lots o problems with it. First of all, the pack diffusion process distorts the pipes and leads to fit-up problems in the assembly. It is not cheap. Welds are a problem. We use it today in regions of plant where no joining is needed.

High-chromium equivalent is good and I think it has been verified in industry. We also have alloys with 1-3% aluminum and welding them is a problem. Similar problem with alloys containing silicon. Also, silicon promotes sigma phase as well. Finally, a continuous coating is good. The laboratory investigations have shown this to be true. But the problem in industry is that to have a high oxygen pressure, we have to generate steam. That means in a reformer you make steam, use it in the process, keep the excess steam there, at the back end condense it and run it around the system again. What are the implications? It takes up space and we need to make the equipment big enough to accommodate the steam. Also, it takes energy to not only make steam but also to condense it. So we want to minimize it but it pushes us in the wrong direction from the metal dusting standpoint. The other way to do this is to periodically brig the system down and steam it out for a day or so. Management is reluctant to do this because a day

of downtime can cost $0.5-1.0M and the issue can cascade down the system where other process subsystems may need to be shut down.

At present the industry deals with the metal dusting issue by designing around the problem. We don't have metallic alloys at locations where metal dusting is expected. If we have a few, we have to live with them. We also change these components from time to time. We use aluminum coatings where possible, where we don't need to join. They work it they are thick enough and if applied properly. There have been failures in them as well. There is limited use of high-chromium equivalent alloys because they are expensive and really not proven right now. We have been doing a lot of laboratory tests but the data are not sufficient enough to reduce the size of the reformer and to recover the high-temperature heat. There is limited us of maintaining high oxygen potential, for reasons I just mentioned.

So if we are going to use the laboratory data, I think we need to close the loop. There is a reasonable understanding of what happens in the metal. But if we are going to build a model using the laboratory data, then there are some holes here. We need to close them. The holes are mainly, as I see them, in the gas phase. We need to develop a material balance around reactors. We have to account for oxygen and the oxide scale development. We need to better understand what is happening in the gas phase, especially what steam-carbon reaction tells us. The other option is to do what ICI is doing, build an $8-10M plant and test it. If we don't have a viable model, I can't use the data right now and the plant option is what we are going to do.

H. J. Grabke

Metal dusting is a problem for heat exchangers in methane reformers, refineries, plants for ammonia, methanol, hydrocarbons, synthesis gases, and direct reduction of iron ores.

In the laboratory studies, we have used mixtures of CO, H2 and H2O to evaluate metal dusting. I have discussed the thermodynamics of the gas phase reactions in my paper. One may also add CO2 to the gas mixture, but I really don't like the tests in which CO alone or CO and H2 alone are used. If you use CO for carburization, then oxygen must stay somewhere and if there are other elements such as Cr or Si present in the alloy, they are oxidized. Using CO or CO and H2 only does not fix the oxygen partial pressure and it is not easy to interpret the results. If CO2 or H2O is used, at least the oxygen pressure can be defined and a steady state may be established, even under non-equilibrium conditions.

Regarding metal dusting, I have explained the reason for it as the tendency for deposition of carbon where carbon transfers from the gas atmosphere into the metal phase. Carbon deposition can be protective but its entering the metal makes the metal disintegrate, leading to metal dusting. Since carbon activity is >1, the surface can be oversaturated with carbon to initiate the process followed by the formation of carbide and its decomposition into graphite and metal particles. The particles are very small and act as effective catalyst for further carbon deposition.

As regards protection, sulfur retards the metal dusting, but it cannot completely stop it, as I have shown in my paper. If a high-alloy steel is exposed to a metal dusting condition at elevated

temperatures, there is competition between the ingress of carbon which would lead to metal dusting and the formation of oxide scales. If the oxide scale is protective and carbon rich and formed fast enough, then metal dusting should be effectively stopped. But this carbon diffusion to the surface is not very fast at the low temperatures. Metal dusting usually occurs at H"600°C, and so the carbon diffusion can be enhanced by a fine-grain microstructure and by surface working. They can also enhance chromium diffusion to the surface. Surface working can be done by grinding, sand blasting, or shot peening. Further, ferritic materials with high Cr contents may be better. Additions of Si and Al can be helpful in formation of oxide scales.

Another issue of concern is the effect of other impurities such as chlorine, hydrogen chloride, sales, and sulfates. These can be detrimental for even the best materials. Cursory study that I did for shell showed strong effects of chlorine but it is not a complete study.

C. W. Thomas

As I said at the time of my talk, we have performed a lot of laboratory tests in the area of metal dusting. Based on these studies, we have come up with several questions for which we would like to seek answers. But I am a bit worried about these questions because on the first impression they might make you think that there has been no progress at all and that we are back to square one. I do not think that is the case at all.

I would like to say that I am not completely in agreement with Farnell that we have to go to pilot plant proving the laboratory studies. I completely understand his and his company's philosophy for metal dusting, but I am saying this in a much more general sense. I think metal dusting is a degradation mechanism where you could make this argument that Farnell made validly, but there are lots of degradation mechanisms where people quite genuinely design plants that don't go through a materials proving exercises. For example, stress corrosion cracking has been a huge problem in industry for over 40 years but plants are being built and operated while developing an understanding of the issue and seeking mitigating avenues.

The first question is why the results from different studies differ, even though they all talk about the same metal dusting degradation. In general, the experimental studies involve exposure of materials to a metal dusting environment and rank the alloys based on their wastage rates. Such studies and the results from these studies are valuable since ultimately engineers, I think, are going to make choices of materials based on these studies. The ranking of alloys in different studies is quite often different which we need to understand and technically justify for the results to be useful for application. More often than not the results from these studies lead to different ranking because the exposure environments may be different, the time of exposures may be different, and the experimental procedures (start up and shut down) may be different. One needs to clarify and understand the differences to justify the differences in ranking. However, most of the studies have shown high-Ni high-Cr alloys to be less susceptible to metal dusting than the Fe-base alloys.

The second question why there is no consistency between the laboratory tests and field exposures. That is a sort of fairly grand statement. It is not absolutely true, but we do see a few strange things going on in plants, which the laboratory tests wouldn't suggest is going to happen.

The correlation between the laboratory tests wouldn't suggest is going to happen. The correlation between the laboratory simulated and the plant environments is a significant issue. We have heard a lot about the gas compositions that have been used in the laboratory test environment. Quite correctly, they are used in my opinion, to make things happen in the laboratory tests. We can't sit around and wait, and I think this is one of the big problems that Farnell faced in their work. They quite rightly, and I can fully understand the philosophy, they wanted to test the gases that they would be using in their plant. They fell into this horrible trap of going for 18 months and expecting the problem to clear up or answered. I think it is quite appropriate in the laboratory to accelerate the damage.

Another issue that we have seen onsite, which is a bit strange, is nominally similar plants at different locations behave entirely differently. I am aware of one plant built in Australia that was similar to the one that has been running in South America. I don't think at this stage we have a firm understanding of how metal dusting changes with changing gas composition. The latter plant was running without any problem while the plant in Australia fell into bits within 30-40 days of operation. I suspect there were subtle differences between the two plants, probably in the process gas environment. There may be perfectly good explanation for and why inconsistencies occur but we don't generally have all the answers beforehand.

In my work, I do lot of creep testing. It is a classic example of where in the laboratory you could accelerate the test because there is an understanding that the relationship between the various conditions that you apply in the laboratory relative to the conditions in service. So I don't think at this stage we have a firm understanding of how metal dusting changes with changing gas composition. We know that there is an incubation period, it takes a long time for things to happen in industry on occasion, and I think we need to understand whether there is a linear relationship between composition and rate of attack or whether there is a threshold.

H. Van Wortel

Several things, of course, have already been said by other speakers, but something I think we should consider is an alternate approach in material selection. When we say we have a good material and start working on it from the start, we should ask whether the alloy was selected based on plant experience. And also consider other factors such as weldability, availability in different product forms in sufficient quantity, and cost.

Second point is that we need to standardize the laboratory test procedure. Everybody has his or her own test facility. That is not the problem but the startup and shutdown procedures, exposure times, and gas chemistry are important. We also have to rank the gas mixtures in terms of their aggressiveness. The laboratory tests should examine the materials from the least to most aggressive environments to establish their suitability for service.

H. J. de Bruyn

I, unfortunately, chose the seat right at the end, so I have a very tough act to follow. I think like a lot of people whoever dealt with metal dusting. I started off working for companies that make fuels and all sorts of liquid products from gas. For that you need some gas. The first

company used to gasify coal and then convert it to liquids. The current company is involved in natural gas conversion.

We, as operating companies with interest in expansion in future, have to look at the economics. Economics tells us that the gas compositions are likely to change. Processes are envisioned with less steam and concepts with less steam are being proposed for the future. The question is, do we have the needed materials or do we have the confidence in the available materials to make those choices and build a plant that will probably cost $5-6B.

One thing that I am really interested in is to relate the published data to the sort of environments that I am interested in. We see a lot of publications and lots of data from laboratory studies. I don't discount them because there are a variety of conditions that influence things. There are startups, shutdowns, massive steam flow, etc. A lot of people think that a lot of steam would be good from an oxidation point of view. If you start thinking about material that has already been carburized, then some of our work and also the work being done in Sweden shows that maybe steam plays a role in the breakdown of this carburized layer. So I'm not so sure if that is positive or negative. But it plays a role in the lifetime of equipment.

I would like to present some information (see Figure 1) that comes from assessment of ammonia plants. The laboratory experiments are done at extremely severe environments with almost no steam while the plant environments can contain as much as 30% or more steam. This makes a big difference in the performance of the alloys in the laboratory versus in plant conditions. Further, we do experiments in the laboratory at atmospheric pressure whereas the plants operate at high pressures. So as a materials person, who has to recommend material choices to my company for the new designs and in new concepts, I find very difficult to bridge this gap and make any judicious recommendations.

So if there's anything that I can ask for people doing research and people doing tests, please try and do it more realistically. Now, I know that our gas interests may be just a small portion of the market available, but you see gas is becoming more and more prominent. And I think there's a lot of value doing more realistic tests. Also, as far as pressure is concerned, we do believe that there are some difficult-to-understand relationships between metal dusting and pressure.

And lastly, as Natesan has mentioned, we know a lot of what is happening in the material, but not so much at the interface between the material and its environment. If we believe Professor Grabke here, then this CO plus H_2 reaction is going to give us a lot of steam locally where that reaction is taking place. The questions is, if that steam is good for oxidation, why doesn't that steam prevent metal dusting? It seems to help. Another argument for the role of steam in laboratory tests.

Not I would like to talk about the trends in industry. At present reformers are running with a peak steam-to-carbon ratio of >1 which maybe lowered down to 1. Trends in the future, we are looking at the economic benefits of building an autothermal reactor (ATR) with a peak steam-to-carbon ratio running at 0.6. There are people who think that they can refine the process to run at a peak steam-to-carbon ratio as low as 0.3. So we are moving in that direction. But we still have

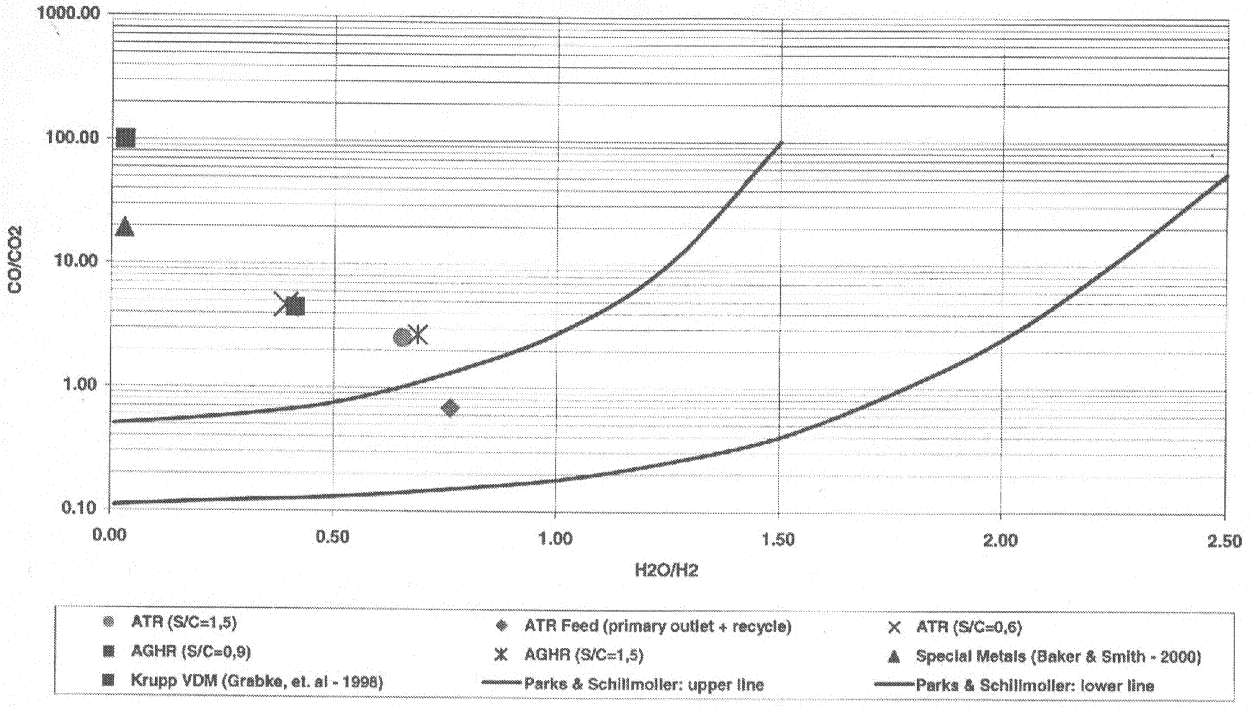

FIGURE 1

different conditions. We have pressures that are higher than this research and we have also gas velocity, even though it might be low, it's still considerably higher than in the laboratory experimental conditions.

Questions and Answers

Question: The presentations are invaluable for the Workshop participants, especially to see what the industry thinks of the research and development on materials to mitigate metal dusting and also the future direction that industry is planning to go in the long run. If one looks at the long term test data presented by industry, it is evident that you can dust any material; you just have to wait for a long time. You might have to wait as long as two years perhaps to dust it. Now, my question to the panelists is, do we have any investigations on the mechanisms which take place after let's say two years which is responsible for this, it's called a breakaway effect or whatever, which spoils the whole story.

Answer: If we know more about this mechanism, I think we can deal with the situation. Perhaps we can develop measures against this kind of breakaway, and perhaps we can really rely on the behavior, and that goes into the direction that we need to deal with to predict the situation, the long-term situation, under these conditions.

Question: If there's not much known about this, the researchers can do some very detailed post-exposure investigation on these long-term-exposed specimens. I understand that the industry might be reluctant in this respect, because they put a lot of money into these tests, and might like to keep this knowledge as their own, but nevertheless this offer from all these scientific laboratories will be useful in order to understand what's going on and really to help the

community in this respect. It is worthwhile to give these specimens to scientists and let them play with them and let them find out what is the actual mechanism.

Answers: It will be interesting to understand if there is a breakaway, when it happens, and what are the conditions that lead to breakaway attack. It is important to know when it starts and people who have analyzed failures rarely relate it to details on the exposure conditions. It is also true that we actually don't know how the material looks after two years of exposure. It is not the same material as in the beginning. We may have changes in the microstructure and in the composition and so on, so I wonder, there might be a way to investigate the development, let's say, of the composition of the subsurface as a function of the exposure time, and also after two years.

In the plant when metal dusting failures occur, the parts are generally removed and new ones are installed. The failed parts are sent for recycling and are rarely analyzed. A postmortem analysis, as we call it, would be very valuable to have the development over time, which is a situation before failure and then, of course, the situation hopefully just right at failure, but we could have lots of them after failure. But I think a key issue, at least for the higher-value material is the oxide scale, and why does it stay intact for two years. That's why we have to find out which are the key parameters that influence the material behavior after two years.

Considering failures in the industry, I think they are mostly caused by some change in conditions or infusion of impurities. And I have also considered several cases. For example, in refineries, the protection by low concentration of sulfur, which is detected up to maybe 600°C, but if the temperature is raised then, maybe only by 25 or 35°C, the protection is lost and the metal dusting can start. Similarly chlorine has been found destroy the protective oxides and can make the alloy susceptible to dusting.

Questions: What is the role of growth stresses on metal dusting degradation?

Answers: I think there are a number of factors that are involved in metal dusting, apart from the composition. Very few studies have explored more deeply into the effects of volume changes because of carburization. We often see materials exhibiting a carburized layer, but only in some areas. The question is, why does that old carburized layer not decompose uniformly? And we do not always find just carburization in the affected areas. We also see very, very perfect spherical regions in the corroded alloys. Why is it so perfectly round? If you look at the alloys, they seem to be a lot more unevenness. The question is, does these spherical areas, perhaps represent some stress relaxation due to composition change? I don't think we have a proper answer for that. I think we need to look a lot more about other types of factors in the material. It's best to look at materials that have not gone through too much degradation.

I think, if I've got your comments correctly, your suggestion is really quite simple. It is just a case of saying, "we don't understand this incubation period, but people are looking at metal dusting on gross effects, they're looking at wastage effects." And what we really need to know, I think, you're saying is that, when does it start? What is it that makes it to start? And, you know, I think on a simplistic way most people probably think it's simple corrosion. I should say it occurs in the metals when the oxide film breaks down. What are the causes for that?

Several points have been raised about these corroded areas. I think they are just caused by the metal dusting starting from one point defect and really spreading radially. And it would certainly be fine to find out what is the reason for the start at this point, but then one must have a continuous observation of the surface from the center, under the metal dusting conditions, really to see where it happens.

I have a great suspicion that the heterogeneities, as I mentioned carbides or nitrides, on the surface are the locations for the start of metal dusting in many cases for some alloys. The study of Rahmel shows that the outgrowth of titanium oxide from a titanium carbide particle on the surface, and it destroys the surface layer. And I have strong suspicions that similar things are happening for Alloy 800, and maybe the reason for it being so susceptible. You know that there are relatively big titanium nitride particles in Alloy 800.

Question: These are questions mainly for the people from industry. One of the things we always talk about is the gas chemistry. We had thermochemical diagrams, oxidation diagrams and things like that. In the industry, I've seen all the plant people who've put in papers, they have a gas chemistry. How do they measure the gas chemistry? Do they measure it at the inlet and/or outlet? Or is it measured at some specific location, by what techniques and how sure you are about the gas chemistry? And how do you measure the steam content? Do you condense the steam and make a mass balance?

Answers: The way we do that, starting at the inlet of the reformers, we know what's going in. Now, in some cases, it's not only methane; sometimes we have refinery gases. So we don't know for sure what the total carbon content is. But in the reformers that use purely steam and methane, we know what's going in. Now, based upon our knowledge of the efficiency of the catalyst and that we do in conjunction with the catalyst vendors, we can calculate what conversion we get at the exit of the reformer.

Now, bear in mind that this catalyst lasts approximately four years or thereabouts, after which time its activity goes down. But when the catalyst is new, we have a real good idea of what comes out of the reformer. This is a calculated number. Coming out of reformers, we're at roughly 1550°F (≈843°C). We then take this gas and quench it to about 600°C in a waste-heat boiler. At that point in time, we can take a sample, that is the basis of the analysis that we're using for the Argonne test program. When we analyze that and compare it to the calculations that we made of the gas coming out of the reformer, it's essentially the same, suggesting that our velocities are so high - and they are very high going through the waste-heat boilers - that we don't change the composition per thermodynamics. That's our position. Now, that changes a little as the activity goes down. So that's how we do it.

We pretty much are in agreement with that. You have to remember that going through this sort of nonequilibrium gas is one of the biggest challenges, and trying to run the laboratory experiment, when you cannot at all get these high-gas velocities you need. You get gas moving a lot more towards equilibrium in a laboratory experiment which you don't necessarily have in a plant and that is a challenge to try and overcome in laboratory experiments.

Question: How do you account for the pressure when you collect, you run the system at say 40 bar, and analyze the gas? Is it by gas chromatograph or some other technique or by mass balance? You're going to collect it at atmospheric pressure, how do you account for the pressure in the gas composition? In other words, does the gas composition change as you reduce the pressure?

Answer: Yes, marginally. I think most of the vendors will now state that in reforming catalysts, modern reforming catalysts, you approach almost equilibrium conditions at the exit of the reformer within a few degrees of equilibrium. And as a first calculation, you may as well just ignore equilibrium approach and say, "If I'm running exit to my primary at 880°C, the gases are in equilibrium at 880°C." It will be at the most a few degrees apart.

Coming out of the secondary reformer or an auto thermal reactor, the gases are so hot that you can almost catalyze it. It's that hot. You would be at equilibrium. When we take samples, often we can get a bit of shifting in the sample line, if it's a high-nickel sample line, and that's easily compensated for. We know the temperature coming out of the reformer, and you know your sample has got an equilibrium temperature on the shift that may be 980°C and you've been reforming at 1000°C. Your gas will be at 1000°C. There's just no question about it. You do the heat and mass balance. You can do a heat and mass balance on the whole plant and accurately tie up the steam that's going in the feed, get that into the secondary, how the shift reactors are working, etc. And the whole thing ties up. There's no doubt we know what the gas composition is, going through these plants.

Question: I was just wondering that, if you do a mass balance, what you are telling me is that you take the amount of carbon, in mass amount of carbon, and put it through the gas phase, and then you look at the carbon that comes out of these, out of the boiler, and you are saying that less than something of 1% of the carbon is deposited on these tubes and things like that? What percent is possible?

Answer: To put some of this into perspective, you've got, say, 1000-ton-a-day ammonia plant. You're putting 5000 tons a day of gas through that waste-heat boiler. Even if you're only making 10 kg a day of carbon, it's part per million of the gas that is reacting to form the carbon going through that boiler. It's significant. And there may be catalytic surfaces available. But there is not enough catalyst available compared to the gas throughput to provide any measurable reaction as you're cooling the gas in the boiler in that sort of device.

In a secondary reformer on that sort of size plant, you've probably 30, 40 cubic meters of catalyst and huge amounts of surface area available to catalysts. There's no way you've got that amount of catalytic material in the waste-heat boilers.

You know, there are instances where people do have steam flow into the waste-heat boiler, and there you occasionally can see a bit of reaction. But it's still small. And it's at the opposite end of the spectrum to the lab tests where you have flow rate of 1 cm/s. We've got 30 m a second in the plant. It's just four to five orders of magnitude different, which is why you see so much reaction.

Question: In these plants, for these components that experience metal dusting problem, what do you expect the lifetime, design lifetime? And how often are you going to shut down for maintenance or inspection? Do you do that periodically? And the second thing is, as a community, whenever you run a plant or are starting up a plant, do you put surveillance specimens? If so are we going to get some samples out periodically to look at?

Answer: Yes, a few answers to that. Typically, in an ammonia plant, you want to run it for four years without any maintenance. A lot of the industry is now pushing out statutory inspections to that period. People are now looking for five years. In terms of lifetime of equipment, you want your waste-heat boiler to last 20+ years without any repair work on it. Yes, lifetime of the plant is actually, you normally design a plant for 20 or 25 years. So that's the theory. That's looking at the internals as well. And typically most waste-heat boilers can achieve that, with the need to occasionally change maybe bypass lines.

In terms of, within that four-year period, nobody wants to shut down, even to take out monitoring samples. You're not going to put samples into a plant and look at them every six months, because that's going to cost three days of production. You're talking millions of dollars, so you can't do that. That's why we're doing the pilot plant, where we can shut it down every three months and take samples. Realistically, in this industry you can't do that. You can get samples, the TNO study has got samples going into a number of plants, but they all come out after long periods of time. And the only time people are willing to shut down more frequently is if it's a big major problem and they need to resolve it to decide what they're going to make as replacement units.

Obviously one of the ways of doing it is to put screening samples in side stream units. yes, people do that, but it's hard. You've got to tap into 1000°C lines, take gas out, cool it, feed it back in. And the samples don't replicate the mechanical stresses and lifetime that the real equipment gets as well. But it's one way of getting it done in industry rather than doing it in labs at real conditions.

There are a lot of commercial interests in a company like ours and are very, very reluctant to give out any results from materials tested. I've had a very, very hard time just being allowed to give some of the alloy producers some feedback on the sort of things that we have expressed here. A little precaution, I had to swear them to secrecy and make sure that that information would not be discussed with any third parties. The information has a lot of economic interest, also there's a lot of competition, especially amongst some gas producers. And I don't think it's an easy task to do.

Question: Just a question, you know, based on what discussions are regarding confidentiality. We have supplied samples and they just don't give us any. Is there that much variation in ammonia production technology or syngas production technology that really it's very advantageous to one company to get technologies that are much different from the other companies? I just want to get a feeling for that. Why is there so much confidentiality in this industry? Is the technology that different, you know?

Answer: I have a client who I spoke to a few months ago, and he was a very happy chap at the time, claiming his plant was making money hand over fist and it was a very good time for them. And his claim was, well, his claim was in part, at least, the reason for their success at that time was that their plant was more reliable. So, yes, this information *is* important.

And I would mirror that. I mean, it's almost frightening to hear Peter Farnell talk about a four-year turnaround cycle, because that's what we do, and we're shooting for five. And it's reliability that we sell. We sell to our customers that our plant's not going to shut down for four or five years. And in the current climate, many of us are dealing with niche markets and highly competitive markets, and that's the edge.

Question: Carbon deposition is the base of a lot of economic problem. There's work to reduce it in the low temperature service. And if carbon doesn't deposit here, that's going to help out from metal dusting standpoint. Is there any work done to try to inoculate the gases, you know, not including sulfur, of course, but to look at something in the gas that could change the kinetics? There has been some work done on the effect of compounds in changing or catalytically enhancing the decomposition of CO. And I was wondering – and a lot of this work was done in direct iron ore reduction, looking at the effects of reducing gases. And my question is, would there be anything to enhance the nonequilibrium, the intermediate compounds that are known such as carbonyls? Are there other intermediates that would forestall or even change the characteristics of the carbon?

Answer: Well, if I may answer, concerning syngas, carbon monoxide, hydrogen, water vapor, carbon dioxide mixtures, the coke deposition or the carbon deposition only occurs if there is a catalytic surface around, and this must usually be a metal surface, and especially very fine particles of iron-nickel, which can catalyze this carbon deposition. If they are not around then there really is no coke deposition. And these particles certainly arise from metal dusting. And as soon as you have metal dusting, the coke deposition increases and you get the coke and you get these reactions and such. That is an important reason for coking.

As has already been noted, we spent a lot of time cleaning the gas, before we even, steam reforming, because the reforming catalysts are finely-divided nickel. So we know what poisons this sort of thing: arsenic, sulfur, lead. Yes, you name it, it's all the sort of materials you don't want to have them, and they get into your cooling system, they're the sort of materials that can attack the metal. And I don't really see anything at the moment that's known to inhibit other than sulfur.

You can put some trace impurity, like the sulfur adsorption, on the surface and block it. And you can do it, but in a syngas plant you'd want a very large cleanup train further down, which is uneconomic.

Question: You hear a lot about Cr equivalent, and one of the speakers also mentioned that, and there are certain formulas published in the literature for Cr equivalent. Do that, formula needs to be modified or something, or how good is it. Just need the panel's opinion on that.

Answer: We are busy with making a new formula, to make it better based on data from, let's say, from laboratory tests and data from practice. So, for instance, in the simple form of it, you only have Cr, Si, and Al. There are other elements in the advanced alloys, which are not really accounted for in the old formula.

Question: Does the refractory afford any protection against metal dusting? The application I'm thinking of is the transition from the manifold to refractory lined transfer line, typical of a syngas plant. It's an academic question, because the thickness at the point where metal dusting might occur is far thicker than required by calculations, but it's just a question that somebody had raised in my company.

Answer: At that stage of the game, the syngas temperatures are generally too high, and metal dusting doesn't occur. There's of course a fundamental problem with refractories in that we apply the refractories on surfaces of metals, usually low alloys that we want to protect. Most of the refractories that we get installed in the plant are permeable to most of the gases, and it can run into an unexpected metal dusting problem on these metal surfaces under the refractories if the metal temperature there is too high.

One uncertainty with refractory design in these plants is that we base thickness of refractories based on values of thermal conductivity measured in air. But now we are exposing that in a syngas plant, which is hydrogen-rich, which is far more conductive. So the values that you normally would use in design, people add quite a bit extra to compensate. And there's no scientific foundation for this. We tried to measure thermal conductivity of alumina refractories in hydrogen environments, and it's extremely difficult and expensive to do. We gave up because it was too expensive. But you add more refractory just to ensure that that metal interface is low enough in temperature not to metal dust.

A lot of people here have been arguing about stagnancy vs. flowing gas and what have you, but it may be that behind the refractory it is *so* stagnant that you get a little bit of metal dusting, which changes the gas composition to a situation which is no longer dusting, and that stagnant area no longer gets flushed out with fresh gas. I would guess that's the sort of thing that happens. Basically, we have an excellent example of this, which was the waste-heat boiler shroud made of 800-H, that Argonne examined. One side, you'd lost 10 mm in a number of years, whereas the backside of it, which is against the refractory, in the same gas environment, but stagnant, no attack. I think velocity is a big issue in propagation of dusting. I heard a big divergence of opinion on that question.

Question: This question is, maybe, for people from industry, because I don't have anything to do with industry. I would like to know, when you build a new plant you, how you select a new material, what are the steps that are most important for choosing this material, in order of importance?

Answer: The first thing we look is how somebody used it previously and whether it has got industrial experience, because nobody wants to be the first to use it. That is the primary consideration in this industry typically, and it's very hard to get beyond that, to get people to accept new things. And then you're into economics, you know; life cycle cost. It may be

expensive up front, but is it going to last the lifetime, or will you accept something cheaper and maintain it. So it tends to be reliability outweighs the upfront capital cost nearly every time in industry. So it's reliability. Will it match the cost? But proof of usage is the first question, always.

It also depends on the complexity of the design. If you have a component that is likely to metal dust, which is relatively simple, like a wall or a plate or a liner, then you're able to accept maintenance and replacement on it. If, on the other hand, if it's a very complicated, spiral-wound heat exchanger, you're not likely to want to do much maintenance on that at all, and you would want to select the optimum material, the best one that is available.

Workshop Summary

K. Natesan

I would like to thank all the speakers, authors, and the attendees for what I think has been a successful and informative proceeding in this workshop. I would also like to thank Charles Sorrell of DOE-OIT and Lee Craig of MTI for their assistance in the organization of this Workshop. Last three days have been a very enlightening experience in that we had a forum in which the researchers, alloy producers, end users, and program sponsors were able to listen to different points of view on the age old problem of metal dusting.

Several papers presented information on the conditions necessary for carbon deposition and/or coking and the need for metal catalyst for continued coking. Several papers discussed the mechanisms for the initiation of metal dusting, but most of them elaborated on pure metals such as iron or nickel whereas the initiation and propagation of metal dusting in complex multicomponent and multiphase alloys may not follow the simple explanations. It is evident that several studies are focused on understanding the behavior of carbon or coke that deposits on metallic materials using sophisticated techniques such as Raman spectroscopy, Infrared spectroscopy, etc. and the role of deposited coke on the initiation process.

Several researchers presented metal dusting data for a variety of alloys in a selected gas mixture, which contained little of no steam. There was significant discussion on the role of gas chemistry in the initiation process and in particular, the importance of steam content in the gas environment on metal dusting. The industry people elaborated on this point and suggested that the laboratory researchers should, as far as possible, simulate the actual reformer environments, which generally contain 25-35% steam. There was very limited information on the role of system pressure on the initiation and propagation of metal dusting, especially on complex alloys. This area needs substantial added effort.

There were a few papers that examined the role of alloying additions in the metal dusting degradation. Silicon and aluminum were identified as beneficial but their effect was not quantified. Several papers were presented on the coatings as a means to minimize the metal dusting attack. But several issues were discussed as the application procedure, specifications, coating integrity, reliability, welding of coated components, etc. The industry people indicated

that coated components were used in specific instances in straight runs in the plants but the cost, reliability, fabrication issues may prohibit their wide usage.

A few papers were presented on the analysis of specific components that have failed by metal dusting in ammonia production systems and in other petrochemical plants. There was consensus from the industry people that the failed components are rarely analyzed in detail and also they generally have inadequate exposure history from the standpoint of temperature, gas chemistry, excursions, etc. The research community felt that the industry should make a strong and proactive effort to secure these failed components and distribute them to various research organizations for detailed analysis. It was felt that such an approach would not only aid focusing the laboratory-oriented research programs but also aid the industry in material selection and in maintaining appropriate operating conditions in plants.

The panel session comprising the panelists' view of the metal dusting research and development and subsequent open forum brought out a lot of issues, some of which are transcribed in this proceedings. Overall, this Workshop met its objectives in setting up a forum for the international participants to discuss the issues, to exchange laboratory-developed and field-generated information, and to possibly develop collaborative approaches to tackle the issues pertaining to metal dusting degradation of metals and alloys.

Author Index

Aas N. 123
Agarwal D. C. 257
Baker B. A. 163
Baumert K. L. 15, 55
Biggs N. 139
Brill U. 257
Cheng H. 15
Chun C. M. 77
Clevenna L. 77
Credson B. J. 269
De Bruyn H. J. 123
Dettenwanger F. 213
Farnell P. W. 269
Grabke H. J. 5, 147, 177, 225
Hertzman S. 109
Hosoya K. 155
Johnson G. L. 55
Kiso T. 155
Klarstrom D. L. 177
Levi T. P. 139
Maroni V. A. 19, 41, 93
McNallan M. 183
Mebrathu T. 55
Minchington I. E. 139
Mochizuki H. 155
Muller-Lorenz E. M. 147, 225
Natesan K. 19, 93, 191, 233
Park Y. S. 183
Pettersson R. 109
Purohit A. 191
Ramanarayanan T. A. 77
Rink D. L. 19, 191, 233
Rosado C. 213
Salot W. J. 191

Schmid B. 123
Schneider A. 225
Schutze M. 213
Smith G. D. 163
Soboroff D. M. 1
Soppet W. K. 19, 233
Sorrell C. 1
Srauss S. 147
Szakalos P. 109
Thomas C. W. 139
Thongtem S. 183
Tomei J. 183
Xiaoping G. 55
Zeng Z. 19, 93, 233

Keyword Index

Alloying Effects, 147, 155, 163
Alonizing, 234
Aluminizing, 215

Boudouard Reaction, 15

Carbon Activity, 21
Carbon Deposition, 27
Carbonyl Formation, 17
Carburization, 249
Catalytic Crystallization, 103
Chemical Industry, 1
Chlorine Effect, 183
ChromePlexing, 234
Chromium Equivalent, 157
Chromizing, 215
CO Disproportionation, 71
Coatings, 213, 233
Corrosion Rate, 84

Failure Analysis, 158, 191

Gas Chemistry, 79, 155
Gas Heated Reforming, 257
Gas Phase Reactions, 20
Gas-metal Reactions, 6
Grinding, 228

Industrial Technologies, 1
Infrared Spectra, 45
Initiation, 36
In-situ Study, 124
Internal Attack, 188
Iron-base Alloys, 26, 147

Kinetics, 5, 183
Low Alloy Steels, 8
Materials Development, 261
Materials of Construction, 2, 257
Mechanisms, 8, 77, 93, 109
Metal Dusting 1, 5, 19, 50, 55, 109, 139, 155, 163, 177, 213, 245, 257
Molecular Spectroscopy, 41

Nickel-base Alloys, 26, 147, 246

Oxidation, 126
Oxide Scale, 228

Pitting Progression, 167
Preoxidation Effect, 239
Pressure Effect, 145
Protection by Sulfur, 226

Raman Spectra, 28
Raman Spectroscopy, 41, 61, 93
Reflectance Spectroscopy, 56

Scanning Electron Microscopy, 96, 110, 123
Siliconizing, 215
Stainless Steel, 109
Steam Carbon Reaction, 15

Theoretical Studies, 15
Thermodynamics, 5, 115, 163

Vision 2020, 2

Wastage Rates, 152, 168, 178, 249
Waste Heat Boiler, 191
Weldment Corrosion, 196
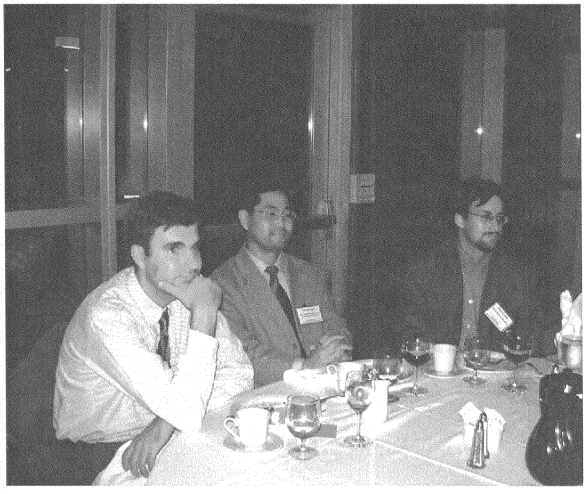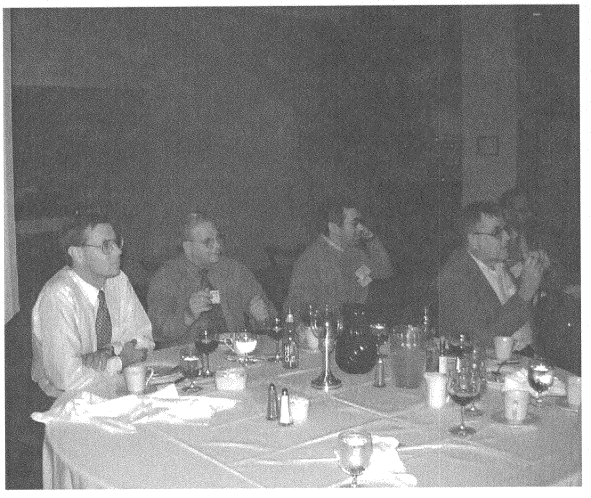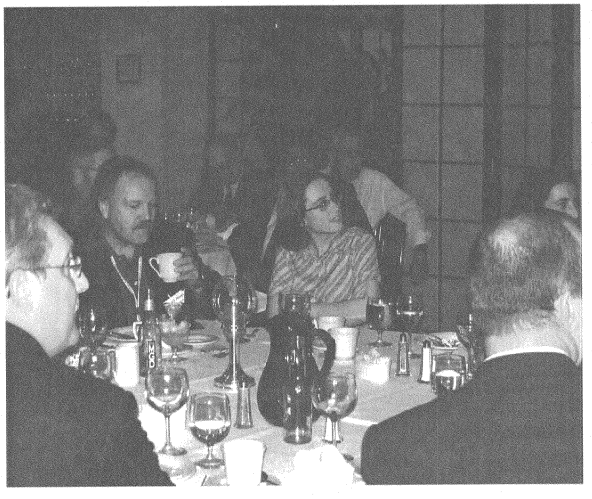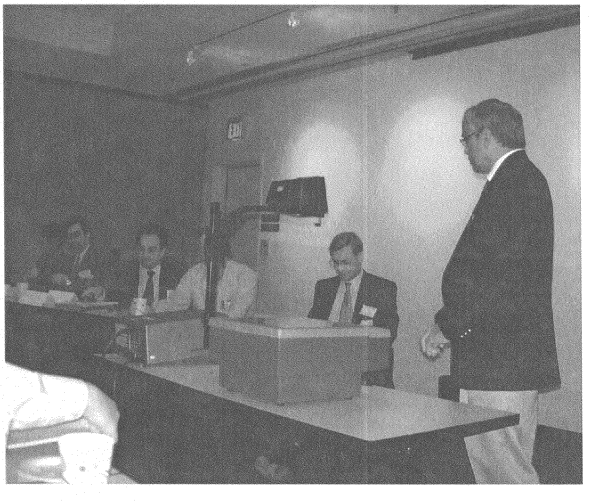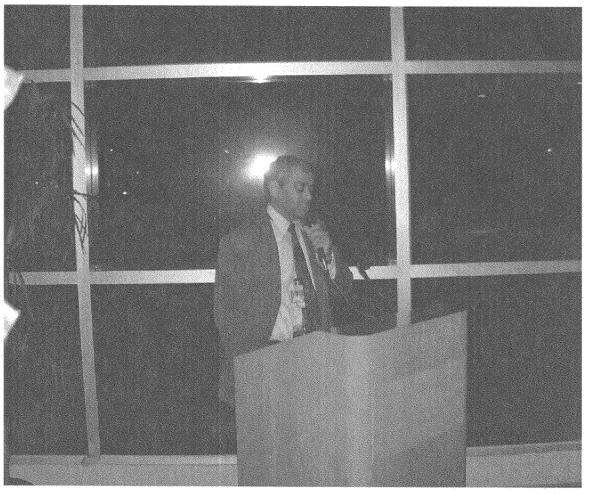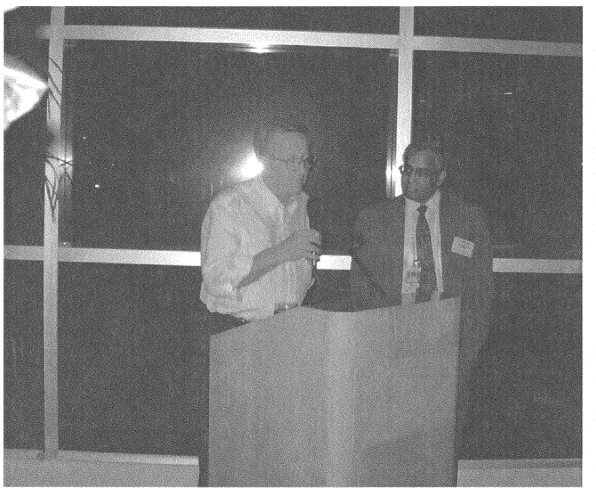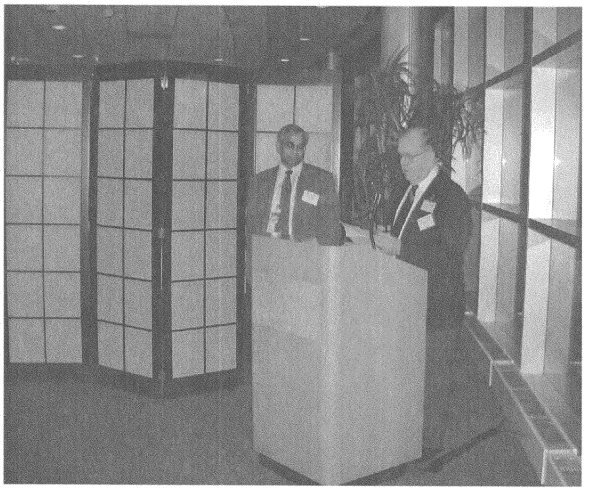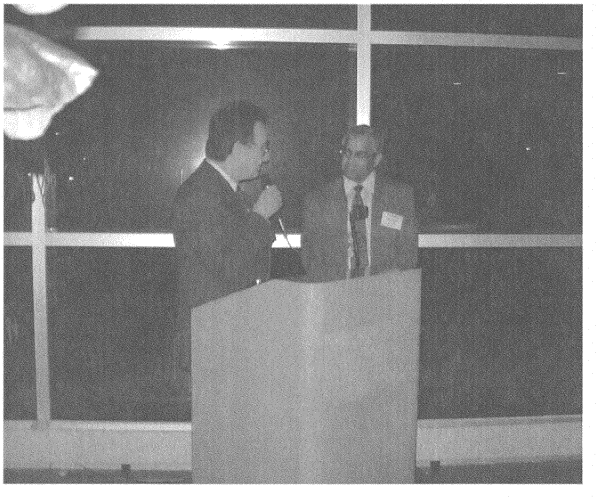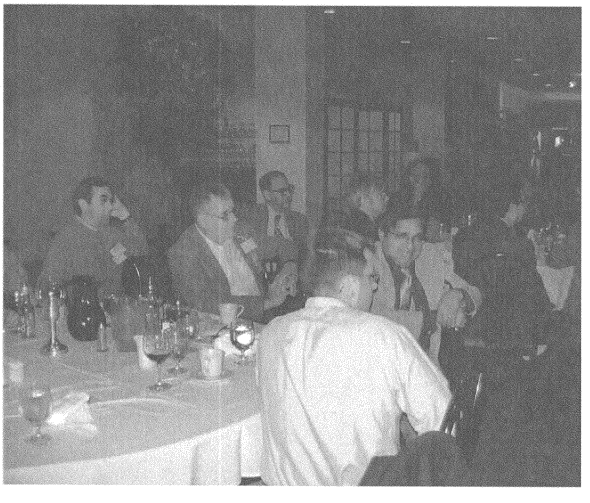
X-ray Diffraction, 93
X-ray Photoelectron Spectroscopy, 58